ELECTRODE EROSION IN HIGH CURRENT, HIGH ENERGY TRANSIENT ARCS

by

ANTHONY LYLE DONALDSON, B.S. in E.E, M.S. in E.E.

A DISSERTATION

IN

ELECTRICAL ENGINEERING

Submitted to the Graduate Faculty
of Texas Tech University in
Partial Fulfillment of
the Requirements for
the Degree of

DOCTOR OF PHILOSOPHY

Approved

Accepted

December, 1990

ACKNOWLEDGEMENTS

I would like to thank Dr. M. Kristiansen for being my Ph.D. advisor and for providing me with the technical support and colleague exposure required for the completion of this work. I would also like to thank Dr. H. Carper, Dr. A. Guenther, Dr. M. Hagler and Dr. C. Whitehead for their helpful criticism and for serving on my Ph.D. committee.

I would also like to thank the following people for various contributions: for lively technical discussions, G. Engel and A. Watson; for help with the various materials tested, J. Koppel and C. Renaud; for the use of the MAX I test facility and results, M. Lehr; for help with the design, construction and testing of the Mark II, V and VI test facilities, E. Kristiansen, D. Garcia, E. Loree, K. Rathbun, L. Stephenson and K. Zinsmeyer; for purchasing and various support activities, C. Burford, G. Igel and D. Reynolds; for drawing the figures, E. Kristiansen; for photography, T. Flores and W. Rains; and for editing and typing portions of the manuscript, M. Byrd, G. Chong, J. Davis, D. Donaldson and C. Spitz. I am especially grateful to D. Srader for the many hours she spent typing much of the initial manuscript, to W. Foong for helping with the viewgraphs and final paper preparation and to D. Garcia for running the majority of the experiments under numerous time constraints. I am also thankful to the following group of excellent undergraduate research

assistants who assisted me with plotting, library research, programming and post experimental analysis of the electrodes: R. Budruk, M. Chandran, R. Conover, A. Darmawirya, M. Engelhardt, W. Foong, L. Heck, G. Jorden, F. Kosari, C. Miller, A. Quarishi, D. Reithmeyer, A. Shaukat, I. Son, H. Tanumihardja, W. Tucker and T. Turner.

I am very thankful for the support and encouragement of my parents Mr. and Mrs. W. Lyle Donaldson and my sisters Susan and Sylvia. I am extremely thankful for my wife Darla, who has prayed, listened and sought to understand the joys and frustrations I experienced during the entire process. Finally, I would like to thank the following members of the Body of Christ who continually supported me in their prayers: S. Adcock, B. Couch, A. Lerner, S. and L. McKinnon, S. and T. Moore, L. and A. Meurer, C. Spitz, M. Stribling-Buskirk, J. Walkup, S. Wootonn, the students at the Wesley Foundation and the Bodybuilders class at Lakeridge UMC. It is to the God of the Lord Jesus Christ Who created me for a purpose and Who I have tried to serve that I dedicate this work.

TABLE OF CONTENTS

ABSTRACT

A review of the experimental and theoretical work performed on understanding electrode erosion in high current transient arcs is given. Over 250 references from the last 40 years are cited, including many recent translations of Russian and German literature. The major mechanisms leading to electrode material melting, vaporization, and removal are identified and discussed as a function of physical and design variables, as well as their effect on electrode erosion rates. A solution to the one-dimensional heat conduction equation, ignoring the effect of electrode joule heating, is discussed and is found to be adequate to explain many experimental results as well as provide a systematic method for classifying different methods used to reduce electrode erosion. Several models which include joule heating due to the skin effect are also evaluated and in both cases rankings of electrode material performance are given. State of the art curves are given for electrode lifetime as a function of charge transfer (0.1 mC to 1 kC per shot) and peak current (1 kA to 1 MA) form the data of 25 different authors.

The author's own experimental results are given for electrode erosion in high current (up to 500 kA), high energy (up to 35 kJ per pulse) transient arcs. Electrode erosion rates were measured for an oscillatory current pulse (100 -250 kHz) as a function of electrode material (over 20

different materials), charge transfer (0.5 to 30 C per shot), peak current (50 to 500 kA), electrode diameter (1.27 to 2.54 cm), gap spacing (0.15 to 2.0 cm), gas type (Air, Ar, He, N_2, SF_6) and gas pressure (0.87 to $3x10^5$ Pa). Scaling laws were derived from the thermal model which agree well with experimental results from several sources. A simple model is also used to predict the minimum in the erosion rate for electrodes composed of two materials.

LIST OF TABLES

LIST OF FIGURES

Figure Page

CHAPTER I

INTRODUCTION

Motivation and Background

For the past few decades there has been and continues to be a considerable interest in the phenomenon associated with electrode erosion resulting from the conduction of high current, high energy arcs [1-9]. Some electric arc applications such as electrical discharge machining [1], mass ablation rockets [2], and plasma erosion devices actually require the occurrence of electrode erosion to achieve certain desired results. However, for a large number of "pulsed power" applications including radar modulators [3], electromagnetic pulse effects simulation, excimer lasers [4], nuclear isotope separation, magnetic field generation, plasma focus devices [5], and particle beam fusion [6], the electric arc takes place in a switching element (typically a "spark gap") and the subsequent electrode erosion is seen as one of, if not the most important, effect limiting the switch, and thus system performance and lifetime.

Although recent advances in other high current switch technologies, namely high power semiconductor devices and back-lit thyratrons (BLT's), have allowed these types of switches to make inroads into the parameter space previously dominated by spark gaps, it appears that for many applications

spark gaps represent the device of choice among users. As recently as 1983, a Tamarron workshop was devoted to assessing the role of the spark gap in high current pulsed power switching applications [7]. Among its conclusions was the fact that the electrode erosion of these devices was not only a key research area but more than likely a rewarding one in terms of the potential for technological advancement. This was primarily due to the recent advent of numerous new materials technologies (both electrode and insulator) and the lack of a unified understanding of the large amount of data already available. Additional Tamarron workshops in 1987 and 1989 discussed in great length the problem of electrode erosion as it related to high current opening switches and arcjet space propulsion technology (albeit for the arcjet at much lower current levels, i.e., 100's of A, but continuous) [8,9]. The opening switch workshop was indicative of the renewed interest in electrode erosion phenomena as a result of the development of electromagnetic launcher technology which often uses the **JxB** induced motion of an electric arc (plasma armature) existing between two electrodes (rails) to accelerate a payload to very high velocities. Although the work reported in this dissertation deals specifically with electrode erosion resulting from stationary arc switching (primarily spark gaps), it will be shown that the models and results can be easily extended to moving arc applications as well. Thus, there remains a considerable interest in understanding the phenomena associated with electrode erosion.

As a result of the importance of electrode erosion in a large number of applications many experiments have been performed to measure erosion rates over a wide range of conditions (see, for example, the references in Chapters 3 and 4, and Appendix A). However, due to the large number and the interdependencies of the parameters affecting electrode erosion, only a limited knowledge of the individual factors listed in Table 1.1 has been obtained. In addition, there has been an apparent lack of awareness in the scientific community of the results of many different experimenters, primarily the work done in the Soviet Union in the 1960's and 1970's. This limited awareness is at least partly due to the unavailability of translations of foreign work, or the lack of easily accessible copies of relevant works. In addition, an urgency is often required in industry and at times research laboratories to develop a specific piece of marketable hardware, of which electrode erosion is only one of several poorly understood phenomena needed for their development. As a result, numerous "apparently" contradictory results have been observed. (I say "apparently" because many of these "discrepancies" can be accounted for with a broader view of the erosion process.) Some of the more obvious "contradictions" are:

1) in comparison with other materials, the erosion of graphite was both the lowest [10-12] as well as the highest [13-15],

Table 1.1 Factors and Specific Parameters Affecting Electrode Erosion

Factor	Parameter		
Pulse:	Waveshape:	Unipolar	(Peak Current, Pulse Length, Risetime, Rate of Rise, Energy)
		Oscillatory	(Frequency, Damping, Peak Current, Charge Transferred)
	Rep-rate:	Single Pulse, Burst or Continuous, Duty Cycle	
Geometry:	Switch:	Exposure to Insulator, Gap Spacing, Volume, Degree of Shock Reflection	
	Electrode:	Mounting, Shape (Hemispherical, Flat, etc.), Size	
Switch Medium*: (Dielectric)	Gas:	Type, Flow Rate and Pattern, Pressure	
Electrode Material Properties:	Thermal:	Conductivity, Density, Heat Capacity, Latent Heats, Melting and Boiling Temperatures	
	Electrical:	Resistivity, Work Function, Permeability	
	Mechanical:	Modulus of Elasticity, Coefficient of Thermal Expansion, Shear Modulus, Poisson's Ratio, Yield Strength, Tensile Strength	
Chemical Compatibility:		Gas-Electrode-Insulator	
External Fields:	Magnetic:	Magnitude, Wave shape (DC, AC, Pulse)	
The One You Forgot!			

*Solid and Liquid Switches are not considered here.

2) numerous dependencies on the pulse parameters have been observed [16-24], and

3) scaling with pressure varies from almost no dependence for some experiments to p^4 for a very narrow range of currents [25].

In addition to the numerous experimental findings, many theoretical models have been developed to explain the erosion process, and several give good agreement with experimental data for a limited set of conditions. The reader is directed to References [26-35] for a review of many of the physical phenomena related to arc-electrode interactions. However, most of the erosion models presented only take into account one or two of what the author considers to be the dominant mechanisms operative under a given set of conditions. In short, various "pieces" of the erosion puzzle are known but the "big picture" remains obscure. Indeed, it appears that much of the literature produced in this country, including the author's earlier work [14], was done in ignorance of at least one major mechanism discussed in detail in the Soviet literature over the last 50 years. Thus, despite a rich history of both theoretical and experimental work there remains a considerable amount of disagreement and uncertainty as to the role and scaling of most of the parameters which affect electrode erosion.

Questions Encountered

During the course of the author's study of electrode erosion numerous questions have been raised at conferences, during private lively discussions, and as a part of the challenge of contract research and consulting obligations. Hearing these questions, and the implied perspectives and assumptions which went into their asking, have proved to be an invaluable aid in guiding the research.

The following is a partial list of the questions which have been posed. It is the author's hope that after having read the discussion of the remainder of this work many of these will have been answered either directly or in a manner which will provide the foundation for the reader to begin to answer them and others which will surface.

Q_1: What is the effect of different variables on electrode erosion?

- pulse parameters
- switch and electrode geometry
- switch medium
- electrode materials and their thermal, electrical, mechanical and chemical properties

Q_2: What variable(s) does the erosion scale with - is it I_p, $\int i dt$, or $\int i^2 dt$?

Q_3: What are the scaling laws for electrode erosion as a function of various pulse parameters?

Q_4: Under what conditions is there a sudden increase in electrode erosion? (e.g., a critical current density?)

Q_5: What is the cause of any sudden increase?

Q_6: How can a sudden increase be avoided?

Q_7: What is the best electrode material?

Q_8: Why is graphite the best material for one set of applications and the worst for another?

Q_9: What about a specific "untried" material? (pyrolytic graphite for example)

Q_{10}: What is the current state of the art?

Q_{11}: What are some methods for reducing the electrode erosion and thus improving the state of the art?

Q_{12}: Did the electrodes melt for the erosion results you are describing?

At times these questions served as a focus for an experimental investigation, while at other times they served to prompt the author to develop a deeper understanding of the overall problem. The saying "a life without reflection is a life without direction and connection"[36] expresses exactly the importance the author found for withdrawing himself from the specifics of the problem in order to place the specifics in their proper context. This was very important because many times the author was tempted to hold onto certain favorite theories, or to address the questions with somewhat pat answers or to assume that the question being asked was the one that needed to be addressed immediately.

Goals and Strategies

Given this background, the goal of this work on high current, high energy, stationary arc electrode erosion was to develop a systematic framework of physical models from which electrode erosion could be described from a physical standpoint and of engineering utility.

It was desired to specifically utilize this framework to:

1. determine the various operating regimes in which each of the various models is likely to be important,
2. determine the detailed role of various variables of interest, including the appropriate scaling relations,
3. clarify the discrepancies of previous experimental results,
4. develop a set of criteria for selecting electrode materials for a given application,
5. design and test "new" state of the art materials, and
6. identify areas for further model development.

In order to achieve these goals the following strategy was followed:

1. perform an exhaustive review of previous electrode erosion work, including obtaining translations of key foreign papers,
2. identify, classify and describe both thermal transport and material removal mechanisms,

3. design and perform experiments which verify the existence of these mechanisms in a particular regime of operation,
4. examine the solutions to the appropriate equations which adequately describe these mechanisms (for example thermal conduction, magnetohydrodynamics, Maxwell's equations, skin effect, etc.),
5. determine the implications of these solutions on the electrode erosion as a function of the engineering variables of interest, and
6. create an extensive database of actual electrode erosion measurements taken under a wide variety of experimental conditions (for example peak current, charge transfer, electrode material, gas pressure, gap spacing, and electrode diameter) to allow for comparison and development of theoretical models.

Scope of the Investigation

Having established the goals and strategies for the study it became important to identify clearly the scope as well. This importance became magnified as it became apparent that the factors and parameters listed in Table 1.1 were related to a plethora of macroscopic physical phenomena, each of which was coupled to the erosion process. These macro-phenomena include the spark gap breakdown and the subsequent arc development, arc-electrode interaction, and dielectric recovery. Just one of the microscopic phenomena, cathode

spots, involved in the understanding of just one of the macro-phenomena, arc-electrode interaction theory, represents a considerable theoretical problem encompassing numerous doctoral dissertations and research efforts extending over a period of a 100 years. Thus, after having identified the various macro-phenomena it became important to decide how they were linked together and the assumptions needed to do this. An initial framework was developed, as shown in Fig. 1.1. Earlier when the goals and strategies were formulated, the author chose to limit his focus to actual thermal and material removal models, keeping in mind that a large number of references related the other macro-phenomena and their models to these as well. This provided the necessary information to determine what variables were needed from non-emphasized phenomena (arc theory for example) in order to describe the inputs of the thermal and material removal models.

In addition to focusing on a few of the more directly related models, it was necessary to select a range of the electrical parameter space. To a large extent this was chosen by the nature of the research funded at the time; namely high energy stationary arc spark gaps. In terms of actual numbers, the majority of the experimental results of this author correspond to peak currents greater than 50 kA and pulse energies greater than 1 kJ. The theoretical results presented in Chapters 2-4 will be shown to extend beyond this range. Comparisons with other experiments and theories outside this

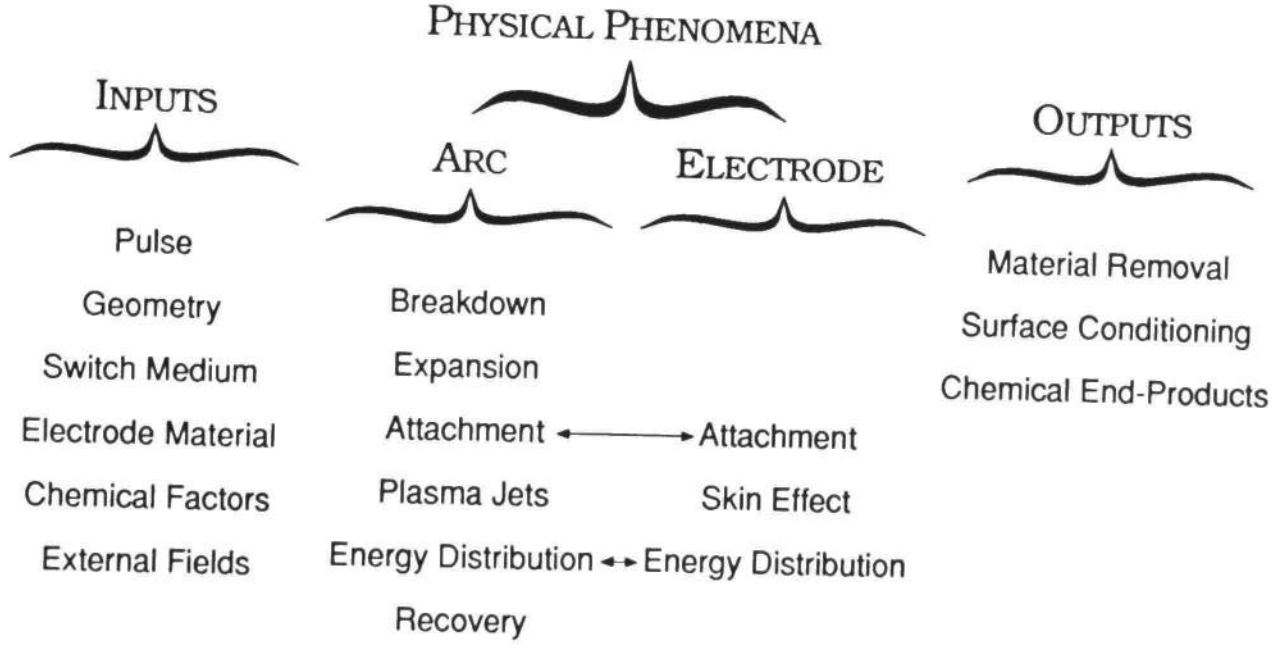

Figure 1.1 Initial Framework: Interrelationship of Various Factors and Models Which Affect Electrode Erosion.

regime are included when they are useful for evaluating the overall processes involved.

Order and Style of Presentation

Chapter 2 contains a review of numerous processes and models for electrode material heating and removal. At the end a "decision tree" for calculating electrode erosion is provided which utilizes most of the models. The decision tree is realized in the form of a series of questions and answers and accompanying flow chart which identify the correct equations needed to calculate the erosion for specific applications. Chapter 3 focuses on one particular erosion mechanism, plasma jet impact heating and ablation, and treats it in detail. A comprehensive review of the literature is again provided in order to acquaint the readers with this very important mechanism which has been overlooked in the United States but which is oftentimes the dominant means of erosion. A large number of the author's own experimental results are given which quite thoroughly substantiate each of the major implications of this mechanism. Chapter 4 presents the author's utilization of some thermal models presented by others to predict electrode erosion parameters of engineering importance. Included are predictions for scaling with pulse parameters, erosion onset conditions as a function of material parameters and pulse conditions, as well as the relative magnitudes of the erosion as a function of materials. For all of these modeling predictions, the author's experimental

results are presented as verification. In addition, the results of other experimentalists, considerably outside the parameter range used by the author, are included to show the scope of the model and its ability to predict the results of numerous experiments. Methods of reducing erosion are also discussed, including the author's own development of a method which led to an order of magnitude reduction in the erosion at high currents.

Numerous appendices are provided to facilitate the chapter discussions. Appendix A is a discussion of the author's investigation of the erosion of over 35 different electrode materials, many of which had never been tested in high current applications. Besides identifying and explaining many aspects of the effect of material on erosion, the author was able to find materials which represent a considerable economic improvement over the current state of the art for a given amount of electrode erosion. In addition, plots of the state of the art for electrode erosion in spark gaps is given which represents a review of over 25 different experimenters' results. Appendix B contains a description of the post experimental calculations and measurement techniques. Appendix C is a paper covering certain specific aspects of chemical erosion which the author presented at the 15th Power Modulator Symposium in 1984. Appendix D is a paper the author co-authored with Dr. Alan Watson concerning this author's experimental verification for Dr. Watson's model of molten material removal. Appendix E presents a derivation for

extending the stationary arc model to moving arc conditions. Appendix F is a short review of various authors' discussion of the importance of joule heating in the electrode. Appendix G and H are the details of the author's derivations for erosion scaling laws and the experimentally observed minimum in composite material electrode erosion as a function of the electrode material composition. Finally, Appendix I presents some miscellaneous experimental results of the author, namely, the effects of gas type, pressure and circuit inductance.

One final note: each chapter is written in a form which makes it complete within itself and suitable, hopefully, for publication. Because the chapters are long, a nomenclature section is provided at the end of each chapter so the reader will not have to find where in the text a variable is first introduced. Additionally, each chapter has its own list of references which include a code, EE#, which corresponds to the author's database of erosion papers.

References

[1] F. van Dijck and R. Snoeys, "A Theoretical and Experimental Study of the Main Parameters Governing the Electro-Discharge Machining Process," *Mechanique*, Num. 301-302, pp. 9-16, 1975. (EE-0832)*

[2] A.L. Donaldson and M. Kristiansen, "An Assessment of Erosion Resistant Cathode Materials with Potential Applications in High Power Electric Propulsion Devices," *AIAA 25th Joint Propulsion Conf.*, Paper # AIAA-89-2515, Monterey, CA, July 10-12, 1989. (EE-1138)

[3] S. Levy, "Spark Gap Erosion Studies," *USAR ELRDL Report # 2454*, U.S. Army Electronics Research and Development Labs, Fort Monmouth, NJ, 1964. (EE-0400)

[4] R.S. Taylor and K.E. Leopold, "UV Radiation-Triggered Rail-Gap Switches," *Rev. of Sci. Instrum.*, vol. 55(1), pp. 52-63, 1984. (EE-1140)

[5] G.R. Neil and R.S. Post, "Multichannel, High Energy Railgap Switch," *Rev. of Sci. Instrum.*, vol. 49(3), pp. 401-403, 1978. (EE-1139)

[6] T.H. Martin, G.W. Barr, J.P. Van Devender, R.A. White and D.L. Johnson, "Pulsed Power Accelerators for Particle Beam Fusion," *IEEE Conf. Record of 14th Pulsed Power Modulator Symposium*, Orlando, FL, pp. 300-304, 1980.

[7] M. Kristiansen and M.O. Hagler, eds., "Proceedings of the US Army Research Office Workshop on Repetitive Spark Gap Operation," Tamarron, CO, Jan. 17-19, 1983. *DTIC No. AD-A132688*.

[8] A. Hyder, E. Clothiaux and M. Kristiansen, "Proceedings of the USAF Workshop on High-Current Opening Switches for EML Application," Tamarron, CO, Mar. 11-13, 1986, published by Space Power Institute, Auburn Univ., Auburn, AL 36849.

[9] M. Kristiansen and L.L. Hatfield, "Proceedings of the Strategic Defense Initiative Organization Workshop on Electrode Erosion in Electric Space Propulsion Engines," Tamarron, CO, March 28-30, 1989, published by Pulsed Power Laboratory, Dept. of Electrical Eng. and Physics/Eng. Physics, Texas Tech Univ., Lubbock, TX 79409-4439.

* EE number refers to the author's annotated bibliography number. It should be included in all correspondence.

[10] A.L. Donaldson, G. Engel and M. Kristiansen, "State-of-the-Art Insulator and Electrode Materials for High Current Switching Applications," *IEEE Trans. on Mag.*, vol. 25, pp. 138-141, 1989.

[11] D. Affinito, E. Bar-Avraham and A. Fisher, "Design and Structures of an Extended Life High Current Sparkgap," *IEEE Trans. on Plasma Science*, vol. PS-7(3), pp. 162-163, 1979. (EE-0785)

[12] G. Marchesi and A. Maschio, "Influence of Electrode Materials on Arc Voltage Waveforms in Pressurized Field Distortion Spark Gaps," *Proceedings of the 5th Int. Conf. on Gas Discharges*, pp. 145-148, Liverpool, UK, 1978. (EE-0860)

[13] K.J. Bickford, K.W. Hanks and W.L. Willis, "Spark Erosion Characteristics of Graphite and CO Gas," *Proceedings of the 15th Power Modulator Symposium*, Baltimore, MD, June 1982. (EE-0783)

[14] A.L. Donaldson, M.O. Hagler, M. Kristiansen, G. Jackson and L.L. Hatfield, "Electrode Erosion Phenomena in a High-Energy Pulsed Discharge," *IEEE Trans. on Plasma Science*, vol. PS-12(1), pp. 28-38, 1984. (EE-0782)

[15] A.L. Donaldson, "Electrode Erosion Measurements in a High Energy Spark Gap," Master's Thesis, Texas Tech University, August, 1982.

[16] J.E. Gruber and R. Suess, "Investigation of the Erosion Phenomenon in High Current, High Pressure Gas Discharges," Institute fur Plasma Physik, Garching bei Munchen, FRG, IPP/4/22, 1969. (EE-0877)

[17] G.M. Goncharenko and Ye. N. Prokhorov, "Erosion of Electrodes Due to Switching of Capacitor-Bank Discharge Circuits," *Trans. of Trudy, Moskovskogo Energeticheskogo Institute, Tekhnika Vysokikh Naprazheniy*, No. 114, Moscow, pp. 86-88, 1972. (EE-0875)

[18] G.S. Belkin and V. Ya. Kiselev, "Influence of Electrode Material on Erosion at High Currents," *Sov. Phys. Tech. Phys.*, vol. 12, pp. 702-703, 1966. (EE-0864)

[19] R. Piejak, H. Wilhelmsen and S.R. Robertson, "Time Resolved Studies of Anode Erosion by High-Current-Density Arcs of Millisecond Duration," *GTE Research Development Report # TR-82-567.2*, August 1982. (EE-0892)

[20] Y. Suzuki, Y. Kawakita, M. Kume and M. Kawai, "A 150-kV, 100-kA Spark Gap Switch for Marx Generators," *Proceedings of the 3rd IEEE Int. Pulsed Power Conf.*, Albuquerque, NM, pp. 444-448, June 1981. (EE-0884)

[21] C. Turner, "Discontinuous Contact Erosion," *Proceedings of the 3rd Int. Research Symp. on Electric Contact Phenomena*, Orono, ME, pp. 309-311, June 1966. (EE-0890)

[22] W.A. Merl and E. Durrwachter, "Concerning Material Losss in Silver Electrodes Caused by Transient Arcing at High Currents in Different Atmospheres," *Proceedings of the 3rd Int. Research Symp. on Electric Contact Phenomena*, Orono, Maine, pp. 259-264, June 1966. (EE-0817)

[23] J. Urbanek, "Mass Loss of Heavy Current Contacts," *Proceedings of the 3rd Int. Research Symp. on Electric Contact Phenomena*, Orono, ME, June 1966. (EE-1096)

[24] M.G. Fey and J. McDonald, "Electrode Erosion in Electric Arc Heaters," *AIChE Symposium Series*, vol. 75(186), pp. 31-37, 1979. (EE-0125)

[25] R.A. Burden and T.E. James, "Statistical Performance Data for a High Current 60 kV Spark Gap Switch," *Proceedings of the 7th Symposium on Fusion Technology*, Grenoble, France, 1972. (EE-0872)

[26] R. Dethlefsen, "Investigation of Electrode Erosion in High Current Arcs," *Aerospace Research Laboratories Report #68-0112*, Wright Patterson AFB, Dayton, OH, 1968. (EE-0908)

[27] T.R. Burkes, M.O. Hagler, M. Kristiansen, J.P. Craig, W.M. Portnoy and E.E. Kunhardt, "A Critical Analysis and Assessment of High Power Switches," *NSWC Report # NP 30/78*, 1978. (EE-0232)

[28] G.V. Butkevich, G.S. Belkin, N.A. Vedeshenkov and M.A. Zhuvoronkov, *Electrical Erosion of High-Current Contacts and Electrodes*, M.:Energy, pp. 1-256, 1978. (EE-1052)

[29] R. Holmes, "Electrode Phenomena," *Chap. 11 in Electrical Breakdown of Gases*, J.M. Meek and J.D. Craggs, eds., John Wiley and Sons, New York, NY, pp. 839-867, 1978. (EE-0081)

[30] P. Predecki, "Investigation of Composite Materials for Repetitive Spark Gap Switch Electrodes," University of Denver, Proposal, 1983. (EE-0906)

[31] G. Ecker, "Electrode Components of the Arc Discharge," *Ergebnisse der Exakten Naturwissenschaften*, vol. 33, pp. 1-104, 1961. (EE-0833)

[32] I.G. Kesaev, "Cathode Processes in Electric Arcs," Nauka Press, Moscow, pp. 1-459, 1968. Translated for Sandia National Labs., Albuquerque, NM, Trans. # Sand 78-601.

[33] V.I. Rakhovskii, "Experimental Study of the Dynamics of Cathode Spots," *IEEE Trans. on Plasma Science*, vol. PS-4(2), pp. 81-102, 1976. (EE-0038)

[34] A.E. Guile, "Arc-Electrode Phenomena," *Proceedings of the IEE, IEE Reviews*, vol. 118(9R), pp. 1131-1154, 1971. (EE-0368)

[35] A.L. Donaldson and M. Kristiansen, "Electrode Erosion Resulting from High Current Arcing," *Proceedings of the First Meeting of the Non-Nuclear Space Power Consortium at Auburn University*, Auburn, AL, Dec. 8-9, 1986.

[36] Steve Moore, Personal Communication, 1988.

CHAPTER II

ELECTRODE EROSION: PROCESSES AND MODELS

This Chapter begins with a listing of the symbols and their definitions. All units are MKSA.

Nomenclature

α_ℓ [m^2/s] - thermal diffusivity of the liquid

$\alpha_{n'}$ [1/s] - modified thermal diffusivity

α_n [$1/^\circ C$] - temperature coefficient of resistivity

α_t [m^2/s] - thermal diffusivity

a_t [$1/^\circ C$] - coefficient of thermal expansion

A_e [m^2] - arc-electrode attachement area

A_m [m^2] - melted area

B [Wb/m^2] - magnetic field density

c [$J/kg^\circ C$] - specific heat

c_ℓ [$J/kg^\circ C$] - specific heat of the liquid

c_{mp} [$J/kg^\circ C$] - specific heat at the melting temperature

C_a [F] - effective gap capacitance

C_t [F] - total system capacitance

δ [m] - skin depth

δ_t - material parameter defined in Eq. (2.22c)

δ_v [m^3/C] - evaporated volume per coulomb

d [m] - distance from the electrode surface to an acoustic interface

d_t [m] - diffusion length

D [m] - geometrical factor used to calculate F_e

D_d [m] - discharge diameter

e [C] - electron charge

η [Ωm] - the electrical resistivity

η_{mp} [Ωm] - the electrical resistivity at the melting temperature

E [N/m^2] - modulus of elasticity

E_a [J] - activation energy

E_m [J] - energy required to melt a material starting at room temperature

EJH - electrode joule heating

Erf - error function

Erfc - the complimentary error function

E_v [J] - energy required to vaporize a material starting at room temperature

f_i - fraction of the total current conducted by the ions

F_e [N] - electromagnetic force at the electrode surface

γ [J/m^2] - surface tension

Γ_{on} - the ratio of the melting and vaporization onset

Γ_{ts} - thermal shock figure of merit

G - shear modulus

h - parameter defined by Eq. (2.22c)

H_s [J] - sublimation energy

I [A] - current

I_p [A] - peak current

I_s [A] - spot current

J [A/m^2] - current density

J_e [A/m^2] - current density in the electrode

J_{eo} [A/m^2] - current density at the electrode surface

J_e [A/m^2] - current density where volume heat source is negligible

J_e^{**} [A/m^2] - current density where the volume and surface heat sources are equal

J_e^{*} [A/m^2] - current density where the evaporation front temperature gradient is zero

J_s [A/m^2] - spot current density

k_1 - a constant which determines the role of the specific heat

k [W/m°K] - thermal conductivity

k_b [J/°K] - Boltzmann constant

k_e - ejection coefficient

k_g - gas dynamic ejection coefficient

k_ℓ - coefficient of liquid removal

k_p - coefficient of particle removal

k_q - fraction of arc generated heat flux which reaches the electrode

k_s - coefficient of solid removal

k_v - coefficient of vapor removal

ℓ [m] - electrode thickness

ℓ_b [m] - distance from the gas bubble center to the electrode surface

ℓ_o [m] - characteristic dimension

L_f [J/m^3] - latent heat of fusion

L_v [J/m^3] - latent heat of vaporization

μ_o [H/m] - magnetic permeability

m_a [kg] - mass ablated

m_a^* - normalized ablated mass

m_i [kg] - ion mass

m_m [kg] - mass melted

m_m^* - normalized melted mass

m_t [kg] - mass melted per spot per pulse

m_v [kg] - mass vaporized

m_v^* - normalized vaporized mass

MLV - model linking variable

M_w - molecular weight

υ - Poisson's ratio

n [kg/m^3] - vapor density

Φ_e [V] - work function of the electrode

p [N/m^2] - vapor pressure

P_p [N/m^2] - plasma pressure at the electrode surface

q [W/m^2] - heat flux

q_c [W/m^2] - conductive heat flux

q_{ch} [W/m^2] - chemical reaction heat flux

q_{cv} [W/m^2] - convective heat flux

q_{ev} [W/m^2] - evaporative heat flux

q_i [W/m^2] - ionic charge

q_j [W/m^2] - plasma jet heat flux

q_m [W/m^2] - magnitude of the heat flux

q_r [W/m^2] - radiative heat flux

q_s [W/m^2] - maximum steady state heat flux

Q [J/m^3] - latent heat per unit volume

Q_e [C] - effective charge transferred

Q_h [J] - thermal energy in the heat flux

r [m] - radial coordinate

r_{bo} [m] - initial gas bubble radius

r_e [m] - electrode radius

r_h [m] - radius of thermal source

r_p [m] - droplet radius

r_s [m] - arc spot radius

R [$J/^\circ C$] - gas constant

R_a [Ω] - arc resistance

R_{ey} - Reynolds number

R_o [Ω] - resistance

ρ [kg/m^3] - electrode density

ρ_g [kg/m^3] - gas density

σ_e [S/m] - electrical conductivity of the electrode

σ_s [N/m^2] - electrode stress

σ_y [N/m^2] - yield strength

τ [s] - time between repetitive pulse initiations

τ_{sw} [s] - time to abrupt drop in conductivity

t [s] - time

t_{eff} [s] - effective evaporation

t_m [s] - time to melt

t_p [s] - pulse time

t_r [s] - resident time of pulse at a given point on the electrode surface

t_t [s] - transition time

T [°K] - temperature

T_b [°K] - boiling temperature

T_e [°K] - electrode temperature

T_{eff} [°K] - an effective melting temperature

T_m [°K] - an effective melting temperature which includes the ambient

T_{max} [°K] - maximum electrode temperature

T_{mp} [°K] - melting temperature

T_o [°K] - ambient or initial temperature

T_s [°C] - spot temperature

u [m/s] - steady state phase front velocity

u_d [m/s] - droplet velocity

u_g [m/s] - gas velocity

u_j [m/s] - jet velocity

u_s [m/s] - velocity of the liquid layer at the gas-liquid boundary

v_e [m^3] - eroded volume

v_i [m/s] - ion velocity

v_l [m^3] - liquid volume

v_o [m/s] - velocity of sound in the electrode

v_p [m/s] - charged particle volume

v_s [m/s] - solid volume

v_v [m/s] - neutral vapor volume

V [V] - voltage

V_{arc} [V] - arc voltage

V_b [V] - breakdown voltage

V_e [V] - voltage drop in front of electrode

V_f [V] - fall voltage

W_a [J] - arc heat energy

W_e [J] - heat energy which is conducted away from the electrode surface

W_{ev} [J] - heat energy which is convected away from the electrode surface

W_e [J] - electrode joule heat energy

W_r [J] - radiated heat energy

W_v [J] - heat energy of vaporization at the electrode surface

x_f - fraction of the total energy which goes into vaporization

z [m] - general coordinate perpendicular to the electrode surface

z_a [m] - depth of ablation

z_f [m] - thickness of film on electrode surface

z_m [m] - depth of melting

z_p [m] - location of the phase front

z_v [m] - depth of vaporization

Introduction

Electrode erosion occurs when electrode material is permanently removed from the electrode surface in one of four forms: charged particles, neutral vapor, liquid or solid. The total volume eroded, v_e, can be expressed as

$$v_e = k_p v_p + k_l v_l + k_v v_v + k_s v_s, \qquad (2.1)$$

where v_p is the charged particle volume, v_v is the neutral vapor volume, v_l is the liquid volume, and v_s is the solid volume. The k's are the coefficients of removal for the various states of matter and may vary from zero, or no removal, to one, or complete removal of all the material in a given state. (Belkin and Kiselev [1] refer to k_l as k_e, or an ejection coefficient.) The material may be removed during or shortly after the applied current pulse. If the molten or vaporized material is removed immediately as it is formed it is said to be removed by ablation. Thus, the erosion process can be thought of as being determined by two sets of mechanisms, namely, those thermal mechanisms which supply energy to the electrode surface and yield the various states of matter from the original solid electrode surface (the v's in Eq. (2.1)) and those material removal mechanisms which determine how much material is actually removed in any given state, (the k's in Eq. (2.1)). The purpose of this chapter is to describe both of these sets of mechanisms. In addition a description is given of a systematic procedure for utilizing the equations for estimating the amount of erosion.

Thermal Mechanisms

Since the onset of electrode erosion usually occurs when enough energy is supplied to the electrode material to invoke a phase change, an important question is: What are the mechanisms responsible for this energy deposition and where do they occur? Figure 2.1 depicts macroscopically the various regions of a typical arc-electrode interaction and Table 2.1 lists the different mechanisms responsible for electrode heating. With the exception of chemical reactions which obtain their energy from the kinetic energy of the individual reactants, all of the energy required for the remainder of the mechanisms can be expressed as the time integrated product of the voltage and the current in the region of interest [2]. Unfortunately, the voltage drop across the arc and the electrodes presents a very difficult measurement problem [3] (not to mention the measurement of the voltage drop in a particular region of the arc). As a result, approximations are often used for the different voltage drops. For example, the voltage drop in region 2 is often assumed to be a constant which is on the order of 10 volts [4]. In general, the voltage will be a function of electrode material, gas type, pressure, gap spacing and current [5], so one needs to realize that these approximations, which usually assume the arc is in a vacuum, are subject to considerable quantitative error.

Joule heating, commonly referred to as I^2R heating, occurs in both the gas (dielectric) and the electrode (conductor). In the electrode the joule heating consists of

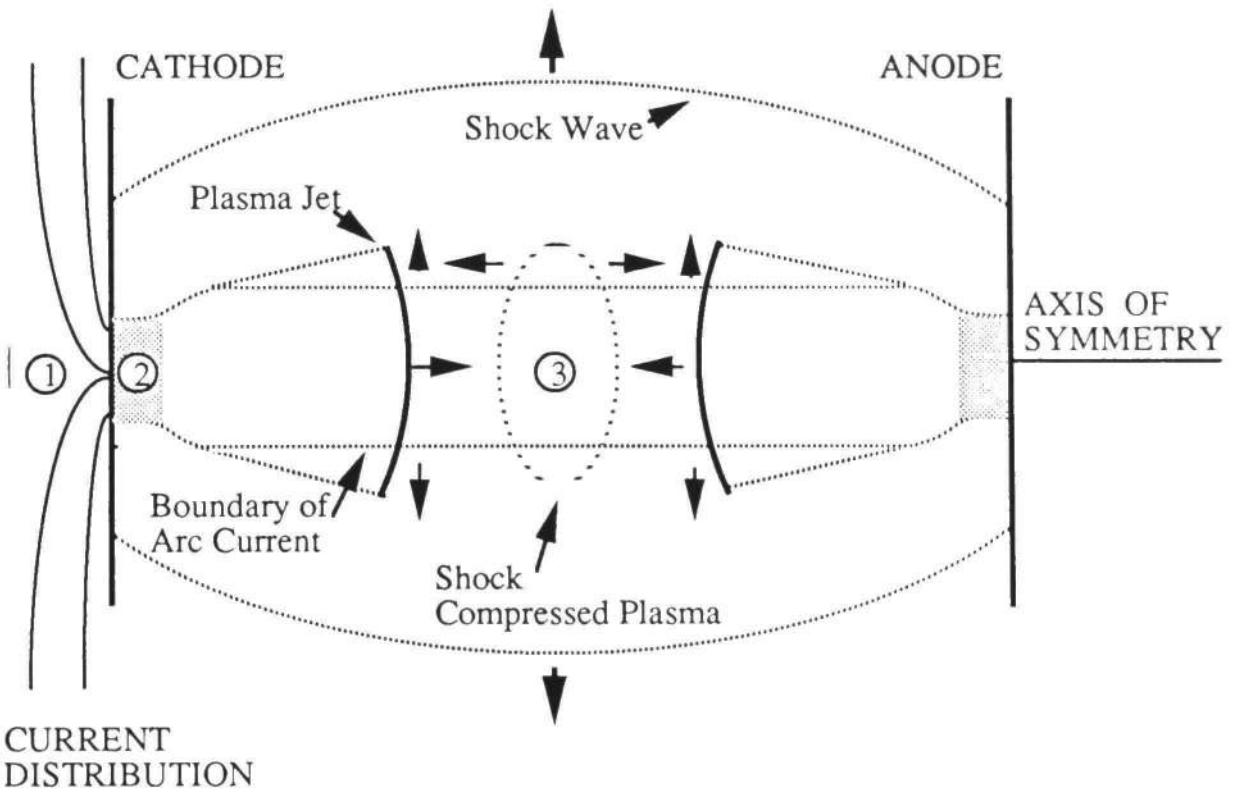

Regions (not to scale)

① Electrode (near the surface)

② Arc Plasma (near the surface)

③ Arc Plasma (center of gap)

Fig. 2.1 Macroscopic Regions of Typical Arc-Electrode Interaction.

Table 2.1 Electrode Heating Mechanisms Due to Arc-Electrode Interaction

Mechanism	Region (see Fig. 2.1)
Joule Heating Within the Electrodes	1
(Enhanced by Local Arc Filamentation and the Skin Effect)	
Joule Heating from the Arc Radiation Turbulent Convection Conduction via Charged Particle Bombardment	2
Plasma Jets (Collective Phenomena Whose Energy is Supplied from the Above Sources)	2, 3
Chemical Attack Exothermic or Endothermic Reactions	2

bulk heating due to the macroscopic current densities ($\leq 5 \times 10^9$ A/m^2) present as well as an effective surface heating which results from the significantly higher microscopic current densities ($\leq 10^{14}$ A/m^2) produced by arc filamentation and in some cases the skin effect. For most materials the joule heating is enhanced further at the electrode surface by the increase in resistivity as a function of temperature when the electrode surface is in either the solid or liquid state. In addition, joule heating in the arc results in thermal energy being delivered to the electrode surface via each of the following mechanisms: radiation, convection and charged particle bombardment.

Plasma jets also comprise a major source of electrode heating in many situations [6]. Plasma jets are high speed ($\sim 10^4$ m/s) directed streams of partially ionized electrode vapor produced in the space adjacent to the electrode surfaces. The individual points of filament attachment at the electrode surface each act as a source of a plasma jet and the effect of all the individual jets can combine hydrodynamically to form one jet [7]. In addition, regions of compression and rarefaction in the plasma between the electrodes (produced by the interaction of the sporadic emission of cathode and anode jets) move back and forth between the electrodes and their "contact" with the electrodes is as likely to be an important a factor on electrode erosion as the initial jet impact [8]. The author's recent experiments which have documented both the existence of these jets and their effect on electrode erosion

in high energy spark gaps are discussed in detail in Chapter 3.

Chemical reactions occurring at the electrode surface can also be a major source of erosion as indicated by preferential erosion of certain electrode constituents [9] and Appendix C, as well as the occurrence of highly altered damage patterns produced when chemically active by-products of the gas and insulator are present [10]. Chemical reactions are known to modify the existing surface material properties in such a way as to alter the resistance of the material to thermal loading. The reaction rates are often very sensitive to the surface temperature as evidenced by the Arrhenius equation

$$k_r = Ae^{-E_a/RT}, \tag{2.2}$$

where k_r is the reaction rate, A is a proportionality constant, E_a is the activation energy and R is the gas constant. Thus, if the reaction is exothermic, a considerable increase in the localized surface heat flux may occur. In addition, for some materials such as Mo or W, oxide layers have a much higher vapor pressure than the metal and even small amounts of oxygen impurities may dramatically increase the evaporation yield [11]. Metallic compounds produced at the electrode surface during arcing in certain background gas combinations have also led to extremely rapid changes in arc velocity and subsequent electrode erosion rates [12]. Thus, electrode-gas chemistry may play an important role in the

electrode erosion but unfortunately most of the experimental results to date have been qualitative in nature.

The role of each of these thermal mechanisms can probably best be described by examining the solution to the heat conduction equation near the electrode surface. Although numerical solutions have been obtained for two dimensional axisymmetric problems [13], the one dimensional equation given below by Eq. (2.3) accurately describes the temperature rise in the electrodes when c and k are considered homogeneous and temperature independent and when the depth of melting is small compared with the radial extent of the melt zone. Thus,

$$\rho c \frac{\partial T(z,t)}{\partial t} = k \frac{\partial^2 T(z,t)}{\partial z^2} + \frac{J_e^2(z,t)}{\sigma_e}, \qquad (2.3)$$

where ρ is the material density, k is the thermal conductivity, c is the specific heat, σ_e is the electrical conductivity, T is the temperature, J_e is the electrode current density, and z is the axial direction perpendicular to the electrode surface. The assumption on c and k has been shown to generate less than a 20% error in the electrode temperature when the material properties c and k are evaluated at half the melting temperature [14]. The criteria for the depth of melting can be expressed as a condition on the diffusion length [13,15], namely,

$$r_h \geq 4 d_t = 4 (k t_p / \rho c)^{1/2}, \qquad (2.4)$$

where r_h is the radius of the heated region of the electrode and d_t is the diffusion length. Furthermore, the electrodes may be considered infinite in the z direction for electrode thicknesses greater than four times d_t [15]. For the materials and time scales encountered in the experiments mentioned in this study these criteria are easily satisfied.

By conservation of heat flux at the electrode surface, Eq. (2.3) is subject to the boundary condition

$$-k \frac{\partial T(0,t)}{\partial z} = q(t) \qquad (2.4a)$$

at the electrode surface before it melts, and

$$-k \frac{\partial T(z_p(t),t)}{\partial z} = q(t) - Q\, dz_p/dt \qquad (2.4b)$$

at the phase interface $z = z_p$. Here Q is the latent heat energy per unit volume for the particular phase and q(t) is the net heat flux entering the electrode surface from all sources, namely

$$q(t) = q_{ch} + q_j + q_c + q_{cv} + q_r - q_{ev} \qquad (2.4c)$$

where q_{ch}, q_j, q_c, q_{cv}, q_r and q_{ev} are the heat fluxes produced at the surface due to chemical reaction (exothermic or endothermic), plasma jet-electrode interaction, conduction by charged particle bombardment, convection, radiation and the net loss due to evaporation, respectively. Although the quantitative modeling of each term of the heat flux is unlikely, the significance of Eqs. (2.3) and (2.4a) is that,

with the exception of the electrode joule heating which appears as a volume source, all of the other thermal mechanisms can affect the solution in a similar manner, namely through an equivalent surface heat source. Thus, q(t) can be given by

$$q(t) = q_{ch}(T_s) + k_q V_{arc}(t) i(t) / A_e(t) - q_{ev}(T_s), \qquad (2.4d)$$

where k_q is the fraction of the total electrically produced heat flux which is received by the electrode surface, V_{arc} is the arc voltage, and $A_e(t)$ is the effective area over which the heat flux acts. Thus, solutions to this equation are direct functions of q(t) and any attempt to understand the erosion should relate the parameters of interest to those parameters which determine the heat flux.

To summarize our understanding at this point, consider Fig. 2.2. Utilizing the general model areas identified in Fig. 1.1 one can see that viewing the erosion problem from a thermal energy perspective has helped to identify specific model linking variables (MLV's) which are the keys to understanding the problem. For example, the solution to the heat conduction problem is basically a function of the heat flux, surface materials properties and the electrode current density. Likewise, the heat flux is determined by the degree of shielding or redistribution of the arc energy with respect to the electrode surface, the arc voltage and current, the area of heat flux interaction with the electrode surface and

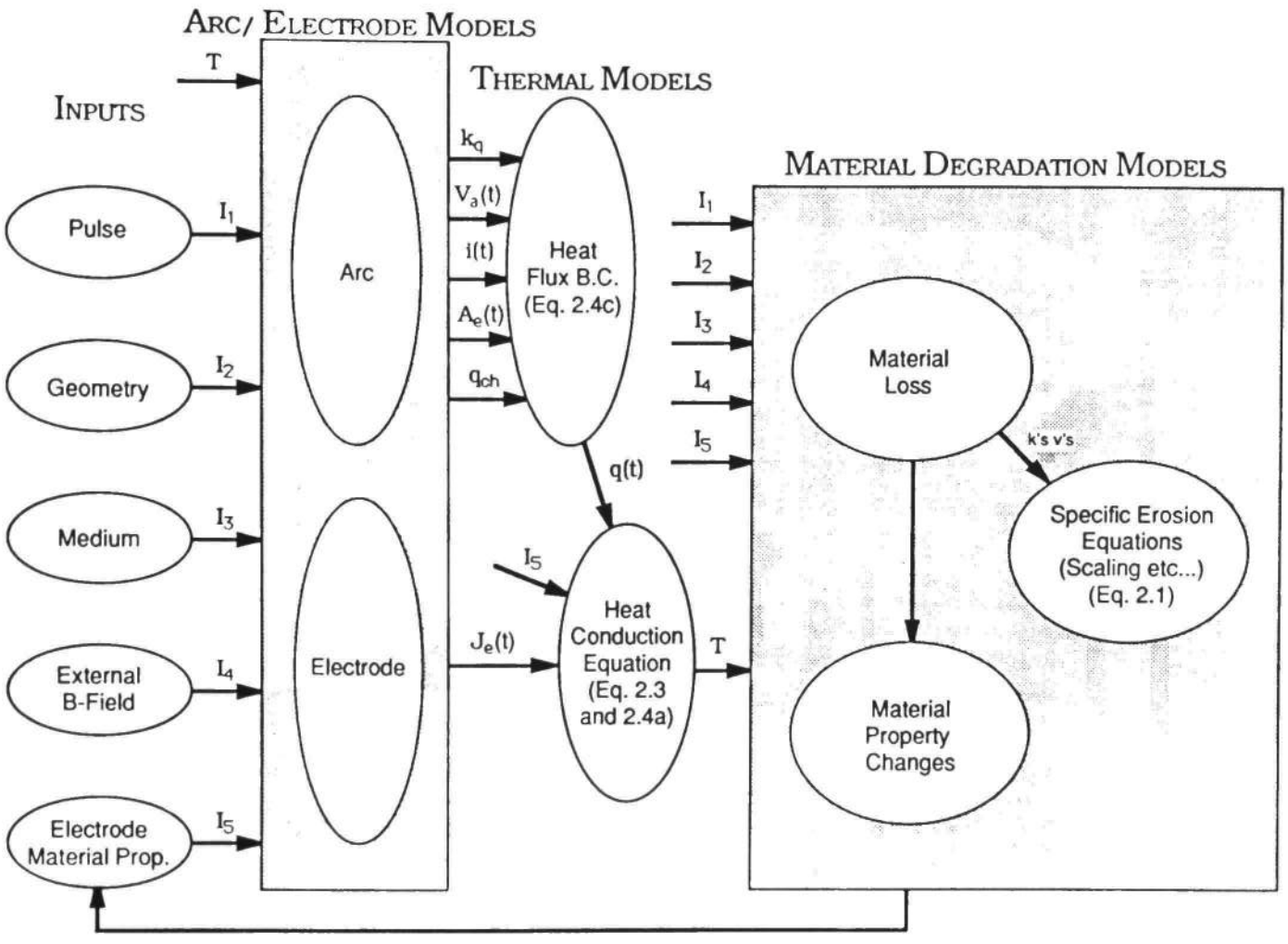

Fig. 2.2 Relationship Between the Various Models Used to Describe the Electrode Erosion Process.

the chemically induced heat flux. At each step in the erosion analysis one can make assumptions on these variables in order to obtain a general understanding of their effect on the overall solution. For example, assuming that the heat flux is given, then the solution to the thermal model may be studied as a function of the heat flux and later the effect of individual variables on the heat flux may be taken into account. One can only hope at this point that this approach may lead to some approximate solutions for the erosion. (In fact it turns out it does!) The next section of this chapter will be devoted to discussing the previously obtained solutions to the thermal model and how they are coupled to the process of material removal.

Thermal Modeling

Many solutions exist for Eq. (2.3), and the more general 3-D heat conduction equation with temperature dependent material properties, depending upon which assumptions are made for the form of $q(t)$, $J_e(t)$, etc. A rather exhaustive review of the literature is given in Ref. [16], and the literature cited there, which encompasses a variety of physical applications including laser and e-beam treatment of materials and reentry ablation, to name a few. Solutions are given in the form of infinite series expansions using various generating functions along with the appropriate recursion relations. These solutions compare nicely with numerical results but in either case it is extremely difficult to

manipulate these solutions to determine scaling laws and other important erosion properties. If necessary, however, one could use these solutions in a "brute force" approach to solve the electrode erosion problem for a given set of conditions. However, the solutions themselves are only as accurate as the approximations made on the MLV's, q(t) for example, so perhaps analytical solutions obtained with various approximations will prove more useful and just as accurate in predicting scaling laws, etc. (In fact they are, as will be shown in Chapter 4.) A review of a large amount of the various analytical approaches which specifically relate to the arc-electrode erosion problem are discussed by Butkevich et al. [17]. The investigations reviewed are primarily Soviet because it appears that they did most of the initial work in the 1960's and 1970's, at least as it relates to arc erosion of contacts and electrodes. The work by Butkevich et al. [17], was written in 1976 but first obtained by the author in 1988. An attempt is made to summarize the most important results of this fairly lengthy document as well as other key papers but the reader is referred to the original works referenced by Butkevich and others when more details are required. It should be noted that many of the papers cited by Butkevich, namely those authored by Belkin, were the ones this author used as early as 1986 to understand much of the thermal nature of the erosion problem prior to obtaining Butkevich's document in 1988.

The solutions given by Belkin [1,18-20], Zingerman [21], Cramer and Roman [15], Raezer [29], Zolotykh [30], Dixon et al. [22], Zien [23], Goloveiko [24] and Watson [25] which are applicable to high current, high energy, transient arcs are discussed below. The solutions given by Belkin consider both a heat flux of constant magnitude, q_m, and pulse duration, t_p, and a time varying heat flux, q(t). In both cases electrode joule heating is ignored. Being a very simple model it is indeed fortunate that the solution is adequate enough to explain a large amount of experimental data. In addition, the solutions provide an excellent framework for evaluating the effect of a particular parameter on electrode erosion. Chapter 4 will be devoted to the reformulation and extension of Belkin's solution to predict erosion parameters of engineering importance, but for now a brief description of the more important aspects of the solution will suffice.

Zingerman [21] solves, analytically, several cases including the melting and the ablation case for a circular heat source. (Belkin assumed a planar heat source.) Cramer and Roman justify the use of the 1-D approximation with negligible electrode joule heating for the evaluation of five known solutions which have different boundary conditions in order to determine the optimum electrode cooling design. Raezer [29] presents the solution to the rep-rated heat flux boundary condition. Zolotykh [30] discusses the solution for an electrode with a different surface layer than the bulk material and finds the criteria whereby the bulk electrode is

not damaged. Dixon et al. [22] solves numerically the case of ablation and melting for a planar heat source. Zien [23] gives a very accurate analytical solution to the ablation problem for time varying heat fluxes of the form $q(t) \sim t^m$ and $q(t) \sim e^t$. All of the solutions mentioned up to this point ignore electrode joule heating.

Goloveiko [24] solves essentially the same case as Belkin but includes the effect of electrode joule heating. A time for transition into the steady state is derived along with a steady state criterion for the critical current densities of which electrode joule heating can be ignored or can become dominant. Watson solves the case where joule heating in the electrode is dominant and includes the effect of fluid motion driven by the **J** x **B** forces acting on the molten metal.

Belkin and Kiselev's Solution

Initially, in 1966, Belkin and Kiselev [1] solved Eq. (2.3) for an arbitrary heat flux, q(t), with negligible electrode joule heating (EJH), by use of an approximation which is very accurate for cases where the depth of melt, z_m, satisfies the condition

$$z_m \leq 0.3 d_t. \tag{2.5}$$

It was shown that this condition is satisfied for problems where the electrode surface temperature is close to the melting point, which is certainly true in high current, high energy arcs. The solution for z_m is given by

$$z_m(t) = (3\rho c T_{mp})^{-1} \int_0^t q(t)\,dt. \qquad (2.6)$$

For the case where q(t) is approximated by

$$q(t) = J_a\, V_{arc}\, [U(t) - U(t-t_p)], \qquad (2.7)$$

and where U(t) is the unit step function, the mass melted, m_m, is given by the equation

$$m_m = V_{arc}\, Q_e / 3 c T_{mp}, \qquad (2.8a)$$

where Q_e is the effective charge transferred (defined as the integral over time of the absolute value of the current). Later Belkin and Kiselev [1] gave a similar expression for the mass melted from an instantaneous heat source, namely

$$m_m = V_{arc} Q_e / 2.07 c T_{mp}. \qquad (2.8b)$$

Belkin's Solution

Belkin [18] also solved numerically the case of a constant heat flux with magnitude, q_m, and pulse width, t_p, which is valid over a wider range of heat fluxes and pulse times than the earlier model because the effect of vaporization is directly accounted for. His results are in good agreement with a large number of experimental results. Belkin's solution, shown in Fig. 2.3, gives the "normalized" amount of melted metal

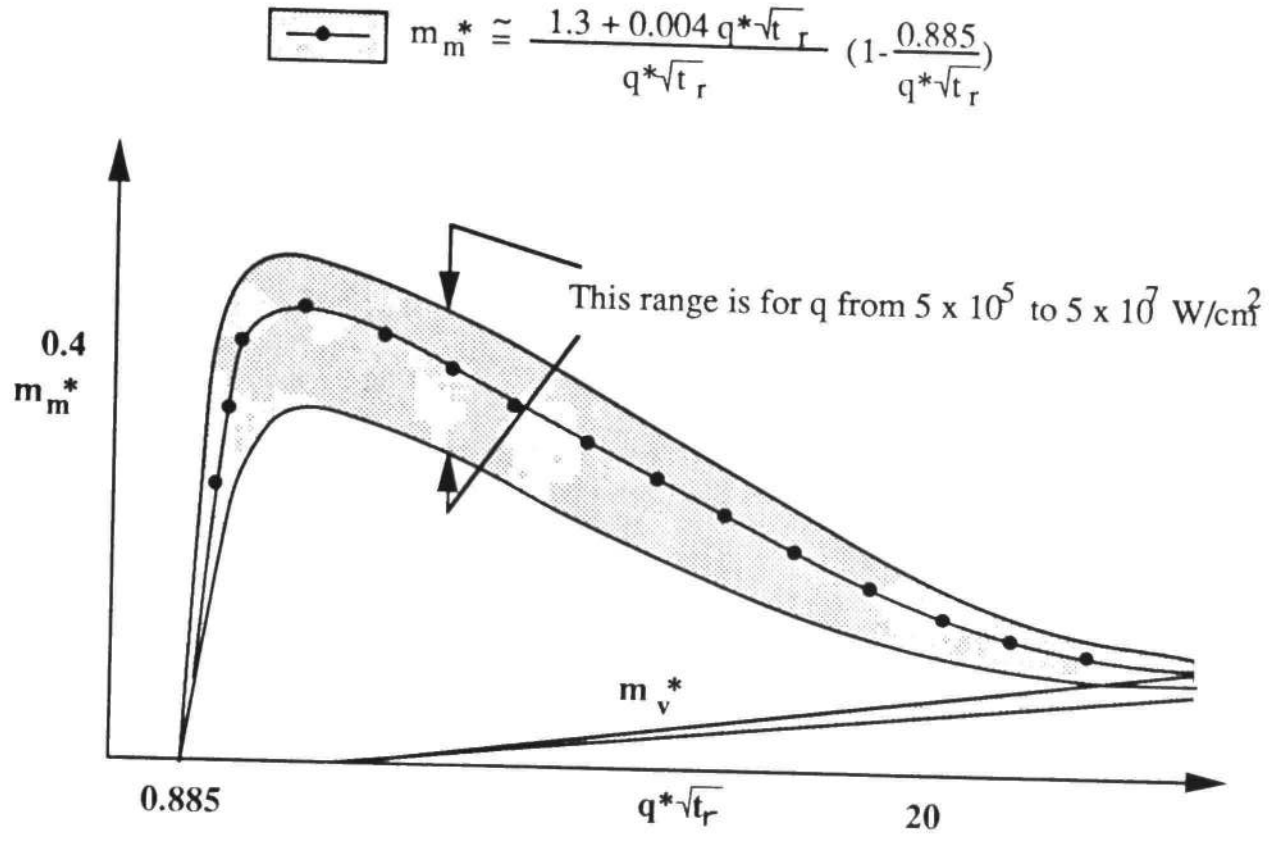

Fig. 2.3 Belkin's Solution [18] for the Electrode Erosion as a Function of Pulse and Material Parameters.

$$m_m^* = m_m/(Q_h/cT_{eff}), \tag{2.9a}$$

and vaporized metal

$$m_v^* = m_v/(Q_h/cT_{eff}), \tag{2.9b}$$

as a function of the quantity

$$q^*(t_r)^{1/2} = q_m(t_r)^{1/2}/(T_{eff}(k\rho c)^{1/2}. \tag{2.10}$$

The quantity, Q_h, is the available energy in the heat flux,

$$Q_h = \int_o^{t_r} q(t)A_e(t)\,dt, \tag{2.11}$$

and T_{eff} is the effective temperature rise,

$$T_{eff} = T_{mp} - T_o, \tag{2.12}$$

where T_{mp} is the melting temperature, T_o is the initial electrode temperature when the heat flux is applied and t_r is the resident time of the pulse (which is equal to the pulse width, t_p, for a stationary arc).

Belkin chose the variable $q^*(t_r)^{1/2}$ because the mass, m_m^*, varies only slightly for a constant $q^*(t_r)^{1/2}$ over a broad range of heat fluxes (from 5×10^5 to 5×10^7 W/cm^2) so that all values of m_m^* lie between two lines (the shaded region). The value of m_m^* is approximated by

$$m_m^* = (1.3 + b(cT_{mp}/(L_v+c_lT_b)))(1 - 0.885/b)/b, \tag{2.13}$$

where $b = q^*(t_r)^{1/2}$, and L_v, c_l, and T_b are the latent heat of vaporization, the specific heat of the liquid metal and the

boiling point, respectively. The value of the m_v^* can also be approximated by

$$m_v^* = cT_{mp}/(L_v + c_l T_b) \qquad (2.14a)$$

for $q^*(t_r)^{1/2} > 50$, and by

$$m_v^* = (cT_{mp}/L_v)(1-3m_m^*) \qquad (2.14b)$$

for $q^*(t_r)^{1/2} \leq 50$.

The existence of a maximum in the dependence of m_m^* on $q^*(t_r)^{1/2}$ was explained as follows: at low $q^*(t_r)^{1/2}$ the metal is heated to the melting temperature at shallow depths and the heat is transported deeper into the metal by thermal conduction. For large $q^*(t_r)^{1/2}$, which corresponds to the heat source being nearly instantaneous, there is intense vaporization near the surface; the larger $q^*(t_r)^{1/2}$, the greater the fraction of both the deposited energy that is removed, and the molten mass which is evaporated. For $q^*(t_r)^{1/2} > 20$ essentially all of the energy goes into vaporization.

The implications of the results from this thermal model (valid for regions where electrode joule heating can be ignored) are as follows:

1. The sudden onset and rapid increase in the amount of molten mass for values of $q^*(t_r)^{1/2}$ between 0.886 and 2 predicts the existence of and may determine the location of the experimentally observed transition region (for example, Belkin and Kiselev [21]) in the erosion rate. The location of the

transition region predicted by this model is given by

$$q(t_r)^{1/2}/T_{eff}(k\rho c)^{1/2}) = (\pi/4)^{1/2} \qquad (2.15)$$

which is a function of three parameters--the heat flux, q, what the authors has defined elsewhere [38] as the melting "impulsivity" of the material, $T_{eff}(k\rho c)^{1/2}$, and the resident time of the pulse, t_r.

2. The model provides in one picture a means for determining the role of each variable of interest since all engineering variables appear in the expressions for the onset condition given above, the total energy, Q_h, and/or another material parameter, cT_{eff}. For example, the gas pressure affects q through the effective area, $A_e(t)$, of the arc-electrode interaction [1]. The higher the pressure the smaller the area and thus the larger q(t). Likewise, rep-rate primarily affects the solution through the variable, T_{eff}, since the initial electrode temperature, T_o, is actually a function of time and increases with increasing rep-rate.

3. The model readily lends itself to classifying the various methods of reducing the amount of molten electrode material into three categories:

   a. choosing materials with high cT_{mp}, L_v, and $(T_{mp}(k\rho c)^{1/2})$ (for a ranking see Chapter 4),

b. reducing or uniformly distributing the heat flux, q, and

c. reducing the residence time of the heat flux, t_r.

Zingerman's Solutions

Zingerman [21] solves Eq. (2.3) for the following cases, after showing that in most cases the electrode joule heating term is negligible.

Case #1: the surface melts but remains until it is removed at the end of the current pulse (by one of several mechanisms),

Case #2: the surface melts but is continuously removed (ablation),

Case #3: the surface melts and vaporizes in a very short period of time (explosive vaporization)

For the first case solutions were found for each of the following boundary conditions:

a) a time varying uniform circular heat flux of radius r_o,

b) a time varying uniform heat flux of infinite extent, and

c) the electrode surface temperature is a constant.

The amount of error was determined for each of the following assumptions:

1) assuming boundary condition b) instead of a),

2) whether or not the latent heat is included, and

3) the assumption that the material properties in the molten liquid can be approximated by the properties at the melting temperature.

In general it was found that:

1) when r_o is greater than three times the diffusion length, d_t, and the depth at which the temperature is to be found, then Case 1b), which has a much simpler solution than Case 1a), is quite accurate,

2) the latent heat of fusion, L_f, may be accounted for by assuming an "effective" melting temperature given by the equation

$$T_m = T_{eff} + k_1 L_f / c, \qquad (2.16)$$

where k_1 is a constant which is a function of the surface temperature and the thermophysical properties of the material but in general is within the range 0.4-0.6. (Note: In previous papers [38], I had taken into account the latent heat using the above equation with $k_1 = 1$, being unaware of Zingerman's solution. After examining Ref. [28] is was apparent that my assumption was in effect an upper limit on the effect of L_f.)

3) the relative error for choosing the properties of the liquid at the melting temperature is very small.

The melting depth, $z_m(t)$, for Case 1a) can be found numerically from the following:

$$2T_{mp}(\pi k\rho c)^{1/2} = \tag{2.17a}$$

$$\left[\int_0^t q(t)\ (t-\tau)^{-1/2} e^{-z_m^2/(4\alpha_t(t-\tau))}\,d\tau - \int_0^t q(t)\ (t-\tau)^{-1/2} e^{-(z_m^2+r_o^2)/(\alpha_t(t-\tau))}\,d\tau\right]$$

For Case 1b), the source is considered infinite, and the second term in Eq. (2.17a) goes to zero, therefore

$$2T_{mp}(\pi k\rho c)^{1/2} = \int_0^t q(t)\ (t-\tau)^{-1/2} e^{(-z_m^2/(4\alpha_t(t-\tau)))}\,d\tau \tag{2.17b}$$

When the heat flux source, q(t), is a constant, equal to q_m, then Eq. (2.17b) can be rewritten as

$$2T_{mp}(\rho_\ell c_\ell k_\ell)^{1/2}/(q_m t^{1/2}) = \int_0^1 (1-y)^{-1/2} e^{n/(y-1)}\,dy, \tag{2.17c}$$

where

$$n = z_m^2(t)/4t\alpha_t. \tag{2.17d}$$

For Case 1c), a constant electrode surface temperature, T_s, the depth of melt, $z_m(t)$, is given by the numerical solution to

$$T_{mp} = T_s[1-Erf(z_m/(2(\alpha_t t)^{1/2}))]. \tag{2.17e}$$

Case 2 was solved for a constant heat flux. The depth of removed molten material is given by

$$z_a(t) = (q_m/(\rho(cT_m + L_f))(t-(t_m/2)(1-\int_0^1 e^{(n/(y-1))}dy)), \qquad (2.18a)$$

where t_m is the time to melting given by

$$t_m = \pi\rho ckT_{mp}^2/q_m^2, \qquad (2.18b)$$

and

$$n = r_o^2/t_m\alpha_t. \qquad (2.18c)$$

Analysis of Eqs. (2.6), (2.17) and (2.18) indicated that the depth of melting, $z_a(t)$, for the ablation case is several times greater than $z_m(t)$ for the melting case.

For Case #3 the following expressions were derived for the onset of explosive vaporization and the depth of material removed as a function of time:

$$q_m \geq 1.8(E_v\rho)(\alpha_t)^{1/2}/(t_r)^{1/2}, \qquad (2.19a)$$

where E_v, the heat energy in the vapor, is given by

$$E_v = L_v + c_t(T_v - T_{mp}) + L_f + c(T_{mp}-T_o), \qquad (2.19b)$$

and z_v, the depth of vaporization is given by

$$z_v(t) = q_m t/\rho E_v. \qquad (2.19c)$$

This result represents an upper limit on the time to vaporization because it was assumed that all the metal within a certain "closed" volume was uniformly heated until it vaporized. In reality, the temperature distribution is uneven (the surface is heated faster) and part of the metal will be vaporized while the rest is still molten. The onset condition

can be compared with the melting onset condition in Eq. (2.15). The ratio of the two onset conditions is given by

$$\Gamma_{on} = 1.8(\alpha_\ell/\alpha_t)^{1/2}(E_v\rho_\ell)/(E_m\rho) \qquad (2.19d)$$

where α_ℓ and α_t are the thermal diffusivities of the liquid and solid metal and E_m is the energy of the molten metal given by

$$E_m = cT_{mp} + L_f. \qquad (2.19e)$$

The ratio, Γ_{on}, for copper is approximately 9.2 which means that an upper limit for the onset of vaporization on Belkin's curves in Fig. 2.1 is when

$$q^*(t_r)^{1/2} = (9.2)(\pi/4)^{1/2} = 8.1. \qquad (2.19f)$$

Cramer and Roman's Solutions

These authors examined known transient solutions [15] of Eq. (2.3) with negligible EJH in order to optimize the electrode thickness and cooling method required to avoid melting of the electrode surface. They used a simple approximation to evaluate the effect of EJH, namely, the temperature rise due to EJH is given by

$$T = \frac{\eta J_e^2 t}{\rho c}, \qquad (2.20a)$$

which for copper is approximately 0.4°C for J_e^2t equal to 8×10^5 A^2s/cm^4. By examining the 1-D uniform heat source solution for an infinite strip source and a circular source they determined that for typical J_e and corresponding arc spot area that one dimensional solutions can be used to determine

optimal cooling. After evaluating the solutions for five different cooling cases they concluded that

1) an electrode is basically infinite if it is greater than four diffusion lengths thick, i.e., cooling does not effect the surface for thick electrodes,
2) active cooling systems are best when the electrode thickness is less than a diffusion length and
3) the "well stirred" boundary condition is hard to achieve in practice due to vapor formation leading to thermal insulation.

The following solution is also given for the temperature decay after the removal of the heat source

$$\frac{T(z=0)}{T_{mp}} = \left(\frac{t}{t_m}\right)^{1/2} - \left(\frac{t}{t_m} - 1\right)^{1/2} \qquad (2.20b)$$

where

$$t_m = \frac{\pi k^2 T_{mp}^2}{4 q_m^2 \alpha_t}. \qquad (2.20c)$$

The temperature drops to 20% of its value in 7 melting times and to 1% in about 1000 melting times for copper.

Raezer's Solution

Raezer [29] obtained an analytical solution for Eq. (2.3) with negligible EJH for the case of a repetitive heat flux of duration, t_p, and interpulse spacing, τ. The boundary conditions for Eq. (2.3) become:

$$T(0,t) = T_o \tag{2.21a}$$

$$T(\ell,0) = T_o \tag{2.21b}$$

$$k\frac{\partial T}{\partial z}(\ell,t) = q_m; \quad j\tau < t < j\tau + t_p \tag{2.21c}$$

$$k\frac{\partial T}{\partial z}(\ell,t) = 0; \quad j\tau + t_p < t < (j+1)\tau, \tag{2.21d}$$

where j = 1, 2, 3 etc., and z = ℓ is the electrode surface exposed to the arc heat flux. These conditions simply imply that the surface is heated by a constant heat flux of magnitude, q_m, for a period, t_p, with a rep-rate given by $1/\tau$. The steady state solution was solved for the temperature at the surface at the end of the pulse by evaluating the following expression:

$$T(\ell,t_p) = \frac{q_m\ell}{k} - \frac{8q_m\ell}{k\pi^2}\sum_{n=0}^{\infty}\frac{1}{(2n+1)^{1/2}}\frac{1-e^{\alpha_n(\tau-t_p)}}{1-e^{\alpha_n\tau}}, \tag{2.21e}$$

where ℓ is the thickness of the electrode and

$$\alpha_n = \frac{(2n+1)^2\pi k}{4\ell^2\rho c} = \frac{(2n+1)^2\pi}{4\ell^2}\alpha_t. \tag{2.21f}$$

The magnitude of the heat flux, q_m, is approximated by

$$q_m = \frac{I_p V_f}{A_e} = J_a V_f \tag{2.21g}$$

Raezer rewrote Eq. (2.21e) in the form

$$\frac{q_m}{q_s} = \left[1 - \frac{8}{\pi^2}\sum_{n=0}^{\infty}\frac{1}{(2n+1)^2}\frac{1-e^{\alpha_n(\tau/t_p-1)t_p}}{1-e^{\alpha_n\tau}}\right]^{-1}, \qquad (2.21h)$$

where q_s is the steady-state heat flux corresponding to a surface temperature, T_{mp}. In practice, q_s is limited by the maximum allowable cooling rate at the back surface of the electrode and not the flux produced by the temperature gradient. A modified version of Raezer's plot [29] of Eq. (2.21h) will be discussed in detail in Chapter 4.

Zolotykh's Solution

Zolotykh [30] presents the analytical solution for the problem of heat propagation for a system consisting of a rod electrode with a surface layer of differing thermophysical properties in order to simulate the effect of films on the erosion of the base electrode. The solution for the temperature is

$$T_2(z,t) = \qquad (2.22a)$$

$$\frac{T_o}{1+\delta_t}\sum_{n=0}^{\infty}\left[(-h)^{n-1}Erfc\left(\frac{(z-n)+(2n-1)z_f(\alpha_{t2}/\alpha_{t1})^{1/2}}{2(\alpha_{t2}t)}\right)\right],$$

where

$$\delta_t = \left(\frac{k_2\rho_2c_2}{k_1\rho_1c_1}\right)^{1/2}, \qquad (2.22b)$$

$$h = \frac{1-\delta_t}{1+\delta_t}, \qquad (2.22c)$$

and the subscripts on k, ρ, c indicate which material they are for; the surface is subscript 1, the bulk is subscript 2. The thickness of the film which is required for $T_2 = T_o$ is given by

$$z_f = 5.8(\alpha_{t1} t_p)^{1/2}. \qquad (2.22d)$$

More will be said about this solution in Chapter 4 when methods of reducing erosion will be treated.

Miscellaneous Solutions

Dixon et al. [22], using ICARUS, a 1-D moving boundary heat flux code developed at LLNL, solved the case of ablation and melting for a planar heat source. The results shown in Fig. 2.4 originally depicted the melt velocity versus time, but have been redrawn to allow a comparison with Belkin's results. One can easily see that the ablation case, as expected, leads to much larger erosion rates (a factor of 3) and reaches a steady state which is very close to the theoretical value given by

$$m_a = V_{arc} Q_e / c T_{mp}. \qquad (2.23)$$

Zien [23] solved analytically the ablation problem for time varying heat fluxes which have the form of $q(t) \sim t^n$ and $q(t) \sim e^t$. The time to the onset of ablation for the case with

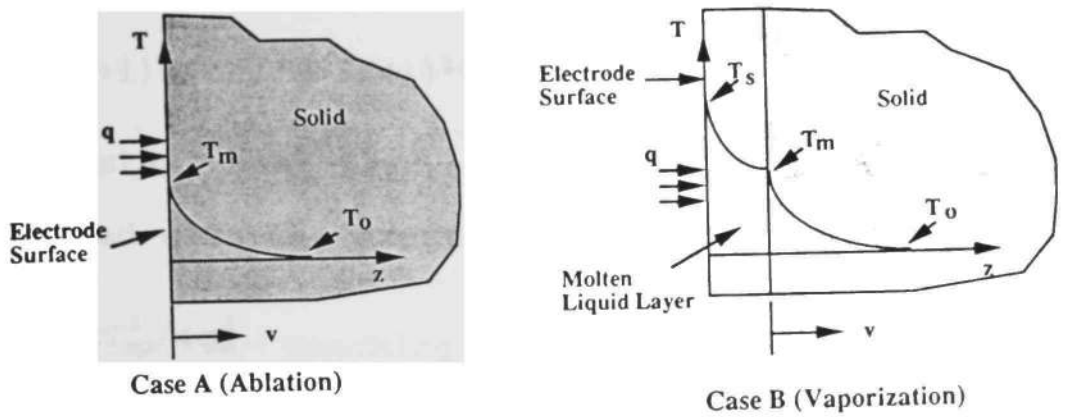

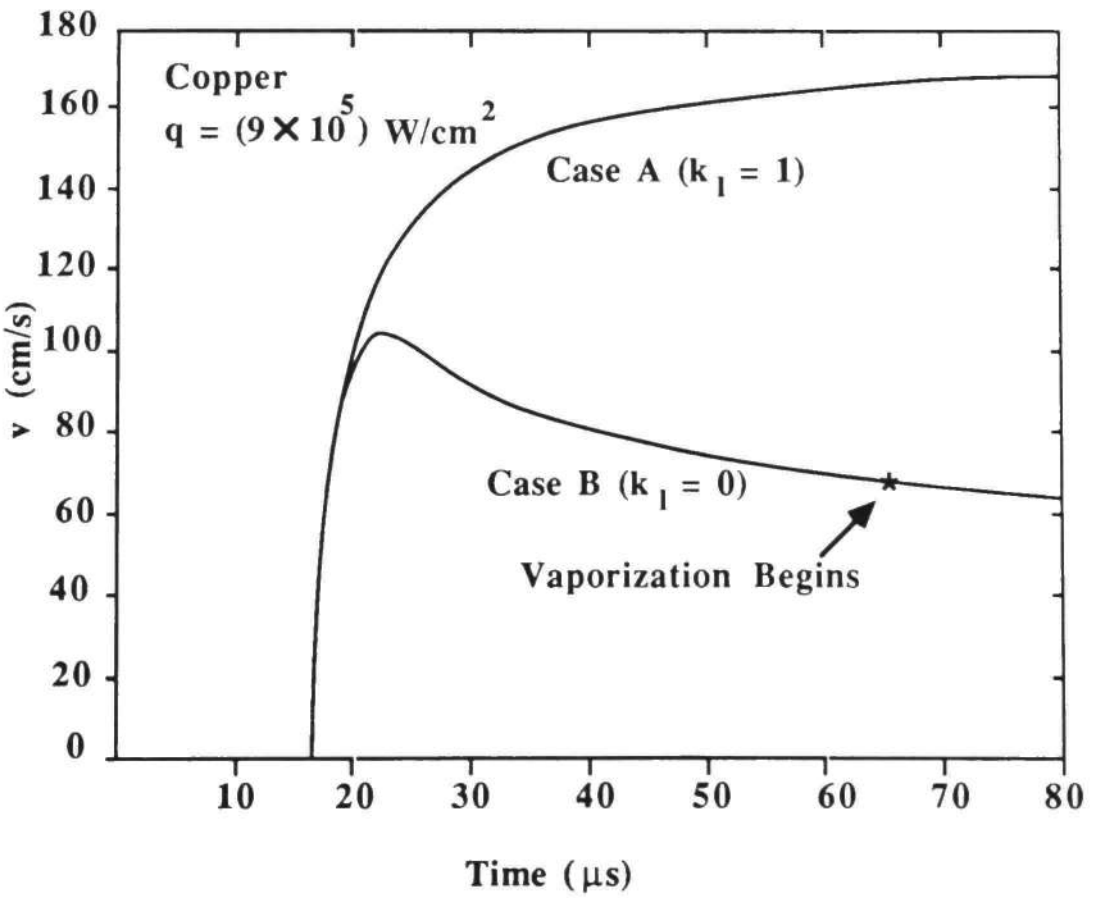

Fig. 2.4 Ablation and Melting Problem Definition and Solutions for a Heat Source by Dixon et al., [22].

$$q(t) = At^n \tag{2.24a}$$

is given by

$$t_m = \left[(n+1)\left(k\rho c/(n+5/4)\right)^{1/2} T_{mp}/A\right]^{\frac{1}{n+1/2}}. \tag{2.24b}$$

For a constant heat flux, n=0 and A=q_m, and the solution can be compared with the exact solution given by Belkin, namely,

$$t_m = \pi k\rho c T_{mp}^2/4q_m^2. \tag{2.24c}$$

Eq. (2.24b) yields

$$t_m = 4k\rho c T_{mp}^2/5q_m^2. \tag{2.24d}$$

Thus, Eq. (2.24b) predicts the exact solution for a constant heat flux (Eq. (2.24c)) within 2%. The author claims an agreement of better than 1% on the temperature field for all n's between 0 and ∞. Similar agreement is found for the exponential case. Thus, if one can model the actual heat flux by either of these forms then a very accurate analytical expression may be obtained for the temperature field and the time to melt in the ablation mode.

Goloveiko's Solution

Goloveiko [24] analytically solved Eq. (2.3), including a temperature dependent electrical resistivity, by making the following approximations. The electrode current density is given by

$$J_e(z,t) = J_{eo}e^{-\delta z}, \tag{2.25}$$

where the parameter, δ, is the reciprocal of the characteristic length for the process which is determined experimentally by measuring the depth of the microscopic holes on the electrode surface. Even with this assumption on J_e the problem defined by Eqs. (2-3) and (2-4b) is nonlinear and has no analytic solution. However, it turns out that at high current densities the high temperature field excited by the surface heat source develops in an extremely thin surface layer, nearly reaching a steady state essentially instantaneously, especially at the vaporization front; the additional temperature increase due to the volume source lags behind considerably. Accordingly, the process may be treated in a somewhat different manner, under the assumption that the steady-state temperature and front velocity, $T(0,t) = T$ and $u(t) = u$, arise instantaneously at the start of the process, and then are stably maintained, while transient phenomena occur everywhere except at the evaporation front itself. After reformulating the problem with these approximations Goloveiko obtained the following expressions for the current density for which the volume heat source is ineffective, J_e^*, the current density for which the surface heat source and volume source are equal, J_e^{**}, and the current density for which temperature gradient at the evaporation front vanishes, J_e^*. These are

$$J_e^* = \frac{\alpha_t \delta \rho}{10 V_f}\left[L_v + C\left(T\ell n^{-1}\left(\frac{10 V_o}{\alpha_t \delta}\right) - T_o\right)\right], \tag{2.26a}$$

$$J_e^{**2} e^{(J_e^{**}/(A^{**}-B^{**}J_e^{**}))} - C^{**}J_e^{**} = D^{**}, \tag{2.26b}$$

with

$$A^{**} = V_f \delta / \eta_{mp} \alpha_\eta T, \tag{2.27a}$$

$$B^{**} = (1-\alpha_\eta T_{mp})(\alpha_\eta T), \tag{2.27b}$$

$$C^{**} = \rho V_o [L_v - C(1-\alpha_\eta (T_{mp}-T_o)/\alpha_\eta)]/2V_f, \tag{2.27c}$$

$$D^{**} = V_o \delta \rho C / 2\alpha_\eta \eta_{mp}; \tag{2.27d}$$

and

$$(A^* + B^* J_e^*)\ell n(C^*/J_e^*) + D^* J^* = E^*, \tag{2.28}$$

with

$$A^* = V_f T_o / \rho L_v, \tag{2.29a}$$

$$B^* = \eta_{mp}(1-\alpha_\eta T_{mp})/\delta \rho C, \tag{2.29b}$$

$$C^* = \rho L_v V_o / V_f, \tag{2.29c}$$

$$D^* = \eta_{mp} \alpha_\eta T / \delta \rho C, \tag{2.29d}$$

and

$$E^* = V_f T_{mp} / \rho L_v. \tag{2.29e}$$

The resistivity of the molten metal, $\eta_e(T)$, is defined by

$$\eta_e(T) = \eta_{mp}[1 + \alpha_\eta (T(0,t) - T_{mp})], \tag{2.30a}$$

where η_{mp} is the resistivity at the melting temperature and α_n is a temperature coefficient. In addition, α_t is the thermal diffusivity defined by

$$\alpha_t = k/\rho c, \tag{2.30b}$$

and v_o is the sound velocity in the metal. The actual calculations by Goloveiko [58], listed in Table 2.2, indicate that $J_e^* \sim J_e^{**} \sim 10^2 J_e^+$ for most metals. The physical meaning of J_e^* is that when $J_e < J_e^*$, the heat flux still penetrates through the evaporation front and into the depth of the electrode; when $J_e = J_e^*$, this process stops; and when $J > J_e^*$, the heat flux moves from the electrode to the evaporation front indicating that the temperature in the electrode exceeds that at the front; i.e., volume superheating occurs.

The steady state front velocity and the transition time to $J_e = J_e^*$ is given by

$$\frac{dz_p}{dt} = V_f J_e^*/\rho L_v \tag{2.31}$$

and

$$t_t > t_t^* = \rho L_v/(\delta(V_f J_e^* - \alpha_t \delta \rho L_v)). \tag{2.32}$$

Thus, one can determine when electrode joule heating becomes significant and the erosion rate when this occurs assuming vaporization is the primary means of material removal.

Table 2.2 Goloveiko's Onset Current Densities for Different Materials [58]

Material	J_e^* (A/cm^2)	$J_e^{**} \sim J_e^*$ (A/cm^2)
Pb	6×10^5	5×10^7
Sn	3×10^6	9×10^7
Cu	6×10^6	1×10^8

Watson's Solution

For the cases where the skin effect enhanced joule heating in the electrode is significant, then Watson [25] has solved the electrode joule heating driven thermal problem combined with the hydromagnetic flow for the amount of molten material flow at the electrode surface. A description of this process will be given in the next section. His results show that the volume flow rate, dv_l/dt, is given by

$$dv_l/dt = I\eta/(2\mu_o\rho cT_{mp})^{1/2} \qquad (2.33)$$

where μ_o is the magnetic permeability.

Material Removal

Up to now only mechanisms for heating the electrode material have been discussed but actual electrode erosion occurs only if the material which changes to the molten or vapor state is removed by a different set of mechanisms, as was indicated earlier in Eq. (2.1). Numerous mechanisms exist which can lead to the following modes of material removal:

1. a large number of atomic particle interactions [26],
2. quiescent evaporation from the bulk surface [11,27,28],
3. explosive evaporation at individual filament attachment sites [29-31],
4. bulk explosive evaporation [32,33],

5. molten droplet ejection [25,34-37],
6. viscous shearing of molten and solid metal [38,39] and
7. solid ejection [40-42].

In this section some of the various mechanisms which have been proposed will be briefly described along with the appropriate equations. For a more detailed description the reader is referred to the numerous references. Because Ecker has written an exhaustive review of the atomic particle interactions [26] and because they probably represent the smallest source of erosion, they will not be discussed here. Since many of the other models are predominantly qualitative in nature, the important material property trends which lead to reduced erosion (k's = 0 in Eq. (2.1)) will be given as well.

Molten

Several mechanisms have been proposed for the removal of the molten electrode material once it has been formed. Gray and Pharney [43] have suggested that the removal of the ionic bombardment force from the molten pool at each filament attachment site results in a recoil force which removes molten droplets from the surface of the pool. The condition for droplet removal is

$$(0.01)I(2V_f m_i/e)^{1/2} \geq 2\pi r_p \gamma, \qquad (2.34)$$

where m_i, r_p and γ are the bombarding ion mass, the radius of the droplet and the surface tension of the melt, respectively. For very low filament currents (I = 0.5 A) this condition was found to be easily satisfied. However, they concluded that a small percentage of the molten material volume is converted into droplets and removed.

McClure [35] proposed the expulsion of molten material from cathode spots by the plasma pressure. The pressure, P_p, is given by

$$P_p = J_s f_i m_i v_i / 2 q_i, \qquad (2.35)$$

where J_s is the cathode spot current density, f_i is the fraction of the total current due to the outgoing ions (~0.1), and m_i, v_i, and q_i are the mean ion mass, velocity and charge, respectively. Typical values of P_p for J_s in the range of 10^{10}-10^{12} A/m^2 are in the range of 10^6-10^8 N/m^2 (10-100 atm). Predicted particle velocities of 10-100 m/s agree quite well with the experimental values of 100 m/s reported by Udris [44].

Petr and Burkes [37] proposed that the removal of molten material could occur when JxB generated acoustic waves interact with the molten surface. The JxB force at the electrode surface initially generates a wave which gets reflected at the electrode holder and returns to the electrode surface. The magnitude of the force at the electrode is given by

$$F_e \sim (\mu_o I^2/2\pi)\ln(r_e/r_s), \qquad (2.36)$$

where r_e and r_s are the electrode and arc spot radii. For molten material to be removed F_e must be greater than the surface tension force and the acoustic wave it generates must arrive back at the electrode before the molten pool solidifies. The later condition is satisfied when

$$t_p \geq d/v_o \qquad (2.37)$$

where t_p is the pulse time, d is the distance to the interface and back, and v_o is the acoustic velocity for the material. The authors were able to experimentally validate this mechanism by changing d.

Watson [25] developed a quite thorough model for molten metal formation and removal, based on the mechanism shown in Fig. 2.5. The radial variation of the JxB forces at the surface of the molten metal, produced by skin effect enhanced joule heating, sets up a pressure gradient which drives material into a standing wave. Interaction of the standing waves from multiple filaments form "fountains" for the removal of molten droplets from the surface. (See the co-authored paper reproduced in Appendix D for the theoretical and experimental results.)

Belkin [27] proposed macroscopic electromagnetic (JxB) forces as a possible cause for molten material removal. He defined an ejection coefficient, k_e, as the ratio of the mass of ejected metal to the mass of melted metal. The following expression was derived for k_e:

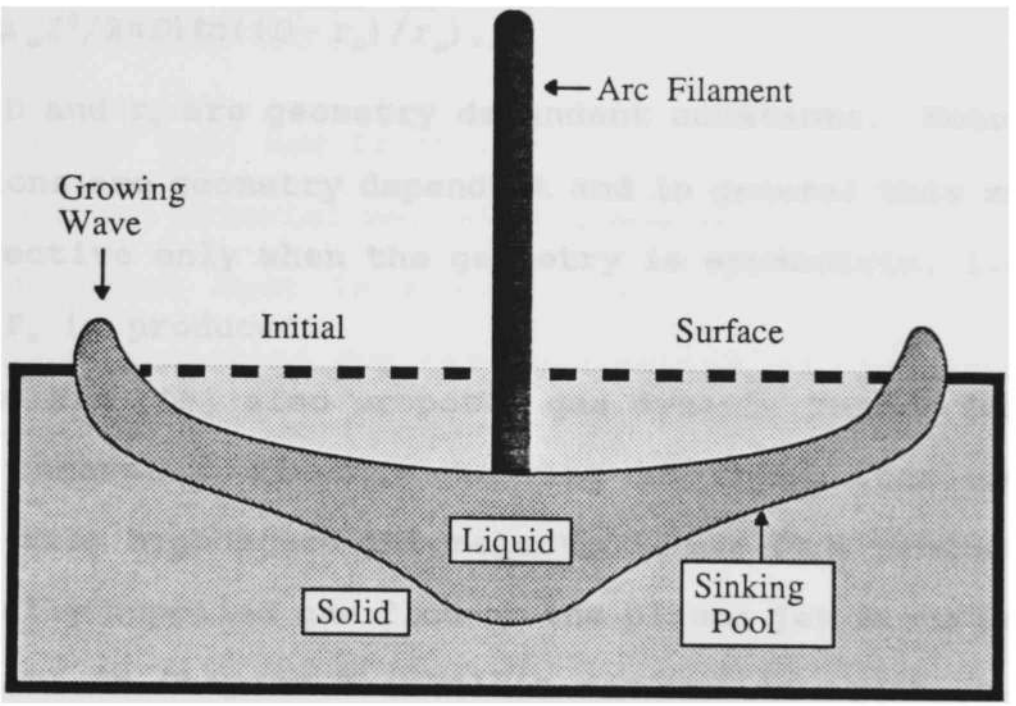

- I^2R heating in electrode material
- Radial variation of $\bar{J} \times \bar{B}$ pressure on molten fluid sets up a standing wave
- Interaction of adjacent waves produces droplet ejection

Fig. 2.5 Watson's Model for Molten Metal Formation and Removal [25].

$$k_e = 1 - 3\pi^2 D_d^3 \gamma \rho c t_{mp} / (16 F_e V_f Q_e), \qquad (2.38)$$

where D_d is the discharge diameter, γ is the surface tension of the molten metal, and F_e is the electromagnetic force acting tangentially to the electrode surface. The force, F_e, is given by

$$F_e = (\mu_o I^2 / 2\pi D) \ln((D - r_o)/r_o), \qquad (2.39)$$

where D and r_o are geometry dependent constants. Note: these equations are geometry dependent and in general this mechanism is effective only when the geometry is asymmetric, i.e., when a net F_e is produced.

Belkin [19] also proposed gas dynamic forces for molten metal removal. Viscous shearing of the molten metal may result from high speed interelectrode gas flow produced by an externally supplied gas flow or the plasma jet flows described in detail in Chapter 3. Belkin derived an equation for the coefficient of ejection for gas dynamic forces for flat surfaced electrodes whose molten mass is given by Eq. (2.8a). The ejection coefficient, k_g, is given by the equation

$$k_g = 1 - \frac{9.3 A_m r_e^2 \rho c T_{mp}}{(R_{ey})^{1/2} u_s t_p V_f Q_e}, \qquad (2.40a)$$

where A_m, r_e, R_{ey}, and u_s are the melted area, the radius of the electrode, the Reynolds number in the y direction (parallel to the electrode surface), and u_s is the velocity of the liquid metal at the boundary between the boundary layer and the liquid flow, given by

$$u_s = \left[F z_m + \frac{0.323 A_m \rho_g u_g^2}{(R_{ey})^{1/2}} - \frac{\gamma A_m}{2 r_e} \right] t / 2 m_m, \qquad (2.40b)$$

where z_m, ρ_g, u_g and m_m are the depth of melt, gas density, gas velocity and the molten mass, respectively. For u_g = 1000 m/s, I = 10 kA, r_e = 1 cm, Q_{eff} = 100 C, t_p = 10 ms and m_m = 0.2 g; molten mass velocities, u_s, of 2 m/s were obtained.

Lebedev [49] and Il'in and Lebedev [32] assumed that all the electrode material melted in a hemispherical crater at the arc attachment spot is a result of EJH. They derived the following expression for the mass melted per spot per pulse, m_t, for a rectangular current pulse

$$m_t = \frac{\rho}{3 (2\pi)^{1/2}} \left(\frac{1}{A+B} \right)^{3/4} I_p^{3/2} t_p^{3/4} \qquad (2.41a)$$

and

$$m_t = \frac{\rho}{3 (2\pi)^{1/2}} \left(\frac{1}{A+B} \right)^{3/4} \left(\frac{C_t V_b^2}{2 R_a} \right)^{3/4} \qquad (2.41b)$$

if the current pulse is generated by a capacitance, C_t, of initial voltage, V_b, discharging through arc resistance R_a, where A and B are material constants. Although they quote several experiments which resulted in the same dependencies on voltage and material properties, their calculated values are one to two orders of magnitude too small. The erosion itself occurs primarily by "explosive" removal of metal droplets. This conclusion was based on the following observations of the electrode processes. For metallic electrodes subject to high

current densities ($5x10^6$ - $2x10^7$ A/cm^2), a time, τ_{sw}, after initiating the discharge, the conductivity abruptly became very small as a consequence of the explosive ejection of molten metal in the form of a jet of very fine particles with velocities u_j of 10^4 to 10^5 cm/s (a function of J_e and τ_{sw}). If the current was switched off before τ_{sw} the melt did not explode but flew apart as coarser droplets with velocities $u_d << u_j$. Although not mentioned by the authors, it is quite possible that the molten crater under the arc spot, which is responsible for the "explosion" could be considered as a system with positive feedback, i.e., as the temperature increases the resistivity increases which leads to more joule heating and thus higher temperatures. Thus, thermal runaway may be achieved which leads to the "explosion."

Zolotykh [33] considered the possibility of molten material removal by the rapid change in the pressure at the electrode surface at the end of the discharge. Schoenbach and Fischer [34] also considered a rapidly changing pressure gradient brought about by an equally rapid channel expansion after the electrode surfaces had superheated (achieved temperatures higher than the melting temperatures because of high local surface pressures). A sudden drop in pressure thus leads to explosive vaporization and droplet removal. Their theoretical result, given in Chapter 3, accurately predicted the velocity scaling with current and also correctly predicted the proper order of different electrode material velocities.

Solid

If thermal energy is supplied to the electrode at a rate which cannot be compensated for by simple ablation or vaporization then thermal stresses may develop within the material which may lead to solid material removal. Several material response regimes exist as described by Rasty et al. [45]; namely, static thermal stress, dynamic thermal stress and thermal shock waves. As the electrode is heated, significant temperature gradients may develop within the material resulting in the generation of internal thermal stresses. The heated portion of the material may try to deform to an equilibrium position where the stresses are minimized but in general the stresses cannot be eliminated entirely. At sufficient heat fluxes, the stresses will become large enough to cause material structural failure, commonly referred to as thermal shock or thermal stress failure. If the heat flux or internal energy source is sufficiently high, the inertia of the heated area keeps it from deforming instantaneously to an equilibrium where the stresses are minimized. Instead stresses in the material oscillate around the equilibrium stress distribution, which increases the peak compression and tension values, resulting in an effective dynamic magnification of the equilibrium stresses. For sufficiently high stress values material structural failure will occur in a manner similar to the static thermal stress case.

For extremely rapid heating, inertia keeps the heated region at the electrode essentially frozen in the bulk leading to large stresses which in turn produce thermal shock waves which propagate into the material. In turn, these compressive shock waves can generate tensile waves at free surfaces of sufficient size to cause material failure (e.g., spall).

Several authors have considered the mechanisms that cause solid material removal. Zolotykh et al. [40], assuming a point thermal source at the surface, solved the thermoelastic potential equation for the various components of the stress tensor. The various stress components were proportional to

$$\sigma_s \sim \frac{G q_m t_p (1+\upsilon)}{\rho c (1-\upsilon)} a_t, \qquad (2.42)$$

where G, υ, and a_t are the shear modulus, Poisson's ratio and the coefficient of thermal expansion of the electrode material. From this it was concluded that the destruction due to thermal stresses is most clearly demonstrated in the case of high T_{mp} materials with low ultimate strength and a relatively high modulus of elasticity and coefficient of thermal expansion. Also a sharp heterogeneity of the thermoelastic properties of individual structural elements in a composite material at high temperatures will increase thermal stress. The authors also stressed the importance of the volume heat source even in cases where it contributes only a small percentage of the amount of heat delivered to the electrode. Its importance arises from the fact that it produces temperature stresses at far greater regions than the

surface heat source because the topography of the thermal stress field is a copy of the thermal field.

Rakhovskii and Yagudaev [41] calculated the stress using

$$\sigma_s = a_t E \nabla T \ell_o, \tag{2.43}$$

where E is the modulus of elasticity and ℓ_o is the characteristic dimension of the region subject to the effect of the thermoelastic wave given by

$$\ell_o \sim (\alpha_t t)^{1/2}. \tag{2.44}$$

Their calculations of the temperature gradients required to remove solid material (10^5K/cm) were found to be in good agreement with measured temperature gradients.

Kapel'yan [42] also considered the fracture of material through the action of internal heat sources produced by joule heating of dissimilar materials, the presence of residual gas bubbles, etc. Thus, upon heating of the electrode vapor, bubbles may be formed close to the electrode surface whose vapor pressure and resulting thermoelastic stresses may lead to failure of the electrode surface. The temperature fields and the resulting thermoelastic stresses are solved using the quasistatic formulation of the thermoelastic potential field. Asymptotic values of the stresses for t = 0 and t = ∞ are given and the time to maximum stress can be found by solving a transcendental equation for which a table of roots is given. However, in general the stress is related to the material parameters by the equation

$$\sigma_s \sim \upsilon G \left(\frac{1+\upsilon}{1-\upsilon}\right) T_b \left(\frac{r_{bo}}{\ell}\right)^3, \tag{2.45}$$

where T_b is the boiling temperature, r_{bo} is the initial radius of the gas bubble and ℓ is the distance from the center of the bubble to the surface. Again, as in Eq. (2.42), it is readily seen that high G, T_b and υ all lead to large stresses.

Stevenson [48] and Behrisch [11] defined a thermal shock figure of merit, Γ_{ts}, as the ratio of the yield strength, σ_y, to the thermal stresses. The temperature gradient is assumed to be proportional to $(\rho ck)^{-1/2}$, which is true for passively cooled electrodes dominated by arc joule heating of the electrode surface. The figure of merit is given by

$$\Gamma_{ts} = \sigma_y \frac{(1-\upsilon)(\rho ck)^{1/2}}{E a_t}. \tag{2.46}$$

Evaporation

Evaporation is perhaps the most straightforward of the mechanisms for electrode erosion because it occurs simply as a result of the increase in the temperature of the electrode as it is heated. The steady state evaporation rate for a clean surface (even a monolayer may alter the results dramatically) can be expressed by

$$\frac{dn(T)}{dt} = k_2 p(T) \left(\frac{M_w}{T}\right)^{1/2}, \tag{2.47}$$

where M_w is the atomic weight of the metal atoms, and the vapor pressure, p(T), is given by

$$p(t) = p_o e^{-(H_s/k_b T)}, \qquad (2.48)$$

where H_s is the heat of sublimation, which has a slight temperature dependence, and k_b is the Boltzmann constant. Vapor pressure data for metals are easily found [50]. The temperature in the above equation is found by solving Eq. (2.3) for the appropriate boundary conditions. This approach represents a considerable reduction of the complexity of the real problem. In general, nonequilibrium evaporation is occurring for large heat fluxes [52]; and vapor shielding of the incoming flux, which may be enhanced by self or externally generated magnetic fields, may also be a factor [53]. However, using fairly straightforward vaporization calculations, several experimentalists have found good agreement over a wide range of pulse conditions between various models and experimental results. Thus, only these later models will be presented here.

Behrisch [11] derived the following expression for the amount of material evaporated from a surface for a heat pulse of time, t_p:

$$n = \frac{dn(T_{max})}{dt} t_{eff}, \qquad (2.49)$$

where dn(T)/dt is found with Eq. (2.47) and t_{eff} is an effective evaporation time given by

$$t_{eff} = 1.8 t_p \left(\frac{k_b T_{max}}{H_s} \right) \left(\frac{T_{max}}{T_{max} - T_o} \right). \quad (2.50)$$

The difficulty in applying this approach a priori is in estimating T_{max} as a function of the pulse conditions. (Experimental verification might be rather simple if one could measure T_{max}, however.)

Holm [54] solves the energy balance equation at the electrode surface for the volume of material vaporized per second in the steady state. Namely,

$$W_e + W_a = W_c + W_v + W_r + W_{cv}, \quad (2.51)$$

where W_a and W_e is the heat energy supplied to the electrode from the arc and generated within the electrode, W_c is the heat energy conducted away, W_v is the energy expended in vaporizing the material and W_r and W_{cv} is the heat lost due to radiation and convection. Holm assumed W_e, W_r, and W_{cv} were negligible. Each of the remaining terms were approximated by the following:

$$W_a = (V_e - \Phi_e) I_s, \quad (2.52)$$

$$W_c = 4 r_s k T_s, \quad (2.53)$$

and

$$W_v = L_v \frac{dv_v}{dt}, \quad (2.54)$$

where V_e is the electrode voltage drop (Holm considered only the cathode), Q_e is the electrode work function, r_s is the spot radius, T_s is the spot temperature, and v_v is the volume

vaporized. The arc attachment is assumed to be a circle so that

$$J_s = I_s/\pi r_s^2. \tag{2.55}$$

Two other variables are introduced; x_f, the fraction of the total energy used for vaporization defined by

$$x_f = W_v/W_a, \tag{2.56}$$

and δ_v, the evaporated volume per coulomb, defined by

$$\delta_v = \frac{dv_v/dt}{I_s} = \frac{(V_e-\Phi_e)x_f}{L_v}. \tag{2.57}$$

Equations (2.51)-(2.57) contain nine variables; I_s, r_s, v_s, x_f, δ_v, k, L_v, V_e and Φ_e. The last four are known material parameters, T_s is assumed to be the boiling temperature, I_s is given, leaving four variables which must be solved using these equations. Thus, one of the four was chosen from experimental results at each current to solve for the remaining three. The results shown in Fig. 2.6 have some interesting ramifications. Namely,

1) the erosion scales with Q_e at high currents (> 1 kA for Cu and W) and approximately with Q_eI at modest currents (1 A - 1 kA),
2) the transition is a result of a higher fraction of the energy going into vaporization, as opposed to conduction, at higher currents,
3) the change in relative order for graphite erosion, versus W and Cu, as the current is increased, is

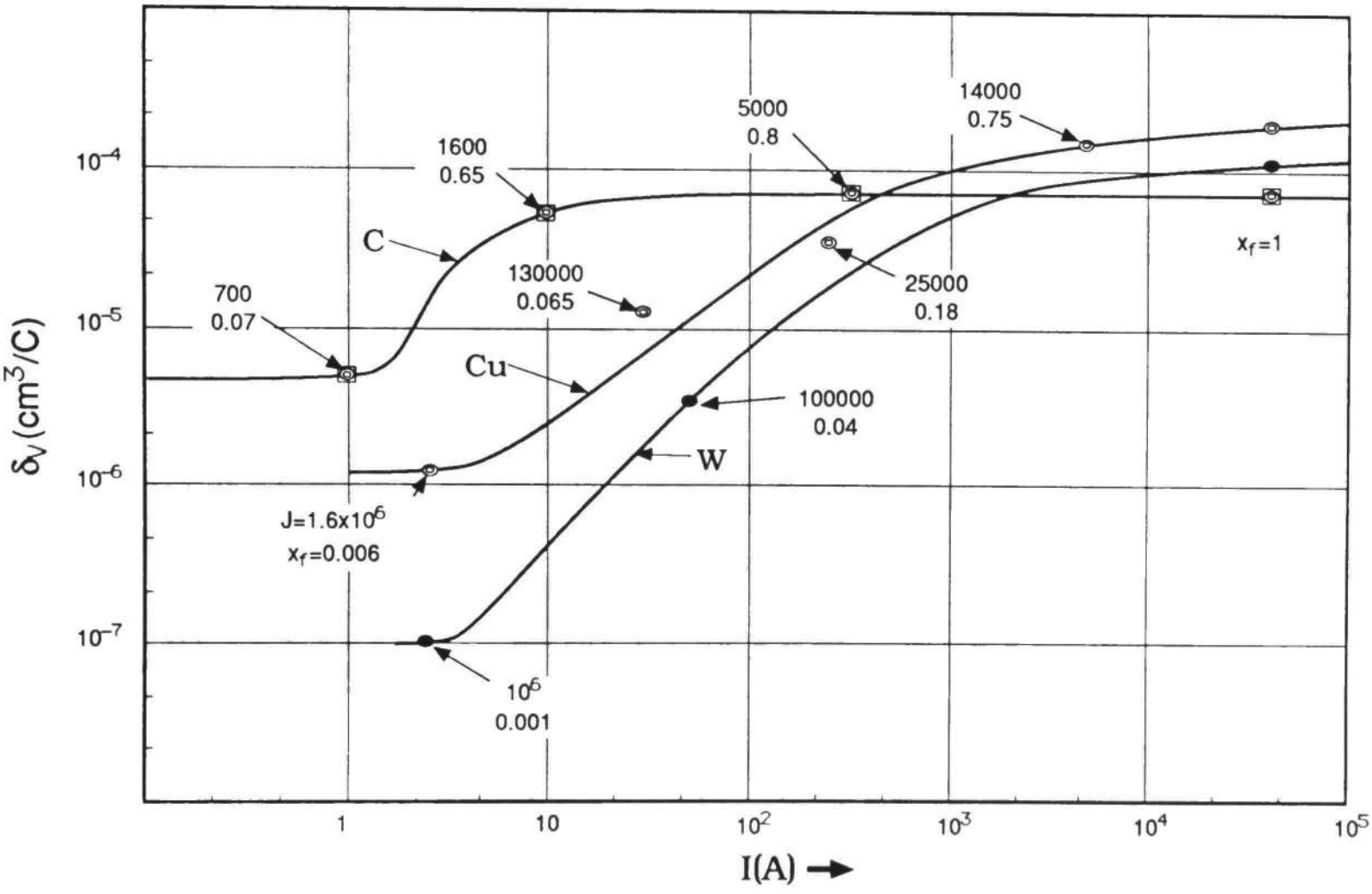

Fig. 2.6 Holm's Solution for the Volume of Vaporized Material Per Coulomb Versus the Current (from Ref. [54]).

due to graphite's lower thermal conductivity, k, and thus higher x_f at lower currents, and

4) the material's erosion is proportional to L_v at high currents.

Jones [55] solved Eq. (2.51) for the case of W_e and $W_{cv} = 0$. He was mainly concerned with very small electrode spacings (0.2 to 0.5 mm) and thus used the expression

$$W_a = C_a V_b^2, \tag{2.58}$$

where C_a and V_b are the effective gap capacitance and discharge voltage, respectively. Predecki [57], utilizing the constant of Jones [55] showed that his model gave erosion values of 2 to 3 orders of magnitude higher than experimental values for larger currents and gap spacings. This is more than likely due to the small fraction of gap energy which actually contributed to the erosion for large gap spacings. Nevertheless, Jones' model proves to be inadequate for our use because of the difficulty in estimating W_a using Eq. (2.58).

The model proposed by Cobine and Burger [56] is similar to that of Jones except that they neglect W_c and W_r as well. The model is used to solve for the erosion of the anode due to vaporization, allowing for a range of electrode temperatures above and below the boiling point. They estimate large total power inputs to the anode (equal to 5×10^4 to $> 10^6$ W/cm^2) by choosing a range of current densities assumed to be constant with time. Using these values to obtain the W_a, the vaporization rate is determined as a function of temperature

by using an evaporation rate chart [50]. For the powers chosen, the anode spot temperature frequently exceeded T_b. This was to be expected because of the high vapor pressures of the electrode surface. The authors compared calculations for erosion rates with those obtained for several materials subjected to a single half cycle of current with peak values of 11 to 26 kA and an electrode gap of 1/32 inch. The erosion rates observed could all be predicted with slightly higher than estimated power ranges. The differences was attributed to droplet loss from "explosive" processes and the motion of the arc "footprint" (assumed to imply plasma pressure).

Osadin [28] solved Eq. (2.3) for negligible EJH, assuming that the erosion was entirely due to vaporization in a vacuum, but that the heat flux due to the evaporation loss was negligible, i.e., the "erosionless" approximation. The electrode surface temperature, $T_e(t)$, as a function of the current pulse, $I(t)$, is given by

$$T_e(t) = T_o + \frac{V_f}{A_e(\pi k \rho c)^{1/2}} \int_0^t \frac{I(\tau)\, d\tau}{(t-\tau)^{1/2}} \qquad (2.59)$$

for $0<t<t_p$, and

$$T_e(t) = T_o + \frac{V_f}{A_e(\pi k \rho c)^{1/2}} \int_0^{t_p} \frac{I(\tau)\, d\tau}{(t-\tau)^{1/2}} \qquad (2.60)$$

for $t>t_p$. (Note: Eq. (2.59) is just Eq. (2.17b) with $z=0$.) The evaporation is in general a nonequilibrium process; however, at low vapor pressures the rate of evaporation is independent of the presence of the vapor, i.e., the rate of

Summary

Despite the large number of processes and models involved, the electrode erosion problem can be formulated in such a way as to predict many parameters of interest for a variety of conditions. Many of the models presented gave good agreement with quantitative values of electrode erosion, and can be used, as the author will show in Chapter 4, to predict scaling laws a priori for a wide variety of conditions. The expertise needed to calculate actual erosion values comes from knowing which model to use for a given set of experimental conditions. Although this expertise will undoubtably come from the reader's careful understanding and practice using the various approaches outlined previously, a somewhat systematic procedure will now be described which should provide a good basis for quantitative electrode erosion analysis. Note: many of the solutions required to aid in this process require numerical solution and careful and at times restrictive assumptions on the heat flux, as well as knowledge of various temperature dependent material properties of the electrode surface.

A somewhat systematic procedure for determining which equations to use may be described with the use of the flow chart shown in Fig. 2.7. The Q's and A's are abbreviations for the following questions and answers (the equations, etc., used to obtain the answers). The questions must be asked in this sequence!

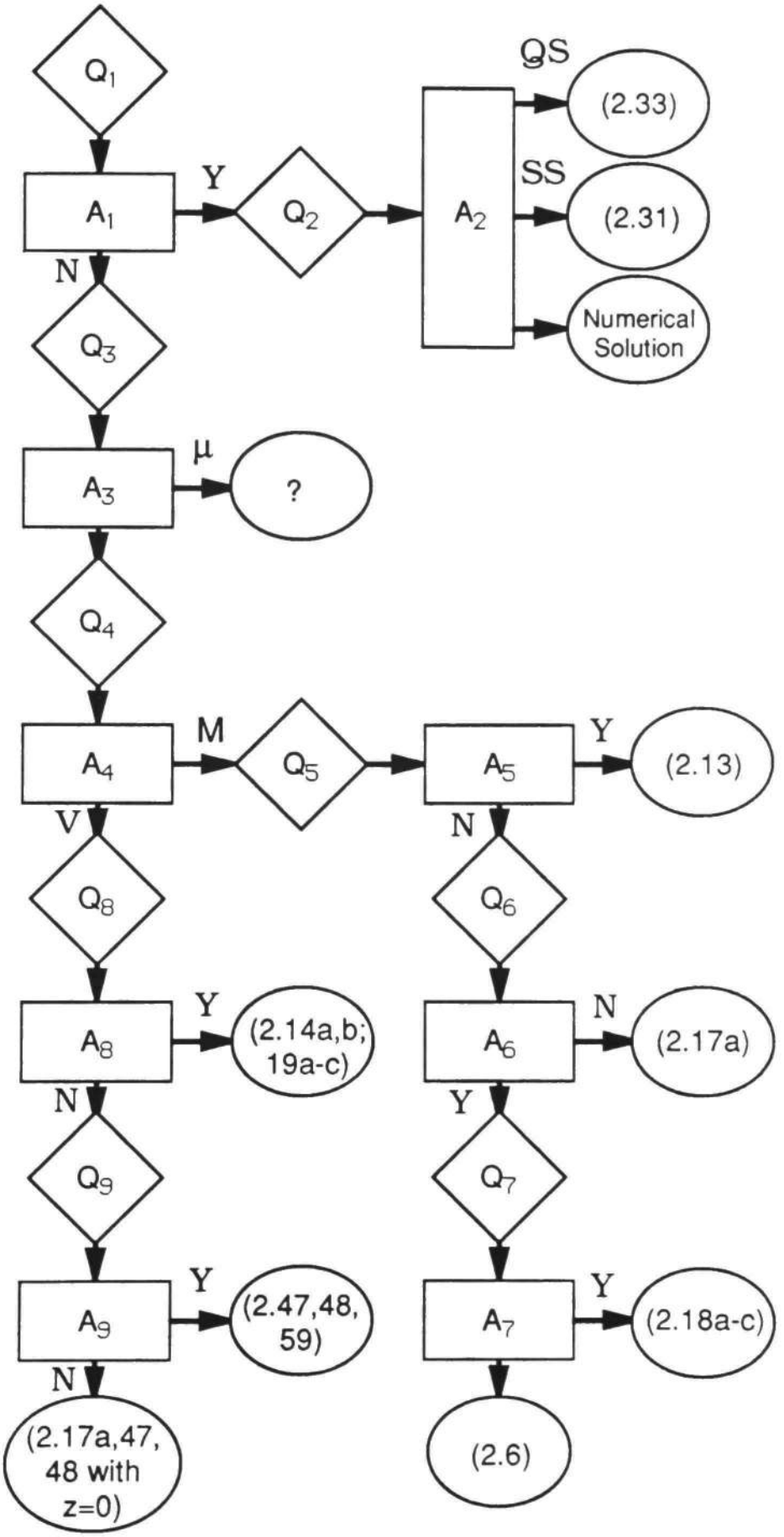

Fig. 2.7 Flowchart of Erosion Solution Selection.

Q_1: Is EJH dominant?

A_1: Eq. (2.20a), Eqn's. (2.26a)-(2.30b) and Appendix E

Q_2: Transient, Quasi-Steady or "Steady-State?"

A_2: Observation of damage (is the radius of arc channel less than the observed molten damage, see Watson [59]), Eq. (2.32), calculation of J_e^* from Eqn's. (2.26a)-(2.30b).

Q_3: Can the erosion be considered as micro or macroscopic?

A_3: Onset condition for macroscopic phenomena is in Eqn's. (2.15) and (2.24a).

Q_4: Is the erosion primarily by vaporization or molten material removal?

A_4: Eqn's. (2.19f) and (2.24c); surface features, debris.

Q_5: Is the heat flux constant?

A_5: The current pulse determines the nature of the heat flux.

Q_6: Is the depth of melting small with respect to the diffusion length?

A_6: Eqn's. (2.4) and (2.5).

Q_7: Is the material ablated?

A_7: Chapter 3, Eqn's. (2.34)-(2.40b).

Q_8: For the vapor case, is the heat flux constant?

A_8: The current pulse determines the nature of the heat flux.

Q_9: For the vapor case, is the depth of melting small with respect to the diffusion length?

A_9: Eqn's. (2.4) and (2.5).

The following solutions result from the results of the answers as indicated in Fig. 2.7, namely:

A_2 (transient): Numerical solution must be implemented on computer, for example see Dixon et al. [60]

A_2 (quasisteady): Eq. (2.33)

A_2 (steady state): Eq. (2.31)

A_3 (microscopic): Not considered in detail in this work, but erosion scales with Q_{eff} (see Chapter 4)

A_5 (yes): Eq. (2.13)

A_6 (no): Eq. (2.17a)

A_7 (yes): Eqn's. (2.18a-c)

A_7 (no): Eq. (2.6)

A_8 (yes): Eqn's. (2.14a,b) and (2.19a-c)

A_9 (yes): Eqn's. (2.47),(2.48) and (2.59)

A_9 (no): Eq. (2.17a) with z=0, T_s instead of T_{mp} and Eqn's. (2.47) and (2.48)

In some cases the results represent a bound on the magnitude of the erosion. Examples of the use of these equations are given in Chapter 4. For other examples, see the chapter written by Belkin in Butkevich et al. [17].

Note: in the above procedure several mechanisms were not considered; solid material removal mechanisms, rep-rate, arc motion etc. Except in the case of catastrophic failure, the solid material removal usually appears as an enhancement of the erosion in the ablation mode (Eq.(2.18a)). Its effect could be included by replacing the amount of energy required to heat the metal to the molten state with the amount of energy needed to heat a mixture of molten and solid material. In other words $\rho(cT_m+L_f)$ in Eq. (2.18a) could be multiplied by a fraction which reflects the reduction in energy required to melt the mixture. The effect of rep-rate can be simulated by calculating the effective initial surface temperature in the steady state using Eqn's. (2.20b and c) and using this value for T_o in any of the equations used for solutions. Equations (2.21a-h) may be used for the conditions specified earlier. The effects of arc motion will be discussed in Appendix E in conjunction with the results presented in Chapter 4.

References

[1] G.S. Belkin and V.Ya. Kiselev, "Electrode Erosion in Pulsed High-Current Discharges," *Sov. Phys. Tech. Phys.*, vol. 11(2), pp. 280-286, 1966. (EE-1038)*

[2] J. Barber, IAP Research Inc., Dayton OH, Personal Communication, June 1986.

[3] H. Akiyama, M. Kristiansen, M.O. Hagler and B. Maas, "Current Voltage Characteristics of a High-Current Pulsed Discharge in Air," *IEEE Trans. on Plasma Science*, vol. 16, pp. 312-316, 1988. (EE-0228)

[4] R. Holmes, "Electrode Phenomena," chapter 11 in *Electric Breakdown of Gases*," J.M. Meek and S.D. Craggs, eds., John Wiley and Sons, New York, NY, pp. 839-867, 1978. (EE-0081)

[5] T.G. Engel, A.L. Donaldson and M. Kristiansen, "The Pulsed Discharge Resistance and Its Functional Behavior," *IEEE Trans. on Plasma Science*, vol. 17(2), pp. 323-329, 1989. (EE-0160)

[6] I.I. Kalyatskiy, V.I. Kurets and E.N. Tarakanovskiy, "The Relationship of Heat Fluxes Entering the Electrode Surfaces During Breakdown of Solids by Pulse Discharges," *Elek. Obrab. Mater.*, vol. 4(4), pp. 45-48, 1976. (EE-1012)

[7] M.A. Sultanov, "Adequacy of the Process of Ablation of Metals Under the Effect of Laser Radiation," *Fiz. Khim. Obrab. Mater.*, vol. 18, pp. 404-405, 1984. (EE-0114)

[8] M.A. Sultanov, "Hydrodynamic Processes in a High-Power Pulsed Discharge," *Sov. Phys. Tech. Phys.*, vol. 21, pp. 815-914, 1976. (EE-0007)

[9] A.L. Donaldson, M. Kristiansen, H. Krompholz, M.O. Hagler, L.L. Hatfield, G.R. Leiker, P.K. Predecki and G.L. Jackson, "Analysis of Electrode Surface Damage in High Energy Spark Gaps," *Proceedings of the 5th IEEE Int. Pulsed Power Conf.*, Arlington, VA, 1985. (EE-1131)

[10] L.B. Gordon, M. Kristiansen, M.O. Hagler, H.C. Kirbie, R.M. Ness, L.L. Hatfield and J.N. Marx, "Material Studies in a High Energy Spark Gap," *IEEE Trans. on Plasma Science*, vol. PS-10(4), pp. 286-293, 1982. (EE-0778)

* EE number refers to the author's annotated bibliography number. These numbers should be used in all correspondence with the author.

[11] R. Behrisch, "Surface Erosion from Plasma Materials Interaction," *J. of Nuclear Materials*, vol. 85, pp. 1047-1061, 1979. (EE-0806)

[12] R.N. Szente, R.J. Munz and M.G. Drouet, "Effect of the Arc Velocity on the Cathode Erosion Rate in Argon-Nitrogen Mixtures," *J. Phys. D: Appl. Phys.*, vol. 20, pp. 747-56, 1987. (EE-0790)

[13] G.S. Belkin, V.Ya. Kiselev and I.D. Finogenova, "Metal Rupture Under the Effect of Concentrated Heat Fluxes," *Sov. J. of Eng. Phys.*, vol. 22(1), pp. 142-146, 1972. (EE-0426)

[14] G.S. Belkin and V.Ya. Kiselev, "On the Selection of the Average/Mean Values of the Thermophysical Parameters During Calculations of Thermal Processes on the Contacts," *Transactions of MEI*, High Voltage Engineering, vol. 114, pp. 83-85, 1972. (EE-1052-228)

[15] K.R. Cramer and W.C. Roman, "Electrode Design Based on Transient Thermal Analysis," *Proceedings of the ASME Winter Annual Meeting*, Los Angeles, CA, Nov. 16-20, pp. 1-3, 1969. (EE-0811)

[16] B.Ya Lyubov and E.N. Sobol, "Heat Transfer Processes in Phase Conversions Under the Action of Intense Energy Fluxes," *Sov. J. of Eng. Phys.*, vol. 45(4), pp. 670-686, 1983. (EE-0342)

[17] G.V. Butkevich, G.S. Belkin, N.A. Vedeshenkov and M.A. Zharvorankov, *Electrical Erosion of High Current Contacts and Electrodes*, M.: Energy, pp. 1-256, 1978. (EE-1052)

[18] G.S. Belkin, "Dependence of Electrode Erosion on Heat Flux and Duration of Current Flow," *Sov. Phys. Tech. Phys.*, vol. 15(7), pp. 1167-1170, 1971. (EE-0435)

[19] G.S. Belkin, "Methodology of Calculating Erosion of High Current Contacts During Action of an Electrical Arc," *Trans. of Electrichestro*, vol. ?(1), pp. 61-64, 1972. FSTC-HT-0787-85. (EE-0870)

[20] G.S. Belkin, "Methods of Approximate Calculations of Erosion Values of Electrodes in Discharges for Switching Large Pulse Currents," *Fiz. Khim. Obrab. Mater.*, vol. 1, pp. 33-39, 1974. (EE-0430)

[21] A.G. Zingerman, "Thermal Theory of the Electrical Erosion of Metals," Trans. of *Izvestiya Vyssykh Uchebnytch Azvedeniy. Elecktromekhanika*, vol. 5(1), pp. 87-98, 1960. FSTC-NT-1427-85. (EE-0352)

[22] W. Dixon, R.C. McCallen, S-W. Kang and R.S. Hawke, "Radiation Induced Ablation for Various Railgun Materials," *LLNL Report # UCID-20902*, Oct. 31, 1986. (EE-0950)

[23] T.F. Zien, "Integral Solutions of Ablation Problems with Time Dependent Heat Flux," *AIAA Journal*, vol. 16(12), pp. 1287-1295, 1978. (EE-0744).

[24] A.G. Goloveiko, "Thermal Processes at the Anode During An Intense Pulsed Discharge," *Sov. J. of Eng. Phys.*, vol. 15(6), pp. 1000-1008, 1968. (EE-0344)

[25] A. Watson, "Electrode Damage from Strong Transient Arcs Due to Surface Material Displaced by Hydromagnetic Flow, I-Basic Principles," to be resubmitted to the *J. of Appl. Phys.*. (EE-0493)

[26] G. Ecker, *Ergebnisse der exakten Naturwissenschaften*, vol. 33, pp. 1-114, 1961. (EE-0833)

[27] G.S. Belkin and V.Ya. Kiselev, "Effect of the Medium on the Electrical Erosion of Electrodes at High Currents," *Sov. Phys. Tech. Phys.*, vol. 23(1), pp. 24-27, 1978. (EE-0402)

[28] B.A. Osadin, "Erosion of the Anode in a Heavy-Current Discharge in Vacuum," *High Temperature Phys. (USSR)*, vol. 3(6), pp. 849-854, 1965. (EE-0345)

[29] S.D. Raezer, "Heat Transfer in Rotated Arcs with Water-Cooled Electrodes," *John Hopkins University Applied Physics Laboratory*, Report # CF-2957, Dec. 5, 1961. (EE-0213)

[30] B.N. Zolotykh, "The Nature of Energy Transfer to Electrodes in a Pulse Discharge with Small Gaps," In the book: *Electrical Contacts*, M: Energy, pp. 5-20, 1964. NASA # TTF-339. (EE-0005)

[31] A.S. Zingerman, "Mechanism of Electrical Erosion," Trans. of *Izvestiya Vysshikh Uchebnykh Zavedeniy. Fizika*. vol. 8(1), pp. 21-30, 1963. FTD-TT-65-950/1+2. (EE-0729)

[32] V.E. Il'in and S.V. Lebedev, "Destruction of Electrodes by Electric Discharges of High Current Density," *Sov. Phys. Tech. Phys*. vol. 7(8), pp. 717-723, 1963. (EE-0339)

[33] B.N. Zolotykh, "The Mechanism of Electrical Erosion of Metals in Liquid Dielectric Medium," *Sov. Phys. Tech. Phys*. vol. 3(12), pp. 1370-1372, 1959. (EE-0749)

[34] K. Schoenbach and H. Fischer, "Explosive Anode Erosion in High Current Sparks," *Applied Optics*, vol. 9, pp. 1695-1697, 1970. (EE-0065)

[35] G.W. McClure, "Plasma Expansion as a Cause of Metal Displacement in Vacuum-Arc Cathode Spots," *J. of Appl. Phys.*, vol. 45(5), pp. 2078-2084, 1974. (EE-0738)

[36] A. Watson, A.L. Donaldson, K. Ikuta and M. Kristiansen, "Mechanism of Electrode Surface Damage and Material Removal in High Current Discharges," *IEEE Trans. on Magnetics*, vol. T-MAG-22, pp. 1779-1803, 1986. (EE-0331)

[37] R.A. Petr and T.R. Burkes, "Erosion of Spark Gap Electrodes," *IEEE Trans. on Plasma Science*, vol. PS-8(3), pp. 149-153, 1980. (EE-0740)

[38] A.L. Donaldson, E. Kristiansen, M. Kristiansen, A. Watson, K. Zinsmeyer, "Electrode Erosion in High Current, High Energy Spark Gaps," *IEEE Trans. on Magnetics*, vol. T-MAG-22, pp. 1441-1447, 1986. (EE-1030)

[39] M.A. Sultanov and L.I. Kiselevskii, "The Mechanism of the Electrode Erosion Produced by Supersonic Flares in a Pulsed Discharge," *High Temperature Phys. (USSR)*, vol. 4(3), pp. 375-379, 1966. (EE-0120)

[40] B.N. Zolotykh, I.P. Korobova and E.M. Strygin, "Contribution of Mechanical Factors to the Erosion Process During Pulse Discharge," Trans. from *Elektronnaya Obrabotka Materialov*, vol. ?(5), pp. 16-24, 1966. (EE-0736)

[41] V.I. Rakhovskii and A.M. Yagudaev, "Electrode Erosion Mechanism in a Pulsed Vacuum Discharge," *Sov. Phys. Tech. Phys.*, vol. 14(2), pp. 227-230, 1969. (EE-0739)

[42] S.N. Kapel'yan, "Fracture of Material Through the Action of an Internal Heat Source," *Sov. J. of Eng. Phys.*, vol. 32(4), pp. 723-728, 1977. (EE-0733)

[43] E.W. Gray and J.R. Pharney, "Electrode Erosion by Particle Ejection in Low-Current Arcs," *J. of Appl. Phys.*, vol. 45 (2), pp. 667-671, 1974. (EE-0743)

[44] Y. Udris "On the Emission of Cathode Material Particles in Low Pressure Arc Discharges", *Proceedings of the 2nd International Conference on Gas Discharges*, IEE, London, pp. 108-112, 1970. (EE-0747)

[45] D.J. Rasty, B. Laub and E.K. Chu, "Modeling of Thermostructural Response of Graphite Materials to High Intensity Laser Heating," *Proceedings of the 27th Aerospace Sciences Meeting*, Reno, Nevada, AIAA paper # 89-0176, 1989. (EE-0724)

[46] P. Predecki, "Investigation of Composite Materials for Repetitive Spark Gap Switch Electrodes," University of Denver, Proposal, 1983. (EE-0906)

[47] C.W. Kimblin, "Erosion and Ionization in the Cathode Spot Regions of Vacuum Arcs," *J. of Applied Phys.*, vol. 44(7), pp. 1078-1973. (EE-1078)

[48] D. Stevenson, "Survey of Candidate Railgun Bore Materials, Railgun Materials Experience, and Arc-Bore Damage Mechanisms," *Sparta, Inc.*, Del Mar, CA, Report # DM-86-02-TR, 1986. (EE-0920)

[49] S.V. Lebedev, "Title Unknown," *Izv. AN Arm. SSR*, vol. ?(3), pp. 33-?, 1950. (EE-0339-2)

[50] R.C. Weast, ed., "*CRC Handbook of Chemistry and Physics*," CRC Press, Boca Rotan, FL, 61st edition, pp. D-218, 219, 1989.

[51] H.S. Carslaw and J.C. Jaeger, *Conduction of Heat in Solids*, Oxford University Press, London, UK, 1959.

[52] Dr. H. Carper, private communication, 1990.

[53] J.G. Gilligan and D. Hahn, "The Magnetic Vapor Shield (MVS) Mechanism for Protection of High-Heat Flux Components in High-Field Tokamaks," *J. of Nuclear Materials*, vol. 145, pp. 391-395, 1987. (EE-0770)

[54] R. Holm, "The Vaporization of the Cathode in the Electric Arc," *J. of Appl. Phys.*, vol. 20, pp. 715-716, 1949. (EE-0373)

[55] F. Llewellyn-Jones, "Electrode Erosion by Spark Discharges," *British J. of Appl. Phys.*, vol. (1), pp. 60-68, 1950. (EE-0424)

[56] J.D. Cobine and E.E. Burger, "Analysis of Electrode Phenomena in the High-Current Arc," *J. of Appl. Phys.*, vol. 26(7), pp. 895-904, 1955. (EE-0422)

[57] G.S. Belkin, "Vaporization of Metal Electrodes by Pulsed Currents," *Sov. Phys. Tech. Phys.*, vol. 13(9), pp. 1256-1260, 1968. (EE-0429)

[58] A.G. Goloveiko, "Pulsed Action of Intense Heat Fluxes and Volume Heat Sources on Metals," *Sov. J. of Eng. Phys.*, vol. 13(2), pp. 124-130, 1967. (EE-0349)

[59] A. Watson, "Fast Rising Heavy Current Spark Damage to Electrodes," *Proceedings of the 2nd IEEE Int. Pulsed Power Conf.*, Lubbock, TX, June, 1979, pp. 471-474. (EE-0737)

[60] W.R. Dixon, "Ablation Analysis for Plasma Armature Railgun Bores," A set of viewgraphs obtained from the author. *Lawrence Livermore National Laboratory*, Livermore, CA, 1986. (EE-0949)

CHAPTER III

THE EFFECT OF ELECTRODE JETS ON ELECTRODE EROSION IN HIGH CURRENT, HIGH ENERGY, TRANSIENT ARCS

This Chapter begins with a listing of the symbols and their definitions. All units are MKSA.

Nomenclature and Abbreviations

A_t [m^2] - area on target for which the jet is retarded

B [Wb/m^2] - magnetic flux density

c [J/kg°C] - specific heat

c_j [J/kg°C] - specific heat of the jet

c_{mp} [J/kg°C] - specific heat at the melting temperature at constant pressure

c_p [J/kg°C] - specific heat at constant pressure

c_v [J/kg°C] - specific heat at constant volume

c_{va} [J/kg°C] - specific heat of the anode vapor

d [m] - electrode diameter

d_m [m] - depth of molten electrode material

DV_+ [cm^3] - erosion of the electrode which is the anode in the first half cycle

DV_- [cm^3] - erosion of the electrode which is the cathode in the first half cycle

DV_{tot} [cm^3] - total erosion of both electrodes

$DV_{\%e}$ - percentage error in total erosion due to measurement error

$DV_{sb\%e}$ - percentage error in V_{sb} corresponding to one standard deviation in the V_{sb} values

δ - overheating factor

e [C] - electron charge

EJE - electrode jet erosion

η [N/m^2] - viscosity of the liquid metal

f_1 [$A^2s^{1.5}$] - an erosion factor derived in Chapter 4 from a thermal model

g [kg/C] - vaporization rate at the electrode surface

γ - ratio of the specific heats, c_p/c_v

HCHETA - high current, high energy transient arcs

I [A] - arc current

I_p [A] - peak current

j [A/m^2] - current density

k_b [J/°K] - Boltzmann's constant

k_c - jet concentration coefficient

k_f - coefficient of friction

k_t [W/m°K] - thermal conductivity

L_f [J/kg] - latent heat of fusion

L_s [J/kg] - latent heat of sublimation

L_v [J/kg] - latent heat of vaporization

m [kg/s] - mass evaporation rate at the electrode surface

m_j [kg] - jet mass

M_a - Mach number, v_j/v_s

M_I [$m/s^{1.5}$] - the "impulsivity" of a material

M_{Il} [$m/s^{1.5}$] - the liquid "impulsivity" of a material

M_{Is} [$m/s^{1.5}$] - the sublimation "impulsivity" of a material

M_{Iv} [$m/s^{1.5}$] - the vaporization "impulsivity" of a material

μ_o [H/m] - magnetic permeability of free space

n_1 [m^{-3}] - electron density at the maximum in the "hump" potential

n_2 [m^{-3}] - electron density at the minimum in the "hump" potential

n_s - a constant indicating the power dependence of erosion on gap spacing

p [N/m^2] - switch pressure

p_t [N/m^2] - pressure in the shock compressed region in front of the target

p_v [N/m^2] - viscous pressure at the liquid-solid interface on the target

Φ_a [eV] - anode work function

q [W/m^2] - heat flux at the electrode surface

q_j [W/m^2] - jet heat flux

q_m [W/m^2] - maximum heat flux on axis

Q_j [J] - energy required to convert a solid into a vapor at a given velocity

Q_m [J] - energy required to heat a material to its melting temperature

Q_v [J] - energy required to heat a material from melting to boiling temperature

r [m] - distance from the axis on the target

ρ [kg/m^3] - total density

ρ_j [kg/m^3] - jet density

s [m] - gap spacing

t_j [s] - action time of the jet

t_p [s] - pulse time

t_{pk} [s] - time to peak current

$t_{v,s}$ [s] - time to vaporize or sublimate the electrode surface

T_a [°K] - arc temperature

T_b [°K] - boiling temperature

T_{eff} [°K] - an effective melting temperature

T_j [°K] - jet temperature

T_{mp} [°K] - melting temperature

T_t [°K] - target temperature

U_{th} [eV] - electron thermal energy

v_1 [m/s] - initial jet velocity at the maximum in the "hump" potential

v_j [m/s] - jet velocity

v_m [m/s] - velocity of the molten metal at the target surface

v_s [m/s] - sound velocity

V_a [V] - anode voltage "fall"

V_c [V] - cathode voltage "fall"

V_f [v] - "fall" voltage (anode or cathode)

V_n [V] - portion of the arc column voltage which is utilized for jet acceleration

V_p [V] - voltage drop across the arc column

V_{sb} [kV] - self-breakdown voltage

W_t [J] - the amount of jet energy transferred to the target

z_s [m] - depth of the target solid layer which can be removed by viscous effects

Introduction

During current conduction in spark gaps having high current, high energy, transient arcs, (HCHETA), directed streams of ionized electrode vapor emerge from the space adjacent to the electrode surfaces. As the streams pass through the cathode and anode fall regions of the arc, they are thought to become superheated (0.3 - 4 x 10^4°K) and achieve supersonic velocities (1-20 km/s), thus, the term "jets" is used. In addition they may interact directly with the opposite electrode surface or indirectly via the formation of oscillating high density disc-shaped plasma regions resulting from anode and cathode jet interaction. The discovery of the existence of the jets has been documented by Sukhodrev [1] to have occurred as early as 1862 [2]. Their existence has found important applications as diverse as an aide for cutting and welding [3], igniters of internal combustion engines [4], plasma torch furnaces [5], stabilization of linear z-pinches [6], and most recently as

a means for accelerating projectiles in electrothermal launchers [7-8]. However, the sole emphasis of this chapter is the description of the role these electrode jets play in the heating and removal of electrode material.

One might ask why such an emphasis was placed on this sole potential mechanism for electrode erosion. At least four reasons exist:

1) A review of foreign literature, primarily Soviet, indicated that there was considerable evidence which showed that under certain conditions electrode jets were the dominant source of material removal and possibly electrode heating as well.

2) The electrode jet erosion mechanism (EJE) was not intuitively obvious as a means of electrode erosion as a result of it being an indirect phenomenon. This is really understating its apparent obscurity--the author himself only considered EJE after having found it discussed in the foreign literature and this after three years of examining the erosion problem. Not to mention that every paper the author found published in English failed to discuss EJE as a means of erosion. (A few mentioned the jets as a source of erosion in the direct sense, i.e., that the jet material itself represented eroded mass).

3) The EJE mechanism had the potential of explaining several phenomena observed in previous erosion experiments, the effect of distance and the effect of the material of the opposite electrode being two examples.

4) It seemed possible to verify the existence of the jets and possibly their effect on erosion for the conditions encountered in the high current, high energy regime with some fairly simple experiments.

Given this situation, it was decided that a review of the literature on electrode jets was needed as well as selecting and performing a set of experiments which would verify the existence and determine the effect of electrode jets on electrode erosion in HCHETA.

The literature review was to identify jet properties, such as temperature, density, velocity and structure, theories for jet production and acceleration mechanisms, and the various jet-jet and jet-electrode interaction phenomena which would lead to material heating and removal. Although, initially any paper discussing the electrode jets was examined (over 100 in all), primarily those papers which had conditions of high current, > 1 kA, or high energy, > 1 kJ, were utilized in the various summaries. The few exceptions had unusual or unique features which made them relevant. The review was performed and the results are presented in the first part of this chapter. From this review a set of experiments was designed and performed which served to verify the existence of EJE in HCHETA. The results of these experiments, which indicate EJE is very important under certain conditions, are given and discussed in the latter part of the chapter.

Summary of Previous Work

Determining the influence of electrode jets on electrode erosion requires the understanding of the mechanisms of jet formation and their acceleration, propagation and the jet-electrode and the jet-jet interaction. In order to substantiate the existence and nature of these mechanisms, and to apply this information to actual jet electrode erosion data, the physical properties of the jet (temperature, density and velocity as a function of space and time) need to be determined or estimated for different discharge conditions. Fortunately, many experiments have been performed which examined some of the jet properties and trends that are most likely to be applicable to high energy or high current transient arcs. It is important to remember that some of these properties are experiment specific and in general are not true for an entire range of experimental parameters. Table 3.1 contains a summary of the experimental conditions which were used to determine various trends and properties of the electrode jets.

Jet Properties

The jets initially start off at the temperature of the electrode surface which may be considerably higher than the boiling point of the electrode material because of the high localized pressures. As they leave the electrode surface the jets expand and are cooled, as evidenced in photographic

Table 3.1 Summary of the Conditions of Electrode Jet Property Experiments

Experimentor(s)	Year	CRN*	Medium	Electrode Materials	Pulse Condition	Misc.
Sobolev	1943	9,0094-6	?	?	?	
Haynes	1948	10,0072	0.066-2 atm H_2	Hg(l), Mo	0.2kA, $\leq$ 5 us	
Mandel'shtam & Raiskii	1949	11,0094	1 atm air, water	Cu, Al, Fe, Mg	10 kA, 0.05 J	
Skeats & Schuck	1954	12,0004	1 atm air	?	15 kA, 60 Hz	
Lee et al.	1957	13,0003	1 atm air	Cu	17 kA	
Sukhodrev & Mandel'shtam	1959	14,0129	1 atm air	Sn	2-10 kJ	
Hermoch	1959	15,0127	?	17 diff.	2 kA	
Grechikhin & Min'ko	1963	16,0122	1 atm air	?	0.2 kJ	1
Ogurtsova et al.	1963	17,0856		Al	300 kA/cm^2	2
Gurov et al.	1964	18,0381	5 x 10^{-5}mm	8 diff.	17 kA, 0.6 kJ	
Kiselevskii & Sultanov	1966	19,0088	1 atm air	Cu	3.6 kJ	
Sultanov & Kiselevskii	1966	20,0121	1 atm air	Cu, Al, +?	6 kA, 0.9 kJ, 70 us	1
Grechikhin & Min'ko	1967	21,0116	?	Cu, Al, Zn	1.3 kJ, 200 us	3

Table 3.1, continued

Experimentor(s)	Year	CRN*	Medium	Electrode Materials	Pulse Condition	Misc.
Balagurov et al.	1967	22,0086	1 x 10^{-5} mm	Al	35 kA, 0.9 kJ	4
Avramenko et al.	1969	23,0087	1 atm air	Cu wires	14 kA, 2 kJ	
Jordan et al.	1970	24,0078	1 atm air	C, Fe	10 kA, 50 Hz	
Abdel-Asis	1973	25,0126	1 atm air	Cu	16 kA, 50 Hz	5
Sultanov	1974	26,0110	1 atm air	?	5.4 kJ	1
Bothwell & Grycz	1974	27,0079	1 atm air	?	40 kA	6
Rykalin et al.	1975	28,0104	0.25-1 atm Ar and He	Ni	6 kA, 650 us	
Sultanov & Semikin	1976	29,0119	1 atm air	Cu, Al	30 kA, 12 kJ 300 us	
Sultanov	1976	30,0007	1 atm air	Cu, Al, Ni, Fe	30 kA, 5.4 kJ	
Yoshiyasu et al.	1983	31,0124	1 atm air	Cu, CuW	12.5 kA, 8 ms	
Sultanov	1984	32,0114	?	?	?	3, 7
Spector et al.	1988	33,0097	2.6 x 10^{-5} atm	steel	24 kA	

*Chapter Reference Number followed by the Annotated Bibliography Reference Number

Misc.: 1 - used an aperture; 2 - used a capillary tube; 3 - used a laser; 4 - for a moving arc on rail electrodes; 5 - used separating contacts; 6 - gas flowing at Mach #0.2-0.8; 7 - collision pinched plasmas.

studies by the appearance of a dark space, and are subsequently reheated by the arc channel [14,21,23]. The jet temperature has been measured to be 3-40 x 10^3°K [9,13,14,17,21,23,29,31,33]. The lower temperatures were obtained when the jet was artificially separated from the arc channel [9]. The jet temperature falls off rapidly with distance [23].

Jet velocities of 0.5-20 km/s have been measured [15-21, 24,26,28,29,33]. In general, the velocity increases with increasing current [18], discharge energy [20,26,29], rate of current rise [34], and/or decreasing gas density [18,20,29]. For lower energy levels the initial velocity is independent of background pressure (0.066 - 2 atm) [10,28] and is not affected by the reversal of the electric field (accomplished by changing from a unipolar to an oscillatory pulse) [10].

The percentage ionization in the jet is a function of electrode material and is often quite high (50-100%) with several experimentalists observing multiply charged particles at low currents (400 A) [35-37]. The measured electron density ranges from 5-50 x 10^{17} /cm^3 [17,23,29,30,33] which is only a factor of two smaller than the theoretical and experimental densities calculated and measured near cathode spots (see references in [37]).

Jet Production and Acceleration

Although the existence of high velocity jets of electrode vapor has been known since the 1860's, the understanding of the mechanism of their production and acceleration has been a subject of considerable interest and ongoing development since that time. As early as 1940 Raiskii [38] discovered that when different materials are simultaneously present in the electrode jet then the velocities are the same, e.g., the jet plasma moves as a unit. The jets can originate from the entire vaporizing electrode surface or from individual points of arc filament attachment. The thermal energy required for jet production is thought to be supplied by electrode or arc joule heating. The frequency of jet emission is high (0.1-10 MHz) resulting from the transient (explosive) nature of each arc filament attachment site [26]. The individual microjets may combine to form a collective macrojet whose velocity is less than the microjet velocity as evidenced by a fine structure on high resolution streak photographs [24,26,32]. In general, the frequency and velocity of jet emission is a function of electrode material, polarity and pulse energy [30]. The jet direction has always been found to be perpendicular to the electrode surface (within a small solid angle and assuming that no external effects, magnetic field, etc., were allowed to influence them) regardless of the angle of the electric field gradient of the arc column [10,12,52]. This result attests to the fact that a large

power impulse to the jet is acquired at the electrode surface. The amount of material released increases with increasing discharge voltage [16].

Following the example of Ecker [39] the jet acceleration mechanisms can be divided into three groups: gas dynamic (GD), where energy is supplied by directed collisions; magnetohydrodynamic (MHD), where energy is supplied by the self magnetic field; and electrodynamic (ED), where energy is supplied by the electric field (either micro or macroscopic). A listing of the jet velocity expressions resulting from most of the proposed accelerating mechanisms is given in Table 3.2. A brief description of each mechanism is given below. To aide in the discussion a graph of the gap potential as a function of gap distance is shown in Fig. 3.1. This graph is taken from Miller [47] and Juttner [49] for a stationary vacuum arc. The author knows of no equivalent graph for high pressure transient discharges.

Finkelnburg [40] proposed that the vapor coming off the electrode surface is heated by collisions in the near electrode plasma and undergoes isobaric expansion in a preferential direction (determined by the electrode surface, i.e., perpendicular to it). Maecker [41] suggested than an axial pressure gradient is produced by plasma pinching from the self-magnetic field. Ecker [39] combined these and numerous other mechanisms known at that time into a single steady-state model. For high current discharges, > 1 kA, the

Table 3.2 A Summary of Jet Velocity Equations

Reference/Accelerating Mechanism*	Velocity Expression
Finkelnburg, 1948 [40], GD	$jV_c/Q_j\rho_j$
Maecker, 1955 [41], MHD	see Holmes
Ecker, 1961 [39], GD & MHD	see simplification by Holmes
Sukhodrev, 1962 [1], GD	$(2(jV_ct-W_c-W_e)/d_m\rho_j)^{0.5}$ where $W_c=2T_b(k_t\rho c_pt/\pi)^{0.5}$ and $W_e=(Q_h+L_m+Q_v+L_v)d_m\rho_j$
Plyutto et al., 1965 [42], EDA	see Moizhes and Nemchinskii with Z=0
Schoenbach, 1971 [34], EGD1+	$2(c_{va}T_a-L_v)^{0.5}$, where $T_a=\pi 10^4(k_t\rho c_p)^{0.5}(V_a+\Phi_a/e+U_{th}/e)((I_p/t_{pk})^{0.33})/4$
Holmes, 1972 [43], GD & MHD	$((j/\rho_j)(\mu_oI/2\pi+g^2j/\rho_j))^{0.5}$
Lyubimov, 1975 [44], EDC	$(2IV_n/m)^{0.5}$
Moizhes and Nemchinskii, 1980 [45], EDA	$(2(Z+1)kT_j\ln(n_1/n_2)/m_j+v_1^2)^{0.5}$
Mesyats, 1982 [46], EGD2	$(4L_s\delta\gamma/(\gamma-1))^{0.5}$

*GD - gasdynamic
MHD - magnetohydrodynamic
EDA - electrodynamic ambipolar
EDG1 - explosive gas dynamic arc heating
EDC - electrodynamic column collisions
EGD2 - explosive gas dynamic electrode heating
+ - for times less than t_{pk} the expression I_p/t_{pk} should be replaced by the current at that time divided by the time.

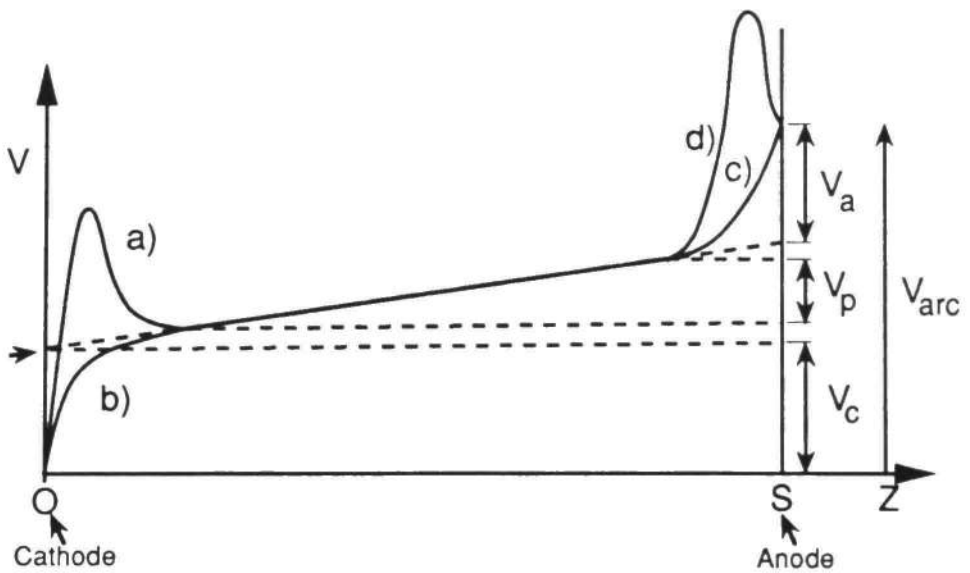

Fig. 3.1 Gap Potential for a Vacuum Arc by Region and Model. (a) - potential "hump" models [42,45,48], b) -standard models [10,40,44], c) no anode spot (lower current and di/dt) [47], d) anode spot (higher current and di/dt) [47]) Note: The location of the top of V_c at z = 0 and the bottom of V_a at z = s are determined by extending the arc voltage line between z_2 and z_3 to z = 0 and z = s.

simplification of Ecker's equations by Holmes [43] may be used to calculate the jet velocities. (Actual calculations will be shown in the results section of this chapter.) The critical parameter in Ecker's model was j/ρ_j. For high j/ρ_j the gas dynamic forces are dominant and for low j/ρ_j the magnetic forces dominate. The effect of current was most dramatic at low j/ρ_j with larger currents resulting in higher velocities, as expected. Sukhodrev [1] calculated the jet velocity, the depth of molten electrode material and the local pressure increase at the electrode surface as a function of time. He included the effect of arc joule heating of the electrode and electrode conduction losses while showing that the effect of electrode joule heating could be ignored. His calculations are in good agreement with experimental results. Plyutto [42] predicts ambipolar acceleration of ions by electrons which assumes the existence of a potential "hump" in the near electrode plasma as shown in Fig. 3.1. Moizhes and Nemchinskii's mechanism [46] is also ambipolar diffusion but their expression for ion energy gain includes a charge multiplication factor, Z+1. Osadin [49] discusses a "quasi-electrostatic" acceleration of ions by a potential "hump" when an "anisotropic plasma layer containing electrons participate in collective oscillatory motion across the layer." Unfortunately, only an abstract of this work was available for comparison. Lyubimov [44] dismisses the idea of a potential "hump" but instead proposes

collisional transfer of energy by electrons to ions in the arc column. Schoenbach [34] suggests that high pressures at the electrode surface enable electrode temperatures greater than the boiling point to exist which result in high internal energies at the electrode surface. When the arc channel expands the rapid drop in pressure causes a sudden release of vapor (explosion). Because of the transient nature of this model the velocity expression is only valid up to the peak time, t_{pk}. Mesyats [46] also relies on large internal energies at the electrode surface to produce an "explosion," however, unlike Schoenbach, his overheating is simply expressed as an overheating factor which is the result of rapid electrode joule heating occurring at the arc filament attachment sites. Unfortunately, most of these expressions have at least one parameter which is hard to determine, namely, ρ_j [1,39-41,43], δ [46], c_{va} [34], $n_{1,2}$ and m_j [42,45], m and V_n [44], Q_j [39], and j [1,39-41,43]. However, in theory, one could compare the predictions of two models which have the same uncertain parameter.

Table 3.3 attempts to clarify these models by including the regions (Fig. 3.1) in space, with respect to the gap potential, where the accelerations discussed take place. For further details the reader is referred to the original papers or the reviews by Haynes [10], Ecker [39], Kesaev [50], Holmes [43], Rakhovskii [51], Butkevich et al. [52], Lyubimov and Rakhovskii [53], and Juttner [49]. It is worth noting that the last two reviews come to conflicting

Table 3.3 Jet Mechanisms by Region

Mechanism	Region	References
Jet Production	0	[1,16,26,30,34,39,46]
Jet Acceleration	0	[1,34,39,46]
	$0-z_2$	[10,39,40,41]
	z_1-z_2	[42,45]
	z_2-z_3	[44,53]
Jet Propagation	z_2-s	[10-12,16,19-22,24-26,29-32,38]
Jet-Electrode Interaction	s	[54-70]

conclusions, namely that the potential "hump" is "extremely artificial" [53] or that it may be very important [49]. It is also very important to keep in mind that many of the calculations which were used to determine the importance of one particular mechanism or another are highly sensitive to current magnitudes. For example, Lyubimov [37] concludes quite correctly that the MHD term may be negligible for hundreds of amperes, however, comparable calculations made in the results section by the author for I_p = 300 kA reveal that MHD forces may indeed dominate.

Jet Propagation and Interaction

In general, jet propagation should be a function of discharge medium density and pressure, gap spacing, and the likelihood of interaction with other jets and obstacles. Early studies by Mandelshtam and Raiskii [11] examined various methods of inhibiting the rapid jet diffusion observed in open air. Included were: 1) the use of a capillary tube to contain one of the electrodes and 2) using water as the discharge medium. Both methods led to a substantial increase in the distance over which the jets were effective. (Note: normally one would anticipate that increasing the density of the medium the jet propagates in would lead to a decrease in effective distance (i.e., if the jet were isolated from the current and allowed to propagate into the dense medium); however, in this case, the arc channel itself was in the medium also, thus producing a

higher current density in the jet accelerating region.) Several authors also found that a periodicity exists in the jet structure in the direction of propagation out of a confined volume (e.g., an aperture or capillary tube) and that it was inversely proportional to the confined volume as well as being a function of the aperture pressure [16,20,21]. Butkevich et al. [52] report about a series of work by Bron and Sushkov for medium to high current arcs (0.1-10's of kA) in which they observe that the "plasma flows" (jets) have a "narrow, sharply outlined and acute beam appearance which testifies, without eliminating thermal processes, about the electromagnetic nature of their acceleration." Although no entrainment of the surrounding gas occurs at the electrode surface [31], the presence of high speed (Mach # 0.2-0.8) gas flow around the jet can produce a shock pattern and turbulence will occur for low currents (< 4 kA) [22]. Recently, several models have been developed which accurately describe the expansion and interaction of cathode plasma jets with background gases and anode vapor [54,55].

Perhaps one of the most important factors in jet propagation is the possible interaction with other jets and obstacles. Anode and cathode jets are emitted at different times and frequencies leading to interactions which produce regions of compression and rarefaction of the interelectrode plasma [12,19,20,25]. These regions may move back and forth at high velocities (0.1-2 km/s) between the electrodes and

may come in "contact" with the electrode surfaces, resulting in enhanced electrode erosion [29-31]. Various barriers, such as paper, ceramics, and metallic discs, have been shown to shield the jet propagation effectively [11,56]. Self-induced and externally applied magnetic fields have also been successful in "bending" the jets to such an extent that jet-jet and jet-electrode interaction could be avoided altogether [12].

Numerous experiments [54-70] have been performed to understand the nature and the importance of jet interaction with a "target" surface (which may be another electrode). To aid in the discussion of these experiments, the various experimental arrangements are shown in Fig. 3.2.

Mandelshtam and Raiskii [11] studied the effect of gap distance, jet material, jet shielding, isolation of the jet from the current conducting channel and various means of reducing the rapid jet diffusion (capillary tubes, different electrode shapes, etc. The conditions were: 0.05 J, 10 kA, air and water medium, and a dominant jet from the cathode. In all the experiments the jet effect was determined to be the dominant erosion mechanism, especially for jets produced in the spark stage (the authors distinguished a spark from an arc by whether the channel has expanded - for a spark the channel has not expanded). Copper jets had the greatest jet erosion effect of all the materials studied (Cu, Fe, Al, Mg). In general, erosion increased rapidly with decreasing gap separation in the range 0.3-4 mm.

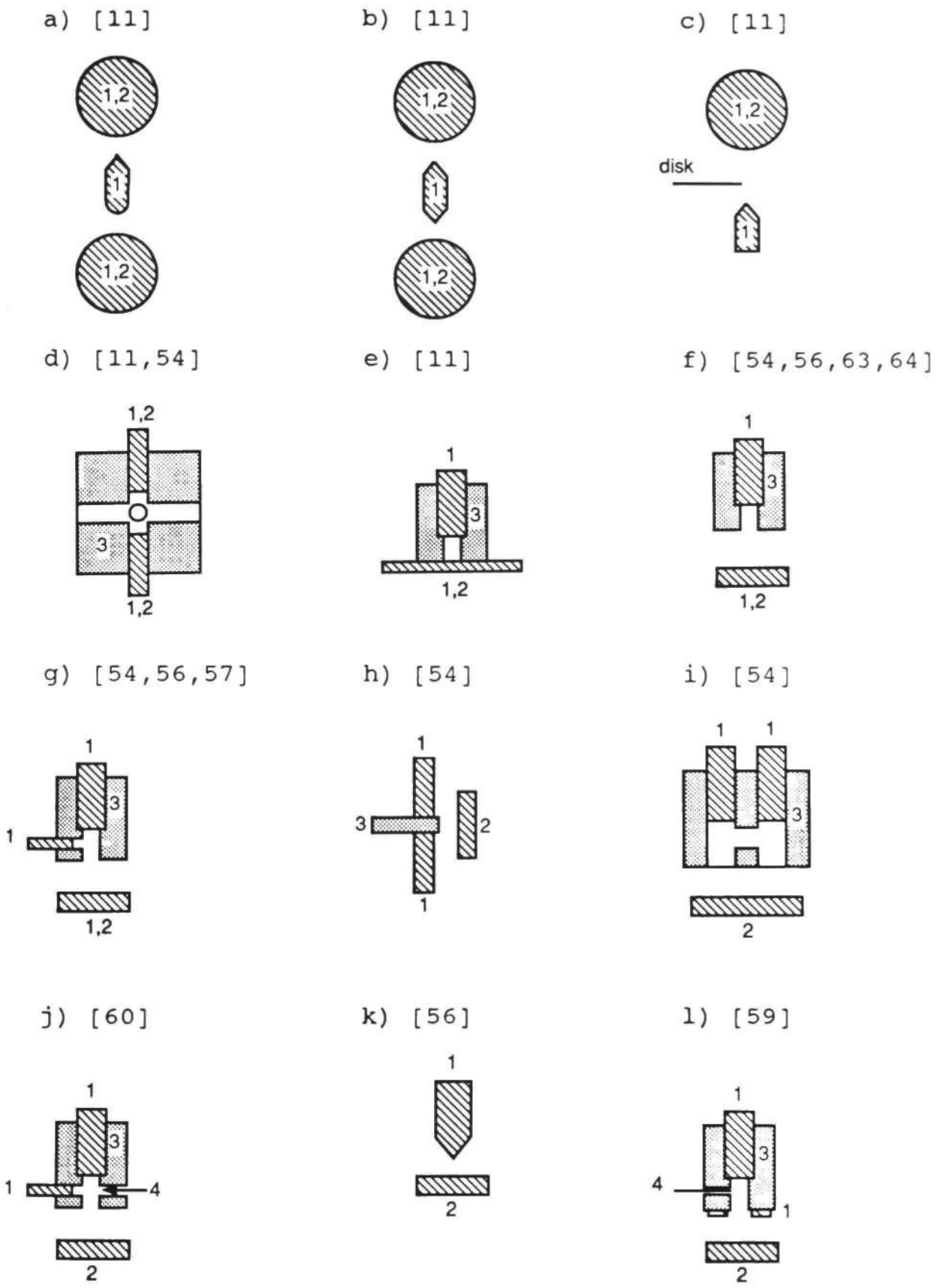

Fig. 3.2. Various Electrode Arrangements Used to Study the Jet Effect. 1 - Electrode, 2 - Target, 3 - Insulator, 4 - Trigger

Hermoch and Krticka [54] utilized several of the geometrical arrangements shown in Fig. 3.2 to study the effect of gap spacing, jet polarity, number of discharges, target and material (Al, Fe and Cu) and the use of a constricting cylindrical cavity. No pulse conditions were specified but the results showed that erosion decreased as distance increased, the anode jet could become more destructive in certain geometries (Fig. 3.2h), the erosion per discharge decreased with each shot, the materials varied in resistance to jet damage (Al<Fe<Cu), and the constricting channel greatly increased the erosion.

Zitka [55] studied the effect of gap spacing (0.001-2.0 cm), and electrode materials (Pb, Zn, Al, Fe, Cu, Sn, Ni). The experimental arrangement was not mentioned although it was some sort of spark gap in open air where one of the electrodes could be moved to expose a fresh surface between each shot. The pulse conditions were 2.5 kA, 63 J and 150 μs. The major conclusions were that the wear of any electrode is a function of the material of the opposite electrode, the amount of molten material increases rapidly with decreasing distance, the pressure formed at the electrode surface led to material expulsion, and the jets produced in the spark stage (defined as the time when the arc voltage is changing) were much more intense than during the arc stage.

The work of Afanas'yev and Goloveyko, is reported in Butkevich et al. [52]. The authors consider that the jet

reaching the opposite electrode does not destroy it mechanically but rather reduces the coefficient of surface tension at the arc spot micro-molten pool which increases the likelihood of liquid metal removal.

Sultanov and Kiselevskii [56] performed some of the first experiments which combined discharges with high current (10 kA) and high energy (3.6 kJ). The jet characteristics were t_j-80 μs, v_j-10 km/s and T_j-10^4°K. The authors gave the following equations for the energy delivered by the jet and the overpressure at the target surface (which was calculated to be 20 atm for M_a=4).

$$W_t \sim v_j T_j (1+(\gamma-1)M_a^2/2) \qquad (3\text{-}1a)$$

$$p_t = p_j[((2M_a^2-1)\gamma+1)/(\gamma+1)]. \qquad (3\text{-}1b)$$

Using three different electrode configurations they concluded that the jet melts a thin layer of the target electrode and then removes it mechanically. The target surfaces could be protected by a thin sheet of writing paper (!), or a thin layer of water or oil. If the jets were supersonic when they hit the target then erosion occurred. This required no jet interaction in the middle of the gap which in turn required asymmetric jet production. One very important result was the fact that the erosion damage pattern due to the jet only was very similar to that for the jet and the current acting together.

Morozov and Kiselevskii [57] studied the effect of supersonic plasma jets on a wide variety of materials (both metallic and non-metallic). The pulse conditions were 10-12 kA, 120 μs and 0.9 kJ. The iron jet had a T_j of $1x10^4$°K with an M_a of 3-3.5 which produced heat fluxes of 10^5 W/cm^2 and shock compressed plasma layers of $2x10^4$°K and 10's of atm at the target surface. The targets were made of Sn, Pb, Zn, Mg, Al, Cu, steel, Ni, W, paper and plastic. The erosion volume, mass and profile were measured. Results for a 1 cm gap spacing indicated that the mass loss was highly dependent on T_{mp} but not T_b which supports a molten metal removal theory. The authors found good agreement with Zitka [55] and others who measured erosion from a pulsed discharge and found that the pressures developed at the electrodes led to molten mass removal.

Belkin and Kiselev [58] studied the effect of coulomb transfer (2-100 C) on the electrode erosion of different materials in a spark gap with a gap spacing of 1.5 mm. They observed a substantial (75%) reduction in the erosion of a copper electrode when the opposite electrode was graphite, which they attributed to the change in electrode jet energy produced by the carbon electrode.

Morozov and Kiselevskii [59] continued their previous studies by examining the nature of the erosion for t_j of 80-120 μs, I_p of 8-90 kA and discharge energies of 50-1800 J. The jet velocities were 4.5 to 14 km/s, and the targets were located 4.5 mm from the jet orifice. They observed that as

the jet energy increased, the percentage of the molten metal removed from the specimen (as opposed to resolidifying) became higher. In addition, photographs were taken of the ejected molten particles which indicated that their number increased with discharge energy.

Pokrovskaya and Plokhikh [86] studied the erosion effect of copper plasma jets on a wide variety (insulators, semiconductors and metals) and large number (25) of materials. The pulse conditions were 1.4 kA, 14.1 ns and 190 J. The target materials were located 0.45 mm from the cathode which resulted in a target heat flux of 8.5×10^{14} W/cm^2. Their results showed that the jet greatly eroded metals and semiconductors, barely eroded crystalline and brittle dielectrics and produced almost no effect on plastic materials. They derived the following expression for the depth of melt from heat conduction theory which agreed nicely with experimental results (although this author could not get their calculated depth of melting, d_m, values from their table of parameters!).

$$d_m = 4(t_p)\ (k_t c/\rho\pi)^{1/2}\ (T_b/(c(T_{mp}-T_o)+L_f)). \qquad (3.2)$$

Sultanov [60] studied the effect of high velocity (6-12 km/s) jets on a wide variety of materials (more than 17 metals and non-metals). For energies up to 1.8 kJ and t_j greater than 10.0 μs the radiant heat flux generated at a steel target varied from 2.6×10^4 W/cm^2 at 4 mm to

$9x10^2$ W/cm^2 at 10 mm. When the jet went sonic the electrodes actually gained mass from the jet. The target materials' resistance to erosion increased with T_{mp} and the energy required to melt the material. The lower than expected erosion values for Al and Cu were attributed to their higher thermal conductivity. Glass performed like the metals whereas the polymers formed bubbles and had much less erosion. The authors agreed that the primary cause of erosion was still melting and subsequent removal of mass by the supersonic flow.

Gurarii et al. [61] studied the disintegration of steel targets by very high velocity (30-35 km/s) plasma jets. Discharge energies of 60 kJ resulted in mean power densities of $5x10^{10}$ W/cm^2 which lasted for 70 μs. The effect of carbon content, heat treatment and specimen temperature on the disintegration pattern were studied. The crater depth at the center of the target was smaller than at the periphery because the material is removed in its molten state by jet forces parallel to the surface whereas at the center the forces are perpendicular. As the materials' resistance to plastic flow (high velocity liquid removing the solid) is increased (by increasing the carbon content) the erosion is less. Thus, for materials with the same thermophysical properties, the mechanical properties determine the resistance to jet erosion. The pressure generated by a liquid layer on a solid is described by the equation:

$$p_v = \eta v_m / z_s, \qquad (3.3)$$

where η is the viscosity of the liquid metal (equal to 2×10^{-3} Nt·s/m^2 for steel). By setting the viscous pressure equal to the critical shear stress at which plastic flow forms (taken to be the yield point of steel - 10^8 N/m^2), the thickness of the solid metal which can be removed by the liquid is calculated to be less than 0.2 μm, which was confirmed by experiment. The crater depth at the periphery increased with temperature which was attributed to a loss in resistance to plastic flow at elevated temperatures.

A series of works by Ageev and Sultanov [63,64] investigated the role of the polarity and the thermal conductivity of the target electrode. The experimental arrangement and conditions were the same as before for Sultanov [60], except that the heat flux was reported to be two orders of magnitude higher, or $3\text{-}5 \times 10^6$ W/cm^2 with M_a=5.6. Seventeen different metal targets (2x2x1 cm) were tested. (The target size was shown not to be a factor). The effect of target polarity was considerable for about half of the materials tested. For all electrodes studied the diameter at the spot diminished and its depth increased for negative polarity (when compared with positive). The authors concluded that the mechanism of erosion for either polarity is the same as for a jet acting on a neutral plate, namely "explosive" liquid and vapor removal by the jet stream. The authors also mention the possibility of an

electron blocking layer forming if the target is an insulator which will reduce the heat flow by electrons to the target which in turn would result in a smaller damage area. In the second work the authors show that for the erosion of a neutral plate the mass of materials ejected beyond the target is directly proportional to the atomic weight of the plate material, there is an inverse linear relationship between the depth of damage and the boiling point and a direct linear relationship between the area of destruction and the thermal diffusivity. The destruction of the target is viewed as a two stage process: "a stationary stage in which the metal is gradually heated, leading to a weakening of the connection of the heated part of the material with the bulk of the substance and a mobile stage in which the metal is ejected from the zone of damage by explosive processes." The first stage is determined by the high temperature shock-compressed plasma interacting with the target which leads to some of the target becoming a superheated liquid. The second stage consists of liquid and gaseous products ejected by the pressure produced by explosion of the superheated liquid metal. The authors were able to predict successfully the evaporation times for each metal as a function of its thermophysical properties. For radiation densities of 10^5 to 10^7 W/cm^2 it was determined that the thermal conductivity cannot be ignored.

Sultanov [65] concludes his studies on jet induced target erosion by observing the plasma properties at the

target surface and the target erosion for three cases: 1) a neutral plate, 2) a plate connected to a large metal mass and 3) a "grounded plate." The erosion is significantly reduced in the latter two cases because an electron blocking layer is not formed and thus small particles and liquid droplets coming from the jet electrode readily attach to the target surface.

The review of the jet-electrode interaction phenomena observed to date indicate the following properties (P1-P5) are true for electrode erosion which is influenced by electrode jets.

P1) a smaller diameter electrode opposite a larger diameter electrode results in enhanced erosion of the larger diameter electrode because of the dominant plasma jet flow from the smaller to the large electrode,

P2) the use of a carbon electrode yields substantially lower erosion at the opposite electrode, due to a lower energy in the carbon jet,

P3) the electrode erosion decreases with increasing distance because of the reduction in jet energy received by the electrode surface,

P4) electrode damage with and without the current flowing through the electrode surface (see Fig. 3.2 g and 1) was similar if a jet was interacting with the surface,

P5) materials subjected to jets had increasing resistance to erosion according to their thermal properties

(higher T_{mp}, latent heats and mechanical properties

(higher yield strengths at elevated temperatures .

The existence of these properties needs to be determined for HCHETA switches. However, before proceeding to the experiments, it would be beneficial to know if a simple comparison of the relative importance of jet heating with other thermal sources indicates whether it may be important.

Relative Importance

Several authors [66-68] compare the energy or heat flux delivered by the jets with other sources. Sukhodrev [1] calculates the amount of energy which goes into the jet production as about 25% of the total delivered to the electrodes, not including ionization, for a jet velocity of 1 km/sec. However, since the jet is ionized and undergoes further heating via collisions in the arc plasma, the amount of energy that it delivers upon impact with the opposite electrode surface could be substantially higher. Zolotykh [66] compares several heat transfer terms--charged particle bombardment, jet or "flare" impact, radiation and gas kinetic energy transfer--for short gap spacings encountered in contact erosion and electro-spark discharging. The energy delivered by the jet was described by

$$W_t = q_j A_t t_j, \text{ or} \qquad (3\text{-}4a)$$

$$W_t = 0.5[c_j \rho_j v_j k_f [T_j(1+(\gamma-1)M_a^2/2)-T_t]A_t t_j]. \quad (3\text{-}4b)$$

After approximating many of the parameters he concluded that the charge bombardment term was the largest and that the jet term was significant, depending on the electrode material. His calculations were for lower energy discharges, and the equations given for the radiation and gas kinetic terms were incorrect in our copy, which made it impossible to compare them at higher energies.

Kalyatskiy et al. [67] also compared various heat transfer terms for low energy discharges--charged particle bombardment, jet impact, radiation, and electrode joule heating. The last two terms are shown to be negligible. His jet term has two components, potential and kinetic, but like Zolotykh [66] the kinetic energy transfer term is shown to be negligible. The comparison calculations were done for breakdown in a solid which he states would increase the jet contribution by possibly two orders of magnitude. Thus, since the jet effect was shown to be two orders of magnitude greater than the charged particle term in solid breakdown the two terms should be approximately the same for open air, low energy discharges.

In order to predict their relative contributions at high energies (i.e., high current) it is necessary to see how each term scales with current. For charged particle bombardment the energy transferred is proportional to the current. To predict the scaling of the jet term the jet

velocity as a function of current needs to be estimated. At high current, assuming that magnetic pinching dominates the jet acceleration, the velocity is found to be given by the expression

$$v_j \propto (\mu_o j I/2\pi\rho_j)^{1/2}, \text{ or} \qquad (3.5a)$$

$$v_j \propto I \text{ (assuming } j \propto I). \qquad (3.5b)$$

Even if one assumes instead that vaporization or the EDC mechanism of Lyubimov [44] (refer to Table 3.2) is responsible for the jet acceleration, the jet velocity still remains proportional to the current. Thus, the two dominant heating terms mentioned by Zolotykh should remain approximately at the same order of importance for high energy discharges. However, because the jet experiments were conducted under conditions which enhanced the jet effect, it still remains to be seen whether the jet heating term or the mechanical action of the jet are important factors in electrode erosion for typical HCHETA switches.

Mark VI Electrode Jet Experiments

Experimental Conditions

In order to perform electrode erosion tests at high currents (up to 750 kA) the Mark VI test facility was constructed. Mark VI consists of a resistively charged

capacitor bank connected in series to a test switch with water cooled electrode holders. When the capacitor bank is charged to the self-breakdown voltage of the test switch it discharges through the switch, producing a slightly damped, oscillatory current pulse, as shown in Fig. 3.3. The operating parameters are given in Table 3.4. A more complete description of the Mark VI test facility is given in Appendix A.

The experiments made use of the three different switch configurations, shown in Fig. 3.4, each designed with a specific purpose in mind. All three switches are axisymmetric. Switch #1 is a standard coaxial spark gap with hemispherical electrodes. This switch was used to generate an electrode data base at high currents and to study enhanced jet effects by using different electrode diameters and materials at the same time. The experimental conditions for Switch #1 are given in Table 3.5. The total coulomb transfer was kept approximately constant by varying the total number of shots for a given current. The effect of peak current was studied by changing the capacitance since the peak current is roughly proportional to the square root of the system capacitance, assuming that the other system variables (inductance and resistance) remain nearly constant. The results of calibration tests discussed in Appendix B showed that this was not always the case, so the ratio of peak current to system capacitance was determined for each value of system capacitance.

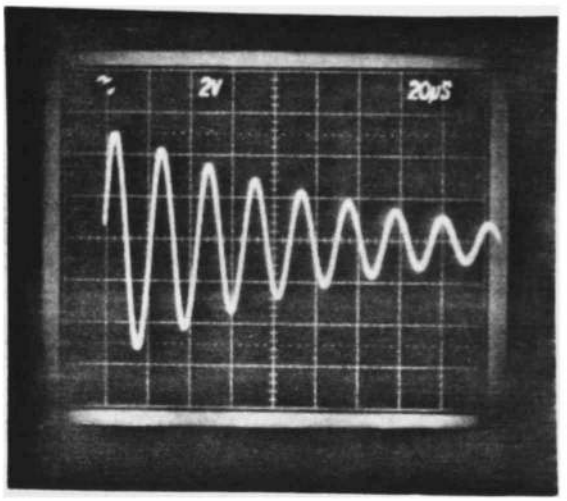

Fig. 3.3 Mark VI Current Waveform. (y axis - 105 kA/div, x axis - 20 μs/div)

Table 3.4 Mark VI System Parameters

Max. Breakdown Voltage	45 kV
Max. Peak Current	750 kA
Max. Energy/shot	56 kJ
Max. Effective Charge/shot	50 C
Max. Stored Charge	2.5 C
Capacitance	1.85 - 55.5 μF
Ringing Frequency	50-250 kHz
Inductance	0.23 μH
Repetition Rate	0.05 - 4 pps

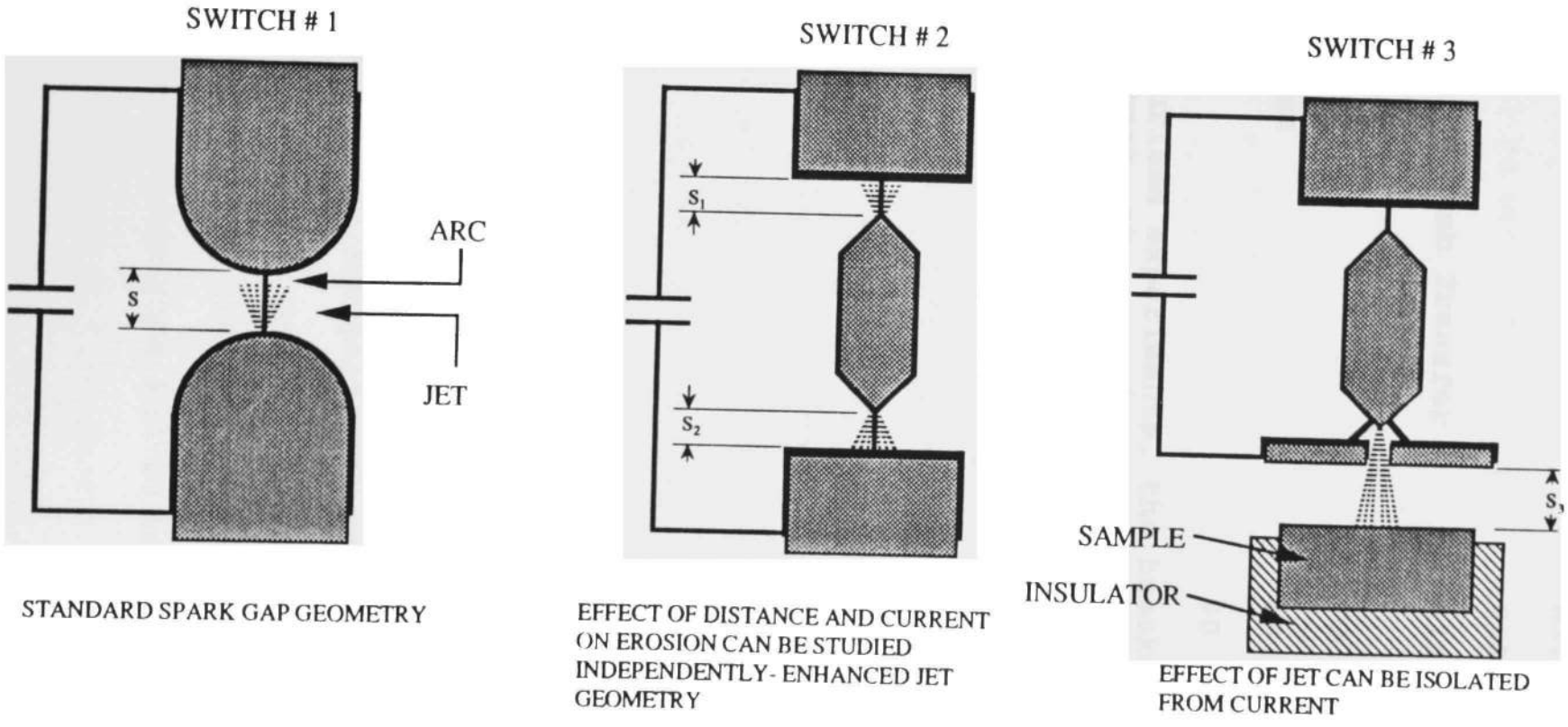

Fig. 3.4 Mark VI Switch Configurations Used to Perform Electrode Jet Experiments. (Note: all three switches are axisymmetric about the vertical axis)

Table 3.5 Switch #1 Operating Conditions for Electrode Jet Experiments

Gas	Air
Gas Pressure	$0.9 - 3.0 \times 10^5$ Pa
Total Effective Coulomb Transfer (for all cases)	1155 C
Number of Shots	50 - 1500
Breakdown Voltage	20 - 35 kV*
Peak Current	80 - 500 kA

*For the pressurized experiments, the breakdown voltage was kept constant, at approximately 32 kV, by varying the gas pressure.

**The experiments ran in open air (0.9×10^5 Pa in Lubbock, TX) or with bottled air for the pressurized case.

Switch #2 [72] was chosen since it allowed the breakdown voltage and thus the total current to be controlled by the distance $s_1 + s_2$, whereas the center electrode could be moved to allow the effect of different distances between the pairs of electrodes to be studied for the same current. The middle electrode was made of copper tungsten, CuW#2 (3W3 [73]), since it needed to last for a large number of shots and would also produce a copper jet which would allow for comparison with other test data. Several different electrode geometries were used with this configuration. Besides the pointed center electrode with flat upper and lower electrodes shown in Fig. 3.4, rounded center and upper electrodes were also used. The pointed electrodes were used when a dominant center electrode jet was needed and rounded electrodes were used when results were to be compared with Switch #1.

Switch #3 [56] was used to isolate the effect of the jet from the current. The distance, s_2, was chosen to be small (0.2 cm) so that the jet would not have to propagate very far (0.45 + s_3 cm) to reach the sample. Thus, s_1 was chosen to be relatively large (2 cm or greater) to keep the total breakdown voltage and peak current high. The center electrode was again chosen to be CuW#2 and the bottom disc electrode was CuW#1 (K-33 [74]). Because of the intense jet heat flux the bottom electrode had to be replaced after each run.

Experimental Results

The results can be divided into two sets of experiments. The first set was designed to determine if the electrode jets existed in our regime of electrode erosion. These experiments were conducted over a limited range of discharge conditions. They were designed to explore the effect on electrode erosion of certain parameters known to affect the jet erosion mechanisms, namely, gap distance, jet material, electrode geometry etc., Once jet existence was established a second set of experiments was run to determine jet effect trends over a larger discharge parameter space.

The initial investigation which indicated that EJE might be taking place in our experiments was a simple baseline study of the erosion of copper electrodes in Switch configuration #1 as a function of the peak current. The experimental values are given in Table 3.6. At first glance the results for the total erosion shown in Fig. 3.5a indicated that the total erosion increased rapidly with peak current, as expected, and that a transition might be occurring as evidenced by a slight change in the slope of the erosion curve (the slopes being almost straight lines on the log-log plot, indicating a constant power dependence) at 220 kA. What the plot failed to reveal was the different nature in the erosion of each electrode which was apparent from the photographs of the electrodes shown in Fig. 3.6. Because of the interesting differences in the appearance of the two electrodes the data were replotted to include the

Table 3.6 Electrode Erosion Data for Cu#1 ($p = 1.8\text{-}3.0 \times 10^5$ Pa)

Run #	Caps (#)	Q_s (mC)	Q_e (C)	I_p (kA)	E_s (kJ)	f_1 (*)	DV+ (x 10^{-5} cm^3/shot)	DV-	DV_{tot}	$DV_{\%e}$	V_{sb} (kV)	$DV_{sb\%e}$
517	1	60.3	1.45	101	0.984	0.207	0.373	0.447	0.820	9.1	32.6	5.2
535	2	114	2.84	146	1.76	0.696	1.79	3.73	5.53	2.7	30.8	7.9
525	3	176	4.20	182	2.79	1.42	17.3	5.63	23.0	0.98	31.7	8.6
529	4	231	5.63	215	3.59	2.42	42.1	11.6	53.7	0.55	31.2	9.1
537	5	279	6.71	217	4.20	3.08	45.9	14.4	60.4	0.61	30.1	9.2
619	5	288	6.95	244	4.50	3.29	73.1	21.1	94.2	0.40	31.2	9.7
515	5	301	7.27	234	4.91	3.60	84.9	29.5	114	0.43	32.6	7.4
676	10	578	11.0	308	9.02	8.52	176	84.8	261	0.29	31.2	9.8
690	20	1090	18.2	351	16.1	19.1	370	301	671	0.22	29.5	10

*The units on f_1 are ($A^2s^{1.5} \times 10^3$).

Table Variables: Caps - the number of 1.8 uF capacitors in the energy storage system, Q_s - stored charge, Q_e - effective or integrated charge, I_p - peak current, E_s - energy stored, f_1 - an erosion factor derived in Chapter 4 from a thermal model, DV_+ - erosion of the electrode which was the anode in the first half cycle, DV_- - erosion of the electrode which was the cathode in the first half cycle, DV_{tot} - total erosion of both electrodes, $DV_{\%e}$ - percentage error in total erosion due to measurement error, V_{sb} - self breakdown voltage, $DV_{sb\%e}$ - percentage error in V_{sb} corresponding to one standard deviation in the V_{sb} values. All variables are defined on a per shot basis.

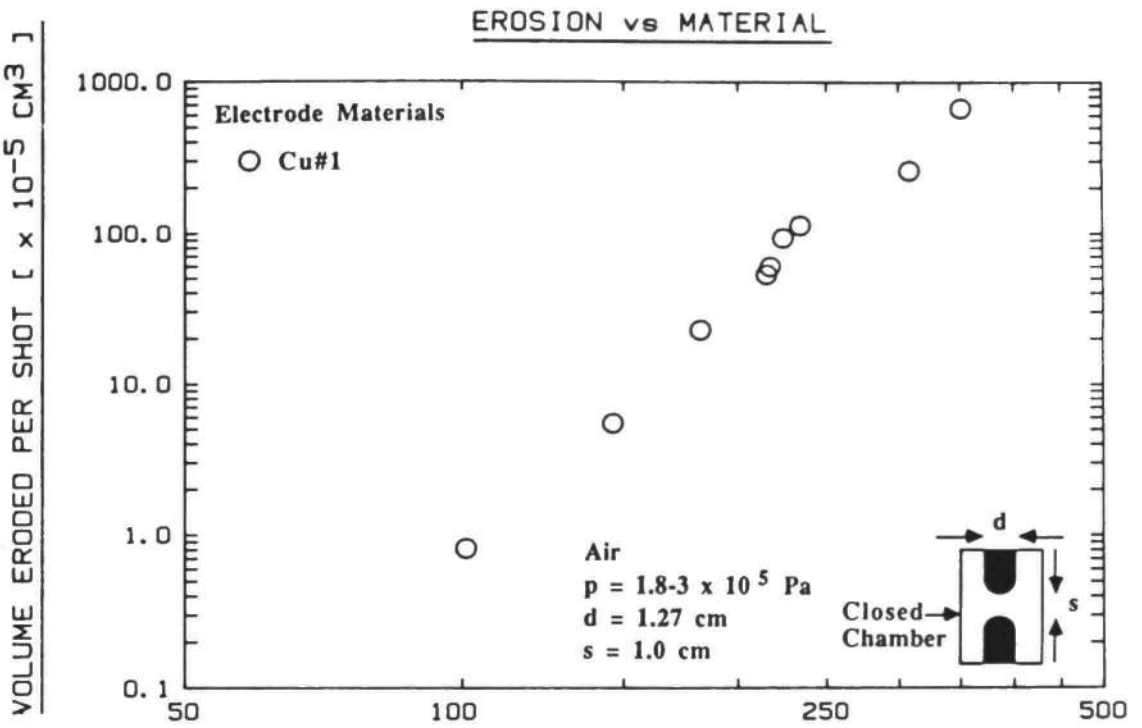

a)

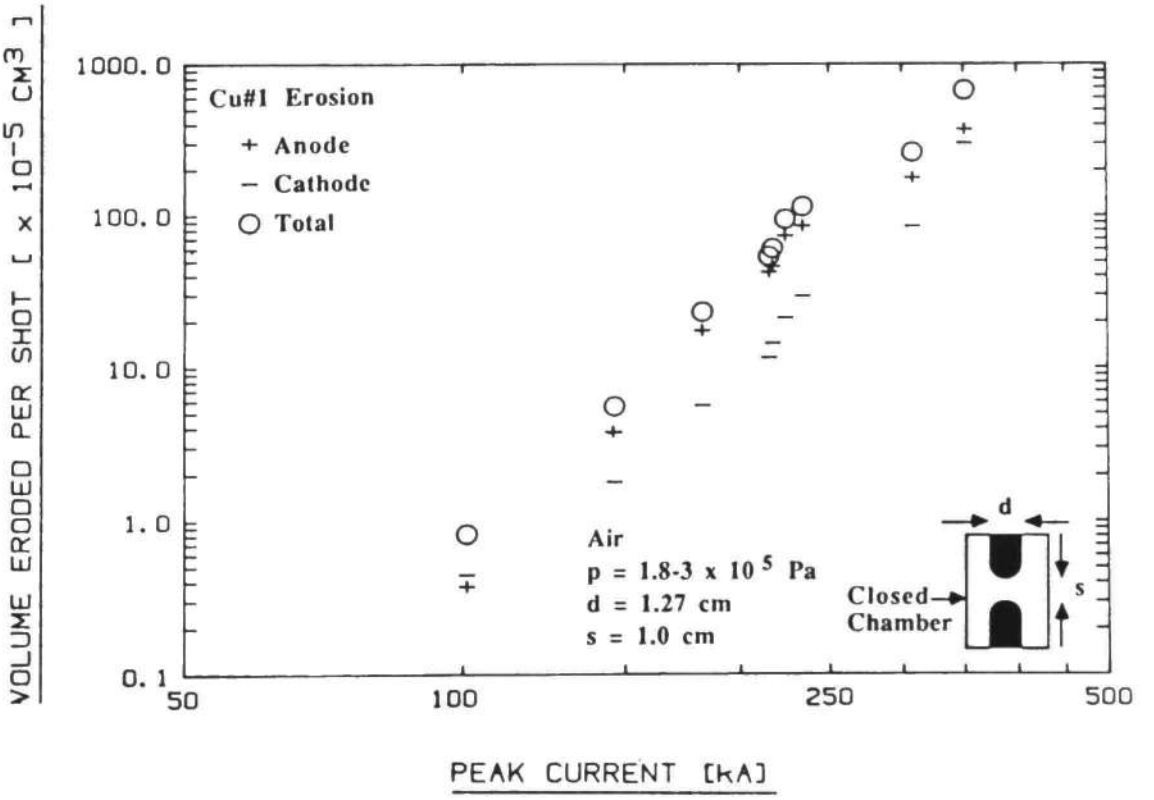

b)

Fig. 3.5 The Erosion of the Baseline Material Cu#1 as a Function of Peak Current in a Pressurized Gap. (for a) total only and b) anode, cathode and total)

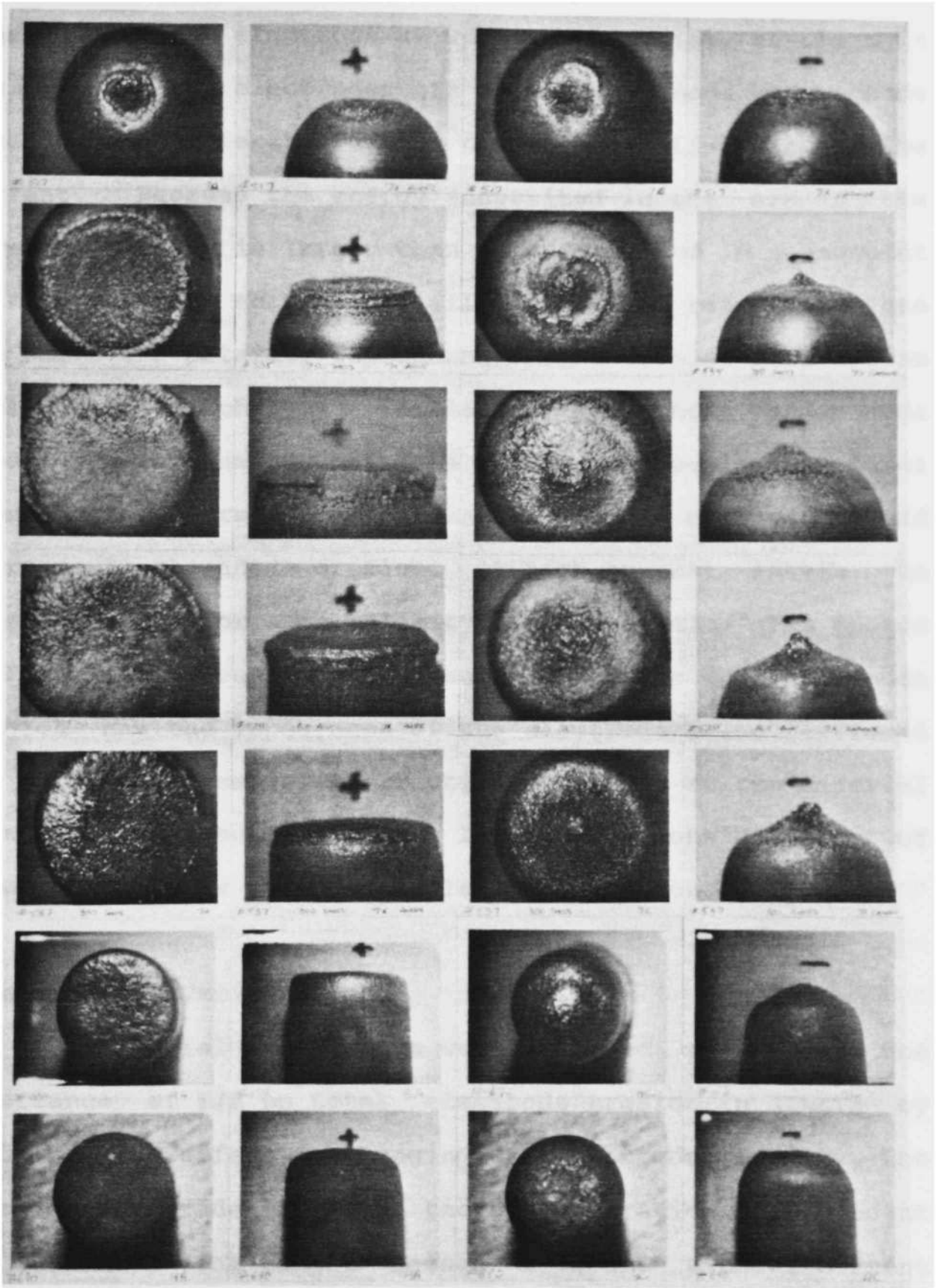

Fig. 3.6 Photographs of Cu #1 Electrodes Used for the Baseline Erosion Tests in a Pressurized Gap. (Left to Right: Anode Top, Anode Side, Cathode Top, Cathode Side; Top to Bottom : Run # 517, 535, 525, 529, 537, 676, 690) Magnification: 517-537 (1.4 x), 676 and 690 (2.5 x).

erosion of each electrode as well as the total, as shown in Fig. 3.5b. The electrodes are designated anode and cathode based on the polarity during the first half-cycle of the current. Because the energy deposited in the arc in the first half cycle is larger than that deposited in subsequent half cycles (due to the initially higher arc resistance) one can observe a polarity dependence in the erosion even for an oscillatory discharge. Initially the cathode and anode erode the same amount but the rapid increase in the total erosion is determined almost entirely by an even more rapid increase in the anode erosion. At high current levels the erosion values for each polarity coincide again. The photos of Fig. 3.6 indicate that the sudden increase in the anode erosion has the appearance of the electrode being flattened by some mechanism which effectively removes molten material parallel to the surface. This led to the consideration of electrode jets as a means of electrode erosion.

Electrode Jet Verification

The initial experiments were designed to evaluate the importance of EJE on total electrode erosion in HCHETA by studying the effect of changing the electrode geometry, the opposing electrode material, the gap separation (independent of current), the target damage with and without current flowing, and the thermal and mechanical properties of the target.

The first experiments consisted in changing the diameter and material of the electrodes. The conditions and results for these experiments are given in Table 3.7 and shown in Figs. 3.7 and 3.8. Experiments # 1 and 2 were made to provide points of reference. Comparing Exp. # 1-3 we see that the cathode erosion is a strong function of the size of the opposite electrode, with a smaller electrode producing greater erosion in the larger electrode. Experiment # 4 indicates that this effect is more a function of the increase in size than of polarity. Experiments # 3 and 5 and Exp. # 4 and 8 indicate that replacing the smaller copper electrode with a carbon one significantly reduces the erosion of the larger electrode, independent of polarity. If one assumes the jet mechanism is operative, then Exp. # 3 together with Exp. # 6 indicates that CuC essentially produces a copper jet, which is expected since copper vaporizes at a lower temperature than graphite. Experiments # 3 and 7 and Exp.# 6 and 11 indicate that CuC is less resistant to erosion than Cu which may be due to the molten copper removing the carbon in the case of CuC. On the other hand, pure carbon is more resistant to erosion than Cu or CuC as indicated by Exp. # 3, 7 and 9. Presumably this is due to the large energy per unit volume required to vaporize the carbon as opposed to melting or vaporizing the copper. All of these results could be explained if the electrode jets play a dominant role in electrode erosion, whereas

Table 3.7 Initial Experimental Results of the Effect of Electrode Diameter and Material on Erosion (Switch #1)

Exp #	Run #	$\langle Q_s \rangle$ (mC)	$\langle I_p \rangle$ (kA)	Anode Type*	Anode Erosion (cm^3)	Cathode Type*	Cathode Erosion (cm^3)
1	514	305	237	Cu, L	0.023	Cu, L	0.026
2	537	279	217	Cu, S	0.14	Cu, S	0.043
3	601	293	228	Cu, S	0.10	Cu, L	0.23
4	600	300	233	Cu, L	0.16	Cu, S	0.073
5	602	280	218	C, S	0.037	Cu, L	0.041
6	653	291	226	CuC, S	0.13	Cu, L	0.23
7	654	269	209	Cu, S	0.084	CuC, L	0.45
8	604	274	213	Cu, L	0.029	C, S	0.029
9	655	271	211	Cu, S	0.063	C, L	0.032
10+	656	278	216	Cu, S	0.083	Cu, L	0.20
11	657	290	226	CuC, S	0.13	CuC, L	0.70

*L indicates 2.54 cm in diameter, S is 1.27 cm in diameter.

+The gap distance was increased from 1.0 cm to 1.5 cm.

For a listing of materials see Chapter 5 where Cu is Cu#1, C is C#1 and CuC is CuC#1. CuC is 85% Cu by weight.

Table Variables: Q_s - stored charge, I_p - peak current.

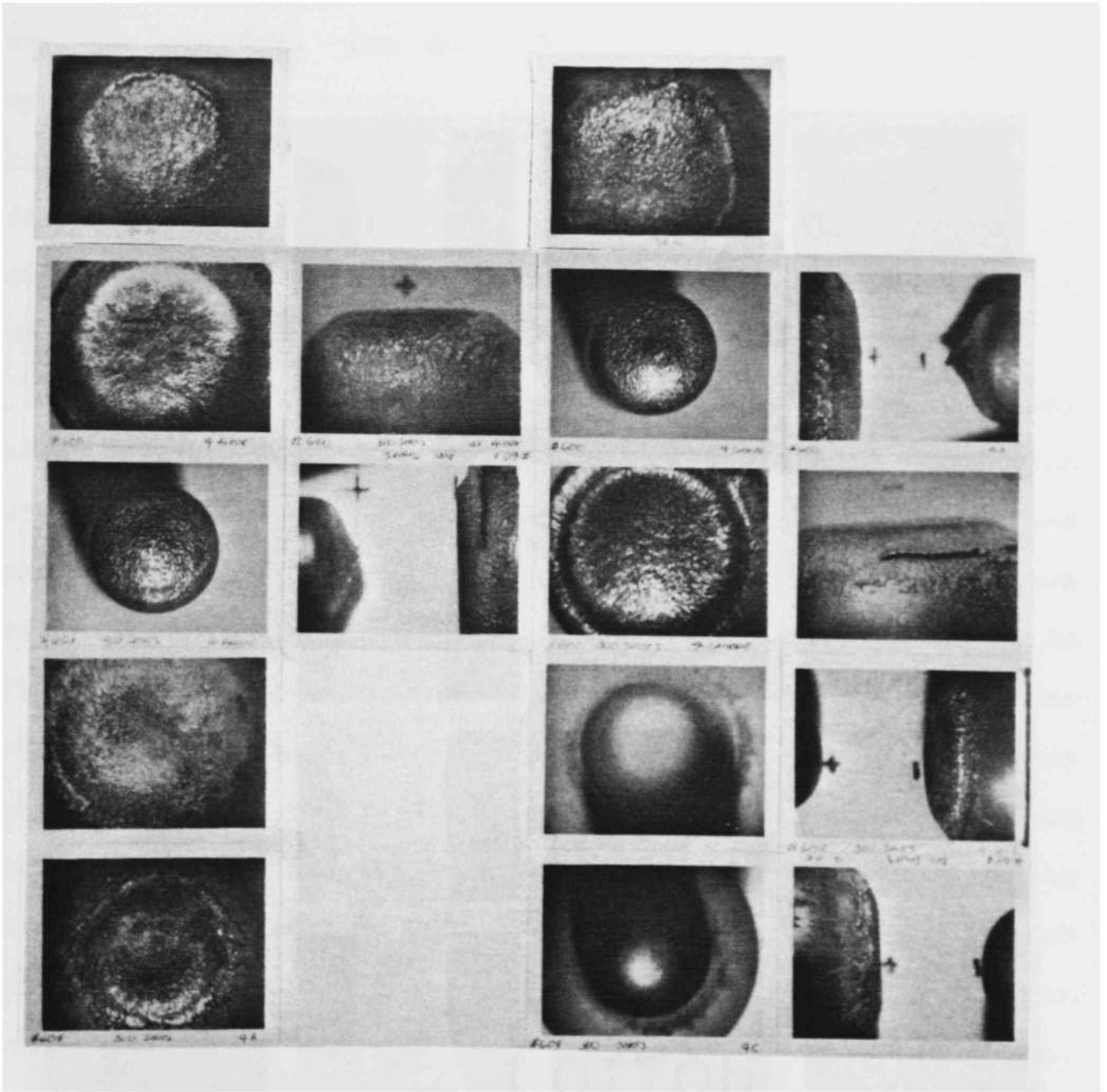

Fig. 3.7 Photographs of the Electrodes Used in Experiment # 1, 3-5, and 8 of Table 3.7. (Left to Right: Anode Top, Anode Side, Cathode Top, Cathode Side; Top to Bottom: Run # 514, 601, 600, 602, 604) Magnification: (1.4x).

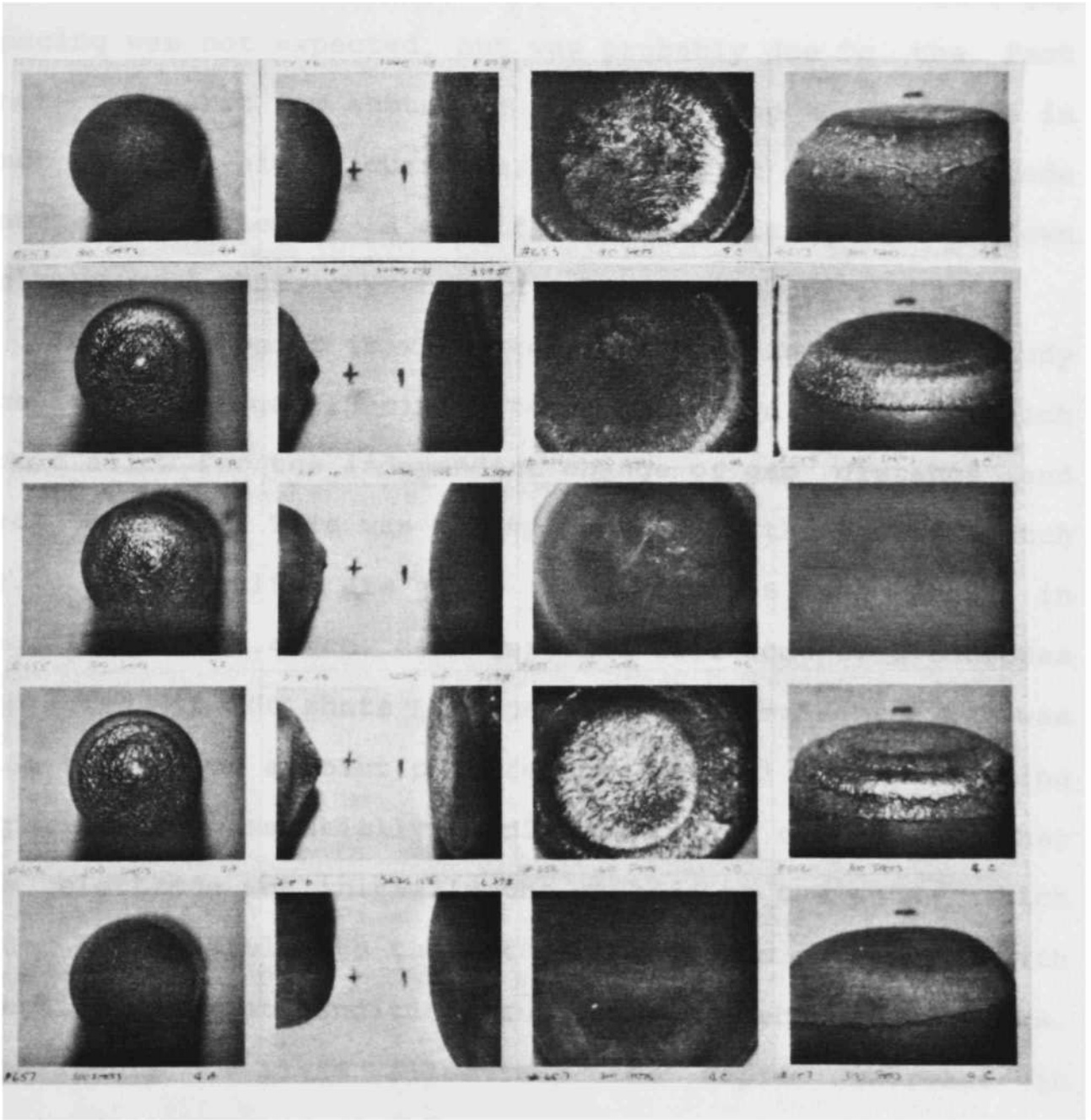

Fig. 3.8 Photographs of the Electrodes used in Experiment # 6, 7, and 9-11 of Table 3.7. (Left to Right: Anode Top, Anode Side, Cathode Top, Cathode Side; Top to Bottom: Run # 653-657) Magnification: (1.4x).

joule heating in the arc or the electrode could not explain the results.

Finally, Exp. # 10, which was designed to test the importance of the gap distance, was inconclusive because the lower erosion values could be attributed to the lower average current. The lower average current at a higher gap spacing was not expected, but was probably due to the fact that the first few shots for the larger gap spacing were in fact at much higher currents, resulting in severe electrode damage which let to a significant reduction in breakdown voltage (and thus, current) in subsequent shots.

At this point it was determined that in order to study the effect of gap spacing, tests had to be designed which would allow for the independent change of gap distance and peak current. This was accomplished with the use of Switch #2. The results are given in Table 3.8 and shown in Fig. 3.9 for 2.45 cm diameter flat Cu#1 copper electrodes subjected to 300 shots in open air. Experiment # 12 was made to provide a point of reference for all the remaining experiments. Essentially no difference was observed whether the electrode was initially the cathode or the anode, which made it possible to test two electrodes at once with identical current conditions and yet different gap spacings. Experiments # 13-16 illustrate the rapid increase in electrode erosion with decreasing distance (the "distance effect") at four different current levels. Figure 3.10 shows this effect quite dramatically for the electrodes of

Table 3.8 Initial Experimental Results of the Effect of Gap Spacing on Erosion (Switch #2)

Exp #	Run #	$\langle Q_s \rangle$ (mC)	$\langle I_p \rangle$ (kA)	s_1 (cm)	s_2 (cm)	s_1 Erosion (cm^3)	s_2 Erosion (cm^3)	n_s
12	630	213	166	0.75	0.75	0.11	0.12	--
13	631	168	130	0.25	1.25	0.10	0.0011*	2.8
14	632	161	125	0.50	1.00	0.052	0.0069	2.9
15	634	187	145	0.75	1.25	0.057	0.012	3.1
16	638	198	154	0.50	1.50	0.12	0.018	1.7

*This represents the lowest volume loss that could be measured and thus may have considerable error.

Table Variables: Q_s - stored charge, I_p - peak current, n_s - power dependence of the erosion with distance (see text), s_1 and s_2 - gap spacings: see Fig. 3-4. All electrodes were subjected to 300 shots.

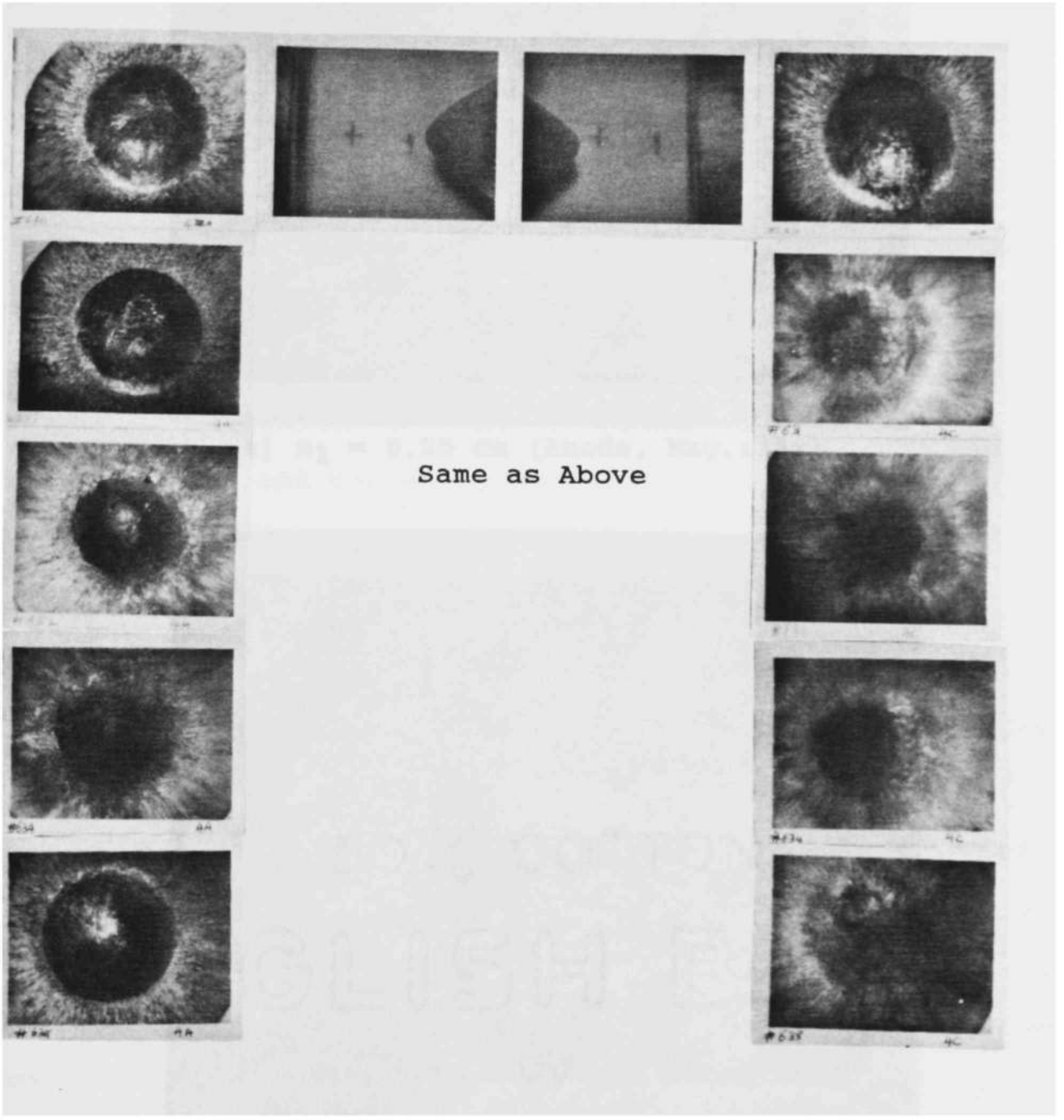

Fig. 3.9 Surfaces of Cu#1, Switch #2, Flat Electrodes Showing the Effect of Gap Separation. (Left to Right: Anode Top, Anode and Trigger Side, Cathode and Trigger Side, Cathode Top; Top to Bottom #630, 631, 632, 634 and 638) Magnification: (1.4x).

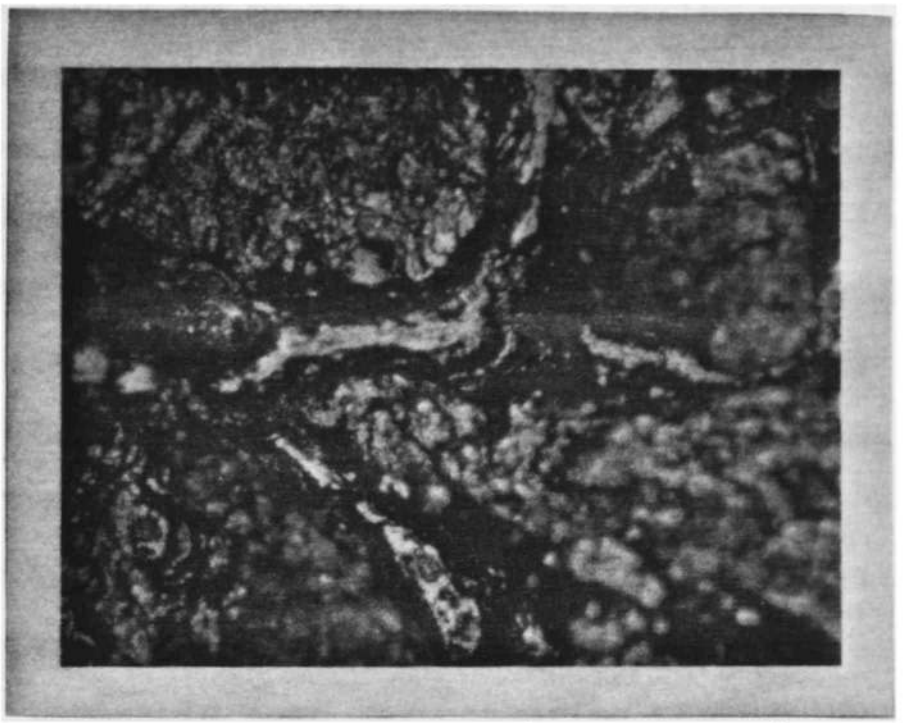

a) s_1 = 0.25 cm (Anode, Mag.:18x)

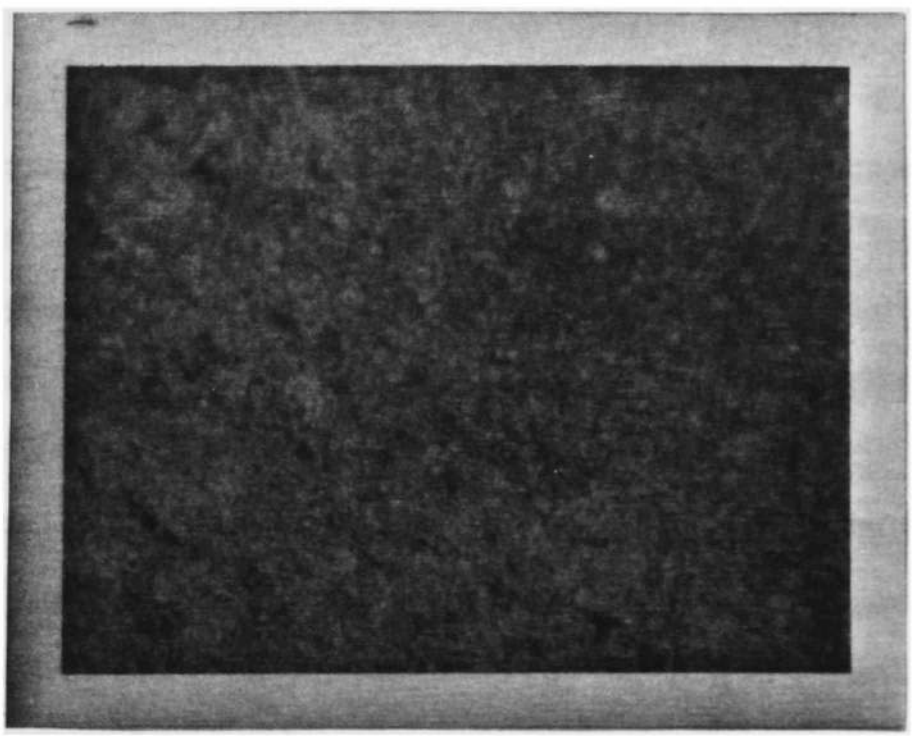

b) s_2 = 1.25 cm (Cathode, Mag.: 18x)

Fig. 3.10 Surfaces of Cu#1 Electrodes Used in Experiment #13. (see Table 3.8 for conditions)

Exp. #13. If one assumes the erosion for these experiments is proportional to $s^{(-n_s)}$ then n_s varies from 1.7 to 3.1 under these conditions. However, one cannot compare the values of two different experiments directly since the current also changes and the erosion is known to have a strong current dependence. In addition, the s_2 erosion values as a function of distance are averaged out when looking at the larger differences in distance ($s_2 - s_1$) at each current. (Note: if the current of Exp. # 14 had been the same as Exp. # 13, i.e., increased, then the s_2 erosion (0.0069 cm^3) would have also been greater, which would have made the threshold seen by comparing the s_2 of Exp. # 14 (0.0069 cm^3) and the s_2 of Exp. # 13 (0.0011 cm^3) even more dramatic.)

The s_1 erosion of Exp. # 12 and 15 and Exp. # 14 and 16 also suggest a significant current threshold effect. Since the distance is constant and the current varies, the erosion dependency on current for copper electrodes can be calculated. By assuming that the erosion is proportional to $I_p^{(n_e)}$ then the power n_e was calculated to be 4.0 and 4.9. (Note: the calculation is very sensitive to errors in the current, so the numbers should only be considered rough estimates.) The results in Fig. 3.6 gave an n_e of approximately 6 in this current range. This indicates that one source of energy driving the erosion rate in this regime could very well be the electrode jets.

The effect of distance and current just described can be shown all in one plot, as seen in Fig. 3.11. The major conclusions from the previous discussion are easily seen, and one can also readily see that a simple power law dependence is inadequate. Also, it is informative to consider two limits, $s = 0$ and $s = \infty$. As s becomes very small a larger portion of the total energy in the arc, i.e., simply $v(t)i(t)dt$, goes into the heating of the electrodes. Thus, one would anticipate, as Fig. 3.11 indicates, that each higher value of current has a higher asymptotic value of erosion. The actual value of the total energy is hard to determine due to the difficulty in measuring v(t) and its variation with electrode spacing. The value of the erosion at any distance divided by the asymptotic value of erosion at $s = 0$ is an indicator of the relative percentage of the arc energy that is coupled into the electrode heating process at that distance. As s increases the effect of EJE should decrease rapidly, and the erosion should also decrease rapidly as long as EJE dominates the erosion. One possible variation from this trend could occur if the jets derive their energy from the arc column region instead of the fall region as has been suggested earlier (see Table 3.3). If this takes place, the jet energy could increase with distance because of the increasing energy in the arc column as the distance increases. This effect would be more likely at higher currents since the jets would be able to retain and deliver

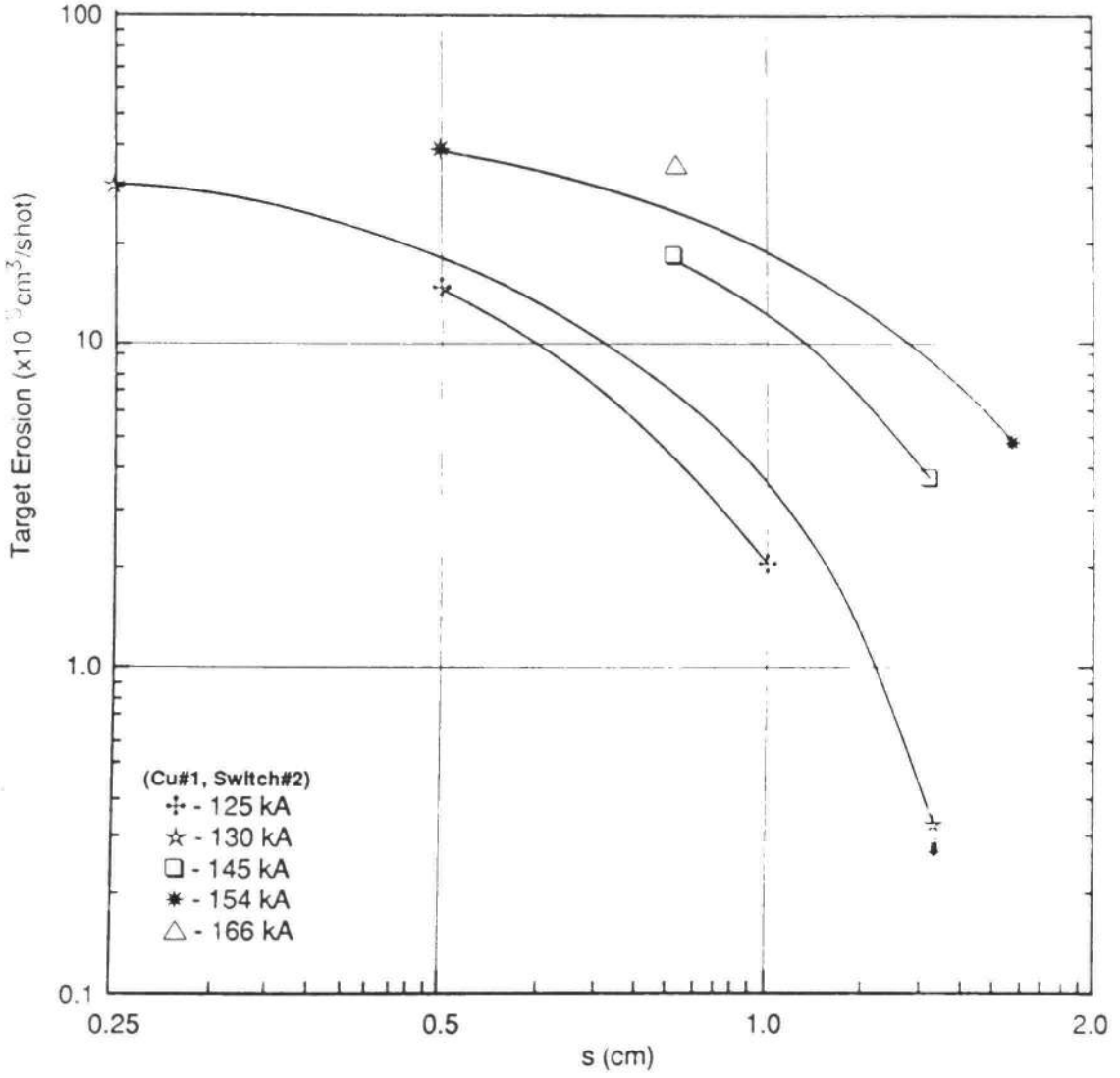

Fig. 3.11 Jet Target Erosion as a Function of Distance and Current. (A curved line is drawn between the two points instead of a straight one because the erosion is known to increase with current and because the results given later in Fig. 3.25 will contain this general shape.)

their energy at the larger distances. An actual increase in erosion could also be observed if the center electrode began transferring a larger amount of its eroded mass to the target electrodes at high currents. However, for average currents of 125-166 kA, Fig. 3.11 shows that the increase of distance led to a rapid decrease in the erosion with each higher current having a corresponding larger distance at which the decrease occurs. This effect is probably due to jet divergence which results in a lower jet energy density with increasing distance of propagation.

Further evidence of the distinct influence of EJE was shown using Switch #3. This switch allows the "target" to "see" only the jet, i.e., no current passes through the target. Figure 3.12 shows the single shot erosion as a function of distance for copper electrodes used in Switch #3. Figure 3.12 also shows similar electrodes used in Switch #2. The damage pattern is essentially the same for both sets of electrodes and is very similar to the pattern produced by air jets on a greased plate, which is shown in Fig. 3.13. Thus the erosion in this current regime and for this electrode geometry seems to be strongly influenced by the electrode jets. It should be noted that Sultanov and Kiselevskii [56] came to the same conclusion under somewhat different conditions.

To study the effect of changing the properties of the electrode material receiving the jet, six materials in addition to copper were tested in Switch #2. The erosion

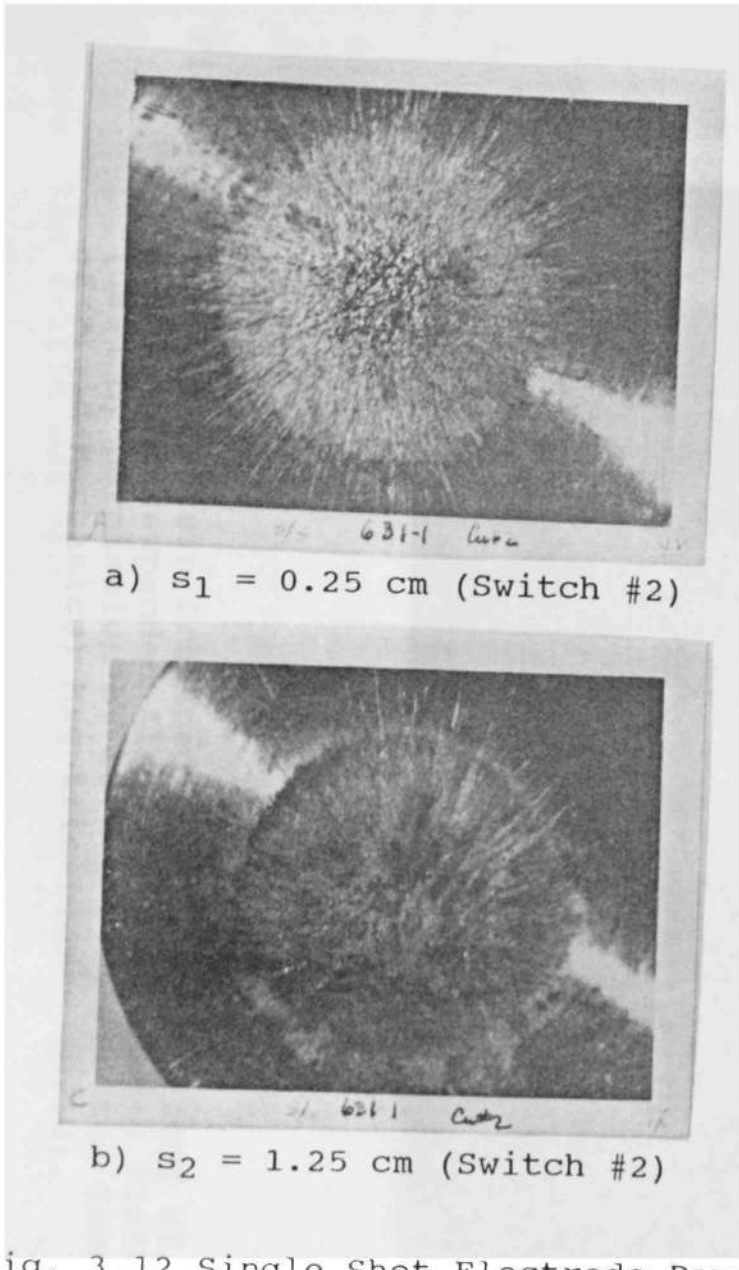

a) s_1 = 0.25 cm (Switch #2)

b) s_2 = 1.25 cm (Switch #2)

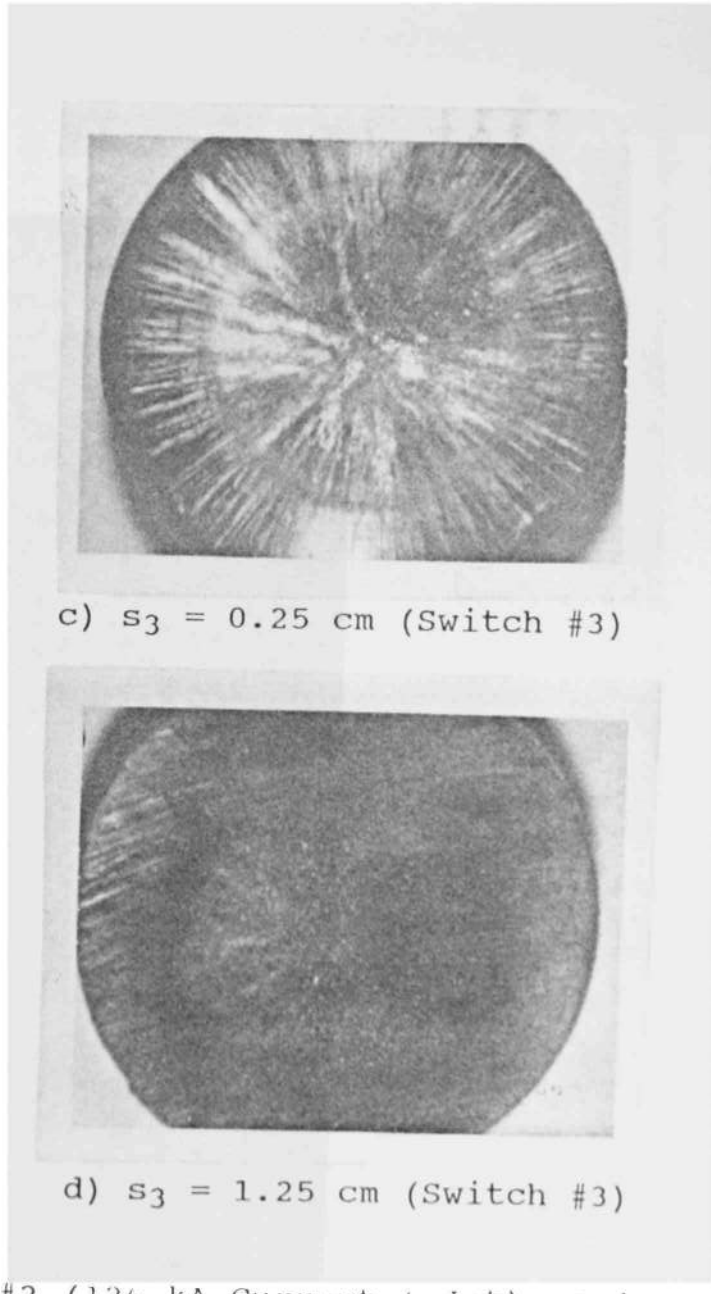

c) s_3 = 0.25 cm (Switch #3)

d) s_3 = 1.25 cm (Switch #3)

Fig. 3.12 Single Shot Electrode Damage for a,b - Switch #2 (126 kA Current + Jet), c,d - Switch #3 (Jet Only).

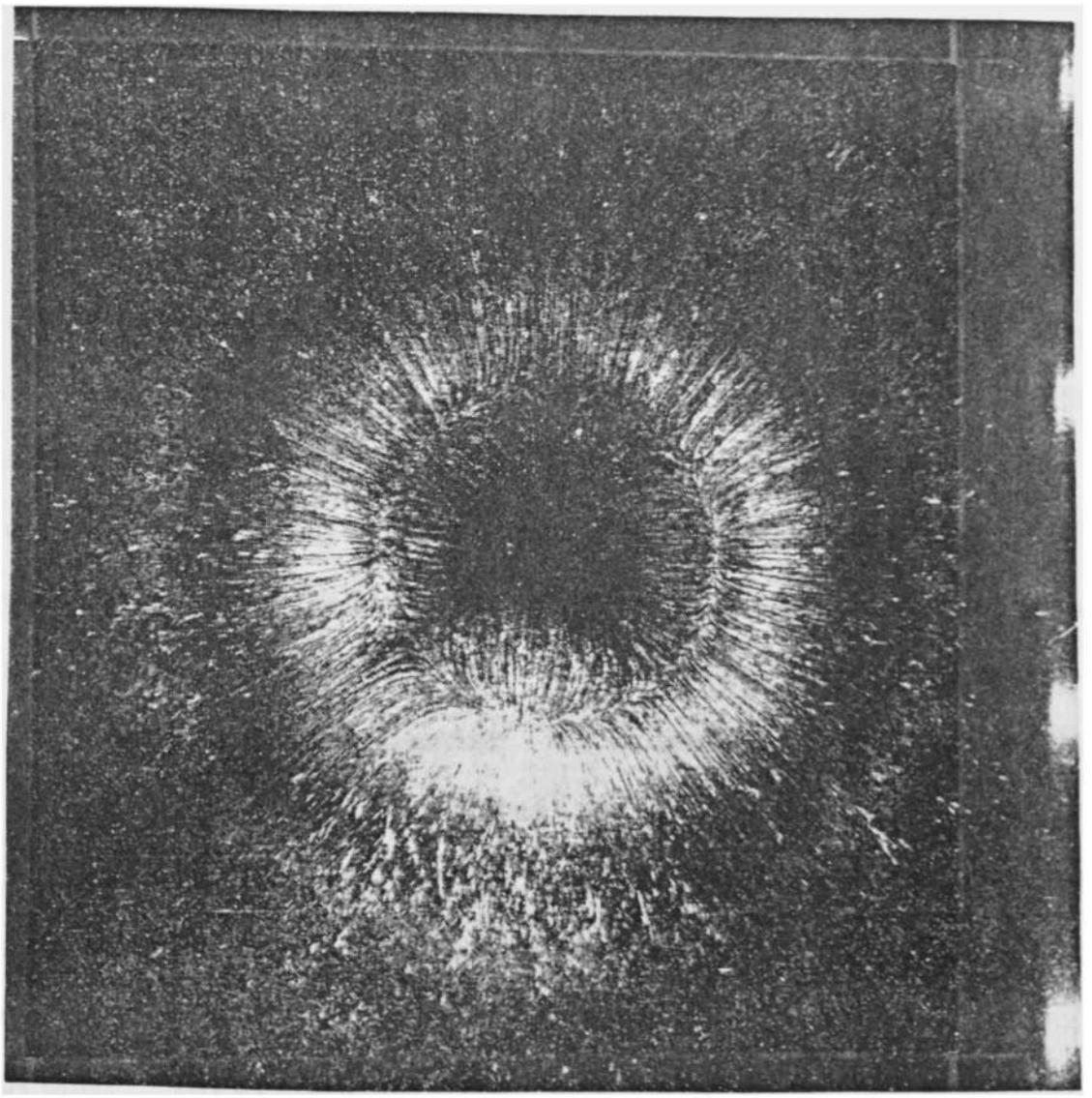

Fig. 3.13 Surface Pattern Produced by the Impingement of a Highly Underexpanded Air Jet on a Greased Plate. (Used by permission of author [72] and the Journal of Fluid Mechanics) Magnification: (0.5x).

results which are given in Table 3.9 show good agreement with the material liquid "impulsivity" or M_{I1} defined by

$$M_{I1} = T_{eff}(k_t \rho c_p)^{0.5}, \qquad (3\text{-}6)$$

where

$$T_{eff} = T_{mp} + L_f/c_{mp}. \qquad (3\text{-}6a)$$

The liquid impulsivity is a measure of the ability of a material to withstand being melted by a source of heat flux. (These terms are derived and discussed in Chapter 4). This agreement makes sense since electrode jets produce an impulse of heat flux at the electrode surface. The electrode surfaces shown in Fig. 3.14 also have damage patterns characteristic of EJE. The performance of composite materials is harder to describe, but it appears that it approaches the performance of the material with the higher impulsivity with the remaining material in the composite acting as an evaporative coolant [75] (this will be discussed in more detail in Appendix B).

Further verification of the existence of supersonic electrode jets and their influence on electrode erosion was obtained with streak photography of the arc discharge in Switch #1. A TRW model 1D streak camera was used with the slit parallel to the electrode axis as shown in Fig. 3.15a. Since the switch was operated in open air in the self break

Table 3.9 Electrode Erosion Data for Various Switch #2 Materials

Run #	Caps (#)	Q_s (mC)	Q_e (C)	I_p (kA)	E_s (kJ)	f_1 (*)	DV+ (x 10^{-5} cm^3/shot)	DV- (x 10^{-5} cm^3/shot)	$DV_{\%e}$ +	$DV_{\%e}$ -	V_{sb} (kV)	$DV_{sb\%e}$
630	5	213	5.14	166	2.46	1.80	36.9 (Cu)	38.4 (Cu)	0.51	0.49	23.1	5.7
631	5	168	4.05	130	1.52	1.11	34.9 (Cu)	0.373 (Cu)	0.54	50	18.2	7.4
632	5	161	3.89	125	1.41	1.03	17.5 (Cu)	2.28 (Cu)	1.1	8.3	17.4	4.4
633	5	177	4.27	138	1.70	1.25	38.5 (SS)	-3.56 (C#1)+	0.54	25	19.2	4.7
634	5	187	4.50	145	1.88	1.38	19.0 (Cu)	4.10 (Cu)	0.98	4.6	20.2	6.4
636	5	171	4.12	133	1.58	1.16	8.21 (Mo)	6.79 (CuC#1)	2.0	2.8	18.9	6.9
637	5	170	4.09	132	1.56	2.41	15.8 (SB)	3.39 (CuW#2)	1.2	3.6	18.4	13
638	5	198	4.78	154	2.12	1.56	39.9 (Cu)	5.97 (Cu)	0.48	3.2	21.4	9.2

*The units on f_1 are ($A^2s^{1.5}$ x 10^3).

+A minus sign indicates this electrode gained mass.

Note: The runs of Table 3.8 are included for comparison purposes. SB is a brass provided by Sandia Laboratories, SS is 304 Stainless Steel. The definitions of the other table variables are given in Table 3.6.

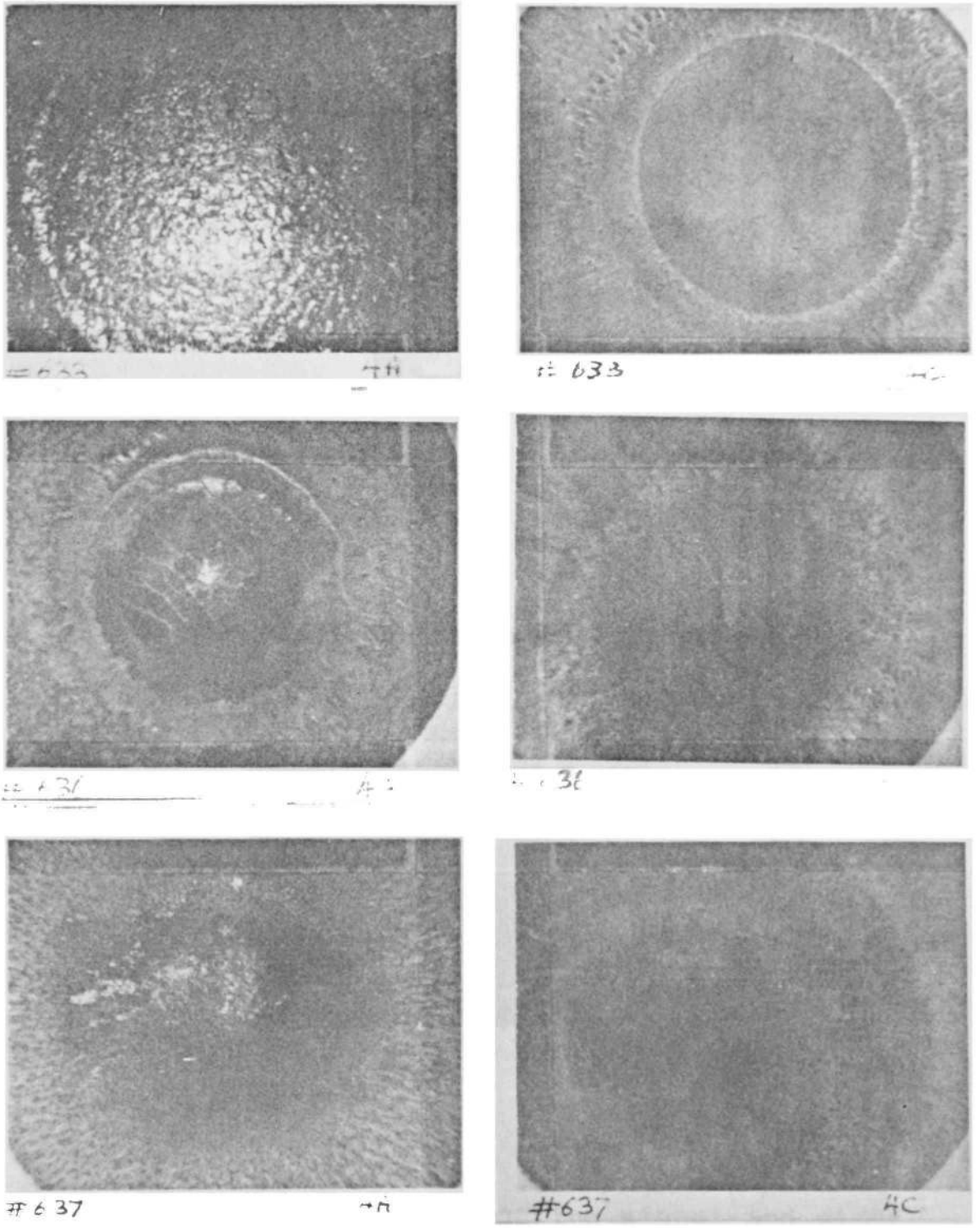

Fig. 3.14 Photographs of the Electrode Surfaces for the Various Materials Tested as Target Electrodes in Switch #2. (Left - Anode Top, Right-Cathode Top; Top to Bottom: Run # 633, 636, 637) Magnification: (2.8x).

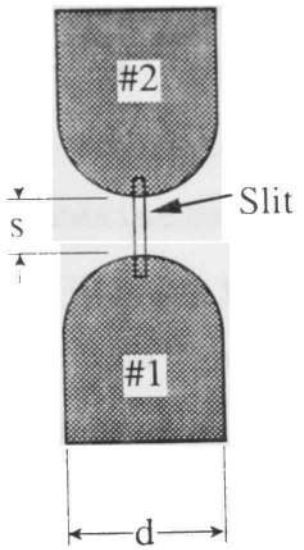

a) the electrode and slit arrangement

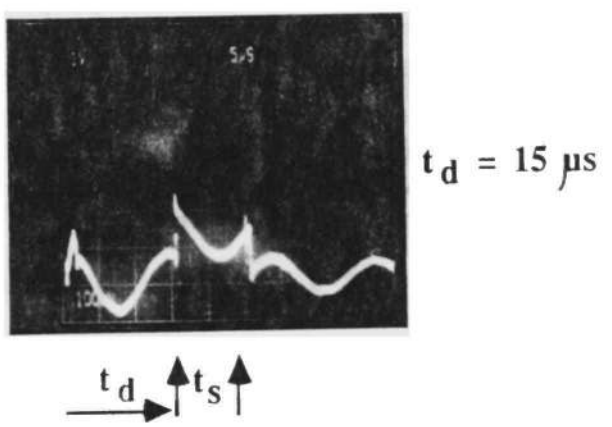

b) superposition of delayed gating signal and di/dt
(t_d - delay time, t_s - streak time)

Fig. 3.15 Experimental Conditions for the Streak Experiments.

mode, a di/dt pickup coil with a delay of 150 ns was used to trigger the camera. The camera delay time was selected to be 10-20 μs since the luminosity during the first 10 μs, corresponding to the first complete cycle of the current, appears to be totally dominated by the initial ionization occurring during the resistive phase of the arc. Thus, pictures which clearly depict the electrode jets could only be obtained for delay times greater than 10 μs. A gating signal was superimposed on the di/dt signal after the delay time so that the portion of the current waveform corresponding to each streak photo could be easily identified, as shown in Fig. 3.15b. The streak time was chosen to be 10 μs since this provided good spatial resolution on the film for the jet velocities which were expected (1-10 km/s). The system capacitance was chose to be 18.5 μF so that a current would result which was large enough to allow the switch to operate in the transition regime where jets should be produced. The electrode geometry varied from symmetrical 1.27 cm diameter electrodes to asymmetrical electrodes with either the cathode or anode being larger in diameter by a factor of 2. The asymmetry was chosen because in previous tests the larger electrode always exhibited the higher erosion rate which was attributed to jet effects. The gap spacing was 1 cm. The electrode materials were CuCrZr and C#1, both of which had been studied in previous erosion tests. Graphite was specifically chosen since erosion on electrodes opposite

graphite had been shown to be substantially reduced over a certain current range.

The important results from the streak studies are shown in Fig. 3.16. For the case of symmetrical electrodes, shown in Fig. 3.16a, a distinct supersonic jet (5 km/s) can be seen emerging from each electrode. The jets interact in the center of the gap, producing a compressed high temperature region, and appear to be partially reflected back to the electrodes. Also detectable is a much slower release of vapor from each electrode surface with a velocity (~0.75 km/s) which is close to the value of the copper vapor thermal expansion velocity into a vacuum at $T = T_b$ (~ 0.80 km/s). For the asymmetrical electrodes shown in Fig. 3.16b, a much faster jet (~10 km/s) is produced at the smaller electrode. The jet trajectory can be traced across the gap until it reaches the opposite (larger) electrode, producing a highly luminous region in front of the larger electrode which lasts longer than the corresponding luminous region at the smaller electrode. The electrode erosion is observed to be much greater at the larger electrode which further tends to support the previous conclusion that the electrode erosion is significantly influenced by the interaction of the electrode jet with the electrode surface, especially in the case of asymmetrical electrodes. In Figs. 3.16c and 3.16d the upper copper electrode (initially the cathode) has been replaced with graphite, which in earlier studies led to a large reduction

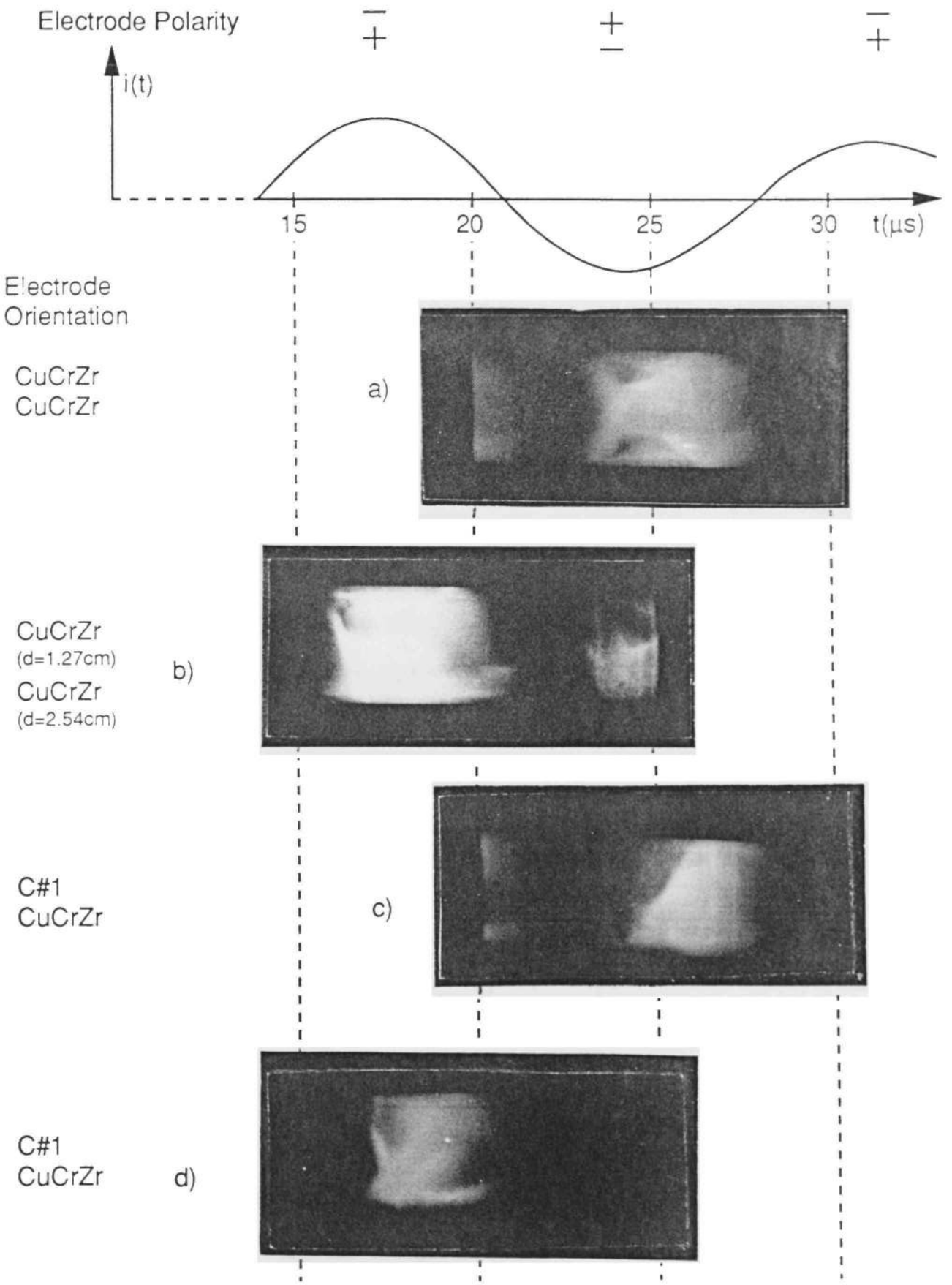

Fig. 3.16 Streak Photographs of Electrode Jets with Varying Electrode Diameter, Electrode Materials, and Delay Times.

in the erosion rate of the copper anode for currents up to 250 kA. Figures 3.16c and 3.16d offer a possible explanation in that, even though a supersonic graphite jet can be seen interacting with the copper electrode, it is generated only when the graphite electrode becomes a cathode on alternate cycles of the current waveform. Thus the copper anode receives significantly less time integrated heat flux than it would have if the cathode had been copper.

In summary, the streak photos along with these initial experiments on the influence of electrode size, material, spacing and configuration indicate:

1) the existence of the supersonic electrode jets,
2) the velocity of the jets is a function of the electrode material, geometry and spacing, and
3) the observed electrode erosion can be explained in part by the interaction of these jets with the electrode surface.

At this point it was decided to conduct further tests to determine the range of these jet effects.

Range of the Electrode Jet Effect

The experience of running the initial baseline test described earlier and shown in Fig. 3.5 indicated that using a pressurized spark gap has several experimental disadvantages including a reduction in the available operating range of the switch. At the lowest capacitance

level in the pressurized gap the higher breakdown voltage obviously resulted in a higher minimum peak current, charge transferred etc., because of the higher pressure. At the higher capacitance levels the higher breakdown voltages and corresponding higher discharge energies led to several catastrophic failures of the switch housing, thus reducing the maximum peak current and charge transfer which could be achieved. Therefore, in order to achieve the widest possible range of experimental discharge parameters, it was decided to operate all the remaining jet effect experiments in open air.

The baseline test was rerun in open air. The results are given in Table 3.10 and are plotted in Fig. 3.17. The plotting variable was changed to stored charge, Q_s, because Q_s is independent of the scale factors used to get Q_e for example. (For conversion to other commonly used plotting variables such as effective charge and peak current one should refer to the data tables in this chapter or in general to the conversion factors which are given in Appendix B.) The open air results plotted in Fig. 3.17 are very similar to those of Fig. 3.5. However, because of the extension of the lower limit of stored charge values from 60 mC down to 40 mC and because the jet effect "turns on" at higher values of charge transfer for lower pressure, one can clearly distinguish a transition from one constant slope erosion regime to another. The transition region, which occurs from 150-250 mC, has a much higher slope and is

Table 3.10 Electrode Erosion Data for Cu#1 Baseline Test ($p = 0.9 \times 10^5$ Pa)

Run #	Caps (#)	Q_s (mC)	Q_e (C)	I_p (kA)	E_s (kJ)	f_1 (*)	DV+ (x 10^{-5} cm^3/shot)	DV- (x 10^{-5} cm^3/shot)	DV_{tot} (x 10^{-5} cm^3/shot)	$DV_{\%e}$	V_{sb} (kV)	$DV_{sb\%e}$
761	1	44.0	1.06	74.0	0.524	0.111	0.227	0.227	0.454	17	23.8	5.1
742	2	75.4	1.88	96.2	0.769	0.304	0.607	0.607	1.21	12	20.4	5.1
647	3	114	2.73	118	1.18	0.599	1.34	0.897	2.24	10	20.6	4.2
1060	4	136	3.33	127	1.26	0.846	1.50	1.20	2.70	11	18.4	9.7
617	5	167	4.02	130	1.51	1.10	2.61	1.49	4.10	9.1	18.0	11
616	5	173	4.17	134	1.62	1.18	5.99	2.24	8.23	4.5	18.7	6.9
625	6	199	4.46	127	1.79	1.25	9.40	2.24	11.6	3.8	18.0	8.8
671	6	195	4.38	125	1.72	1.21	9.80	2.67	12.4	3.6	17.6	9.4
624	7	222	4.38	129	1.91	1.30	5.18	4.66	9.84	5.3	17.2	8.2
626	8	275	5.37	141	2.56	1.80	61.0	7.83	68.8	0.8	18.6	7.4
666	10	320	6.09	171	2.77	2.62	69.4	9.69	79.0	0.9	17.3	6.9
677	20	566	9.45	182	4.33	5.14	61.0	75.5	137	1.1	15.3	10
878	20	559	9.33	180	4.22	5.02	63.1	113	176	0.8	15.1	12
620	30	746	10.7	196	5.02	6.96	136	206	342	0.7	13.4	14
+687	30	1240	17.7	326	13.8	19.1	394	526	920	0.2	22.3	11

*The units on f_1 are ($A^2s^{1.5} \times 10^3$).

+Switch #2 ("Piggyback")

Table variables are defined in Table 3.6.

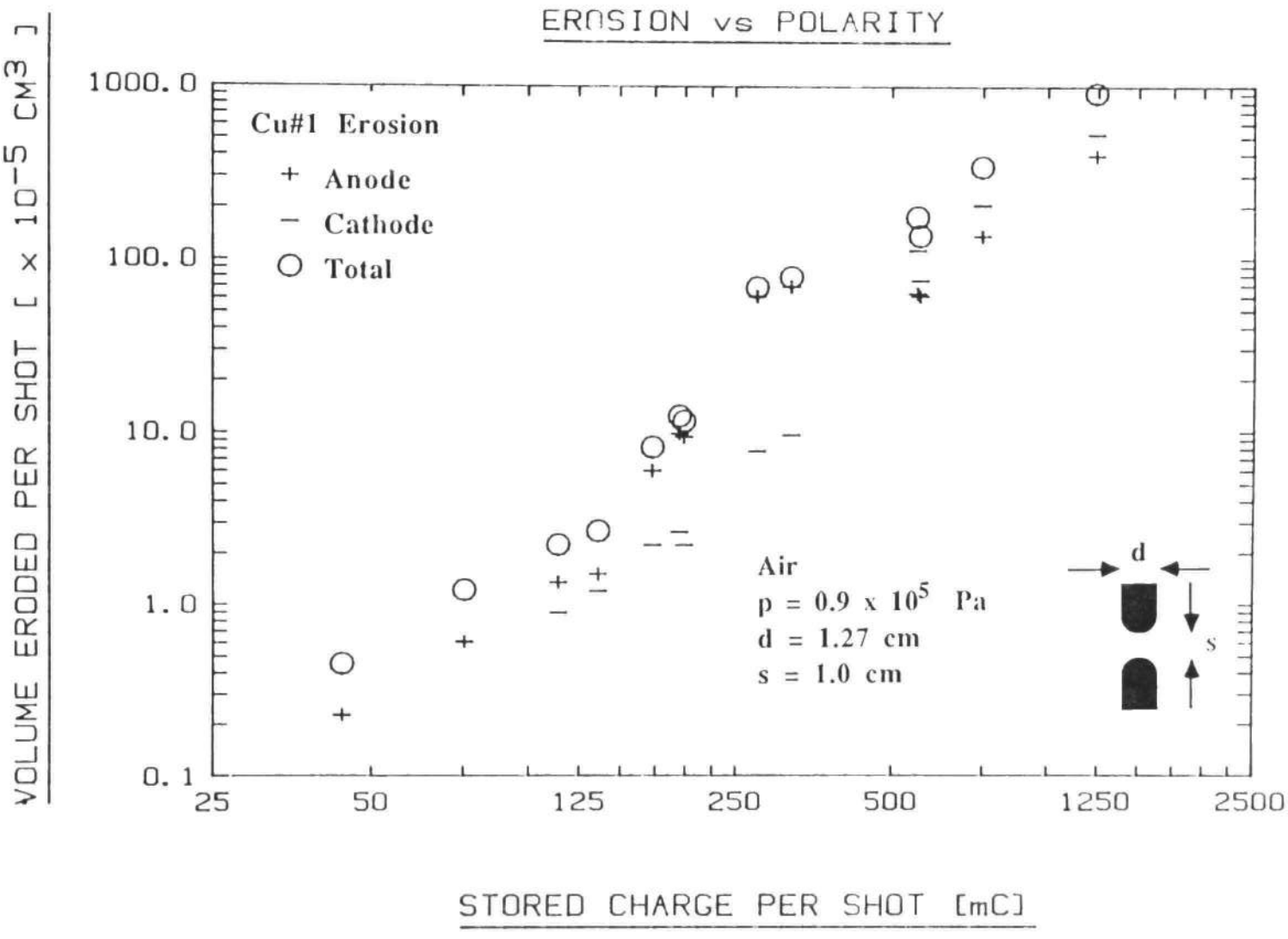

Fig. 3.17 Electrode Erosion Baseline Test Results for Cu#1 in Open Air Showing the Effect of Initial Polarity.

distinguished by a rapid increase in the anode erosion rate. In Fig. 3.18 the photographs of the electrodes in this transition region again seem to indicate that the cathode jet may be efficiently removing the molten anode material. At still higher charge levels, 500 mC, the sudden increase in the cathode erosion, as further evidenced by the flattening of the cathode, could be explained by the onset of the anode jet. To confirm this hypothesis and to determine the range of jet interaction an attempt was made to try and isolate as many of the jet interaction properties (P1-P5), discussed earlier, as possible. Note: the tables and photographs of the electrodes for these experiments are grouped together at the end of this section.

The first experiment consisted of increasing the diameter of the electrodes from 1.27 cm to 2.54 cm. According to the theories for jet acceleration discussed earlier this should have reduced the jet impact velocity and subsequent electrode damage by reducing the **j x B** accelerating force since increasing electrode diameter has the effect of reducing both j and B. This effect may be partially offset by the fact that the larger diameter electrode intercepts more of the jet energy. The results plotted in Fig. 3.19 indicate that increasing the diameter had the effect of reducing the electrode erosion only in the transition region which is where the jet influence should be the greatest. To determine which electrode diameter was producing this effect the erosion was measured for the case

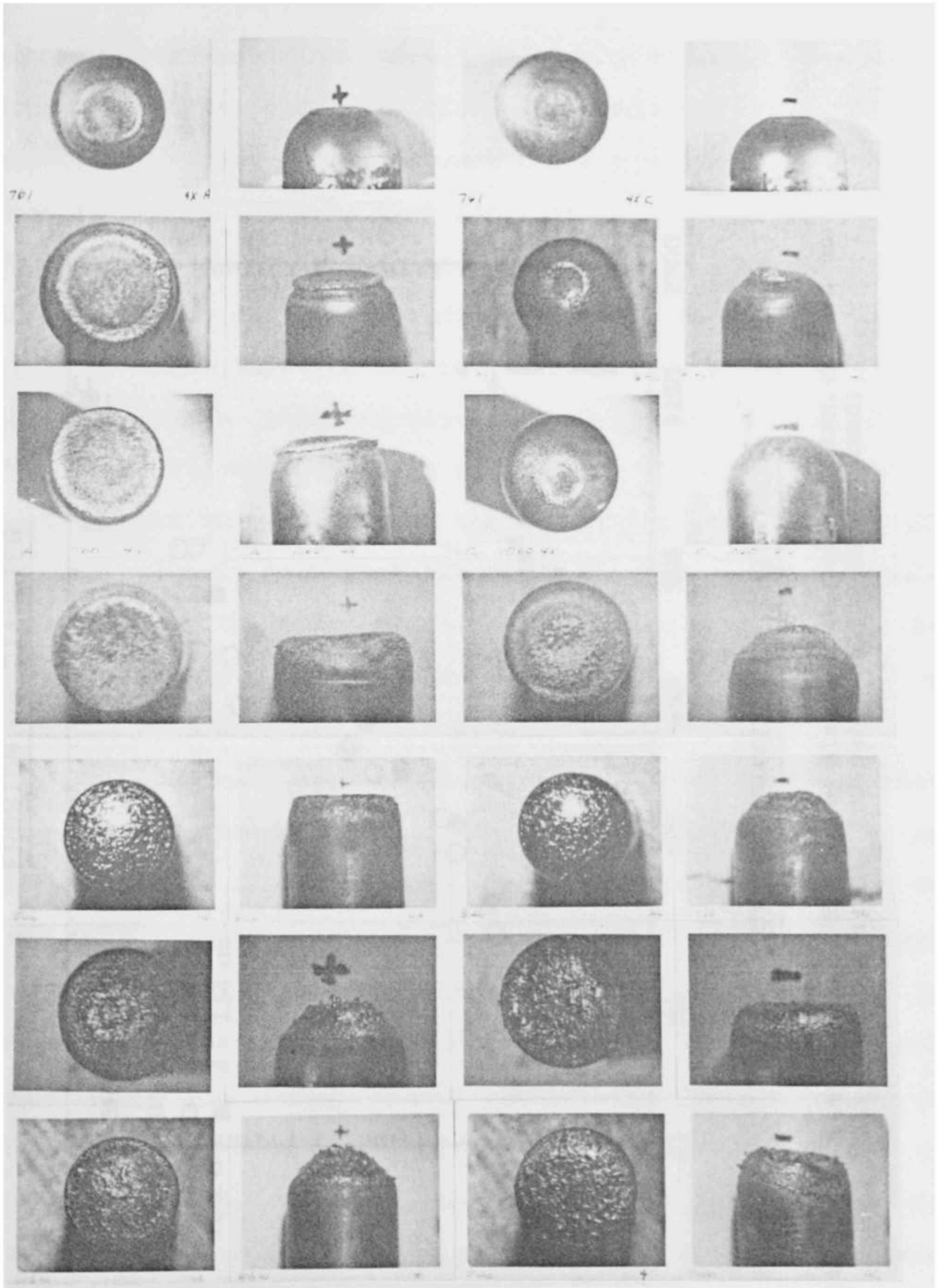

Fig. 3.18 Photographs of Cu#1 Electrodes Used for the Baseline Open Air Erosion Tests. (Left to Right: Anode Top, Anode Side; Cathode Top, Cathode Side; Top to Bottom: Run #761, 647, 1060, 626, 666, 878, 620)

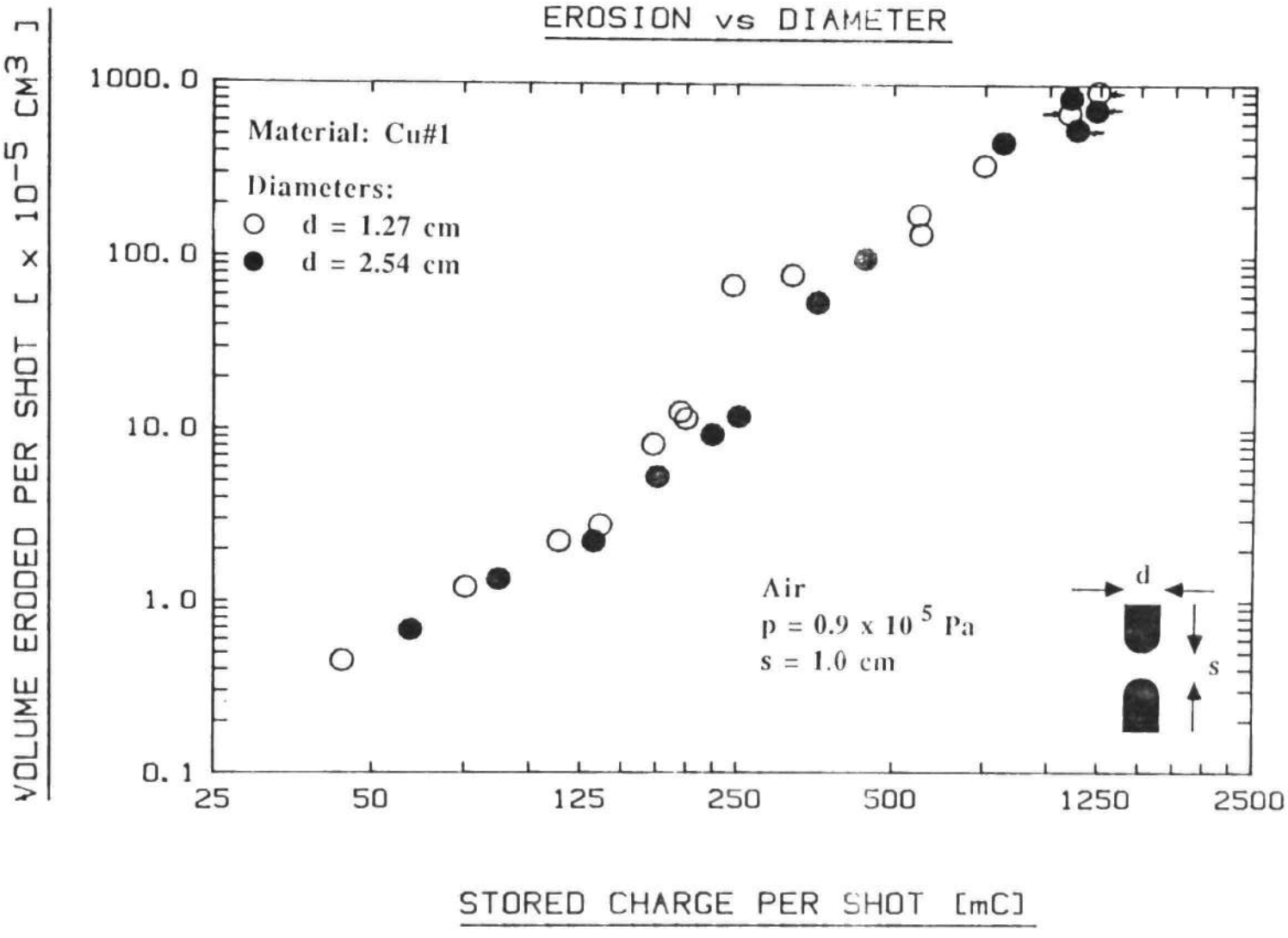

Fig. 3.19 The Effect of Electrode Diameter on Cu#1 Erosion. (A dash on the plotting symbol indicates Switch #2 was used)

of asymmetrical electrodes. Figure 3.20 shows the anode erosion for the four possible cases involving two different diameters. Case #2 and #4 were those plotted in Fig. 3.19. Case #1 and #4 indicate that for a large cathode the anode diameter has no effect on the anode erosion. Case #1 and #2 indicate that the cathode diameter has an effect on the 1.27 cm anode erosion in the transition region with the larger cathode yielding significantly less anode erosion. For the 2.54 cm anode, case #3 and #4, the same effect is observed but it extends past the transition region. These results clearly show that the anode erosion is considerably dependent on the size of the opposite electrode. Of the mechanisms thought to produce electrode erosion it is believed that only EJE would produce these results.

To determine if the initial polarity is also important the cathode erosion was studied for the same four cases as shown in Fig. 3.21. The one difference between Figs. 3.20 and 3.21 is that a small anode does not produce increased cathode erosion if the cathode is also small. This can be explained since the cathode jet will be dominant for electrodes of equal size. Thus, cathode erosion is independent of the anode diameter for anodes of equal or greater diameter. However, case #1 and #2 together indicate that cathode erosion is a function of anode diameter when the anode diameter is smaller and that the dependence exists in the transition region and beyond. Thus, for certain specific cases it can be said that the electrode erosion is

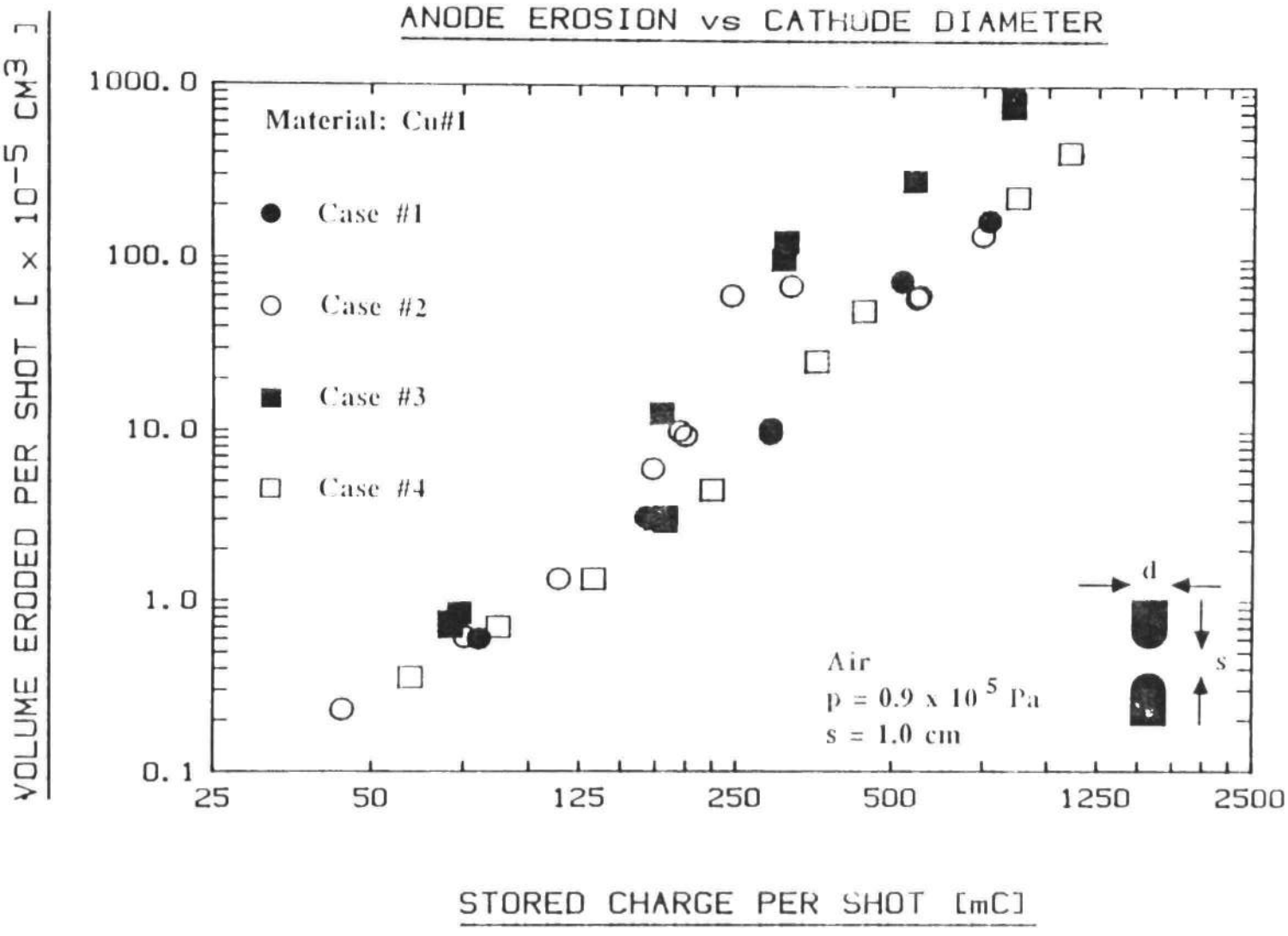

Fig. 3.20 Cu#1 Anode Erosion vs. Cathode Diameter. (Case #1: d_+ = 1.27 cm, d_- = 2.54 cm, Case #2: $d_+ = d_-$ = 1.27 cm, Case #3: d_+ = 2.54 cm, d_- = 1.27 cm, Case #4: $d_+ = d_-$ = 2.54 cm.) (d_+ and d_- are the anode and cathode diameters)

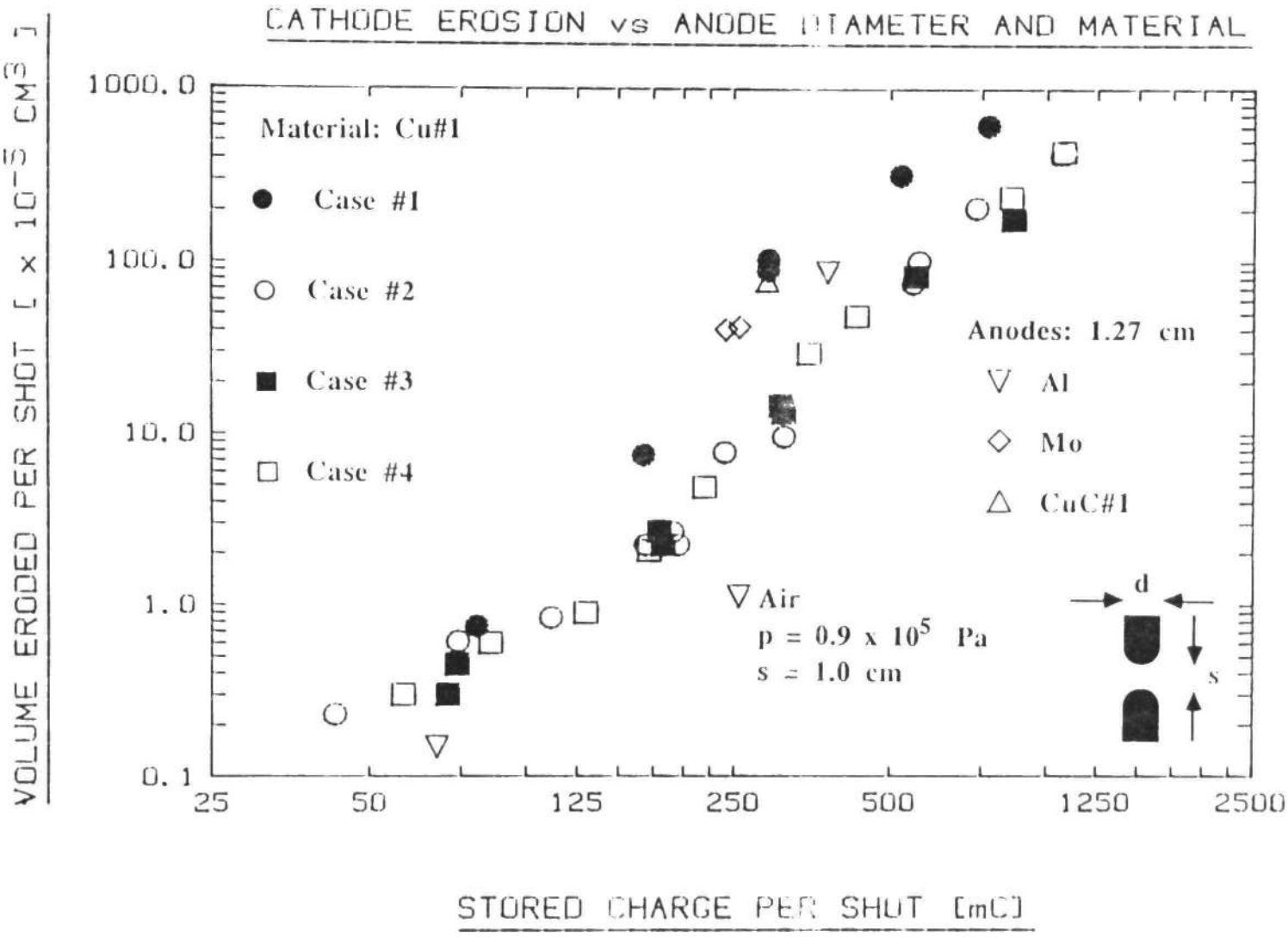

Fig. 3.21 Cu#1 Cathode Erosion vs. Anode Diameter and Material, Case Description the Same as for Fig. 3.20.

significantly influenced by the size of the opposite electrode because of the jet effect.

The effect of the anode material on the cathode erosion is also shown in Fig. 3.21. A small diameter anode opposite a large diameter cathode was chosen in order to insure that an anode jet would be the dominant cause of cathode erosion. Three materials were utilized: aluminum, copper-graphite (CuC#1) and molybdenum. The Mo and CuC results were similar to that for copper, as expected, but the Al results showed a significant reduction in the cathode erosion over a wide range of stored charge, especially at lower values. Examination of the copper cathode showed large amounts of aluminum indicating that its lower melting temperature led to its early transfer into the gap and onto the cathode so that the copper cathode never needed to supply much of its material for charge conduction. The use of a low melting point additive has been suggested by Gruber and Suess [71] as a means of reducing erosion.

The next experiment consisted of replacing the copper cathode with graphite. Graphite should reduce the jet energy by virtue of its low atomic weight and high sublimation energy (see the discussion section). Also the streak photograph of Fig. 3.16c indicated that graphite electrodes do not necessarily produce the electrode jets at the same conditions as copper electrodes. The results plotted in Fig. 3.22a and b for two different electrode diameter sizes indicate that the use of a graphite cathode

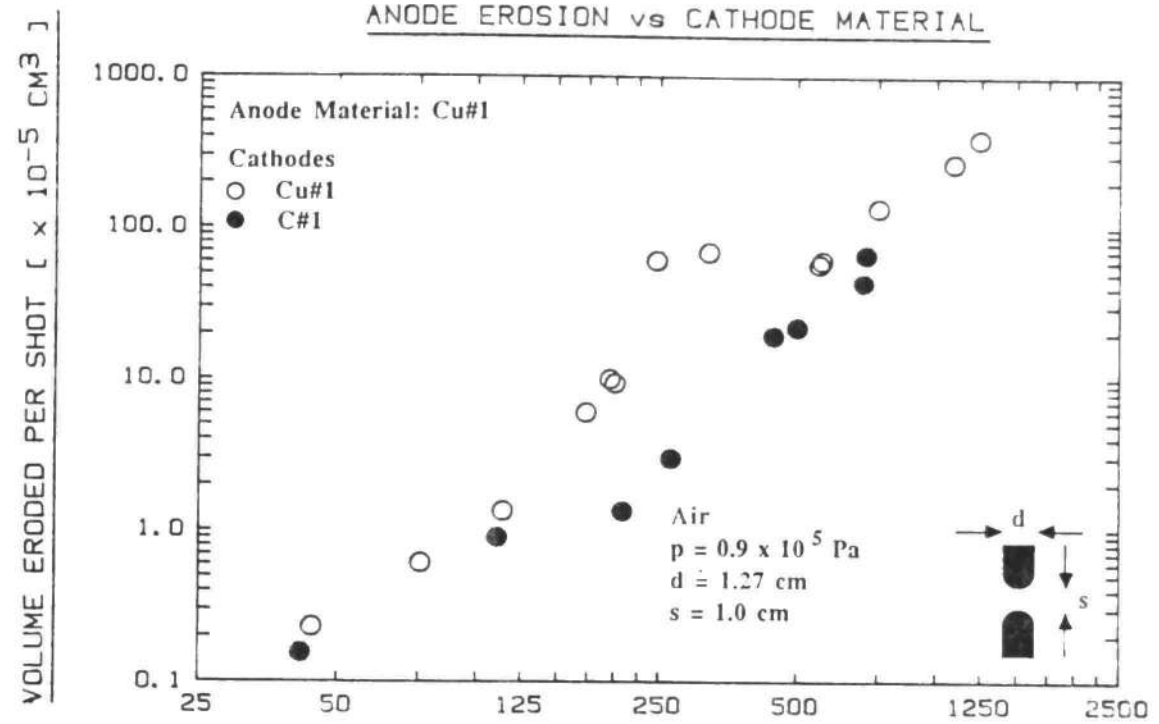

a) d = 1.27 cm

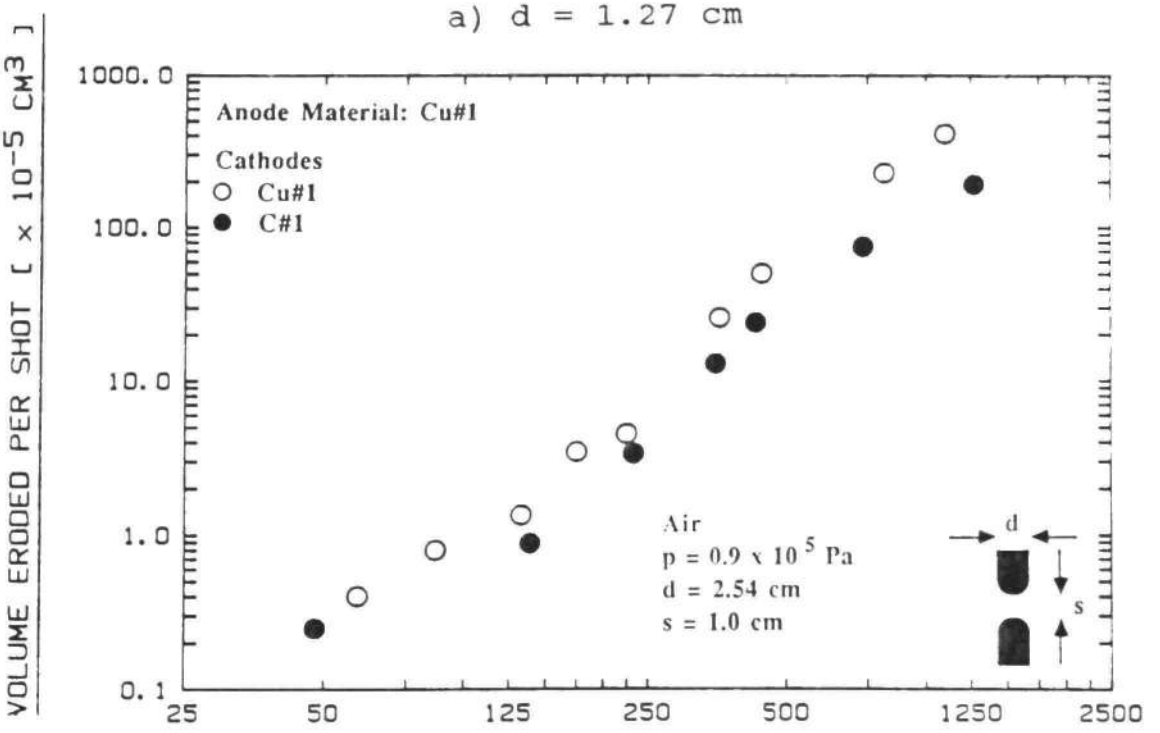

b) d = 2.54 cm

Fig. 3.22 Cu=1 Anode Erosion vs. Cathode Material for Two Different Diameters.

caused a shift in the transition region to higher values of stored charge. This shift results in a reduction in electrode erosion in the previous transition region by over an order of magnitude for the smaller diameter case. This result is consistent with the results of Fig. 3.19 in that one would expect the reduction to be the greatest in the region where EJE dominates. Beyond the transition region the erosion is reduced by up to a factor of three. This last result indicates that the electrode material is more important than the electrode diameter for determining the electrode erosion for the case of symmetric electrodes.

Switch #3 was used to determine the trends for the erosion from the jet only. The results plotted in Fig. 3.23 indicate that the erosion decreases rapidly with increasing distance or decreasing current (decreasing capacitance). The apparent inversion of the 37 μF and 55.5 μF results is a consequence of the higher breakdown voltages, and thus, higher average peak currents obtained for the 37 μF runs. The reason for the lower average self-breakdown voltages for higher values of capacitance is a result of the greater electrode surface damage (macroscopic surface protrusions, produced by the first few shots of the higher discharge energies. When comparing these results with any of the other jet plus arc results it is important to remember that the geometry used was necessary to obtain jet only results, and thus, in general, does not lend itself to a direct comparison.

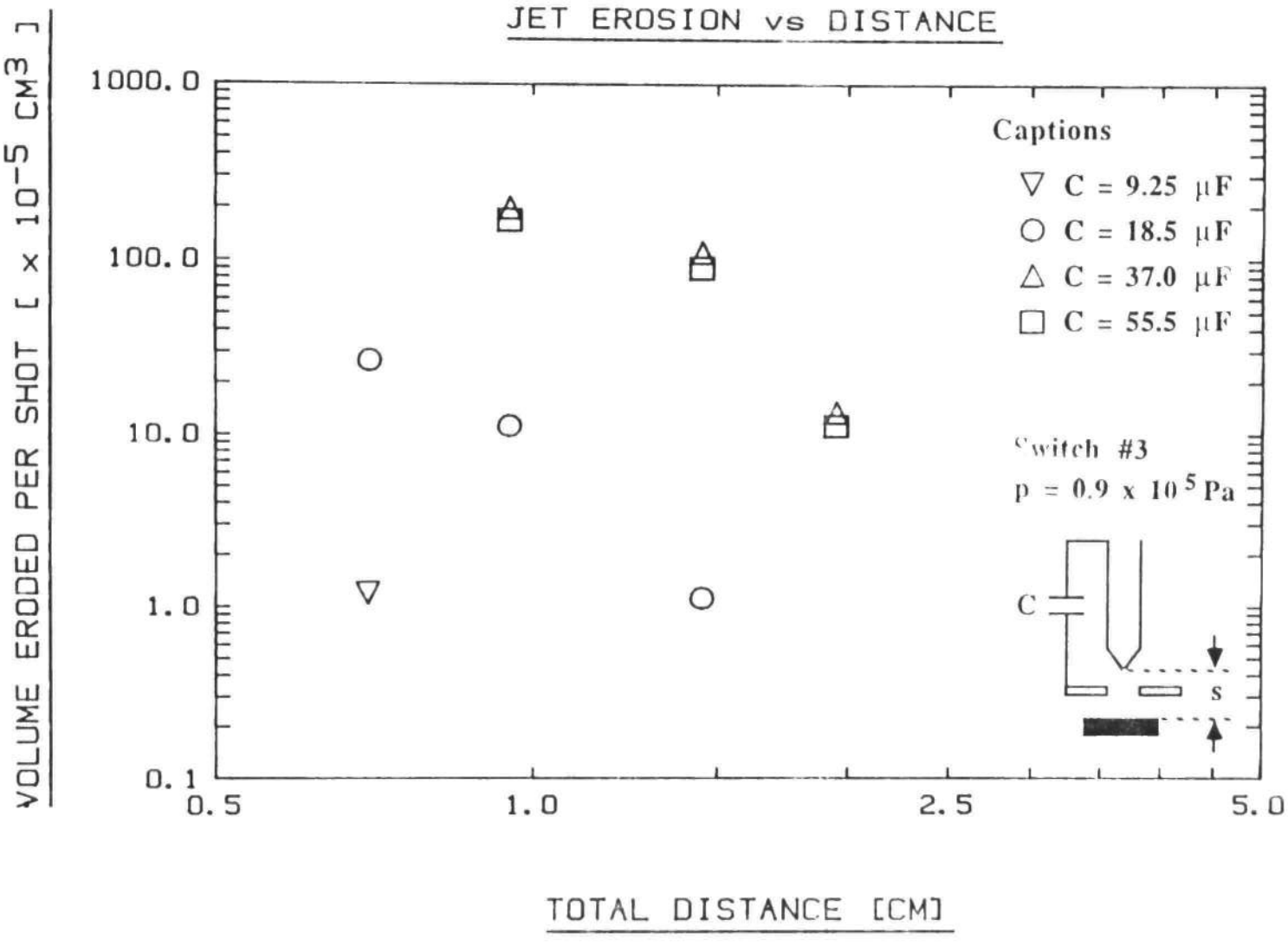

Fig. 3.23 Cu#2, Flat Electrode, Jet Only Erosion vs. Distance in Switch #3.

Both the effect of jet material and gap separation were studied in the experiments shown in Fig. 3.24. Switch #2 was used to generate erosion data at two gap spacings for the same current conditions. Pointed electrodes were used since this geometry enhances the jet effect to such an extent that the initial polarity dependence on jet production is dominated by an initial geometry dependence. Thus, the overlap of the points where both gap spacings were the same indicate that the initial polarity is not important for this geometry, as expected. This allows one to compare the data for the same run which have different gap spacings. The center electrodes were chosen to be graphite and CuW#2 because they eroded less than other materials, and thus maintained their pointed shape longer and also because the jet material produced, graphite and copper, gave highly contrasting results in earlier experiments. The center electrode was pointed so that the jet it produced would dominate the erosion of the opposite electrode. Thus, it was no surprise that for all cases the erosion on the electrode opposite the graphite center electrode was significantly lower than the erosion on the electrode opposite the CuW center electrode. The slopes of the graphite data and the CuW data indicate that both sets of data might coalesce at very high and very low values of the stored charge. We were unable to use higher values of the stored charge for the graphite electrodes because they shattered--presumably from electrode joule heating induced

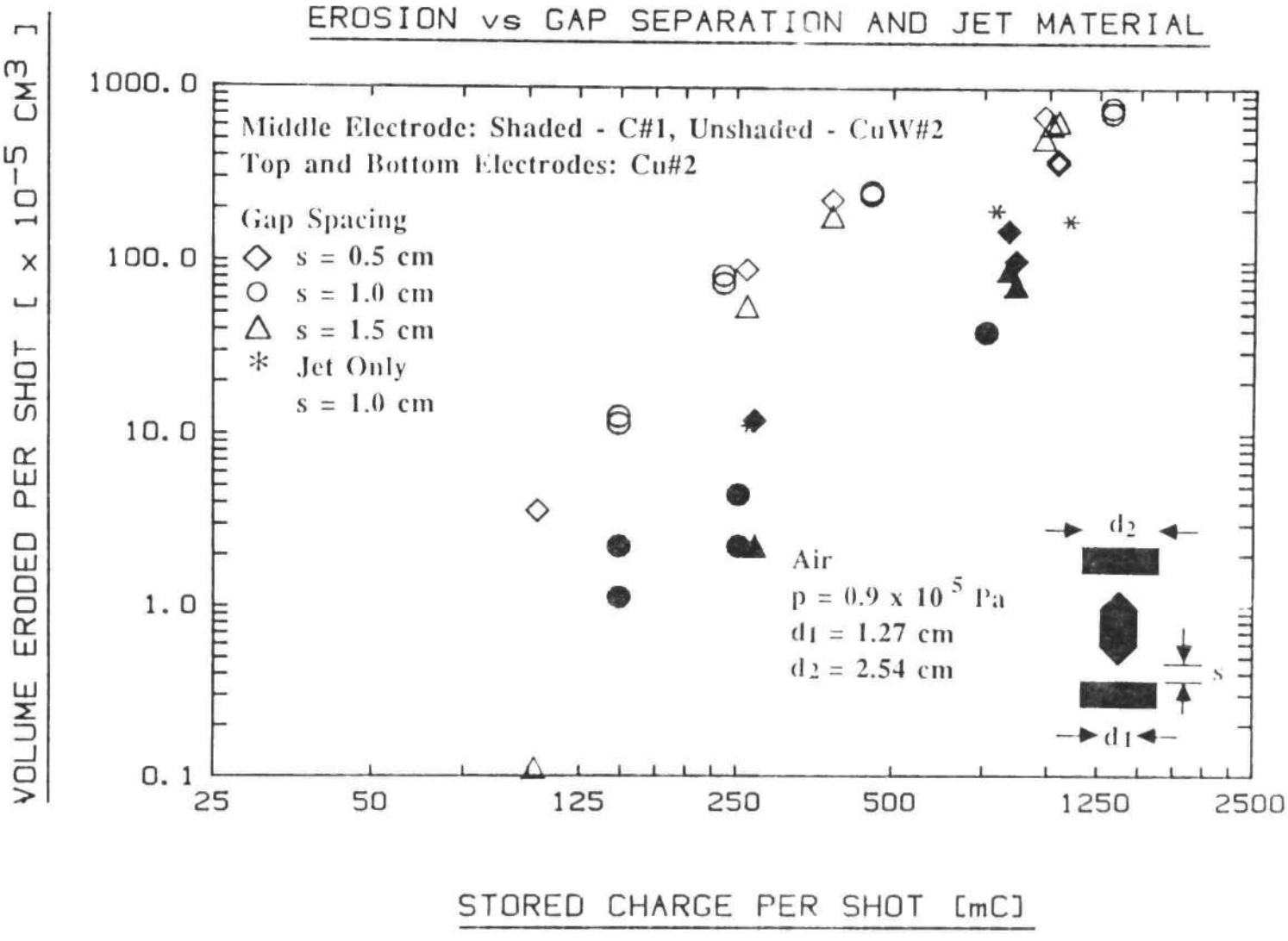

Fig. 3.24 The Effects of Gap Separation and Jet Material on Cu#2, Flat Electrode Erosion in Switch #2.

temperature stresses or acoustic shocks [76]. For lower values of stored charge the measured net erosion was close to zero or zero (which could not be plotted). However, it is believed that significant mass transfer took place from the center electrode to the target electrode, so that the erosion was actually greater, although the amount is uncertain. (Note: for the results which were plotted, the mass transfer factor was considered secondary because of the large values of electrode erosion which were encountered.)

The relevant data points from the jet only erosion data of Switch #3 were also plotted in Fig. 3.24. The jet erosion values ranged from two to eight times lower than the erosion obtained with the jet plus the arc. At first glance this might lead one to conclude that the jet portion of the erosion is not dominant. However, the Switch #3 geometry which was used to produce the jet-only results may shield a significant portion of the jet energy (as evidenced by the severe destruction of the disk electrode). Given this condition, it is likely that EJE may account for a considerable amount of the electrode erosion. Finally, with a few exceptions the erosion increases as gap spacing decreases; however, the distance effects shown in Fig. 3.24 were not conclusive.

To see more easily the combined effects of distance and current for all the Switch #2 and #3 electrodes which had CuW#2 center electrodes, the results shown in Fig. 3.23 and Fig. 3.24 were added to the plot of Fig. 3.11 to produce

Fig. 3.25. (Note: The erosion values for the 1 cm tests which were approximately the same for each target electrode are plotted as a single point with a (x 2) indicator.) Because the experiments used copper supplied by two different manufacturers, designated Cu#1 and Cu#2, a standard test run was conducted for both materials. The result, designated by a "T" on the plot, indicates that Cu#2 has a slightly higher erosion than Cu#1, but not enough to hinder the observation of major trends. (The reason two materials were used was the result of a supply problem during the middle of testing. The difference was not considered significant enough to warrant the rerunning of the entire set of Cu#1 experiments.)

The major observations are as follows:

1) The jet only erosion results (Switch #3) were very close to the combined jet and current results of Switch #2 for lower values of current (<150 kA), for higher currents the jet erosion was substantially less but appeared to coalesce (dotted lines) with the Switch #2 results at low gap spacings. In all cases the jet only erosion decreased more rapidly with increasing gap separation. For several runs with the same gap separation, the run with the higher current had less erosion. This was probably due to material transfer from the center electrode. For example, the 2.0 cm runs with currents of 266 and 321 kA saw the center electrode erosion increase from 38 to 50 x 10^{-5} cm^3/shot which is considerably larger than the 14 x 10^{-5} cm^3/shot

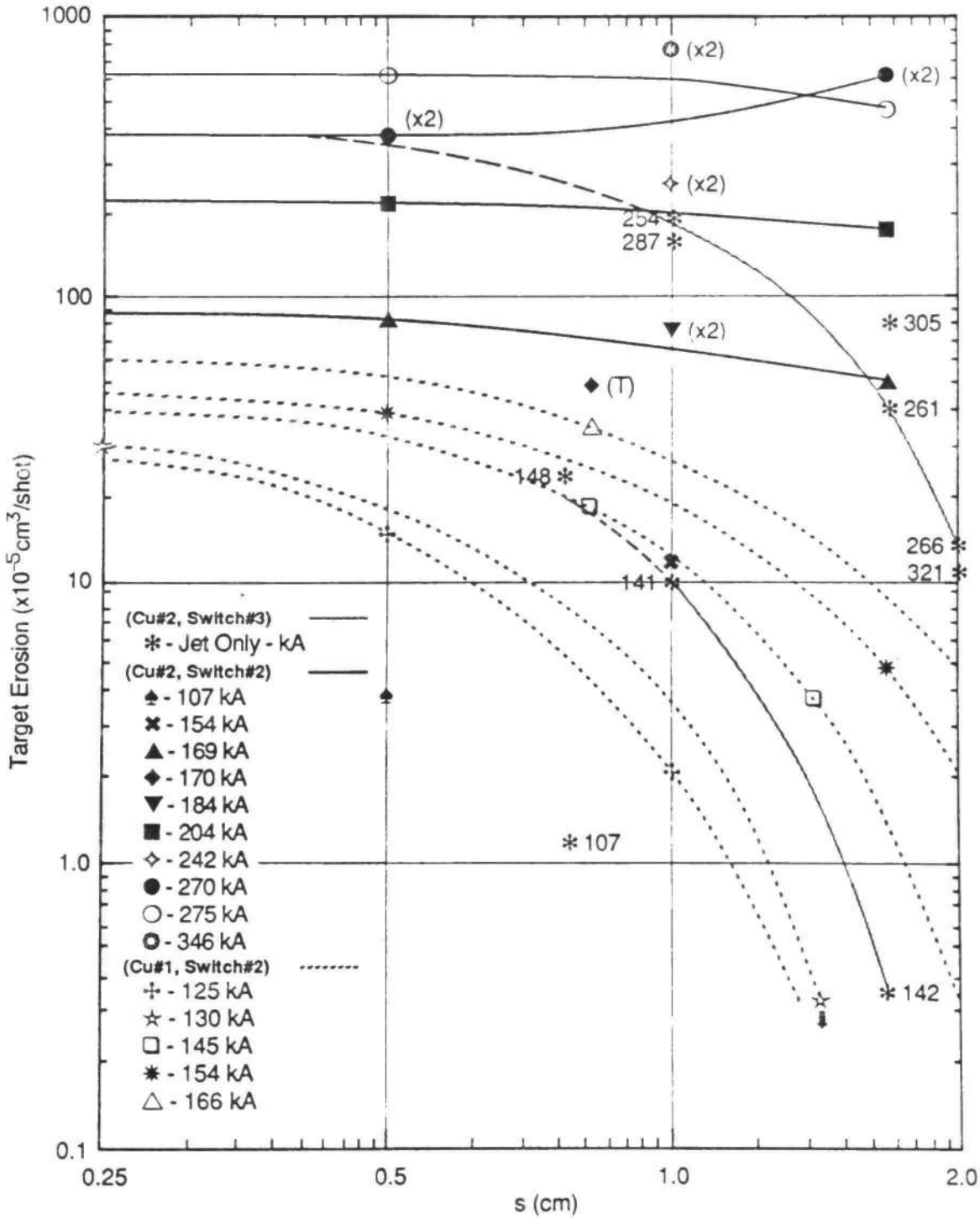

Fig. 3.25 The Effect of Gap Separation and Peak Current on Cu # 1 and # 2 Flat Electrode Erosion in Switch # 2 and # 3.

lost on the electrodes, and thus, could mask the actual erosion.

2) The Switch #2 erosion decreased rapidly with increasing distance only for currents less than 165 kA. For larger currents the erosion either dropped much less rapidly or actually increased. The one case where it increased (run # 622) was rerun (622-1), with exactly the same result, then rerun again (622-2) with the gap spacings s_1 and s_2 reversed which effectively reversed the initial polarity. This time the erosion decreased with increasing gap spacing which indicated there is a polarity effect at high currents. Possible explanations for this phenomenon were discussed with Fig. 3.12 earlier.

3) In all cases Switch #2 erosion increased with increasing current for a given gap separation.

Further experiments designed to determine the effect of distance consisted of varying the gap spacing from 0.5 cm to 2.0 cm in the standard rounded electrode configuration of Switch #1 and #2. The results are shown in Figs. 3.26 and 3.27. (A plot of the Fig. 3.26 data was made using the form of Fig. 3.25 but was not included because no trends beside those seen in Fig. 3.26 were seen.) In Fig. 3.26 one can clearly see that the rapid increase in the erosion can be enhanced (s = 0.5 cm) or virtually eliminated (s = 2.0 cm) in the transition region by changing the gap spacing. The fact that gap separation is apparently important only in the transition region could be due to the fact that this is

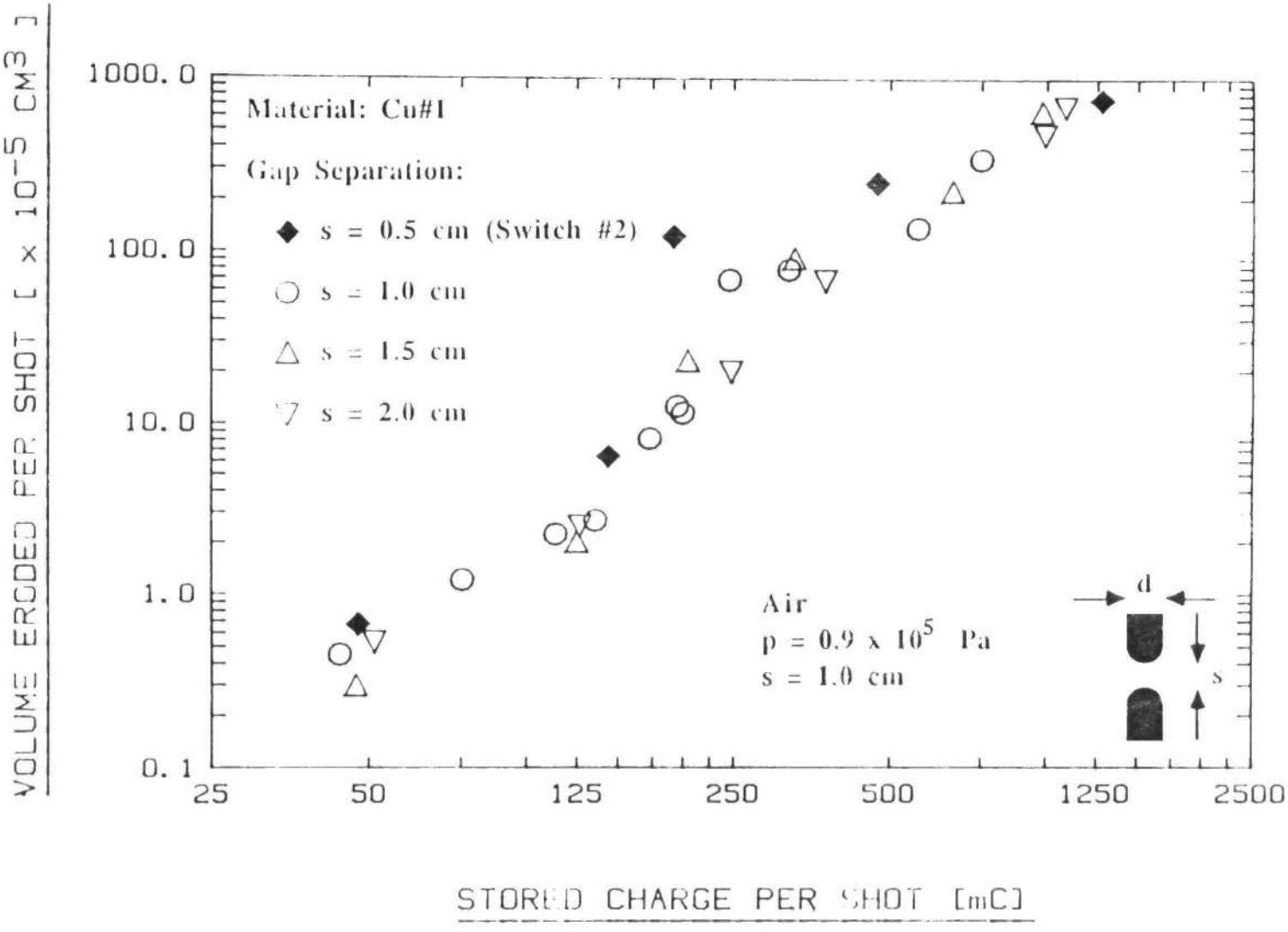

Fig. 3.26 Cu#1 Electrode Erosion vs. Gap Separation in Switch #1 and 2.

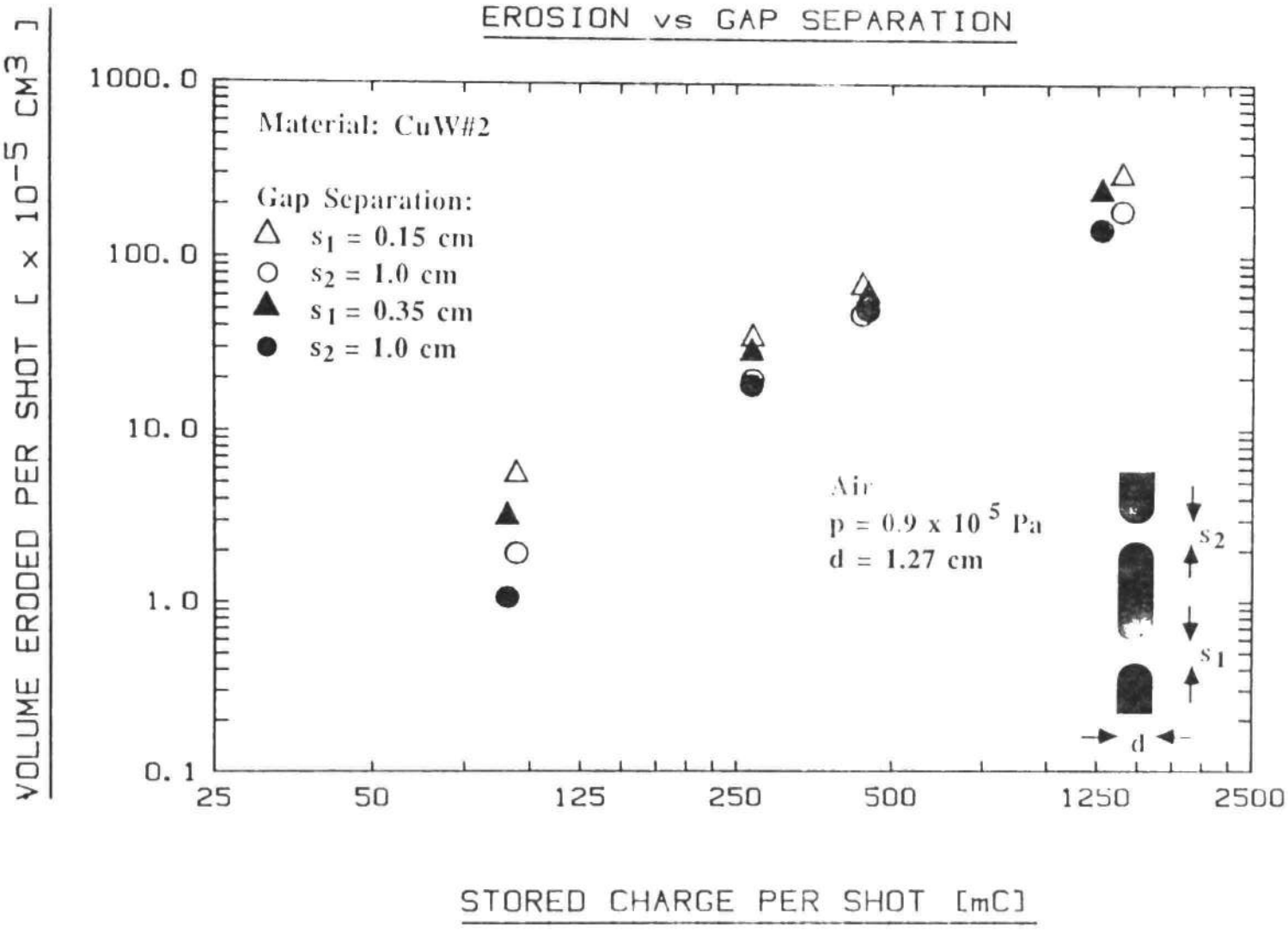

Fig. 3.27 CuW#2 Electrode Erosion vs. Gap Separation in Switch #2.

where EJE is taking place. If this is true then the reverse may also prove to be useful from an engineering standpoint, i.e., if one observes that the gap spacing is having a major effect on erosion, then EJE may be the cause. In Fig. 3.27 it appears that the erosion decreases with increasing distance, as expected, and that the gap distance has its greatest effect at the lower stored charge levels, for reasons which are still unknown. Since the breakdown voltage for both cases is approximately the same it is unclear why the 1 cm erosion for the 1 cm plus 0.35 cm case is less than the erosion for the 1 cm plus 0.15 cm case.

Earlier it was concluded that EJE occurred primarily by the removal of molten material by the jet stream. If this is true for our conditions then increasing a material's mechanical strength at elevated temperatures should improve its resistance to EJE. The final jet experiment consisted of measuring the total erosion for several different materials with improved high temperature mechanical properties. The materials were Cu#1, the baseline material, CuCrZr and CuZr [77], two high strength copper alloys, Cu-Nb#1 [73], which is 18% by weight extruded niobium filaments, and Cu+Al_2O_3 [77], a dispersion strengthened copper 0.3% (#1) and 1.1% (#2) by weight Al_2O_3.

The electrode erosion for these materials is shown in Fig. 3.28. (A listing of the mechanical properties is given in Appendix A.) As expected, the materials with the higher yield strengths at elevated temperatures showed less erosion

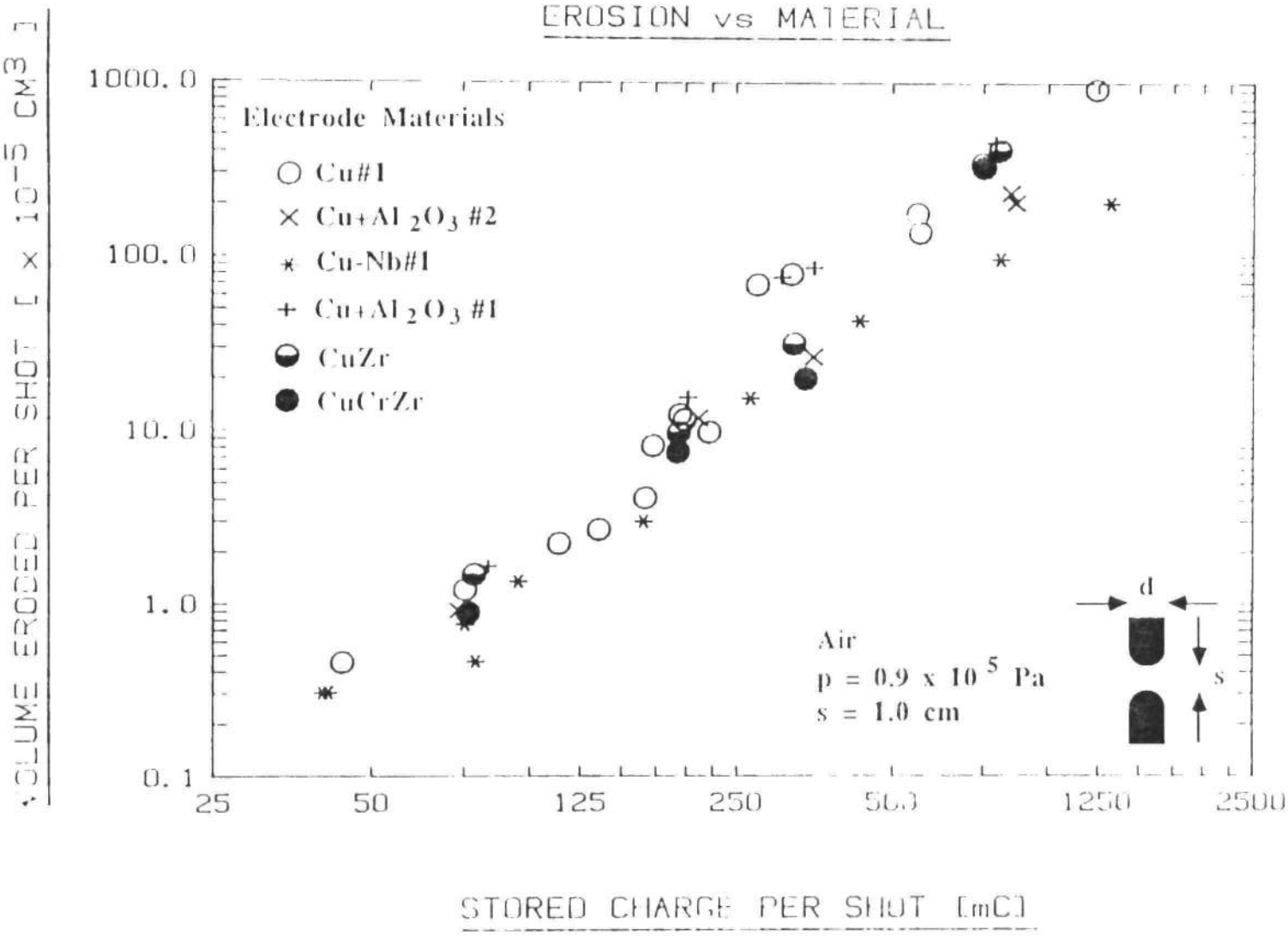

Fig. 3.28 Electrode Erosion for Several Materials with Different High Temperature Mechanical Strengths.

in the transition region. The materials with the best high temperature mechanical properties, Cu-Nb#1 and $Cu+Al_2O_3$#2, exhibit improved erosion beyond the transition region as well. Photographs of the electrode surfaces indicate that the improvement in the erosion characteristics in the transition region was probably due to the retention of heated electrode material, which however, in the case of Cu#1 was apparently removed by EJE.

The photographs and tables for the results just discussed are shown in Fig. 3.29 through Fig. 3.38 and listed in Tables 3.11 through 3.19.

EJE Implications on the Effect of Gas Type and Pressure

The EJE experiments seemed to indicate that because of the presence of the electrode jets, the gap separation could become a dominant factor on electrode erosion, especially in the transition region where potentially a large percentage of the electrode surface is near or at the melting temperature. If this is true, then one might suspect that for small gap spacings the method of voltage holdoff becomes a secondary consideration when predicting the erosion performance. To test this hypothesis, three different methods of voltage holdoff of a 0.15 cm gap were utilized: 10^5 Pa (1 atm) of SF_6 gas, 2-3 x 10^5 Pa of pressurized air and the use of the "piggyback," switch #2, gap arrangement

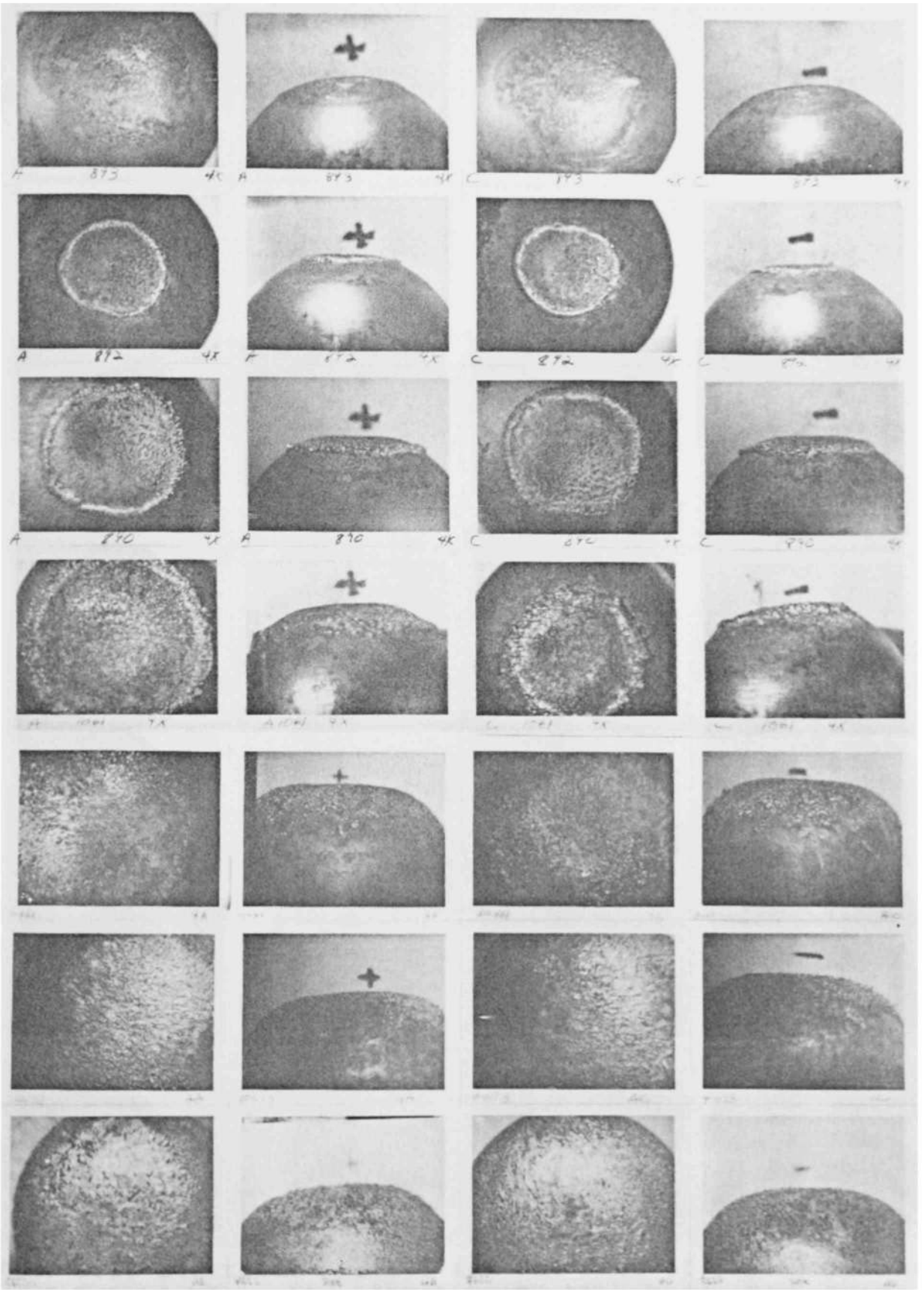

Fig. 3.29 Electrode Surface for the Plot of Fig. 3.19 and Table 3.11. (Left to Right: Anode Top, Anode Side, Cathode Top, Cathode Side; Top to Bottom: Run # 893, 892, 890, 746, 661, 693, 622)

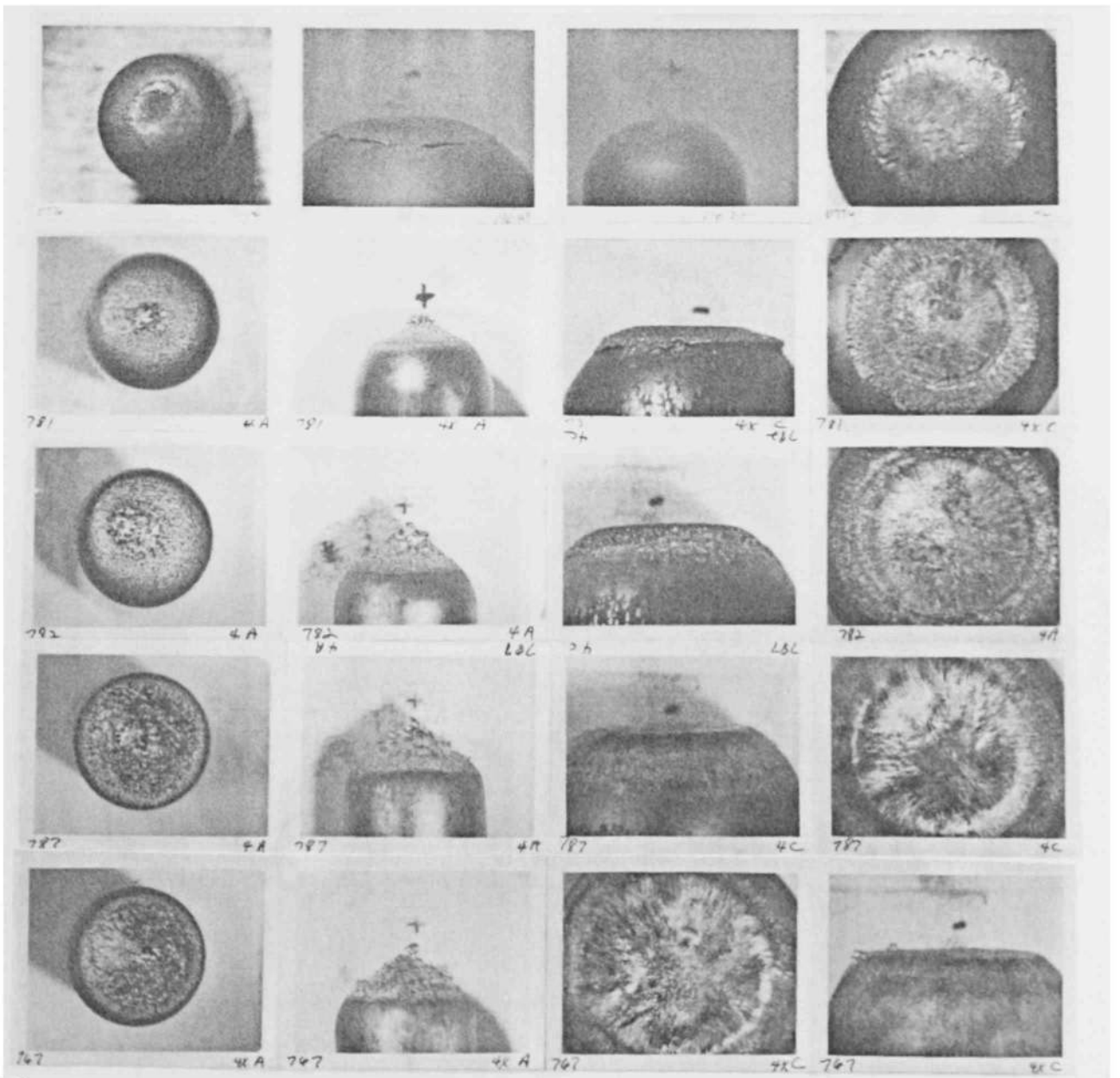

Fig. 3.30 Electrode Surface for the Plot of Fig. 3.20 and Table 3.12. (Left to Right: Anode Top, Anode Side, Cathode Top, Cathode Side; Top to Bottom: Run # 776, 781, 782, 787, 767)

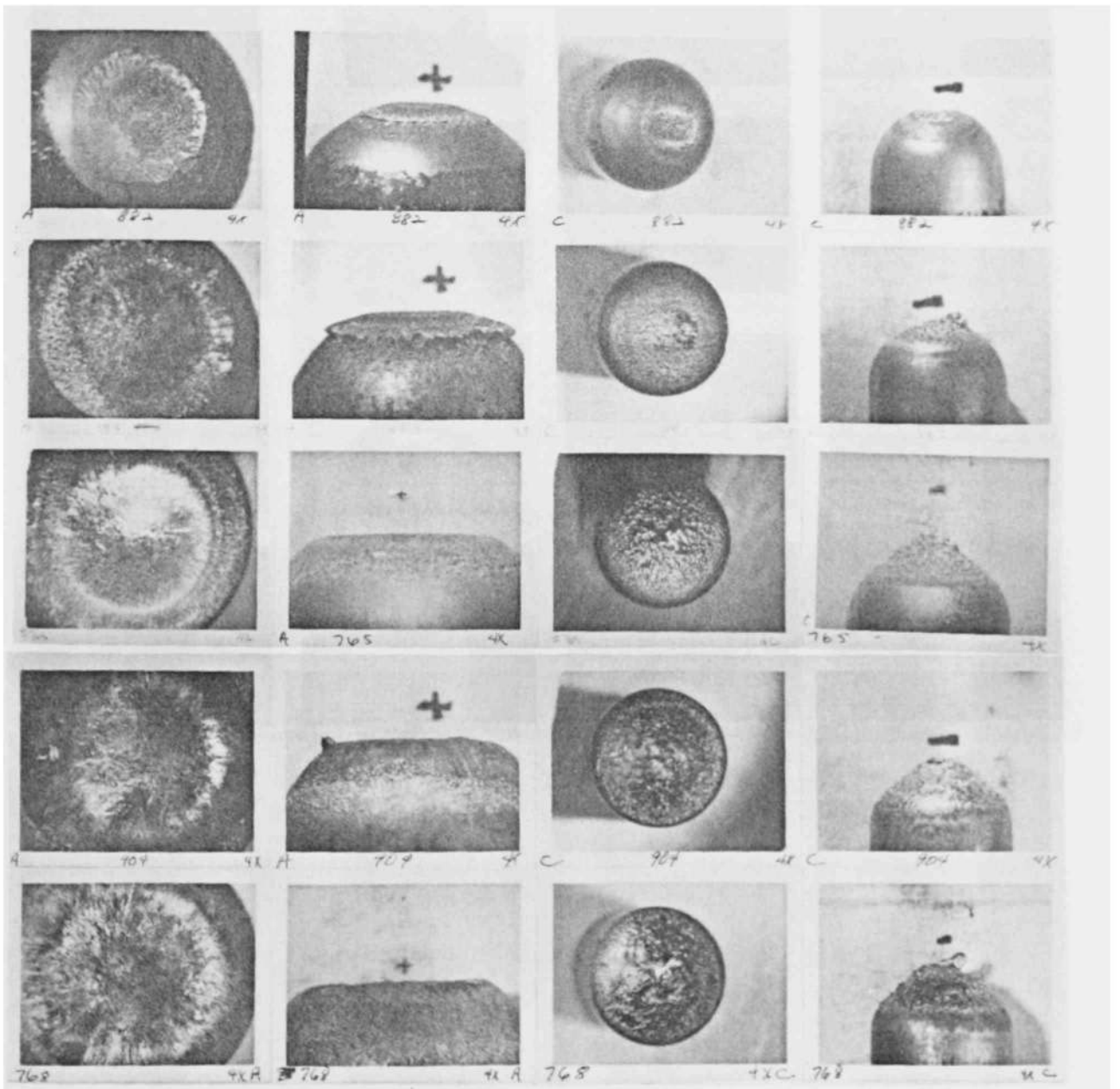

Fig. 3.31 Electrode Surface for the Plot of Fig. 3.20 and Table 3.12. (Left to Right: Anode Top, Anode Side, Cathode Top, Cathode Side; Top to Bottom: Run # 882, 883, 765, 904, 768)

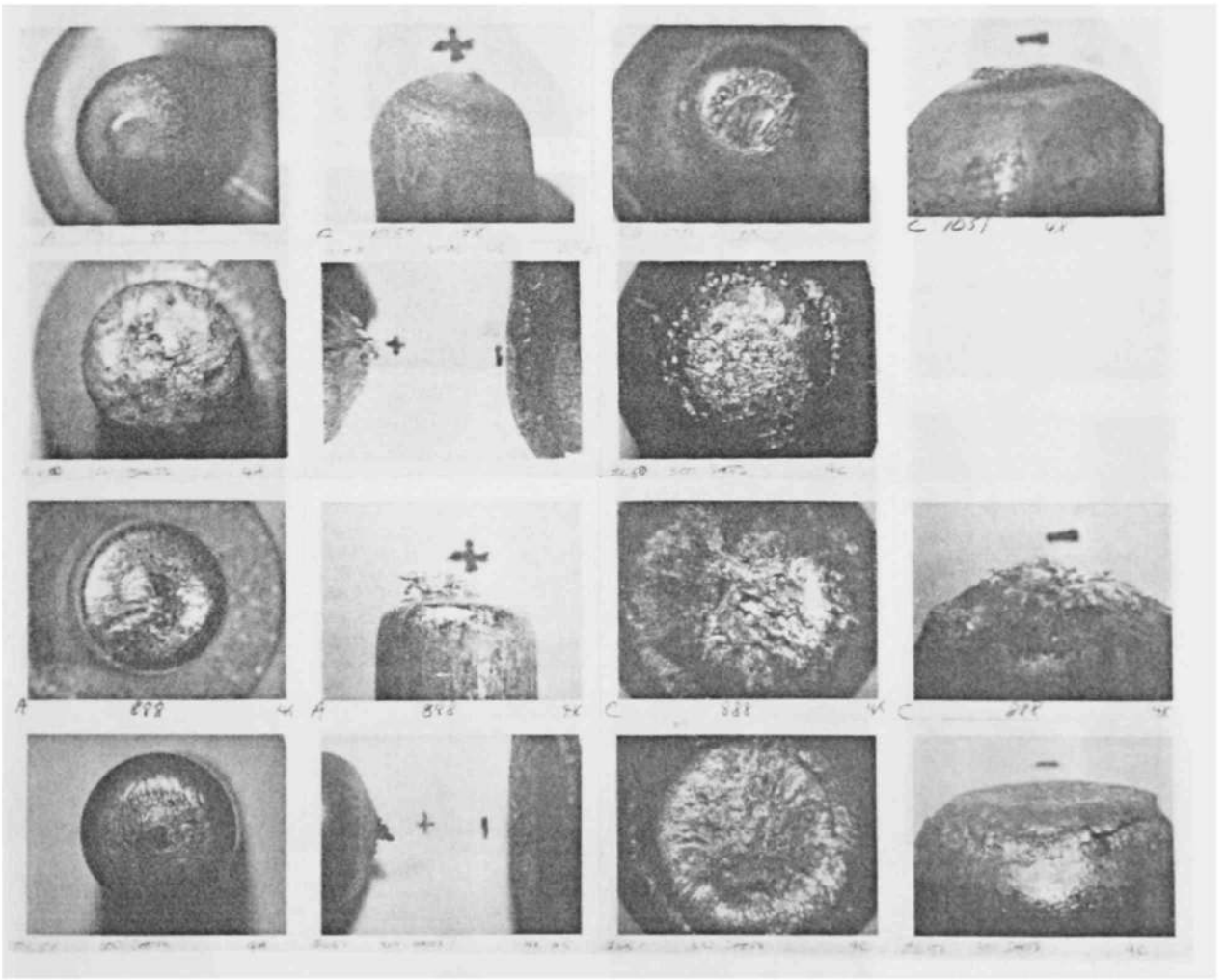

Fig. 3.32 Electrode Surface for the Plot of Fig. 3.21 and Table 3.13. (Left to Right: Anode Top, Anode Side, Cathode Top, Cathode Side; Top to Bottom: Run # 1051, 650, 888, 651, 652, 653)

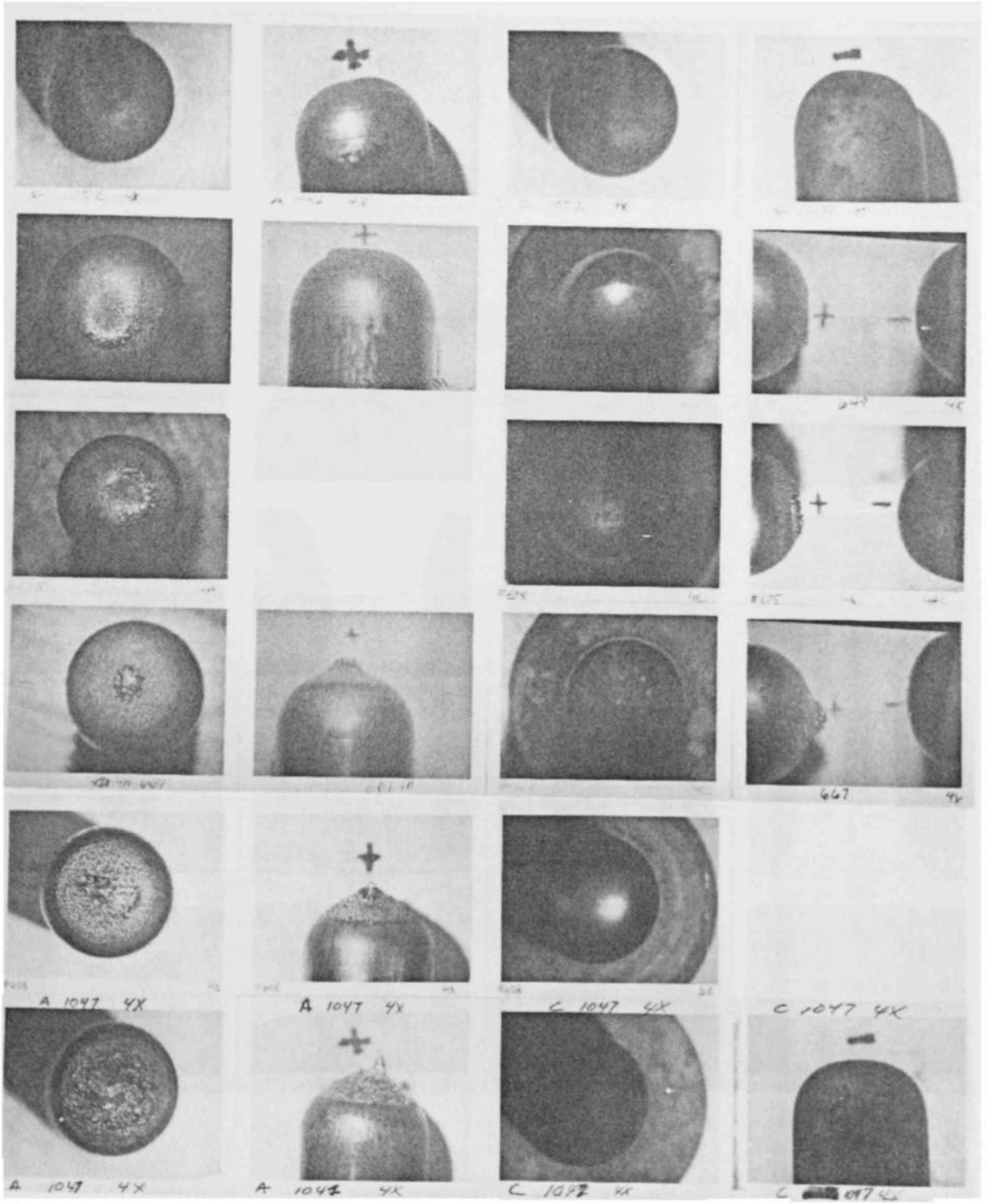

Fig. 3.33 Electrode Surface for the Plot of Fig. 3.22 and Table 3.14. (Left to Right: Anode Top, Anode Side, Cathode Top, Cathode Side; Top to Bottom: Run # 1052, 649, 685, 667, 628, 1047)

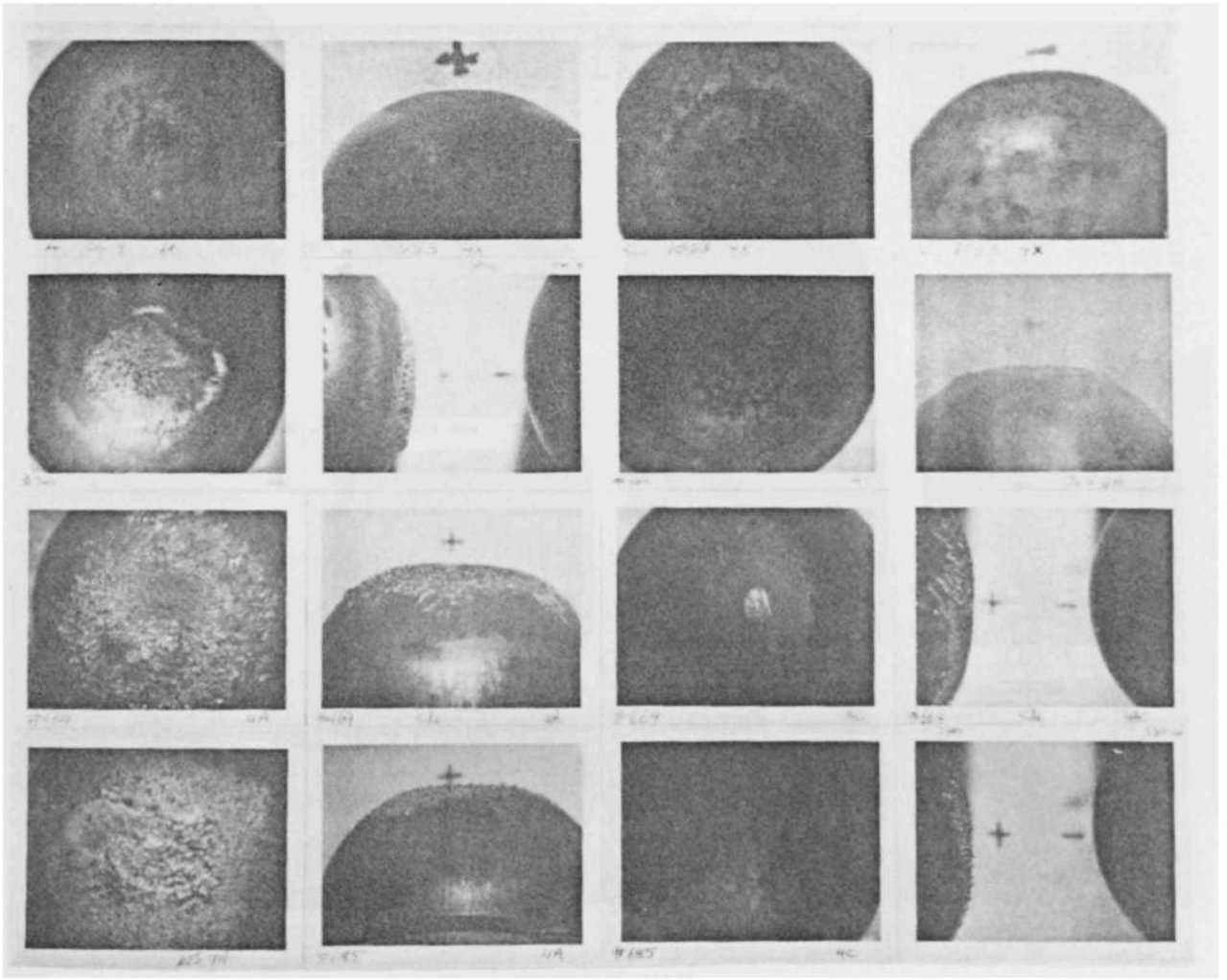

Fig. 3.34 Electrode Surface for the Plot of Fig. 3.22 and Table 3.14. (Left to Right: Anode Top, Anode Side, Cathode Top, Cathode Side; Top to Bottom: Run # 1053, 744, 644, 685)

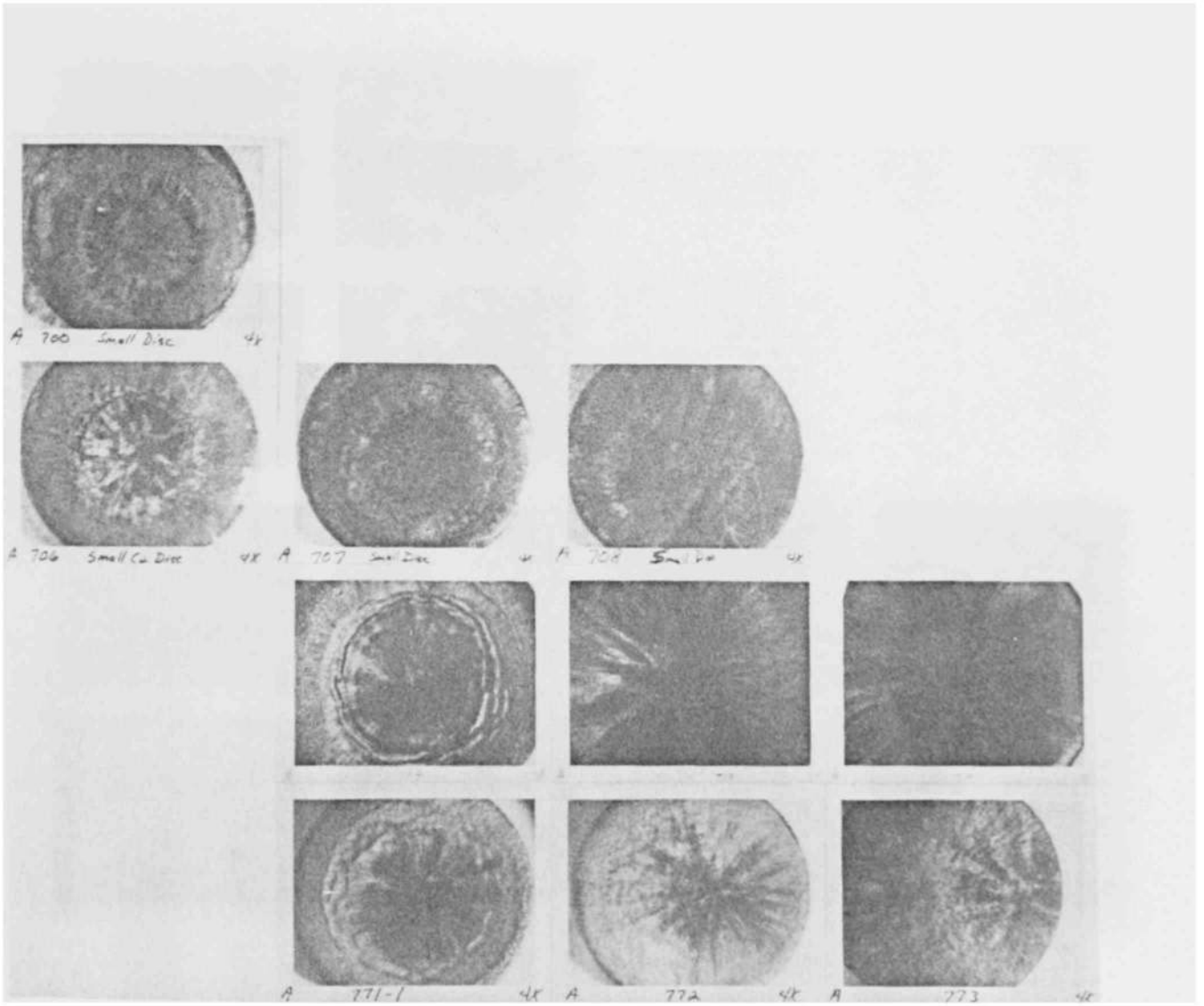

Fig. 3.35 Electrode Surface for the Plot of Fig. 3.23 and Table 3.15. (Left to Right: s = 0.7, 0.95, 1.45, 1.95 cm; Top to Bottom: # Caps - 5, 10, 20, 30; Run # See Table 3.15)

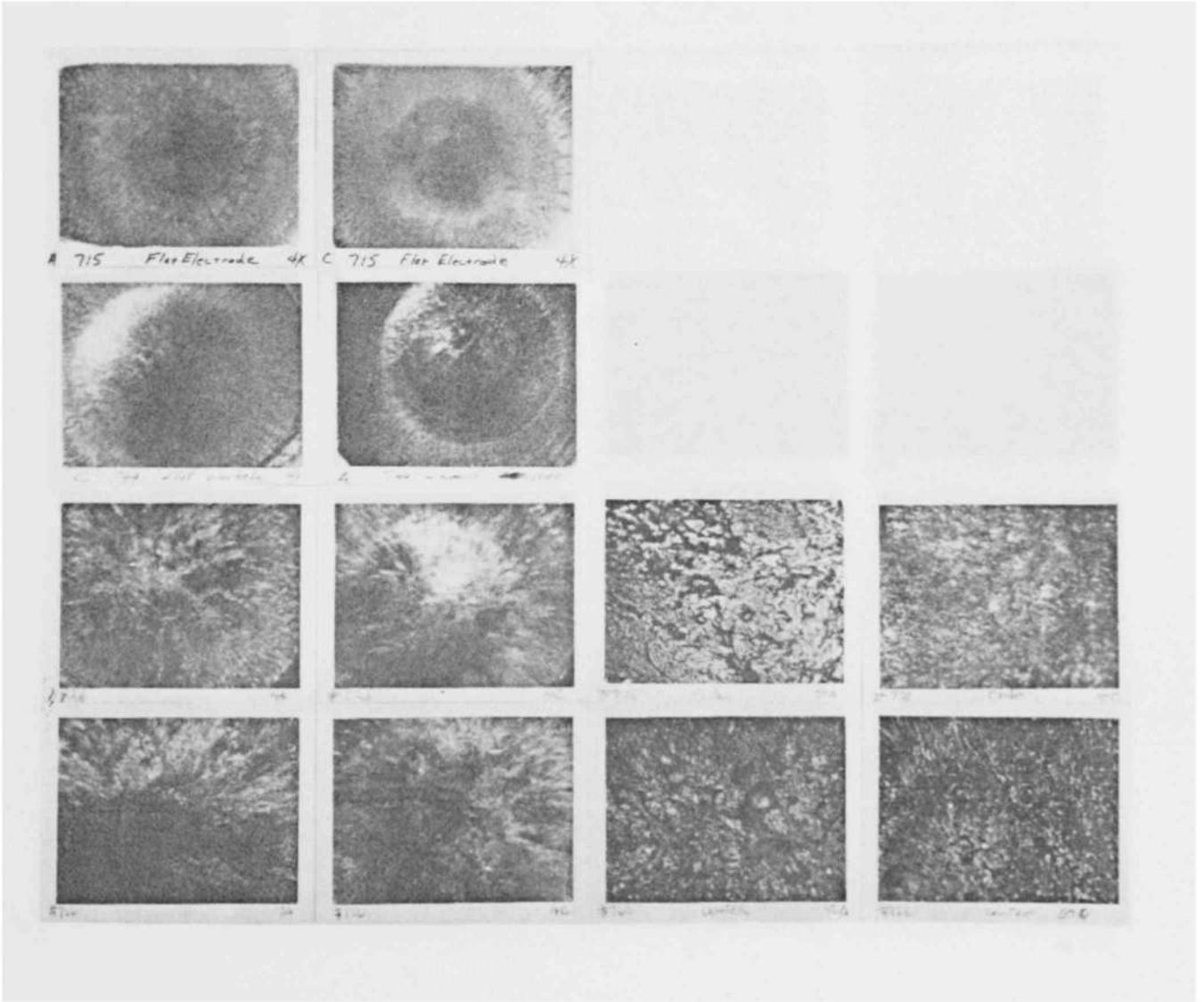

Fig. 3.36 Electrode Surface for the Plot of Fig. 3.24 and Table 3.16. (Left to Right: Anode (1.4x), Cathode (1.4x), Anode (18x), Cathode (18x); Top to Bottom: Run # 715, 739, 726, 722)

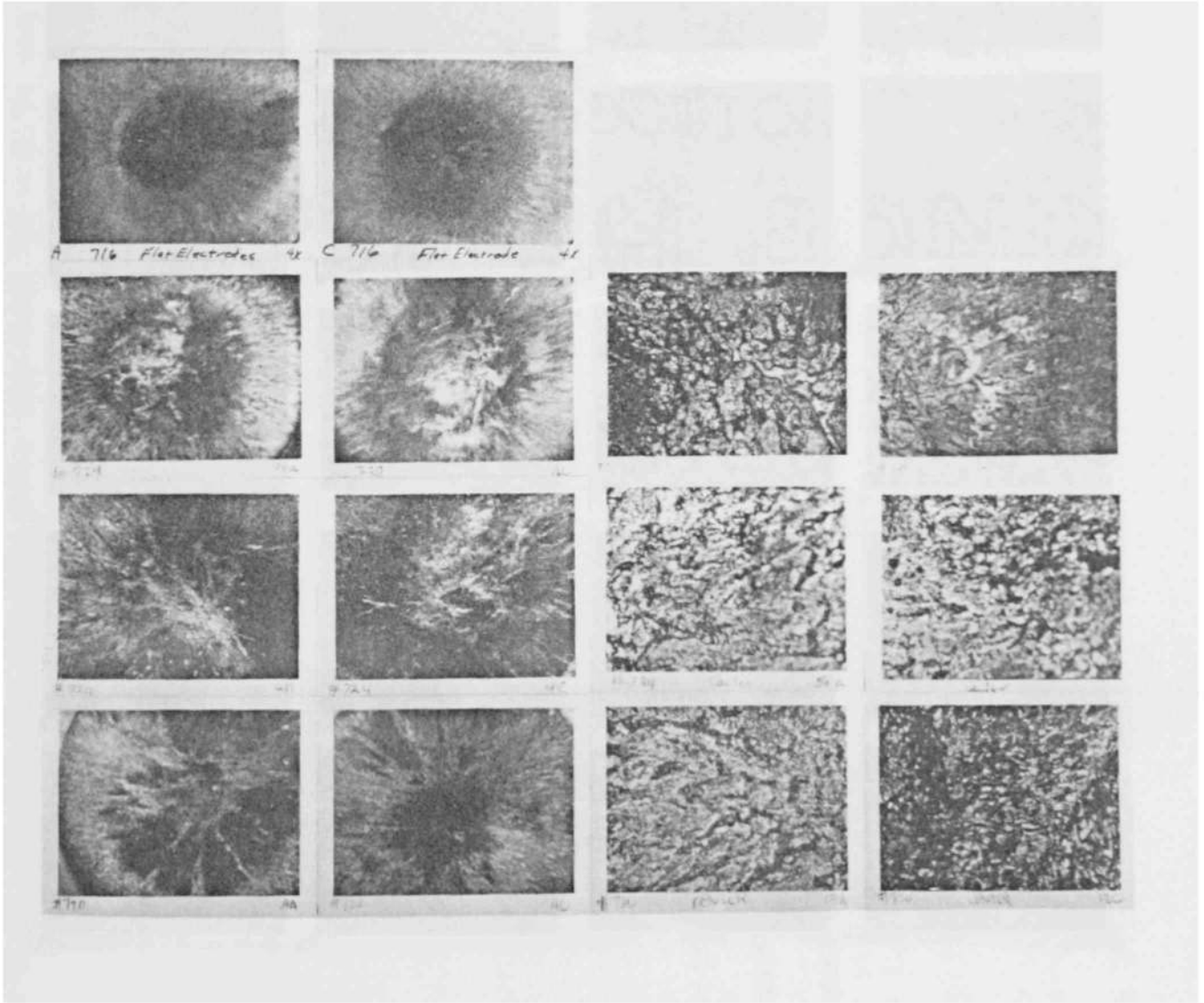

Fig. 3.37 Electrode Surface for the Plot of Fig. 3.24 and Table 3.16. (Left to Right: Anode (1.4x), Cathode (1.4x), Anode (18x), Cathode (18x); Top to Bottom: Run # 716, 729, 724, 720)

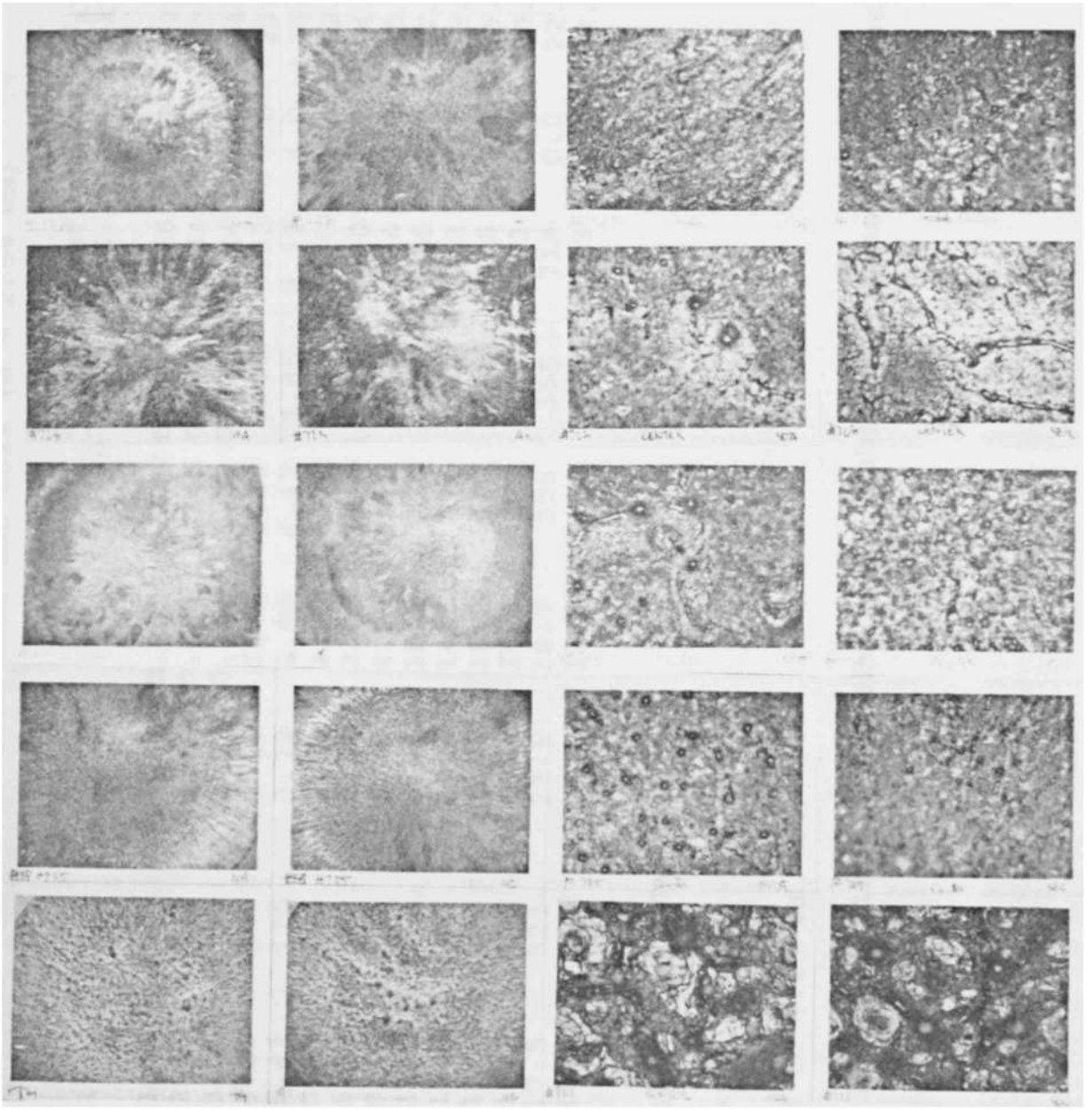

Fig. 3.38 Electrode Surface for the Plot of Fig. 3.24 and Table 3.16. (Left to Right: Anode (1.4x), Cathode (1.4x), Anode (18x), Cathode (18x); Top to Bottom: Run # 727, 723, 728, 725, 721)

Table 3.11 Electrode Erosion Data for Cu#1 (d = 2.54 cm)

Run #	Caps (#)	Q_s (mC)	Q_e (C)	I_p (kA)	E_s (kJ)	f_1 (*)	DV+ (x 10^{-5} cm^3/shot)	DV-	DV_{tot}	$DV_{\%e}$	V_{sb} (kV)	$DV_{sb\%e}$
893	1	59.4	1.43	99.9	0.955	0.202	0.376	0.300	0.676	11	32.1	3.8
892	2	87.3	2.17	111	1.03	0.404	0.746	0.597	1.34	11	23.6	3.7
743	3	133	3.18	137	1.59	0.810	1.34	0.895	2.24	10	24.0	4.4
890	4	176	4.30	165	2.10	1.42	3.24	2.08	5.32	5.6	23.8	4.5
641	5	224	5.41	175	2.72	2.00	4.47	4.85	9.32	4.0	24.3	4.4
1061	6	251	5.62	160	2.83	1.99	6.71	4.92	11.6	3.9	22.6	5.1
746	8	358	6.98	183	4.32	3.04	25.6	29.4	55.0	1.2	24.2	4.9
661	10	443	8.41	236	5.29	4.99	50.0	48.4	98.4	0.8	23.9	6.2
693	20	814	13.6	262	8.95	10.7	228	239	466	0.3	22.0	8.8
622	30	1080	15.4	283	10.4	14.5	474	488	962	0.2	19.4	16
681	30	1100	15.8	290	11.0	15.2	412	434	846	0.3	19.9	17
**736	30	1130	16.1	296	11.4	15.8	273	280	553	0.4	20.3	8.6
**737	30	1230	17.5	323	13.6	18.7	358	358	718	0.0	22.1	8.2
+683	30	1260	18.0	332	14.4	19.8	426	483	909	0.3	22.7	9.7

*The units on f_1 are ($A^2s^{1.5}$ x 10^3).

**Switch #2 ("Piggyback")

+ Gap distance increased to 1.25 cm.

Note: Data for d = 1.27 cm is listed in Table 3.10. Table variables are defined in Table 3.6.

Table 3.12 Electrode Erosion Data for Cu#1 Asymmetric Electrodes

Run #	Caps (#)	Q_s (mC)	Q_e (C)	I_p (kA)	E_s (kJ)	f_1 (*)	DV+ (x 10^{-5} cm^3/shot)	DV- (x 10^{-5} cm^3/shot)	DV_{tot} (x 10^{-5} cm^3/shot)	$DV_{\%e}$ +	$DV_{\%e}$ -	V_{sb} (kV)	$DV_{sb\%e}$
Case #1: Anode - (Cu#1, d = 1.27 cm), Cathode - (Cu#1, d = 2.54 cm)													
776	2	80.3	2.00	102	0.87	0.343	0.60	0.75	1.35	13	10	21.7	6.6
781	6	168	3.75	107	1.27	0.888	3.11	7.55	1.07	7.1	2.9	15.1	14
764	10	292	5.54	155	2.31	2.16	9.69	89.5	99.2	3.8	0.42	15.8	11
782	10	292	5.54	155	2.31	2.16	10.4	104	114	3.6	0.36	15.8	10
787	20	523	8.73	168	3.69	4.39	79.0	319	398	0.94	0.23	14.1	15
767	30	771	11.1	204	5.36	7.51	166	615	781	0.67	0.18	13.9	15
Case #2: Anode and Cathode - (Cu#1, d = 1.27 cm) (See Table 3.10 and Fig. 3-17)													
Case #3: Anode - (Cu#1, d = 2.54 cm), Cathode - (Cu #1, d = 1.27 cm)													
882	2	70.7	1.76	90.2	0.675	0.267	0.749	0.299	1.05	10	25	19.1	6.1
910	2	73.6	1.83	93.9	0.733	0.289	0.90	0.45	1.35	8.3	17	19.9	5.9
883	6	183	4.11	117	1.52	1.06	3.13	2.24	5.37	7.2	10	16.5	8.4
907	6	180	4.03	115	1.46	1.03	13.5	2.71	16.2	1.7	8.3	16.2	8.0
906	10	309	5.87	165	2.58	2.43	105	14.8	120	0.35	2.5	16.7	8.6
765	10	313	5.95	167	2.65	2.50	124	13.4	137	0.30	2.8	16.9	7.5
1130+	10	318	6.05	170	2.74	2.59	58.2	11.2	69.4	1.3	6.7	17.2	10
904	20	552	9.23	178	4.12	4.91	300	92.5	393	0.25	0.81	14.9	18
1048	30	851	12.2	224	6.52	9.06	875	199	1070	0.13	0.56	15.3	18
Case #4: Anode and Cathode - (Cu#1, d = 2.45 cm) (See Table 3.11 and Fig. 3-19)													

*The units on f_1 are ($A^2s^{1.5} \times 10^3$).

+The diameter of the cathode surface was initially 2.54 cm instead of 1.27 cm, (the diameter of the electrode shaft was still kept at 1.27 cm).

Table variables are defined in Table 3.6

Table 3.13 Electrode Erosion Data for Large Diameter Cu#1 Cathodes (d = 2.54 cm) vs. Different Anode Materials

Run #	Caps (#)	Q_s (mC)	Q_e (C)	I_p (kA)	E_s (kJ)	f_1 (*)	DV- (x 10^{-5} cm^3/shot)	$DV_{\%e}$ -	V_{sb} (kV)	$DV_{sb\%e}$
Anode:	Al (d = 1.27 cm)									
1051	2	67.8	1.69	86.4	0.620	0.245	0.149	50	18.3	6.0
650	5	256	6.18	199	3.55	2.60	1.13	17	27.7	19
888	20	380	6.35	122	1.96	2.32	88.0	0.85	10.3	33
Anode:	Mo (d = 1.27 cm)									
651	5	242	5.84	188	3.17	2.32	40.6	44	26.2	18
652	5	257	6.20	200	3.57	2.62	42.0	0.45	27.8	13
Anode:	CuC#1 (d = 1.27 cm)									
653	5	290	7.00	226	4.56	3.34	78.2	0.24	31.4	3.8

*The units on f_1 are ($A^2s^{1.5}$ x 10^3).

Table variables are defined in Table 3.6.

Table 3.14 Electrode Erosion Data for Cu#1 Anodes vs. Cathode Material

Run #	Caps (#)	Q_s (mC)	Q_e (C)	I_p (kA)	E_s (kJ)	f_1 (*)	DV+ (x 10^{-5} cm^3/shot)	$DV_{\%e}$	V_{sb} (kV)	$DV_{sb\%e}$
Cu #1 Cathode (d = 1.27 cm) Results in Table 3.10 and Fig. 3-17.										
Cathode:	C#1 d = 1.27 cm			Anode:	Cu#1 d = 1.27 cm					
1052	1	41.5	1.00	69.8	0.466	0.099	0.15	25	22.4	2.7
649	3	111	2.65	115	1.11	0.567	0.90	13	20.0	5.5
675	6	208	4.65	133	1.94	1.37	1.34	17	18.7	8.4
667	10	265	5.01	141	1.89	1.78	2.98	13	14.3	17
628	20	444	7.43	143	2.66	3.18	19.4	3.9	12.0	20
752	20	500	8.34	160	3.37	3.99	22.1	3.3	13.5	15
1047	30	689	9.86	181	4.28	5.92	47.0	2.4	12.4	20
794-2	30	701	10.0	184	4.43	6.10	64.9	1.7	12.6	18
Cu#1 Cathode (d = 2.54 cm) Results in Table 3.11 and Fig. 3-19.										
Cathode:	C#1 d = 2.54 cm			Anode:	Cu#1 d = 2.54 cm					
1053	1	48.0	1.16	80.6	0.621	0.132	0.228	17	25.9	2.5
744	3	139	3.36	146	1.76	0.912	0.88	12	25.3	3.1
644	5	233	5.61	181	2.94	2.15	3.36	5.5	25.2	5.6
745	8	351	6.84	180	4.16	2.93	12.8	5.0	23.7	4.9
664	10	429	8.16	229	4.98	4.70	23.8	1.6	23.2	7.0
685	20	733	12.2	236	7.25	8.61	74.6	1.0	19.8	11
698	30	1270	18.1	332	14.4	19.9	191	0.86	22.8	10

*The units on f_1 are ($A^2s^{1.5}x10^3$).

Table variables are defined in Table 3.6.

Table 3.15 Electrode Erosion Data from the Jet Only for Cu#1 Samples in Switch #3 vs. Distance

Run #	Caps (#)	Q_s (mC)	Q_e (C)	I_p (kA)	E_s (kJ)	f_1 (*)	s (cm)	DV_s ($x10^{-5}$	DV_j cm^3/shot)	$DV_{\%e}$	V_{sb} (kV)	$DV_{sb\%e}$
700	5	138	3.32	107	1.03	0.751	0.70	1.12	7.21	50	14.9	11
706	10	278	5.29	148	2.10	1.97	0.70	26.3	19.8	4.2	15.0	11
707	10	266	5.05	141	1.91	1.79	0.95	11.2	20.2	5.0	14.4	17
708	10	267	5.08	142	1.93	1.81	1.45	0.00	12.3	100	14.4	12
713	20	791	13.2	254	8.46	10.0	0.95	197	37.5	0.57	21.4	6.0
714	20	811	13.6	261	8.90	8.92	1.45	42.5	38.9	2.6	21.9	5.4
718	20	828	13.8	266	9.27	9.23	1.95	13.4	37.5	8.4	22.4	4.4
771-1	30	1090	15.6	287	10.7	14.8	0.95	168	45.7	1.1	19.7	4.3
772	30	1160	16.6	305	12.1	16.8	1.45	89.5	50.5	2.1	20.9	6.9
773	30	1220	17.4	321	13.4	18.5	1.95	11.2	48.1	17	22.0	6.5

*The units on f_1 are ($A^2s^{1.5}$ x 10^3).

Note: s is shown in Fig. 3.23, DV_s is the erosion of the target sample, DV_j is the erosion of the electrode producing the jet (the center one - see Fig. 3.23). Other table variables are defined in Table 3.6.

Table 3.16 Electrode Erosion Data for Cu#1 vs. Gap Separation and Jet Material in Switch #2

Run #	Caps (#)	Q_s (mC)	Q_e (C)	I_p (kA)	E_s (kJ)	f_1 (*)	DV+ (x 10^{-5} cm^3/shot)	DV- (x 10^{-5} cm^3/shot)	DV_{tot} (x 10^{-5} cm^3/shot)	$DV_{\%e}$	V_{sb} (kV)	$DV_{sb\%e}$
s+ = 0.5 cm, s- = 1.5 cm, Jet Material: CuW#2												
715	3	104	1.47	107	0.965	0.492	3.59	0.00	3.59	6.3	18.7	9.4
739	6	266	5.95	169	3.18	2.23	87.7	53.7	141	0.32	23.9	
726	10	383	7.28	204	3.96	3.53	226	183	410	0.55	20.7	8.9
722-1	30	1010	14.4	266	9.18	12.7	386	621	1010	0.55	18.2	8.5
722	30	1040	14.8	273	9.69	13.4	369	649	1020	0.55	18.7	12
s+ = s- = 1.0 cm, Jet Material: CuW#2												
716	3	149	3.55	154	1.99	1.02	11.5	12.6	24.1	0.93	26.8	11
729	5	237	5.71	184	3.03	2.22	82.8	74.6	157	0.71	25.6	12
724	10	455	8.64	242	5.59	4.97	242	253	495	0.45	24.6	6.6
720	30	1320	18.8	346	15.6	21.6	724	777	1500	0.36	23.7	6.6
s+ = 0.5 cm, s- = 1.5 cm, Jet Material: C#1												
727	10	271	5.15	144	1.99	1.86	12.0	2.24	14.2	5.3	14.7	7.3
723	30	836	12.0	220	6.29	8.76	151	89.5	240	2.3	15.1	9.6
723-1	30	864	12.3	227	6.72	9.26	101	72.7	173	3.2	15.6	6.4
s+ = s- = 1.0 cm, Jet Material: C#1												
728	5	148	3.58	115	1.19	0.87	1.12	2.24	3.36	33	16.0	6.0
725	10	254	4.83	13.5	1.75	0.164	4.47	2.24	6.71	11	13.7	14
721	30	760	10.9	200	5.20	7.23	39.1	39.1	78.2	7.2	13.7	10
s = 0.95 cm, Switch #3 - with CuW#2 Jet Only												
707	10	266	5.05	141	1.91	1.79			11.2	5.0	14.4	17
713	20	791	13.2	254	8.46	10.0			197	0.57	21.4	6.0
771-1	30	1090	15.6	287	10.7	14.8			168	1.1	19.7	4.3

*The units on f_1 are ($A^2s^{1.5}$ x 10^3).

Table variables are defined in Table 3.6.

Table 3.17 Electrode Erosion Data for Cu#1 vs. Gap Separation

Run #	Caps (#)	Q_s (mC)	Q_e (C)	I_p (kA)	E_s (kJ)	f_1 (*)	DV+ (x 10^{-5} cm^3/shot)	DV-	DV_{tot}	$DV_{\%e}$	V_{sb} (kV)	$DV_{sb\%e}$
Switch #2, s = 0.5 cm												
1055	1	46.6	1.12	78.4	0.587	0.124	0.378	0.303	0.681	11	25.2	3.6
751	3	144	3.43	149	1.86	0.95	4.00	2.46	6.46	3.5	25.9	3.7
750	6	192	4.67	179	2.48	1.67	41.3	82.2	124	0.36	25.9	3.3
749	10	472	8.96	251	6.02	5.35	117	133	250	0.30	25.5	4.9
1063	30	1280	18.3	336	14.7	20.4	313	443	756	0.03	23.0	7.8
s = 1.0 cm (see Table 3.10)												
s = 1.5 cm												
1056	1	45.8	1.10	76.9	0.566	0.120	0.163	0.163	0.327	25	24.7	6.2
648	3	125	3.00	130	1.41	0.725	1.35	0.674	2.02	11	22.6	9.6
673	6	204	4.57	130	1.88	1.32	19.7	3.59	23.3	1.9	18.4	15
668	10	328	6.23	175	2.91	2.74	12.7	79.0	91.7	0.81	17.7	11
679	20	658	11.0	212	5.85	6.97	115	110	225	0.66	17.8	11
+621	30	809	11.6	213	5.90	8.19	143	192	336	0.35	14.6	14
621-1	30	976	14.0	257	8.58	11.9	342	304	647	0.67	17.6	17
s = 2.0 cm												
1054	1	51.3	1.24	86.3	0.712	0.151	0.302	0.226	0.528	14	27.7	3.1
740	3	127	3.02	131	1.44	1.31	1.80	0.677	2.48	9.1	22.8	14
741	6	248	5.55	158	2.76	1.94	14.3	5.82	20.1	2.2	22.3	9.0
1050	10	376	7.14	200	3.81	3.59	43.3	24.6	67.9	1.1	20.3	12
1049	30	993	14.2	261	8.89	12.3	172	300	472	0.47	17.9	9.0
769	30	1090	15.5	286	10.6	14.7	271	416	687	0.33	19.6	8.3

+Cooling water flowing through the upper and lower electrodes was accidentally shut off.

*The units on f_1 are ($A^2s^{1.5}$ x 10^3).

Table variables are defined in Table 3.6.

Table 3.18 Electrode Erosion Data for CuW#2 vs. Gap Separation in Switch #2

Run #	Caps (#)	Q_s (mC)	Q_e (C)	I_p (kA)	E_s (kJ)	f_1 (*)	DV+ (x 10^{-5} cm^3/shot)	DV- (x 10^{-5} cm^3/shot)	DV_{tot} (x 10^{-5} cm^3/shot)	$DV_{\%e}$	V_{sb} (kV)	$DV_{sb\%e}$
855	2	94.4	2.35	120	1.20	0.474	3.08	2.70	5.78	1.7	25.5	2.7
856	6	268	6.01	171	3.24	2.27	17.6	18.2	35.8	0.80	24.2	2.7
857	10	439	8.33	234	5.20	4.90	36.0	35.1	71.1	0.68	23.7	9.0
858-1	30	1410	20.1	371	17.9	24.7	136	140	275	0.52	25.4	2.5
848	2	90.7	2.26	116	1.11	0.44	1.84	1.45	3.29	2.9	24.5	3.1
847	6	267	5.99	170	3.22	2.25	15.3	14.1	29.4	0.98	24.1	4.1
846	10	449	8.54	239	5.46	5.13	30.8	32.7	63.4	0.76	24.3	5.4
845-1	30	1390	19.8	365	17.3	24.0	111	117	228	0.63	25.0	4.5

*The units on f_1 are ($A^2s^{1.5}$ x 10^3).

Table variables are defined in Table 3.6.

Table 3.19 Electrode Erosion Data vs. High Temperature Mechanical Strength

Run #	Caps (#)	Q_s (mC)	Q_e (C)	I_p (kA)	E_s (kJ)	f_1 (*)	DV+ (x 10^{-5} cm^3/shot)	DV-	DV_{tot}	$DV_{\%e}$	V_{sb} (kV)	$DV_{sb\%e}$
Cu-Nb#1												
885	1	40.4	0.974	68.0	0.442	0.094	0.151	0.151	0.302	25	21.8	12
763	1	41.4	0.999	69.7	0.464	0.098	0.151	0.151	0.302	25	22.4	13
805	2	79.1	1.97	101	0.845	0.334	0.306	0.153	0.458	33	21.4	16
775-1	2	75.4	1.88	96.1	0.768	0.303	0.455	0.304	0.759	20	20.4	2.0
879	4	166	4.05	155	1.86	1.26	1.51	1.51	3.02	10	22.4	4.7
754	6	267	5.97	170	3.2	2.25	8.14	7.24	15.4	2.9	24.0	4.7
627	10	434	8.25	231	5.10	4.79	21.0	21.8	42.8	1.8	23.5	4.4
732	20	812	13.6	261	8.91	10.6	49.5	46.5	96.4	1.6	22.0	7.0
748	30	1320	18.9	348	15.8	21.8	124	77.4	201	1.9	23.8	7.6
CuZr												
877	2	78.6	1.96	100	0.835	0.329	0.905	0.603	1.51	10	21.2	3.7
875	6	194	4.35	124	1.70	1.19	7.16	2.68	9.94	4.5	17.5	12
872	10	324	6.16	173	2.84	2.68	20.9	11.2	32.1	2.3	17.5	12
871	30	806	11.5	212	5.86	8.09	141	273	414	0.5	14.5	15
CuCrZr												
876	2	77.3	1.92	98.6	0.807	0.318	0.451	0.451	0.902	17	20.9	9.6
874	6	195	4.36	124	1.71	1.20	4.29	3.43	7.71	5.6	17.5	22
873	10	344	6.54	183	3.20	3.01	12.0	8.26	20.3	3.7	18.6	16
870	30	759	10.9	200	5.19	7.23	116	215	331	0.7	13.7	16

*The units on f_1 are ($A^2s^{1.5}$ x 10^3).

Table variables are defined in Table 3.6.

Table 3.19, continued

Run #	Caps (#)	Q_s (mC)	Q_e (C)	I_p (kA)	E_s (kJ)	f_1 (*)	DV+ (x 10^{-5} cm^3/shot)	DV-	DV_{tot}	$DV_{\%e}$	V_{sb} (kV)	$DV_{sb\%e}$
$Cu+Al_2O_3$#1												
815	2	83.5	2.08	107	0.942	0.374	1.07	0.610	1.68	9.1	22.6	3.0
814	6	202	4.53	129	1.84	1.29	4.47	11.2	15.7	2.8	18.2	9.3
731	10	307	5.84	164	2.55	2.41	14.2	12.7	76.8	2.8	16.6	8.5
813	10	354	6.72	188	3.38	3.18	70.1	17.2	87.2	0.9	19.0	7.0
788	30	791	11.3	208	5.64	7.80	121	338	458	4.8	14.3	16
$Cu+Al_2O_3$#2												
820	2	73.3	1.82	93.5	0.725	0.286	0.449	0.449	0.898	17	19.8	3.0
821	6	212	4.76	135	2.03	1.42	8.05	3.58	11.6	4.1	19.1	9.9
792	10	353	6.70	188	3.36	3.17	11.2	14.9	26.1	2.9	19.1	10
791-1	30	848	12.1	223	6.48	8.95	116	110	226	1.0	15.4	15
791-2	30	867	12.4	228	6.78	9.38	96.2	103	199	1.1	15.6	12

Cu#1 See Table 3.10

*The units on f_1 are ($A^2s^{1.5}$ x 10^3).

Table variables are defined in Table 3.6.

in open air (0.87×10^5 Pa). Several people [78,79] have speculated that the use of SF_6 may lead to increased erosion because of chemical attack, embrittlement, etc., of the electrode surface, and in general it is believed that increasing the pressure of a switch leads to increased erosion because the current density, and therefore the heat flux, at the surface is greater [80]. However, the author wondered if perhaps the gap spacing required to hold off the voltage, and thus the energy or current switched, was the dominant factor. In other words, for the same breakdown voltage the SF_6 switch would have a much smaller gap spacing than another gas, such as air, at the same pressure.

The results for these three holdoff techniques are given in Table 3.20 and shown in Fig. 3.39. For CuW#2 electrodes, over a wide range of stored charge, the erosion for all three techniques was essentially the same! This indicates that at least for high energy, small gap spacing systems, i.e., the ones where EJE exists, that electrode gas chemistry and gas pressure appear to play a secondary role in the electrode erosion. The erosion results for CuW#2 electrodes run in an open air gap at 1 cm are shown in Fig. 3.40. A comparison with Fig. 3.39 shows the erosion decreases with increasing gap separation which further indicates that the distance is the critical factor when switching the same stored charge.

Table 3.20 Electrode Erosion Data for Different Methods of Voltage Holdoff Using CuW#2 Electrodes

Run #	Caps (#)	Q_s (mC)	Q_e (C)	I_p (kA)	E_s (kJ)	f_1 (*)	DV+ (x 10^{-5} cm^3/shot)	DV- (x 10^{-5} cm^3/shot)	DV_{tot} (x 10^{-5} cm^3/shot)	$DV_{\%e}$	V_{sb} (kV)	$DV_{sb\%e}$
Air (0.87 x 10^5 Pa), (bottom of Switch #2 "Piggyback"), s_1 = 0.15 cm												
855	2	94.4	2.35	120	1.20	0.474	16.0	10.7	26.7	0.4	25.5	2.7
856	6	268	6.01	171	3.24	2.27	136	136	272	0.1	24.2	2.7
857	10	439	8.33	234	5.20	4.90	340	307	647	0.07	23.7	9.2
858	30	1390	19.9	366	17.4	24.2	1170	1390	2560	0.07	25.1	3.6
858-1	30	1410	20.1	371	17.9	24.7	1260	1600	2860	0.05	25.4	2.5
SF_6 (10^5 Pa) s = 0.15 cm												
854	2	111	2.75	141	1.65	0.651	2.83	2.83	5.65	25	29.9	8.9
853	6	276	6.17	176	3.42	2.40	15.9	16.7	32.6	0.9	24.8	11
852-1	10	469	8.92	250	5.95	5.61	31.8	49.8	106	1.3	25.4	16
Air (2-3 x 10^5 Pa) s = 0.15 cm												
861	2	107	2.67	137	1.55	0.614	3.38	3.57	6.95	1.4	29.0	5.2
862	6	324	7.25	207	4.72	3.32	23.1	20.5	43.5	0.7	29.2	5.0
863	10	509	9.68	271	7.01	6.72	56.7	52.9	110	0.4	27.5	8.4
Air (0.87 x 10^5 Pa), Switch #1, s = 1.0 cm												
914	1	46.8	1.13	78.8	0.592	0.126	0.245	0.245	0.489	10.0	25.3	9.3
804	2	84.0	2.09	107	0.952	0.376	1.07	0.972	2.04	4.8	22.7	8.6
915	4	181	4.43	116	2.22	1.03	4.40	4.78	9.18	2.1	24.5	8.2
779	6	262	5.85	166	3.07	2.15	11.5	12.4	23.9	1.2	23.5	7.6
730	10	367	6.97	195	3.64	3.42	26.9	21.6	48.5	1.0	19.8	8.5
916	20	868	14.5	279	10.2	12.1	65.4	63.4	129	0.7	23.4	6.7
783	30	1330	19.0	350	15.9	22.1	95.2	111	206	0.7	24.0	5.3

*The units on f_1 are ($A^2s^{1.5}$ x 10^3).

Table variables are defined in Table 3.6.

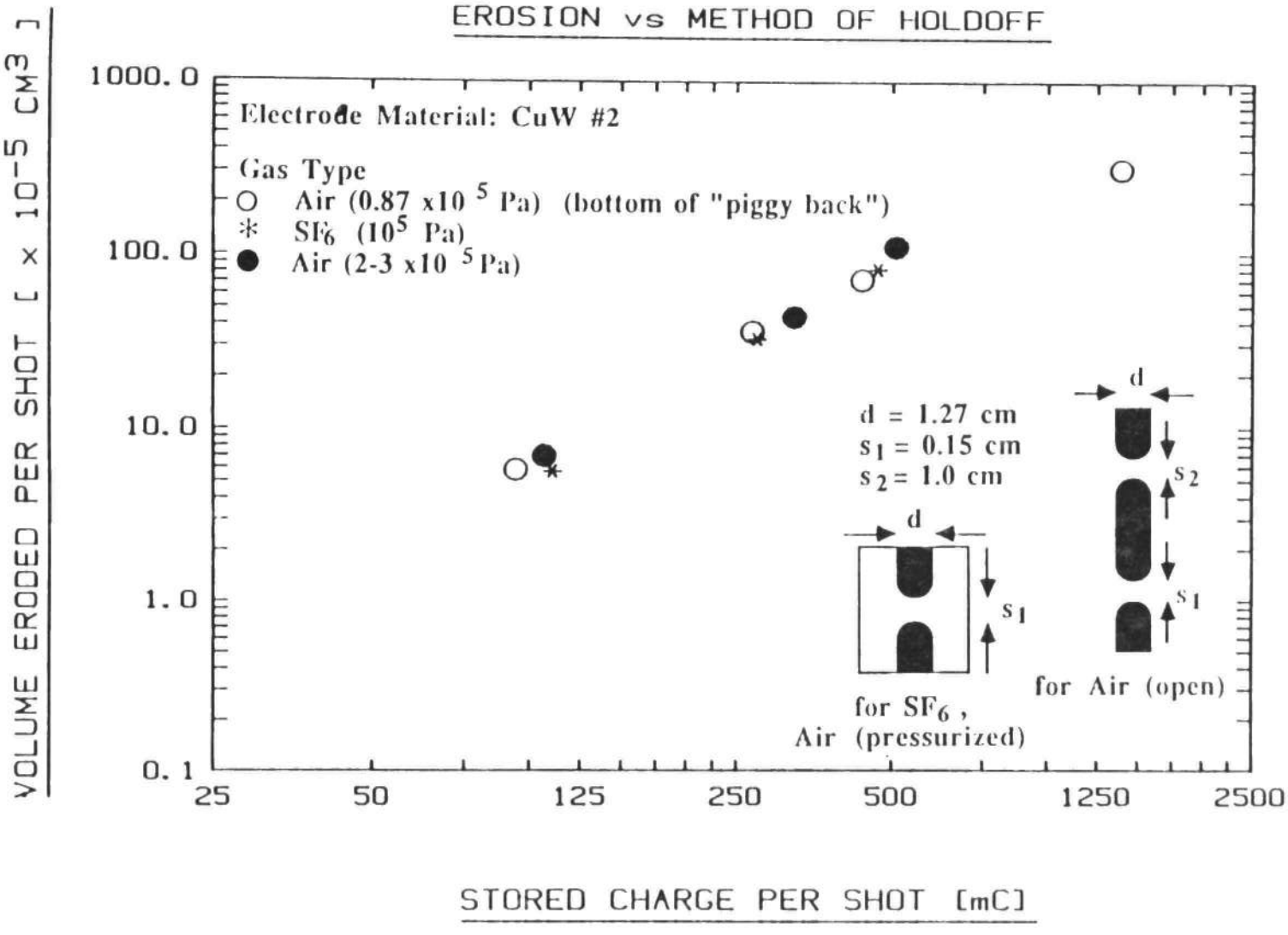

Fig. 3.39 Electrode Erosion vs. the Method of Voltage Holdoff.

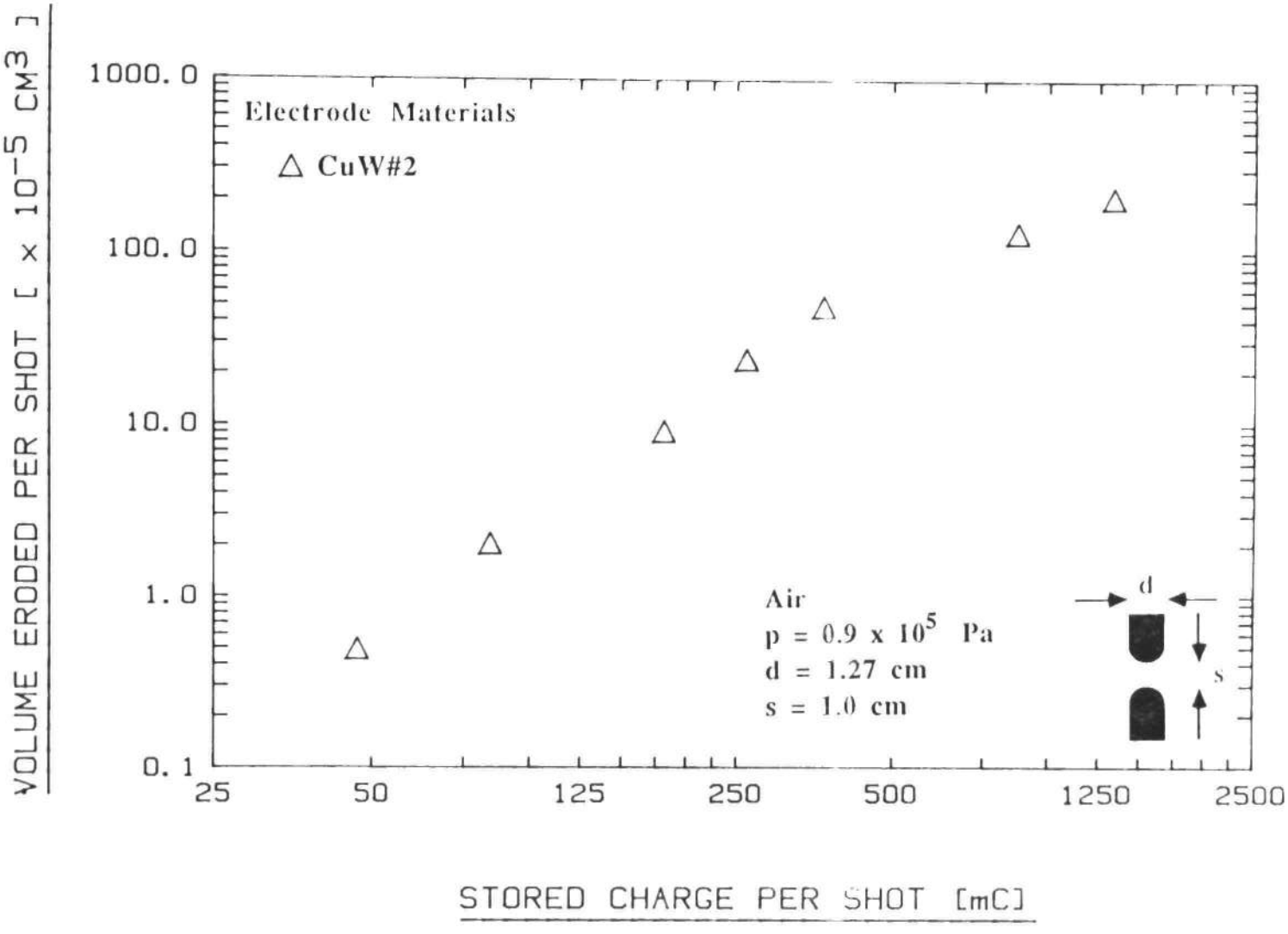

Fig. 3.40 Erosion for CuW#2 Switch #1 Electrodes in Open Air.

Further Discussion

The EJE experiments conducted with HCHETA indicate that all of the jet properties (P1-P5) previously observed under other discharge conditions were present, which implies that EJE is an important factor in the overall erosion process. The enhanced erosion of the larger electrode in an asymmetric electrode combination has been examined in more detail for air and oil filled high current contacts [81,82]. Observations made from the framing photographs support our conclusion that the jet production, motion, and interaction is significantly influenced by the electrode diameters, independent of polarity. Presumably the different geometries can affect both j and B, and thus the jet velocity, although this has not been verified.

The copper and carbon jet velocity values (5-10 km/sec) obtained from our streak photos are consistent with the theoretical results of Ecker [39] which predicts that magnetic pinching will dominate for high current arcs. Figure 3.41 shows the results of Ecker's velocity equation (see Table 3.2) for both polarities of copper and carbon electrodes. Two limiting cases were considered by Ecker: Case a--the effective evaporation rate is zero, and case b--the evaporation rate is proportional to j as determined by Cobine and Burger [83]. For the high currents considered here (> 100 kA), the equations of Ecker reduce to:

$$v_+^2 = (j/\rho j)[(2 \times 10^{-7})I + 10^{-10}(j/\rho j)] \qquad (3.7a)$$

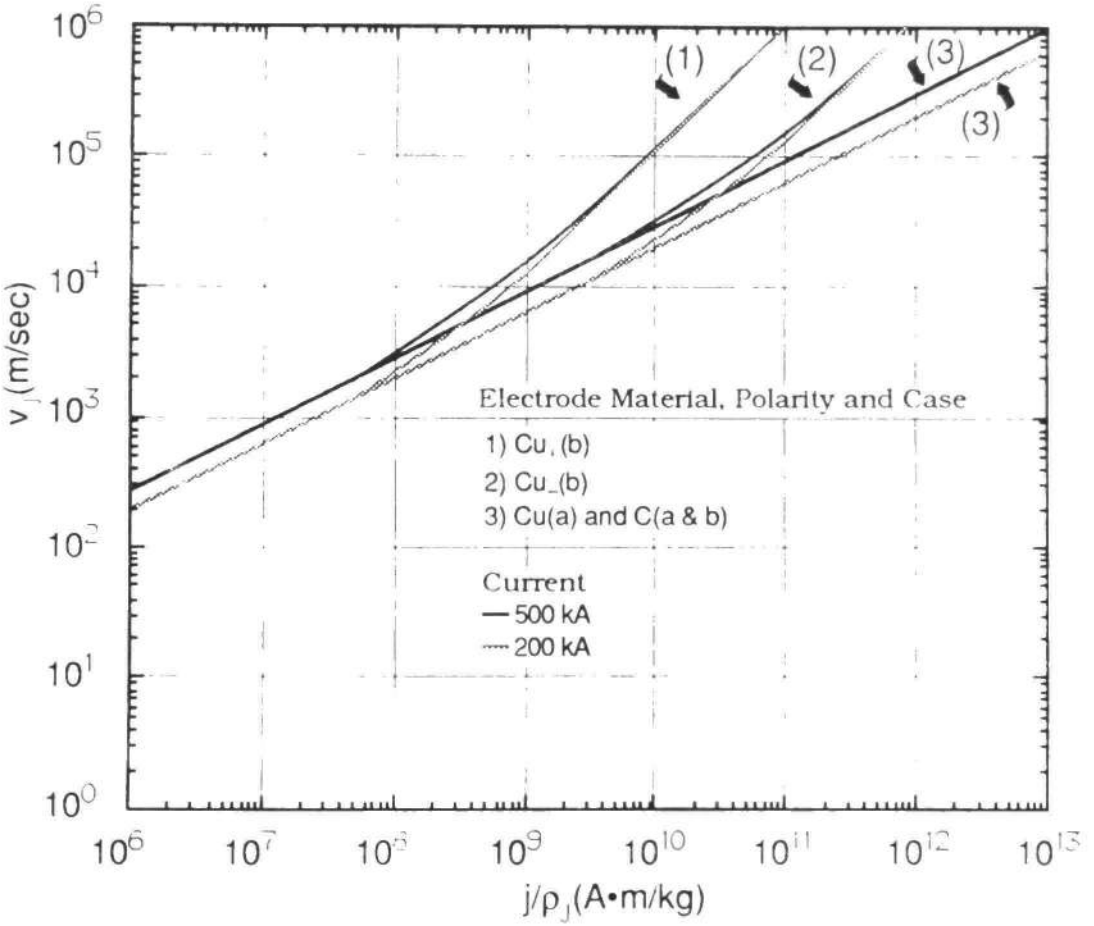

Fig. 3.41 Theoretical Predictions for the Electrode Jet Velocities. (Calculated Using Ecker's Equations [39]) Case (a): the electrode evaporation rate is zero (the lower limit), case (b): the electrode evaporation rate is proportional to j (the upper limit).

$$v_-^2 = (j/\rho_j)[(2 \times 10^{-7})I + 10^{-12}(j/\rho_j)] \quad (3.7b)$$

for copper, and

$$v_+^2 = (j/\rho_j)[(2 \times 10^{-7})I + 4 \times 10^{-14}(j/\rho_j)] \quad (3.8a)$$

$$v_-^2 = (j/\rho_j)[(2 \times 10^{-7})I + 4 \times 10^{-16}(j/\rho_j)] \quad (3.8b)$$

for carbon. These equations use a steady state evaporation rate of 2×10^{-7} kg/C for carbon and 1×10^{-5} kg/C for copper. The first term in the brackets is the j x B term and the second is the evaporation pressure gradient term. the difference in the anode, v_+, and cathode, v_-, velocity equations is a result of the assumption that the arc constricts by a factor of ten at the cathode. For higher currents higher constriction is expected which decreases the importance of the evaporation effect through the constriction factor but increases it through the increase in the evaporation rate. The electrode erosion rates measured in our experiments indicate that if one assumes all the mass loss is due to evaporation (which represents an upper limit) then the evaporation rate is 1.9×10^{-8} kg/C for carbon in the 1-10 C range and 4×10^{-8} kg/C at 1 C and 1.8×10^{-7} kg/C, at 5 C, for copper. Using these values Eqn's. (3.7a,b) and (3.8a,b) become

$$v_+^2 = (j/\rho_j)[(2\times10^{-7})I + 3.2\times10^{-14}(j/\rho_j)] \quad (3.9a)$$

$$v_-^2 = (j/\rho_j)[(2\times10^{-7})I + 3.2\times10^{-16}(j/\rho_j)] \quad (3.9b)$$

for copper, and

$$v_+^2 = (j/\rho_j)[(2\times10^{-7})I + 3.5\times10^{-16}(j/\rho_j)] \quad (3.10a)$$

$$v_-^2 = (j/\rho_j)[(2\times10^{-7})I + 3.5\times10^{-18}(j/\rho_j)] \quad (3.10b)$$

for carbon. For the ranges of j/ρ_j plotted in Fig. 3.41 all of these results are represented by a single line given by Eq. (3.5) for magnetic pinching effects only. Using current densities of 400 kA/cm^2 at 200 kA, determined from the macroscopic erosion traces on the electrodes, and average vapor densities of $10^{-3}\rho_s$, the approximation used by Zolotykh [68], one obtains a j/ρ_j of 4×10^8 A·m/kg for copper. This value of j/ρ_j yields jet velocities of 4 km/sec and 6 km/sec for the cathode and anode, respectively. This is in extremely good agreement with the experimental results. For carbon the j/ρ_j may be about the same order since j is decreased but so is the ρ_j. (The inability to distinguish the erosion traces made it more difficult to determine j.) This result is consistent with the experimental results which showed comparable jet velocities when the carbon jets were present.

The observed absence of the carbon anode jet in the streak photos could indicate that the anode current density

may be less than the carbon cathode current density at a given current. For a constant heat flux to the electrode surface, q, given by

$$q = V_f \cdot j, \tag{3.11}$$

the time to onset of vaporization or sublimation is given by

$$t_{v,s} = (M_I/q)^2(\pi/4), \tag{3.12}$$

where

$$M_I^2 = M_{Il}^2 + M_{Iv}^2, \tag{3.12a}$$

with

$$M_{Iv} = (L_v/c_p + T_b - T_{mp})(k_t \rho c_p)^{0.5}, \tag{3.12b}$$

and M_{Il} as defined in Eq. (3.6). The material properties k_t, ρ, and c_p are evaluated in the liquid state. For the case of sublimation (i.e., for carbon),

$$M_I = M_{Is}, \tag{3.13}$$

where

$$M_{Is} = (L_s/c_p + T_b)(k_t \rho c_p)^{0.5}. \tag{3.13a}$$

These quantities are discussed in more detail in Chapter 4. However, Eq. (3.12) indicates that increasing M_I or decreasing j causes $t_{v,s}$ to increase. Since carbon has the highest M_I for all the elements (see Appendix A for a listing), and j may be less as well, it is not surprising that no carbon anode jet was seen. (Note: for carbon the M_I is largely determined by its high sublimation energy.) The energy in the carbon jet, and thus, its ability to erode the opposite electrode, is substantially less than other materials. This is easily seen because the jet energy is directly proportional to the time that the jet exists, t_j, where t_j is given by the equation

$$t_j = t_p - t_{v,s}. \qquad (3.14)$$

Thus, for a given pulse time, t_p, t_j is smaller for larger $t_{v,s}$. This could explain why the carbon electrode was observed to produce substantially less erosion of opposite electrodes. Another explanation could be the lower atomic weight of carbon. If the jet energy is determined by collisional processes (electron to ion energy transfer), as suggested by Lyubimov [37] and Moizhes and Nemchinskii [45], then materials with lower atomic weights would have lower jet energies (i.e., for a fixed electron velocity (temperature), the ions ideally could achieve the same velocity as the electrons and their mass would then determine their energy).

Measurements of the heat flux by Ageev and Sultanov [64] support the conclusion that the jet flux is comparable to the arc-electrode heat flux. For a 10 kA discharge they were able to measure jet heat fluxes of 3-5 x 10^6 W/cm^2. (Belkin [84] reports typical values for a high current (100 kA) high energy discharge in air to be approximately the same order.) However, the jet experiments in [64] were done for a geometry which enhanced the jet effect, thus, under normal conditions one might conclude like Butkevich et al. [52] that "the energy transferred by the plasma jet is substantially less than the energy introduced into the electrode by the arc, and therefore it is most probable that the change in erosion due to the jet action is a result of enhancing the overshoot of molten metal, or by more effectively carrying out vapors of metal from the gap region." This conclusion is supported by our experimental results for materials with the same thermophysical (properties) but higher mechanical strength. If the jets were producing larger heat fluxes to the electrode surfaces then all the materials would show similar erosion, which they did not. However, if the EJE is primarily a mechanical removal of high temperature or molten material then the materials with the higher mechanical strengths at elevated temperatures should erode less, which they did.

Suggestions for Future Work

Having established that EJE can be a dominant erosion mechanism under certain conditions, the suggestions for future work in the area of EJE are based upon the following questions which still remain partly unanswered. Namely:

Q1) What is (are) the acceleration mechanism(s) of the jet for a given set of pulse conditions?

Q2) Under what conditions (materials, pulse, geometry) are the anode and cathode jets produced?

Q3) What are the ways the jet effect can be minimized in actual switching devices?

Q4) When is the jet-driven distance-effect the dominant means of erosion?

In order to answer these questions the following experiments should be considered:

E1) Determine the onset conditions for jet formation for various regimes of operation (pulse widths, electrode materials, gas type, peak currents, using a unipolar pulse. Streak photos using narrow band filters designed to eliminate continuum radiation should be one of the main diagnostics. The electrodes could be seeded with another material to aid this technique, if necessary. Results should be correlated with existing models for the onset of vaporization of a heated metal surface. The unipolar tests should be followed up with oscillatory pulse tests to determine the onset for both polarities. Existing unipolar thermal models could then be adapted to include oscillatory

(time varying) heat flux parameters. Additional diagnostics might include spectroscopic techniques which have been utilized for this purpose by Sultanov [30].

E2) Various means of shielding the electrode from the jet should be considered. For example, a simple baffle might be designed which could be injected/ejected in much the same way as a gun cartridge. Perhaps a replaceable thin film or "paper" on the electrode surface or a ceramic ribbon with punched holes could be used between the electrodes. (This might sound absurd, but one should remember that Sultanov and Kiselevskii [56] showed that paper could shield an electrode surface from the jet.) The feasibility of this concept has been shown by Malyuta and Mezhevov [85] who utilized a ceramic disk with a hole in it for their high current (10 kA) spark gap design, albeit for the purpose of enhancing the gas flow velocity in the arc region in order to aid the recovery switch. Other methods of shielding, such as altering the B-field with self or externally produced fields, should also be tried.

E3) The gas type experiments of Fig. 3.39 should be repeated for copper electrodes since they are more likely to experience greater molten material removal by electrode jets when compared with CuW. Other gases should also be tried, such as N_2, which gave lower erosion in other experiments, in order to determine when the distance effect dominates over gas chemistry effects.

References

[1] N.K. Sukhodrev, "On Spectral Excitation in a Spark Discharge," *Transactions (Trudy) of the P.N. Lebedev Physics Institute*, Volume XV-Research on Spectroscopy and Luminescence Part 3, Chapter 4, pp. 29-44, Consultants Bureau, New York, 1962. (EE-0097)*

[2] W. Feddersen, "Ueber die Elektrische Flaschenentladung," *Poggendorffs Annalen*, vol. 116, pp. 132-171, 1862. (EE-1080)

[3] R.C. Eschenbach, N.A. Barcza and K. J. Reid, "Plasma Torches and Plasma Torch Furnaces," *Plasma Technology in Metallurgical Processing*, Iron and Steel Society, Pittsburg, PA, Chapter 7, pp. 77-87, 1987. (EE-0111)

[4] P.R. Smy, R.M. Clements, J.P. Dale, D. Simeoni and D.R. Tophan, "Efficiency and Erosion Characteristics of Plasma Jet Igniters," *J. Phys. D: Appl. Phys.*, vol. 16, pp. 783-791, 1983. (EE-0100).

[5] M.A. Sultanov, "Evaluation of Heat Fluxes in Electrodes with High-Current, High-Power Pulsed Discharges," Institute of Chemistry, Academy of Sciences of the Tadzhik SSR. Article # 3465-76, Deposited September 30, 1976. Submitted to Viniti: All-Union Institute of Scientific-Technical Information. Abstract found translated in *High Temperature (USSR)*, 14(6), pp. 1198, 1976. (EE-0137)

[6] J.G.H. Salge, T.H.G.G. Weise, U.E. Braunsberger, H. Fien, M.J. Loffler, W. Witt, D. Zwingel, and K. Zocha, "Mass Acceleration by Plasma Pulses," *IEEE Transactions on Magnetics*, vol. 25(1), pp. 495-499, 1989. (EE-0096)

[7] J.G.H. Salge, T.H.G.G. Weise, U.E. Braunsberger, M.J. Loffler and W. Witt, "Plasma-Pulse-Acceleration Experiments," *Proceedings of the 6th IEEE Pulsed Power Conference*, Arlington, VA, pp.25-28, June, 1987, (EE-0095)

[8] A. Loeb and Z. Kaplan, "A Theoretical Model for the Physical Processes in the Confined High Pressure Discharges of Electrothermal Launchers," *IEEE Trans. on Magnetics*, vol. 25(1), pp. 342-346, 1989. (EE-0098)

*The EE number corresponds to the paper number used in the Annotated Bibliography written by the author. All communication should include this number.

[9] N.N. Solbolev, "Unknown Title," *Sov. Phys. - JETP*, vol. 13, pp. 531-?, 1943. (EE-0094-6)

[10] J. R. Haynes, "The Production of High Velocity Mercury Vapor Jets by Spark Discharge," *Physical Review*, vol. 73(8), pp. 891-903, 1948. (EE-0072)

[11] S.L. Mandelshtam and S.M. Raiskii, "The Mechanism of the Electrical Erosion of Metals," Translation of *Izvestiya Akademii Nauk SSSR*, seriya fizicheskaya, vol. 13(5), pp. 549-565, 1949. Distributed by US Army FSTC, 220 7th St., NE, Charlottesville, VA 2901-5396, Document # FSTC-HT-1230-85. (EE-0094)

[12] W.F. Skeats and C.L. Schuck, "Measurement of Current Density in the High-Current Arc," *Trans. of AIEE*, vol. 73, pp. 848-856, 1954. (EE-0004)

[13] T.H. Lee, W.R. Wilson and J.C. Sofianek, "Current Density and Temperature of High-Current Arcs," *Trans. of AIEE*, vol. 76, pp. 600-608, 1957. (EE-0003)

[14] N.K. Sukhodrev and S.L. Mandelshtam, "On the Temperature of Electrode Vapors in a Spark Discharge," *Optics and Spectroscopy (USSR)*, vol. 6(6), pp. 473-476, 1959. (EE-0129)

[15] V. Hermoch, "Vapor Jets of Electrode Materials During a Brief Electrical Discharge with a High Current Strength," Translation of *Chekloslovatskiy fizicheskiy zhurnal*, vol. 9, pp. 221-228, 1959. Distribution: see reference 11. (EE-0127)

[16] L.I. Grechikhin and L.Ya. Min'ko, "Structure of the Plasma Jet from a Pulsed Discharge," *Sov. Phys. Tech. Phys.*, vol. 7(9), pp. 784-787, 1963. (EE-0122)

[17] N.N. Ogurtsova, I.V. Podmoshenskii and V.M. Shelemina, "Characteristics of the Plasma Jet of a Powerful Capillary Discharge," *Optics and Spectroscopy (USSR)*, vol. 15, pp. 404-406, 1963. (EE-0856)

[18] S.V. Gurov, T.Z. Dzhafarov, A.A. Malinin, B.A. Osadin and Yu. F. Tainov, "Electrode Processes in a High Current Discharge in Vacuum," *Sov. Phys. Tech. Phys.*, vol. 9(5), pp. 665-670, 1964. (EE-0381)

[19] L.I. Kiselevskii and M.A. Sultanov, "Study of the Plasma Formations Resulting from Jet Interaction in a High-Power Impulsive Discharge," *Sov. J. Mech. and Tech. Phys.*, vol. 7(4), pp. 96-98, 1966. (EE-0088)

[20] M.A. Sultanov and L.I. Kiselevskii, "Interaction of Supersonic Jets Under Pulse Conditions," *High Temperature (USSR)*, vol. 4(1), pp. 34-38, 1966. (EE-0121)

[21] L.I. Grechikhin and L.Ya. Min'ko, "Similarity between Physical Processes in a Pulsed Discharge and in the Effect of Laser Radiation on a Metal," *Sov. Phys. Tech. Phys.*, vol. 12(6), pp. 846-849, 1967. (EE-0116)

[22] A.Ya. Balagurov, A.G. Ershov, V.L. Levtov, L.V. Leskov, A.M. Petrov, V.V. Savichev and V.A. Chivilev, "Investigation of a Pulsed Plasma Rail Gun," *Sov. Phys. Tech. Phys.*, vol. 12(2), pp. 193-198, 1967. (EE-0086)

[23] V.B. Avramenko, B.B. Davydov and L.Ya. Min'ko, "Plasma Formation Near an Electrode During a High-Current Pulsed Discharge with Separate Flares," *High Temperature (USSR)*, vol. 7(1), pp. 12-16, 1969. (EE-0087)

[24] G.R. Jordan, B. Bowman and D. Wakelam, "Electrical and Photographic Measurements of High Power Arcs," *J. Phys. D: Appl. Phys.*, vol. 3, pp. 1089-1099, 1970. (EE-0078)

[25] A.M. Abdel-Asis, "On the Influence of Contact Dimensions on the Loss of Metal Switching of Alternating Currents in Oil and in Air," *IEEE Trans. on Parts, Hybrids, and Packaging*, vol. PHP-9(1), pp. 53-37, 1973. (EE-0126)

[26] M.A. Sultanov, "Supersonic Plasma Jet from a High-Power Pulsed Discharge," *Sov. Phys. Tech. Phys.*, vol. 19(4), pp. 478-482, 1974. (EE-0110)

[27] I.R. Bothwell and B. Grycz, "High Current A.C. Arcs in Uniform Air Flow," The University of Liverpool, Department of Elec. Eng. and Elect., Arc Discharge Research Project,*Report ULAP-T28*, Sept. 1974. (EE-0079)

[29] M.A. Sultanov and L.D. Semikin, "Oscillatory Processes in a High-Power Pulsed Discharge," *Sov. Phys. Tech. Phys.*, vol. 20(8), pp. 1089-1093, 1975. (EE-0119)

[30] M.A. Sultanov, "Hydrodynamic Processes in a High-Power Pulsed Discharge," *Sov. Phys. Tech. Phys.*, vol. 21 (7), pp. 815-821, 1976. (EE-0007)

[31] H. Yoshiyasu, S. Murata, S. Yamagata, T. Wada and Y. Shibuya, "Experimental Study of Electrode Vapour Flow in a Free-Burning Arc," *J. Phys. D: Appl. Phys.*, vol. 16, pp. 2213-2221, 1983. (EE-0124)

[32] M.A. Sultanov, "Adequacy of the Process of Ablation of Metals Under the Effect of Laser Radiation and Collision-Pinched Plasma," *Physics and Chemistry of Materials Processing (USSR)*, vol. 18(4), pp. 35-38, 1984. (EE-0114)

[33] N. Spector, Z. Kaplan, A. Loeb, B. Brill and J. Levinson, "Confined High Pressure Discharge Experiments," *IEEE Trans. on Magnetics*, vol. 25(1), pp. 538-540, 1989. (EE-0097)

[34] K. Schönbach and Fischer, "Explosive Erosion in High-Current Sparks," In-house translation of *Zeitschrift fur Angewandte Physik*, vol. 32 (4), pp. 253-257, 1971. (EE-0065)

[35] W.O. Davis and H.C. Miller, "Analysis of the Electrode Products Emitted by dc arcs in a Vacuum Ambient," *J. of Appl. Phys.*, vol. 40, pp. 2212-2221, 1969. (EE-1068)

[36] M.P. Zektser and G.A. Lyubimov, "Fast Plasma Jets from the Cathode Spot in a Vacuum Arc," *Sov. Phys. Tech. Phys.* vol. 24 (1), pp. 1-5, 1979. (EE-0077)

[37] G.A. Lyubimov, "Dynamics of Cathode Vapor Jets," *Sov. Phys. Tech. Phys.* vol. 22 (2), pp. 173-177, 1977. (EE-0076)

[38] S.M. Raiskii, "Propagation of Vapors of the Materials of Electrodes During the Spark Discharge," *Sov. Phys. JETP*, vol. 10 (8), pp. 907-9, 1940. (EE-1089)

[39] G. Ecker, "Electrode Components of the Arc Discharge," *Ergebnisse der Exakten Naturwissenschaften*, vol. 33, pp. 1-104, 1961. (EE-0833)

[40] W. Finkelnburg, "A Theory of the Production of Electrode Vapor Jets by Sparks and Arcs," *Physical Review*, vol. 74 (10), pp. 1475-1477, 1948. (EE-0101)

[41] H. Maecker, "Plasma Streams Produced by Self Magnetic Compression and its Importance for the Mechanism of High Current Arcs," *Appl. Sci. Research*, vol. 5, pp. 231-6, 1955. (EE-1060)

[42] A.A. Plyutto, V.N. Ryzhkov and A.T. Kapin, "High Speed Plasma Streams in Vacuum Arcs," *Sov. Phys. - JETP* , vol. 20 (2), pp. 328-337, 1965. (EE-0011)

[43] R. Holmes, "Electrode Phenomenon," Chapter 11 in *Electrical Breakdown of Gases*, J.M. Meek, J.D. Craggs, ed., John Wiley and Sons, New York, NY, pp. 839-867, 1978. (EE-0081)

[44] G.A. Lyubimov, "Mechanism of Acceleration of Cathodic Vapor Jets," *Sov. Phys. Dokl.*, vol. 20 (12), pp. 830-832, 1975. (EE-0074).

[45] B.Ya. Moizhes and V.A. Nemchinskii, "Erosion and Cathode Jets in a Vacuum Arc," *Sov. Phys. Tech. Phys.*, vol. 25 (1), pp. 43-48, 1980. (EE-0080)

[46] G.A. Mesyats, "Fast Processes on the Cathode in a Vacuum Discharges," *Proceedings of the 10th Int. Symp. on Discharges and Electrical Insulation in Vacuum*, Columbia, SC, pp. 37-43, 1982. (EE-0066)

[47] H.C. Miller, "Vacuum Arc Phenomena," *IEEE Trans. on Plasma Sci.*, vol. PS-5(3), pp. 181-196, 1977. (EE-1070).

[48] B.Juttner, "Vacuum Arcs," *Proceedings of 17th Int. Conf. on Phenomena in Ionized Gases*, Budapest, Hungary, pp. 17-30, July 8-12, 1985. (EE-0073)

[49] B.A. Osadin, "Mechanism of Acceleration of an Erosion Plasma," Article #3026-77, Deposited July 25, 1977. Submitted to Viniti: All-Union Institute of Scientific-Technical Information. Abstract found translated in *High Temperature (USSR)*, vol. 15(5), pp. 965, 1977. (EE-0075)

[50] I.G. Kesaev, "Cathode Processes in Electric Arcs," Nauka Press, Moscow, pp. 1-459, 1968. Translated for Sandia National Labs, Albuquerque, NM, Trans. # Sand 78-601. (EE-601)

[51] V.I. Rakhovskii, "Experimental Study of the Dynamics of Cathode Spots," *IEEE Trans. on Plasma Science*, vol. PS-4(2), pp. 81-102, 1976. (EE-0038)

[52] G.V. Butkevich, G.S. Belkin, N.A. Vedeshenkov and M.A. Zhavoronkov, *Electrical Erosion of High-Current Contacts and Electrodes*, M.: Energy, pp. 1-256, 1978. (EE-1052)

[53] G.A. Lyubimov and V.I. Rakhovskii, "The Cathode Spot of a Vacuum Arc," *Sov. Phys. Usp.*, vol. 21(8), pp. 693-718, 1978. (EE-0360)

[54] V. Hermoch and K. Krticka, "The Erosion Action of Jets of Neutral Particles, Arising During Electrical Condensor Discharges," Translation of *Chekhoslovatskiy fizicheskiy zhurnal*, vol. 3(2), pp. 149-151, 1953. Distribution: see reference 11, FSTC-HT-0026-85. (EE-0959).

[55] B.H. Zitka, "Erosion Effect of Condensed Discharges in a Dielectric Medium," Translation of *Chekhoslovatskiy fizicheskiy zhurnal*, vol. 3(3), pp. 241-254, 1953. (EE-0085).

[56] M.A. Sultanov and L.I. Kiselevskii, "The Mechanism of the Electrode Erosion Produced by Supersonic Flares in a Pulsed Discharge," *High Temperature (USSR)*, vol. 4(3), pp. 361-366, 1966. (EE-0120)

[57] V.A. Morozov and L.I. Kiselevskii, "Destruction of Materials by Supersonic Pulse Capillary Discharge Plasma Jets," *Eng. Phys. J. (USSR)*, vol. 13(5), pp. 338-341, 1967. (EE-0118)

[58] G.S. Belkin and V.Ya. Kiselev, "Influence of Electrode Material on Erosion at High Currents," *Sov. Phys. Tech. Phys.*, vol. 12(5), pp. 702-703, 1967. (EE-0864)

[59] V.A. Morozov and L.I. Kiselevskii, "On the Destruction of Metals by a Pulsed Plasma Jet," Translation of *Doklady Akademii Nauk USSR*, vol. 12(5), pp. 413-416, 1968. Distribution: see reference 11, FSTC-HT-0152-86. (EE-0742)

[60] M.A. Sultanov, "Mechanism of Erosion of Certain Solid Substances Under the Effect of a Supersonic Flow of Plasma as a Function of Their Thermophysical Properties," *High Temperature (USSR)*, vol. 8(5), pp. 906-909, 1970. (EE-0130)

[61] V.N. Gurarii, P.S. Nosarev and S.E. Netsvetaev, "Disintegration of Carbon Steel by High-Velocity Plasma Jets," *Eng. Phys. J. (USSR)*, vol. 24(4), pp. 439-441, 1973. (EE-0734)

[62] O.B. Bron and L.K. Sashkov, *Electrical Erosion of High-Current Contacts and Electrodes*, M.: Energy, pp. 202-206, 1978. (EE-1052)

[63] V.A. Ageev and M.A. Sultanov, "Role of the Polarity of the Electrodes in the Erosion Mechanism of Metal Plates," *High Temperature (USSR)*, vol. 11(3), pp. 447- 450, 1973. (EE-0134)

[64] V.A. Ageev and M.A. Sultanov, "Mechanism of Ablation of Metals by a Supersonic Plasma Torch in Relation to Their Thermal Conductivity," *High Temperature (USSR)*, vol. 12 (1), pp. 15-20, 1974. (EE-0138)

[65] M.A. Sultanov, "Method for Reducing Ablation in a Supersonic Plasma Flow," *Sov. Phys. Tech. Phys.*, vol. 22(10), pp. 1287-1289, 1977. (EE-0133)

[66] J.L. Meunier and M.G. Drouet, "Experimental Study of the Effect of Gas Pressure on Arc Cathode Erosion and Redeposition in He, Ar, and C from Vacuum to Atmospheric Pressure," *IEEE Trans. on Plasma Sci.*, vol. PS-15, pp. 515-519, 1987. (EE-1063)

[67] R.L. Boxman and S. Goldsmith, "Momentum Interchange Between Cathode-Spot Plasma Jets and Background Gases and Vapors and its Implications on Vacuum-Arc Anode-Spot Development," *IEEE Trans. on Plasma Sci.*, vol. PS-18(2), pp. 231-236, 1990. (EE-1064)

[68] B.N. Zolotykh, "On Nature of the Energy Transfer to Electrodes in the Pulsed Discharge with Small Gaps/Intervals," In the book: *Electrical Contacts*, M., "Energy," pp. 5-20, 1964. Translation #NASA TTF 339. (EE-0005)

[69] I.I. Kalyatskiy, V.I. Kurets and E.N. Tarakanovskiy, "Relation of Heat Flows Going to the Surface of Electrodes During the Breakdown of Solids by Pulse Discharge," Translation of *Elektronnaya Obrabotka Materialov*, vol. 4, pp. 45-48, 1976, (EE-1012). Distribution: see reference 11, FSTC-HT-1061-84. (EE-0367)

[70] N.N. Rykalin, A.V. Nikolaev and I.D. Kulagin, "Heat Flow in a Body Interacting with a Plasma Jet," *High Temperature (USSR)*, vol. 3(6), pp. 811-817, 1965. (EE-0136)

[71] J.E. Gruber and R. Suess, "Investigation of the Erosion Phenomena in High Current, High Pressure Gas Discharges," *Max-Planck Institute for Plasma Physics*, Garching bei Munchen, IPP 4/72, Dec. 1969.

[72] Contacts Metals Welding, Inc., manufacturer, P.O. Box 2266, Indianapolis, IN 46206.

[73] Schwarzkopf Development Corp., distributor, 140 Lowland Street, Holliston, MA 01746. (Manufactured by Metallwerk Plansee, Austria.)

[74] C. duP. Donaldson and R.S. Snedeker, "A Study of Free Jet Impingement. Part 1. Mean Properties of Free and Impinging Jets," *J. Fluid Mech.*, vol. 45(2), pp. 281-319, 1971. (EE-0108)

[75] "CUWODUR - Contact Materials and Contact Components," Company Brochure, DoDuCo, D7530 Pforzheim, in Altgefall 12, FRG.

[76] P. Chao, W. Weber, and S.K. Lam, "Mechanical Behavior of Poco Graphite as Spark Gap Electrodes," *Physics International Laboratory Notes*, 2700 Merced, San Leandro, CA 94577-0599, 1987.

[77] SCM Metal Products, Manufacturer, Western Reserve Building, W. 9th Street, Cleveland, OH 44113.

[78] L.B. Gordon, M. Kristiansen, M.O. Hagler, H.C. Kirbie, R.M. Ness, L.L. Hatfield and J.N. Marx, "Material Studies in a High Energy Spark Gap," *IEEE Trans. on Plasma Science*, vol. PS-10(4), pp. 286-292, 1982. (EE-0778)

[79] Y. Suzuki, Y. Kawakita, M. Kume and M. Kawai, "A 150-kV, 100 kA Spark Gap Switch for Marx Generators," *Proceedings of the 3rd Int. Pulsed Power Conf.*, Albuquerque, NM, pp. 444-448, 1981. (EE-0884)

[80] G.S. Belkin and V. Ya Kiselev, "Effect of the Medium on the Electrode Erosion at High Currents," *Sov. Phys. Tech. Phys.*, vol. 23(1), pp. 24-24, 1978. (EE-0402)

[81] A.M. Abdel-Asis, "On the Influence of Contact Dimensions on the Loss of Metal During Switching of Alternate Currents in Oil and in Air," *IEEE Trans. on Parts, Hybrids and Packaging*, vol. PHP-9(1), pp. 53-57, 1973. (EE-0126)

[82] H.W. Turner and C. Turner, "Material Transfer Between Heavy Current Contacts," *Proceedings of the 10th Int. Conf. on Elec. Contact Phenomena*, Chicago, IL, pp. 61-70, 1980. (EE-0131)

[83] J.D. Cobine and E.E. Burger, "Analysis of Electrode Phenomena in the High-Current Arc," *J. of Applied Phys.*, vol. 26(7), pp. 895-900, 1955. (EE-0422)

[84] G.S. Belkin, "Dependence of Electrode Erosion on Heat Flux and Duration of Current Flow," *Sov. Phys. Tech. Phys.*, vol. 15(7), pp. 1167-1170, 1971. (EE-0435)

[85] D.D. Malyuta and V.S. Mezhevov, "Discharger with High Pulse Repetition Frequency," Plenum Publishing Corp., translation of Pribory i Teknika Exksperimenta, Vol. 4, pp. 89-90, 1980. (EE-1215)

[86] L.M. Pokrovskaya and N.I. Plokhikh, "Erosion by Plasma Jet," *J. of Spectroscopy, (USSR)* ,vol. 11 (3), pp. 1006-1009, 1969. (EE-1050)

CHAPTER IV

UTILIZATION OF A THERMAL MODEL TO PREDICT ELECTRODE EROSION PARAMETERS OF ENGINEERING IMPORTANCE

This chapter begins with a listing of the symbols and their definitions. All units are MKSA.

Nomenclature

A_e [m^2] - area of arc attachment on the electrode surface

AJH - arc joule heating

c [J/kg°C] - specific heat of the solid at constant temperature

c_b [J/kg°C] - specific heat at the boiling temperature

c_ℓ [J/kg°C] - specific heat of the liquid

c_{mp} [J/kg°C] - specific heat at the melting temperature

C - coulombs

C_t [F] - total system capacitance

Γ_e - the experimental ratio of the ablation erosion to the vaporization erosion

Γ_t - the theoretical ratio of the ablation erosion to the vaporization erosion

d [m] - diameter of electrode rod

e_f [m^3] - filament erosion

e_{tot} [m^3] - total erosion

E_a [J] - energy released in the arc

E_e [J] - energy released in the electrode

E_m [J] - the energy required to melt 1 m^3 of electrode material

E_v [J] - the energy required to vaporize 1 m^3 of electrode material

EJH - electrode joule heating

f_1 - an erosion scaling factor derived from thermal considerations

I_a [A] - arc current

I_e [A] - electrode current

I_f [A] - filament current

I_p [A] - peak arc current

J [A/m^2] - current density

J_{cta} [A/m^2] - critical risetime current density for AJH

J_{cte} [A/m^2] - critical risetime current density for SEEEJH

J_e [A/m^2] - electrode current density

J_{eo} [A/m^2] - electrode surface current density

J_{ess} [A/m^2] - steady state electrode current density

J_{mo} [A/m^2] - melting onset current density for AJH

J_{vo} [A/m^2] - vaporization onset current density for AJH

J_1 [A/m^2] - melting onset current density for SEEEJH

J_2 [A/m^2] - vaporization onset current density for SEEEJH

k [$W/m^\circ K$] - thermal conductivity of the solid

k_{j1} [A^2s/m^4] - melting onset constant for EJH only

k_{j2} [A^2/sm^4] - melting onset constant for SEEEJH only

k_ℓ [$W/m^\circ K$] - thermal conductivity of the liquid

k_{mo} [A^2s/m^4] - melting onset constant for AJH

k_{moe} [A^2s/m^4] - experimental value of k_{mo}

k_{mot} [A^2s/m^4] - theoretical value of k_{mo}

k_{vo} [A^2s/m^4] - vaporization onset constant for AJH

ℓ [m] - electrode thickness

ℓ_a [m] - arc attachment length

L [$V/^\circ K$] - Wiedemann-Franz-Lorentz Law constant

L_f [J/kg] - latent heat of fusion

L_v [J/kg] - latent heat of vaporization

μ [H/m] - magnetic permeability

n_f - number of filaments

q_ℓ [W/m^2] - heat flux lost at back of electrode ($z=\ell$)

q_m [W/m^2] - magnitude of the heat flux

q_s [W/m^2] - maximum cooling rate

q^* - normalized heat flux

q_{ch} [W/m^2] - effective heat flux due to chemical reactions

Q [C] - charge transfer

Q_e [C] - effective charge transfer

M_I [$N/^\circ Ks^{0.5}$] - thermal "impulsivity"

M_{Im} [$N/^\circ Ks^{0.5}$] - thermal melting "impulsivity"

M_{Iv} [$N/^\circ Ks^{0.5}$] - thermal vaporization "impulsivity"

ρ [kg/m^3] - electrode material density

ρ_ℓ [kg/m^3] - density of the liquid metal

r_o [m] - arc attachment radius

R_a [Ω] - arc resistance

R_e [Ω] - electrode resistance

R_f [Ω] - filament resistance

σ_e [S/m] - electrical conductivity

SEEEJH - skin-effect enhanced electrode joule heating

τ [s] - current pulse periodicity

t [s] - time

t_1 [s] - melting onset time for SEEEJH

t_2 [s] - vaporization onset time for SEEEJH

t_d [s] - effective dwell time of the arc on the electrode surface

t_p [s] - pulse time (width)

t_{rt} [s] - rise time onset time

T [°K] - temperature

T_b [°K] - boiling temperature

T_m [°K] - effective melting temperature which includes the effect of latent heat

T_{mp} [°K] - melting temperature

T_o [°K] - initial temperature

T_v [°K] - effective vaporization temperature which includes the effect of latent heat

v_a [m^3] - volume ablated

v_a^* - normalized ablated volume

v_{as} [m^3] - steady state ablation volume

v_e [m^3] - eroded volume

v_e^* - normalized eroded volume

v_m [m^3] - volume melted but not removed

v_m^* - normalized volume melted but not removed

v_o [m/s] - arc velocity

v_v [m^3] - volume vaporized

v_v^* - normalized vaporized volume

v_{vs} [m^3] - steady state vaporization volume

V_a [V] - arc voltage

V_f [V] - fall voltage

V_{fi} [V] - filament voltage

x - graphical coordinate representing $q^*(t_p)^{1/2}$

x_1 - value of x for the onset of melting or vaporization

x_2 - value of x where the thermal process begins to be steady state

y_{ss} - steady state value of the vertical graphical coordinate which represents the normalized eroded volume

z [m] - direction perpendicular to the electrode surface

k_f, k_f^*, k_f^{**}, k_s - various constants

Introduction

The electrode erosion produced by high current, high energy, transient arcs is one of the most important factors limiting lifetime and affecting performance in spark gaps and electro-magnetic mass drivers. Despite a rich history of both theoretical and experimental work there remains a considerable amount of disagreement and uncertainty as to the role and scaling of many of the factors which affect electrode erosion. More often than not the engineer attempts to determine empirical scaling laws in terms of an experimental variable, (Q_e, I_p, dI_a/dt, $\int I_a^2\, dt$, etc.). Unfortunately, if one approaches electrode erosion from a thermal management point of view, then a single one of these variables is inadequate to describe the scaling phenomena. However, numerical and analytical solutions to the appropriate thermal equations should indicate which and how these factors affect the erosion process. Thus, the purpose of this chapter is to examine the implications of a previously obtained solution of the thermal differential equation for heat conduction at the electrode surface in order to determine and predict the onset conditions for various thermal mechanisms, the scaling laws for the actual erosion and the importance of various material properties as a function of differing pulse conditions. The theoretical results will be compared with the experimental data of the author and others [1-10].

The Thermal Model

For high current, high energy pulses, energy is transferred to the electrode via numerous mechanisms including conduction, radiation and convection from arc joule heating (AJH), electrode joule heating (EJH), skin effect enhanced EJH (SEEEJH) chemical reaction heating (CRH), and plasma jet impact heating (PJIH), to name a few. Each of these mechanisms was discussed in detail or alluded to in Chapters 2 and 3.

A numerical solution for the condition of dominant AJH with a constant heat flux was found in part by Belkin [13] (melting and vaporization) and Dixon [14] (ablation) and is shown in Fig. 4.1. The solution indicates that there are two limiting cases for material removal: ablation, v_a^*, where all the melted electrode material is removed as it is formed, and vaporization, v_v^*, where the molten material, v_m^*, remains on the electrode surface until it begins to vaporize. The axis variables v_e^* and $q^*(t_p)^{1/2}$ were normalized by Belkin [13] so that they are unitless and so that the normalized eroded volume, v_e^*, approaches one of the steady state values, v_{as}^* or v_{vs}^*, unity as t_p increases. The normalized variables are given by

$$v_a^* = v_a c T_m / q_m t_p A_e, \qquad (4.1a)$$

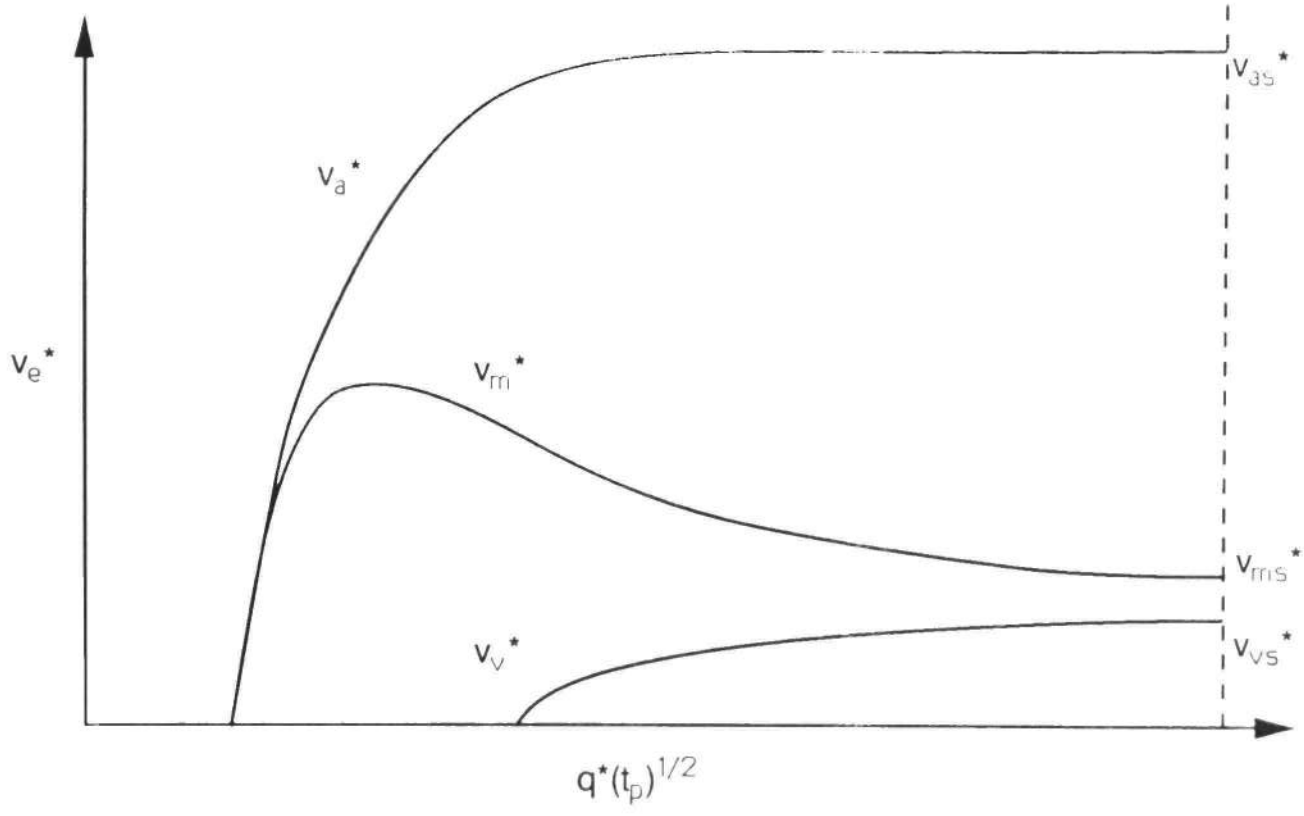

Fig. 4.1 Ablation, Melting and Vaporization Front Locations as a Function of the Applied Heat Flux. The heat flux is assumed to have constant magnitude, q_m, and constant cross sectional area, A_e, for the pulse duration, t_p.

$$v_m^* = V_m c T_m / q_m t_p A_e, \tag{4.1b}$$

$$v_v^* = v_v c T_m / q_m t_p A_e, \tag{4.1c}$$

and

$$q^* = q_m / M_{Im}; \tag{4.1d}$$

where an effective melting temperature, T_m, is defined by

$$T_m = T_{mp} - T_o + L_f / c_{mp}, \tag{4.1e}$$

and the melting thermal "impulsivity", M_{Im}, is given by

$$M_{Im} = T_m (k \rho c)^{1/2}. \tag{4.1f}$$

In the above equations T_{mp}, T_o, k, ρ, c and L_f are the electrode melting temperature, initial surface temperature, thermal conductivity, specific density, heat capacity and latent heat of (Note: Eq. 4.1d contains the correction term, L_f/c_{mp}, to account for the latent heat of fusion which Belkin chose not to include.) In order to relate the results in terms of the electrical pulse parameters, the heat flux, q_m, present at the electrode surface from all sources is approximated by the expression

$$q_m = [V_f I_p / A_e] [U(t) - U(t-t_p)], \tag{4.2}$$

where U(t) is the unit step function. The quantities V_f and A_e are often assumed to be constant and, for estimation purposes, are on the order of 10 volts and 1 cm^2. It is these equations and the solutions in Fig. 4.1 which will be used to derive thermal damage onset conditions and scaling laws for

electrode erosion as a function of material properties and pulse conditions.

Model Predictions

Scaling Laws

At the very onset of the electrode erosion work, one of the primary objectives was to determine the scaling laws for erosion as a function of one of the electrical discharge parameters (peak current, charge stored or transferred, etc.). Before discussing the experimentally observed erosion scaling laws one should remember that it is essential to know the experimental conditions used to change the scaling variable. For example, if additional capacitance is added to the energy store to increase the peak current, then for an oscillatory discharge with a small damping factor, Q_e is proportional to I_p^2 (see derivation in Appendix B). If the gas pressure is used to increase the peak current by increasing the breakdown voltage, then Q_e is proportional to I_p. For a unipolar pulse, in either case, Q_e is proportional to I_p. These considerations have led to much confusion when they have been ignored. For the results discussed below, the scaling laws obtained from each author's original works have been reformulated in terms of Q_e, I_p and t_p, taking into account the correct relationships between the scaling variables.

Several experimenters [1-4] have found erosion to scale linearly with Q_e when I_p was kept constant. Of these, the oscillatory current results for Belkin, and Gruber and Suess

were for large charge transfers (>1 C) and small gap spacings (~1.5 mm). Suzuki et al. [5] reported a dependence of $I_p^{2.3}$ or $Q_e^{2.3}$, but two cases of only two points each were used. Many dependencies have been reported for contact erosion, $I_p^{1.5}t_p$ [6], Q_eI_p [7], and $Q_eI_p^{1.7}$ [8], but some of these are undoubtedly influenced by time varying gap separation. Fey and McDonald [9] observed $I_p^{2.24}$ Q_e dependencies for electrode erosion in arc heaters with externally applied magnetic fields influencing the arc attachment. It should be mentioned that most of the experimenters mentioned above observed transition regions where the erosion increased rapidly (proportional to I_p^3 to I_p^6) over a very small range of I_p or Q_e. One group of authors [9] possibly missed one of these transition regions when assigning a straightline fit to their data. After examining the results from the solution to the heat conduction equation shown in Fig. 4.1, one can predict these dependencies with rather straightforward considerations. First, however, it will be useful to review the basis for previous approaches for the scaling of electrode erosion.

Early efforts at determining the scaling of erosion as a function of current attempted to relate the erosion to the total energy in the arc, E_a, or the electrode, E_e, or both. For example, in general

$$E_a(t) = \int_0^t V_a(t)\, I_a(t)\, dt, \tag{4.3}$$

and

$$E_e(t) = \int_0^t V_e(t)\, I_e(t)\, dt, \tag{4.4}$$

where I_a, I_e, V_e and V_a are the absolute values of the arc and electrode current and voltage, which usually are functions of time. By assuming that the erosion scaled linearly with the arc or electrode energy, which is not true except for specific conditions, then the following solutions were obtained for the eroded volume v_e, each solution having its own assumptions. If the arc energy is dominant (AJH erosion mechanism is dominant) then

$$v_e \propto V_a Q_e, \tag{4.5}$$

for a constant arc voltage, V_a, where Q_e is the effective charge transferred, and for a constant arc resistance, R_a,

$$v_e \propto R_a \int I_a^2(t)\, dt. \tag{4.6}$$

If the electrode energy is dominant (EJH or SEEEJH dominates the erosion) then

$$v_e \propto V_e Q_e, \tag{4.7}$$

for a constant electrode voltage, V_e, and

$$v_e \propto R_e \int I_e^2(t)\, dt, \tag{4.8}$$

for a constant electrode resistance, R_e, where V_e and R_e are defined for some region close to the surface where the current density is the highest and thus the electrode heating is most likely to result in the production of molten electrode material. Since the energy density is usually needed to

calculate material heating, the expressions for $I_e(t)$ are often divided by an effective arc-electrode interaction area, $A_e(t)$, to get the current density, $J_e(t)$.

The approach outlined above has numerous disadvantages including:

1) the assumption that v_e scales linearly with the energy available - Holmes [13] has rightly noted that only a small fraction of the available energy is actually needed to produce the erosion observed,
2) the assumption of constant V_a, R_a, V_e, and R_e; in effect this is the same as removing the transient part of the solution which in many cases can be shown to be a dominant factor, and
3) the inability to correctly define an effective electrode volume, area or depth for which these processes are acting (which again is really time dependent).

Despite these inadequacies, several authors quote experimental results which agree with Eq. (4.5). They are most likely able to do so because of one or more of the following reasons:

1) they make the assumption that the portion of the arc energy which accounts for the electrode heating is that which occurs in the electrode "fall" region of the arc, thus, V_a becomes V_f, a constant,
2) they are conducting experiments where the gap spacing is very small, which implies that a high

percentage of the arc energy actually does result in electrode heating, or

3) they are conducting experiments for relatively long pulse times (i.e., pulse times which result in a constant arc voltage).

In addition, the fine structure of the arc attachment needs to be considered. As was mentioned in the introductory chapter, different regions exist for the erosion process, partially defined by whether the arc attachment to the electrode surface can be considered from a macroscopic or microscopic point of view (the arc attachment defined by the arc diameter or the filament diameter, respectively). In actuality, the high current arc is known to consist of many individual filaments, each of which is attached to the electrode and forms a microscopic crater [14,15]. Whether the erosion at each crater site is due to AJH, EJH, or SEEEJH the total erosion is a function of the filament current and the temporal history of each attachment site [16,17]. Under certain circumstances, it has been shown that the current per filament and the attachment lifetime are approximately constant [14,15]. If this is the case then the following proof will show that regardless of the erosion dependence on the current at each individual attachment site (i.e., any mechanism, EJH or AJH), the total erosion will be proportional to Q_e since the total number of sites would be a linear function of current.

In general, the total erosion, e_{tot}, is a product of the number of filaments, n_f, and the erosion produced per filament, e_f, e.g.,

$$e_{tot} = n_f e_f. \tag{4.9}$$

If one defines a filament time, t_f, resistance, R_f, and current, I_f, then Eq. (4.8) becomes

$$e_f = k_f R_f \int_0^{t_f} I_f^2(t)\, dt, \tag{4.10}$$

where k_f is a proportionality constant. Equation (4.10) becomes

$$e_f = k_f^* I_f^2 t_f. \tag{4.11a}$$

where

$$k_f^* = k_f R_f. \tag{4.11b}$$

Substituting Eq. (4.11a) into Eq. (4.9) yields

$$e_{tot} = n_f k_f^* I_f^2, \tag{4.12}$$

but with

$$n_f I_f t_f = Q_e, \tag{4.13}$$

then

$$e_{tot} = k_f^* I_f Q_e. \tag{4.14}$$

Also, for AJH, with a filament voltage, V_{fi},

$$e_f = k_f V_{fi} \int_0^{t_f} I_f dt, \tag{4.15}$$

or

$$e_f = k_f^{**} I_f t_f. \tag{4.16a}$$

with

$$k_f^{**} = k_f V_{fi}. \tag{4.16b}$$

Substituting Eq. (4.16b) into Eq. (4.9) yields

$$e_{tot} = n_f k_f^{**} I_f t_f. \tag{4.17}$$

However, with Eq. (4.13), Eq. (4.17) becomes

$$e_{tot} = k_f^{**} Q_e. \tag{4.18}$$

Thus, in either case the total erosion, for the situation where each filament's erosion acts independently, is proportional to the total effective charge transfer. The thermophysical properties only enter Eqn's. (4.14) and (4.18) through the constants of proportionality, k_f^*, and k_f^{**}. Earlier work by the author [13] assumed that this was always the case, but in reality many other dependencies have been observed macroscopically [1-10]. Thus, either the initial assumption that the erosion could be expressed by Eqn's. (4.3)-(4.8) is wrong or the macroscopic phenomena are determined by a different set of criteria. It can be shown that any dependency could have been picked for the erosion of the filament as a function of the filament current and the total erosion would still have been proportional to Q_e. Thus, it is apparent that the macroscopic arc, whose individual filaments act collectively, must be described by equations

other than Eqn's. (4.3)-(4.8) if one is to account for dependencies other than Q_e. The approach chosen by the author, to accomplish just that, was to examine the solutions to the heat conduction equation given by Belkin [11] in order to predict scaling (i.e., start with the physics of heat transfer to get the desired relationship with respect to the engineering variables and not vice versa).

Appendix G contains the derivation of the scaling laws for erosion by ablation and vaporization. The results indicate that both v_a and v_v are bounded by scaling laws proportional to Q_e and $Q_e I_p (t_p)^{1/2}$ (defined as f_1) in the transient regime after the initiation of melting and are proportional to Q_e in the steady state. In the thermal steady state, the expression for v_a and v_v are

$$v_a = \frac{V_f Q_e}{\rho C T_m} = \frac{V_f Q_e}{E_m}, \tag{4.19}$$

and

$$v_v = \frac{V_f Q_e}{\rho (C T_m + C_{mp} T_v)} = \frac{V_f Q_e}{E_v}, \tag{4.20}$$

where E_m and E_v are the energies required to melt and vaporize the electrode, respectively.

The ratio of v_a/v_v should give the relative difference in magnitudes between the eroded volumes when ablation occurs instead of vaporization. The ratio, Γ_t, is

$$\Gamma_t = v_a/v_v = 1 + \frac{C_{mp}T_v}{cT_m}. \qquad (4.21)$$

The value of this ratio is 10 for Cu, 8.33 for W and Mo and 9.72 for Nb. Thus one would expect the erosion values for ablation to be approximately one order of magnitude higher than the values for vaporization.

Onset Conditions

The details of the mechanisms of electrode erosion were covered in Chapter 2. The various thermal mechanisms for which an onset has been determined are arc joule heating (AJH), electrode joule heating (EJH), and skin effect enhanced EJH (SEEEJH). The other thermal source, chemical reaction heating (CRH), has not been adequately quantified for the electric arc conditions. The performance of an electrode material may be characterized by knowing which of these heating mechanisms is dominant as a function of pulse conditions and by knowing the limit on material removal which occurs for each mechanism. Thus, the onset conditions which determine when the various heating mechanisms begin to have an effect on the erosion are very important. In a recent paper by Nemes and Randles [19] the onset conditions for material damage resulting from laser irradiation of a surface were characterized as a function of material properties and pulse conditions. It was that work which led the author to reexamine the way he and others have characterized the onset conditions for electric arc damage.

The onset condition for thermal damage for the case where AJH of the electrode surface is dominant is described by the equation

$$q^*(t_p)^{1/2} = (\pi/4)^{1/2}, \tag{4.22}$$

where t_p is the current pulse width and q^* is the normalized heat flux defined by Eq. (4.1d). Substituting Eqn's. (4.14) and (4.2) back into Eq. (4.22), squaring both sides and setting I_p/A_e equal to the current density, J, a constant, one obtains:

$$J^2 t_p = (\pi/4)(M_{Im}^2)/V_f^2, \tag{4.23}$$

or

$$J^2 t_p = k_{mo}, \tag{4.24}$$

where k_{mo} is a melting onset constant given by Eq. (4.23). It should be noted that the melting temperature was used to define this onset, but any temperature in which a significant reduction in the thermal strength of the material is experienced could define a thermal damage onset constant, k_{to}. A similar expression can be derived for the onset of vaporization, namely,

$$J^2 t_p = k_{vo}, \tag{4.25}$$

where

$$k_{vo} = k_{mo} + (\pi/4)(M_{Iv}^2)/V_f^2, \tag{4.26}$$

where the vaporization impulsivity, M_{Iv}, is defined by

$$M_{Iv} = T_v(k_\ell \rho_\ell c_\ell)^{1/2}, \tag{4.27}$$

$$T_v = T_b - T_{mp} + L_v/c_b, \tag{4.28}$$

and where k_ℓ, ρ_ℓ, c_ℓ, T_b, L_v, c_b are the material's thermal conductivity, density, and specific heat as a liquid; and the boiling temperature, latent heat of vaporization, and specific heat at the boiling temperature, respectively. (All of the material parameters are assumed to be constant with temperature for a given state.) Equations (4.24) and (4.25) are plotted in Fig. 4.2 using t_p and J^2 as the x and y axis, respectively. The region of no thermal degradation is shaded and the onset takes the form of a straight line under the assumptions used. Having considered arc joule heating, let us now consider adding the effect of electrode joule heating (EJH).

Intuitively, including the effects of EJH should have the effect of lowering the damage onset condition if the EJH significantly modifies the electrode temperature distribution in the region of no thermal degradation from AJH. Several people have examined the effect of EJH [20-28]. A brief review of these works is given in Appendix F. Of these, Dethlefsen [29], Avsyesoch [25] and Goloveiko [26] all gave onset conditions. Goloveiko's approach, which was presented in Chapter 2, requires the solution of some transcendental equations and will not be considered here. Dethlefsen's and Avsyesoch's criteria differ by only a constant. Their criteria were reevaluated by the author [10]

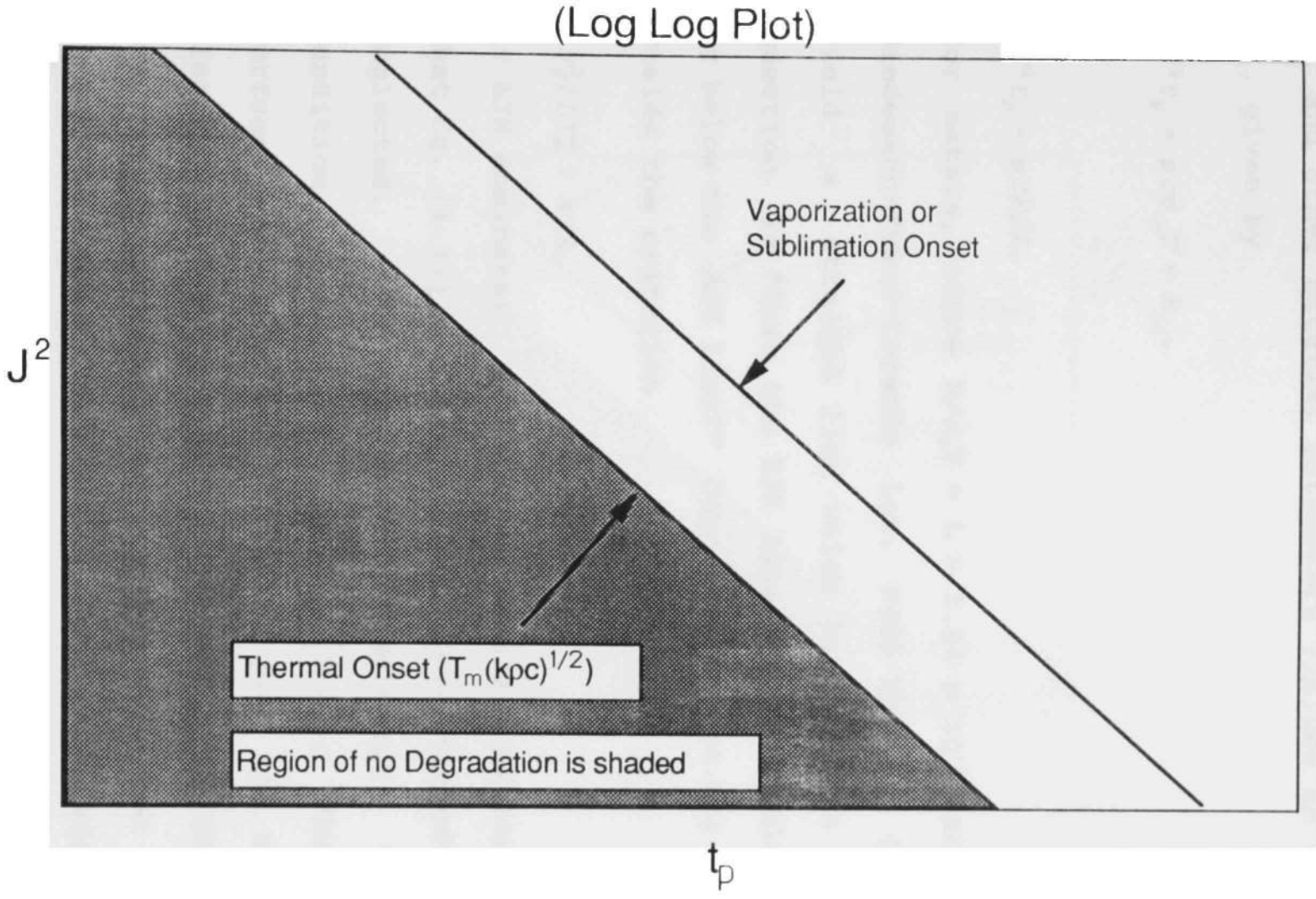

Fig. 4.2 Material Performance for Arc Joule Heating. Assumptions: spatially and temporally constant heat flux, EJH is negligible.

in terms of J^2 and t_p for plotting purposes. Rewriting Dethlefson's criteria in terms of the electrical conductivity, σ_e, and other material parameters yielded an onset constant, k_{j1}, given by

$$J^2 t_p = \rho c \sigma_e T = k_{j1}, \tag{4.29}$$

or

$$J^2 t_p = \rho c k / L, \tag{4.30}$$

for metals, since $k/\sigma_e T = L = 2.24 \times 10^{-8} (\text{volt/K})^2$, by the Wiedemann-Franz-Lorentz Law. Note that Eq. (4.31) will also yield a straight line which is shown on Fig. 4.3. The question is "Does the EJH line from Dethlefsen lie above or below the AJH line?" Comparing Eq. (4.30) with Eq. (4.23) yields the criterion

$$V_f^2 / L T_m^2 > \pi/4, \tag{4.31}$$

if AJH dominates. For all the metals considered it was found that Eq. (4.31) was easily satisfied, therefore, EJH can be neglected. It should be remembered that the onset condition represented by Eq. (4.31) is for the electrode surface. Thus, at some distance from the surface of the electrode a condition will arise where the EJH will dominate over the propagation of the AJH from the surface. This effect has been observed in contact erosion [37] but has not been modeled for the conditions studied here.

Using a simple "skin" heating model, the author has derived a relationship for when SEEEJH will begin to become

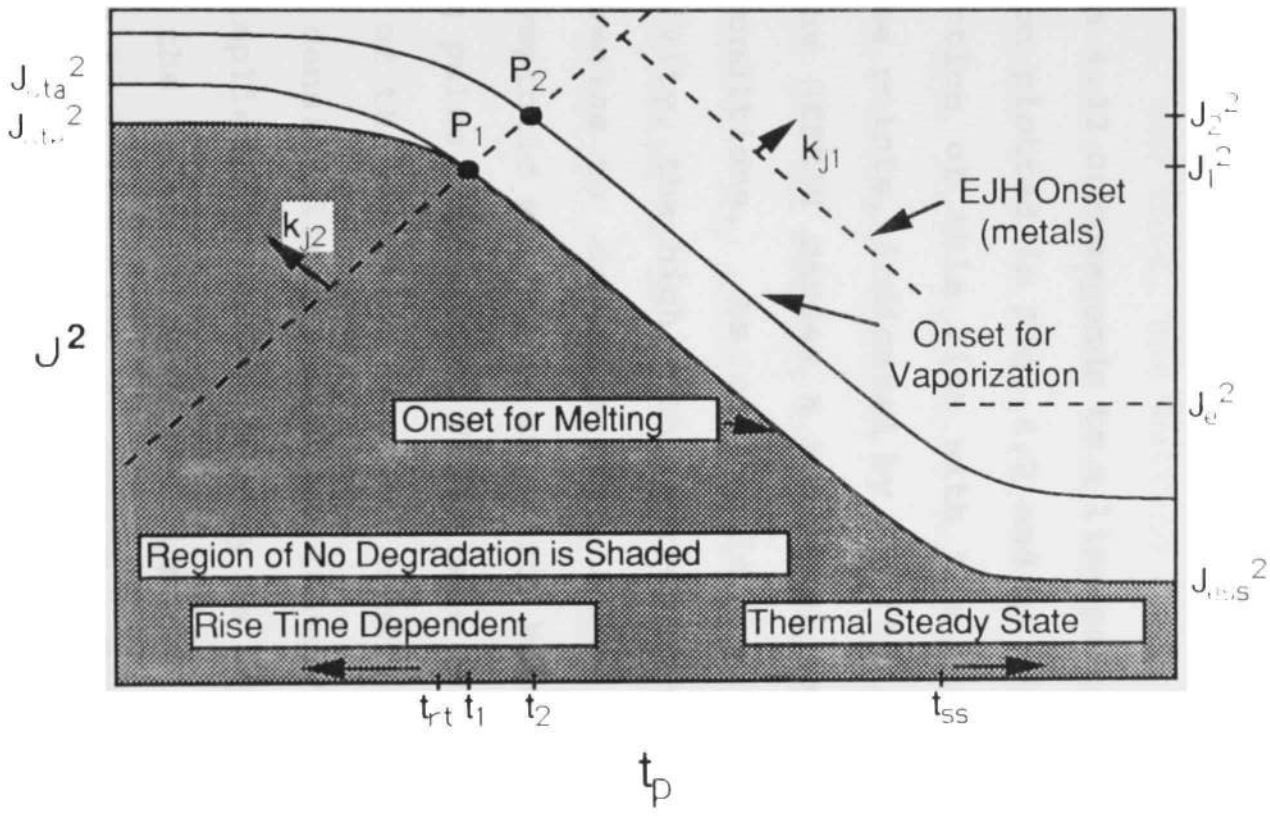

Fig. 4.3 Material Performance for Electrode and Arc Joule Heating. (For symbol definitions see the text.)

important at the electrode surface. The details are given in Appendix F but the result is

$$J^2 = k_{j2} t_p, \tag{4.32}$$

where k_{j2} is the SEEEJH onset constant given by

$$k_{j2} = 20\pi^2 V_f^2 \sigma_e / \mu. \tag{4.33}$$

Equation 4.32 corresponds to a line perpendicular to the other criterion plotted in Fig. 4.2 and is shown in Fig. 4.3. The intersection of this line with the thermal onset criterion marks the points, indicated by P_1: (t_1, J_1) and P_2: (t_2, J_2) at which the SEEEJH causes a reduction in the overall thermal onset conditions. As one would expect, the higher the conductivity, the higher the current which is needed before SEEEJH begins to dominate over AJH.

Asymptotic solutions exist for both high current density and long pulse times. The first case is indicated by the flat portion of the curve on the left hand side of Fig. 4.3. This current density limit, which is independent of pulse length, simply implies that enough energy is supplied during the rise time of the pulse to melt the surface. This limit could be produced for either AJH or SEEEJH. For AJH Eq. (2.24) could be used to determine the AJH critical current density, J_{cta}. For SEEEJH the author has not derived an expression but intuitively believes that the SEEEJH critical current density, J_{cte}, is less than J_{cta}. The way that Fig. 4.3 is drawn it appears that the onset curve for melting begins to flatten out

to the asymptotic value J_{cte} when $t_p < t_{rt}$, the time when the risetime determines the onset, (i.e., $t_{rt} \sim t_1$). In general this may not be true. If $t_{rt} << t_1$ then the curve should look like the one in Fig. 4.4. The shape of this curve from t_{rt} to t_1 simply indicates that due to SEEEJH a higher amount of energy for a fixed arc current gets transferred to the electrode, and thus, the melting curve shifts to the left.

The other asymptote, shown as a flat portion on the right hand side of Fig. 4.3, is for long t_p, e.g., thermal steady state. This limit says that for some critical steady state electrode current density, J_{ess}, the heat entering the electrode at the melting temperature is just balanced by the heat removed. Any additional current increases would lead to surface melting as the latent heat of fusion is overcome. The current density, J_{ess}, for melting due to AJH only is given by

$$J_{ess} = MAX((k(T_{mp}-T_o)/\ell) , q_t) / V_f, \qquad (4.34)$$

where MAX indicates the maximum of the argument in parenthesis, ℓ is the electrode thickness and q_t is the total heat flux lost from the electrode by conduction, radiation and convection. For reasonable values of ℓ, q_t is the larger of the two terms, and in practice values of 20 kW/cm^2 can be achieved. A similar expression could be derived for erosion due to vaporization. The J_{ess} for EJH has been derived by Rich [20] and Zekster [27]. Again they differ only by a constant with Zekster predicting a higher current density. For EJH to

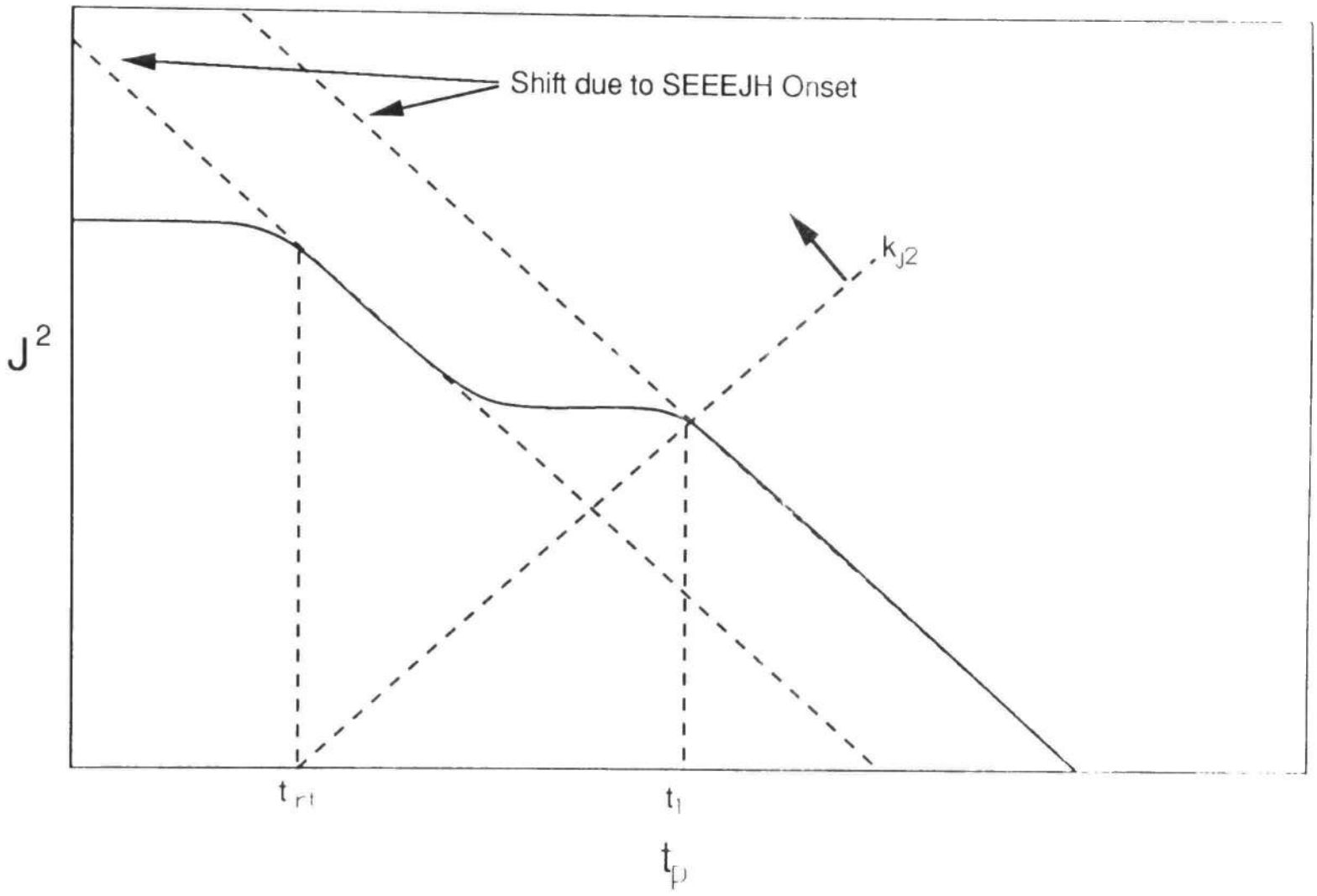

Fig. 4.4 Modification of Fig. 4.2 for the Case When the Risetime Threshold Time, t_{rt}, is Much Smaller than the Pulsetime for SEEEJH Onset, t_1.

dominate over AJH, the electrode current density, J_e, must satisfy the condition

$$J_e > V_f \sigma_e / r_o. \qquad (4.35)$$

where r_o is the radius of the arc attachment. Since J_e is much larger than J_{ess} for all materials for the current densities considered, the steady state onset criterion is determined by Eq. (4.34), namely, $J_{ess} \sim 2$ kA/cm^2.

The material onset constants for several materials were calculated by the author [10] and are given in Table 4.1. These values are only estimates because of the assumptions made in the derivations, i.e., temperature independent material properties, constant current density, fall voltage, etc.

Values for the onset current densities which result in melting (J_{mo}) and vaporization (J_{vo}) are given in Table 4.2 for a pulse time of 10 μs. Also, calculated are the intersection points, labeled P1 and P2 in Fig. 4.3, for the onset of SEEEJH given by (J_1,t_1) and (J_2,t_2). In practice, actual onset current densities may be considerably less, (a factor of 5) due to the inhomogeneous nature of the current density in the arc.

The effects of repetition-rate on the onset melting conditions can be calculated using the results of Raezer [28] which were discussed in Chapter 2. Equation (2.21h) was an expression for the maximum heat flux, q, as a function of the pulse length, t_p, the pulse periodicity, τ, the maximum

Table 4.1 Material Onset Constants for Various Electrode Heating Mechanisms

Material	k_{mo} (A^2s/m^4) x 10^{13}	k_{vo} (A^2s/m^4) x 10^{15}	k_{j1} (A^2s/m^4) x 10^{16}	k_{j2} (A^2/m^4s) x 10^{28}
Cu	2.41	1.75	6.1	7.47
W	7.49	3.71	2.1	2.26
C	---	1.23	0.053	0.011
Mo	3.25	1.47	5.3	2.26
Nb	1.01	0.684	1.6	0.98

Note: V_f is chosen to be 10 volts, $r_a = 10^{-3}$ m.

These values are only estimates because of the assumptions made in the derivations, i.e., constant current density, fall voltage, etc.

Table 4.2 Onset Condition for the Various Thermal Processes

Material	J_{mo}^*	J_{vo}^*	J_1^+	J_2^+	t_1^*	t_2^*
Cu	0.16	1.3	3.7	11	18	150
W	0.27	1.9	3.6	9.6	57	400
C	----	1.1	---	1.9	---	3500
Mo	0.18	1.2	2.9	7.7	38	250
Nb	0.10	0.82	1.8	5.1	32	260

Units: J-(x 10^{10} A/m^2), t-(x 10^{-9} s).

* calculated with t_p chosen to be 10 μs.

+ calculated with the arc area chosen to be 10^{-6} m^2.

cooling rate, q_s, and the thermal diffusivity, α_t. This equation has been rewritten in terms of the current density, J, by choosing V_f = 10 volts, q_s = 20 kW/cm^2 and A_e = 0.5 cm^2. Figure 4.5 shows this equation for copper electrodes on a plot of J^2 versus t_p. For the case of a single pulse, $\tau/t_p = \infty$, the conditions for the melting onset are exactly the same as in Fig. 4.2. As the ratio of τ/t_p decreases the onset condition is lowered until for τ/t_p = 10 the onset curve changes very little for short pulse lengths. This is consistent with the fact that in the limit as τ/t_p = 1, or a continuous heat flux, the onset curve should be a straight line corresponding to a steady-state condition. The effect of repetition-rate can be seen by considering the maximum J^2 for a fixed t_p. Picking t_p = 10 μs, a repetition-rate of 1000 pps gives a maximum J^2 of ~ 2 x 10^8 A^2/cm^4. For a repetition-rate of 100 pps the maximum J^2 is increased to 6.4 x 10^9 A^2/cm^4. Thus the onset conditions are lowered as τ/t_p is reduced or the repetition-rate is increased.

The effect of arc motion on the onset conditions is discussed in Appendix E for a simple case where the arc velocity is constant, independent of current level. The results, shown in Fig. 4.6, indicate that the onset condition shifts to a higher value of J, for a fixed t_p, by the amount

$$k_s = v_o t_p / \ell_a, \tag{4.36}$$

where v_o is the arc velocity and ℓ_a is the length of the arc attachment in the direction of motion.

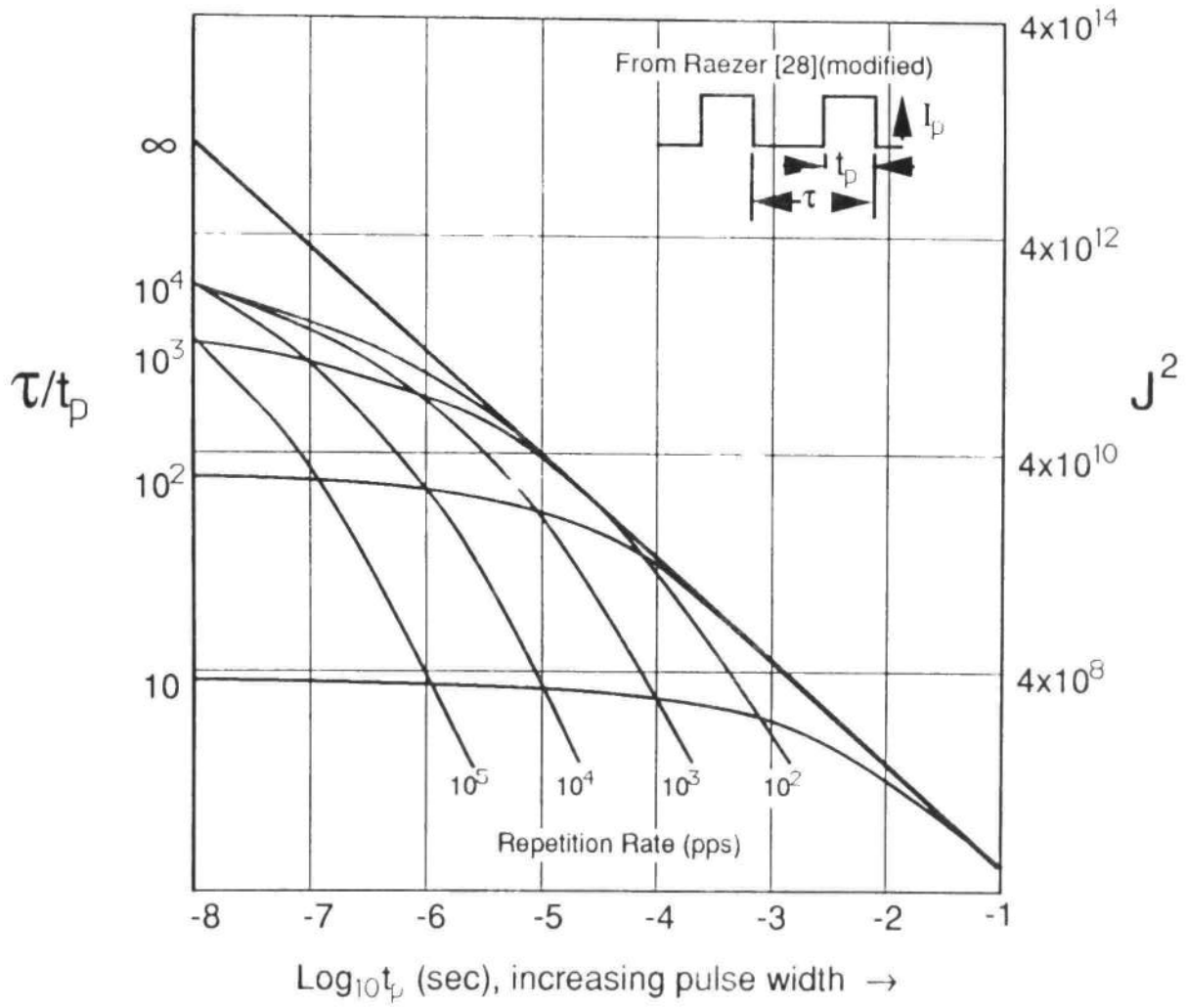

Fig. 4.5 Maximum Current Density Allowed before Melting Occurs as a Function of Pulse Width. (Modified from Raezer [28])

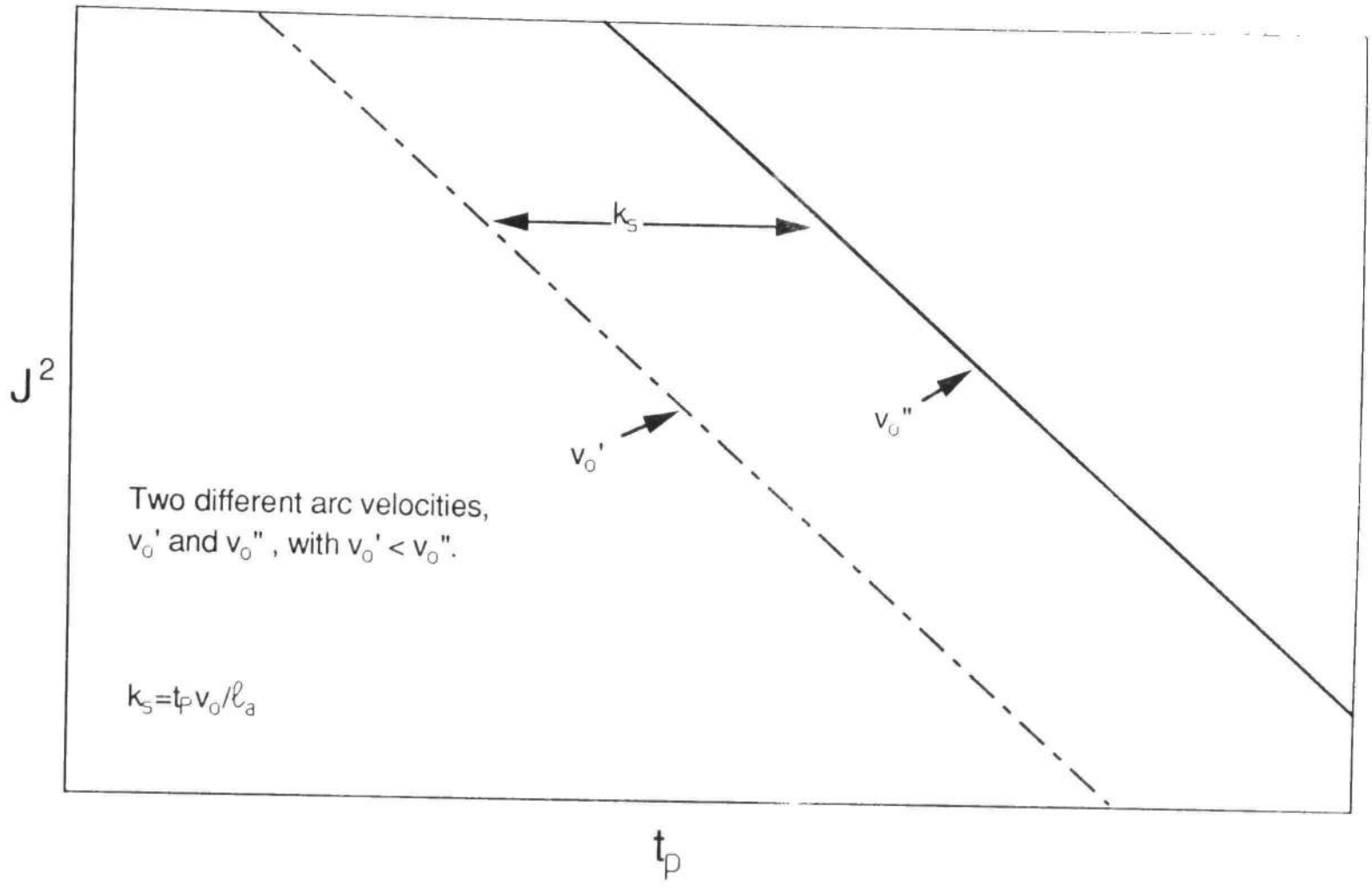

Fig. 4.6 The Effect of Arc Motion on the Thermal Onset Condition. (see Appendix E for the Details)

Erosion Magnitudes

After having determined, as a function of material properties and pulse parameters (J^2, t_p), which regime of electrode damage that one is in, it would be important to know what relative erosion might be expected from different materials. For the case where EJH is important the author has derived expressions from the theories of Watson [29] and Comstock and Williams [21] for the amount of molten metal formed. The derivations are given in Appendix F but the results are shown here in Table 4.3 for several electrode materials.

For the case of thermal steady state AJH, i.e., $q^*(t_p)^{1/2} >> (\pi/4)^{1/2}$, then Eqn's. (4.19) and (4.20) indicated that the energy to melt, E_m, is the figure of merit when the electrode ablates; and the energy to vaporize, E_v, is the figure of merit when the electrode vaporizes. Table 4.4 lists values of E_m and E_v for several electrode materials.

For thermal transient AJH the following expressions are derived in Appendix G for the volume eroded as a function of the pulse and material properties. Note: the results cannot be reduced to a single material parameter because these are a function of both E_m and k_{mo} or E_v and k_{vo}. Namely, from Appendix G, for ablation

$$v_a(x) = y_{ss}\left(\frac{x-x_1}{x_2-x_1}\right)\left(\frac{V_f Q_e}{E_m}\right) \qquad (4.37)$$

when $x_1 \leq x \leq x_2$, and

Table 4.3 Material Erosion Parameters for Electrode Joule Heating

	$(\sigma_e/\rho^{1/4})(E_m)^{1/2}$*	$E_m(\sigma_e)^{1/2}$**
Cu	3.63×10^{11}	2.83×10^{13}
W	1.46×10^{11}	3.87×10^{13}
Mo	1.55×10^{11}	2.93×10^{13}
Nb	6.20×10^{10}	1.54×10^{13}
C+	6.42×10^{8}	9.61×10^{11}

Note: The higher the number the less the erosion.
* Derived from Watson [29]. In earlier publications the factor $\rho^{1/4}$ was accidentally not included.
** Derived from Comstock and Williams [21].
\+ For carbon the energy to vaporize, E_v, is used instead of the energy to melt, E_m.

Table 4.4 Material Erosion Parameters for Arc Joule Heating

Material	E_m* ($\times 10^9$ J/m^3)	E_v** ($\times 10^{10}$ J/m^3)
Cu	5.53	5.37
W	12.5	10.3
Mo	9.61	7.75
Nb	8.07	7.70
C	---	7.47

*$E_m = \rho(cT_{mp}+L_f) = \rho cT_m$.
**$E_v = (E_m + \rho(c_{mp}(T_b-T_{mp})+L_v) = E_m + \rho c_{mp}T_v$.
Note: the higher the number the lower the erosion.

$$v_a(x) = \frac{V_f Q_e}{E_m} \tag{4.38}$$

when $x \geq x_2$. The parameters x, x_1, x_2 and y_{ss} are given in Appendix G, but in general they are functions of k_{mo}, E_m, and $q^*(t_p)^{1/2}$. Also, for vaporization,

$$v_v(x) = y_{ss}\left(\frac{x-x_1}{x_2-x_1}\right)\frac{V_f Q_e}{E_m}, \tag{4.39}$$

when $x_1 \leq x \leq x_2$, and

$$v_v(x) = \frac{V_f Q_e}{E_v}, \tag{4.40}$$

when $x \geq x_2$. The parameters x, x_1, x_2 and y_{ss} are again given in Appendix G, but in general are functions of k_{vo}, E_v and $q^*(t_p)^{1/2}$. Note: Eqn's. (4.37) - (4.40) were normalized with respect to the same variables, E_m on the y-axis, and M_{Im} on the x-axis, so the two solutions could be plotted on the same axis as in Fig. 4.1. Intuitively, however it makes more physical sense to normalize the y-axis with E_v and the x-axis with M_{Iv} where the "impulsivities" are defined by

$$M_{Im} = T_m(k\rho c)^{1/2} = V_f\left(\frac{4k_{mo}}{\pi}\right)^{1/2}, \tag{4.41}$$

and

$$M_{Iv} = V_f\left(\frac{4k_{vo}}{\pi}\right)^{1/2}. \tag{4.42}$$

Experimental Results

Scaling Laws

Figures 4.7-4.10 represent electrode erosion results for four out of over 40 electrode materials tested to date. Erosion for the other materials exhibits similar trends and will be presented in Appendix A. The results show a transition from one constant slope line to another, in which both lines indicate a linear variation of the erosion with f_1 as predicted from theory. Earlier results discussed in Chapter 3 showed that the transition is a result of the increase in molten material removal by the plasma jets. Thus, the dashed line extended from the lower branch of the erosion "S" curve should represent erosion primarily by vaporization and the upper solid line should represent erosion primarily by ablation. The ratio between these two curves, Γ_{e1}, should approach the value Γ_t. The calculated and theoretical values of this ratio are extremely close and are given in Table 4.5. The plotted symbol with a dot in the center represents the results from a proprietary switch design which effectively eliminates most of the molten material removal by keeping the jet from ablating or heating the surface. Not only did the shielded erosion considerable lower than expected (a factor of two to four which results in much higher Γ_{e2} values), but the scaling was the same with or without shielding. The lower erosion could be a result of 1) the fact that the jet actual does delever a substantial amount of heat energy to the electrode and thus, its removal reduces the erosion, 2) a

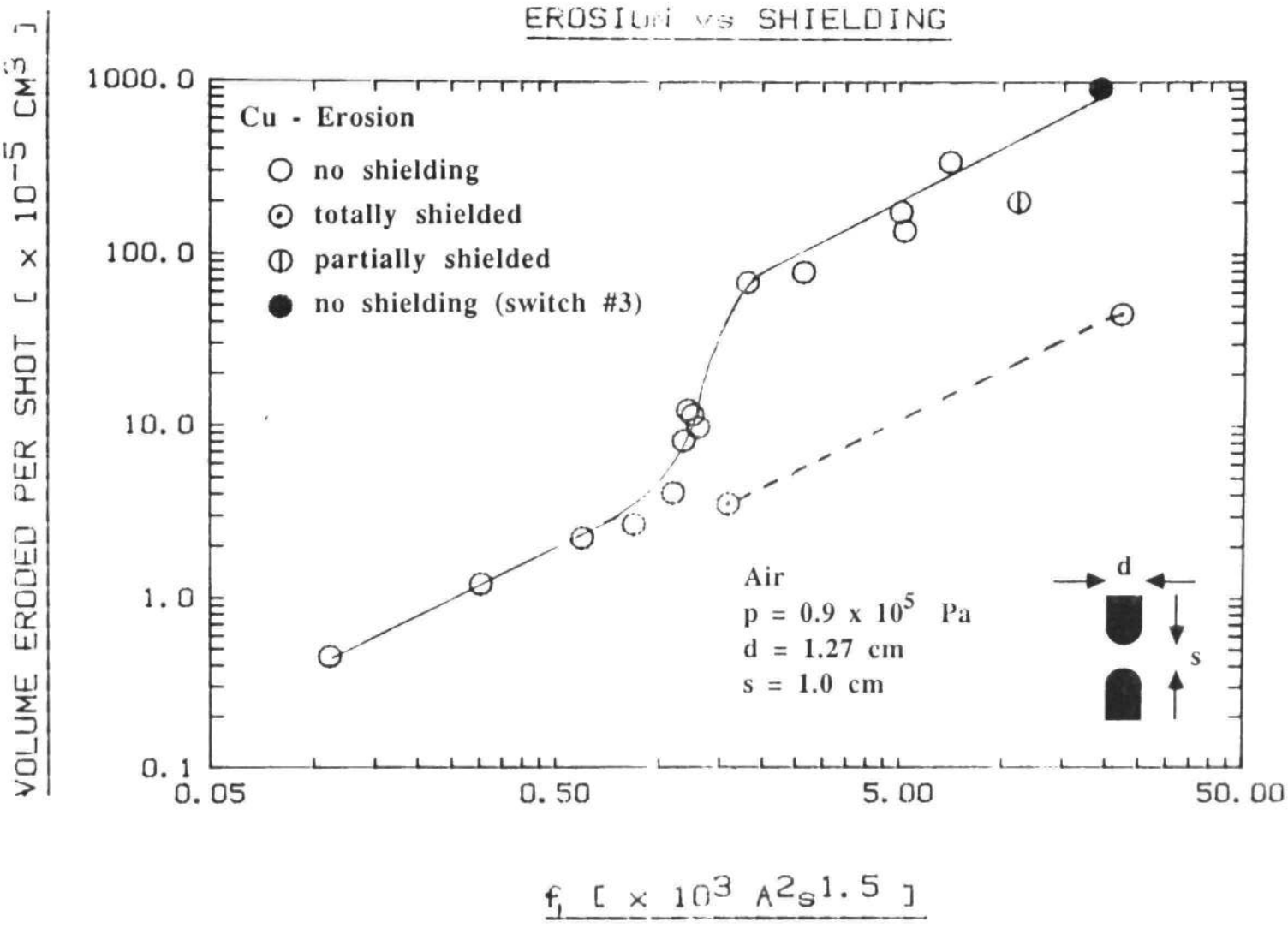

Fig. 4.7 Scaling of Electrode Erosion for Copper Electrodes. (Dashed line is the vaporization scaling with a proprietary switch, the solid line is the Mark VI result.)

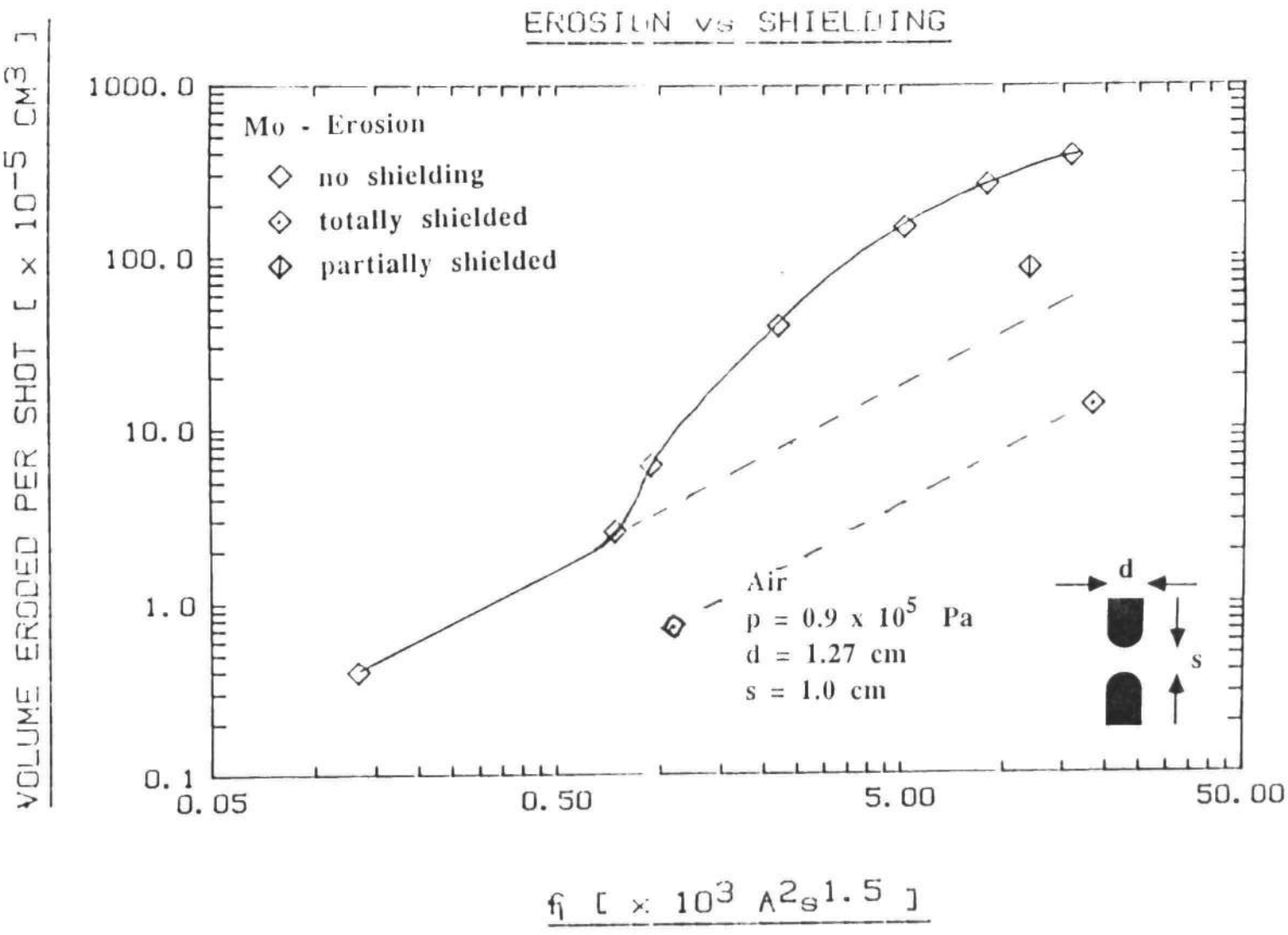

Fig. 4.8 Scaling of Electrode Erosion for Molybdenum Electrodes. (Dashed line is the vaporization scaling with a proprietary switch, the solid line is the Mark VI result.)

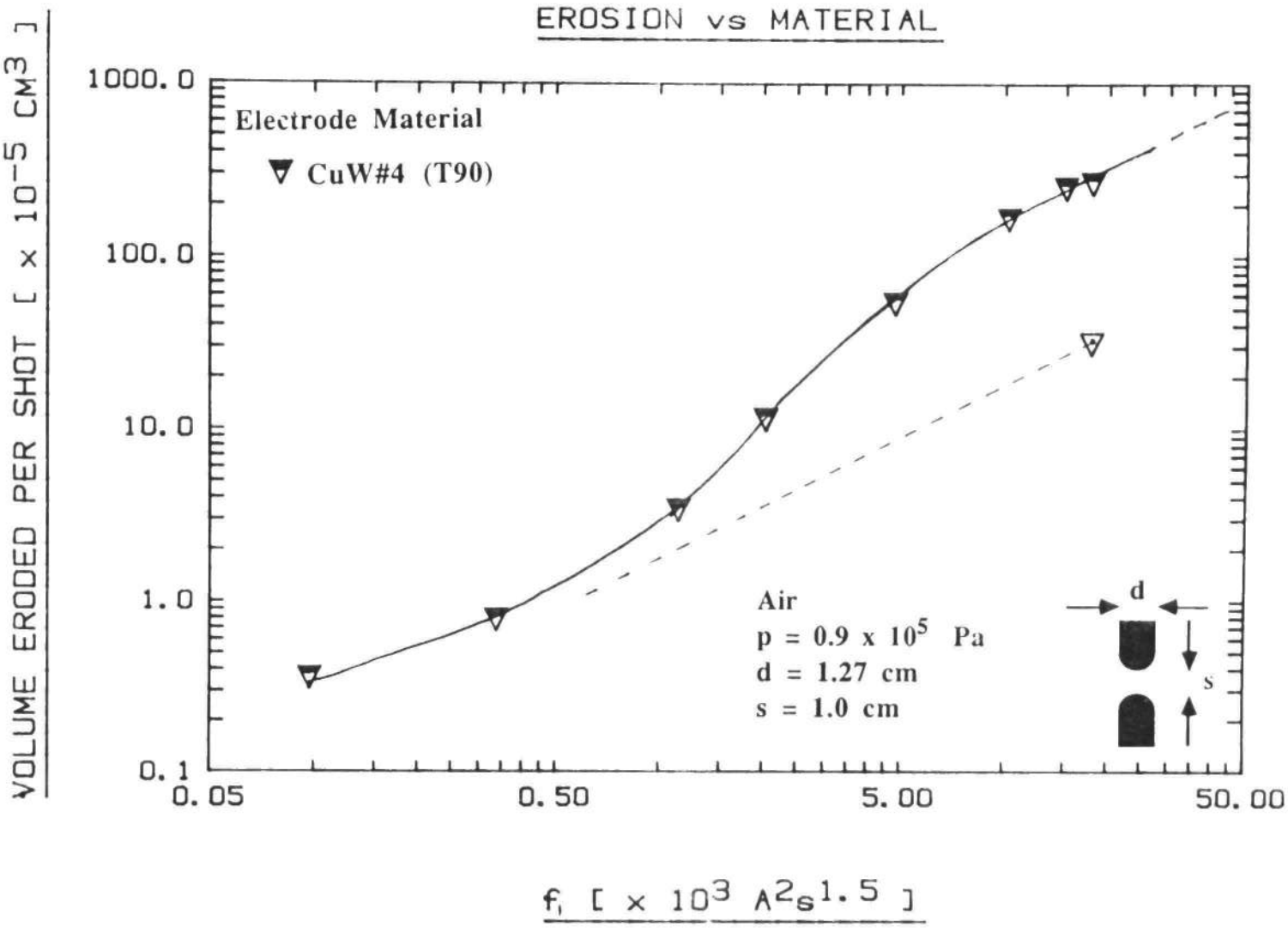

Fig. 4.9 Scaling of Electrode Erosion for Copper-Tungsten Electrodes. (Dashed line is the vaporization scaling with a proprietary switch, the solid line is the Mark VI result.)

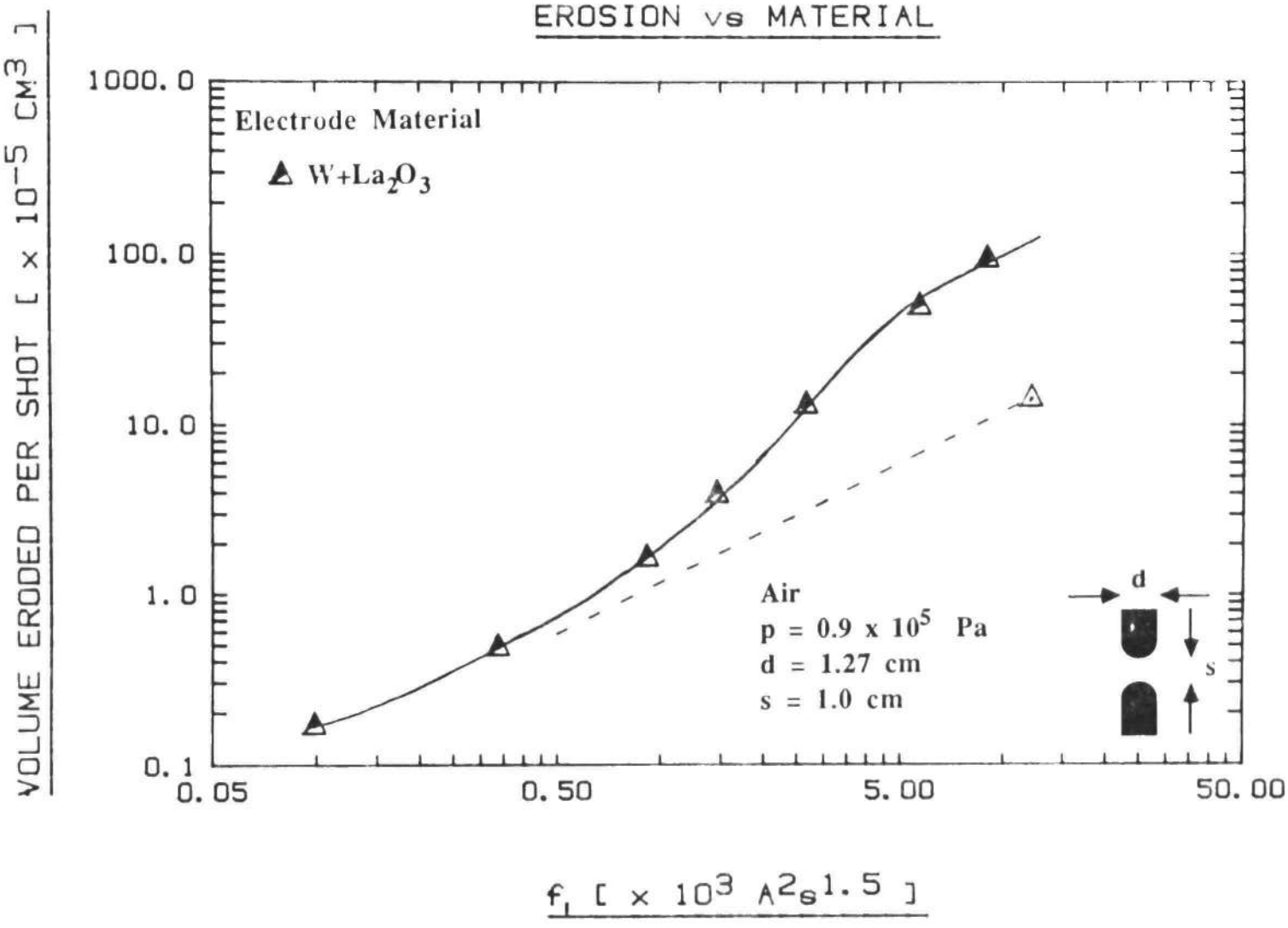

Fig. 4.10 Scaling of Electrode Erosion for $W+La_2O_3$ Electrodes. (Dashed line is the vaporization scaling with a proprietary switch, the solid line is the Mark VI result.)

Table 4.5 Experimental (Γ_{e1} and Γ_{e2}) and Theoretical (Γ_t) Values of the Ratio of the Electrode Ablation to the Electrode Vaporization

Material	Γ_t	Γ_{e1}	Γ_{e2}
Cu	10	10	22
$W+La_2O_3$	8.3	8.1	8.1
CuW*	8.3	8.3	8.3
Mo	8.3	7.0	35

* 90% W by weight

lowering of the current density and thus, the heat flux to the electrode surface, 3) the lower branch of the "S" curve does have a subtantial amount of molten material removed, or 4) the decomposition of the shield leads to a protective coating on the electrode.

Figure 4.11 illustrates the ability of the theory to predict the erosion trends of other experimentalists, namely Gruber and Suess [1]. The transition from a vaporization to an ablation dominated erosion is again clearly seen with the slope of each erosion curve being linear with increasing f_1. In addition, the value of the tungsten erosion was predicted quite accurately (the dotted line) using the ratio of v_v for tungsten compared with v_v for copper. The pulse conditions for these experiments were oscillatory like ours, however, the I_p and t_p were considerably different. This result indicates that the parameter f_1 is good for scaling over a wide range of conditions. (Note: for calculation of f_1 in both cases the width of the first half period was used).

Figure 4.12 illustrates the ability of the theory to correlate the electrode erosion results for significantly different experimental conditions. The three different experimental conditions are summarized in Table 4.6. The data for $Q_e < 25$ was performed on the Mark VI; for $25 < Q_e < 60$, on the MAX I, and for $Q_e > 150$ on a spark gap developed at Physics International Corp [56]. The data were plotted vs. Q_e instead of f_1 because the scaling at high Q_e levels should be proportional to Q_e not f_1. Although the exact scaling is hard

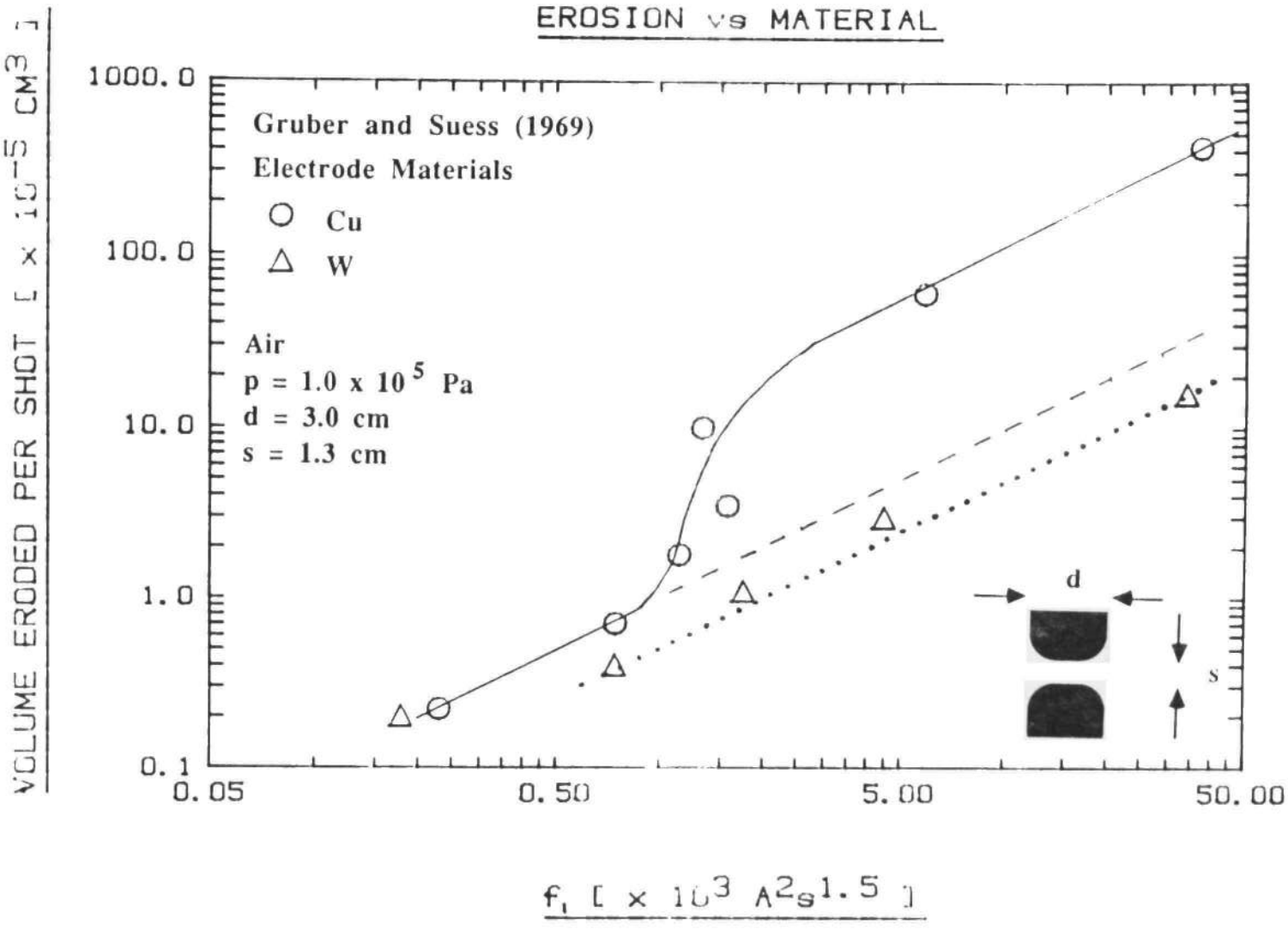

Fig. 4.11 Scaling of Electrode Erosion for the Copper and Tungsten Electrodes Tested by Gruber and Suess [1]. (Solid line is the actual measured results, dashed line is the predicted results for erosion by vaporization only, dotted line is the theoretical prediction of the tungsten erosion using our model.)

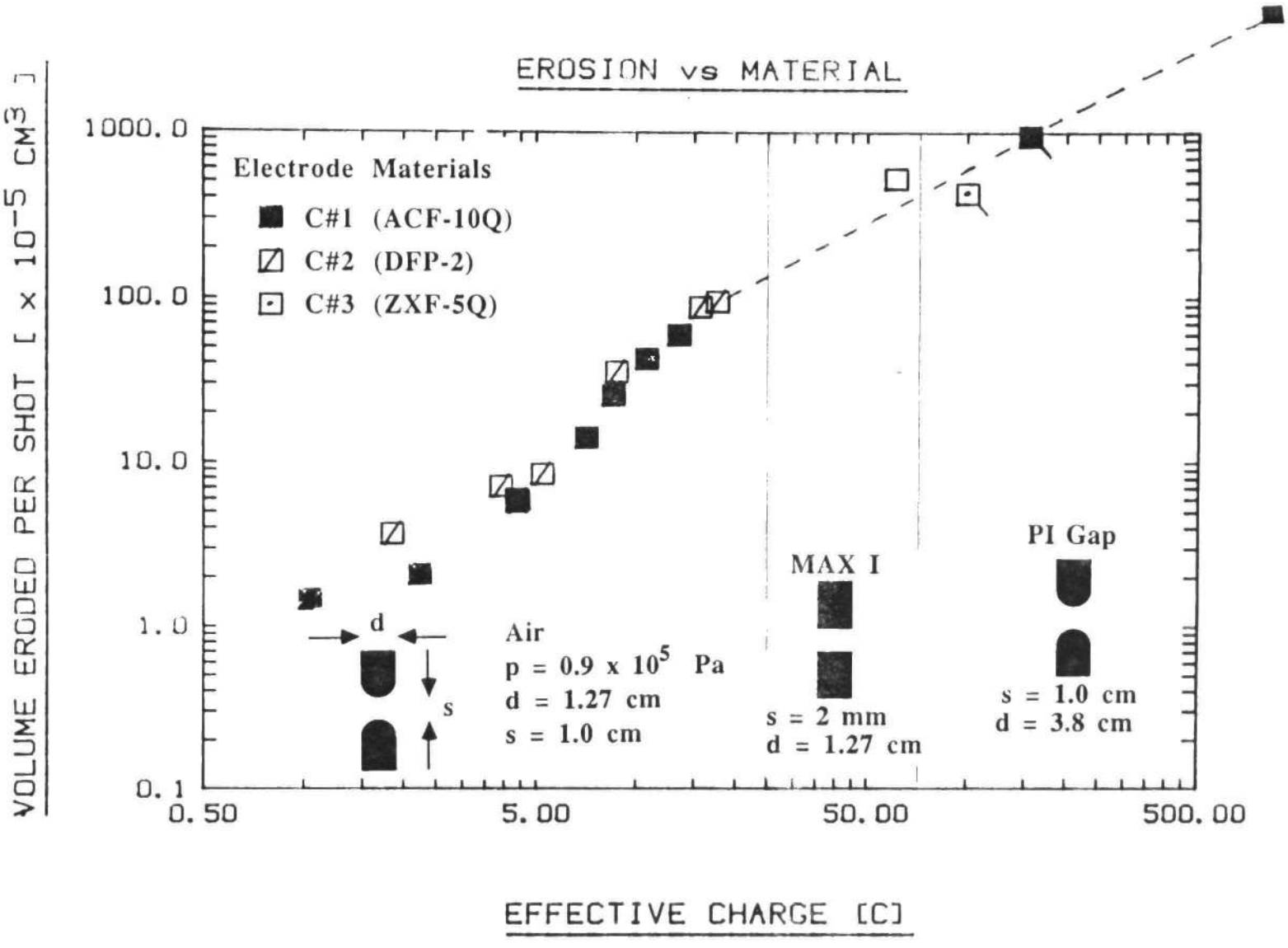

Fig. 4.12 Erosion Results for Graphite Electrodes Used on Three Different Experiments.

Table 4.6 Experimental Conditions for 3 Different Test Switches. (Mark VI, MAX I, and Physics International-PI [56])

Parameter	Mark VI	MAX I	PI
I_p (kA)	< 500	< 300	< 325
Q_e (C)	< 50	< 58	< 900
E_s (kJ)	< 48	< 17	< 250
Frequency (kHz)	< 250	8	> 3.7
Gap Spacing	1 cm	0.2 cm	0.95
Electrode Type	d*=1.27 cm (round tip)	d=1.27 cm (flat)	d=3.8 cm (round or flat)

*d is the diameter of the electrode rod.

to determine because the majority of the data are on the knee of an "S" curve, it appears that the PI data lie on a line proportional to Q_e, extended from the Mark VI data point with the the highest Q_e, as predicted.

Onset Conditions

The ability of the theory to predict the onset of enhanced erosion is somewhat limited in practice by the error involved in estimating the effective arc attachment area. The theory was also derived for a square pulse, which often is not the case. In addition, other mechanisms besides the heat flux may lead to a sudden increase in the erosion (i.e., jet impact erosion, for example). Nonetheless, the author has found that despite these sources of error the theory does predict with a fair degree of accuracy the onset of enhanced erosion. For example Table 4.7 contains the data of five different experimentalists who observed a sudden increase in the erosion. The theoretical values of k_{mo} are very close, especially for the data of Gremmel [30] and Piejak, et al., [4] who used unipolar pulses.

Erosion Magnitudes

Earlier it was shown that the thermal model could predict accurately the difference between erosion due to vaporization and melting. Now the model will be used to predict relative differences in the erosion for different materials subjected to the same current pulse. Finally we will attempt to predict

Table 4.7 Comparison of Experimental and Theoretical Values of the Onset Constant k_{mo}

Experimenter	Type of Pulse	Electrode Material	I_{po} (kA)	Q_e (C)	t_p (ms)	A_e ***	k_{mot}	k_{moe} ($x10^{13}A^2s/m^4$)
Gremmel [30]	Unipolar*	Cu	4-6	8.8-13.2	2.2	5	2.4	1.4-3.1
		Mo	6-8	13.2-17.6	2.2	5	3.3	3.1-5.0
		W	8-10	17.6-22	2.2	5	7.5	5.0-8.8
Gruber and Suess [1]	Oscillatory	Cu	60	4.4	---	10	2.4	2.6
Piejak [4]	Unipolar*	Cu	8** (4-4.8)	20-24	5	6	2.4	2.3-3.2
Donaldson [10]	Oscillatory	Cu	120	3.3	---	8.4	2.4	5.6
		Mo	112	3.1	---	8.4	3.3	4.9
Belkin and Kiselev [3]	Oscillatory	Cu	25	10	---	31	2.4	2.65
		Mo	276	12	---	31	3.3	3.4
		Ti	464	34	---	31	0.2	?

k_{mot} is the theoretical value of k_{mo}, k_{moe} is the experimental value of k_{mo}, I_{po} is the onset peak current, and $k_{mo} = J^2 t_p = \frac{I_{po}^2 t_p}{A_e^2}$ or $\frac{Q_e I_{po}}{A_e^2}$.

*The waveform was very close to a square wave.
**The average current was about 0.5-0.6 I_p for the pulse time used in the calculations. (This average was used in the calculation of k_{moe}.)
***Units on A_e are ($\times 10^{-5} m^2$).

quantitatively the amount of erosion. Figure 4.13 shows the electrode erosion results obtained by the author for four materials: Cu, Mo, W+La_2O_3, and C. Assuming that graphite sublimes and the rest of the materials melt, the relative differences in the erosion are calculated and shown in Table 4.8 alongside the experimental results measured by the author. Next, in Table 4.9, a comparison is made of the experimental results and the values predicted in Chapter 2 using various theories.

As expected the results all lie between the limits represented by vaporization and molten material being removed at the end of the pulse. It appears that one is able to use this method to get quantitative erosion values for large Q_e. Prediction of composite erosion will be discussed in Appendix A.

Methods of Reducing Erosion

The thermal model indicates there are three main ways to reduce the amount of material which is likely to be eroded:

1) choosing materials with high k_{mo}, k_{vo}, E_m and E_v,
2) reducing or uniformly distributing the heat flux, and
3) reducing the residence time of the heat flux.

Experimental evidence exists which supports all three of these methods. For example, Affinito [32], Marchesi and Maschio [33] and the author [31], have all found graphite, the material with the highest material rankings, to yield the

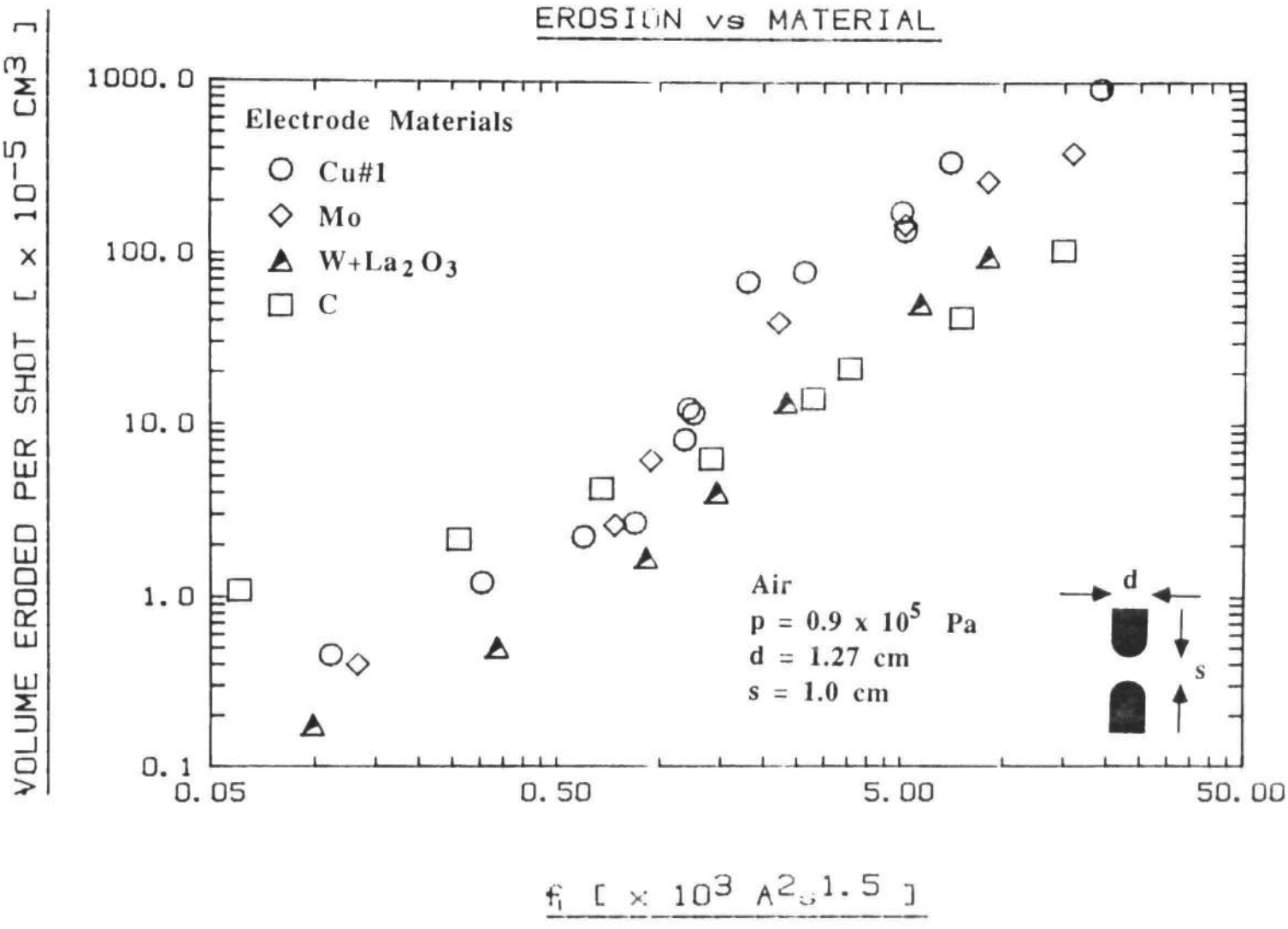

Fig. 4.13 Erosion for 1.27 cm Diameter Electrodes Made of Cu, Mo, W+La_2O_3 and C.

Table 4.8. Relative Magnitudes of Erosion vs. Material for High Current Conditions

Material	Theoretical[+]	Experimental
Cu	1 (14)	1 (7.7)
Mo	0.57 (8.1)	0.66 (5.1)
W	0.44 (6.3)	0.43 (3.3)[*]
C	0.07 (1)	0.13 (1)

[*]Results for $W+La_2O_3$.

[+]Erosion magnitudes normalized for Cu and (C).

Table 4.9 Comparison of Various Models' Ability to Predict Quantitatively the Erosion

Material	Q_e (C)	Actual Erosion[*]	Theory #1	Theory #2	Theory #3
Cu	18.4	8-10	11	33	3.3
Mo	16.1	3.9	5.6	16.8	2.07
W	17.1	2.7	4.6	13.8	1.64
C	15.6	1.1	---	---	2.1

Theory #1 by Belkin $v_e \propto \frac{V_f Q_e}{3E_m}$ (lower limit for melt removal, assuming the material is removed at end of pulse).

Theory #2 by Belkin $v_e \propto \frac{V_f Q_e}{E_m}$ (upper limit for melt removal, assuming liquid ablation).

Theory #3 by Belkin $v_e \propto \frac{V_f Q_e}{E_v}$ (lowest limit, assuming vaporization).

[*](x 10^{-3} cm^3/shot)

lowest erosion in the high current regime for all the materials tested. (Note: one must compare graphite's k_{vo} and E_v to other materials' k_{mo} and E_m since graphite sublimes while the other materials may have some ablative loss.) Gruber and Suess [1], not having tested graphite, obtained the lowest erosion for tungsten, the material with the second highest ranking. The author has also found tungsten compounds to give low erosion (see the results in Appendix A). It should be noted that several experimenters found graphite to have the highest erosion rates [18,35]. However, it will be shown in Appendix A that this can be a result of its low thermal conductivity which plays an increasingly important role at lower currents. (Earlier the author thought the high erosion was due to enhanced joule heating in the electrode resulting from graphite's high resistivity but this is not the case.)

Several methods have also been successful at altering the heat flux, including:

1) making use of larger electrodes [36]
2) utilizing electrode additives which give a lower V_{arc}, such as Sb [37],
3) using a saturable inductor (albeit at much lower currents) in the discharge circuit which reduces the commutation energy in the arc by limiting the current rise during the voltage collapse [38,39],
4) operating at a reduced pressure [40], (Belkin and Kiselev found a minimum in the erosion around 10^2 Pa),

5) using Ar or He as the switch gas [41,42],

6) applying an external magnetic field which can shield the heat flux from the surface [43,44],

7) adding materials, such as LaB_6, to the electrodes which decrease the time for the arc voltage collapse and also serve to distribute the current over the electrode surface [45] and

8) alter the gap geometry so that a shield can be added which keeps the plasma jets from reaching and ablating the opposite electrode.

This last technique was explored in detail by the author and was responsible for the order of magnitude reduction in the erosion indicated in Figs. 4.7-4.11. The exact design and material utilized for the jet shielding are proprietary, but Table 4.10 summarizes the improvement. Very little optimization of the design has been tried, but already over an order of magnitude reduction has been achieved for certain conditions.

In applications where the pulse duration is long enough to enable significant arc motion during the discharge, the effect of moving the arc has been shown to reduce electrode erosion significantly [46,47]. Several researchers have predicted an erosion dependence proportional to $(v_a)^{-1/2}$ [11,48,49], where v_a is the arc velocity. The author's own treatment of the theory is given in Appendix H. At present several different state of the art switches utilize arc motion to reduce the erosion [50,51]. For extremely high coulomb

Table 4.10 Reduction in Electrode Erosion Utilizing a Novel Change in the Spark Geometry which Effectively Shields the Electrodes from Plasma Jets

Run #	Material	Charge (mC)	Standard Design Erosion (cm^3/shot)	Novel Design Erosion (cm^3/shot)
1156	Cu	224	$2x10^{-4}$	$3.54x10^{-5}$
1153	Cu	1130	$1x10^{-2}$	$4.47x10^{-4}$
*1152	Cu	938	$4x10^{-3}$	$2.01x10^{-3}$
*1151	Mo	977	$3.5x10^{-3}$	$8.61x10^{-4}$
1155	Mo	1200	$4x10^{-3}$	$1.37x10^{-4}$
1159	Mo	244	$1.8x10^{-4}$	$3.91x10^{-6}$
1161	Mo	1170	$3.9x10^{-3}$	$9.78x10^{-6}$
1154	Cu-Nb#4	1420	$2x10^{-3}$	$2.92x10^{-4}$
*1150	CuW+Ir	1130	$1.4x10^{-3}$	$5.54x10^{-4}$
1148-1	C	1190	$1.0x10^{-3}$	$8.50x10^{-4}$
1146	CuW#4	1200	$3.0x10^{-3}$	$3.24x10^{-4}$
1147	$W+La_2O_3$	977	$1.3x10^{-3}$	$1.61x10^{-4}$
*1149	Cu-Cr#1	932	$1.0x10^{-3}$	$6.30x10^{-4}$

*Used a different method of shielding which was only partially successful.

switching applications, producing arc motion may well be one of the best approaches to increasing electrode life.

Another approach to reducing erosion is to provide a sacrificial material which absorbs some the arc energy. Among the methods proposed:

1) the addition of additives which absorb energy through endothermic reactions [52],
2) flowing liquid through a capillary electrode [53], and
3) the formation of a regenerative film on the electrode surface [54].

The first technique has been suggested for use in electromagnetic launcher studies [52]. The second was successful at lower currents [55]. The last technique was achieved accidentally by the author, and it may be quite promising. The solution to the thermal problem presented by 3) was treated in Chapter 2.

Conclusions

With the utilization of some simple equations the erosion scaling laws for several pulse shapes and different materials can be predicted with considerable accuracy. The erosion was found to scale with f_1, defined as $Q_e I_p (t_p)^{1/2}$, for modest values of Q_e (1-25 C), and scale as Q_e for larger values of charge or for very small gap spacings (Gruber and Suess [1]). Onset conditions for enhanced erosion were predicted from theory for a wide variety of conditions. The relative magnitudes of the

erosion for different materials at $Q_e \sim 25$ C was found to be closely predicted by the energy required to melt or vaporize the material. In addition, modifying the switch geometry to shield the electrodes from each others plasma jets, led to a reduction in the erosion at high currents by over one order of magnitude. Thus a simple thermal model has proved to be adequate for predicting numerous erosion parameters of engineering importance.

References

[1] J.E. Gruber and R. Suess, "Investigation of the Erosion Phenomenon in High Current, High Pressure Gas Discharges," *Institute fur Plasma Physik, Garching bei Munchen*, FRG, IPP/4/22, 1969. (EE-0877)*

[2] G.M. Goncharenko and Ye. N. Prokhorov, "Erosion of Electrodes Due to Switching of Capacitor-Bank Discharge Circuits," *Trans. of Trudy, Moskovskogo Energeticheskogo Institute, Tekhnika Vysokikh Naprazheniy*, No. 114, Moscow, pp. 86-88, 1972. (EE-0875)

[3] G.S. Belkin and V. Ya. Kiselev, "Influence of Electrode Material on Erosion at High Currents," *Sov. Phys. Tech. Phys.*, vol 12, pp. 702-703, 1966. (EE-0864)

[4] R. Piejak, H. Wilhelmsen and S.R. Robertson, "Time Resolved Studies of Anode Erosion by High-Current-Density Arcs of Millisecond Duration," *GTE Research Development Report # TR-82-567.2*, August 1982. (EE-0892)

[5] Y. Suzuki, Y. Kawakita, M. Kume and M. Kawai, "A 150-kV, 100-kA Spark Gap Switch for Marx Generators," *Proceedings of the 3rd IEEE Int. Pulsed Power Conf.*, Albuquerque, NM, pp. 444-448, June 1981. (EE-0884)

[6] C. Turner, "Discontinuous Contact Erosion," *Proceedings of the 3rd Int. Research Symp. on Electric Contact Phenomena*, Orono, ME, pp. 309-311, June 1966. (EE-0890)

[7] W.A. Merl and E. Durrwachter, "Concerning Material Losss in Silver Electrodes Caused by Transient Arcing at High Currents in Different Atmospheres," *Proceedings of the 3rd Int. Research Symp. on Electric Contact Phenomena*, Orono, ME, pp. 259-264, June 1966. (EE-0817)

[8] J. Urbanek, "Mass Loss of Heavy Current Contacts," *Proceedings of the 3rd Int. Research. Symp. on Electric Contact Phenomena*, Orono, ME, pp. 301-308, June 1966. (EE-1096)

[9] M.G. Fey and J. McDonald, "Electrode Erosion in Electric Arc Heaters," *AIChE Symposium Series*, vol. 75(186), pp. 31-37, 1979. (EE-0125)

* EE number refers to the author's annotated bibliography number. It should be included in all correspondence.

[10] A.L. Donaldson and M. Kristiansen, "Utilization of a Thermal Model to Predict Electrode Erosion Parameters of Engineering Importance," *Proceedings of the 19th Power Modulator Symposium*, San Diego, CA, June 24-27, 1990. (EE-1135)

[11] G.S. Belkin, "Dependence of Electrode Erosion on Heat Flux and Duration of Current Flow," *Sov. Phys. Tech. Phys.*, vol. 15(7), pp. 1167-1170, 1971. (EE-0435)

[12] W. R. Dixon, R.C. McCallen, S-W. Kang and R.S. Hawke, "Radiation Induced Ablation Rate for Various Railgun Materials," *Lawrence Livermore National Laboratory Report #UCD-20902*, 1986. (EE-0950)

[13] R. Holmes, "Electrode Phenomena," Chap. 11 in *Electrical Breakdown of Gases*, J.M. Meek and J.D. Craggs, ed., John Wiley and Sons, New York, NY, pp. 839, 1978. (EE-0081)

[14] R. Basharov, E.N. Gavrilovskaya, O.A. Malkin and E.S. Trekhov, "Erosion of Cathode Material in a Pulsed Discharge Between Parallel Electrodes," *Sov. Phys. Tech. Phys.*, vol. 12(10), pp. 1383-1390, 1966. (EE-0779)

[15] J.C. Sherman, R. Webster, J.E. Jenkins and R. Holmes, "The Spontaneous Formation of Cathode Spots in High-Current Triggered Vacuum Switches and an Estimate of the Cathode Spot Current Density on Copper," *Proceedings of the 4th Int. Conf. on Gas Discharges*, Swansea, U.K., pp. 94-97, 1976. (EE-0032)

[16] V.E. Il'in and S.V. Lebedev, "Destruction of Electrodes by Electric Discharges of High Current Density," *Sov. Phys. Tech. Phys.*, vol. 7(8), pp. 717-721, 1963. (EE-0339)

[17] A.E. Guile, "Joule Heating in Emitting Sites on Various Nonrefractory Arc Cathodes," *Proceedings of the IEE*, vol. 127(7), pp. 452-457, 1980. (EE-0321)

[18] A.L. Donaldson, M.O. Hagler, M. Kristiansen, G. Jackson and L. Hatfield, "Electrode Erosion Phenomena in a High-Energy Pulsed Discharge," *IEEE Trans. on Plasma Science*, vol. PS-12(1), pp. 28-38, 1984. (EE-0782)

[19] J.A. Nemes and P.W. Randles, "Energy Deposition Phenomena in Partially Transparent Solids," *J. of Thermophysics and Heat Transfer*, vol. 3(2), pp. 160-166, 1989. (EE-0889)

[20] J.A. Rich, "Resistance Heating in the Arc Cathode Spot Zone," *J. of Appl. Phys.*, vol. 32(6), pp. 1023-1031, 1961. (EE-0337)

[21] W.D. Comstock and E.M. Williams, "Current Distribution in the Cylindrical Source Plane-Electrode Configuration, *Trans. of AIEE Comm. and Elec.*, vol. 43(6), pp. 252-256, 1959. (EE-0338)

[22] A.S. Zingermann, "The Role of Joule-Lenz Heat in the Electrical Erosion of Metals," translation of *Sov. Phys. Tech. Phys.*, vol. 25(11), pp. 1931-1943, 1955, FSTC-HT-703-86. (EE-0418)

[23] R.E. Kidder, "Nonlinear Diffusion of Strong Magnetic Fields into a Conducting Half-Space," *Lawrence Livermore National Laboratory Document #UCRL-5467*, Livermore, CA, 1959. (EE-0792-1)

[24] R. Dethlefsen, "Investigation of Electrode Erosion in High Current Arcs," *Aerospace Research Laboratories Report # 68-0112*, Wright-Patterson AFB, Dayton, OH, June 1968. (EE-0416)

[25] O.I. Avsyesoch, "The Heat Processes on Electrodes During Pulse Discharges," In the book *Electrical Contacts*, M. Energiya, pp. 65-70, 1967. (EE-0367-2)

[26] A.G. Goloveiko, "Thermal Processes at the Anode During an Intense Pulse Discharge," *Sov. J. of Eng. Phys.*, vol. 15(6), pp. 1168-1174, 1968. (EE-0344)

[27] M.P. Zekster, "Effect of Joule Heat Liberation in a Metal Cathode on the Temperature of the Cathode Arc Spot," *High Temperature (USSR)*, vol. 15(1), pp. 190-193, 1977. (EE-0355)

[28] S.D. Raezer, "Heat Transfer in Rotated Arcs with Water-Cooled Electrodes," *John Hopkins University Applied Physics Laboratory Report # CF-2957*, Dec. 5, 1961. (EE-0213)

[29] A. Watson, *Contribution to Annual Technical Report, SDI Power Conditioning*, DNA Contract # 001-85-C-0184, Texas Tech University, 1986. (EE-1137)

[30] M.D. Bryant and Y.G. Yune, "The Complete Temperature Field in Carbon Graphite Electrical Brushes Due to Frictional and Electrical Power Dissipation," *Proceedings of the 1987 Int. Current Collector Conf.*, Balcones Research Center, Austin, TX, Nov. 1987. (EE-0946)

[31] H. Gremmel, "Das Abbrandverhalten der Elektroden von Starkstromlichtbögen bei kurzer Lichtbogendauer," Ph.D. Dissertation, Maschinenwesen der Technischen Hochschule Carolo-Wilhelmina zu Braunschweig, 1963. (EE-0905)

[32] D. Affinito, E. Bar-Avraham and A. Fischer, "Design and Structures of an Extended Life High Current Sparkgap," *IEEE Trans. on Plasma Science*, vol. PS-7, pp. 162-163, 1979. (EE-0785)

[33] G. Marchesi and A. Maschio, "Influence of Electrode Materials on Arc Voltage Waveforms in Pressurized Field Distortion Spark Gaps," *Proceedings of the 5th Int. Conf. on Gas Discharges*, pp. 145-148, Liverpool, U.K., September 1978. (EE-0860)

[34] A.L. Donaldson, G. Engel and M. Kristiansen, "State-of-the-Art Insulator and Electrode Materials for High Current Switching Applications," *IEEE Trans. on Mag.*, vol. 25, pp. 138-141, 1989. (EE-1139)

[35] K.J. Bickford, K.W. Hanks and W.L. Willis, "Spark Erosion Characteristics of Graphite and CO Gas," *Proceedings of the 15th Power Modulator Symp.*, Baltimore, MD, pp. 89-92, June 1982. (EE-0783)

[36] J. Harrison, private communication, Maxwell Laboratories, 9244 Balboa Ave., San Diego, CA, 92123, 1986.

[37] G.S. Belkin and M.E. Danilov, "Measurement of the Energy Introduced into the Electrodes During the Burning of an Arc in Vacuum," *High Temperature (USSR)*, vol. 11(3), pp. 533-536, 1973. (EE-0242)

[38] S. Levy, "Spark Gap Erosion Studies," *U.S. Army Electronics Research and Development Labs Report # 2454*, Fort Monmouth, NJ, April 1964. (EE-0767)

[39] R.A. Dougal, G.D. Volakakis and M.D. Abdalla, "Magnetically Driven Vacuum Switching," *Proceedings of the 6th Pulsed Power Conference*, Arlington, VA, pp. 21-24, 1987. (EE-0756)

[40] G.S. Belkin and V. Ya. Kiselev, "Effect of the Medium on the Electrical Erosion of Electrodes at High Current," *Sov. Phys. Tech. Phys.*, vol. 23(1), pp. 24-27, 1978. (EE-0402)

[41] A.L. Donaldson, D. Garcia and M. Kristiansen, "Influence of Gas Type and Pressure on Electrode Erosion in High Energy, High Current Switching," presentation given at *1987 IEEE Int. Conf. on Plasma Science*, June 1-3, Arlington, VA, 1987. (EE-0403)

[42] G.S. Belkin, "Vaporization of Metal Electrodes by Pulsed Currents," *Sov. Phys. Tech. Phys.*, vol. 13(9), pp. 1256-1261, 1969. (EE-0429)

[43] A.E. Konovalev, "Effect of a Transverce Magnetic Field on the Heat Flux to the Electrodes of a Sharply-Defined Discharge," *High Temperature (USSR)*, vol. 7(4), pp. 563-567, 1969. (EE-0947)

[44] J.G. Gilligan and D. Hahn, "The Magnetic Vapor Shield (MVS) Mechanism for Protection of High-Heat Flux Components in High-Field Tokamaks," *J. of Nuclear Materials*, vol. 145, pp. 391-395, 1987. (EE-0770)

[45] S.V. Antonov, G.G. Gnesin, G.V. Levchenko, R.B. Luban and V.I.Rakhovskii, "Arc Erosion of Cathodes Containing Inclusions of Emission-Active Phase", *Sov. Phys. Tech. Phys.*, vol. 27(2), pp. 173-177, 1982. (EE-0595)

[46] Y.S. Pavlov and S.A. Smirnov, "Electrodes for High-Current Commutators", *Pribory I Tecknika Eksperimenta*, vol. ?(120), pp. 118-120, 1971. Consultant Bureau, a division of Plenum Publishing Corp., 227 West 17th St., New York, NY, 10011. (EE-0760)

[47] F. Labrenz, "Erosion of Switching Electrodes by Rotating Arcs in SF_6," *Unknown Conference*, pp. 326-330, 1981. (EE-0880)

[48] V.I. Krylovich and T.N. Abramenko, "Heat Transfer from a Rapidly Moving Arc Spot," *High Temp. (USSR)*, vol. 4 (1), pp. 71-77, 1966. (EE-0187)

[49] F.M. Lehr, B.D. Smith, A.L. Donaldson and M. Kristiansen, "The Influence of Arc Motion on Electrode Erosion in High Current, High Energy Switches," *Proceedings of the 6th IEEE Pulsed Power Conference*, Arlington, VA, pp. 529-533, June 29-July 1, 1987. (EE-1140)

[50] S.H. Choi and J.H. Lee, "An Inverse-Pinch Switch for High Coulomb Transfer," *Proceedings of the 10th Int. Symposium on Discharges and Electrical Insulation in Vacuum*, Columbia, SC, pp. 273-278, 1982. (EE-0763)

[51] J. Harrison, private communication, Maxwell Laboratories, 9244 Balboa Ave., San Diego, CA, 92123, 1990.

[52] M.R. Palmer and S. Taylor, "Cooling of Solid and Plasma Armatures by Chemical Bond Breaking," *Proceedings of the 1st EM Gun Armature Workshop*, Air Force Armament Laboratory, Eglin AFB, FL, pp. 254-260, 1986. (EE-0761)

[53] H.K. Kocher and D. Stockel, "Material Transfer of Composite Contact Materials," *IEEE Trans. of Components, Hybrids and Manufacturing Tech.*, vol. CHMT-2(1), pp. 15-19, 1979. (EE-0469)

[54] V.P. Vilister and M.L. Sedova, "The Process of Formation of Protective Films at an Electrode Instrument During Electro-Spark Operations," translation of *Fizika i Khimiya Obrabotki Materialov*, vol. ?(2), pp. 19-25, 1967, FSTC-HT-1184-86. (EE-1116)

[55] F.S. Goucher, "Spark Gap Switches for Radar," *Bell System Tech. J.*, vol.25, pp. 563-569, 1946.

[56] T. Naff, private communication, Physics International Company, 2700 Merced St., P.O. Box 1538, San Leandro, CA, 94577, 1989.

APPENDIX A

ELECTRODE EROSION RESULTS FOR NUMEROUS ELECTRODE MATERIALS

This Appendix contains the data and plotted erosion results versus stored charged, Q_s, and the theoretically derived factor, $Q_e I_p (t_p)^{1/2}$ (defined as f_1), for more than 40 electrode materials tested in the Mark VI and MAX I switches. A brief description of the materials is given along with tables listing their composition and the various suppliers. In addition, a plot comparing the best material from the erosion results of over 25 experimentalists is given to identify the current state of the art.

Material Selection

Early on, the testing of different electrode materials was seen as an integral part of the overall work on electrode erosion for the following reasons:

1) the tests would facilitate the engineering goal of identifying and developing materials with increased lifetime,
2) the tests would allow the author to determine in one standardized study the relative performance of a large number of materials with vastly different thermal, electrical and mechanical properties and thus,

3) the material tests would supplement the work of others and thereby provide a means of comparing and developing various erosion theories (models and mechanisms).

Because of these reasons materials were selected for inclusion in the study because:

1) they were elements whose thermophysical properties were well known (Cu, Mo, C, W),
2) they had been tested by others under a variety of conditions (Cu, Mo, C, W, CuW, CuC, xxx +LaB_6),
3) they were recommended by various manufacturers, suppliers or other experimenters, and
4) they appeared to have properties which the models predicted would yield reduced erosion.

To date over 40 materials have been tested based on these considerations. A listing of these materials along with their generic name, composition, density and marking symbol is given in Table A.1.

Once a material was selected a supplier had to be located. This might sound trivial, but several of the materials selected had never been manufactured before or were not standard commercial items, while others required locating sources outside the country. A listing of the suppliers and manufacturers is given in Table A.2.

Midway through the testing the materials were divided into seven groups or classifications:

1) Cu, Cu Alloys and Mo,

Table A.1 Materials Used in Erosion Studies

Material*	Composition (by wt.)	Density ($x10^3 kg/m^3$)	Label
Al (UN1396)	> 90% Al	2.70	
C#1 (ACF-10Q)	100% C	1.88	
C#2 (DFP-2)	100% C	1.88	
Cu#1,2,3 (C10200)	> 99% Oxygen-free Cu	8.94	
Cu#4 (C15000)	99.8% Cu, 0.15% Zr	8.94	
Cu#5 (C15715)	99.8% Cu, 0.15% Al_2O_3	8.90	
Cu#6 (C15760)	99.4% Cu, 0.60% Al_2O_3	8.90	
Cu#7 (C18100)	99% Cu, 0.9% Cr, 0.1% Zr	8.94	
CuC#1 (DFP-1C)	85% Cu, 15% C	2.97	
CuC#2 (GRAPHOR3)	97% Cu, 3% C	8.90	
Cu+LaB_6	97% Cu, 3% LaB_6	8.68	
CuMo (Cu50Mo)	50% Cu, 50% Mo	9.54	
Cu-Cr	85% Cu, 15% Cr	8.57	
Cu-Nb#1 (E-15)	85% Cu, 15% Nb	8.88	
Cu-Nb#2	85% Cu, 18% Nb	8.75	
Cu-Nb#3	85% Cu, 18% Nb	8.75	
Cu-Nb#4	85% Cu, 15% Nb	8.90	
Cu-Nb#1+LaB_6	83% Cu, 15% Nb, 3% LaB_6	8.28	
Cu-Ta#1	85% Cu, 15% Ta	9.50	
Cu-Ta#2	85% Cu, 15% Ta	10.4	
CuW#1 (K-33)	68% W, 32% Cu	14.0	
CuW#2 (3W3)	67% W, 33% Cu	13.9	
CuW#3 (30W3)	80% W, 20% Cu	15.6	
CuW#4 (T-90)	90% W, 10% Cu	17.3	
CuW+Ir	66% W, 31% Cu, 3% Ir	14.1	
CuW+LaB_6	66% W, 31% Cu, 3% LaB_6	12.4	
CuW+Re	66% W, 31% Cu, 3% Re	14.1	
CuW+Sb	66% W, 31% Cu, 3% Sb	13.2	
Mo	100% Mo	10.2	
Mo+LaB_6	97% Mo, 3% LaB_6	9.84	
SS#1 (304)	68% Fe, 10% Cr, 10% Ni	8.00	
SS#2 (316L)	65% Fe, 17% Cr, 12% Ni	8.00	
SS#3 (440-C)	80% Fe, 17% Cr, 1% Ni	7.60	
SS#4 (450)	75% Fe, 15% Cr, 6% Ni	7.80	
SS#5 (20 Cb-3)	42% Fe, 33% Cr, 19% Ni	8.10	
TiB_2#1		4.50	
W#1	90% W, 10% Ni-Fe-Co	16.2	
W#2	90% W, 10% Ni-Fe-Co	17.1	
W#3 (CMW1000)	90% W, 6% Ni, 4% Cu	17.0	
W+ThO_2#1,2,3	98% W, 2% ThO_2	18.9	
W+La_2O_3	98% W, 2% La_2O_3	18.6	
W+LaB_6	98% W, 2% LaB_6	16.7	

Table A.1, continued

Material*	Composition (by wt.)	Density ($x10^3 kg/m^3$)	Label
$W+Y_2O_3$	98% W, 2% Y_2O_3	17.9	
W+? (WS-2)	Proprietary	18.3	
$W+BaO_2$	98% W, 2% BaO_2	11.9	

*The manufacturer's designation, when available, is given in parentheses.

Table A.2 Suppliers of Electrode Materials Tested

Source	Contacts	Materials Supplied
A.D. Mackay Inc. P.O. Box 1612 104 Old Kings Hwy. N. Darien, CT 06820	Tom Skerrett 203/655-7401	Al
Air Force Wright Aeronautical Labs. Wright-Patterson AFB OH 45433-6563	Chuck Oberly 513/255-2923	Cu-Nb#2+Nb Clad
Carpenter Technology Steel Division Reading, PA 19603	Bob Draznick 215/371-2000	SS#1 SS#4 SS#2 SS#5 SS#3
CMW, Inc. 570 Alaska Ave. Torrance, CA 90503	Lloyd G. Barnes 213/775-3264	Mo W#3 Cu#4 Cu#7
Coppermetal Products[1] 801 Pittsburgh Dr. Delaware, OH 43015	Jorma Sermala I.I. Koppinen 614/363-1981	Cu#1 CuZr CuZrCr
DoDuCo Postfach 480 D-7530 Pforzheim, FRG	Dr. E. Durrwachter Telex: 7 83741-0	CuC#2
Dornier-System GmbH Postfach 1360 7990 Freidrichshafen 1, FRG	Dr. Schmidberger Dr. Schäfer Telex: 734209-0	W#1 W#2
G. Rau GmbH and Co. Postfach 1440 Kaiser-Friedrich-Str. 7 D-7530 Pforzheim, FRG	Dr. Tautzenberger Telex: 783835	Samples of Nb, W fibers in copper
Gallagher P.O. Box 2463 2230 E. Murphy St. Odessa, TX 79763	Von Trotter 915/337-5336	Cu#2

[1]A subsidiary of Outokumpu Oy of Finland.

Table A.2, continued

Source	Contacts	Materials Supplied
Iowa State University Dept. of Mech. Eng. 2025 Black Eng. Bldg. Ames, IA 50011-2160	S. Bahadur 515/294-7658	Cu-Cr, Cu-Nb#4, Cu-Ta#2
Maxwell Laboratories[2] 9244 Balboa Ave. San Diego, CA 92123	Dr. R. Dethlefsen 619/576-7880	CuC#2 TiB_2#1
Metallwerk Plansee GmbH Siebenburgerstrasse 23 D-8923 Lechbruck FRG	Mr. Langenwalder Dr. W. Glatzle Telex: 59747 plan d	Cu-Nb#1 CuMo Cu-LaB_6 Mo+LaB_6 Cu+LaB_6 CuW#1 W+ThO_2#3 CuW+Re W+LaB_6 CuW+Sb W+BaO_2 CuW+Ir W+Y_2O_3 W+La_2O_3 CuW+LaB_6 Cu-Nb#1+LaB_6
Philips Elmet Corp. 1560 Lisbon Road Lewiston, ME 04240	Audrey Hobbs 1-800-343-8008	W+ThO_2#1
Physics Department Wichita State Univ. Wichita, KS	Jim Ho 316/689-3190	Cooperated on Cu-Nb effort with Supercon
Rembar Comp. Inc. 67 Main St. Dobbs Ferry, NY 10522	Dean McCarthy 914/693-2620 Telex 883-864	W+ThO_2#2
Poco Graphite, Inc. A Unocal Company 1601 South State St. Decatur, TX 76234	Jeff Kopel 817/627-2121 800/433-5547	C#1 C#2 CuC#1
SCM Metal Products Western Reserve Bldg. 1468 W. 9th St. Cleveland, OH 44113	Edward Weber 216/344-8432	Cu#5 Cu#6

[2]Not normally a supplier of electrode materials, but in this case they supplied samples of materials they were evaluating. Their CuC#2 was Doduco's material.

Table A.2, continued

Source	Contacts	Materials Supplied
Schwarzkopf Dev. Corp.[3] 140 Lowland St. Holliston, MA 01746	Joe Hladick	See Metallwerk list
Supercon Inc. 830 Boston Turnpike Shrewsbury, MA 01545	Charles Renaud Eric Gregory 508/842-0174	Cu-Nb#2+Nb Clad[4] Cu-Nb#2 Cu-Nb#3
Williams and Co. Inc. P.O. Box 10911 Nashville, TN 37210	Frank Philpot 615/883-9440	Cu#3

[3]A distributor for Metallwerk Plansee of Austria.

[4]Material supplied in cooperation with Chuck Oberly.

2) Graphite,

3) CuW Composite,

4) In-Situ Extruded Fibers,

5) Tungsten Alloys,

6) Materials with an LaB_6 admixture and

7) Miscellaneous.

In the following section a description is given of the materials in each of these classifications.

Material Description

Cu Alloys (Cu#4-Cu#7): To increase the mechanical properties at elevated temperatures various alloys of copper are utilized. In the case of Cu#5 and Cu#6 a small percentage of Al_2O_3 results in a substantial increase in the yield strength by causing dislocations in the metal to spiral around Al_2O_3 sites rather than propagate straight through the material. Enhanced mechanical properties can be maintained up to 700°C using this technique [1]. Because the percentage of copper is still very high (> 99%) these materials still have excellent thermal and electrical conductivities.

Graphite: Unlike Cu and Mo which are elements whose properties are fairly standardized for a given degree of purity, graphite properties vary widely (up to an order of magnitude in some cases) depending on the manufacturing process. Other results have shown that C#1 is a superior electrode material [2] and C#2, which was recommended by the manufacturer, serendipitously had a thermal conductivity which

was almost 50% higher than C#1. In general, graphite has proved to be an excellent material because its erosion occurs via sublimation which requires a larger amount of energy than those materials which are removed in the molten state.

CuW Composites: Although manufacturing techniques vary, the best of these materials are formed by infiltrating copper into a press sintered tungsten "skeleton" matrix. Because the melting temperature of tungsten is higher than the boiling temperature of copper, the copper must be vaporized in order to be removed. Since the energy required to vaporize copper is much greater than that required to melt copper or tungsten, the composite material gives substantially less erosion. (See Appendix H for a model of this process.) The composites also have better conductivity and are more machinable than pure tungsten. A tradeoff exists between erosion and crack formation as a function of the tungsten grain size [5]. Antimony (Sb) was added because it has lowered the arc voltage in vacuum arcs [3]. Rhenium (Re) and Iridium (Ir) [4], though expensive, serve as "wetting" agents for tungsten to copper, i.e., the conductivity between the two elements is increased.

In-Situ Extruded Fibers: Originally developed for superconducting magnets because of their excellent conductivity and record setting yield strengths [6], these materials were tested for the first time in high current applications by the author. Ideally these materials consist of fibers of an in-situ material (niobium, chromium or tantalum) which were formed in bulk copper through various extrusion processes. I

say ideally because SEM photographs of several of the materials supplied to us indicated that little or no elongation of the in-situ material had occurred. (See the discussion in the next section.)

Tungsten Alloys: As can be seen from Table A.1, various alloys have been used. Almost all of the materials are press sintered alloys. The material W#2 is unique in that it was annealed, which resulted in a structure with tungsten fibers running parallel to the rod axis. In general the alloys posses higher conductivity and greater machinability when compared with pure tungsten. The materials indicated with a plus (+) were selected because of their lower work functions and or high electron emission rates.

LaB_6 additives: LaB_6 is a good emitter of electrons, especially at high temperatures [7]. Its addition to CuW led to a significant decrease in the erosion in previous experiments [8]. In general, it is thought that it reduces erosion by one or more of the following mechanisms:

1) decreasing the arc voltage, thereby decreasing the dissipation in the arc at a given current level,
2) increasing the rate of the arc voltage collapse during arc initiation, thus reducing the dissipation in the first half cycle of the discharge, and
3) producing a more uniform and diffuse current density distribution across the surface of the electrode due to the profusion of electron emitting sites.

Supercon's Analysis of the In-Situ Materials

The following section is a verbatim description by Charlie Renaud at Supercon Inc. of the in-situ materials tested by the author. It is included because many of the materials were not what they were purported to be.

Cu-Nb#1: Transverse section (Fig. A.1a)--I had to etch this sample rather heavily to bring out the Nb. It appears to be a powder metallurgy material of rather low volume % of Nb. The Nb spacing appears to be too great to be effective in a strengthening role. Average particle size is 4-5μm. Distribution of Nb appears homogeneous. Longitudinal section (Fig. A.1b)--the majority of Nb particles have been elongated, but some remain undeformed. This is probably due to oxygen content. Particles are ~ 16 μm long giving an aspect ratio of only 4:1.

Cu-Nb#1 + LaB_6: Transverse section (Fig. A.2a)--this sample appears to be a powder met product with Nb particles greater than 30 μm in diameter. Also present are inclusions, presumably LaB_6, ~ 5-20 μm in diameter. No indication of filamentization. Longitudinal section (Fig. A.2b)--very similar to transverse section. Close examination of the entire cross section revealed that a handful of the smallest LaB_6 inclusions have filamentized, but no indication of any filamentization by the Nb.

Cu-Nb#2: Transverse section (Fig. A.3)--this cross section looks very familiar. Polishing tends to smear over

a) 550X

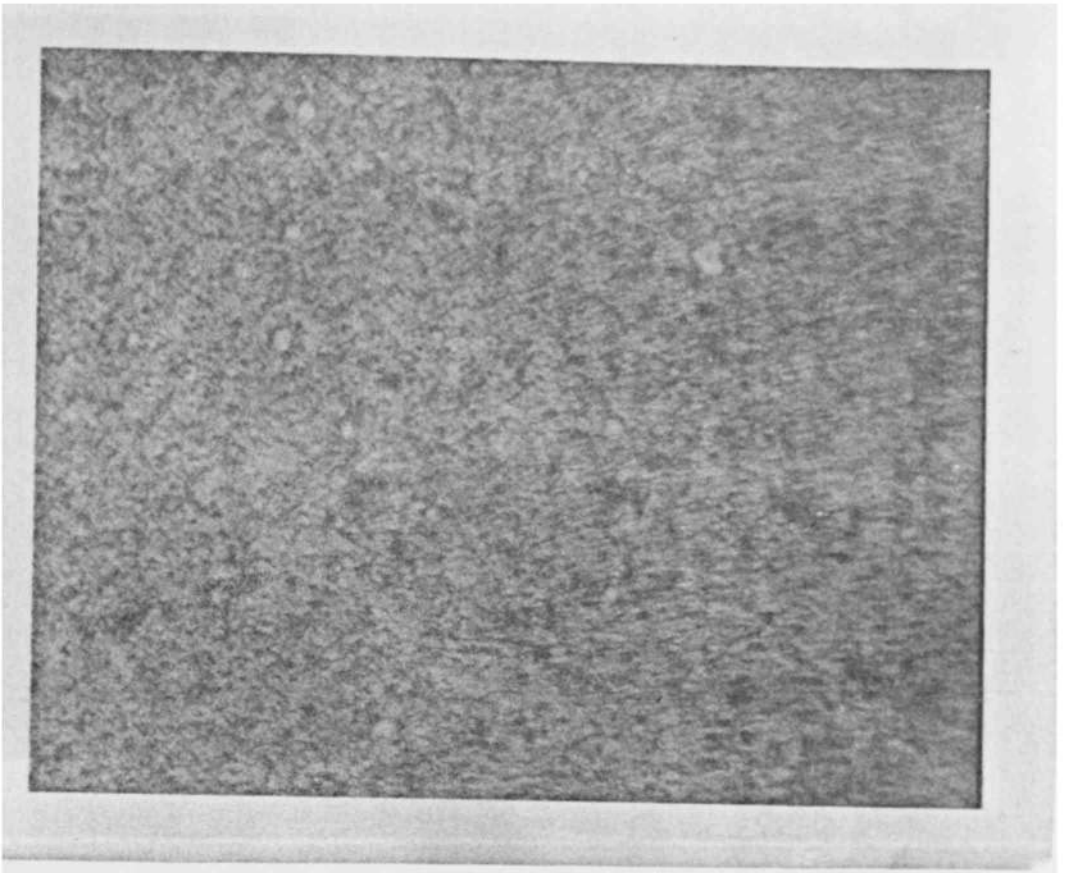

b) 400X

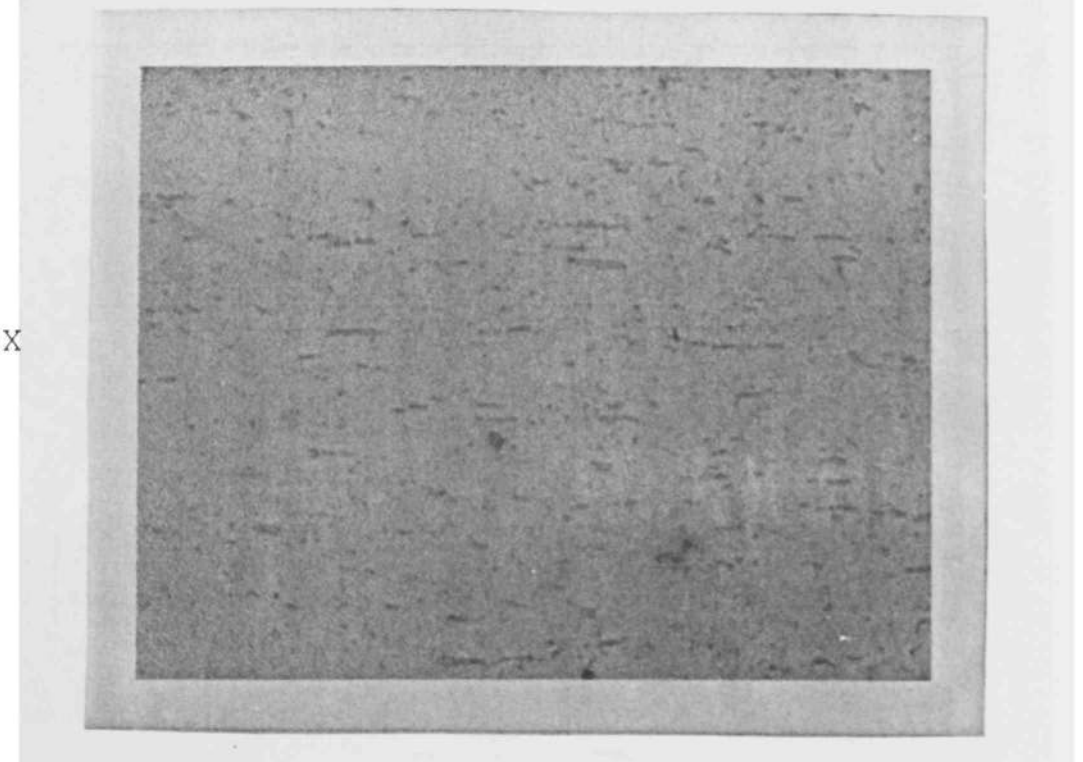

Fig. A.1 Cu-Nb#1 Electrode: a) Transverse, b) Longitudinal.

a) 450X

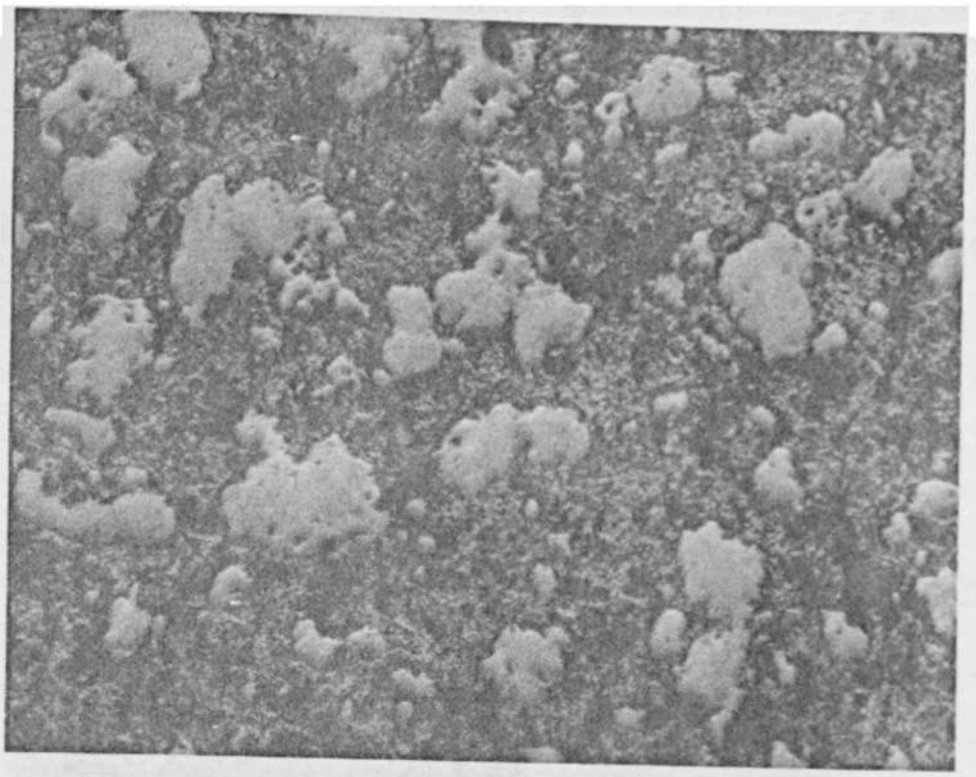

b) 200X

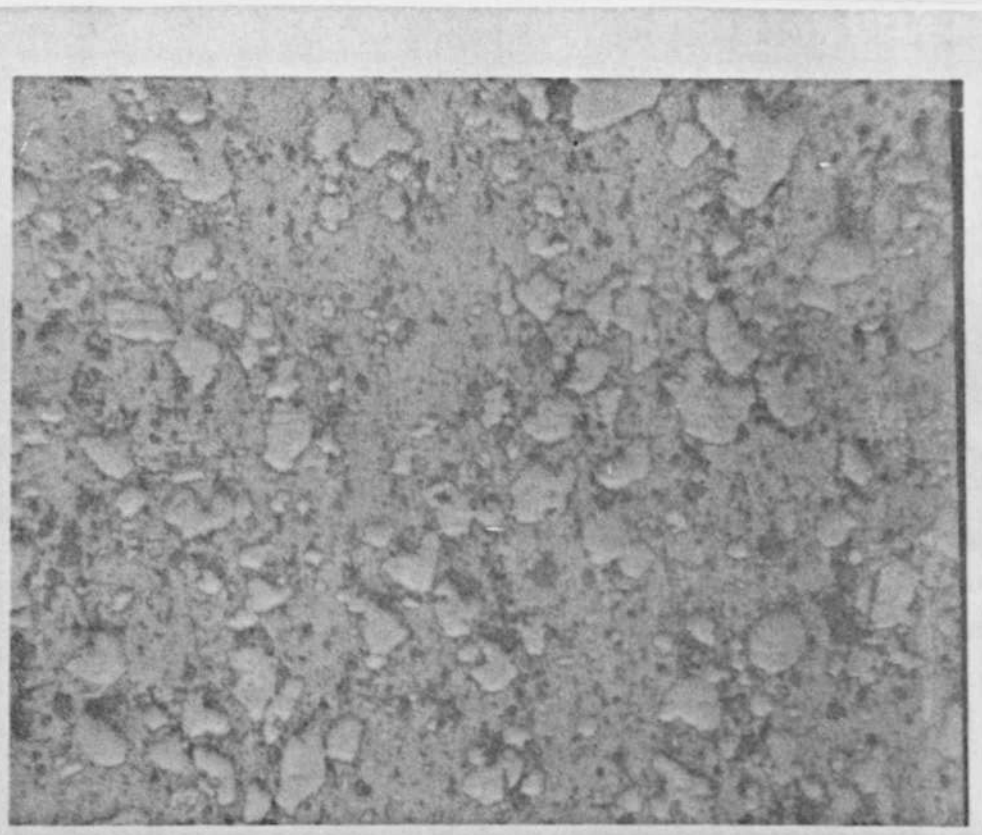

Fig. A.2 Cu-Nb#1+LaB_6 Electrode: a) Transverse, b) Longitudinal.

a) 200X

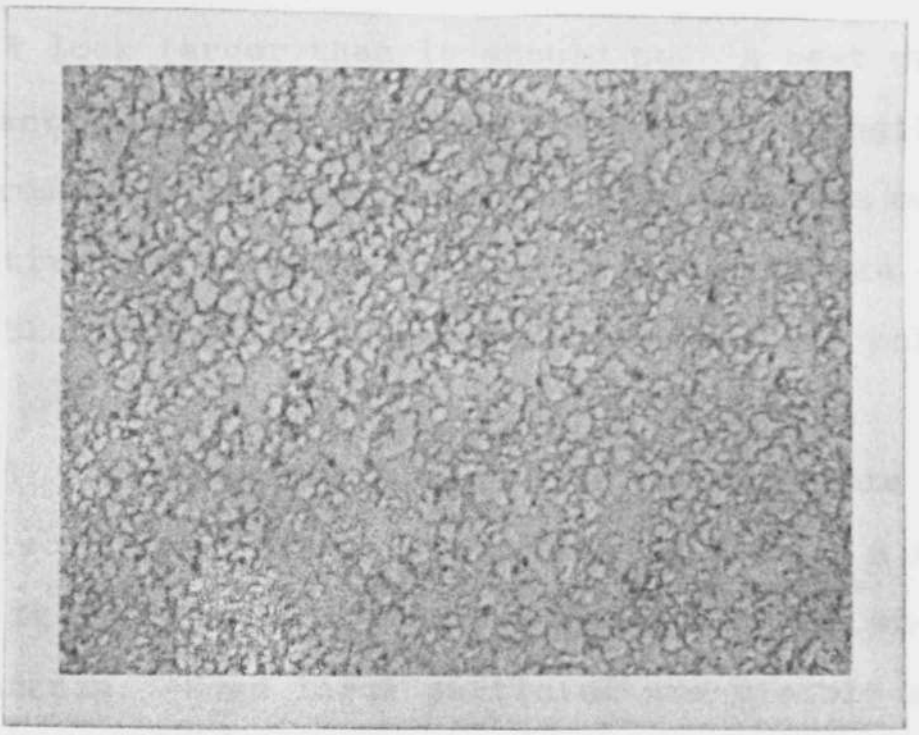

b) 100X

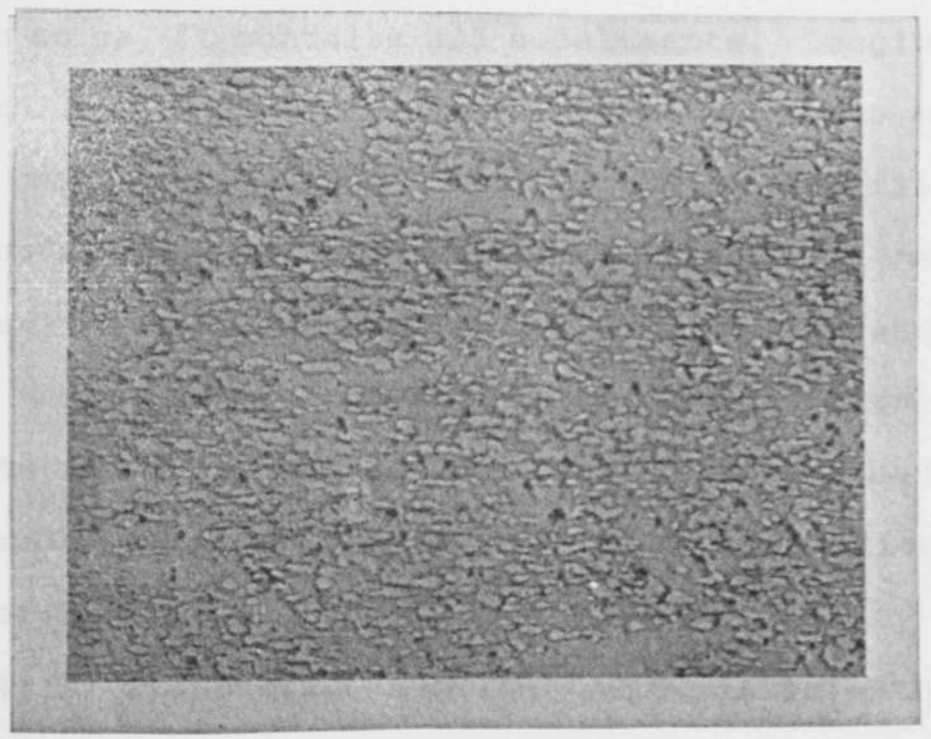

Fig. A.3 Cu-Nb#2 Electrode: a) Transverse, b) Longitudinal.

the Nb filaments into one another making resolution of individual, closely spaced filaments difficult. It also makes the volume % look larger than it should be. A best guess of true filament diameters would be ~ 6 μm. Longitudinal section: Breakup of the cast dendritic structure has occurred and filamentization has commenced. The filaments are ~ 60 μm long. The black spots in the photomicrographs are polishing artifacts.

Cu-Nb#3: Transverse section (Fig. A.4a)--this microstructure also looks familiar. I believe this to be a restack of CuNb#2. It has obviously undergone a significant amount of cold work strain. Some large particles are visible and are most likely the result of filament coarsening during the HIP'ing and extrusion processes. If this is the sample that I believe it to be, it contains 823 subelements. Longitudinal section (Fig. A.4b)--at 1000 X most of the filaments are too small to be resolved optically. Most of the smaller filaments are submicron in diameter. The presence of large filaments is due to filament coarsening and the lack of applied strain (η = 1.4 since extrusion). Filament coarsening is significant for filaments under 300 nm, and filament diameters have been known to double or even triple. This cross section is a candidate for SEM.

Cu-Nb#4: Transverse section (Fig. A.5a)--this is restacked material. Very heavy coring is present within the hexagonal subelements. Coring can be a result of either 1) segregation during melting due mostly to cooling rate, or 2)

a) 400X

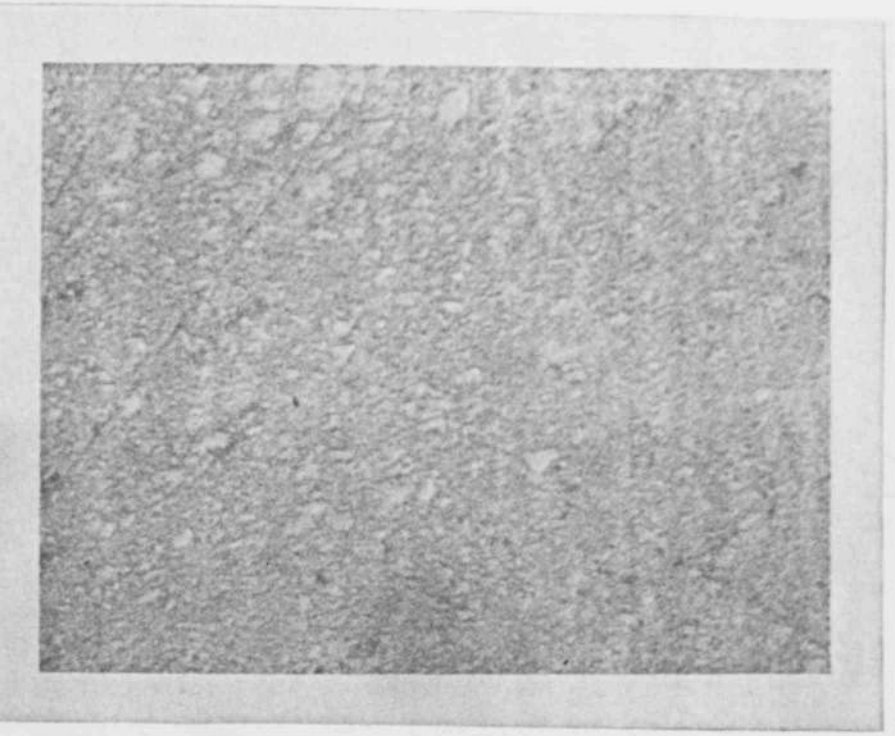

b) 1000X

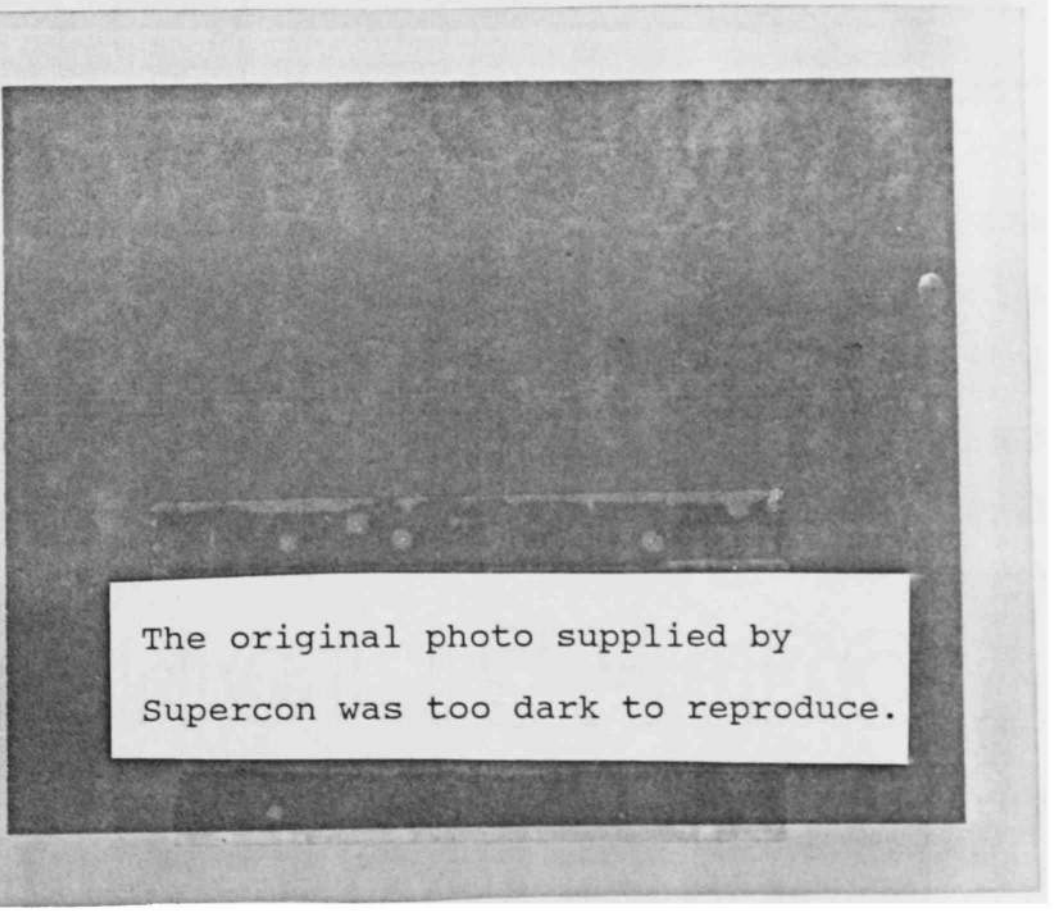

Fig. A.4 Cu-Nb#3 Electrode: a) Transverse, b) Longitudinal.

a) 90X

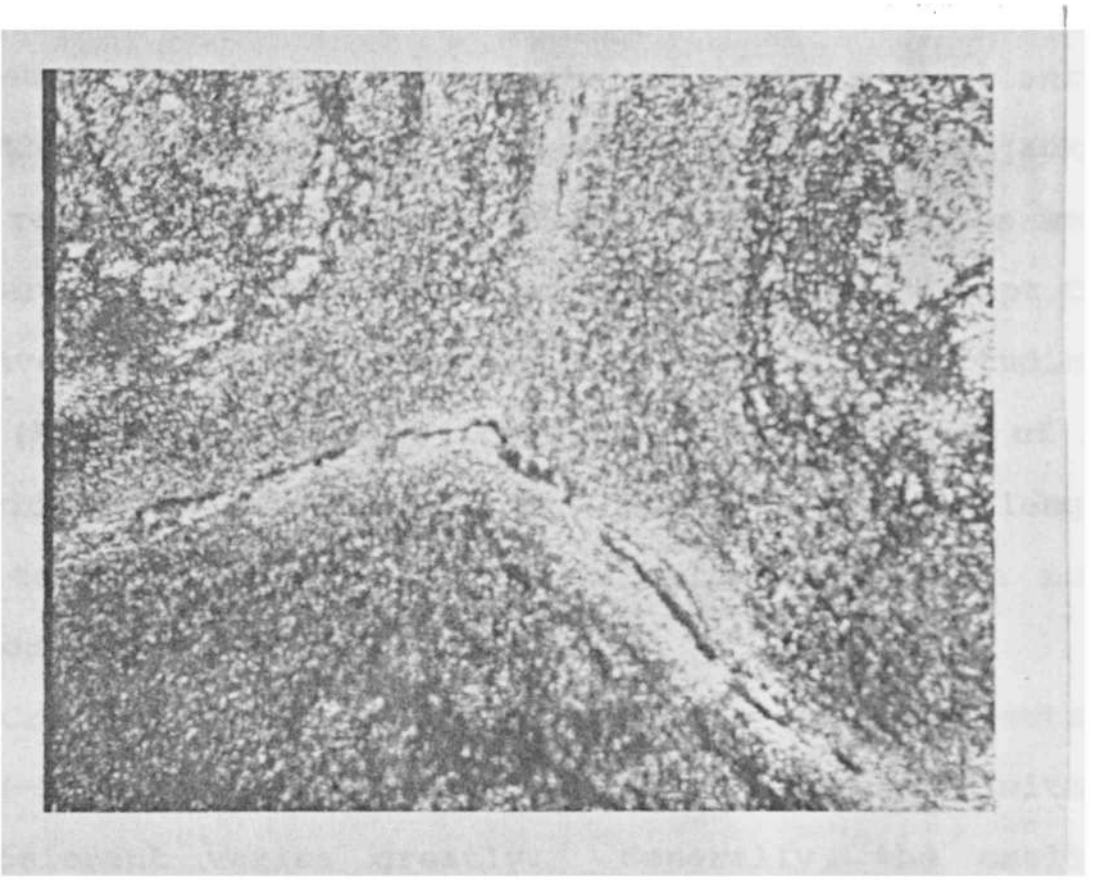

b) 200X

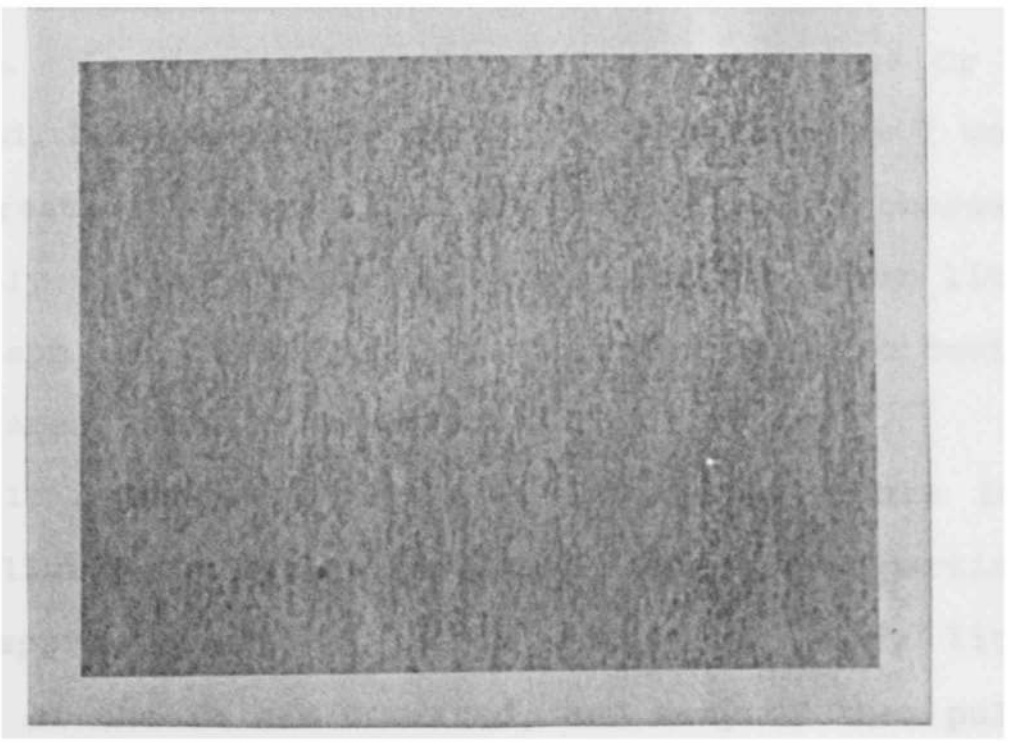

Fig. A.5 Cu-Nb#4 Electrode: a) Transverse, b) Longitudinal.

a build up of material in dead zones during extrusion due to improper die angle. Many large Nb particles exist in the cored areas. Boundaries between the subelements are clearly seen in the photomicrograph as the primary Cu drawing jacket was not removed prior to restacking. These boundaries were also clearly seen in the other restacked materials except Cu-Nb#3. Average filament diameter is ~ 5 μm. Longitudinal section (Fig. A.5b)--almost complete filamentization of Nb with a wide range of diameters and lengths. Average length appears to be ~ 40 μm. Nb distribution seems much more homogeneous than in transverse section.

Cu-Cr: Transverse section (Fig. A.6a)--this is a restack of 61 Cu-Cr hexagonal subelements. The homogeneity within each subelement varies greatly. Generally, the smaller filaments are located toward the outside where the greater concentration of filaments occurs. Average filament diameter is ~ 10 μm. Longitudinal section (Fig. A.6b)--the Cr has filamentized, but the aspect ratio is not as high as I would expect for restacked material. Either the filaments coarsened significantly during the second extrusion, or very little strain was applied to the primary extrusion prior to hexing. Average filament length was measured to be 37 μm.

Cu-Ta#1: Transverse section (Fig. A.7a)--this is a powder metallurgy product, with widely dispersed Ta particles measuring approximately 27 μm in diameter. Very little deformation of the Ta has occurred, and many of them pulled out during polishing. A Cu core of 6 mm diameter is present.

a) 400X

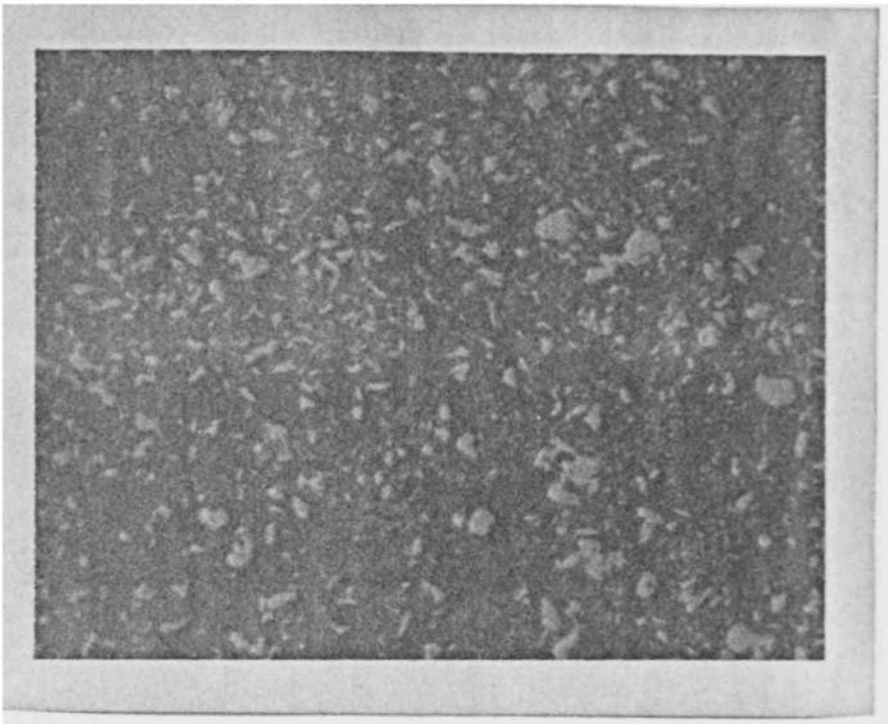

b) 400X

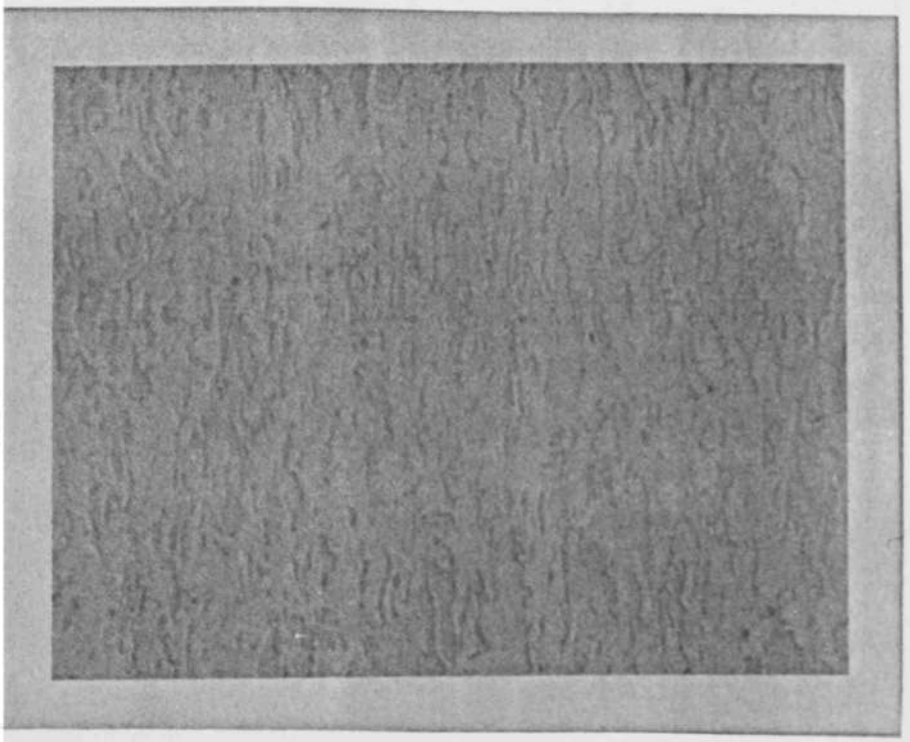

Fig. A.6 Cu-Cr Electrode: a) Transverse, b) Longitudinal.

a) 72X

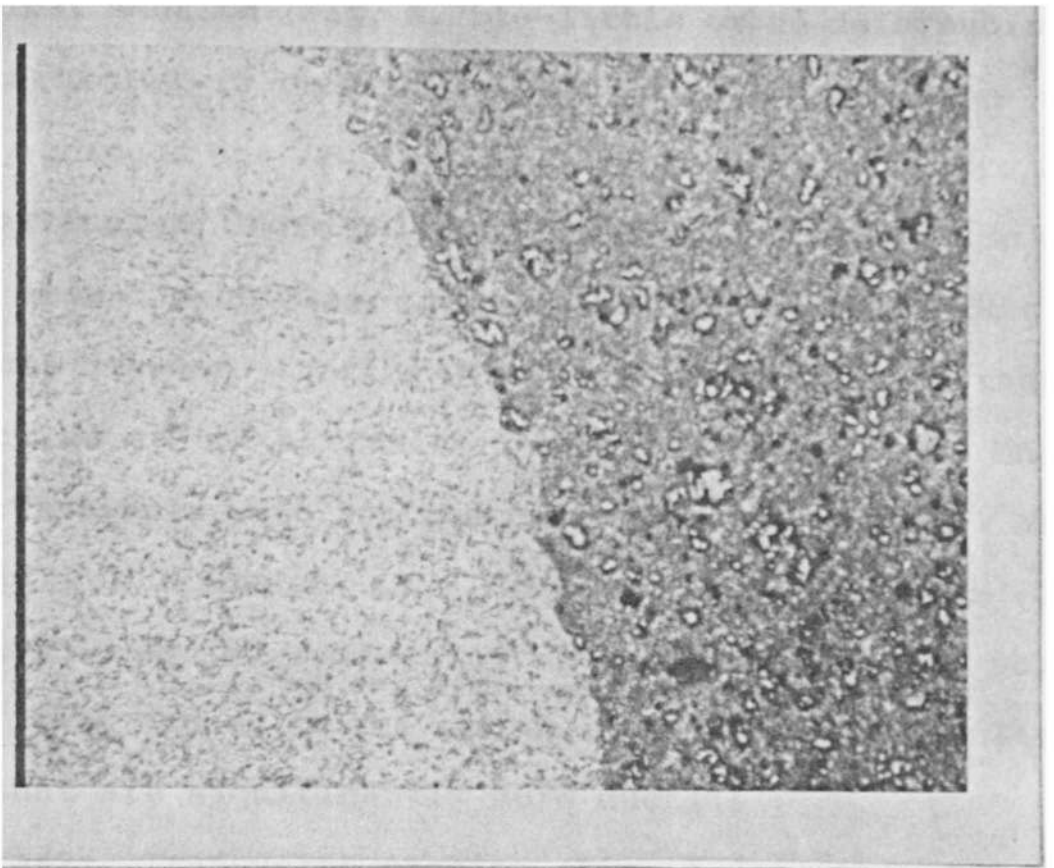

b) 200X

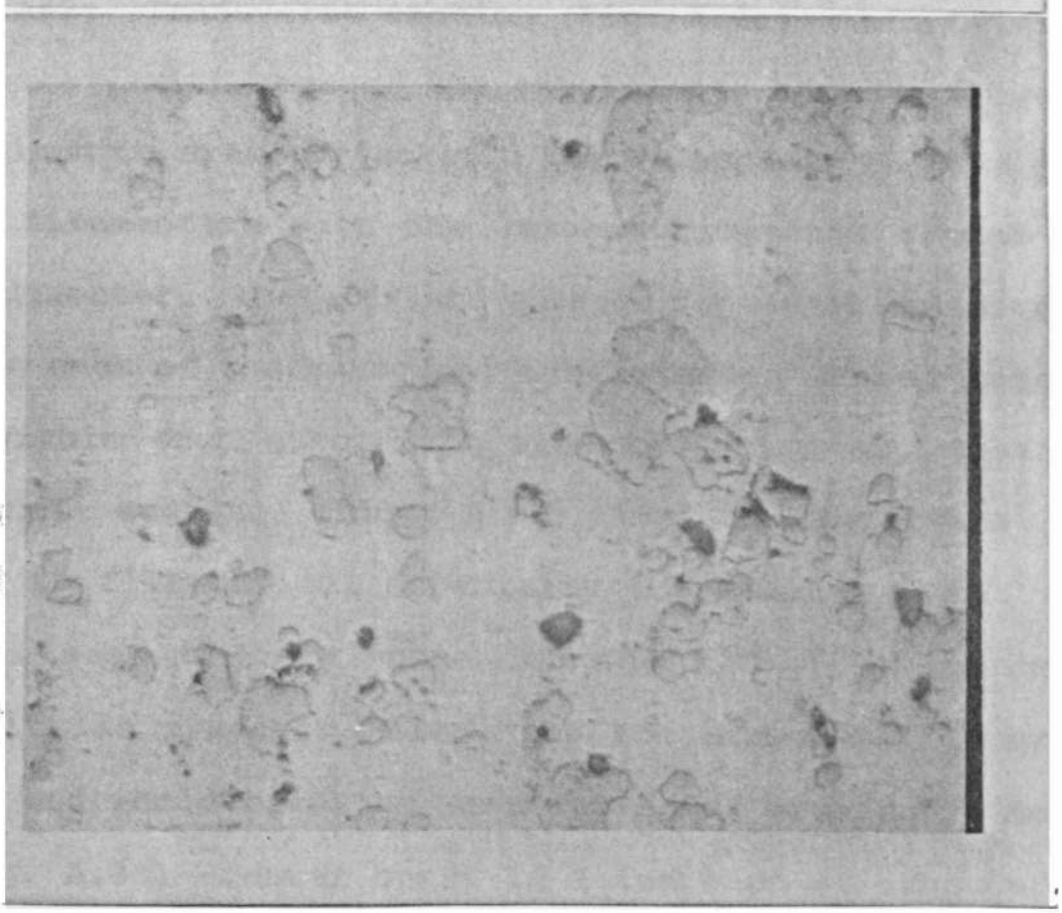

Fig. A.7 Cu-Ta#1 Electrode: a) Transverse, b) Longitudinal.

Longitudinal section (Fig. A.7b)--little or no deformation of the Ta particles is observed. The Cu core penetrates only partially through the section, so it is probably an improperly cropped extrusion. More pullouts occurred and many voids were observed around particles. This leads me to suspect that the differences between the flow stress of the matrix and that of the particles at the extrusion temperature were great enough that the Ta simply went for the ride during extrusion. Also, the use of small powders is a mistake. Large powders (250-500 μm) will require restacking, but the surface to volume ratio is lower and so is the oxygen content. This results in powders that are significantly more ductile.

Cu-Ta#2: Transverse section (Fig. A.8a)--this material was restacked, with some of the subelements showing evidence of a retained Cu drawing jacket. The Ta appears to have just begun to filamentize with the largest filaments around 10-12 μm in diameter. There exists a large degree of inhomogeneity within each of the hexagonal subelements. The Ta concentration within each subelement also tends to vary greatly. Longitudinal section (Fig. A.8b)--the Ta particles are beginning to filamentize, especially the smaller ones. The large ones seem to have "gone for the ride." Significant inhomgeneity is present. Also, the rod experienced "center bursting" and would break up with continued drawing. Center burst (Fig. A.8c)--center burst is a function of area reduction, die angle and friction. As we are fond of saying, "the outside doesn't know what the inside is doing." It is

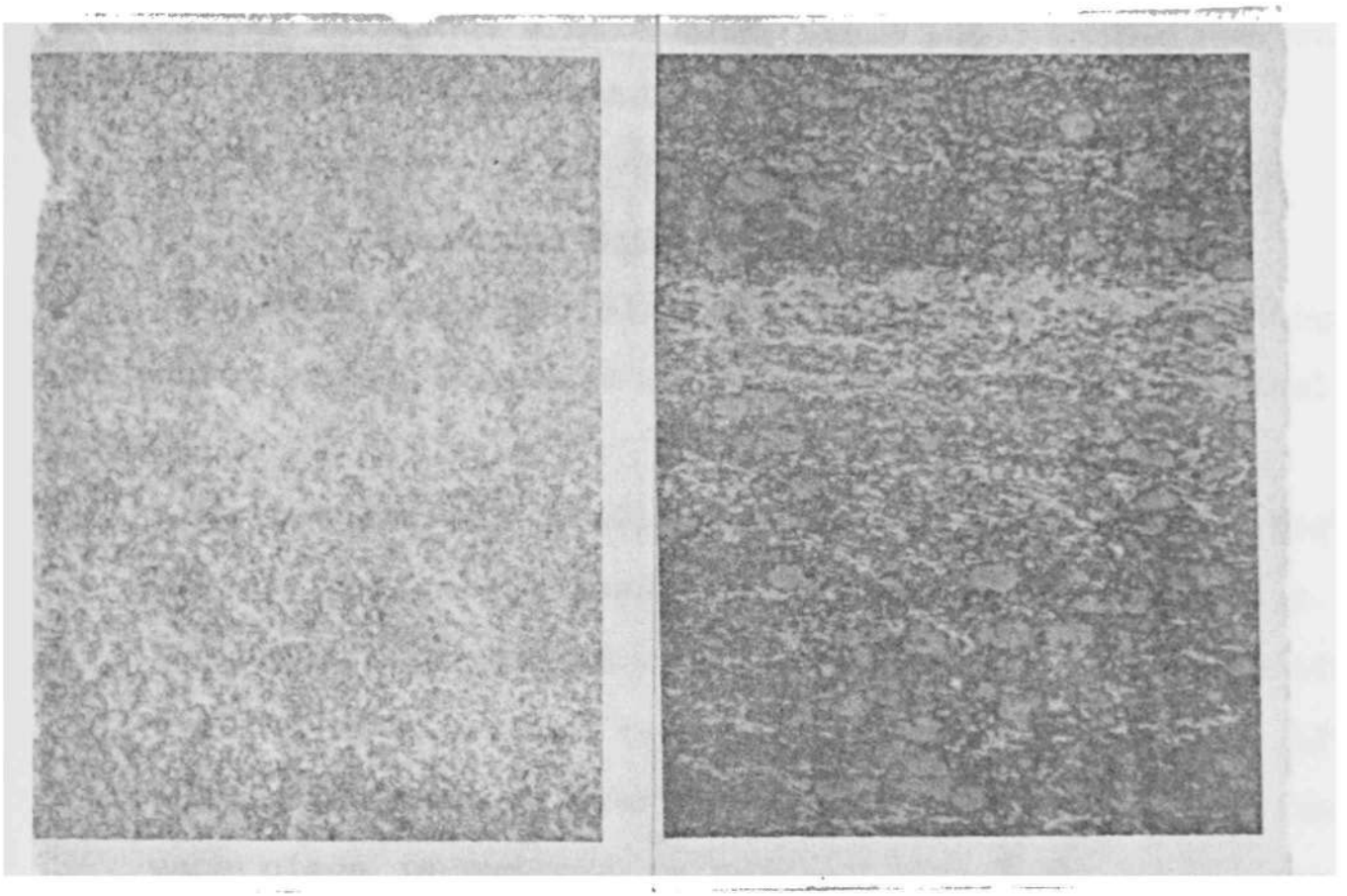

a) 200X

b) 200X

c) 30X

Fig. A.8 Cu-Ta#2 Electrode: a) Transverse, b) Longitudinal, c) Center Burst (indicated by the void).

prevalent in powder met materials, or materials where a soft outer layer surrounds a hard core. This distinctive chevron pattern is periodic throughout the extrusion.

Electrode Material Preparation

Upon receipt of the electrode materials, the following procedures are performed to prepare the electrodes for actual testing:

1) Each material is assigned a specific dot pattern for identification purposes, for a listing see Table A.1. The pattern is stamped with a metal punch on both ends of the rod of electrode material (this guarantees that if one end is cut off then the rod is still marked!). As each piece is cut off to make an electrode it is also marked on its side.
2) A sample piece, approximately 1-2 cm long is cut off for documentation and further testing purposes.
3) The sample is weighed and measured in order to calculate the experimental value of the density used for each material. This is very important because the theoretical densities assume that the material has no porosity. (For example carbon has a theoretical density of 2.25 gm/cm^3 which is 20% greater than the actual density of 1.88-gm/cm^3).
4) As many sets of 3.8-5 cm (1.5-2") long electrodes are cut from the rod as possible.

5) The electrode pieces have one end machined to a hemispherical tip, while the other end is usually drilled and tapped. (For brittle or extremely hard materials, such as high percentage tungsten alloys, the materials are not drilled and tapped.)

6) The machined surface is polished with Norton "No-Fil Adalox 400-A grit sandpaper." The degree of polishing is not critical since the surface the arc "sees" for each shot is dominated by the damage produced on previous shots.

7) In most cases water is used as the lubricant during the electrode machining, however, if machine oil is required for cutting, then the electrodes are cleaned ultrasonically using Buehler Ultramet cleaner.

8) The electrodes are weighed using one of the two scales described in Appendix B depending on the sensitivity required, time available and the total mass to be weighed.

9) Occasionally the electrode tip is cut off for further analysis but usually the tip is resurfaced by removing at least 3 mm from the electrode surface.

10) In some cases additional data are taken on the sample piece such as hardness, optical micrographs, and SEM photographs of the cross section and surface.

Experimental Conditions for Electrode Material Testing

The standard experimental conditions for the electrode materials testing are given in Table A.3. Figures A.9 and A.10 show the experimental facility and the test switch. In order to change the peak current, charge or energy per shot the capacitance is varied simply by adding 1.8 μF capacitors to the energy store in a symmetric fashion. There are seven standard capacitance configurations settings which are used for most materials: 1, 2, 4, 6, 10, 20, and 30 caps. For the baseline tests using Cu#1 electrodes, runs were also made for 3, 5, 7 and 8 caps. In all cases the amount of charge transferred through the electrodes is kept approximately constant by varying the number of shots, N_s, as a function of the number of caps, N_c, such that

$$N_c N_s = 1500. \qquad \text{(A.1)}$$

For the earlier graphite runs, where only the less sensitive balance ($\Delta m > 10$ mg) was available, the number of shots was sometimes doubled to increase the total eroded mass to a measurable level. For all of these cases the effect of N_s on the erosion was shown to be negligible. In addition to the seven standard runs performed on the Mark VI an additional eighth run was performed for most materials using the MAX I energy storage system run in the stationary arc, oscillatory discharge mode. The MAX I data provided a comparison for different pulse conditions which was needed to verify scaling

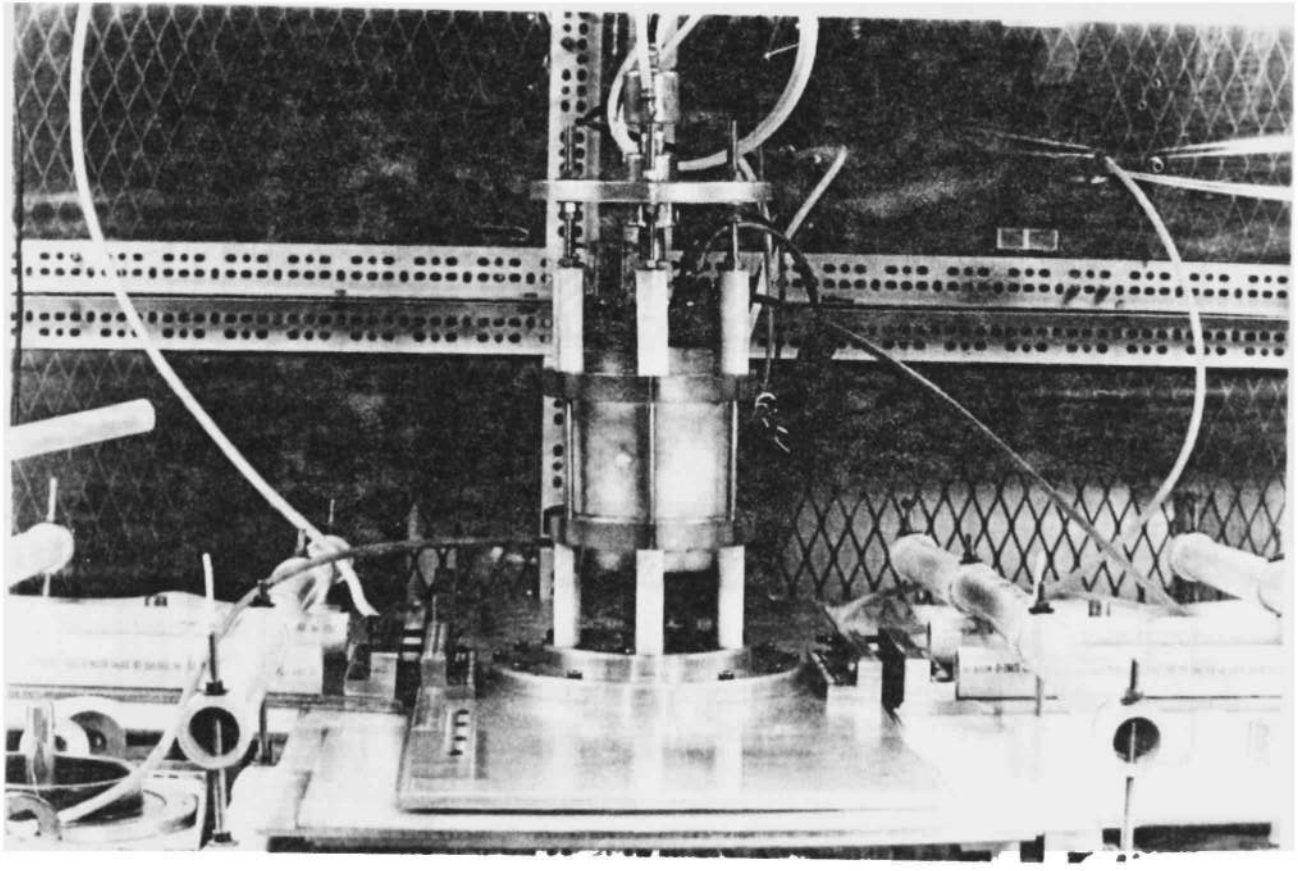

Fig. A.9 Mark VI Experimental Facility.

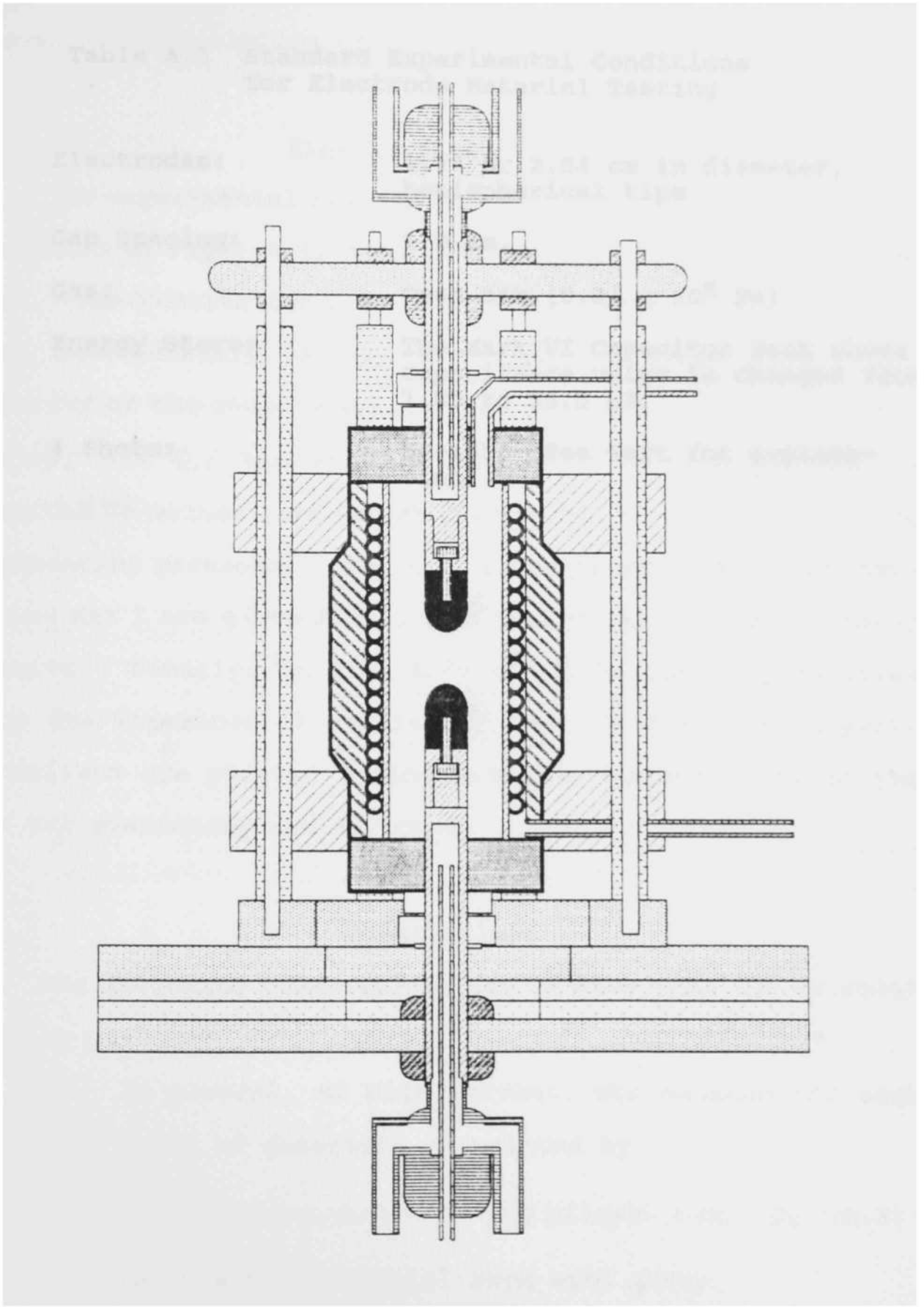

Fig. A.10 Cross-Section of Mark VI Switch = 1 Spark Gap (Watercooled, Pressurized Version).

Table A.3 Standard Experimental Conditions for Electrode Material Testing

Electrodes:	1.27 or 2.54 cm in diameter, hemispherical tips
Gap Spacing:	1.0 cm.
Gas:	Open Air (0.87×10^5 Pa)
Energy Store:	The Mark VI Capacitor Bank whose capacitance value is changed from 1.85 to 55.5 μF.
# Shots:	50-1550 (See text for explanation)

models. The MAX I pulse conditions are given in Table A.4. A complete description of the MAX I system is given in [9].

Experimental Results

The experimental results for most of the materials tested are shown in Figs. A.11-A.56 and listed in Tables A.5 through A.41. The results for 2.54 cm diameter CuC#1 (see Fig. A.57) were inadvertantly placed at the end of Table A.41. The majority of the results are plotted versus f_1, the theoretical factor, and Q_s, the stored charge. The erosion rate is reported in volume lost per shot since this is the significant engineering parameter. The 1.27 cm diameter results for Mark VI and MAX I are given first, followed by the 2.54 cm diameter results. Finally, in Fig. A.58 and A.59 the best material from the experimental results of over 25 different experimentalists are plotted to indicate the current state of the art for stationary arc switches.

Observations

The following observations can be made from the material erosion results:

1) In general, at high current, the erosion for each group of materials is related by

$$C < (Cu\text{-}90\%, W\ Alloys, CuW) < (W+, Cu\ Alloys) < Mo < Cu \quad (A.2)$$

for the best material from each group.

Table A.4 MAX I System Parameters (Oscillatory Mode)

Voltage	6 kV
Peak Current	300 kA
Energy Stored	17.3 kJ
Effective Charge Transfer	58 C*
Ringing Freq.	8 kHz
Pulse Duration	500 μs
Gap Spacing	2 mm
# Shots	1-10
Gas	Open Air

*Considerable error is involved in this calculation. Values may range from 40-90, depending on the gain factor assumed. (The previous author used 52, the present author uses 60 - a geometric mean between the limits.)

The gain factor is defined as the effective charge multiplication factor, 10, times 6 (to account for 6 kV). This factor is then multiplied by the amount of capacitance in mF to get the effective charge in C.

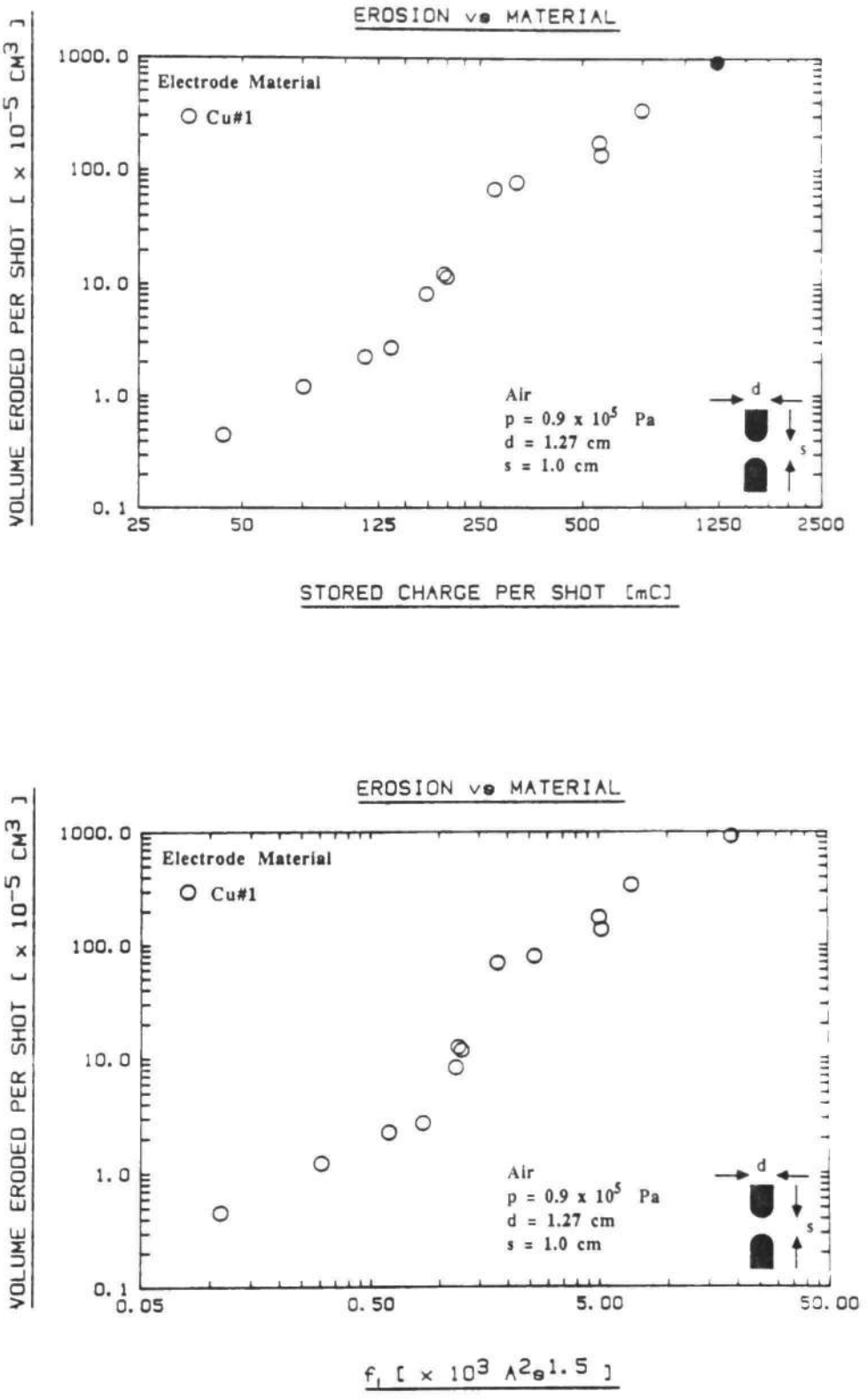

Fig. A.11 Erosion for Cu#1 1.27 cm Diameter Electrodes vs. a) Stored Charge and b) f_1.

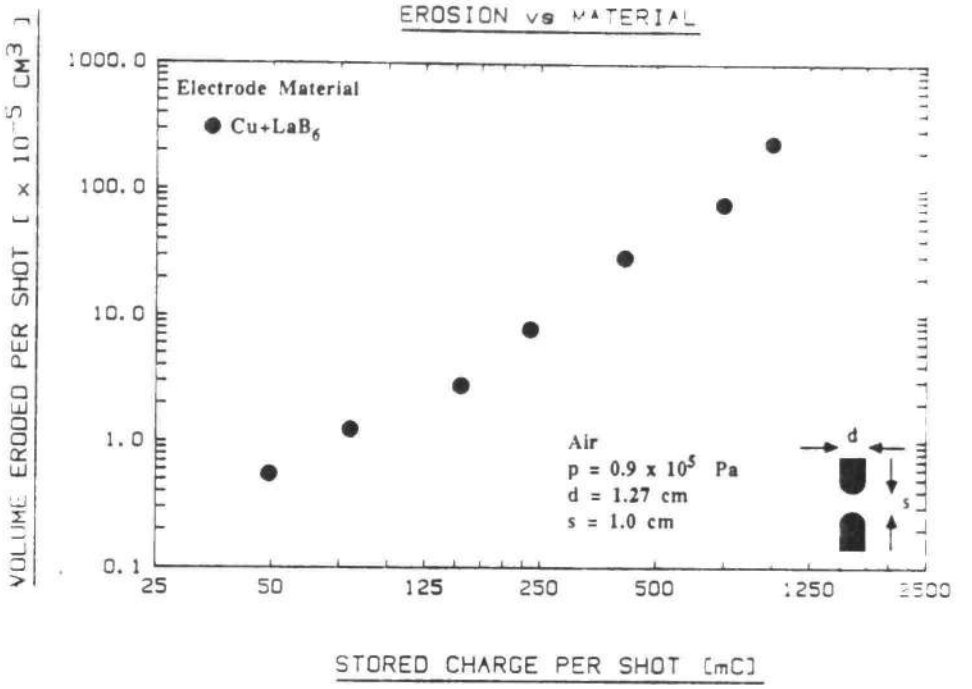

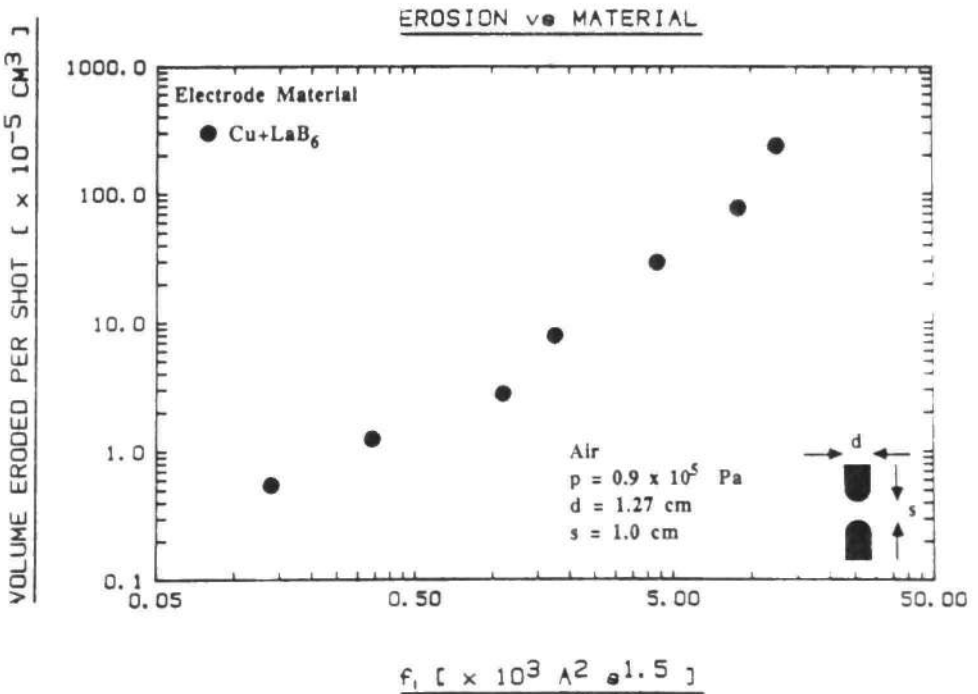

Fig. A.12 Erosion for $Cu+LaB_6$ 1.27 cm Diameter Electrodes vs. a) Stored Charge and b) f_1.

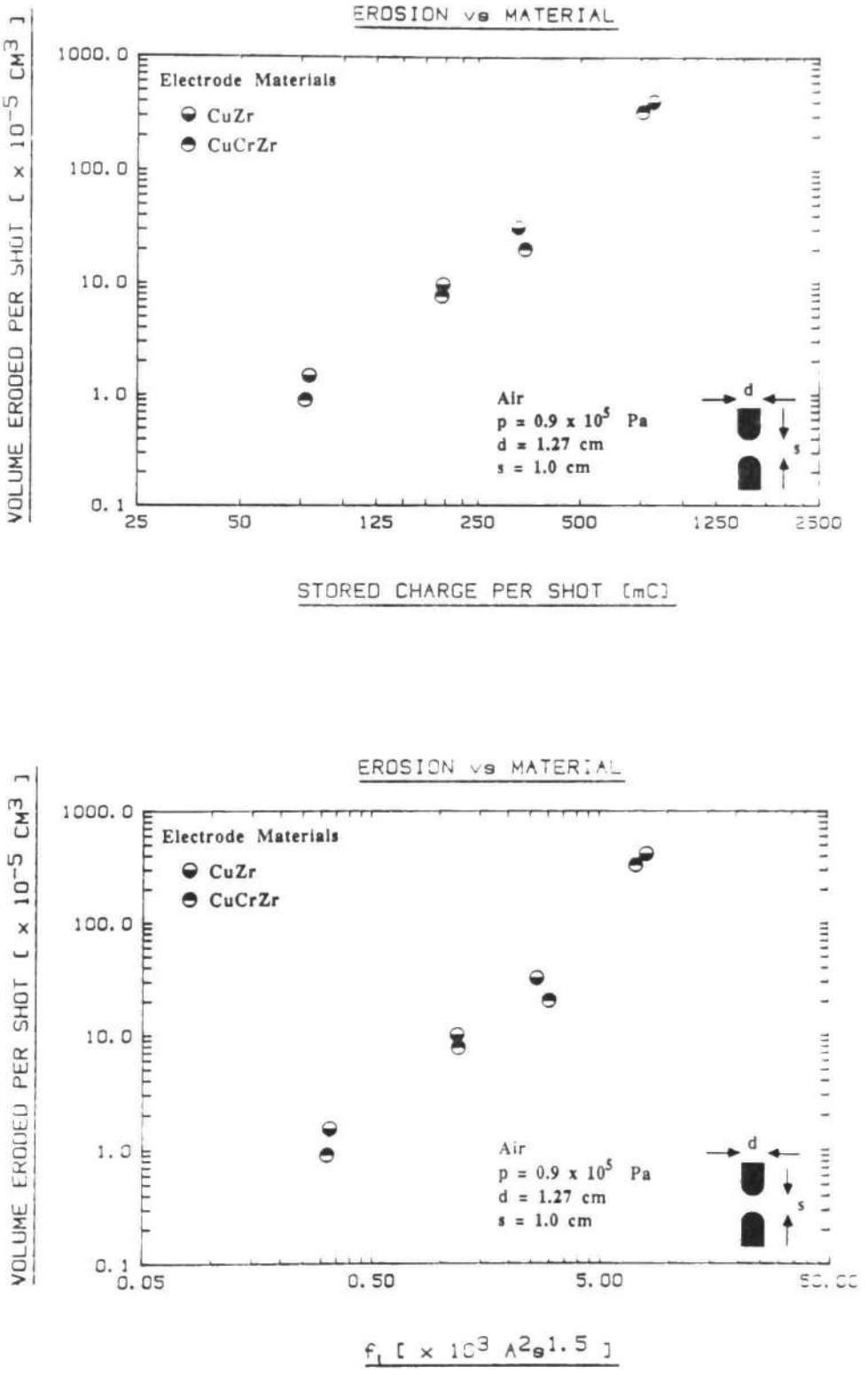

Fig. A.13 Erosion for CuZr and CuCrZr 1.27 cm Diameter Electrodes vs. a) Stored Charge and b) f_1.

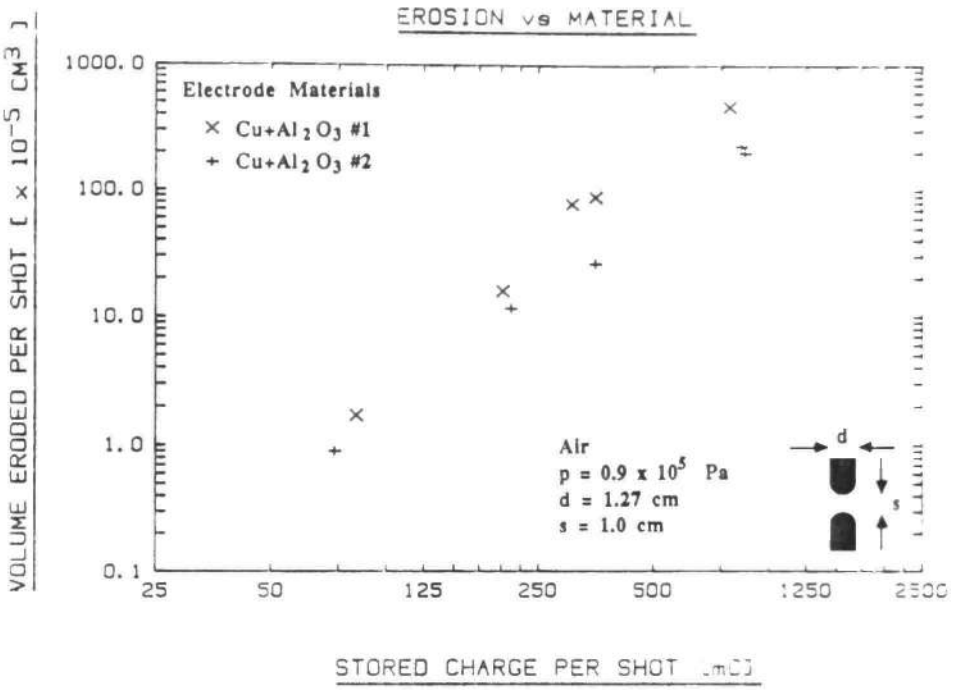

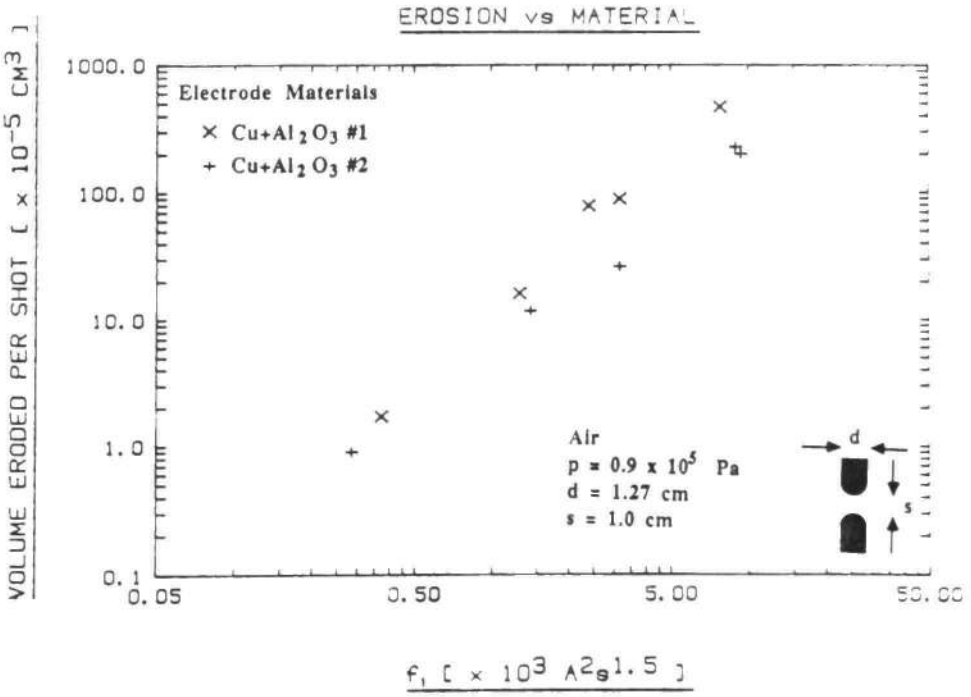

Fig. A.14 Erosion for $Cu+Al_2O_3$#1 and =2 1.27 cm Diameter Electrodes vs. a) Stored Charge and b) f_1.

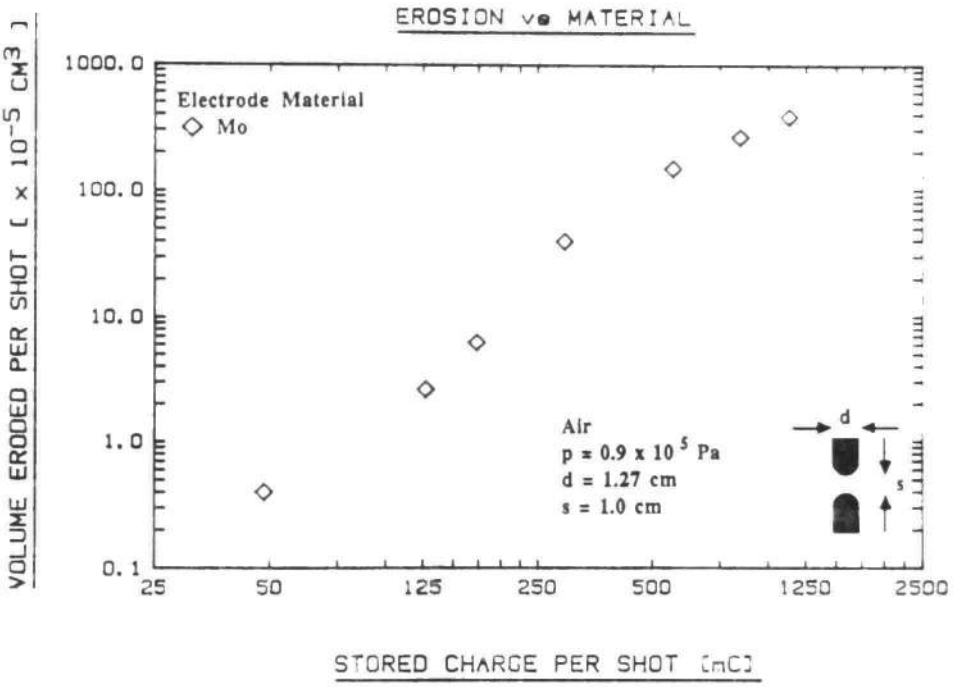

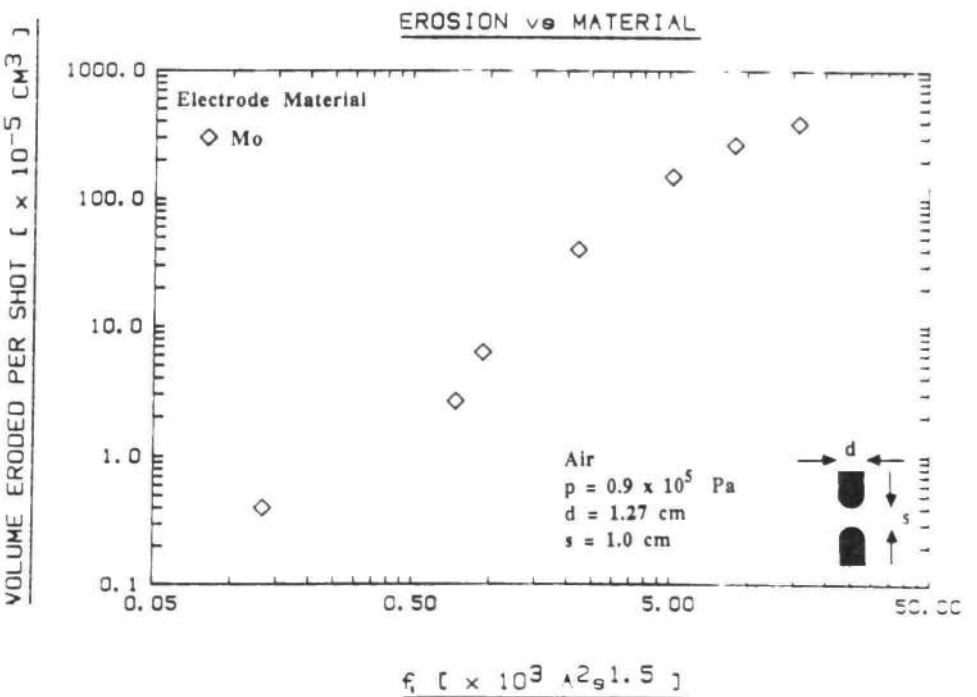

Fig. A.15 Erosion for Mo 1.27 cm Diameter Electrodes vs. a) Stored Charge and b) f_1.

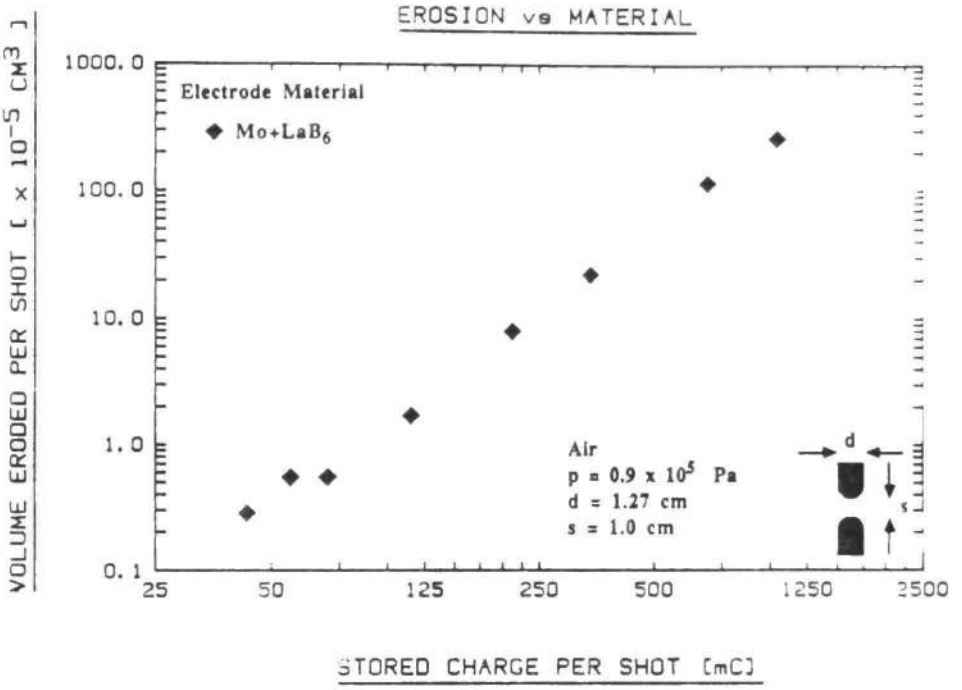

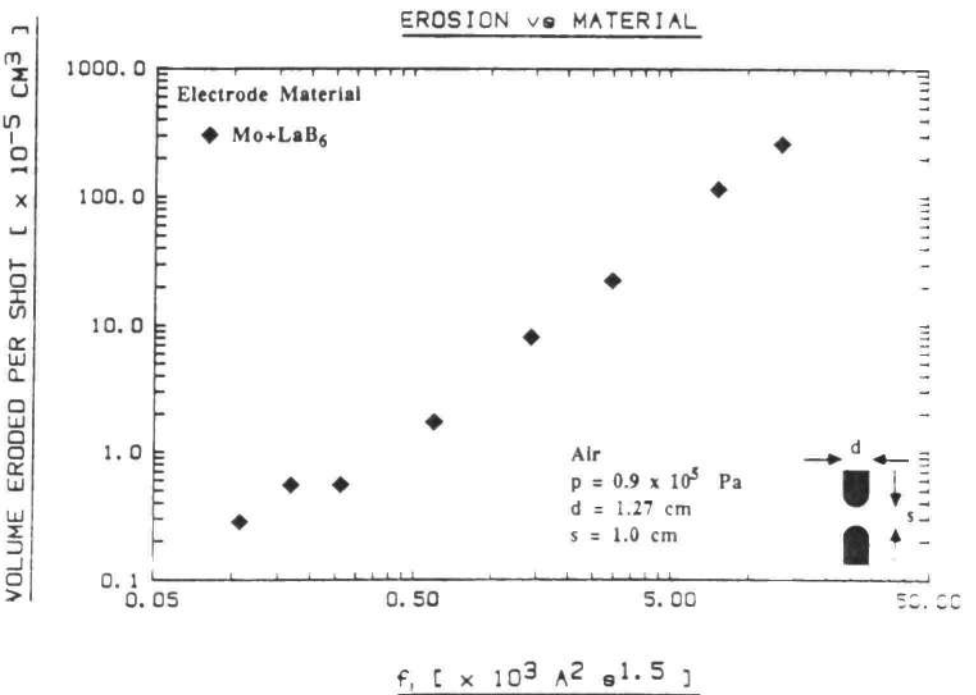

Fig. A.16 Erosion for $Mo+LaB_6$ 1.27 cm Diameter Electrodes vs. a) Stored Charge and b) f_1.

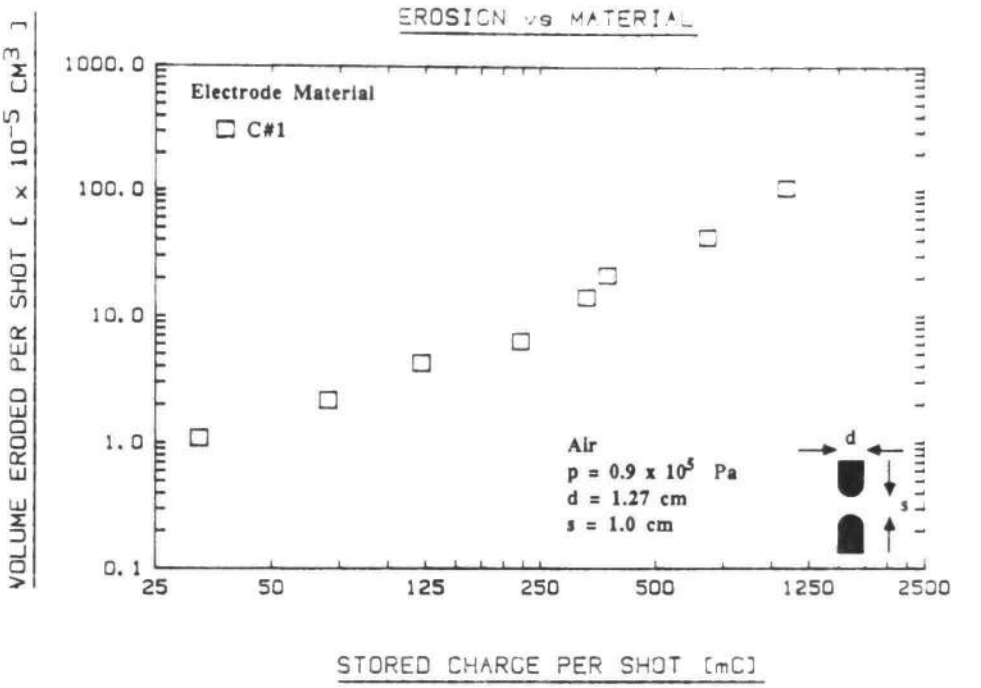

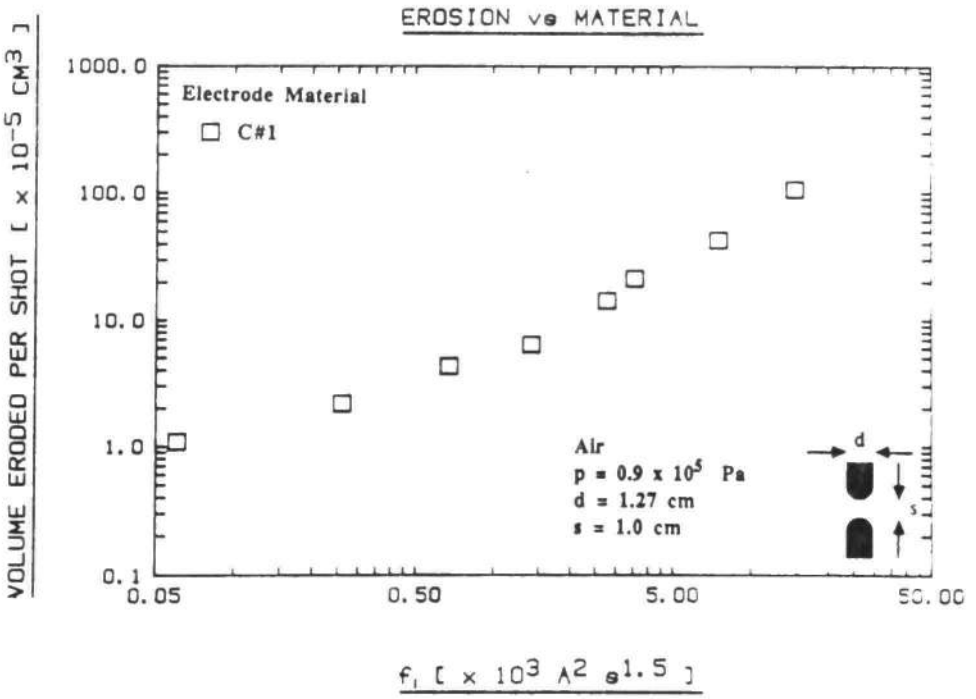

Fig. A.17 Erosion for C#1 1.27 cm Diameter Electrodes vs. a) Stored Charge and b) f_1.

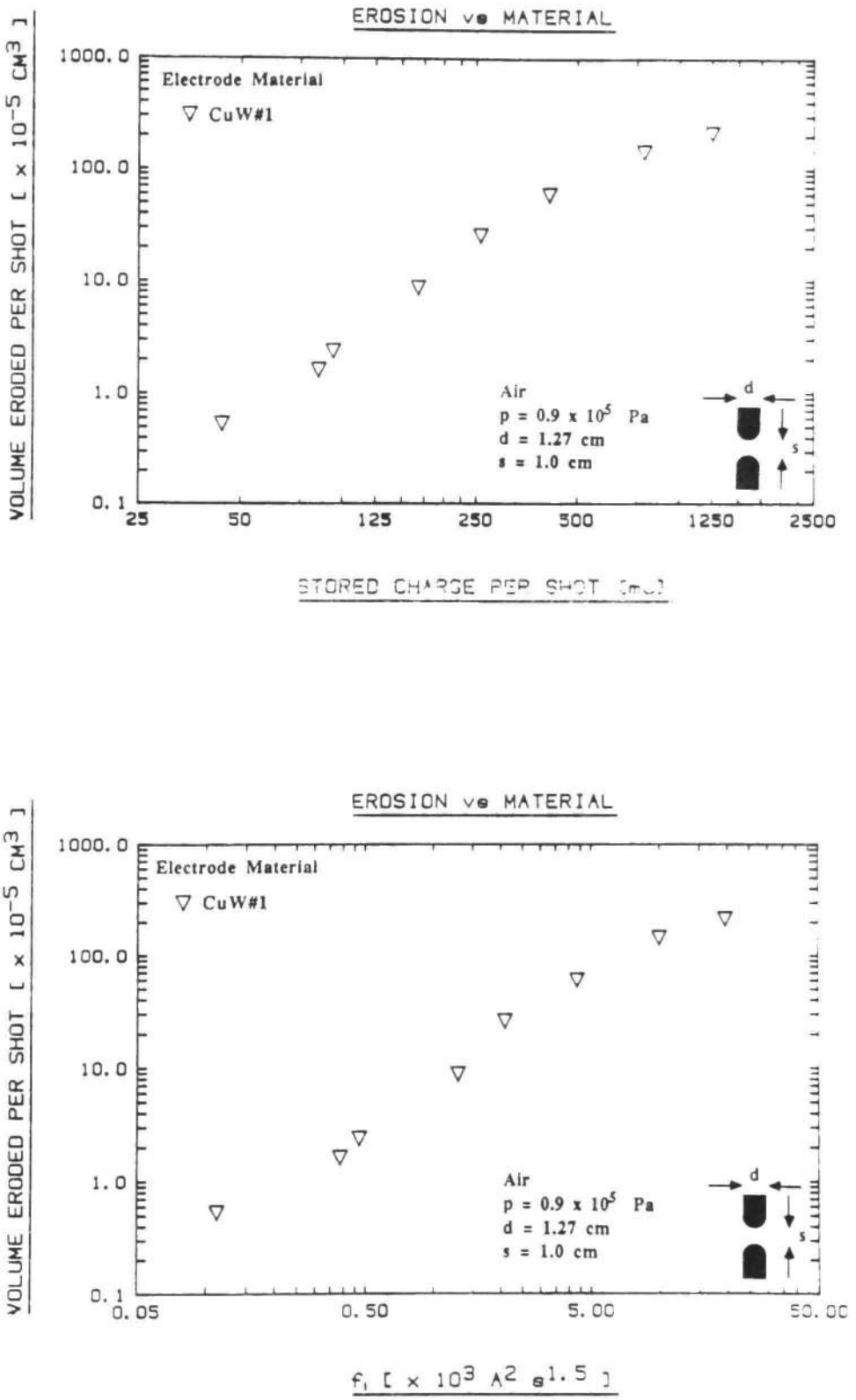

Fig. A.18 Erosion for CuW#1 1.27 cm Diameter Electrodes vs. a) Stored Charge and b) f_1.

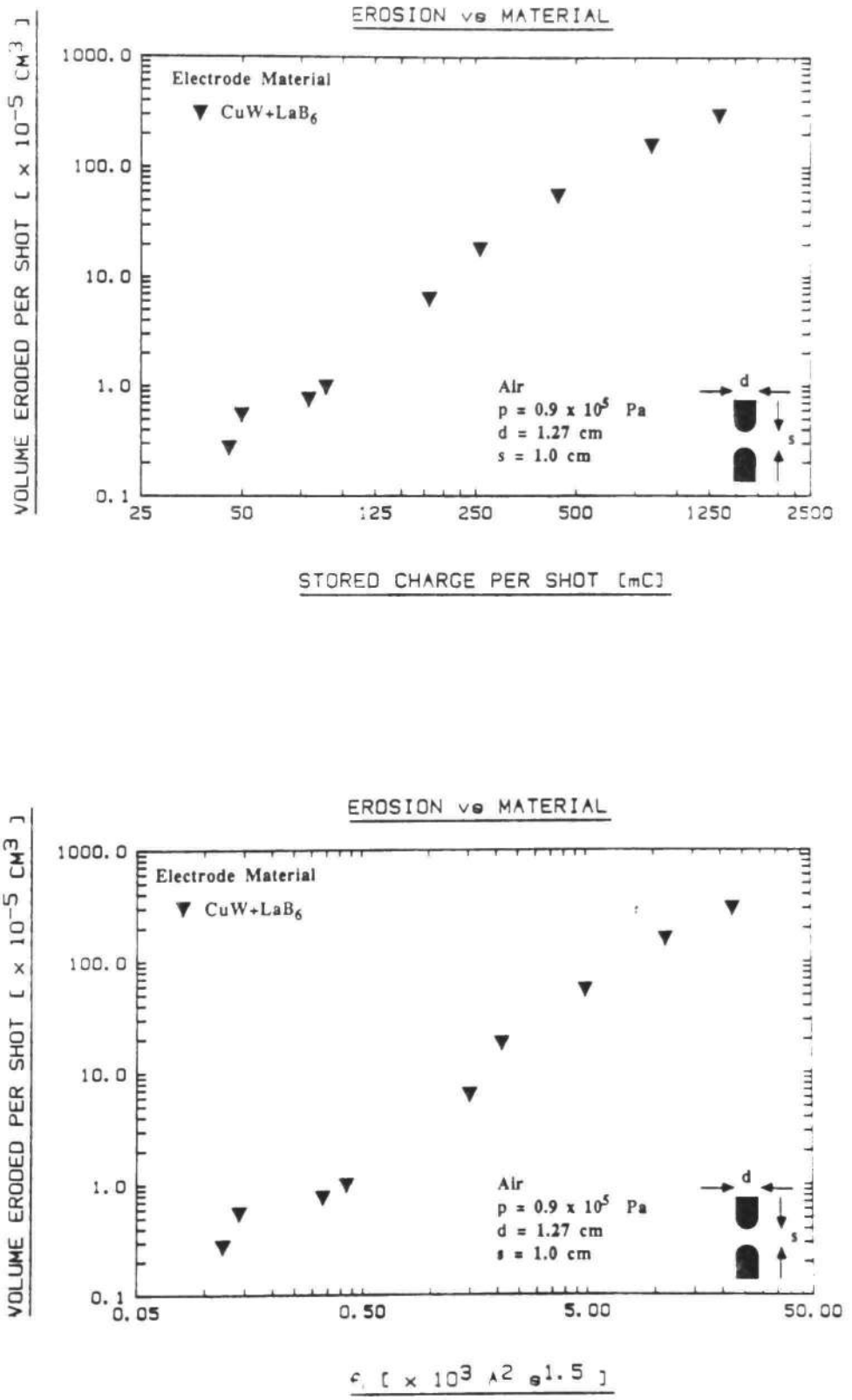

Fig. A.19 Erosion for CuW#1+LaB_6 1.27 cm Diameter Electrodes vs. a) Stored Charge and b) f_1.

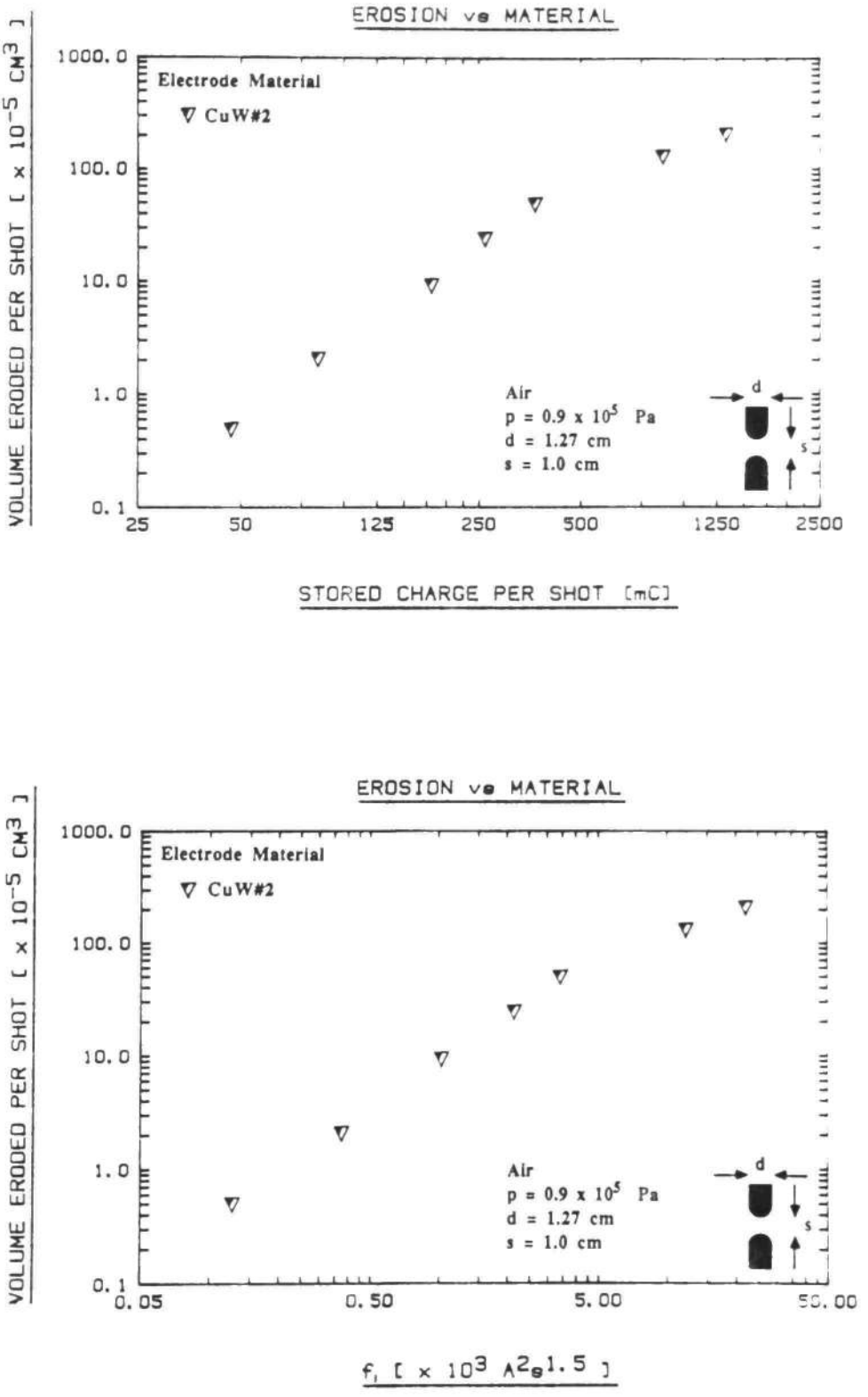

Fig. A.20 Erosion for CuW#2 1.27 cm Diameter Electrodes vs. a) Stored Charge and b) f_1.

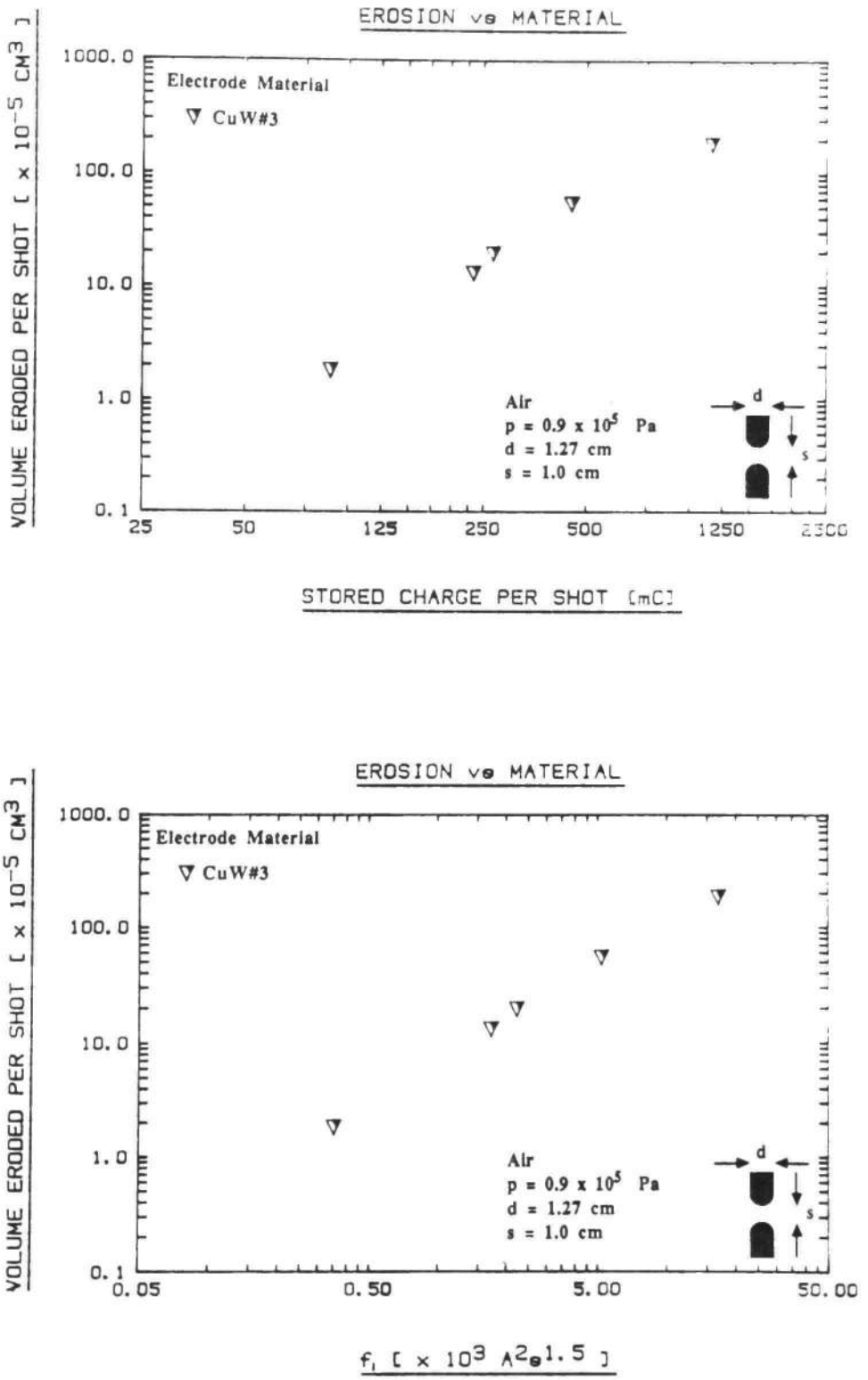

Fig. A.21 Erosion for CuW#3 1.27 cm Diameter Electrodes vs. a) Stored Charge and b) f_1.

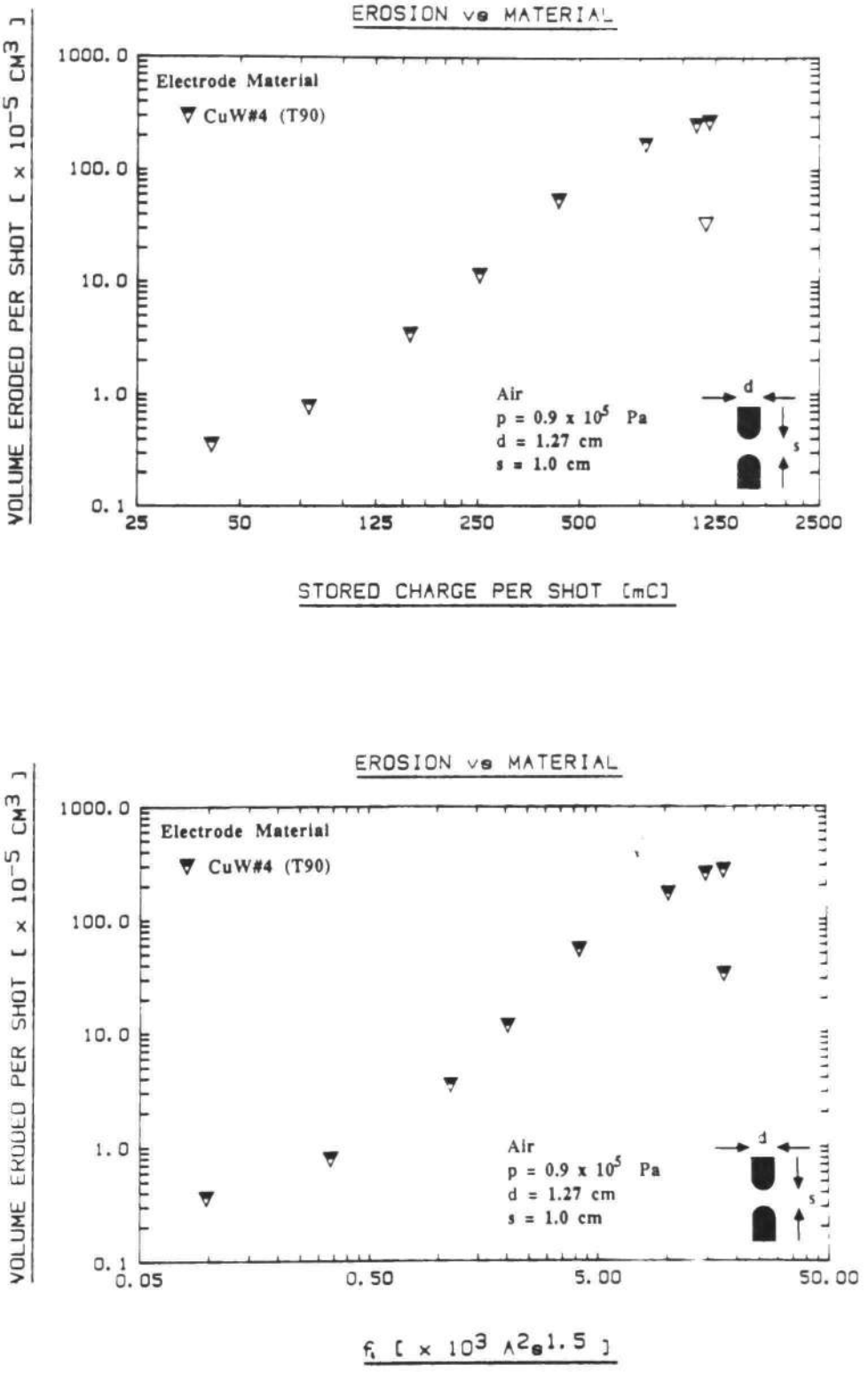

Fig. A.22 Erosion for CuW#4 1.27 cm Diameter Electrodes vs. a) Stored Charge and b) f_1.

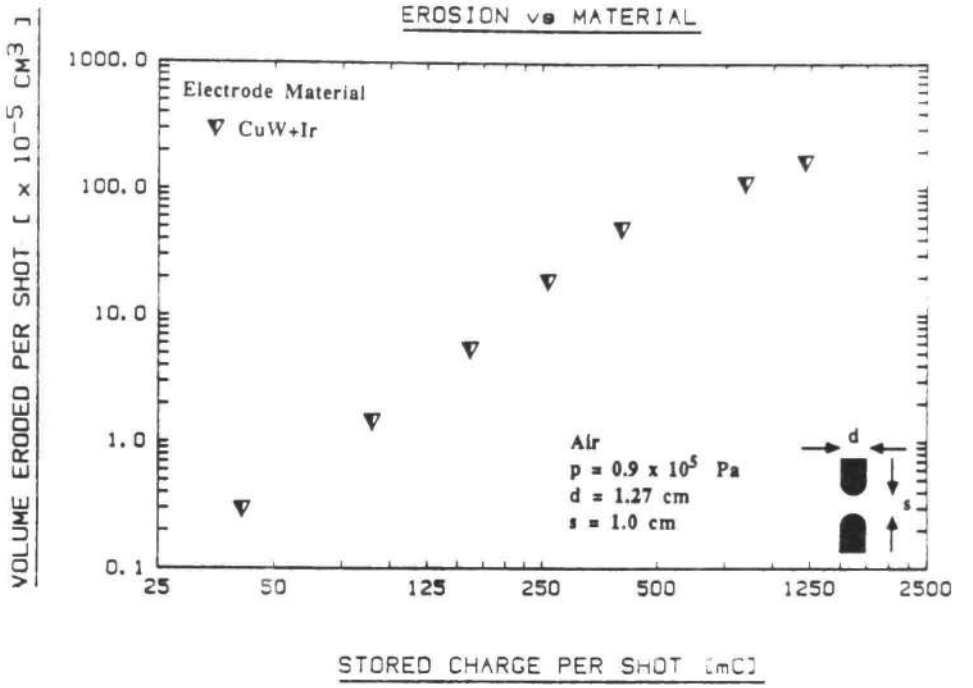

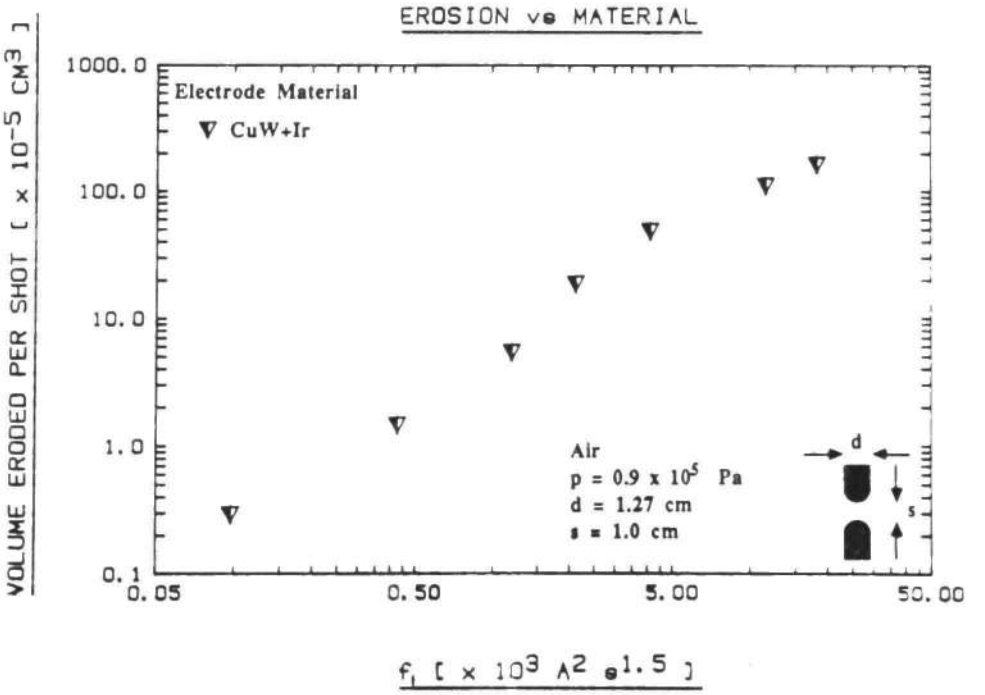

Fig. A.23 Erosion for CuW+Ir 1.27 cm Diameter Electrodes vs. a) Stored Charge and b) f_1.

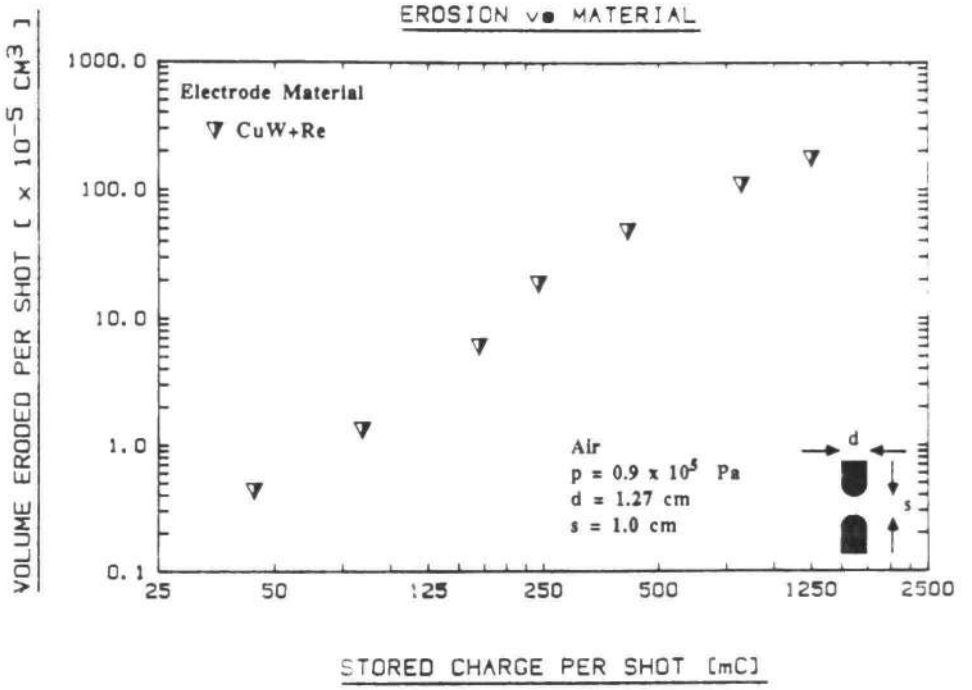

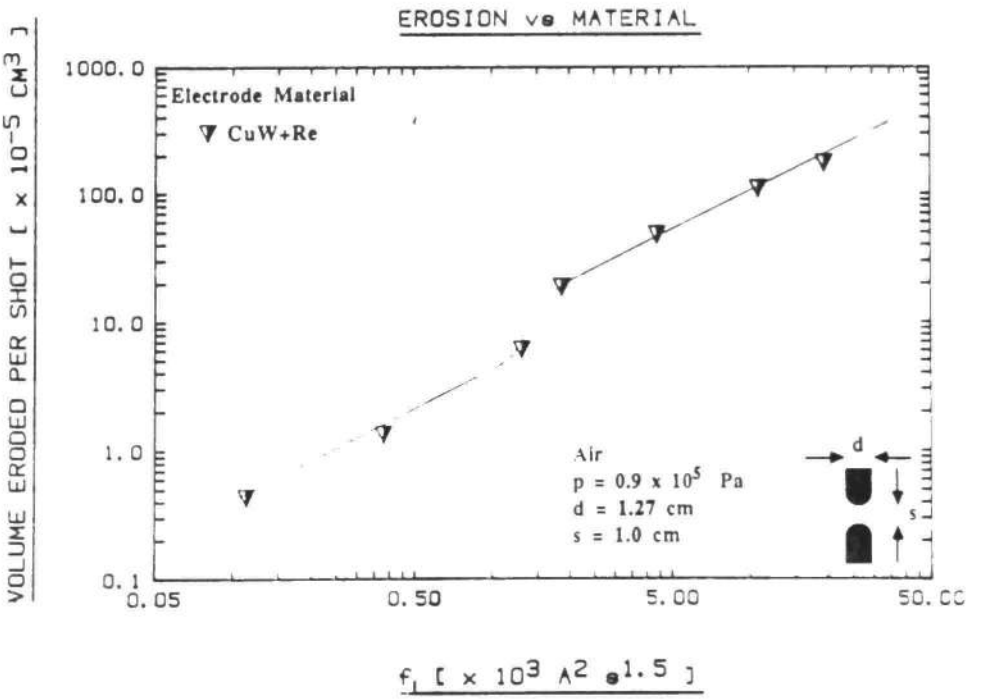

Fig. A.24 Erosion for CuW+Re 1.27 cm Diameter Electrodes vs. a) Stored Charge and b) f_1.

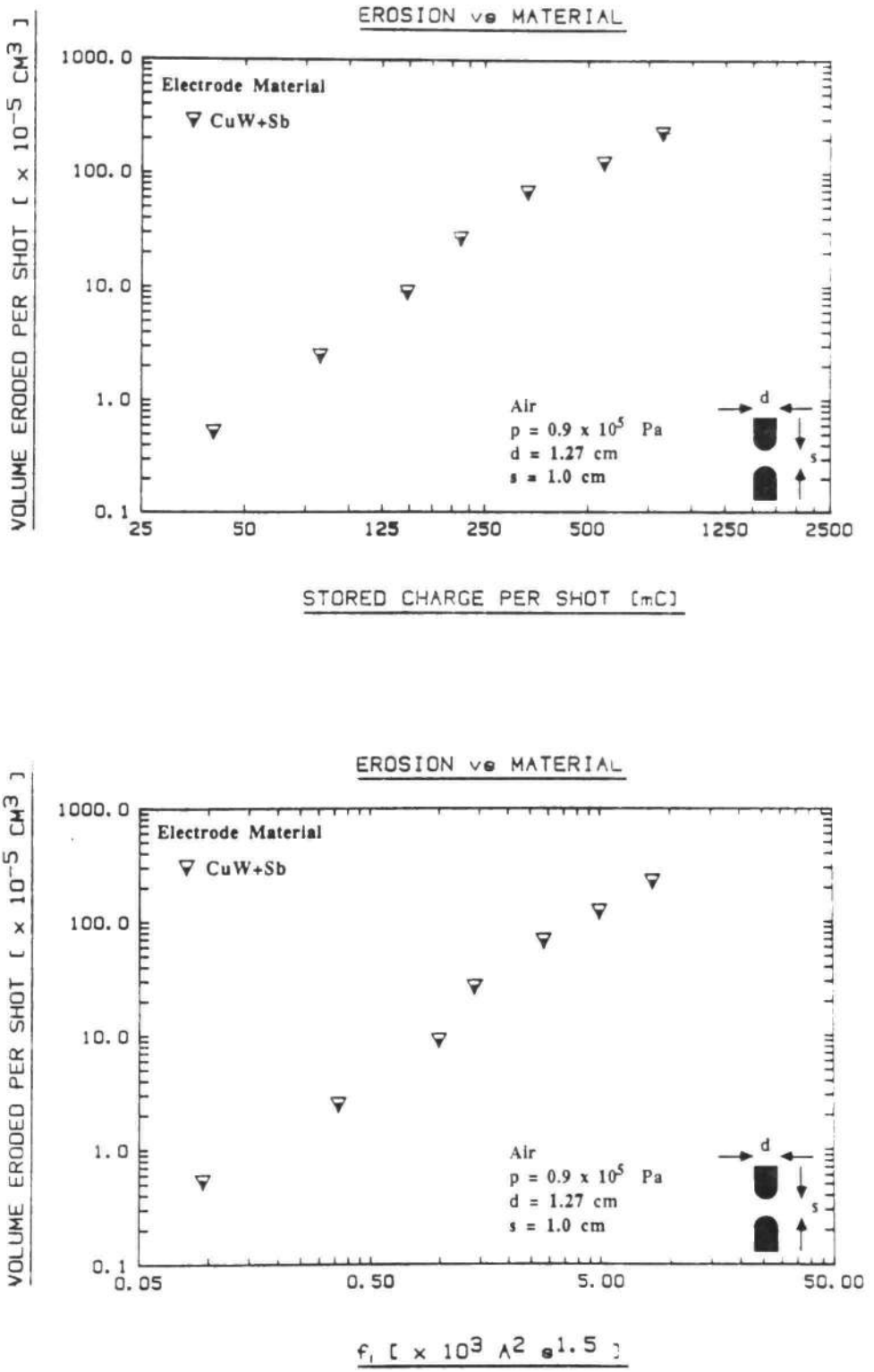

Fig. A.25 Erosion for CuW+Sb 1.27 cm Diameter Electrodes vs. a) Stored Charge and b) f_1.

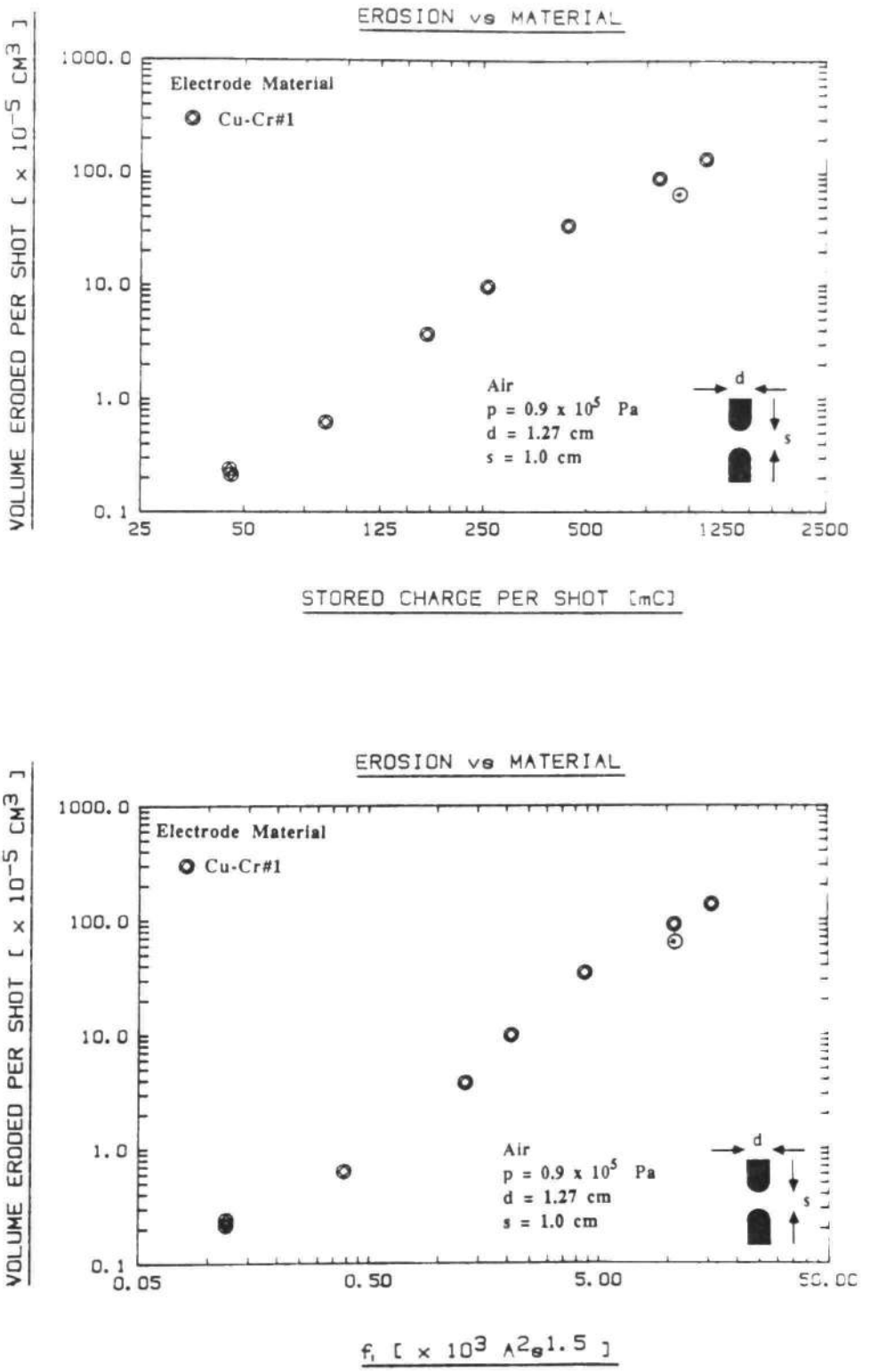

Fig. A.26 Erosion for Cu-Cr 1.27 cm Diameter Electrodes vs. a) Stored Charge and b) f_1.

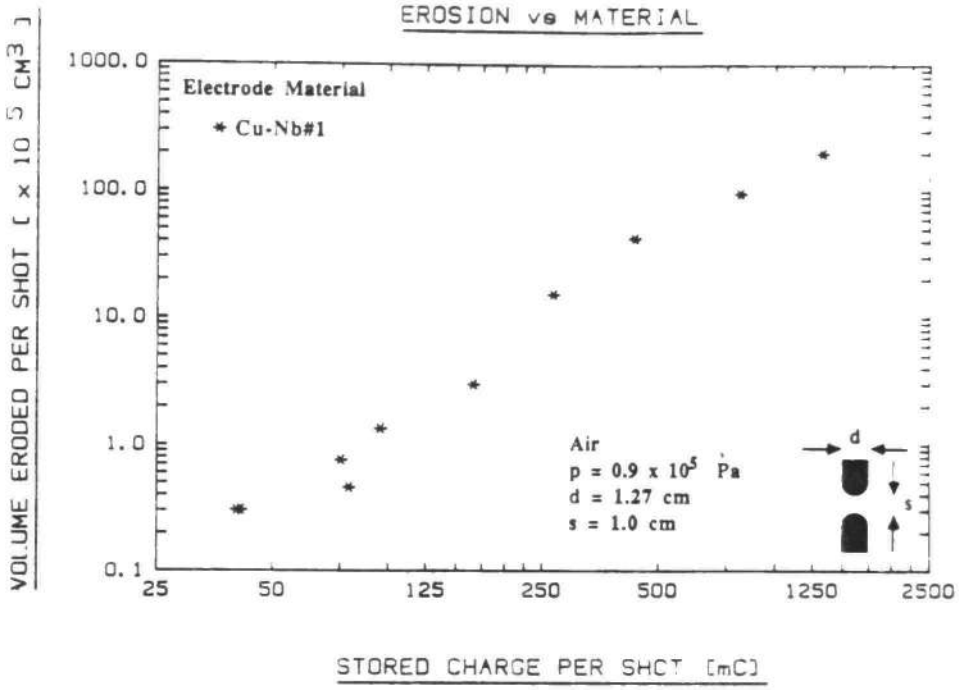

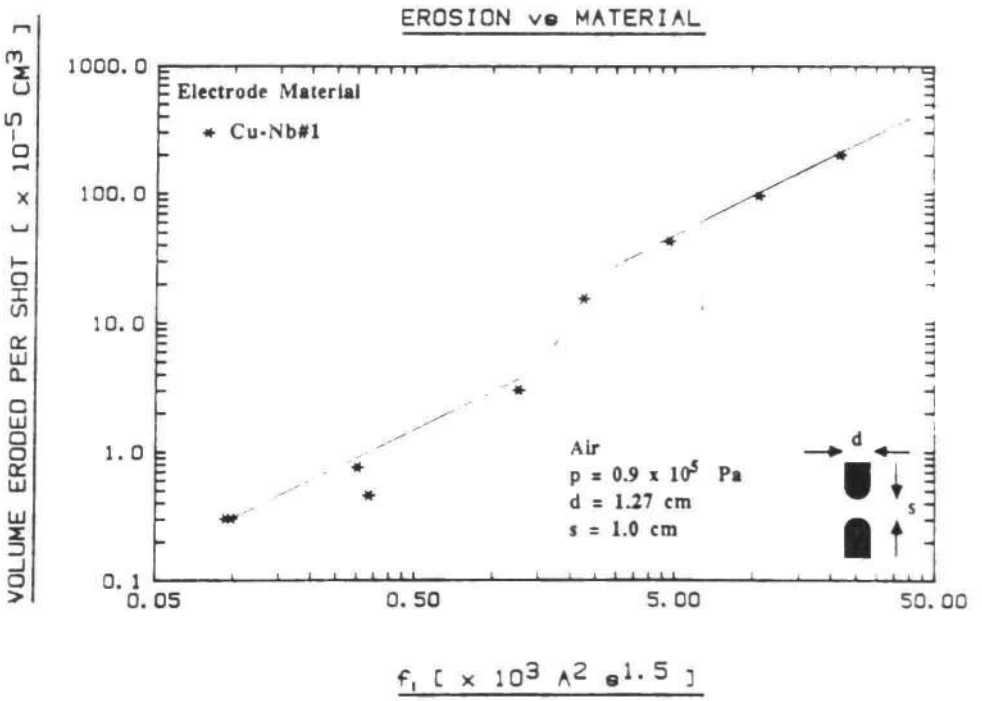

Fig. A.27 Erosion for Cu-Nb#1 1.27 cm Diameter Electrodes vs. a) Stored Charge and b) f_1.

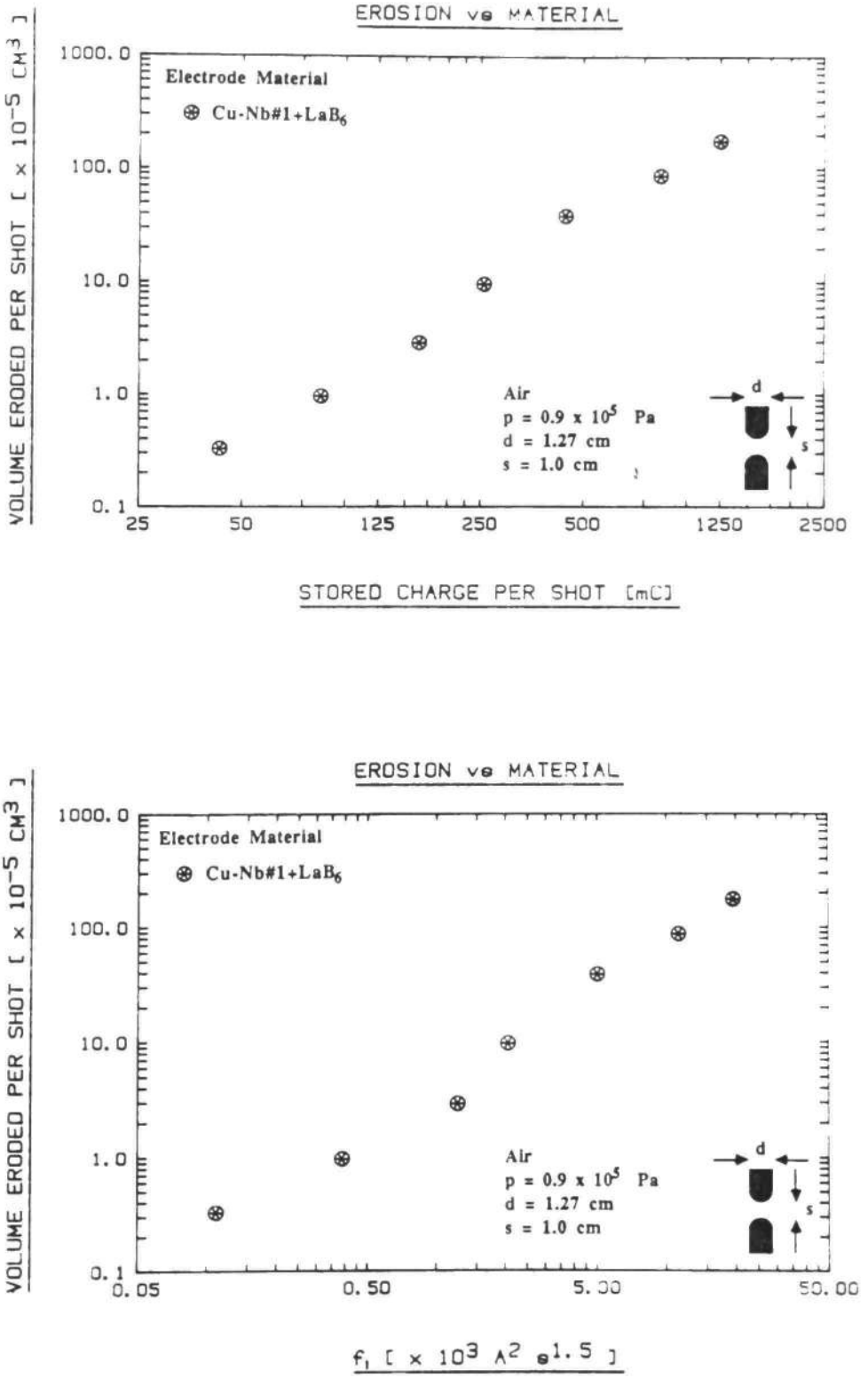

Fig. A.28 Erosion for Cu-Nb#1+LaB_6 1.27 cm Diameter Electrodes vs. a) Stored Charge and b) f_1.

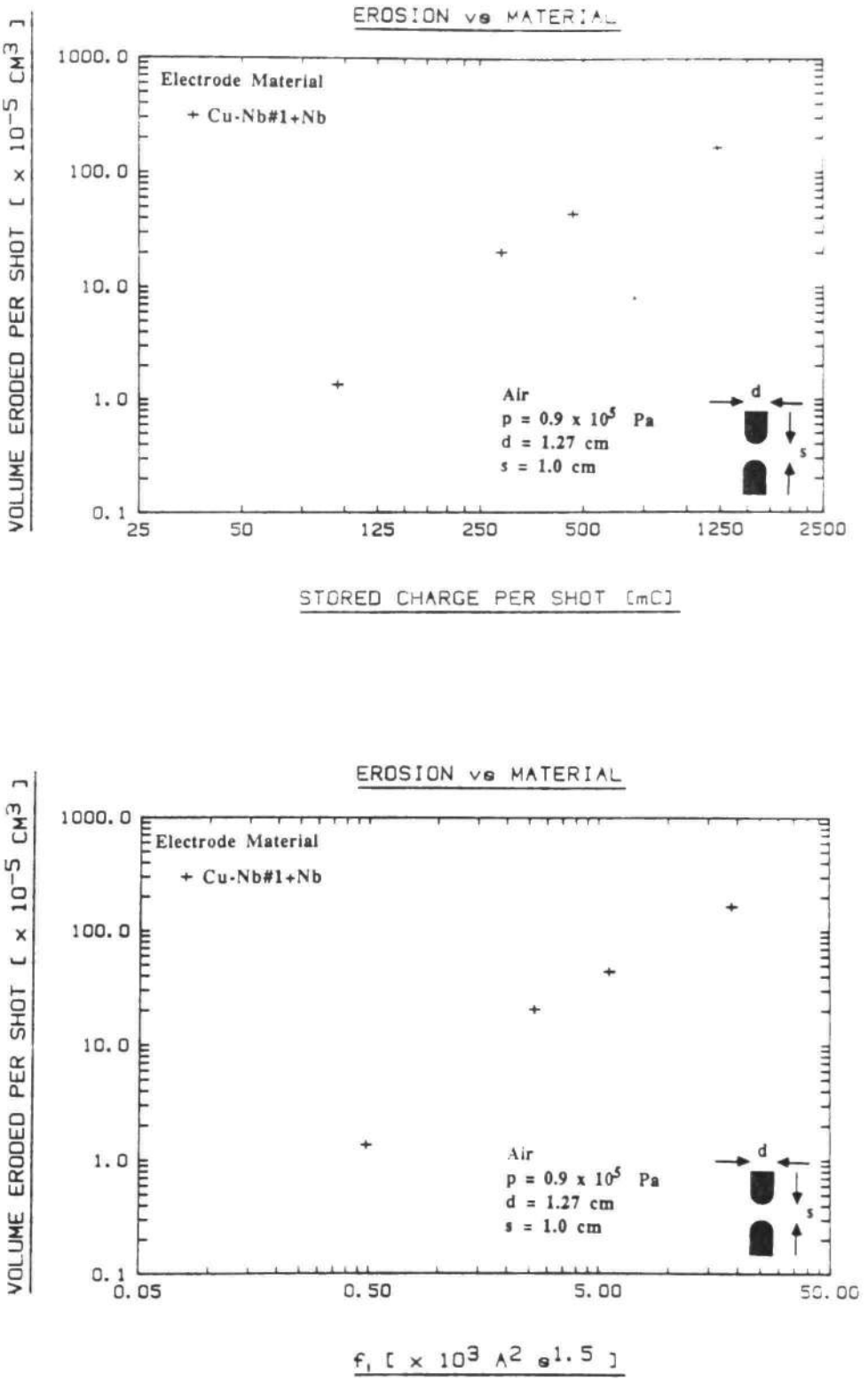

Fig. A.29 Erosion for Cu-Nb#1+Nb Clad 1.27 cm Diameter Electrodes vs. a) Stored Charge and b) f_1.

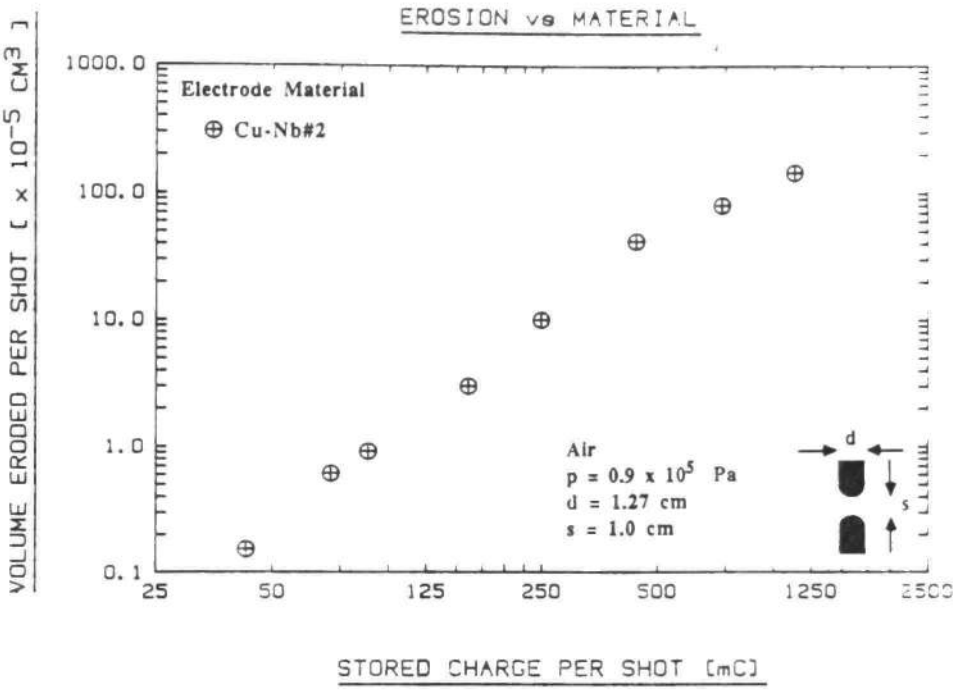

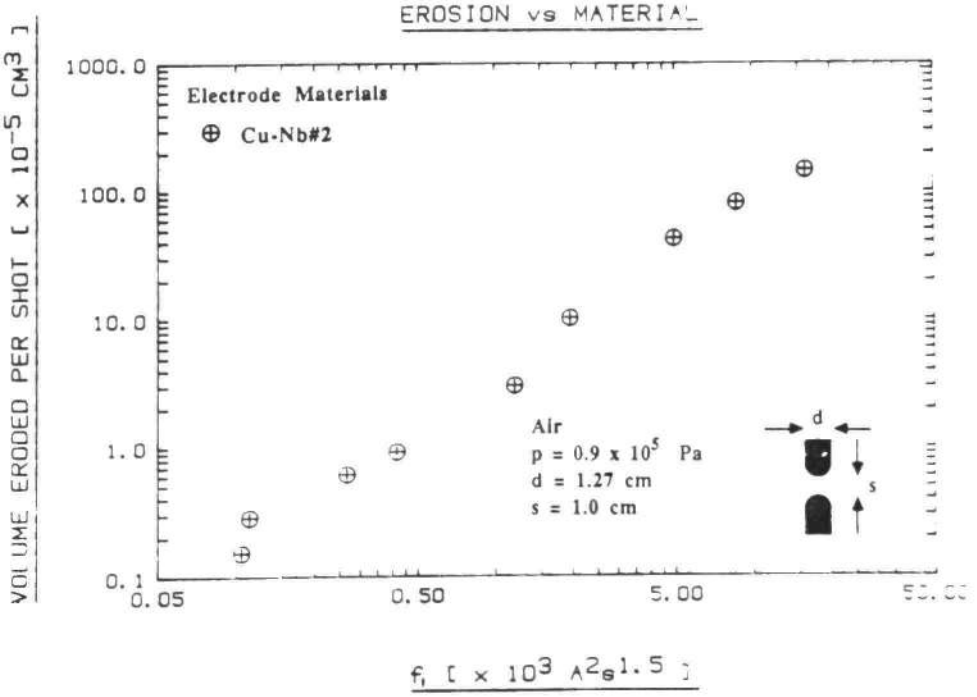

Fig. A.30 Erosion for Cu-Nb#2 1.27 cm Diameter Electrodes vs. a) Stored Charge and b) f_1.

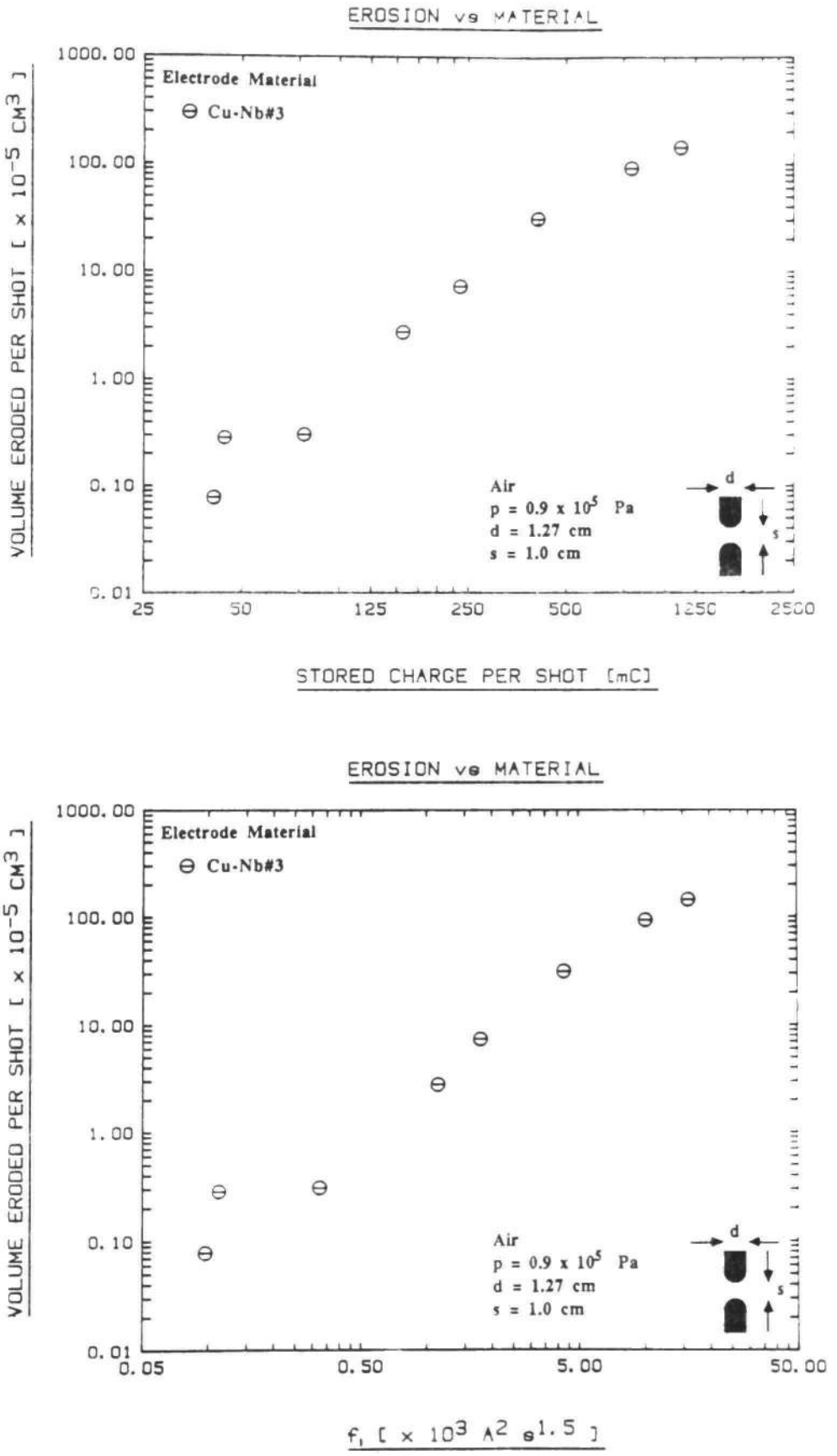

Fig. A.31 Erosion for Cu-Nb#3 1.27 cm Diameter Electrodes vs. a) Stored Charge and b) f_1.

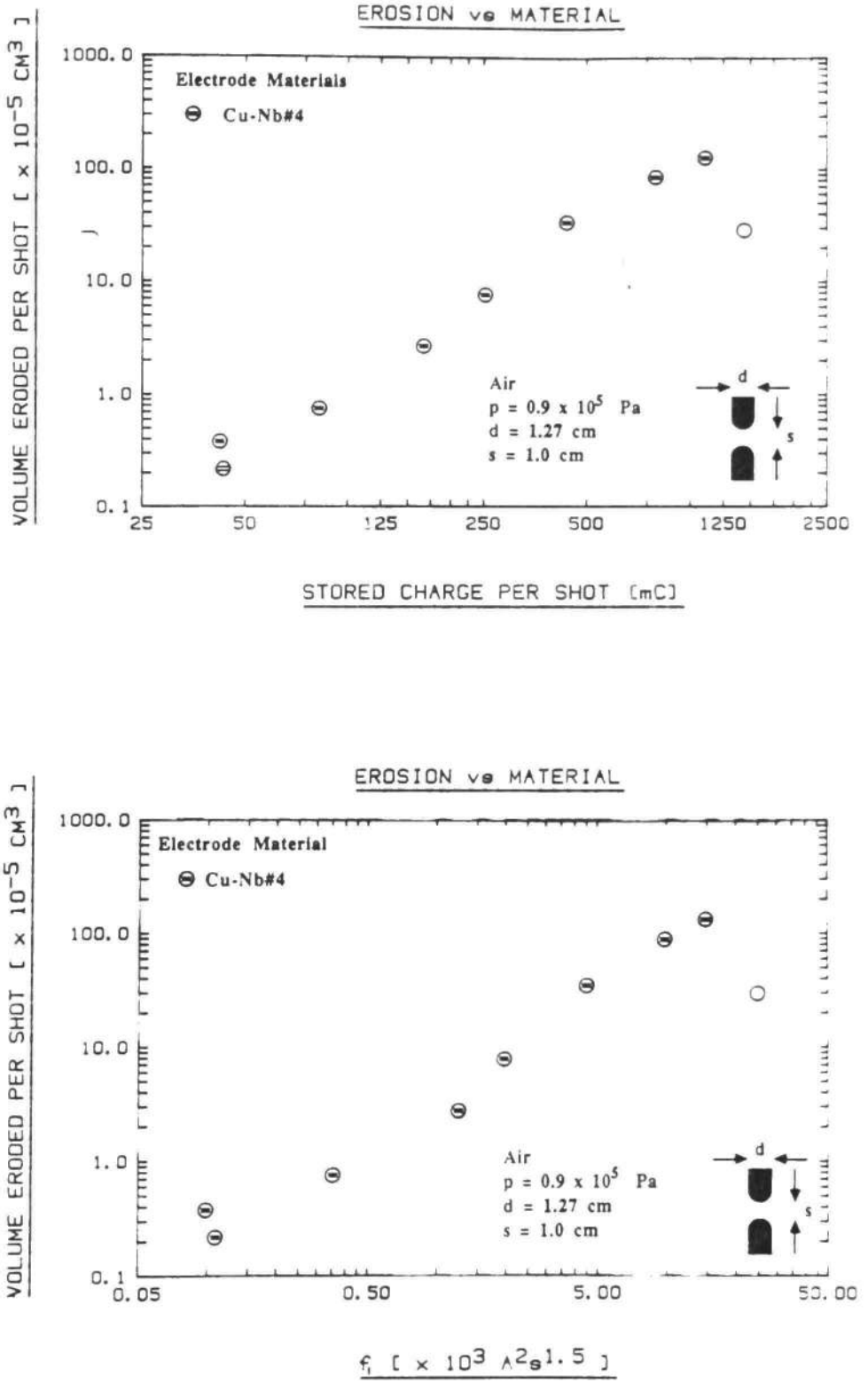

Fig. A.32 Erosion for Cu-Nb#4 1.27 cm Diameter Electrodes vs. a) Stored Charge and b) f_1.

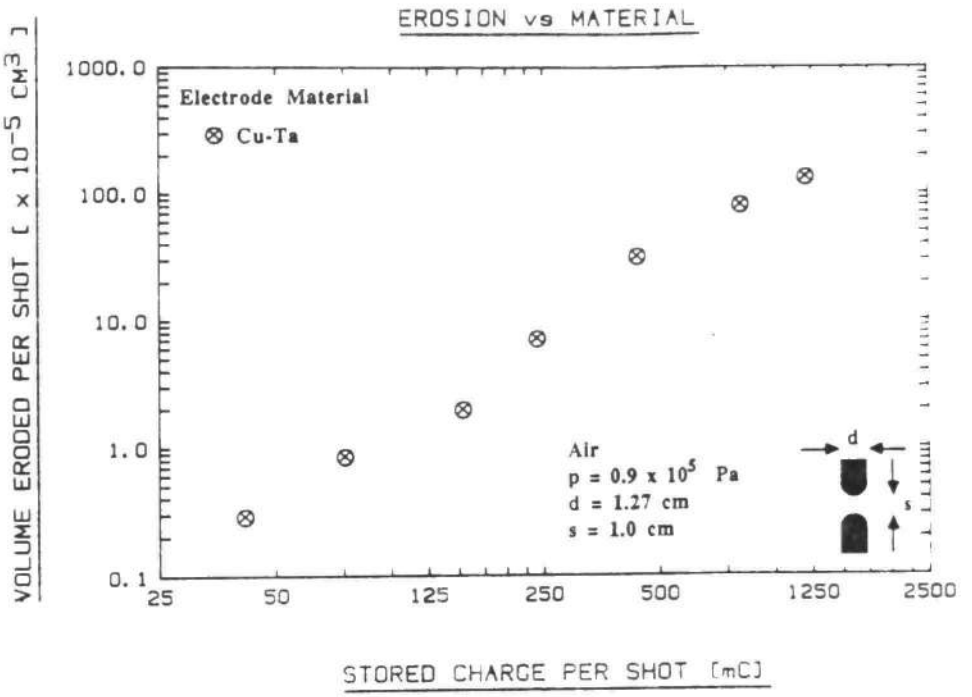

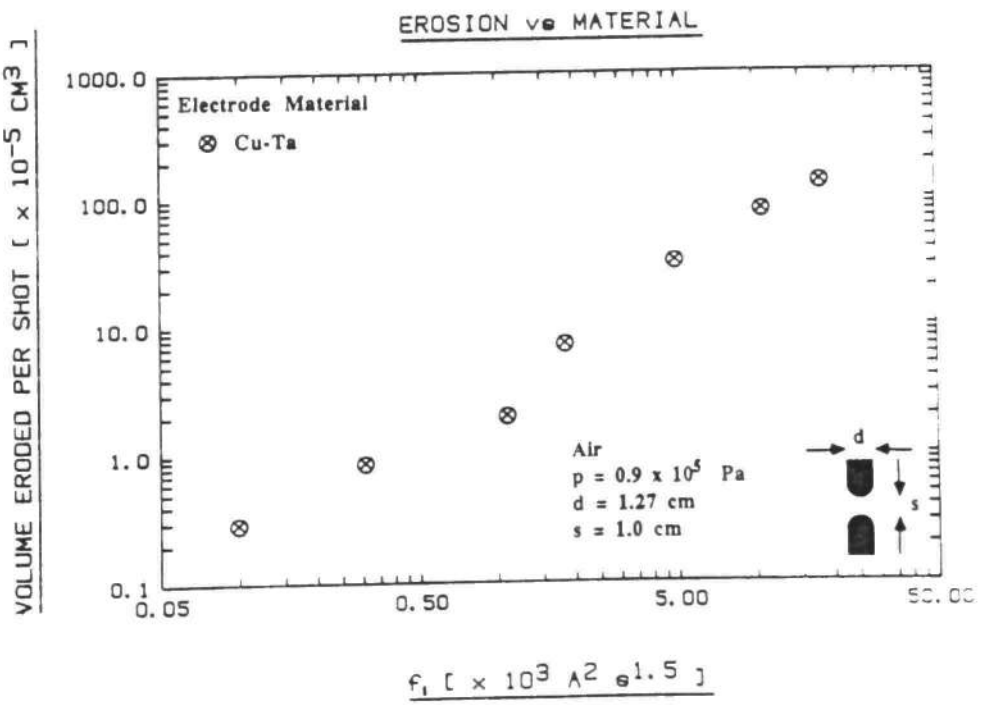

Fig. A.33 Erosion for Cu-Ta#1 1.27 cm Diameter Electrodes vs. a) Stored Charge and b) f_1.

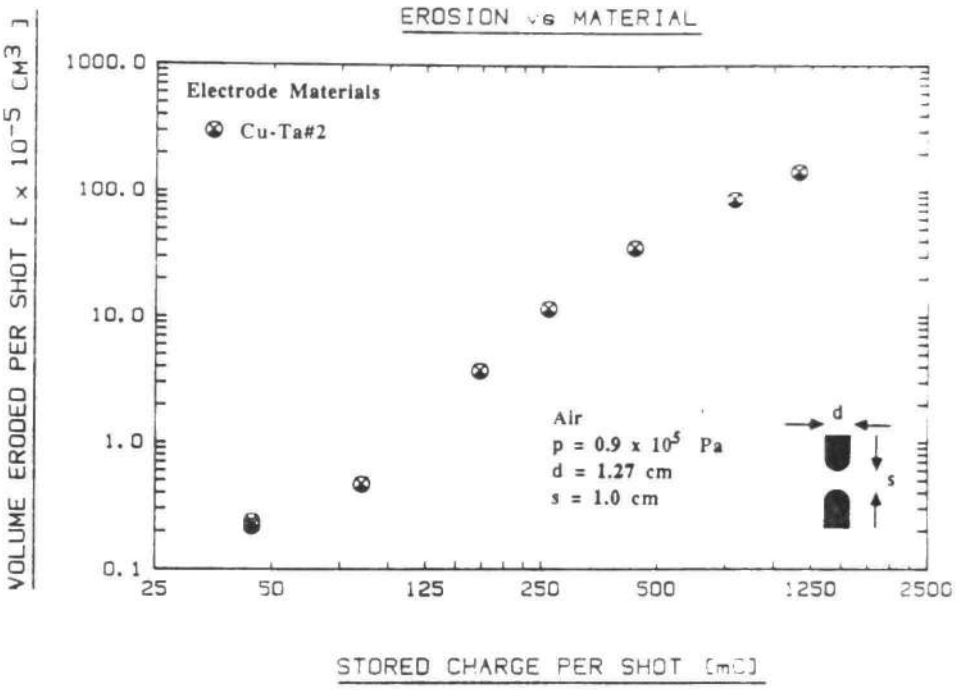

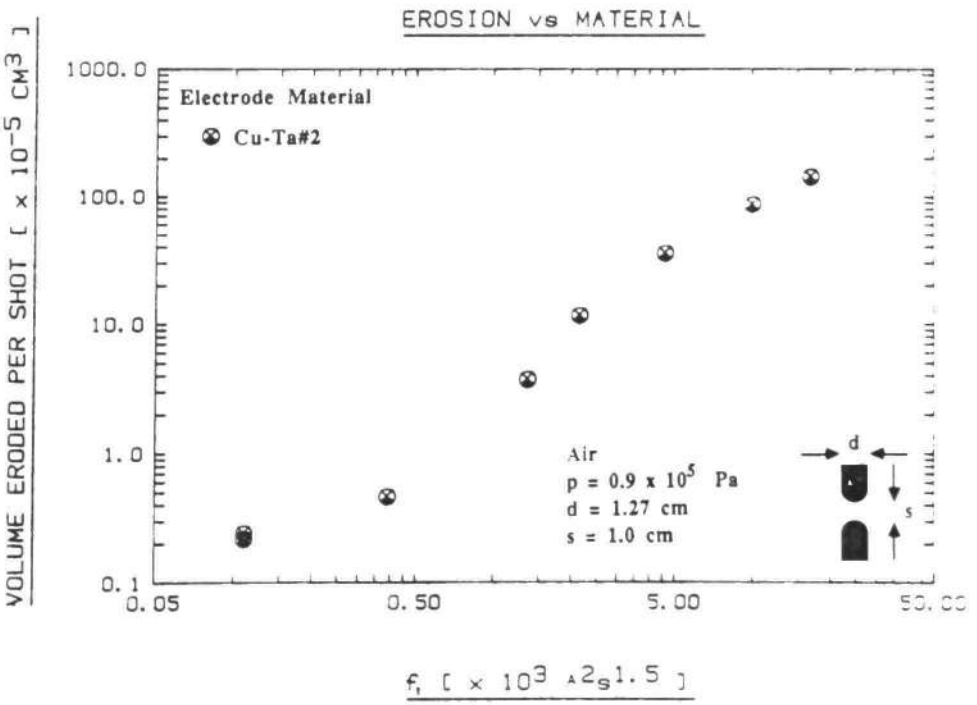

Fig. A.34 Erosion for Cu-Ta=2 1.27 cm Diameter Electrodes vs. a) Stored Charge and b) f_1.

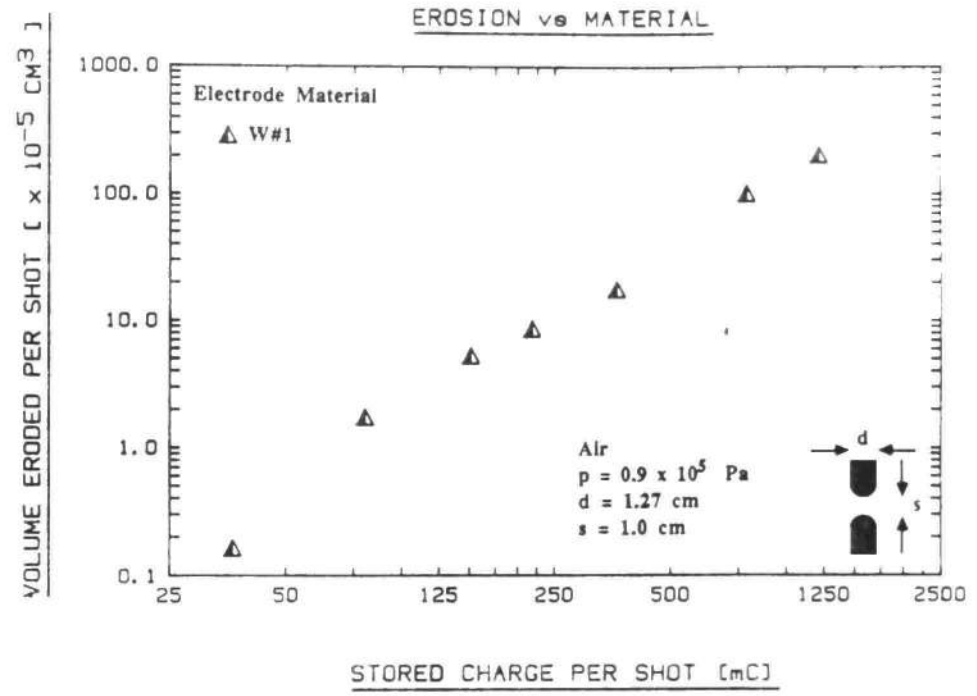

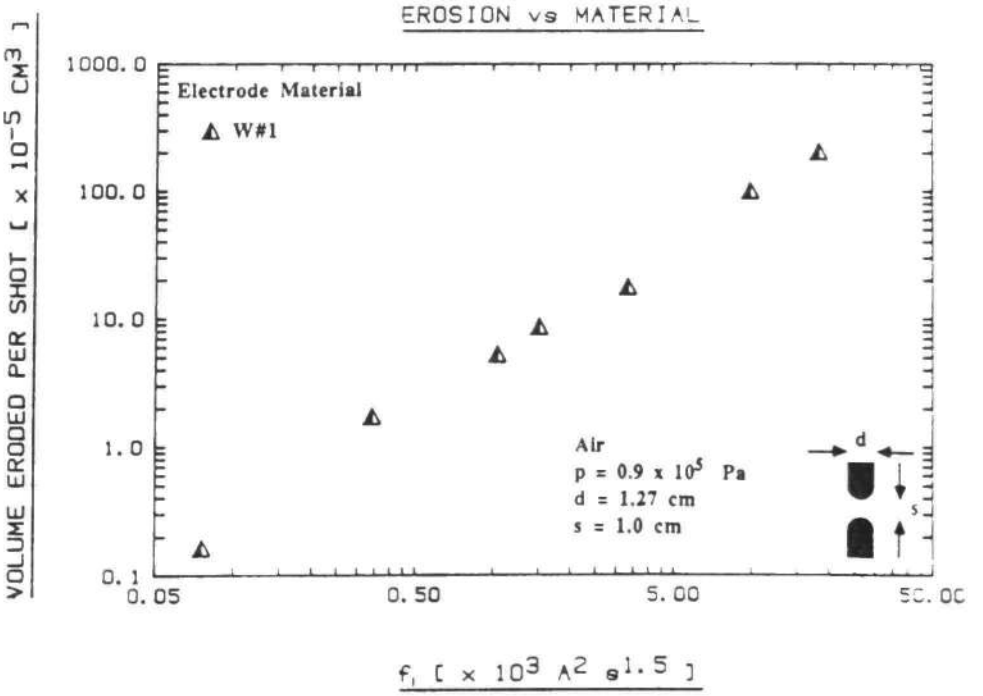

Fig. A.35 Erosion for W#1 1.27 cm Diameter Electrodes vs. a) Stored Charge and b) f_1.

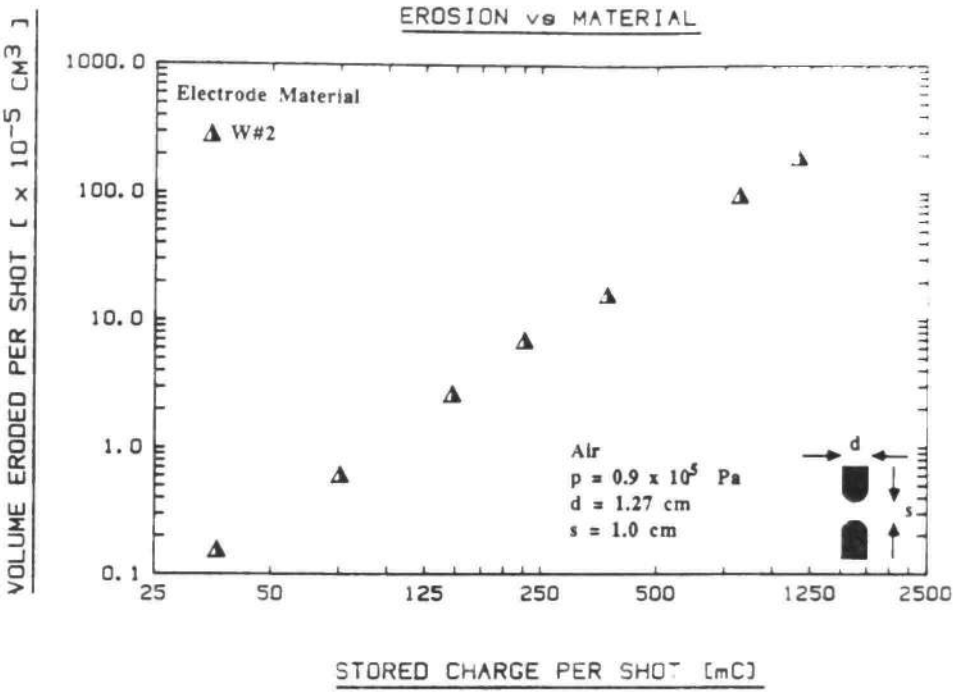

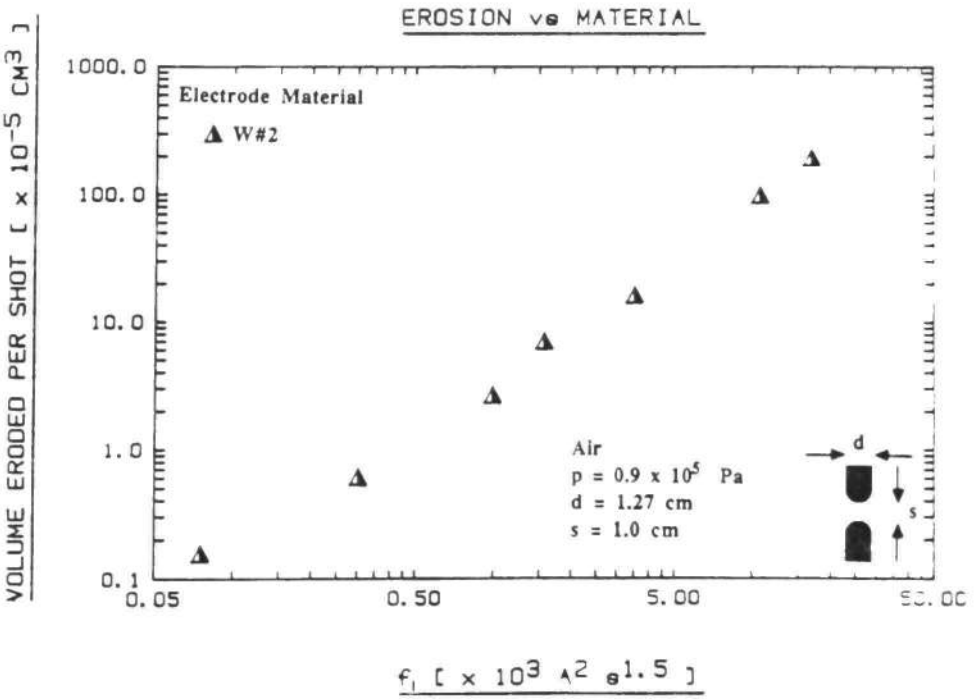

Fig. A.36 Erosion for W#2 1.27 cm Diameter Electrodes vs. a) Stored Charge and b) f_1.

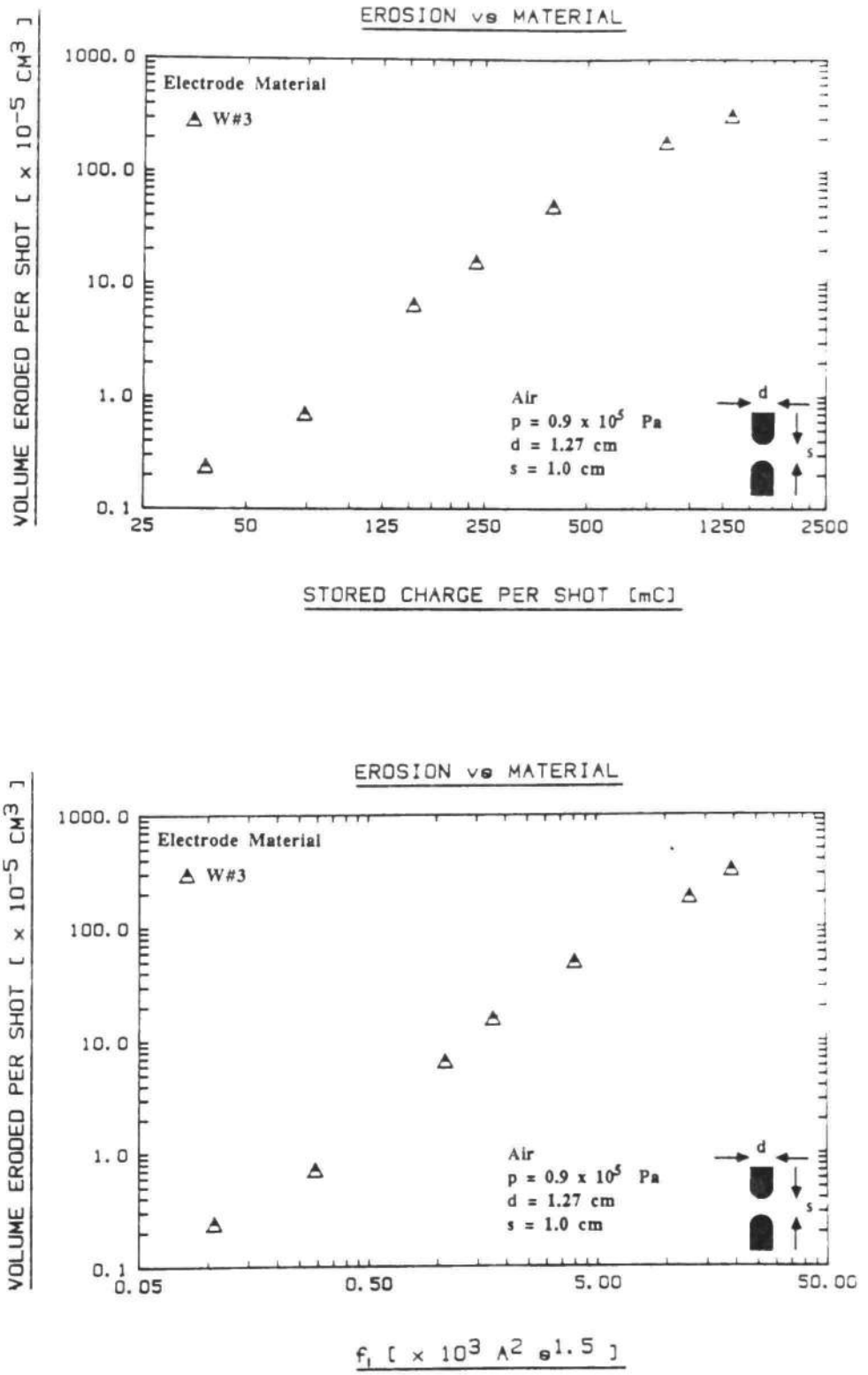

Fig. A.37 Erosion for W#3 1.27 cm Diameter Electrodes vs. a) Stored Charge and b) f_1.

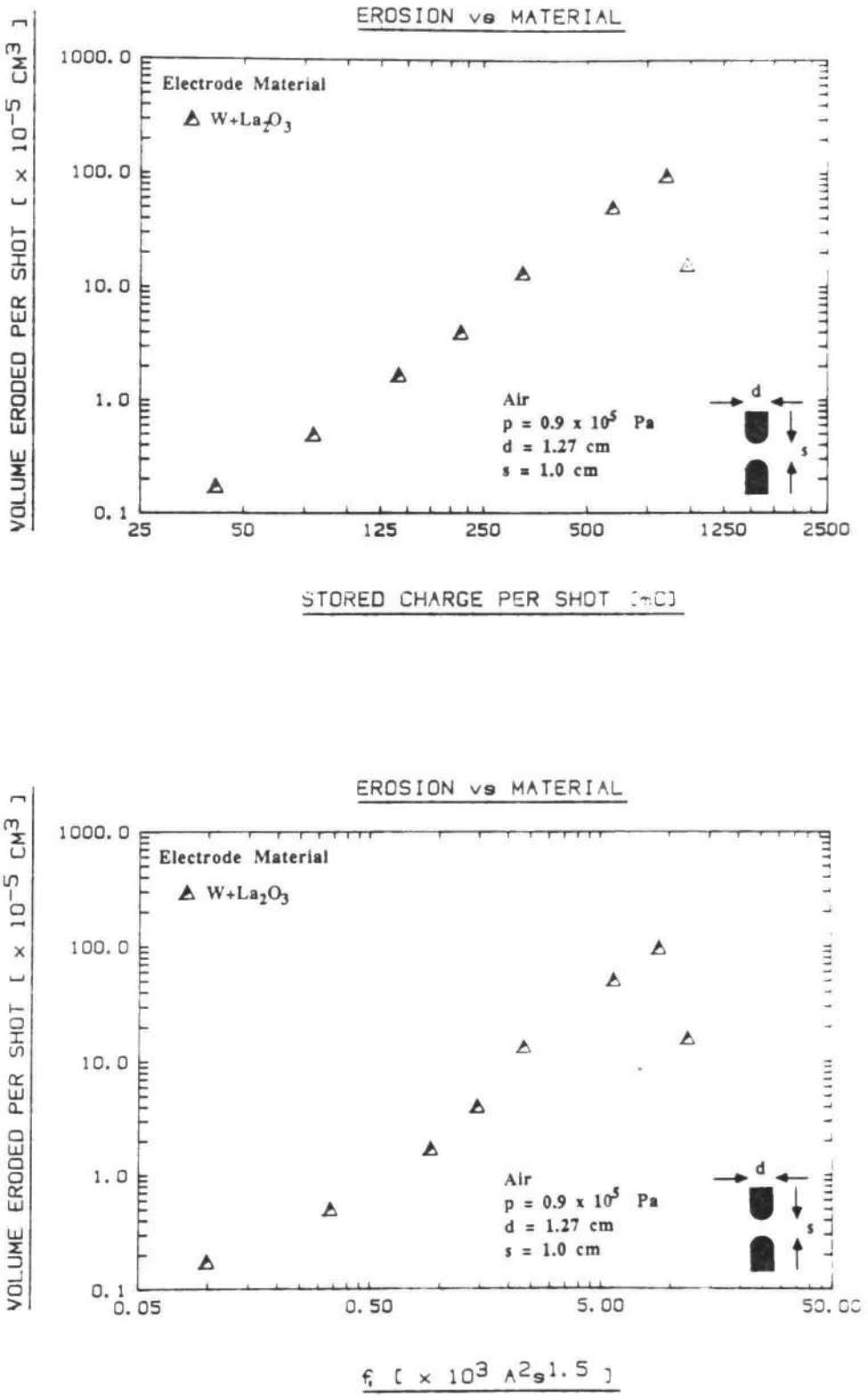

Fig. A.38 Erosion for $W+La_2O_3$ 1.27 cm Diameter Electrodes vs. a) Stored Charge and b) f_1.

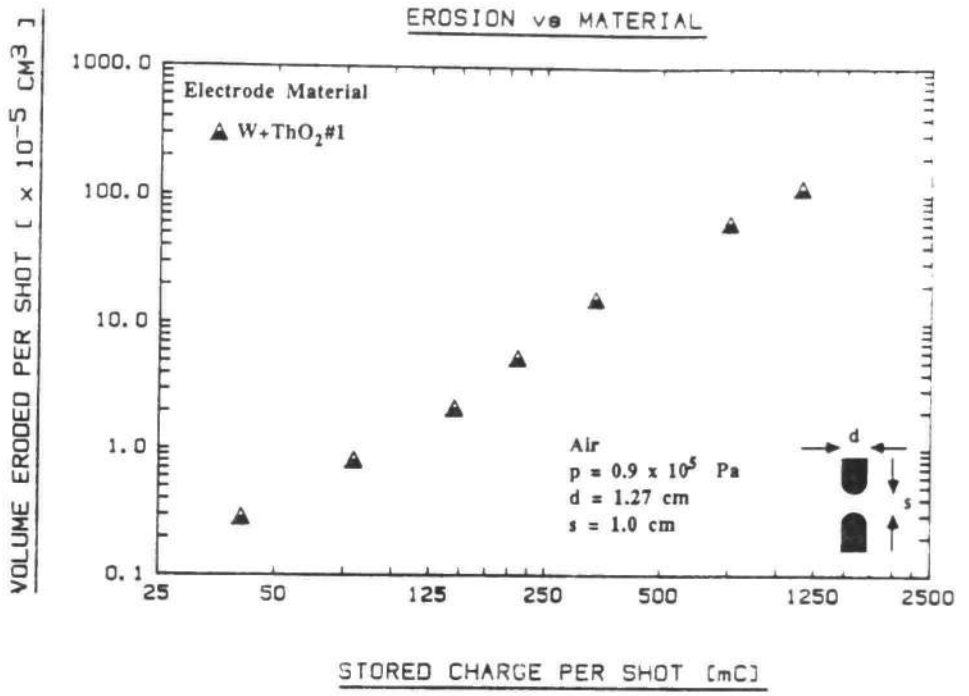

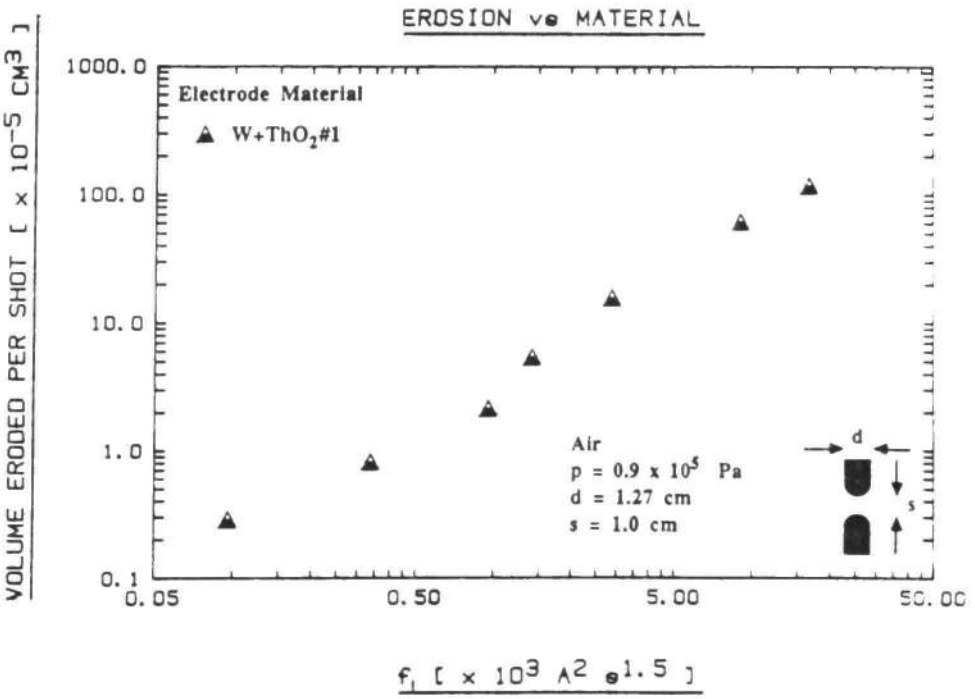

Fig. A.39 Erosion for W+ThO_2#1 1.27 cm Diameter Electrodes vs. a) Stored Charge and b) f_1.

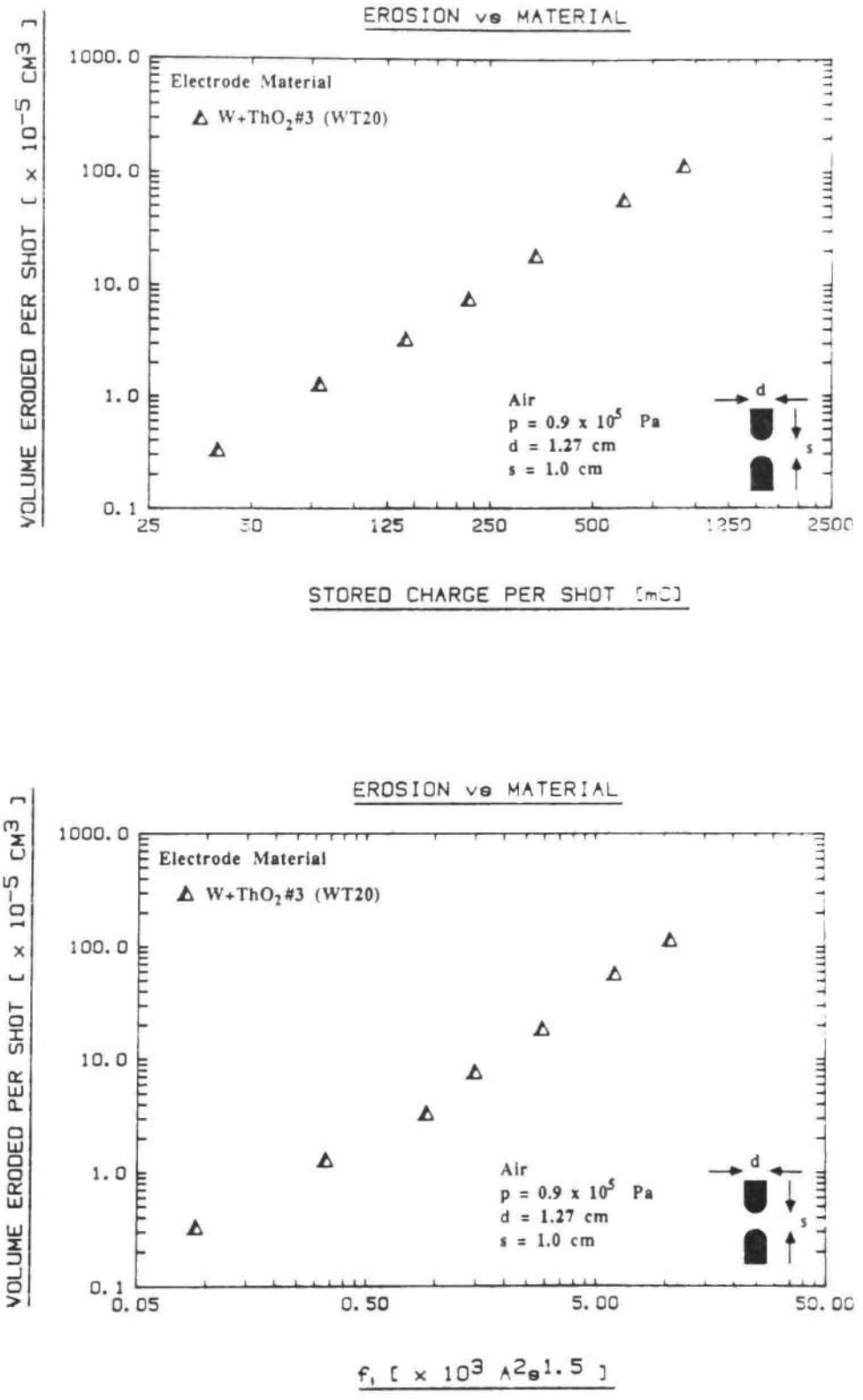

Fig. A.40 Erosion for W+ThO_2#3 1.27 cm Diameter Electrodes vs. a) Stored Charge and b) f_1.

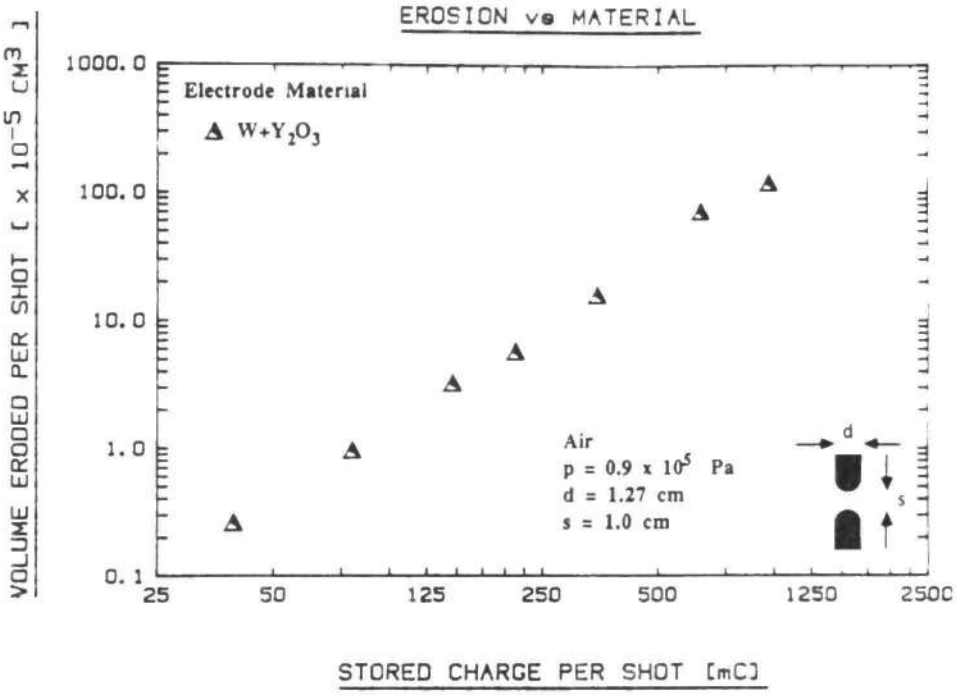

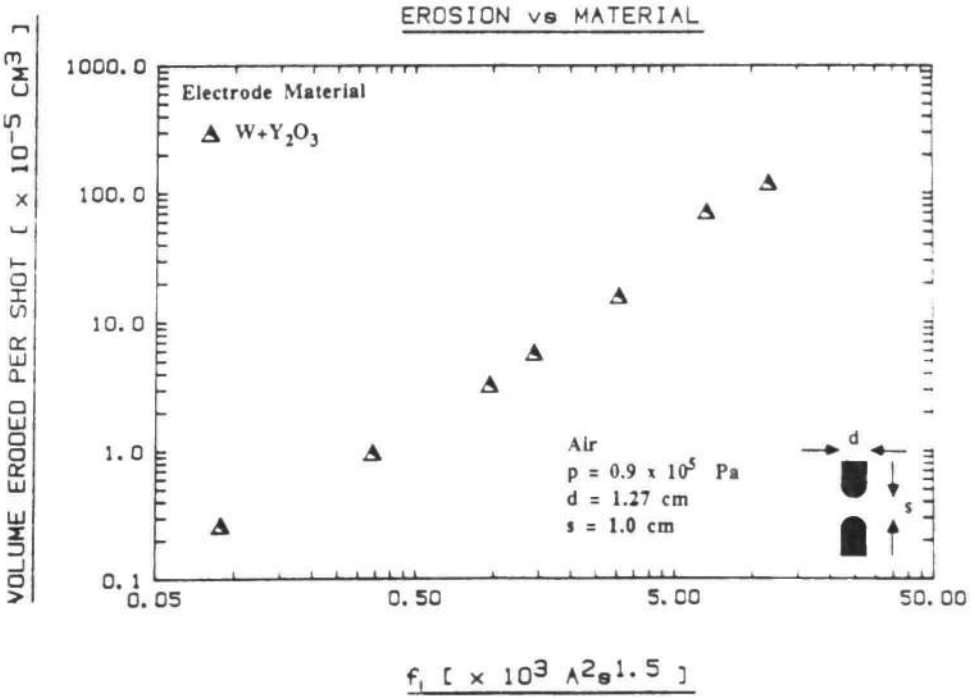

Fig. A.41 Erosion for $W+Y_2O_3$ 1.27 cm Diameter Electrodes vs. a) Stored Charge and b) f_1.

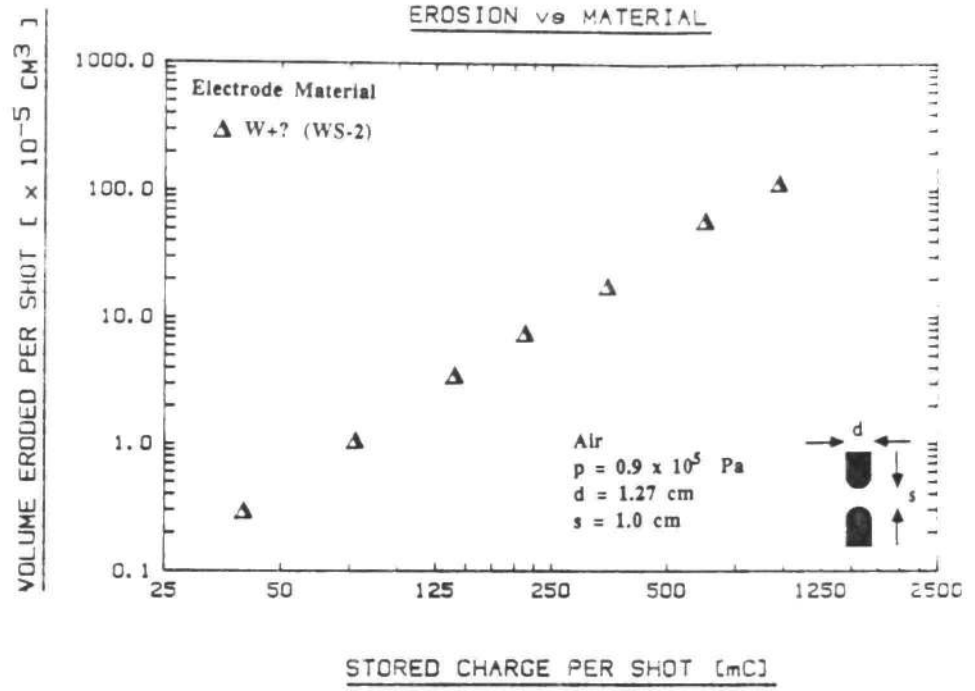

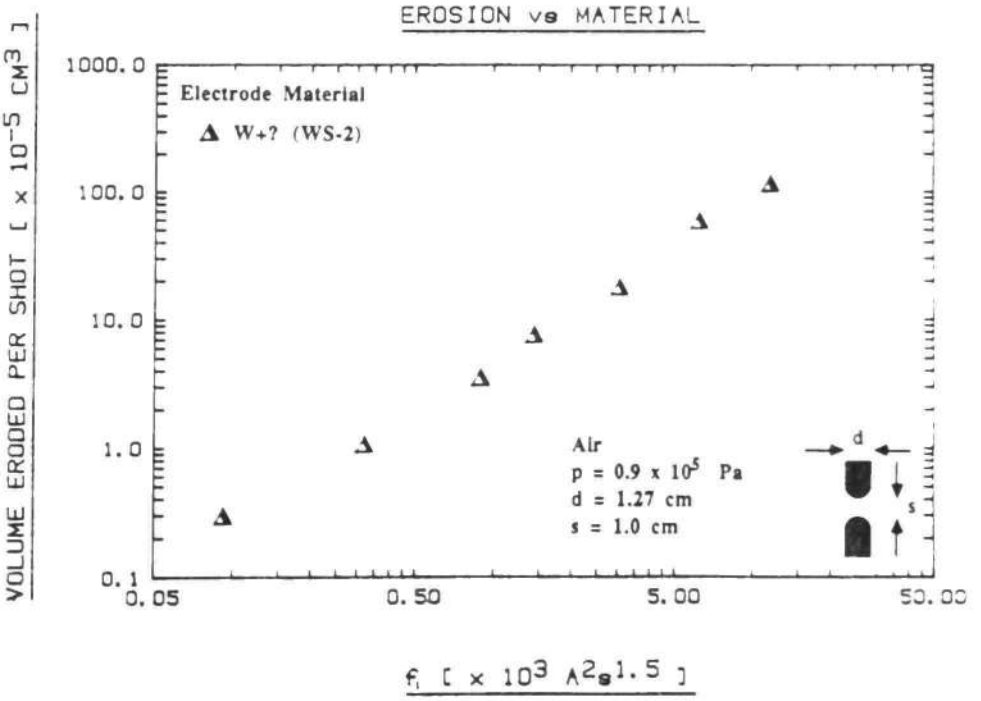

Fig. A.42 Erosion for W+?(WS-2) 1.27 cm Diameter Electrodes vs. a) Stored Charge and b) f_1.

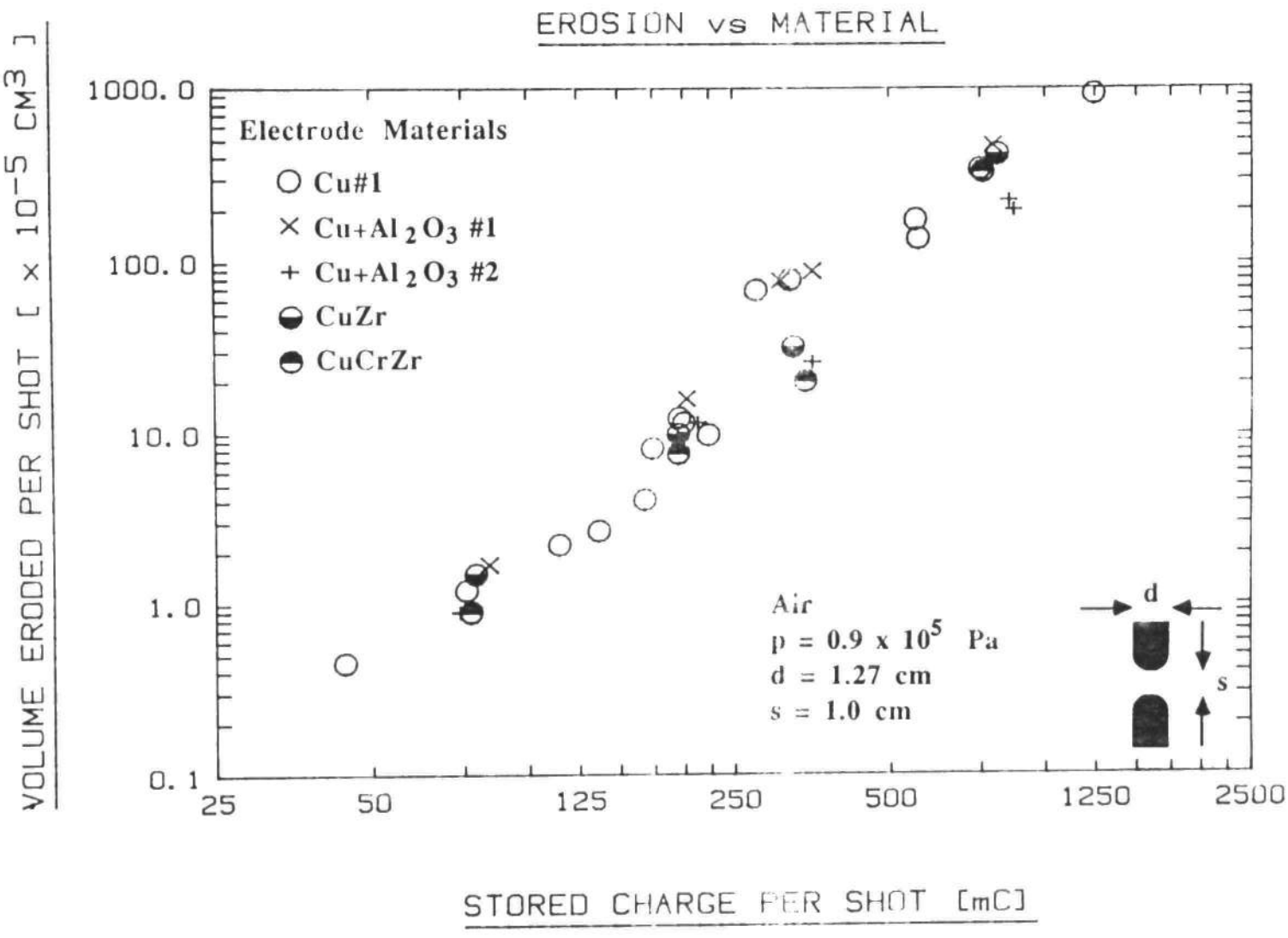

Fig. A.43 Comparison of 1.27 cm Diameter Cu Alloy Electrode Erosion vs. Stored Charge.

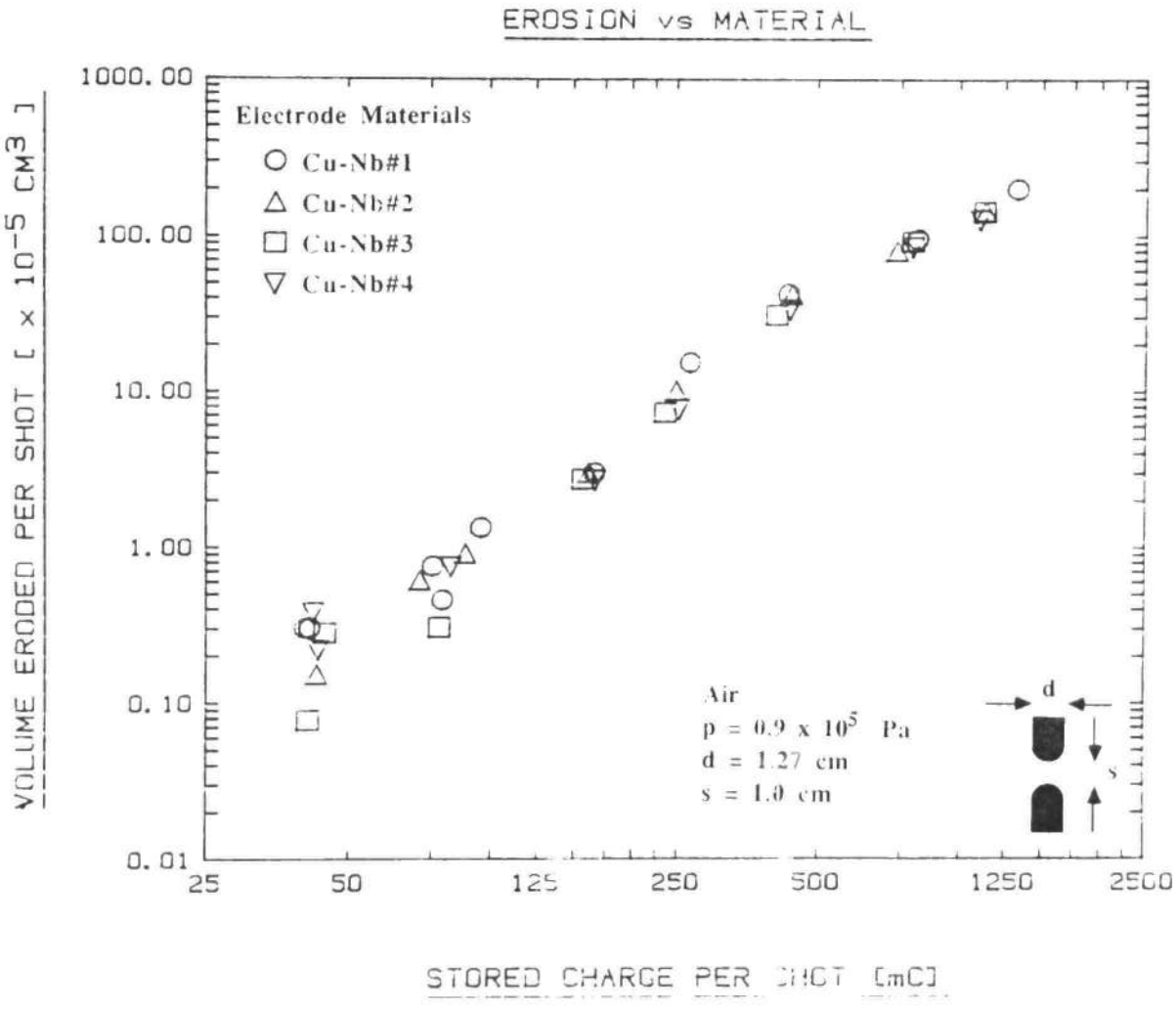

Fig. A.44 Comparison of 1.27 cm Diameter Cu-Nb Electrode Erosion vs. Stored Charge.

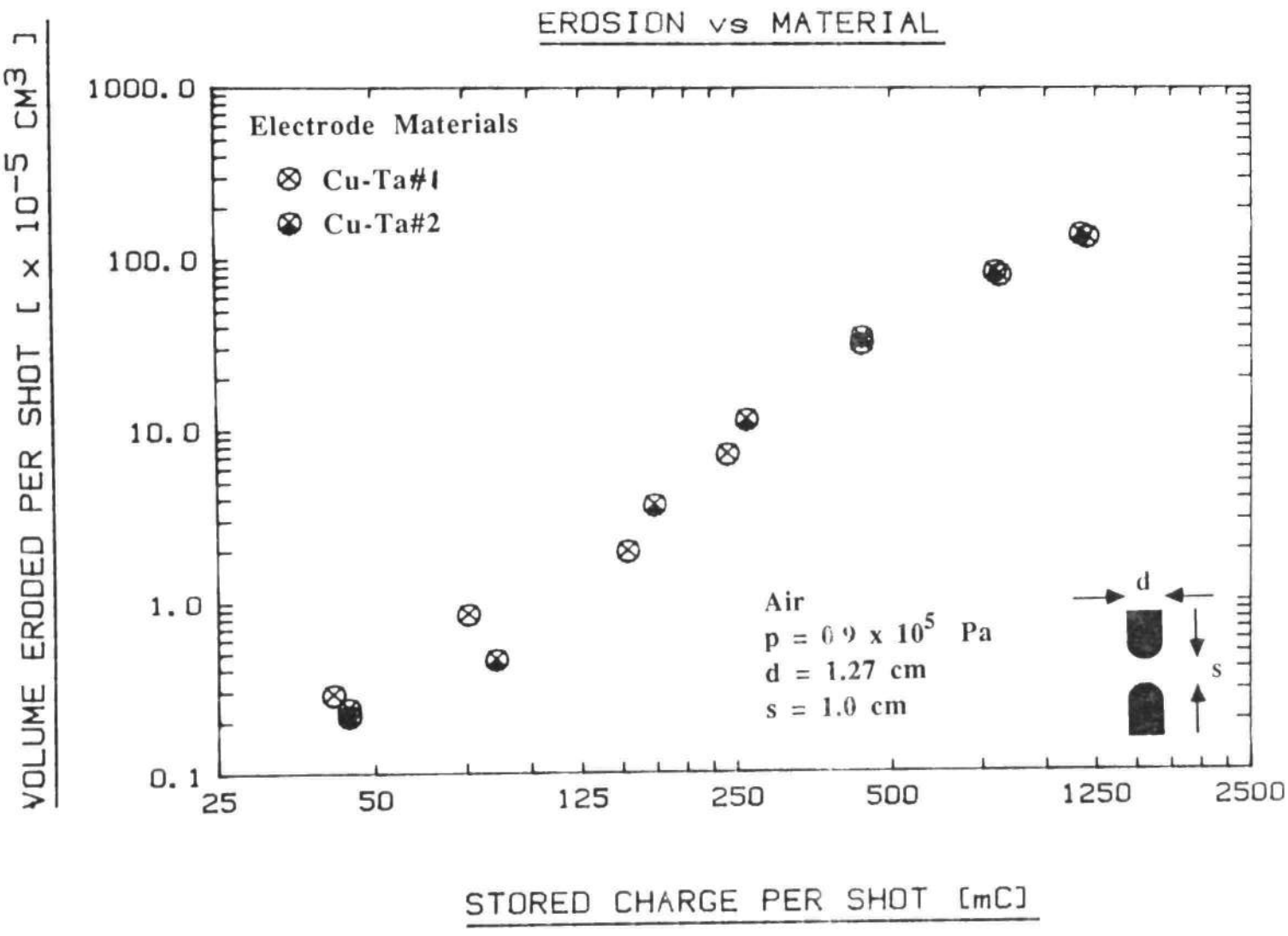

Fig. A.45 Comparison of 1.27 cm Diameter Cu-Ta Electrode Erosion vs. Stored Charge.

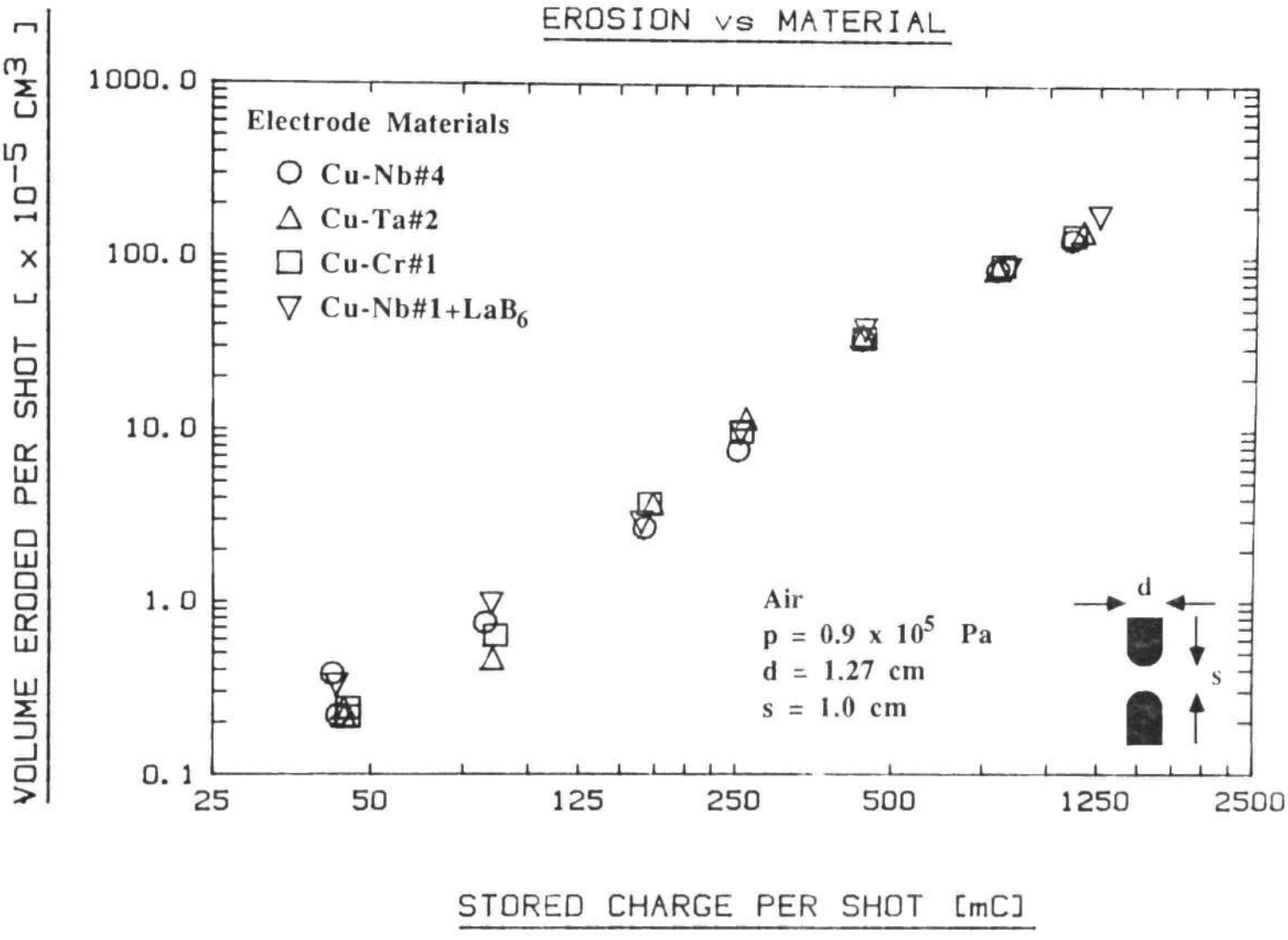

Fig. A.46 Comparison of 1.27 cm Diameter In-Situ Electrode Erosion vs. Stored Charge.

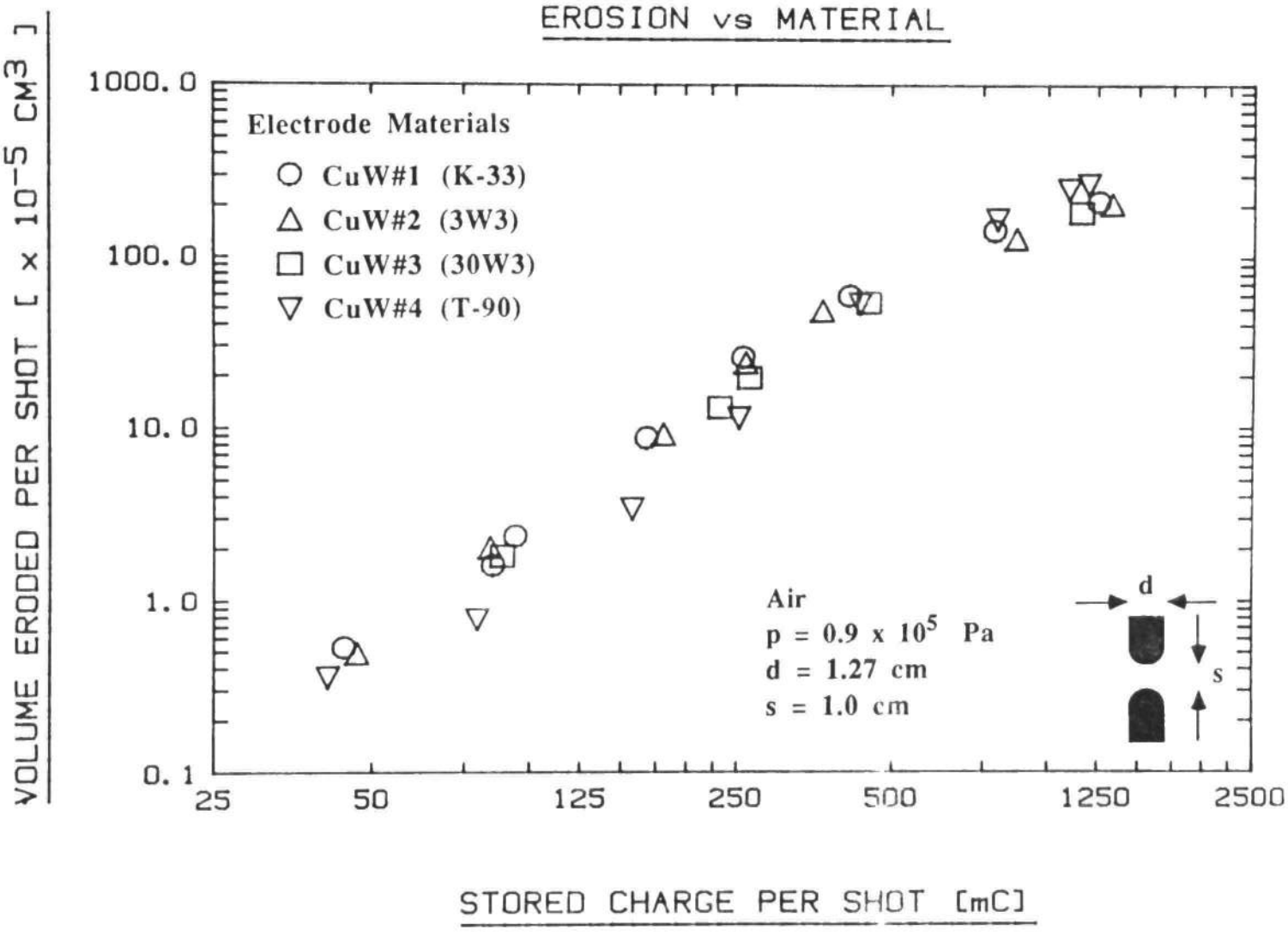

Fig. A.47 Comparison of 1.27 cm Diameter CuW Electrode Erosion vs. Stored Charge.

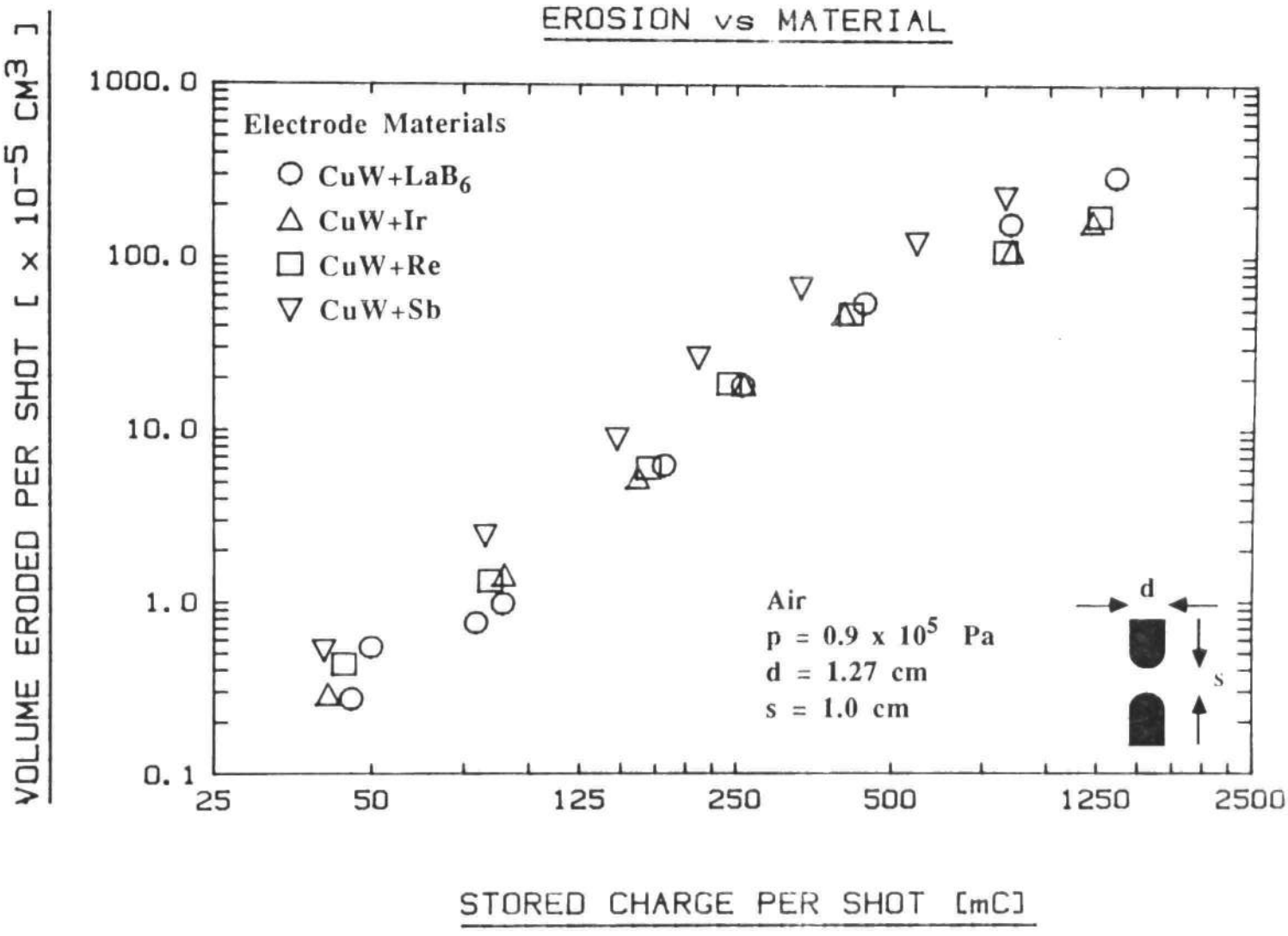

Fig. A.48 Comparison of 1.27 cm Diameter CuW+Rare Earth Oxide Electrode Erosion vs. Stored Charge.

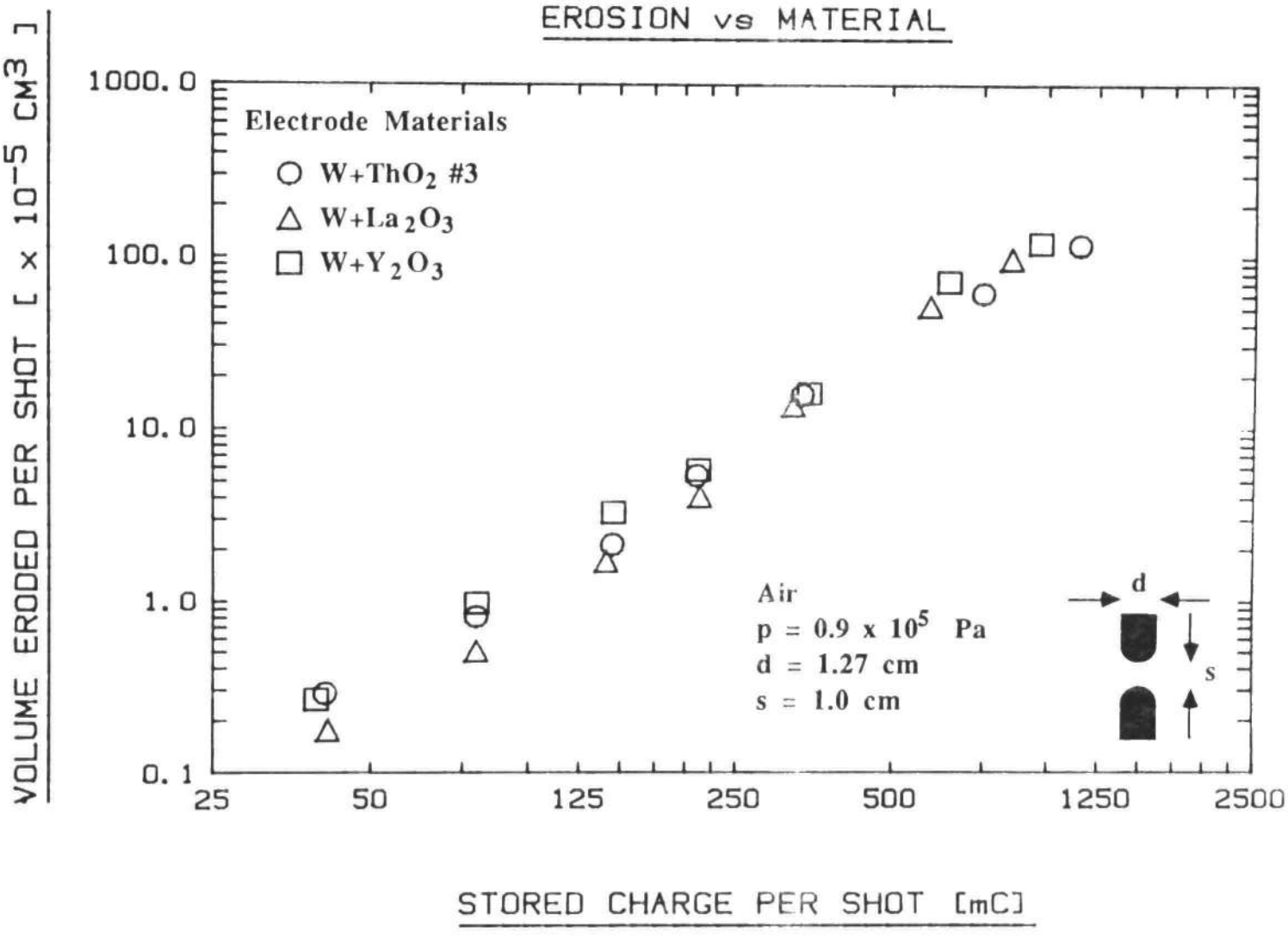

Fig. A.49 Comparison of 1.27 cm Diameter W+Rare Earth Oxides Electrode Erosion vs. Stored Charge.

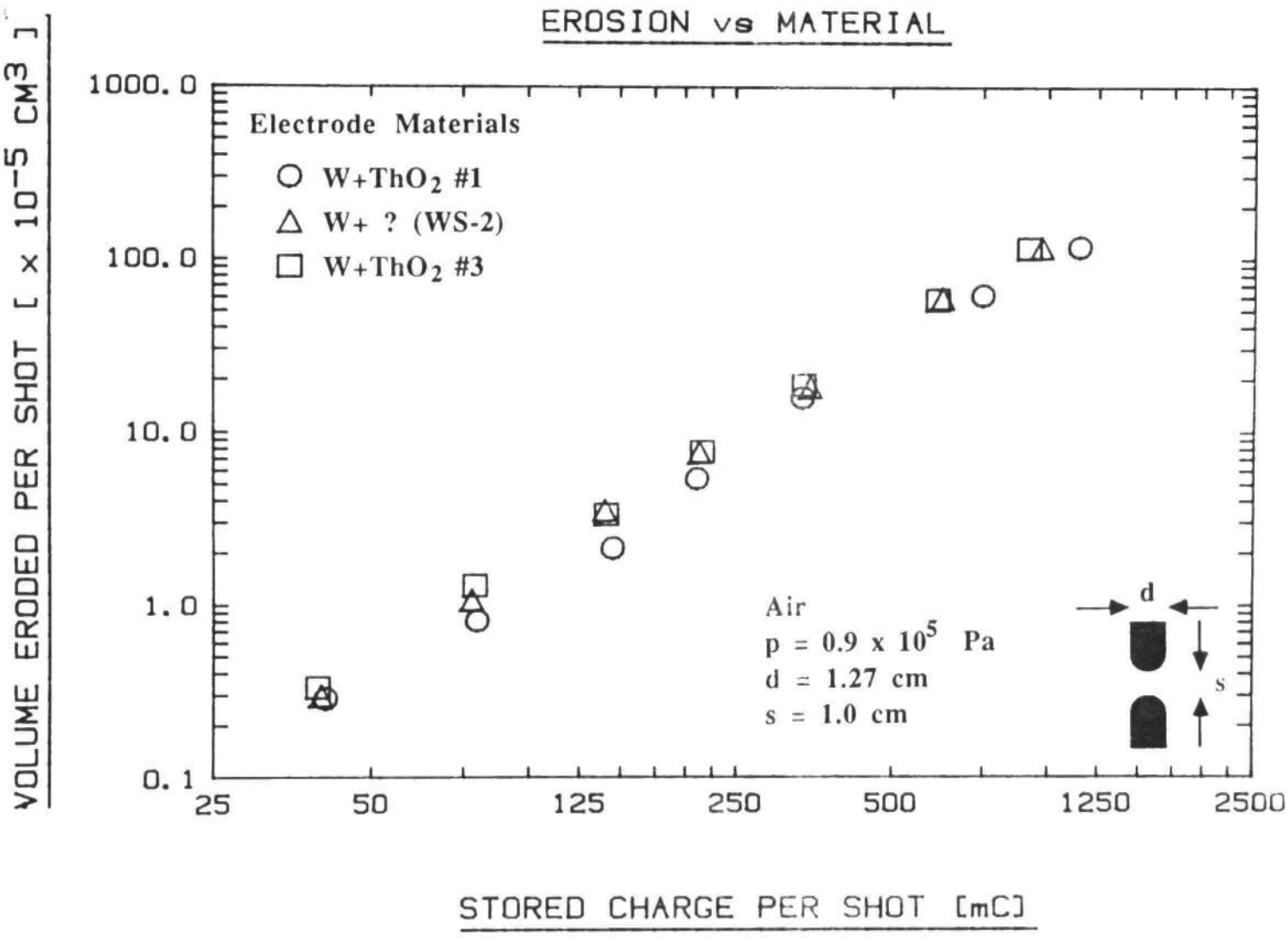

Fig. A.50 Comparison of 1.27 cm Diameter W+ThO_2 Electrode Erosion vs. Stored Charge. (W+? indicates a proprietary material)

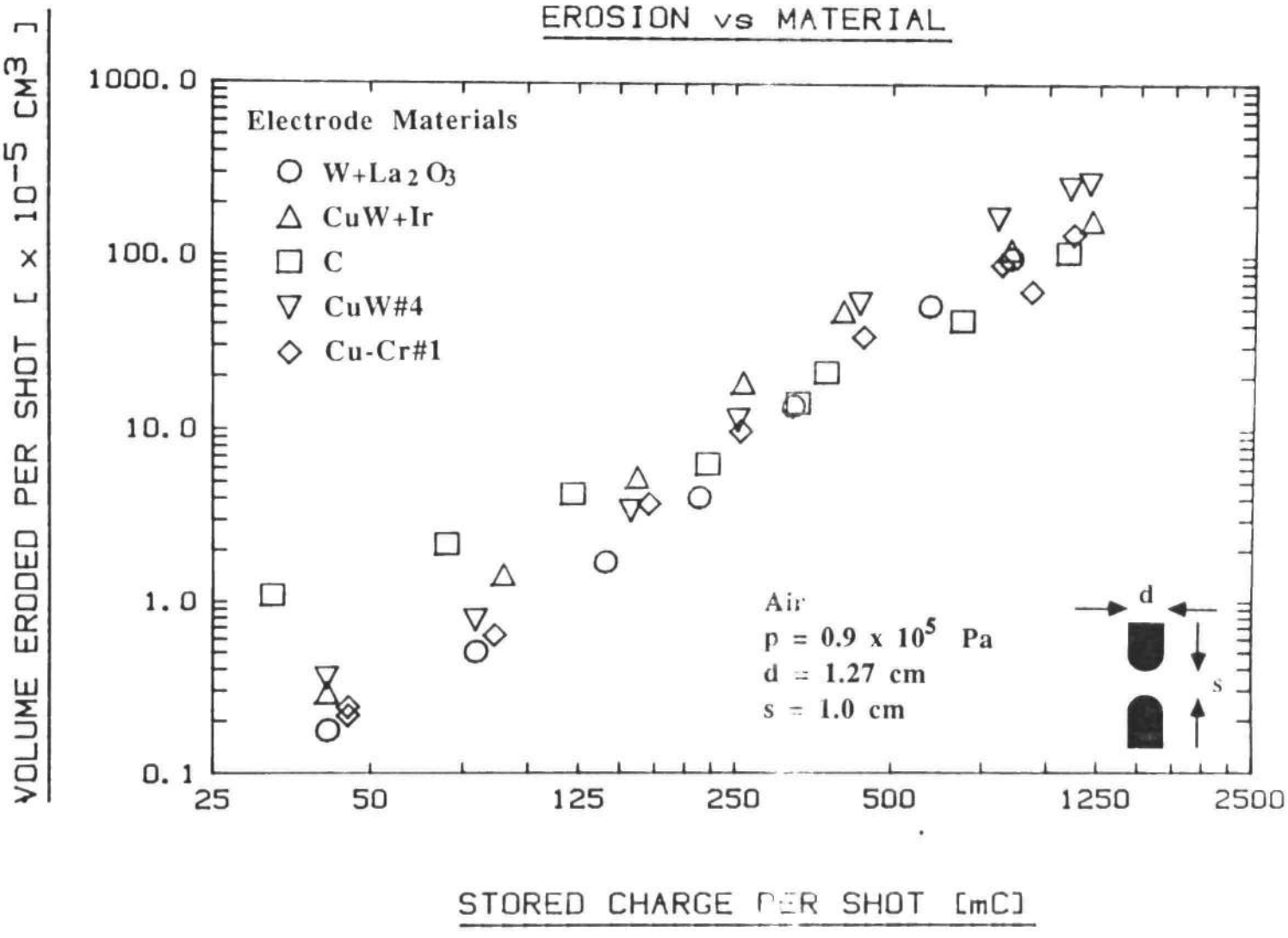

A.51 Comparison of 1.27 cm Diameter Electrode Erosion of the Best of Each Type of Material vs. Stored Charge.

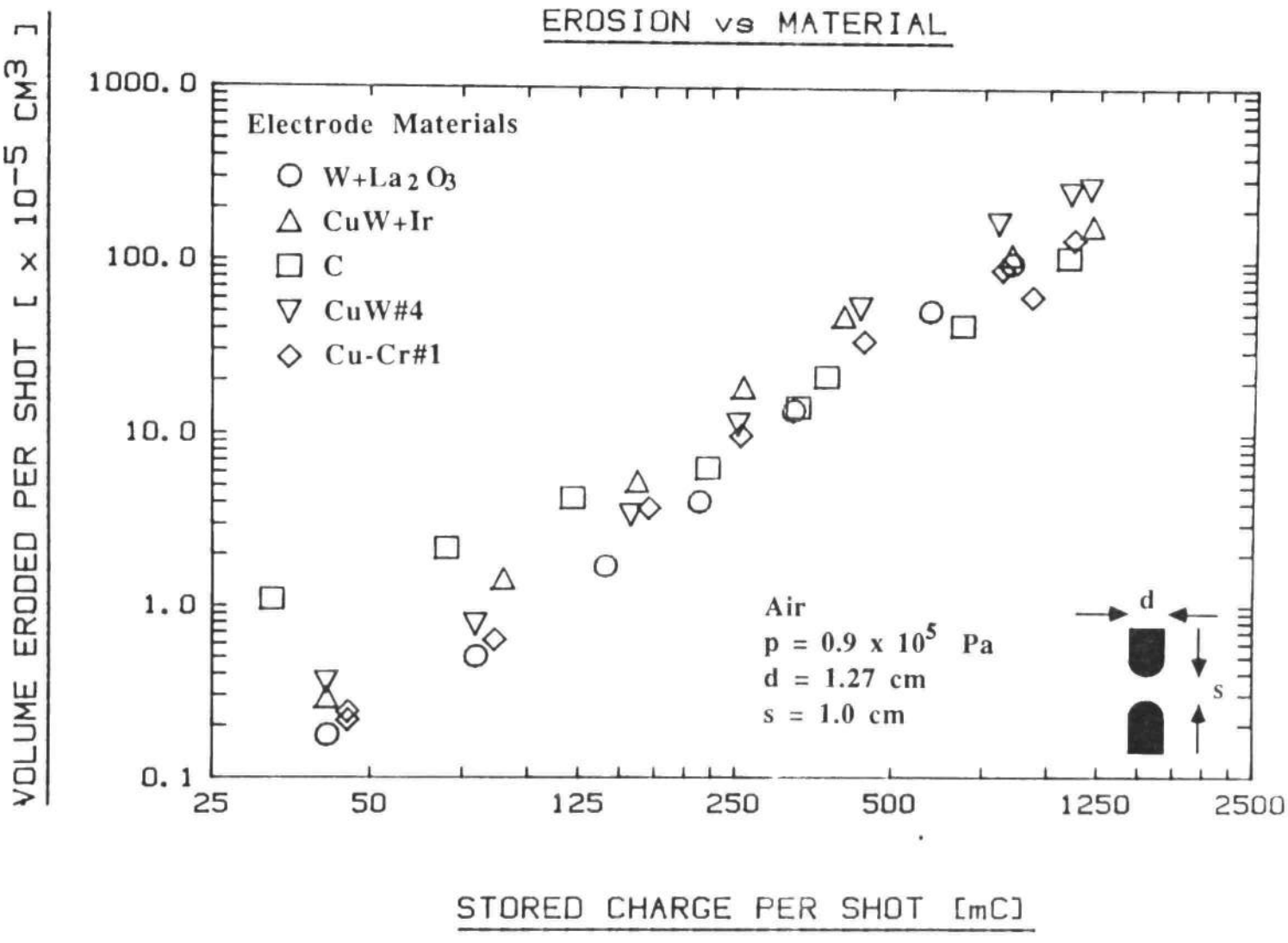

A.51 Comparison of 1.27 cm Diameter Electrode Erosion of the Best of Each Type of Material vs. Stored Charge.

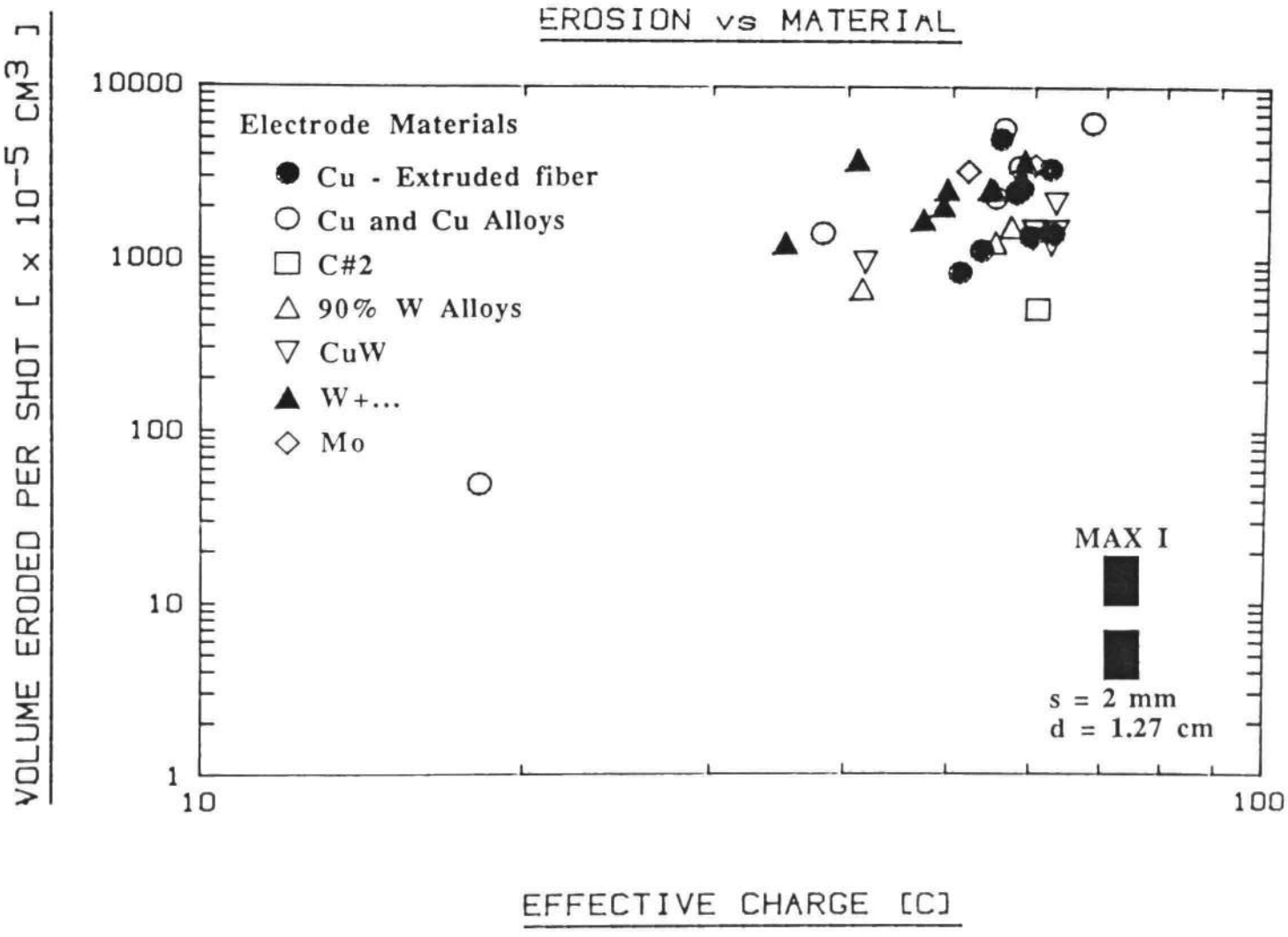

Fig. A.52 MAX I Electrode Erosion Results vs. Effective Charge.

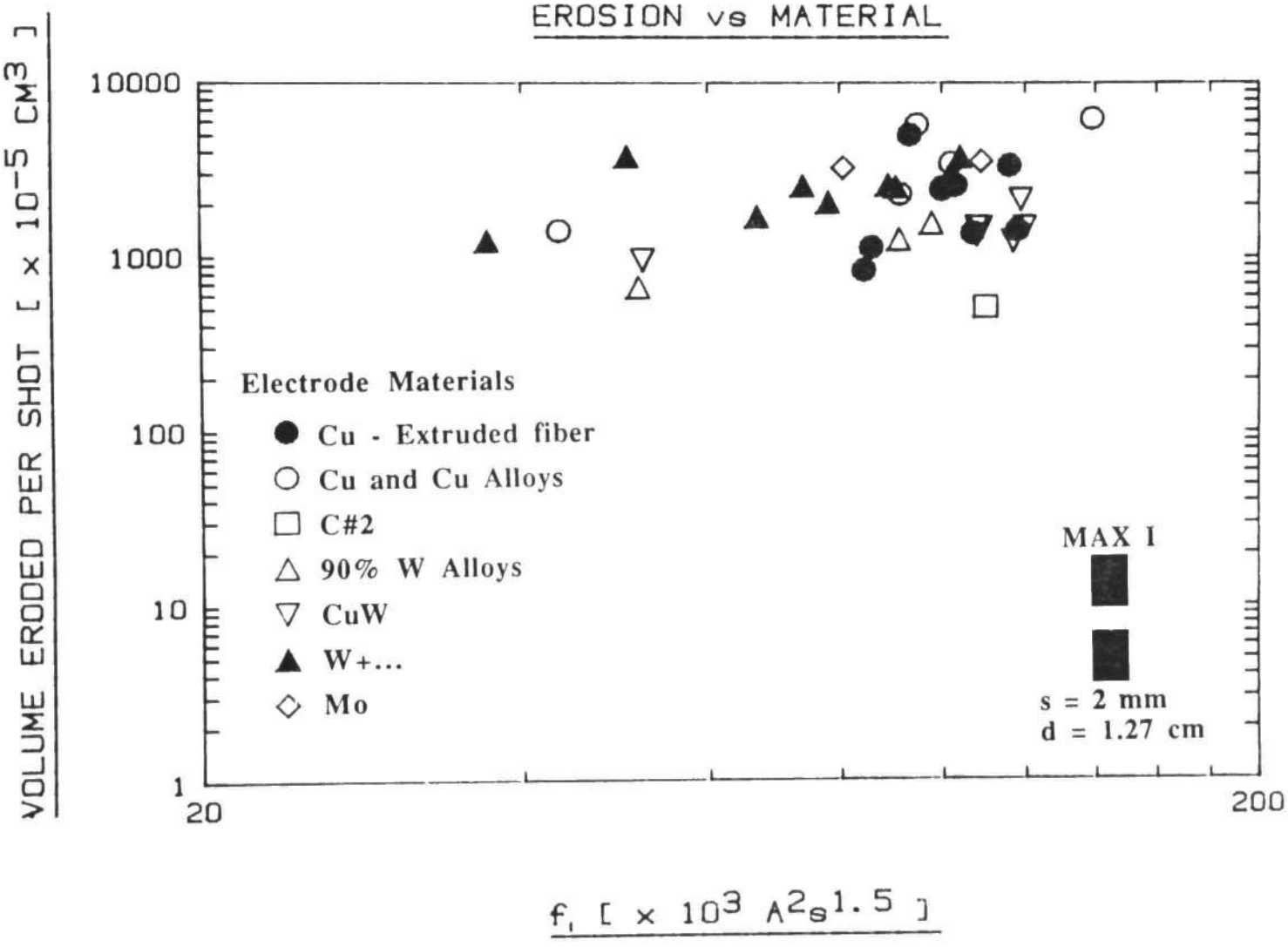

Fig. A.53 MAX I Electrode Erosion Results vs. f_1.

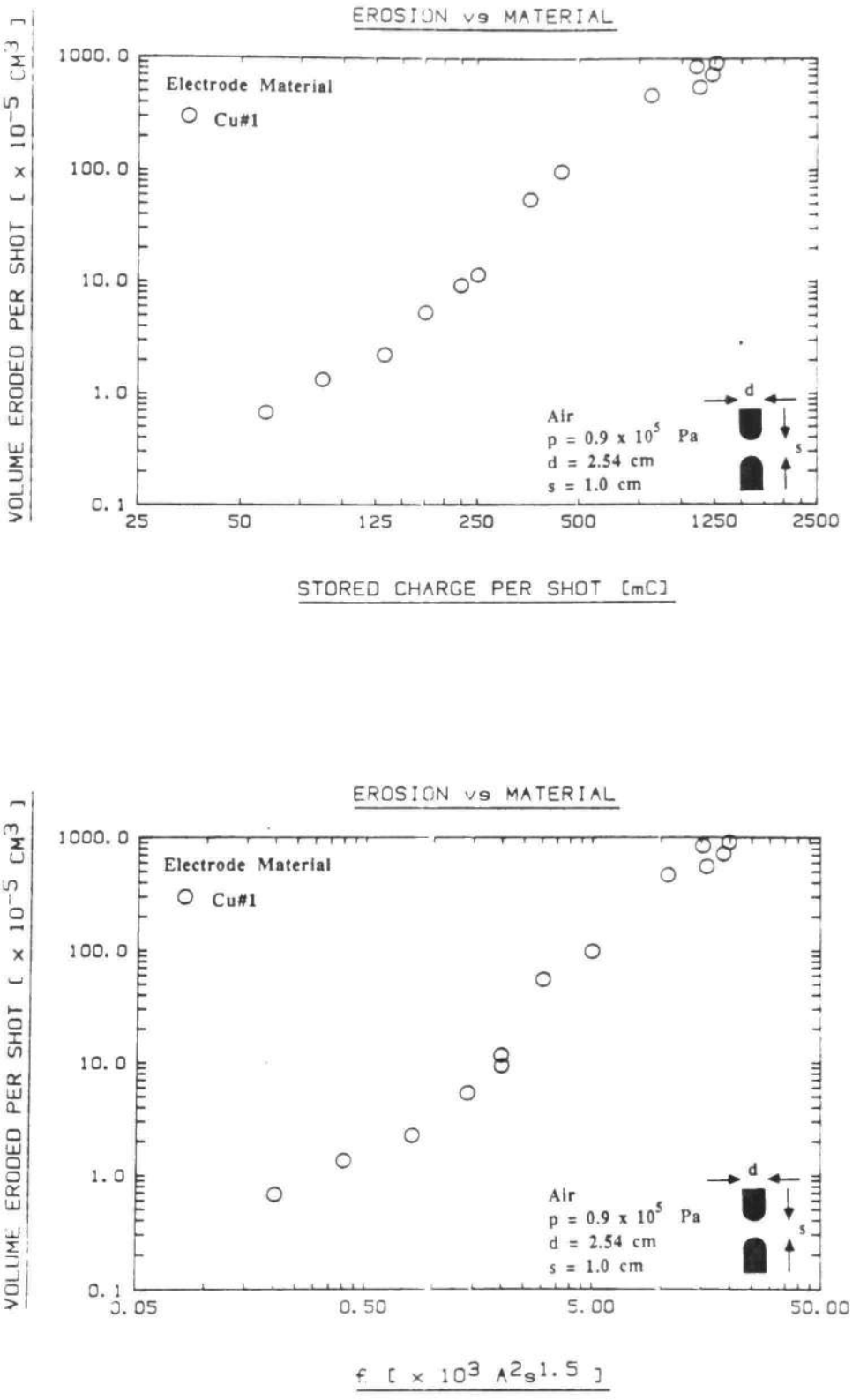

Fig. A.54 Cu#1 2.54 cm Diameter Electrode Erosion vs. a) Stored Charge and b) f_1.

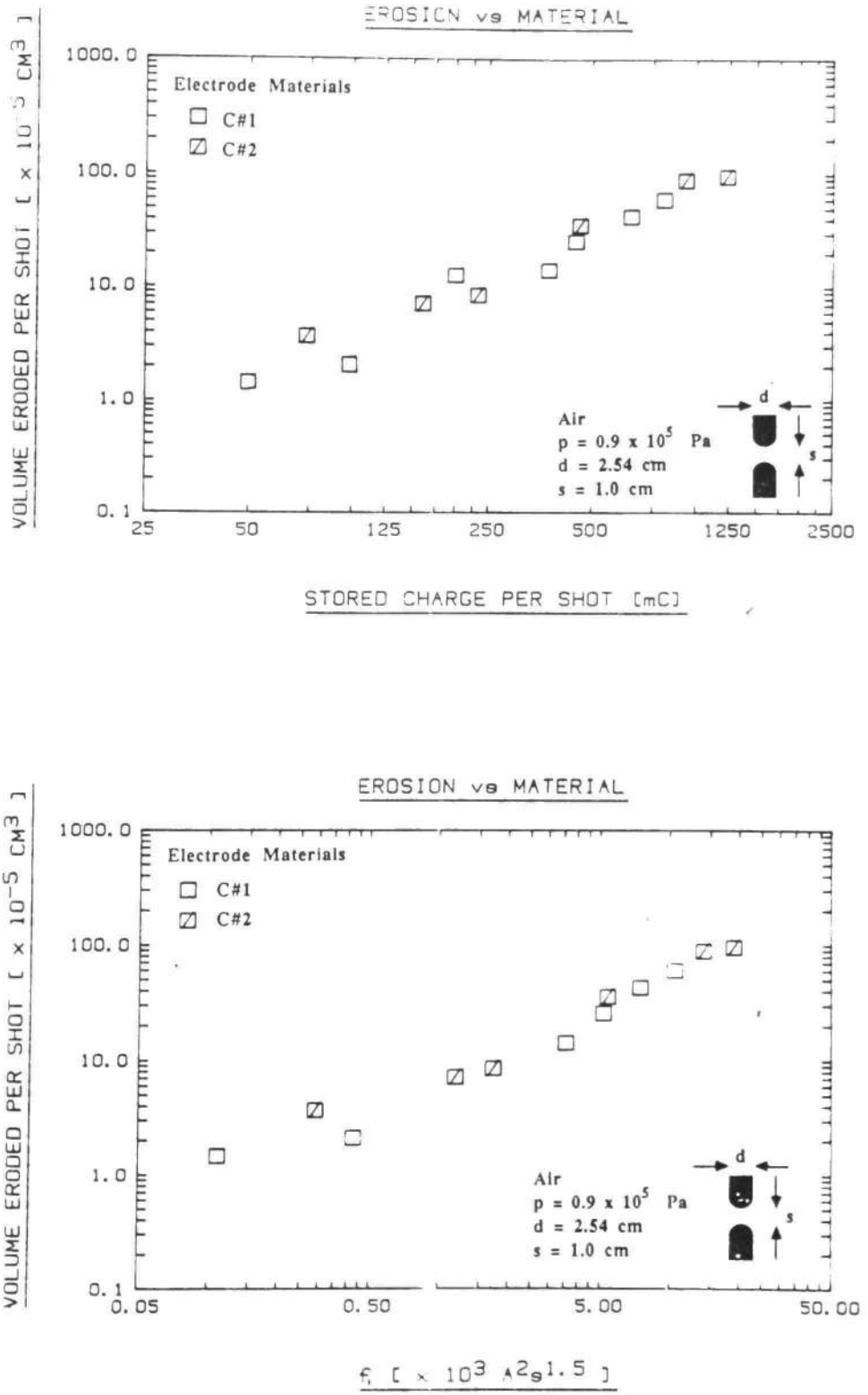

Fig. A.55 C#1 and C#2 2.54 cm Diameter Electrode Erosion vs. a) Stored Charge and b) f_1.

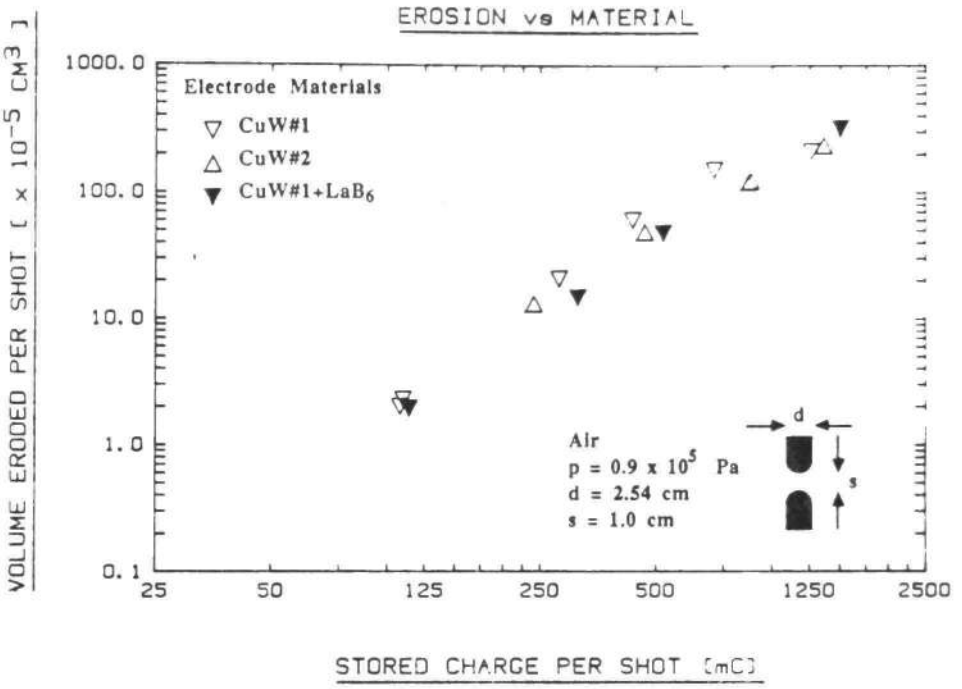

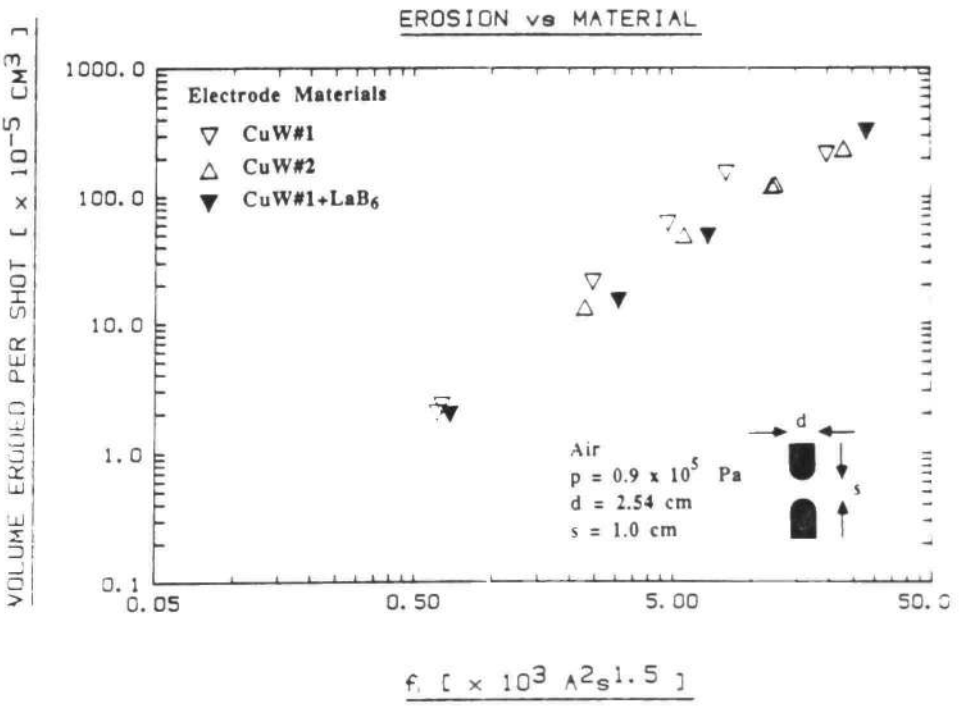

Fig. A.56 CuW=1, CuW#2 and CuW#1+LaB_6 2.54 cm Diameter Electrode Erosion vs. a) Stored Charge and b) f_1.

Table A.5 Electrode Erosion Data for Cu#1 Baseline Test ($p = 0.9 \times 10^5$ Pa)

Run #	Caps (#)	Q_s (mC)	Q_e (C)	I_p (kA)	E_s (kJ)	f_1 (*)	DV+ (x 10^{-5} cm^3/shot)	DV- (x 10^{-5} cm^3/shot)	DV_{tot} (x 10^{-5} cm^3/shot)	$DV_{\%e}$	V_{sb} (kV)	$DV_{sb\%e}$
761	1	44.0	1.06	74.0	0.524	0.111	0.227	0.227	0.454	17	23.8	5.1
742	2	75.4	1.88	96.2	0.769	0.304	0.607	0.607	1.21	12	20.4	5.1
647	3	114	2.73	118	1.18	0.599	1.34	0.897	2.24	10	20.6	4.2
1060	4	136	3.33	127	1.26	0.846	1.50	1.20	2.70	11	18.4	9.7
617	5	167	4.02	130	1.51	1.10	2.61	1.49	4.10	9.1	18.0	11
616	5	173	4.17	134	1.62	1.18	5.99	2.24	8.23	4.5	18.7	6.9
625	6	199	4.46	127	1.79	1.25	9.40	2.24	11.6	3.8	18.0	8.8
671	6	195	4.38	125	1.72	1.21	9.80	2.67	12.4	3.6	17.6	9.4
624	7	222	4.38	129	1.91	1.30	5.18	4.66	9.84	5.3	17.2	8.2
626	8	275	5.37	141	2.56	1.80	61.0	7.83	68.8	0.8	18.6	7.4
666	10	320	6.09	171	2.77	2.62	69.4	9.69	79.0	0.9	17.3	6.9
677	20	566	9.45	182	4.33	5.14	61.0	75.5	137	1.1	15.3	10
878	20	559	9.33	180	4.22	5.02	63.1	113	176	0.8	15.1	12
620	30	746	10.7	196	5.02	6.96	136	206	342	0.7	13.4	14
+687	30	1240	17.7	326	13.8	19.1	394	526	920	0.2	22.3	11

*The units on f_1 are ($A^2s^{1.5} \times 10^3$).

+Switch #2 ("Piggyback")

Table variables are defined in Table 3.6.

Table A.6 Electrode Erosion Data for Cu+LaB_6

Run #	Caps (#)	Q_s (mC)	Q_e (C)	I_p (kA)	E_s (kJ)	f_1 (*)	DV+ (x 10^{-5} cm^3/shot)	DV-	DV_{tot}	$DV_{\%e}$	V_{sb} (kV)	$DV_{sb\%e}$
912	1	49.2	1.19	82.7	0.645	0.139	0.313	0.235	0.548	14	26.6	11
866	2	79.8	1.99	102	0.862	0.341	0.772	0.463	1.24	12	21.6	12
908	4	1150	3.78	145	1.63	1.10	1.84	0.922	2.76	11	21.0	12
867	6	235	5.26	150	2.49	1.75	5.53	2.30	7.83	5.9	21.2	7.7
868	10	414	7.87	220	4.63	4.35	16.1	13.1	29.2	0.3	22.4	6.4
902	20	745	12.4	240	7.50	8.90	35.3	41.5	76.8	2.0	20.1	9.7
869	30	998	14.3	263	8.97	12.5	89.9	147	237	1.0	18.0	14

*The units on f_1 are $A^2s^{1.5}$.

Table variables are defined in Table A.5.

Table A.7 Electrode Erosion Data for CuZr and CuCrZr

Run #	Caps (#)	Q_s (mC)	Q_e (C)	I_p (kA)	E_s (kJ)	f_1 (*)	DV+ (x 10^{-5} cm^3/shot)	DV- (x 10^{-5} cm^3/shot)	DV_{tot} (x 10^{-5} cm^3/shot)	$DV_{\%e}$	V_{sb} (kV)	$DV_{sb\%e}$
CuZr												
877	2	78.6	1.96	100	0.835	0.329	0.905	0.603	1.51	10	21.2	3.7
875	6	194	4.35	124	1.70	1.19	7.16	2.68	9.94	4.5	17.5	12
872	10	324	6.16	173	2.84	2.68	20.9	11.2	32.1	2.3	17.5	12
871	30	806	11.5	212	5.86	8.09	141	273	414	0.5	14.5	15
CuCrZr												
876	2	77.3	1.92	98.6	0.807	0.318	0.451	0.451	0.902	17	20.9	9.6
874	6	195	4.36	124	1.71	1.20	4.29	3.43	7.71	5.6	17.5	22
873	10	344	6.54	183	3.20	3.01	12.0	8.26	20.3	3.7	18.6	16
870	30	759	10.9	200	5.19	7.23	116	215	331	0.7	13.7	16

Table A.8 Electrode Erosion Data for Cu+Al_2O_3#1 and #2

Run #	Caps (#)	Q_s (mC)	Q_e (C)	I_p (kA)	E_s (kJ)	f_1 (*)	DV+ (x 10^{-5} cm^3/shot)	DV- (x 10^{-5} cm^3/shot)	DV_{tot} (x 10^{-5} cm^3/shot)	$DV_{\%e}$	V_{sb} (kV)	$DV_{sb\%e}$
Cu+Al_2O_3#1												
815	2	83.5	2.08	107	0.942	0.374	1.07	0.610	1.68	9.1	22.6	3.0
814	6	202	4.53	129	1.84	1.29	4.47	11.2	15.7	2.8	18.2	9.3
731	10	307	5.84	164	2.55	2.41	14.2	12.7	76.8	2.8	16.6	8.5
813	10	354	6.72	188	3.38	3.18	70.1	17.2	87.2	0.9	19.0	7.0
788	30	791	11.3	208	5.64	7.80	121	338	458	4.8	14.3	16
Cu+Al_2O_3#2												
820	2	73.3	1.82	93.5	0.725	0.286	0.449	0.449	0.898	17	19.8	3.0
821	6	212	4.76	135	2.03	1.42	8.05	3.58	11.6	4.1	19.1	9.9
792	10	353	6.70	188	3.36	3.17	11.2	14.9	26.1	2.9	19.1	10
791-1	30	848	12.1	223	6.48	8.95	116	110	226	1.0	15.4	15
791-2	30	867	12.4	228	6.78	9.38	96.2	103	199	1.1	15.6	12

*The units on f_1 are $A^2s^{1.5}$.
Table variables are defined in Table A.5.

Table A.9 Electrode Erosion Data for Mo

Run #	Caps (#)	Q_s (mC)	Q_e (C)	I_p (kA)	E_s (kJ)	f_1 (*)	DV+ (x 10^{-5} cm^3/shot)	DV-	DV_{tot}	$DV_{\%e}$	V_{sb} (kV)	$DV_{sb\%e}$
760	1	48.2	1.16	81.0	0.628	0.133	0.20	0.20	0.400	17	26.0	8.8
881	4	127	3.11	119	1.10	0.740	1.57	1.05	2.62	10	17.2	22
733	6	173	3.87	110	1.35	0.942	3.52	2.74	6.26	6.3	15.6	11
623	10	294	5.59	157	2.34	2.21	19.6	20.2	39.8	1.6	15.9	13
887	20	565	9.44	182	4.32	5.14	75.7	73.1	149	0.87	15.3	8.3
735	30	848	12.1	223	6.48	8.95	122	143	264	0.74	15.3	13
+736	30	1130	16.1	296	11.4	15.8	207	178	385	0.51	20.3	8.6

Table A.10 Electrode Erosion Data for Mo+LaB_6

Run #	Caps (#)	Q_s (mC)	Q_e (C)	I_p (kA)	E_s (kJ)	f_1 (*)	DV+ (x 10^{-5} cm^3/shot)	DV-	DV_{tot}	$DV_{\%e}$	V_{sb} (kV)	$DV_{sb\%e}$
894-1	1	43.1	1.04	72.5	0.503	0.107	0.141	0.141	0.282	25	23.3	12
895	2	56.0	1.40	71.5	0.425	0.168	0.274	0.274	0.549	25	15.2	12
953	2	69.9	1.74	89.2	0.660	0.261	0.275	0.275	0.550	25	18.9	6.7
896	4	115	2.80	107	0.892	0.599	0.854	0.854	1.71	17	15.5	20
897	6	212	4.76	136	2.03	1.43	3.8	4.22	8.01	5.3	19.1	12
898	10	341	6.48	182	3.15	2.97	16.3	6.10	22.4	3.0	18.4	11
899	20	689	11.5	222	6.41	7.63	46.1	69.1	115	1.2	18.6	11
901	30	1040	14.9	274	9.81	13.5	118	142	260	0.78	18.8	10

+Piggyback

*The units on f_1 are $A^2s^{1.5}$.

Table variables are defined in Table A.5.

Table A.11 Electrode Erosion Data for C#1

Run #	Caps (#)	Q_s (mC)	Q_e (C)	I_p (kA)	E_s (kJ)	f_1 (*)	DV+ (x 10^{-5} cm^3/shot)	DV-	DV_{tot}	$DV_{\%e}$	V_{sb} (kV)	$DV_{sb\%e}$
911	1	32.5	0.784	54.7	0.29	0.061	0.54	0.543	1.09	17	17.6	2.3
802	2	70.0	1.74	89.3	0.66	0.261	1.44	0.722	2.17	33	18.9	3.3
884	4	122	2.97	114	1.00	0.679	2.14	2.14	4.27	17	16.5	4.9
801	6	222	4.98	142	2.23	1.41	4.26	2.13	6.38	33	20.0	2.9
905	10	331	6.28	176	2.96	2.78	7.09	7.09	14.2	25	17.9	6.7
800	10	375	7.12	199	3.79	3.56	10.6	10.6	21.3	17	20.2	3.2
886	20	684	11.4	220	6.32	7.50	24.8	17.7	42.5	8.2	18.5	6.0
795	30	1090	15.6	287	10.7	14.8	53.2	53.2	106	10	19.7	10

*The units on f_1 are $A^2s^{1.5}$.

Table variables are defined in Table A.5

Table A.12 Electrode Erosion Data for CuW#1

Run #	Caps (#)	Q_s (mC)	Q_e (C)	I_p (kA)	E_s (kJ)	f_1 (*)	DV+ (x 10^{-5} cm^3/shot)	DV-	DV_{tot}	$DV_{\%e}$	V_{sb} (kV)	$DV_{sb\%e}$
762	1	44.2	1.07	74.3	0.528	0.112	0.289	0.241	0.531	9.1	23.9	7.8
955	2	85.1	2.12	109	0.98	0.388	0.761	0.856	1.61	5.9	23.0	4.4
774	2	93.9	2.34	120	1.19	0.472	1.33	1.05	2.38	4.0	25.4	7.2
880	4	168	4.10	157	1.91	1.29	4.57	4.19	8.76	2.2	22.7	4.4
753	6	258	5.77	164	2.99	2.09	13.5	12.3	25.8	1.1	23.2	9.6
780	10	414	7.87	220	4.63	4.35	30.0	29.5	59.5	0.8	22.4	10
733	20	789	13.2	254	8.42	10.0	72.1	72.1	144	0.66	21.3	9.9
738	30	1250	17.9	330	14.1	19.6	97.1	115	213	0.67	22.6	8.2

Table A.13 Electrode Erosion Data for CuW#1+LaB_6

Run #	Caps (#)	Q_s (mC)	Q_e (C)	I_p (kA)	E_s (kJ)	f_1 (*)	DV+ (x 10^{-5} cm^3/shot)	DV-	DV_{tot}	$DV_{\%e}$	V_{sb} (kV)	$DV_{sb\%e}$
973	1	45.7	1.10	76.9	0.565	0.120	0.163	0.109	0.272	20	24.7	8.2
913	1	49.8	1.20	83.7	0.670	0.142	0.273	0.273	0.544	10	26.9	9.6
954	2	79.2	1.97	101	0.847	0.334	0.433	0.324	0.757	14	21.4	5.1
777	2	89.2	2.22	114	1.08	0.425	0.546	0.437	0.982	11	24.1	8.8
909	4	182	4.44	170	2.24	1.51	3.59	2.69	6.28	3.6	24.6	7.9
778	6	258	5.78	165	3.00	2.11	9.08	9.08	18.2	1.8	23.3	5.6
614	10	442	8.40	235	5.28	4.96	28.0	26.9	54.9	0.98	23.9	5.2
903	20	841	14.0	270	9.55	11.3	75.4	81.9	157	0.69	22.7	5.4
766	30	1340	19.2	353	16.3	22.5	136	158	294	0.55	24.2	8.1

*The units on f_1 are $A^2s^{1.5}$.

Table variables are defined in Table A.5.

Table A.14 Electrode Erosion Data for CuW#2

Run #	Caps (#)	Q_s (mC)	Q_e (C)	I_p (kA)	E_s (kJ)	f_1 (*)	DV+ (x 10^{-5} cm^3/shot)	DV-	DV_{tot}	$DV_{\%e}$	V_{sb} (kV)	$DV_{sb\%e}$
914	1	46.8	1.13	78.8	0.592	0.126	0.245	0.245	0.489	10.0	25.3	9.3
804	2	84.0	2.09	107	0.952	0.376	1.07	0.972	2.04	4.8	22.7	8.6
835	2	105	2.62	134	1.50	0.590	0.873	0.873	1.75	5.5	28.5	12
915	4	181	4.43	116	2.22	1.03	4.40	4.78	9.18	2.1	24.5	8.2
779	6	262	5.58	166	3.07	2.15	11.5	12.4	23.9	1.2	23.5	7.6

Table A.15 Electrode Erosion Data for CuW#3

839	2	88.8	2.21	113	1.07	0.353	0.953	0.866	1.82	4.8	24.0	4.4
838	6	233	5.23	149	2.45	1.72	6.68	6.43	13.1	2.0	21.0	4.0
838-1	6	266	5.95	169	3.18	2.23	9.77	9.77	19.5	1.3	23.9	2.8
837-1	10	452	8.59	241	5.52	5.20	27.8	26.5	54.3	1.4	24.4	4.1
840	30	1160	16.6	305	12.1	16.8	86.6	97.1	184	0.71	20.9	11

Table A.16 Electrode Erosion Data for CuW#4

1094	1	41.3	0.994	69.4	0.460	0.0976	0.198	0.158	0.356	11	22.3	3.7
1097	2	79.6	1.98	102	0.857	0.339	0.387	0.387	0.777	10	21.5	7.3
1102	4	158	3.86	148	1.69	1.14	1.86	1.55	3.41	4.5	21.4	4.0
1080	6	254	5.69	162	2.91	2.04	5.35	6.05	11.4	2.0	22.9	3.7
1073	10	435	8.26	232	5.11	4.82	25.1	28.6	53.7	0.7	23.5	4.2
1071	20	800	13.4	257	8.64	10.3	82.6	84.9	168	0.5	21.6	10
1067+	30	1100	15.7	288	10.8	15.0	130	123	252	0.5	19.7	10
1067-1	30	1200	17.1	315	12.9	17.9	132	137	269	0.4	21.6	10

+No cooling of anode electrode.

*The units on f_1 are $A^2s^{1.5}$.

Table variables are defined in Table A.5.

Table A.17 Electrode Erosion Data for CuW+Ir

Run #	Caps (#)	Q_s (mC)	Q_e (C)	I_p (kA)	E_s (kJ)	f_1 (*)	DV+ (x 10^{-5} cm^3/shot)	DV- (x 10^{-5} cm^3/shot)	DV_{tot} (x 10^{-5} cm^3/shot)	$DV_{\%e}$	V_{sb} (kV)	$DV_{sb\%e}$
948	1	41.2	0.993	69.3	0.459	0.097	0.145	0.145	0.290	17	22.3	6.2
927	2	89.7	2.23	114	1.09	0.427	0.764	0.669	1.43	6.7	24.2	6.1
950	4	162	3.95	151	1.77	1.19	2.66	2.66	5.32	3.6	21.9	4.1
925	6	259	5.81	165	3.03	2.12	9.10	9.38	18.5	1.5	23.4	4.5
921	10	403	7.65	214	4.38	4.12	25.8	22.2	48.0	1.1	21.8	3.8
952	20	845	14.1	272	9.66	11.5	55.9	54.0	110	0.86	22.8	5.7
918	30	1210	17.3	318	13.2	18.2	79.6	82.4	162	0.88	21.8	9.1

Table A.18 Electrode Erosion Data for CuW+Re

Run #	Caps (#)	Q_s (mC)	Q_e (C)	I_p (kA)	E_s (kJ)	f_1 (*)	DV+ (x 10^{-5} cm^3/shot)	DV- (x 10^{-5} cm^3/shot)	DV_{tot} (x 10^{-5} cm^3/shot)	$DV_{\%e}$	V_{sb} (kV)	$DV_{sb\%e}$
975	1	44.3	1.07	74.5	0.531	0.113	0.240	0.192	0.432	11	24.0	10
977	2	84.4	2.10	108	0.963	0.381	0.663	0.663	1.33	7.1	22.8	7.3
979	4	170	4.14	158	1.94	1.31	3.03	3.03	6.05	3.1	22.9	6.2
981	6	243	5.44	155	2.66	1.87	9.34	9.34	18.7	1.5	21.9	7.1
982	10	416	7.90	221	4.67	4.39	25.0	22.6	47.6	0.99	22.5	5.4
985	20	822	13.7	264	9.13	10.8	54.9	54.0	109	0.85	22.2	5.1
987	30	1250	17.9	329	14.0	19.5	84.9	89.1	174	0.81	22.5	5.2

*The units on f_1 are $A^2s^{1.5}$.

Table variables are defined in Table A.5.

Table A.19 Electrode Erosion Data for CuW+Sb

Run #	Caps (#)	Q_s (mC)	Q_e (C)	I_p (kA)	E_s (kJ)	f_1 (*)	DV+ (x 10^{-5} cm^3/shot)	DV-	DV_{tot}	$DV_{\%e}$	V_{sb} (kV)	$DV_{sb\%e}$
947	1	40.6	0.980	68.3	0.446	0.095	0.260	0.260	0.520	10	22.0	6.5
926	2	82.7	2.06	105	0.923	0.363	1.12	1.32	2.44	4.2	22.3	6.7
949	4	148	3.60	138	1.47	0.994	4.45	4.45	8.90	2.3	19.9	8.5
923	6	212	4.75	135	2.02	1.42	11.5	14.9	26.4	1.2	19.1	12
920	10	334	6.36	178	3.02	2.85	32.9	34.4	67.2	0.75	18.1	14
951	20	556	9.29	179	4.18	4.97	51.6	70.8	122	0.83	15.0	17
919	30	823	11.8	216	6.09	8.45	108	117	224	0.68	14.8	19

*The units on f_1 are $A^2s^{1.5}$.

Table variables are defined in Table A.5.

Table A.20 Electrode Erosion Data for Cu-Cr#1

Run #	Caps (#)	Q_s (mC)	Q_e (C)	I_p (ka)	E_s (kJ)	f_1 (*)	DV+ (x 10^{-5} cm^3/shot)	DV-	DV_{tot}	$DV_{\%e}$	V_{sb} (kV)	$DV_{sb\%e}$
1093-1	1	45.3	1.09	76.2	0.56	0.12	0.122	0.093	0.215	0.4	24.6	7.2
1093	1	45.3	1.09	76.2	0.56	0.12	0.16	0.079	0.24	33	24.5	6.6
1090	2	86.5	2.12	110	1.01	0.39	0.31	0.31	0.63	25	23.4	4.6
1087	4	171	4.16	159	1.97	1.32	1.87	1.87	3.74	8.3	23.1	2.9
1084	6	257	5.75	164	2.96	2.09	4.67	5.13	9.80	4.7	23.1	3.2
1077	10	442	8.39	206	5.27	4.36	17.1	17.1	34.2	2.3	23.9	1.8
1064	20	815	13.6	262	8.98	10.7	46.7	43.6	90.2	1.7	22.0	8.4
1061	30	1117	16.0	294	11.2	156	65.3	70.0	135	1.7	20.1	11
1149**	30	932	13.3	245	7.83	10.8	30.3	32.7	63.0	3.7	16.8	12

*Units on f_1 - x 10^3 $A^2s^{1.5}$

**Shielded Electrode Experiment

Note: run 1093-1 was rerun using a weighing scale with greater accuracy to reduce measurement error.

Table A.21 Electrode Erosion Data vs. Cu-Nb#1

Run #	Caps (#)	Q_s (mC)	Q_e (C)	I_p (kA)	E_s (kJ)	f_1 (*)	DV+ (x 10^{-5} cm^3/shot)	DV- (x 10^{-5} cm^3/shot)	DV_{tot} (x 10^{-5} cm^3/shot)	$DV_{\%e}$	V_{sb} (kV)	$DV_{sb\%e}$
Cu-Nb#1												
885	1	40.4	0.974	68.0	0.442	0.094	0.151	0.151	0.302	25	21.8	12
763	1	41.4	0.999	69.7	0.464	0.098	0.151	0.151	0.302	25	22.4	13
805	2	79.1	1.97	101	0.845	0.334	0.306	0.153	0.458	33	21.4	16
775-1	2	75.4	1.88	96.1	0.768	0.303	0.455	0.304	0.759	20	20.4	2.0
879	4	166	4.05	155	1.86	1.26	1.51	1.51	3.02	10	22.4	4.7
754	6	267	5.97	170	3.2	2.25	8.14	7.24	15.4	2.9	24.0	4.7
627	10	434	8.25	231	5.10	4.79	21.0	21.8	42.8	1.8	23.5	4.4
732	20	812	13.6	261	8.91	10.6	49.5	46.5	96.4	1.6	22.0	7.0
748	30	1320	18.9	348	15.8	21.8	124	77.4	201	1.9	23.8	7.6

*The units on f_1 are ($A^2s^{1.5}$ x 10^3).

Table variables are defined in Table A.5.

Table A.22 Electrode Erosion Data for Cu-Nb#1 + LaB_6

Run #	Caps (#)	Q_s (mC)	Q_e (C)	I_p (kA)	E_s (kJ)	f_1 (*)	DV+ (x 10^{-5} cm^3/shot)	DV-	DV_{tot}	$DV_{\%e}$	V_{sb} (kV)	$DV_{sb\%e}$
946	1	43.1	1.07	72.4	0.515	0.110	0.164	0.164	0.327	25	23.3	6.4
928	2	85.1	2.12	109	0.980	0.388	0.485	0.485	0.970	17	23.0	6.1
943	4	165	4.02	154	1.84	1.24	1.29	1.61	2.91	11	22.3	3.1
924	6	256	5.72	163	2.94	2.06	4.83	4.83	9.66	5.0	23.0	4.3
922	10	444	8.44	237	5.34	5.03	20.1	18.5	38.6	2.1	24.0	3.4
939	20	838	14.0	270	9.49	11.3	43.5	43.5	87.0	1.9	22.6	6.2
917	30	1250	17.9	329	14.1	19.5	74.9	101	176	1.4	22.5	8.7

*The units on f_1 are $A^2s^{1.5}$.

Table variables are defined in Table A.5.

Table A.23 Electrode Erosion Data for Cu-Nb#1+Nb

Run #	Caps (#)	Q_s (mC)	Q_e (C)	I_p (kA)	E_s (kJ)	f_1 (*)	DV+ (x 10^{-5} cm^3/shot)	DV-	DV_{tot}	$DV_{\%e}$	V_{sb} (kV)	$DV_{sb\%e}$
816	2	95.4	2.38	122	1.23	0.488	0.751	0.601	1.35	11	25.8	8.6
817	6	288	6.45	184	3.74	2.63	10.4	9.91	20.3	2.2	26.0	6.4
818	10	467	8.88	249	5.90	5.56	22.5	21.0	43.5	1.7	25.3	4.4
819	30	1230	17.6	323	15.6	18.9	85.6	78.8	164	1.4	22.1	9.3

Table A.24 Electrode Erosion Data for Cu-Nb#2

Run #	Caps (#)	Q_s (mC)	Q_e (C)	I_p (kA)	E_s (kJ)	f_1 (*)	DV+ (x 10^{-5} cm^3/shot)	DV-	DV_{tot}	$DV_{\%e}$	V_{sb} (kV)	$DV_{sb\%e}$
936	1	42.8	1.03	72.0	0.496	0.105	0.077	0.077	0.153	50	23.2	9.7
1128	1	44.4	1.07	74.6	0.533	0.113	0.137	0.149	0.286	0.3	24.0	6.5
934	2	70.8	1.76	90.3	0.677	0.267	0.306	0.306	0.612	13	19.1	12
929	2	88.5	2.20	113	1.06	0.417	0.460	0.460	0.919	17	23.9	8.2
935	4	161	3.94	151	1.76	1.19	1.51	1.51	3.02	10	21.8	3.2
930	6	249	5.58	159	2.80	1.96	5.49	4.57	10.1	4.5	22.4	5.1
931	10	441	8.39	235	5.27	4.96	21.5	20.7	42.2	1.8	23.9	3.3
933	20	734	12.3	236	7.29	8.68	38.1	42.7	80.8	1.9	19.8	11
932	30	1130	16.2	298	11.5	16.0	72.5	72.5	145	1.5	20.4	8.1

*The units on f_1 are ($A^2s^{1.5}x10^3$).

Table variables are defined in Table A.5.

Table A.25 Electrode Erosion Data for Cu-Nb#3

Run #	Caps (#)	Q_s (mC)	Q_e (C)	I_p (kA)	E_s (kJ)	f_1 (*)	DV+ (x 10^{-5} cm^3/shot)	DV- (x 10^{-5} cm^3/shot)	DV_{tot} (x 10^{-5} cm^3/shot)	$DV_{\%e}$	V_{sb} (kV)	$DV_{sb\%e}$
1013	1	41.1	0.992	69.2	0.458	0.097	0.000	0.078	0.078	100	22.2	7.5
1013-1	1	44.6	1.07	75.0	0.537	0.113	0.152	0.129	0.281	0.3	24.1	7.3
1012	2	78.0	1.94	99.5	0.823	0.324	0.153	0.153	0.306	50	21.1	4.8
1012-1	2	80.3	2.00	102	0.871	0.343	0.371	0.213	0.585	0.3	21.7	5.5
1011	4	157	3.83	147	1.67	1.13	1.52	1.22	2.74	11	21.2	5.0
1010	6	236	5.29	151	2.51	1.77	4.10	3.19	7.30	6.2	21.3	4.9
1009	10	410	7.79	218	4.55	4.27	16.0	15.2	31.2	2.4	22.2	4.1
1007	20	794	13.3	255	8.53	10.1	47.1	45.6	92.7	1.6	21.5	7.5
1008	30	1130	16.1	297	11.5	15.9	73.0	70.7	144	1.6	20.3	8.6

Table A.26 Electrode Erosion Data for Cu-Nb#4

Run #	Caps (#)	Q_s (mC)	Q_e (C)	I_p (ka)	E_s (kJ)	f_1 (*)	DV+ (x 10^{-5} cm^3/shot)	DV- (x 10^{-5} cm^3/shot)	DV_{tot} (x 10^{-5} cm^3/shot)	$DV_{\%e}$	V_{sb} (kV)	$DV_{sb\%e}$
1091-1	1	43.2	1.04	72.6	0.50	0.11	0.117	0.102	0.219	0.3	23.4	5.8
1091	1	42.2	1.02	71.0	0.48	0.10	0.15	0.23	0.38	20	22.8	7.1
1088	2	82.6	2.06	105	0.92	0.36	0.45	0.30	0.75	20	22.3	7.6
1085	4	167	4.07	156	1.88	1.27	1.50	1.20	2.70	11	22.5	4.3
1082	6	253	5.67	161	2.88	2.02	4.06	3.61	7.67	5.9	22.8	3.6
1075	10	438	8.33	233	5.20	4.61	17.2	16.5	33.7	2.2	23.7	1.7
1065	20	794	13.3	255	8.53	10.1	44.9	40.4	85.4	1.8	21.5	7.9
1070	30	1104	15.8	291	11.0	15.2	59.5	68.3	128	1.7	19.9	10

*Units on f_1 - x 10^3 $A^2s^{1.5}$

Table variables are defined in Table A.5.

Note: run 1091-1, was rerun using a weighing scale with greater accuracy to reduce measurement error.

Table A.27 Electrode Erosion Data for Cu-Ta#1

Run #	Caps (#)	Q_s (mC)	Q_e (C)	I_p (kA)	E_s (kJ)	f_1 (*)	DV+ (x 10^{-5} cm^3/shot)	DV-	DV_{tot}	$DV_{\%e}$	V_{sb} (kV)	$DV_{sb\%e}$
945	1	41.6	1.00	70.0	0.469	0.099	0.143	0.143	0.287	25	22.5	6.1
944	2	75.7	1.89	96.6	0.775	0.307	0.424	0.424	0.848	17	20.5	7.9
942	4	154	3.77	144	1.61	1.09	1.13	0.844	1.97	14	20.9	4.5
941	6	241	5.40	154	2.62	1.84	3.79	3.37	7.16	5.9	21.7	4.4
940	10	440	8.36	234	5.23	4.92	16.8	14.7	31.6	2.2	23.8	1.3
938	20	815	13.6	262	8.97	10.7	39.3	40.7	80.0	1.8	22.0	7.2
937	30	1210	17.2	317	13.1	18.1	63.2	69.5	133	1.6	21.7	9.1

Table A.28 Electrode Erosion Data for Cu-Ta#2

Run #	Caps (#)	Q_s (mC)	Q_e (C)	I_p (ka)	E_s (kJ)	f_1 (*)	DV+ (x 10^{-5} cm^3/shot)	DV-	DV_{tot}	$DV_{\%e}$	V_{sb} (kV)	$DV_{sb\%e}$
1092-1	1	44.5	1.07	74.7	0.53	0.11	0.117	0.100	0.217	0.4	24.0	7.6
1092	1	44.4	1.07	74.6	0.53	0.11	0.16	0.079	0.24	33	24.0	6.8
1089	2	85.3	2.12	109	0.98	0.39	0.31	0.16	0.46	33	23.0	4.7
1086	4	173	4.22	161	2.02	1.36	2.16	1.55	3.71	8.3	23.4	3.1
1083	6	261	5.85	167	3.07	2.16	6.01	5.55	11.6	4.0	23.5	2.6
1076	10	437	8.31	233	5.17	4.61	17.7	17.7	35.5	2.2	23.6	1.7
1063	20	791	13.2	254	8.45	10.0	43.2	43.2	86.3	1.8	21.4	8.6
1062	30	1160	16.6	305	12.1	16.8	74.0	69.4	143	1.6	20.9	9.3

*Units on f_1 - x 10^3 $A^2s^{1.5}$

Table variables are defined in Table A.5.

Note: run 1092-1 was rerun using a weighing scale with greater accuracy to reduce measurement error.

Table A.29 Electrode Erosion Data for W#1

Run #	Caps (#)	Q_s (mC)	Q_e (C)	I_p (kA)	E_s (kJ)	f_1 (*)	DV+ (x 10^{-5} cm^3/shot)	DV-	DV_{tot}	$DV_{\%e}$	V_{sb} (kV)	$DV_{sb\%e}$
959	1	36.3	0.876	61.1	0.357	0.076	0.083	0.083	0.165	25	19.6	7.6
961	2	80.1	1.99	102	0.867	0.341	0.910	0.827	1.74	4.8	21.6	7.1
963	4	151	3.68	141	1.54	1.04	2.64	2.64	5.28	3.1	20.4	3.8
965	6	218	4.89	139	2.15	1.51	4.70	3.96	8.66	2.9	19.7	5.3
967	10	362	6.88	193	3.54	3.33	9.49	8.25	17.7	2.3	19.6	5.8
969	20	784	13.1	252	8.30	9.87	58.6	42.9	101	0.82	21.2	5.6
971	30	1210	17.3	318	13.1	18.2	105	100	205	0.60	21.8	6.7

Table A.30 Electrode Erosion Data for W#2

Run #	Caps (#)	Q_s (mC)	Q_e (C)	I_p (kA)	E_s (kJ)	f_1 (*)	DV+ (x 10^{-5} cm^3/shot)	DV-	DV_{tot}	$DV_{\%e}$	V_{sb} (kV)	$DV_{sb\%e}$
960	1	36.3	0.874	61.0	0.355	0.075	0.079	0.079	0.157	25	19.6	7.2
962	2	75.4	1.88	96.1	0.768	0.303	0.231	0.384	0.615	13	20.4	7.6
964-1	4	147	3.60	138	1.47	0.994	1.41	1.25	2.66	5.9	19.9	5.4
966	6	226	4.99	142	2.23	1.57	4.21	2.80	7.01	3.3	20.1	6.0
968	10	372	7.07	198	3.74	3.52	8.51	7.74	16.2	2.4	20.1	5.7
970	20	817	13.6	263	9.02	10.7	49.8	48.3	98.1	0.79	22.1	5.2
972	30	1160	16.7	306	12.2	16.9	95.8	99.3	195	0.60	21.0	4.5

*Units on f_1 are $A^2s^{1.5}$.

Table variables are defined in Table A.5.

Table A.31 Electrode Erosion Data for W#3

Run #	Caps (#)	Q_s (mC)	Q_e (C)	I_p (kA)	E_s (kJ)	f_1 (*)	DV+ (x 10^{-5} cm^3/shot)	DV-	DV_{tot}	$DV_{\%e}$	V_{sb} (kV)	$DV_{sb\%e}$
1021	1	38.0	1.17	63.8	0.390	0.106	0.120	0.120	0.240	17	20.5	4.0
1022	2	73.8	1.84	94.1	0.736	0.291	0.317	0.396	0.712	11	19.9	6.7
1023	4	154	3.75	144	1.60	1.08	3.77	2.83	6.60	2.4	20.8	6.2
1024	6	235	5.26	150	2.48	1.75	8.73	7.08	15.8	1.5	21.2	4.5
1025	10	396	7.52	211	4.23	3.99	26.3	23.6	49.9	0.79	21.4	5.5
1026	20	847	14.1	272	9.68	12.7	97.5	88.1	186	0.42	22.9	6.0
1027	30	1320	18.8	346	15.6	19.4	164	162	325	0.36	23.7	8.1

Table A.32 Electrode Erosion Data for W+La_2O_3

Run #	Caps (#)	Q_s (mC)	Q_e (C)	I_p (kA)	E_s (kJ)	f_1 (*)	DV+ (x 10^{-5} cm^3/shot)	DV-	DV_{tot}	$DV_{\%e}$	V_{sb} (kV)	$DV_{sb\%e}$
1107	1	41.4	1.00	69.7	0.464	0.0986	0.105	0.0703	0.176	20	22.4	3.4
1110	2	79.6	1.98	101	0.855	0.336	0.288	0.216	0.504	14	21.5	3.3
1113	4	141	3.45	132	1.35	0.911	1.00	0.715	1.71	8.4	19.1	7.5
1116	6	214	4.80	137	2.07	1.46	2.36	1.72	4.08	5.3	19.3	6.0
1135	10	324	6.15	172	2.83	2.66	6.81	6.81	13.6	2.6	17.5	8.3
1138	20	592	10.0	190	4.74	5.68	23.6	27.9	51.6	1.4	16.0	12
1141	30	849	12.1	223	6.50	8.95	52.7	45.3	98.0	1.1	15.3	16

*The units on f_1 are ($A^2s^{1.5}$ x 10^3).

Table variables are defined in Table A.5.

Table A.33 Electrode Erosion Data for W+ThO_2#1

Run #	Caps (#)	Q_s (mC)	Q_e (C)	I_p (kA)	E_s (kJ)	f_1 (*)	DV+ (x 10^{-5} cm^3/shot)	DV-	DV_{tot}	$DV_{\%e}$	V_{sb} (kV)	$DV_{sb\%e}$
1046	1	40.5	0.976	68.0	0.443	0.094	0.156	0.137	0.293	0.1	21.9	3.2
1045	2	79.0	1.97	101	0.844	0.334	0.411	0.406	0.818	0.09	21.4	2.9
1044	4	145	3.53	135	1.41	0.953	1.12	1.02	2.14	0.07	19.6	5.9
1043	6	211	4.73	135	2.01	1.41	3.06	2.33	5.40	0.04	19.0	6.9
1042	10	337	6.40	179	3.07	2.88	6.92	8.72	15.7	0.02	18.2	8.2
1041	20	749	12.5	241	7.58	9.01	13.9	17.4	61.7	0.01	20.2	8.2
1040	30	1150	16.5	304	20.0	16.6	63.4	58.1	118	0.01	20.8	9.0

Table A.34 Electrode Erosion Data for W+ThO_2#3

Run #	Caps (#)	Q_s (mC)	Q_e (C)	I_p (kA)	E_s (kJ)	f_1 (*)	DV+ (x 10^{-5} cm^3/shot)	DV-	DV_{tot}	$DV_{\%e}$	V_{sb} (kV)	$DV_{sb\%e}$
1095	1	39.6	0.954	66.6	0.424	0.0899	0.185	0.148	0.332	11	21.4	3.2
1098	2	78.9	1.96	101	0.841	0.332	0.649	0.649	1.30	0.6	21.3	2.5
1101	4	141	3.45	132	1.35	0.911	1.67	1.67	3.34	4.2	19.1	7.9
1081	6	216	4.84	138	2.10	1.48	4.08	3.65	7.73	2.8	19.5	6.7
1074	10	339	6.44	180	3.11	2.91	8.95	9.67	18.6	1.9	18.3	11
1066	20	613	10.2	197	5.09	6.01	27.2	30.8	58.0	1.2	16.6	10
1069	30	919	13.1	242	7.60	10.5	53.7	62.3	116	0.9	16.6	11

*The units on f_1 are ($A^2s^{1.5}$ x 10^3).

Table variables are defined in Table A.5.

Table A.35 Electrode Erosion Data for $W+Y_2O_3$

Run #	Caps (#)	Q_s (mC)	Q_e (C)	I_p (kA)	E_s (kJ)	f_1 (*)	DV+ (x 10^{-5} cm^3/shot)	DV-	DV_{tot}	$DV_{\%e}$	V_{sb} (kV)	$DV_{sb\%e}$
1108	1	39.4	0.950	66.2	0.420	0.0889	0.152	0.114	0.265	14	21.3	2.6
1111	2	79.9	1.99	102	0.863	0.341	0.450	0.525	0.975	7.7	21.6	4.2
1114	4	146	3.56	136	1.44	0.968	1.64	1.64	3.29	4.6	19.7	5.6
1117	6	213	4.77	136	2.05	1.44	3.13	2.68	5.82	3.8	19.2	6.7
1136	10	348	6.61	185	3.27	3.07	7.83	8.20	16.0	2.3	18.8	10
1139	20	644	10.8	207	5.60	6.68	25.4	47.0	72.3	1.0	17.4	13
1142	30	966	13.8	254	8.40	11.6	45.9	74.9	121	0.9	17.4	10

Table A.36 Electrode Erosion Data for WS-2

Run #	Caps (#)	Q_s (mC)	Q_e (C)	I_p (kA)	E_s (kJ)	f_1 (*)	DV+ (x 10^{-5} cm^3/shot)	DV-	DV_{tot}	$DV_{\%e}$	V_{sb} (kV)	$DV_{sb\%e}$
1096	1	42.9	1.03	72.2	0.498	0.105	0.187	0.150	0.337	11	23.2	5.8
1099	2	78.1	1.94	99.6	0.824	0.324	0.353	0.282	0.635	11	21.1	3.8
1103	4	139	3.38	129	1.30	0.872	1.32	1.02	2.34	6.2	18.7	7.9
1104	6	211	4.74	135	2.01	1.42	3.07	2.85	5.92	3.7	19.0	7.7
1079	6	212	4.75	135	2.03	1.42	2.62	2.62	5.24	4.2	19.1	6.6
1078	10	330	6.28	176	2.95	2.78	10.2	8.40	18.6	2.0	17.9	8.2
1072	20	582	9.71	187	4.57	5.43	22.6	30.0	52.6	1.4	15.7	12
1068	30	862	12.3	227	6.69	9.26	51.5	54.8	106	1.0	15.5	13

The units on f_1 are ($A^2s^{1.5}$ x 10^3).

Table variables are defined in Table A.5.

Table A.37 MAX I Experimental Results

Run #	Material	# shots	Q_s (C)	f_1 ($x10^3 A^2 s^{1.5}$)	V_{br} (kV)	Q_e (C)	v_e ($x10^{-5} cm^3$/shot)
401	W+ThO_3#1	1	5.86	104	6.1	58.6	3770
402	W+ThO_2#2	1	5.81	102	6.05	58.1	3020
403	W+Y_2O_3	1	3.50	37.1	3.65	35.0	1240
404	W+La_2O_3	1	5.47	90.4	5.7	54.7	2540
405	Cu-Nb#4	1	5.33	85.7	5.55	53.3	1140
406	Cu-Ta#2	1	5.95	107	6.2	59.5	1380
407	Cu-Cr	1	5.09	84.3	5.3	50.9	846
408	W+?(WS-2)	1	5.42	88.8	5.65	54.2	2600
409	Cu#1	2	5.60	94.7	5.83	56.0	5760
410	Cu+Al_2O_3#1	5	6.79	139	7.07	67.9	6240
411	Cu+Al_2O_3#2	1	5.80	102	6.04	58.0	3470
412	Cu-Nb#1+LaB_6	1	6.20	116	6.46	62.0	3380
413	Cu-Nb#2	4	5.76	100	6.00	57.6	2510
414	Cu-LaB_6	1	5.50	91.3	5.73	55.0	2300
415	CuW#3	4	6.30	120	6.56	63.0	1490
416	CuW#2	8	5.98	108	6.27	59.8	1490
417	CuW#1+LaB_6	6	6.28	119	6.54	62.8	2150
418	CuW+Ir	6	5.98	108	6.23	59.8	1340
419	CuW+Sb	15	4.16	52.1	4.33	41.6	965
420	CuW#1	9	6.00	109	6.25	60.0	1480
421	Cu-Ta#1	3	5.56	93.2	5.79	55.6	5050

Table A.37, continued

Run #	Material	# shots	Q_s (C)	f_1 ($x10^3 A^2 s^{1.5}$)	V_{br} (kV)	Q_e (C)	v_e ($x10^{-5} cm^3$/shot)
422	Mo	10	5.17	80.6	5.38	51.7	3270
423	$Mo+LaB_6$	2	6.00	109	6.25	60.0	3560
424	Cu-Nb#1	5	5.76	100	6.00	57.6	2450
425	W#1	4	5.69	97.7	5.93	56.9	1560
426	W#2	5	5.49	91.0	5.72	54.9	1260
427	CuW+Re	2	6.22	117	6.48	62.2	1240
428	Cu-Nb#3	6	5.83	103	6.08	58.3	2600
429	$W+ThO_2$#3	1	4.94	73.8	5.15	49.4	2570
430	W#3	6	4.90	78.0	5.10	49.0	2060
433	CuW#4	1	4.13	51.5	4.30	41.3	669
434	CuZr	1	3.79	43.4	3.95	37.9	1420
435	CuCrZr	1	1.82	10.0	1.90	18.2	49.2
436	C#2	1	6.05	110	6.30	60.5	516
437	Cu-Nb#3	1	6.24	118	6.5	62.4	1430
438	$W+LaB_6$	1	4.70	668	4.90	47.0	1710
439	$W+BaO_2$	1	4.08	50.3	4.25	40.8	3800

Table A.38 Electrode Erosion Data for Cu#1 (d = 2.54 cm)

Run #	Caps (#)	Q_s (mC)	Q_e (C)	I_p (kA)	E_s (kJ)	f_1 (*)	DV+ (x 10^{-5} cm^3/shot)	DV- (x 10^{-5} cm^3/shot)	DV_{tot} (x 10^{-5} cm^3/shot)	$DV_{\%e}$	V_{sb} (kV)	$DV_{sb\%e}$
893	1	59.4	1.43	99.9	0.955	0.202	0.376	0.300	0.676	11	32.1	3.8
892	2	87.3	2.17	111	1.03	0.404	0.746	0.597	1.34	11	23.6	3.7
743	3	133	3.18	137	1.59	0.810	1.34	0.895	2.24	10	24.0	4.4
890	4	176	4.30	165	2.10	1.42	3.24	2.08	5.32	5.6	23.8	4.5
641	5	224	5.41	175	2.72	2.00	4.47	4.85	9.32	4.0	24.3	4.4
1061	6	251	5.62	160	2.83	1.99	6.71	4.92	11.6	3.9	22.6	5.1
746	8	358	6.98	183	4.32	3.04	25.6	29.4	55.0	1.2	24.2	4.9
661	10	443	8.41	236	5.29	4.99	50.0	48.4	98.4	0.8	23.9	6.2
693	20	814	13.6	262	8.95	10.7	228	239	466	0.3	22.0	8.8
622	30	1080	15.4	283	10.4	14.5	474	488	962	0.2	19.4	16
681	30	1100	15.8	290	11.0	15.2	412	434	846	0.3	19.9	17
**736	30	1130	16.1	296	11.4	15.8	273	280	553	0.4	20.3	8.6
**737	30	1230	17.5	323	13.6	18.7	358	358	718	0.0	22.1	8.2
+683	30	1260	18.0	332	14.4	19.8	426	483	909	0.3	22.7	9.7

*The units on f_1 are ($A^2s^{1.5}$ x 10^3).

**Switch #2 ("Piggyback")

+ Gap distance increased to 1.25 cm.

Table variables are defined in Table A.5.

Table A.39 Electrode Erosion Data for CuC#1 (d = 2.54 cm)

Run #	Caps (#)	Q_s (mC)	Q_e (C)	I_p (kA)	E_s (kJ)	f_1 (*)	DV+ (x 10^{-5} cm^3/shot)	DV-	DV_{tot}	$DV_{\%e}$	V_{sb} (kV)	$DV_{sb\%e}$
1059	2	88.8	2.21	113	1.07	0.419	0.900	0.450	1.35	33	24.0	4.5
646	5	232	2.90	180	2.90	1.10	21.0	15.5	36.4	3.0	25.0	5.4
662	10	395	7.50	210	4.21	3.96	85.3	92.0	177	1.3	21.3	16
684	20	660	11.0	212	5.88	6.97	359	400	759	0.6	17.8	18
684-1	20	690	11.5	222	6.43	7.63	382	368	750	0.6	18.6	18
689	30	1030	14.7	271	9.57	13.2	918	825	1740	0.0	18.6	16

Table A.40 Electrode Erosion Data for C#1 and C#2 (d = 2.54 cm)

Run #	Caps (#)	Q_s (mC)	Q_e (C)	I_p (kA)	E_s (kJ)	f_1 (*)	DV+ (x 10^{-5} cm^3/shot)	DV-	DV_{tot}	$DV_{\%e}$	V_{sb} (kV)	$DV_{sb\%e}$
C#1												
645	5	200	4.81	155	2.16	1.58	7.45	5.32	12.8	8.5	21.6	3.5
665	10	373	7.09	199	3.76	3.55	7.09	7.09	14.2	25	20.2	4.6
747	10	451	8.57	240	5.50	5.17	13.9	11.7	25.6	4.2	24.4	4.0
691	20	646	10.8	208	5.65	7.45	21.3	21.3	42.6	17	17.5	9.3
692	20	807	13.5	260	8.81	10.5	31.7	28.2	59.9	2.9	21.8	6.5
C#2												
891	2	73.7	1.84	94.1	0.74	0.29	1.84	1.84	3.68	10	19.9	5.5
889	4	161	3.92	150	1.75	1.18	3.58	3.58	7.16	10	21.7	3.7
1062	6	233	5.22	149	2.45	1.72	4.26	4.26	8.51	25	21.1	6.5
784	10	461	8.75	245	5.74	5.39	17.7	17.7	35.5	10	24.9	3.8
785	20	932	15.6	300	11.7	14.0	46.1	42.6	88.7	4.0	25.2	7.4
793	30	1230	17.6	323	13.6	18.9	53.2	42.6	95.7	11	22.2	12

The units on f_1 are $A^2s^{1.5}$.

Table variables are defined in Table A.5.

Table A.40 Electrode Erosion Data for C#1 and C#2 (d = 2.54 cm)

Run #	Caps (#)	Q_s (mC)	Q_e (C)	I_p (kA)	E_s (kJ)	f_1 (*)	DV+ (x 10^{-5} cm^3/shot)	DV- (x 10^{-5} cm^3/shot)	DV_{tot} (x 10^{-5} cm^3/shot)	$DV_{\%e}$	V_{sb} (kV)	$DV_{sb\%e}$
C#1												
645	5	200	4.81	155	2.16	1.58	7.45	5.32	12.8	8.5	21.6	3.5
665	10	373	7.09	199	3.76	3.55	7.09	7.09	14.2	25	20.2	4.6
747	10	451	8.57	240	5.50	5.17	13.9	11.7	25.6	4.2	24.4	4.0
691	20	646	10.8	208	5.65	7.45	21.3	21.3	42.6	17	17.5	9.3
692	20	807	13.5	260	8.81	10.5	31.7	28.2	59.9	2.9	21.8	6.5
C#2												
891	2	73.7	1.84	94.1	0.74	0.29	1.84	1.84	3.68	10	19.9	5.5
889	4	161	3.92	150	1.75	1.18	3.58	3.58	7.16	10	21.7	3.7
1062	6	233	5.22	149	2.45	1.72	4.26	4.26	8.51	25	21.1	6.5
784	10	461	8.75	245	5.74	5.39	17.7	17.7	35.5	10	24.9	3.8
785	20	932	15.6	300	11.7	14.0	46.1	42.6	88.7	4.0	25.2	7.4
793	30	1230	17.6	323	13.6	18.9	53.2	42.6	95.7	11	22.2	12

Table A.41 Electrode Erosion Data for CuW#1 and CuW#1+LaB_6 (d = 2.54 cm)

Run #	Caps (#)	Q_s (mC)	Q_e (C)	I_p (kA)	E_s (kJ)	f_1 (*)	DV+ (x 10^{-5} cm^3/shot)	DV-	DV_{tot}	$DV_{\%e}$	V_{sb} (kV)	$DV_{sb\%e}$
CuW#1												
953	2	85.1	2.12	109	0.980	0.388	0.761	0.856	1.61	5.9	23.0	4.4
806	2	110	2.74	140	1.63	0.644	1.24	1.05	2.29	4.2	29.7	5.6
806-1	2	108	2.68	137	1.57	0.617	0.957	1.06	2.01	4.8	29.1	8.9
807	6	280	6.26	178	3.52	2.47	11.4	9.43	20.9	1.4	25.2	7.0
808	10	435	8.27	232	5.12	4.82	30.0	31.0	61.0	0.78	23.5	11
694	20	710	11.9	228	6.82	8.11	74.7	76.8	152	0.71	19.2	16
697	30	1260	18.0	332	14.3	19.8	109	104	213	0.68	22.7	12
CuW#2												
640	5	240	5.78	187	3.11	2.29	6.97	6.25	13.2	1.8	25.9	7.7
663	10	467	8.87	249	5.89	5.55	26.0	23.1	49.0	0.98	25.2	4.8
696	20	867	14.5	279	10.2	12.1	59.6	61.5	121	0.79	23.4	8.6
695	20	882	14.7	284	10.5	12.5	56.7	67.3	124	0.78	23.8	7.8
686	30	1360	19.4	357	16.6	23.0	112	124	236	0.61	24.5	7.2
CuW+LaB_6												
809	2	114	2.84	145	1.75	0.692	1.08	0.866	1.95	5.5	30.8	8.2
810	6	313	7.01	200	4.41	3.10	8.11	6.81	14.9	2.2	28.2	5.5
811	10	521	9.90	277	7.35	6.89	24.8	23.7	48.5	1.1	28.2	3.8
770	30	1500	21.5	395	20.3	28.2	165	157	321	0.50	27.0	7.8

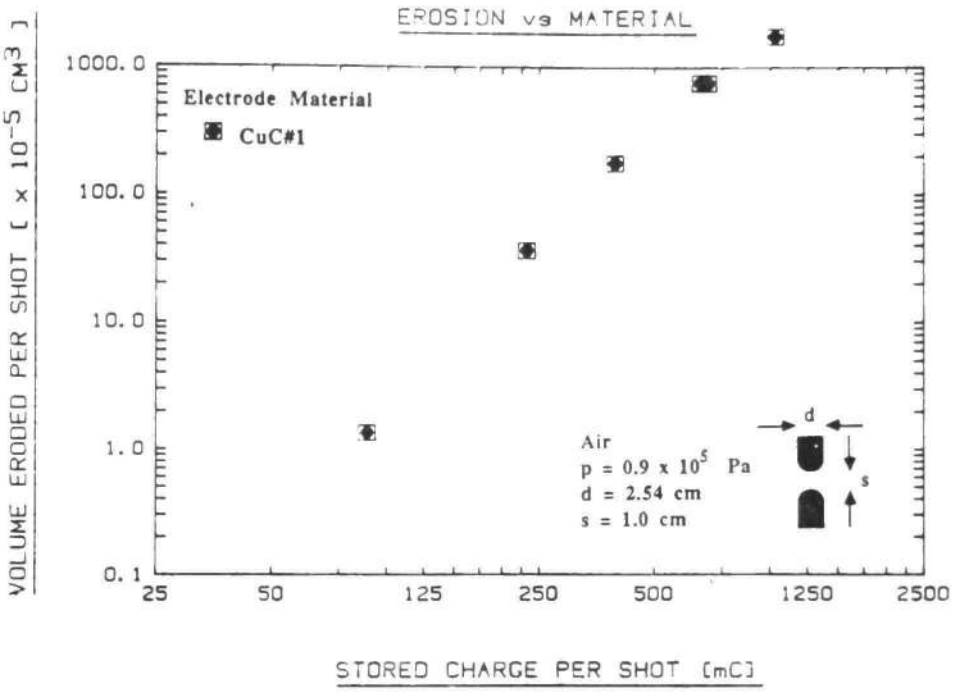

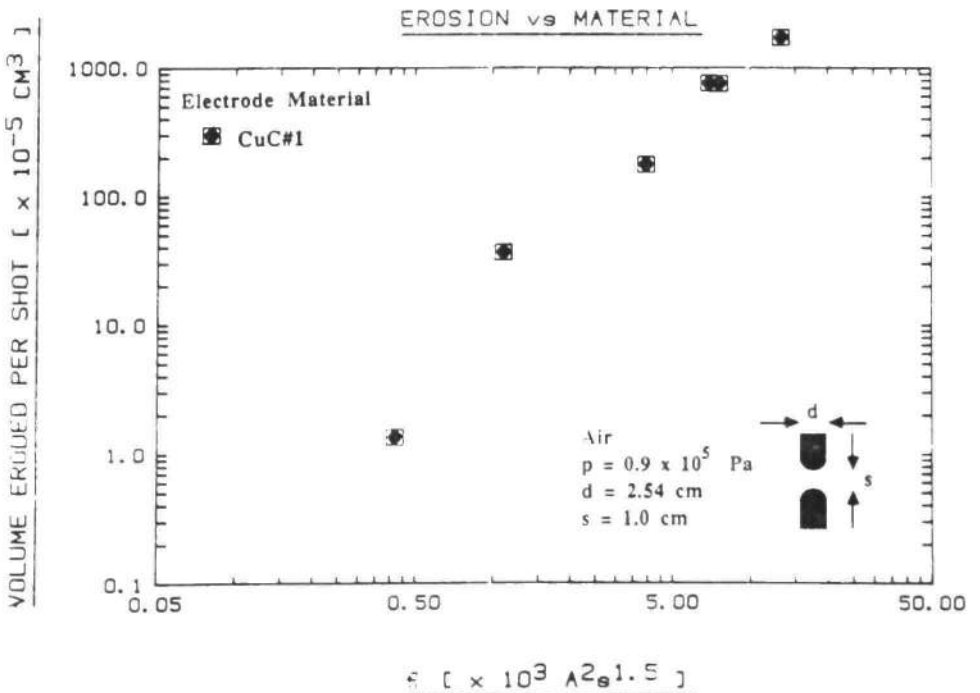

Fig. A.57 Erosion for CuC#1 2.54 cm Diameter Electrodes vs. a) Stored Charge and b) f_1.

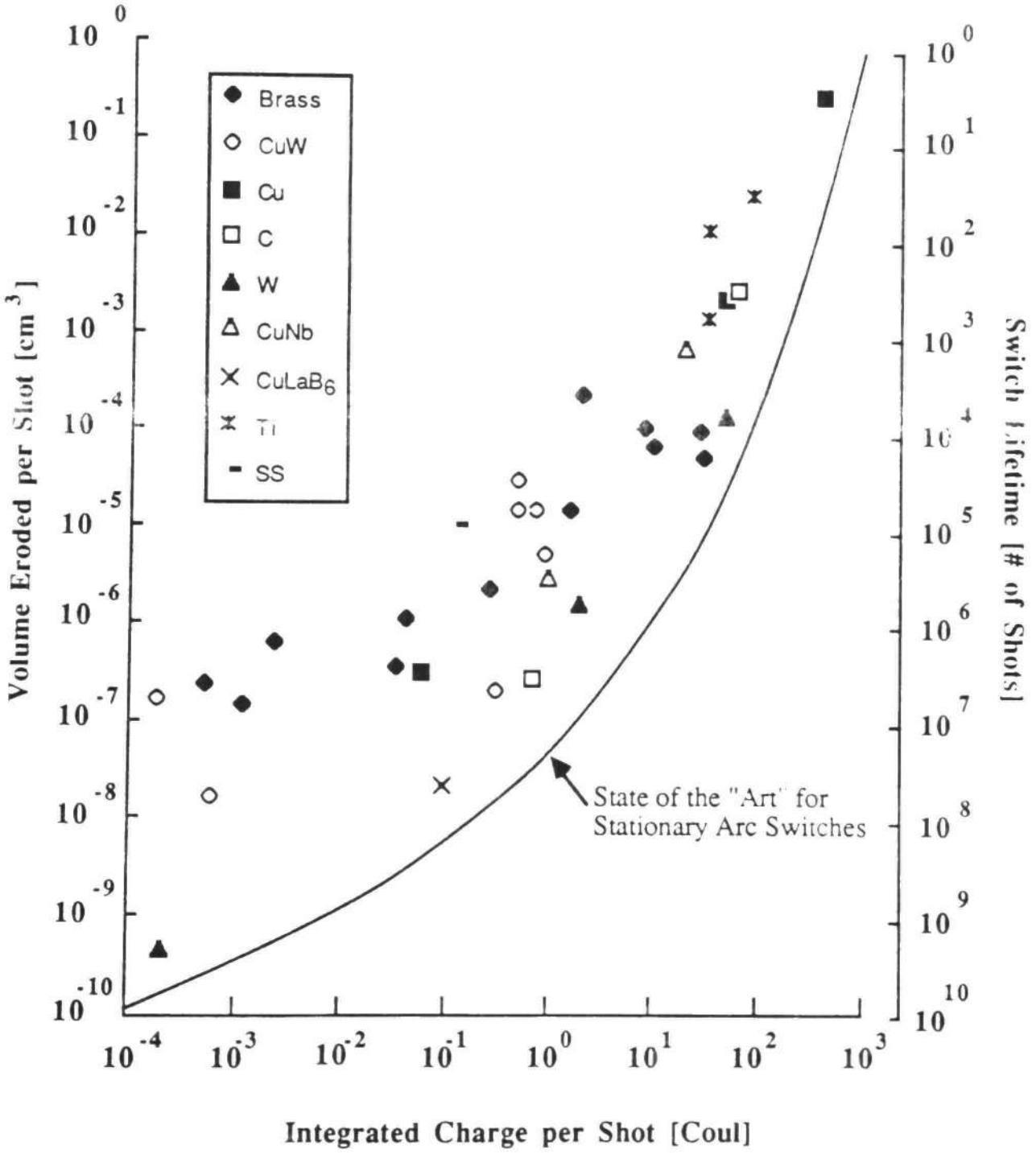

Fig. A.58 Comparison of the Electrode Erosion of the Best Material for Different Experimentalists vs. Effective Charge.

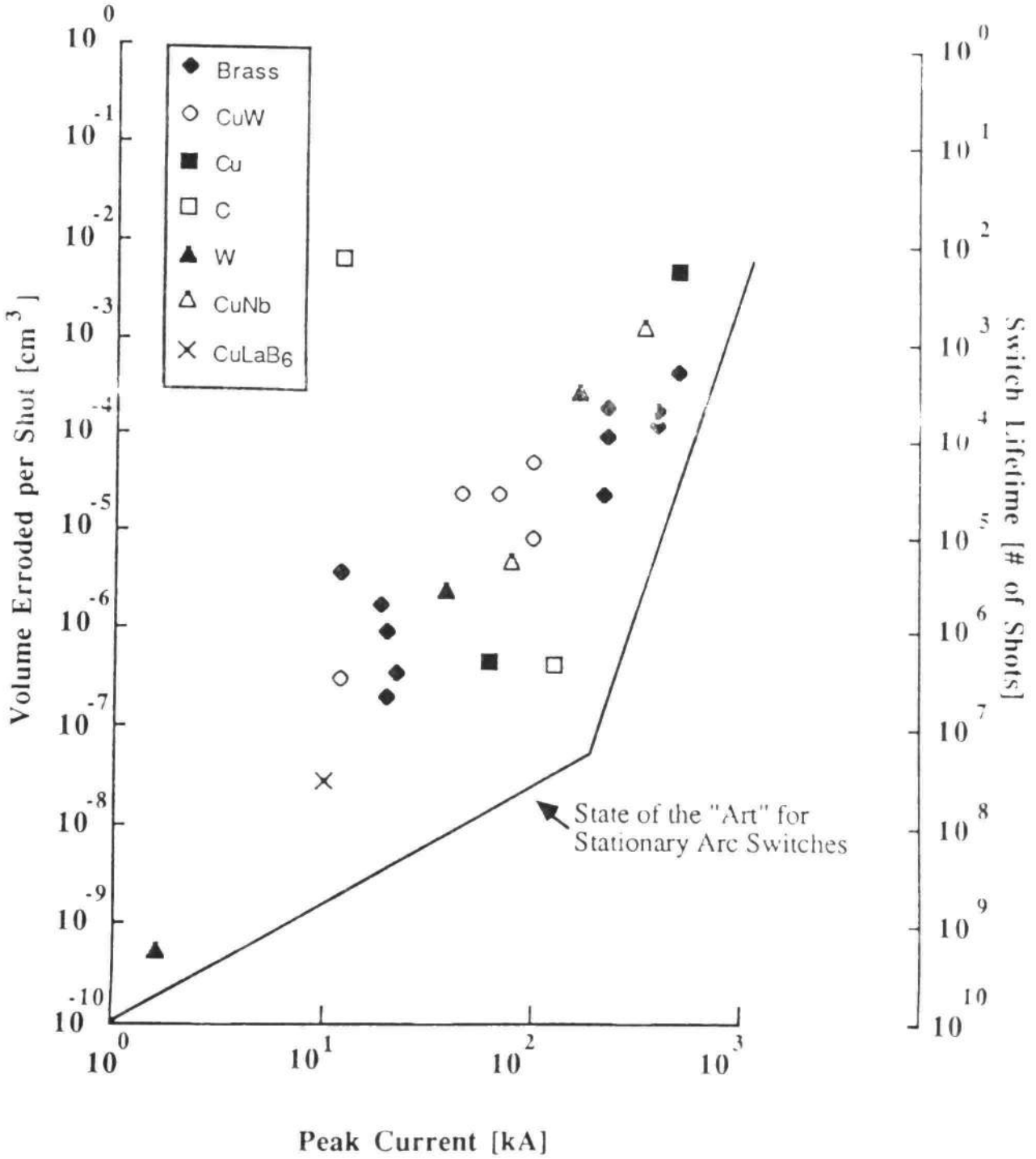

Fig. A.59 Comparison of the Electrode Erosion of the Best Material for Different Experimentalists vs. Peak Current.

2) For lower currents, the material's thermal conductivity is important, which accounts for the reversal in the position of graphite (from best to worst) and the relative values of the two graphites. This effect is also seen in the work of Gruber and Suess [10] for stainless steel electrodes.

3) There is a wide dispersion in the in-situ material results due to the large differences in the manufacturing techniques.

4) The in-situ materials are equal in erosion to, and thus better economically than, CuW composites.

References

[1] "Glidcop," *SCM Metal Products Company Brochure*, Western Reserve Building, W. 9th Street, Cleveland, OH 44113. (EE-9999)

[2] D. Affinito, E. Bar-Avraham and A. Fischer, "Design and Structure of an Extended Life High Current Sparkgap," *IEEE Trans. on Plasma Science*, vol. PS-7(3), pp. 162-163, 1979. (EE-0785)

[3] G.S. Belkin and M.E. Danilov, "Measurement of the Energy Introduced into the Electrodes During the Burning of an Arc in Vacuum," *High Temperature (USSR)*, vol. 11(3), pp. 533-356, 1973. (EE-0242)

[4] S. Levy, "Spark Gap Erosion Studies," *U.S. Army Electronics Research and Development Labs Report # 2454*, Fort Monmouth, NJ, April 1964. (EE-0767)

[5] Y. Suzuki, Y. Kawakita, M. Kume and M. Kawai, "A 150-kV, 100-kA Spark Gap Switch for Marx Generators," *Proceedings of the 3rd IEEE Int. Pulsed Power Conf.*, Albuquerque, NM, pp. 444-448, June 1981. (EE-0884)

[6] "CuNb Microcomposite Conductor," *Supercon Inc. Company Brochure*, 830 Boston Turnpike, Shrewsbury, MA 01545.

[7] M. Kristiansen and L. Hatfield, "SDI Power Conditioning," *Annual Technical Report for the Defense Nuclear Agency on Contract #001-85-C-0184*, pp. 3-6, June 15, 1987.

[8] V.I. Krizhanovskii, A.I. Kuz'michev, G.V. Levchenko, R.B. Luban, and A.I. Shendakov, "Investigation of the Erosion Resistance of Cathode Materials Containing an Admixed Emission Active Phase in the High-Current Vacuum-Arc Regime," *Sov. Phys. Tech. Phys.*, vol. 26, pp. 1204-1208, 1981. (EE-0596)

[9] F.M. Lehr, "Electrode Erosion from High Current, High Energy Moving Arcs," M.S. Thesis, Texas Tech University, pp. 1-68, August 1988.

[10] J.E. Gruber and R. Suess, "Investigation of the Erosion Phenomenon in High Current, High Pressure Gas Discharges," *Institute für Plasma Physik Report # IPP/4/22*, Garching bei Munchen, FRG, 1969. (EE-0877)

APPENDIX B

EXPERIMENTAL CALCULATIONS AND ELECTRODE WEIGHING

Tables B.1-B.3 contain the explanation of the variables involved and the calculations required to obtain the erosion rates. The electrode weighing procedure is described below along with the possible sources and amounts of error.

Two scales were used to weigh the electrodes. The first, a Mettler PE-3600, has a sensitivity of 10 mg and a capacity of 400 g. It had the advantage of being in the same location as the experiment which insures a quick turnaround. The other scale, a Mettler H-10, has a theoretical sensitivity of 100 μg (a practical sensitivity of 1 mg was actually achieved) and a capacity of 160 g. Besides the limited capacity (almost all of the 2.54 cm diameter electrodes exceeded this limit) it had the disadvantage of being located across campus. However, for most of the one and two cap runs, which yield lower values of erosion, it was worth the extra time involved to obtain the more precise weighing.

The accuracy of the scales was checked using a set of standard masses. The results, shown in Table B.4 indicate that although the error (Δm) increases with mass the percentage error ($\Delta m/m$) actually decreases. The overall error in the erosion measurements using the scales is even smaller than this table indicates since it is the change in mass which is actually used in the erosion calculations (e.g., approximately

Table B.1 Explanation of Table Nomenclature

Run #	A different run # is assigned to each experiment. If an experiment is rerun for any reason, it is usually indicated by the old run # - 1. For example 1013 became 1013-1 when we used a more sensitive balance. Run #'s 400-499 were run on the MAX I system. Run #'s 500-599 were run on the Mark V system. Run #'s 600-1200 were run on the Mark VI system.
Caps	The # of capacitors connected to the switch is indicated. Each capacitor is 1.85×10^{-6}F. Whenever possible a symmetric connection is utilized.
Q_s	The total charge stored in 10^{-3} Coulombs.
Q_e	The effective charge transferred in Coulombs.
I_p	The peak current in kiloamps.
E_s	The energy stored in kilojoules.
f_1	A derived parameter which predicts performance.
DV_+	The volume eroded for the electrode which is initially the anode ($\times 10^{-5}$ cm^3/shot).
DV_-	The volume eroded for the electrode which is initially the cathode ($\times 10^{-5}$ cm^3/shot).
DV_{tot}	The total volume eroded ($\times 10^{-5}$ cm^3/shot).
$DV_{\%e}$	The percentage error in the volume measurement due to the weighing limitations.
V_{sb}	The self breakdown voltage in kilovolts.
$DV_{sb\%e}$	The percentage error in the voltage corresponding to one standard deviation.
t_1	The time for the first half cycle of the current waveform in 10^{-6} sec.

Table B.2 Calculations

C_{tot}	(# Caps)(1.85 x 10^{-6})
Q_s	(# Caps)(1.85 V_{sb})
Q_e	(SFQ)(Q_s x 10^{-3})
I_p	(V_{sb})(SFI)
E_s	(Q_s)(V_{sb})/2000
D_{v-}	(Cathode mass loss)/((density)(# shots))
D_{v+}	(Anode mass loss)/((density)(# shots))
D_{vtot}	D_{v-} + D_{v+}
f_1	(Q_e)(I_p)((t_1)$^{1/2}$)

Note:SFI and SFQ are the scale factors used to convert breakdown voltage to current and charge. (See Table B.3 for their values.)

Table B.3 Calibration Tables

# Caps	SFQ	SFI	# shots	t_1*
1	24.1	3.11	1500	2
2	24.9	4.72	750	2.82
3	23.9	5.74	500	3.46
4	24.4	6.91	375	4
5	24.1	7.19	300	4.47
6	22.4	7.08	250	4.9
7	19.7	7.51	225	5.29
8	19.5	7.59	188	5.66
10	19.0	8.60	150	6.32
20	16.7	11.9	75	8.94
30	14.3	14.6	50	11

*An effective time defined as the first half-cycle time in us. The factors SFQ and SFI are scale factors used to convert measured breakdown voltages to charge and current.

Table B.4 Electrode Scale Calibration

Calibration (g)	Δm (H-10) (g)	ΔM(PE-3600) (g)	Δm/m (H-10) (%)	Δm/m (PE-3600) (%)
0.010	0.0000	0.00	< 0.5	< 50
0.020	0.0000	0.00	< 0.25	< 25
0.030	0.0000	0.00	< 0.17	< 17
0.050	0.0000	0.00	< 0.10	< 10
0.100	0.0000	0.00	< 0.05	< 5
0.200	0.0002	0.00	≤ 0.1	< 2.5
0.300	0.0003	0.00	≤ 0.08	< 1.7
0.500	0.0003	0.00	≤ 0.06	< 1.0
1.000	0.0000	0.00	< 0.005	≤ 0.5
5.000	0.0003	0.01	≤ 0.006	≤ 0.2
10.000	0.0001	0.02	≤ 0.001	≤ 0.2
20.000	0.0002	0.06	≤ 0.001	≤ 0.3
100.000	0.0001	0.15	≤ 0.0001	≤ 0.15

Note: If the Δm was zero then the largest value of an undetectable mass was used for Δm to calculate Δm/m for each scale, e.g. 0.005 for the PE-3600 and 0.00005 for the H-10. The Δm/m values are multiplied by 100 to obtain the %. For Δm values equal to zero a less than (<) symbol is used for Δm/m, for Δm values not equal to zero a less than or equals (≤) symbol is used for Δm/m.

the same measurement error is likely to occur for the electrode both before and after weighing and thus the errors may cancel each other).

The weighing error resulting from handling and mounting was determined by weighing several different electrode materials before and after handling and mounting. The results for electrodes which are bolted on, $\Delta m_1/m$, clamped on, $\Delta m_2/m$, and handled in between weighings, $\Delta m_3/m$ are given in Table B.5. The results indicate that clamping yields a significantly lower error and that simple handling of the electrodes may produce as much error as mounting them. The lower error for the clamping may be a result of the harder electrode materials (W alloys) which required clamping using a collet-like device instead of bolting.

Table B.5 Handling and Mounting Weighing Error

Material	$\frac{\Delta m_1}{m}$	$\frac{\Delta m_2}{m}$	$\frac{\Delta m_3}{m}$
Cu#1	1.6×10^{-5}	--	4.3×10^{-6}
Cu	1.6×10^{-5}	--	3.0×10^{-5}
CuW#3	5.0×10^{-6}	--	5.0×10^{-6}
W#1	0*	--	5.6×10^{-6}
C#2	6.8×10^{-5}	1.4×10^{-5}	4.1×10^{-5}
W+ThO_2#1	--	1.3×10^{-6}	--
W+La_2O_3	--	6.0×10^{-7}	--
W+Y_2O_3	--	1.0×10^{-6}	--
W+LaB_6	--	2.1×10^{-6}	--
W+BaO_2	--	1.4×10^{-5}	--

*$< 4 \times 10^{-7}$

APPENDIX C

ANALYSIS OF ELECTRODE SURFACE DAMAGE IN HIGH ENERGY SPARK GAPS*

A.L. Donaldson, M. Kristiansen, H. Krompholz, and M.O. Hagler
Department of Electrical Engineering/Computer Science
L.L. Hatfield and G.R. Leiker
Department of Physics
Texas Tech University
Lubbock, Texas 79409 USA
P.K. Predecki
University of Denver
Denver, Colorado 80208 USA
G.L. Jackson
The BDM Corporation
Huntsville, Alabama 35805 USA

*Originally presented at the 5th IEEE Pulsed Power Conf. in Arlington, VA, June 1985. The work was published in the conference proceedings and was supported by AFOSR.

Abstract

The surfaces of stainless steel electrodes used in a high energy, gas-filled spark gap have been analyzed using Auger Electron Spectroscopy (AES) and Scanning Electron Microscopy (SEM). The analysis of electrode cross-sections revealed areas of enhanced erosion and crack formation as a result of temperature cycling of the arc and enhanced chemical attack along manganese "stringers" which were present in the stainless steels. The depth of the cracks was considerably less in nitrogen (20 μm) than in air (80 μm) and except at the cracks the damage was generally less than 10 μm. The use of low sulphur steels and cutting the electrodes so that the stringers ran parallel to the surface both proved to be

effective means of eliminating crack formation, thus reducing the chance of electrode failure.

Introduction

The surface damage and subsequent electrode erosion resulting from high energy arcs has been of interest for a considerable time as a major factor limiting the lifetime of spark gaps used as switching components in a variety of pulsed power systems. Recent work on electromagnetic launchers ("rail guns") has renewed the interest in understanding electrode erosion, especially for very high currents (> 100 kA). The work reported here contains results on material effects likely to play a role in electrode reliability in the high current regime.

In order to thoroughly study the processes and effects resulting in electrode surface damage, the following questions should be addressed:

- What effect was observed?
- What is its importance to spark gap performance (via electrode erosion for example)?
- What is (are) the cause(s)?
- How can it be corrected/altered/designed around?

A listing of some of the surface alterations which have occurred are given in Table C.1 along with a brief summary of their significance.

Table C.1 Listing of Surface Damage/Alteration Effects

Effect	Significance
Material Removal (Erosion)*	Increase in Breakdown Voltage
Micro Cracks (Hexagonal "Riverbed")*	Possible Fracturing of Electrode, Bulk Material Removal; Subsequent Failure to Operate
Material Transfer Electrode to Electrode*	Surface Stability & Erosion Rate, A Function of Opposite Electrode
Macro Cracks*	Fracturing of Electrode Subsequent Failure to Operate
Macro Protrusions	Reduction in Breakdown Voltage
Micro Protrusions	Alteration of Breakdown Voltage Stability
Chemical Compound Formation on Surface	Alteration of Breakdown Voltage Stability
Micro Craters	None, Except the Sum Leads to Net Material Removal

*Likely to be of increasing importance at very high currents.

Specifically, the work reported here will concentrate primarily on one of these effects, namely, surface cracking and the resulting hexagonal structure in stainless steel.

Experimental Setup

The electrode erosion experiments described below were performed on the Mark II energy storage and spark gap system. The spark gap was coaxial in design and was essentially like the one shown in Fig. C.1. (Some modifications have been made to allow for water cooling of the electrodes and inner gap housing in order to remove the bulk heat at high rep-rates and high Coulomb transfer.) The spark gap was designed for frequent electrode and insulator replacement and to allow for accurate control of the electrode alignment and gap spacing.

The hemispherically shaped electrodes are all 2.5 cm in diameter and were attached to a stainless steel (304) electrode holder. The insulator inserts provide protection for the main gap housing and studies of the surfaces of these inserts have given information about the insulator damage resulting from the discharge byproducts [1]. A detailed description of the spark gap assembly and diagnostic systems are given elsewhere [2]; however, the operating parameters for the gap are summarized in Table C.2.

The analysis of the elctrodes was performed using several pieces of equipment including a PHI model 595 Auger Electron Spectrometer, a JEOL JSM-2 Scanning Electron Microscope and an Olympus BHM Optical Microscope.

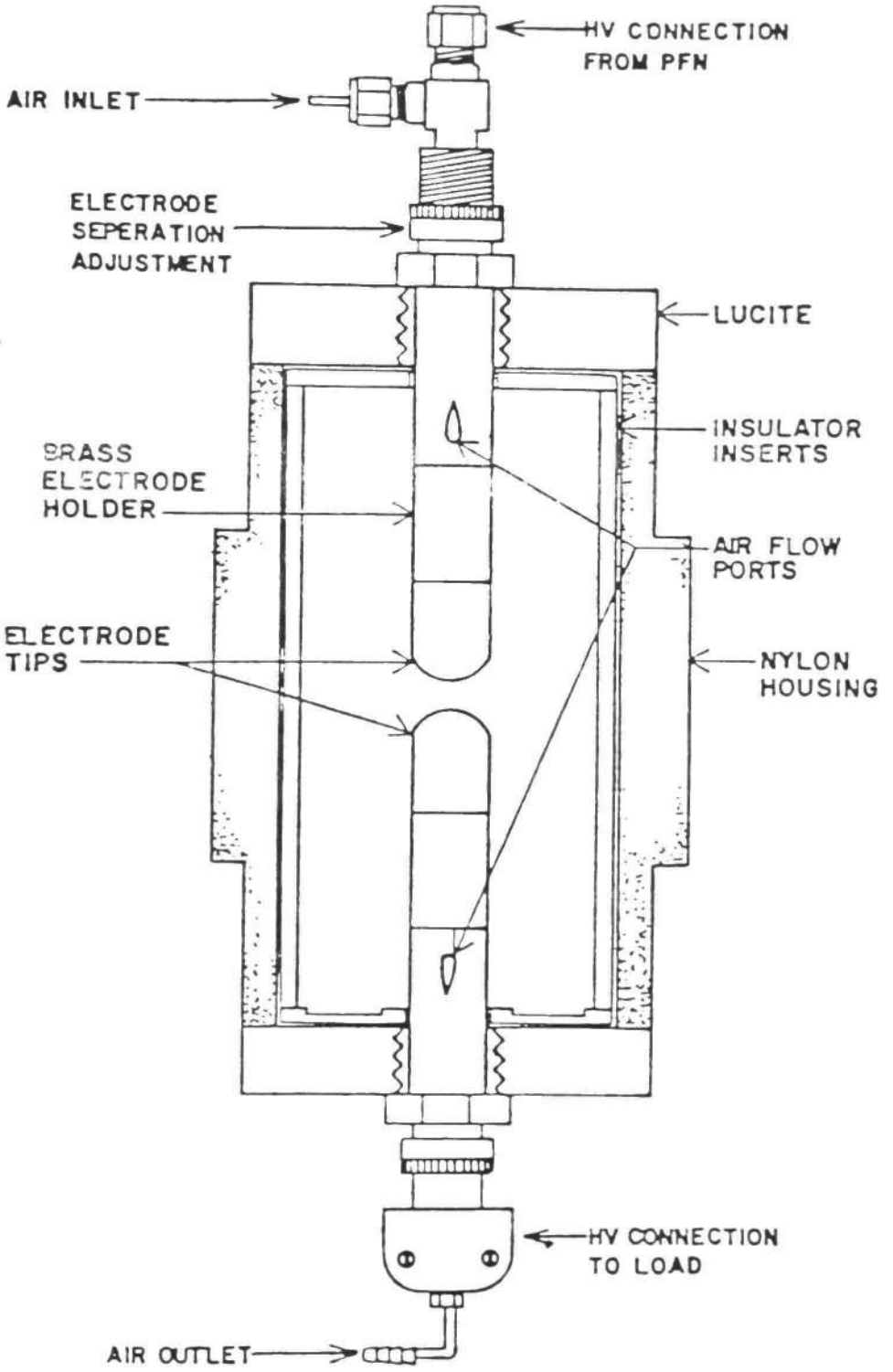

Fig. C.1 Mark II Spark Gap (Original).

Table C.2 Mark II Operating Conditions

Gap Spacing	< 0.75 cm
Voltage	< 30 kV
Current	< 25 kA
Capacitance	21 μF
Charge/Shot	0.6 Coul
Energy/Shot	< 9 kJ
Pulse Width	25 μs
Rep-Rate	5 pps
Pressure	1 atm (absolute)

Results

Previous experiments performed by the authors [3] have shown that stainless steel (304) electrodes subjected to 50,000 shots showed a significant reduction in electrode erosion (1.5 to 0.7 μcm^3/coul) when the switching gas was changed from air to nitrogen. The surfaces of these electrodes, shown in Fig. C.2, indicate a regular surface pattern with cracks similar in appearance to a dried up river bed.

The cross sections of these electrodes, shown in Fig. C.3, reveal cracks with depths of approximately 80 μm for electrodes run in air and 20 μm for electrodes run in nitrogen. At first it was thought that the cracks were due solely to temperature cycling in the material with the "hexagonal" pattern resulting from the biaxial tensile forces present during resolidification of the molten surface. (A simple calculation showed that a temperature change of 200°C could lead to crack formation.)

However, further examination of the cracks shown in Fig. C.4, revealed that the crack orientation was coincident with manganese "stringers" present in the steel, which are perpendicular to the surface (parallel to the length of the rod from which the electrode tip was cut).

Auger analysis of the cracks indicated that the manganese acted as a "getter" for the sulphur present in the steel which at high temperatures resulted in a chemical reaction leading to material removal at the manganese sites. However, since

(a) 2mm

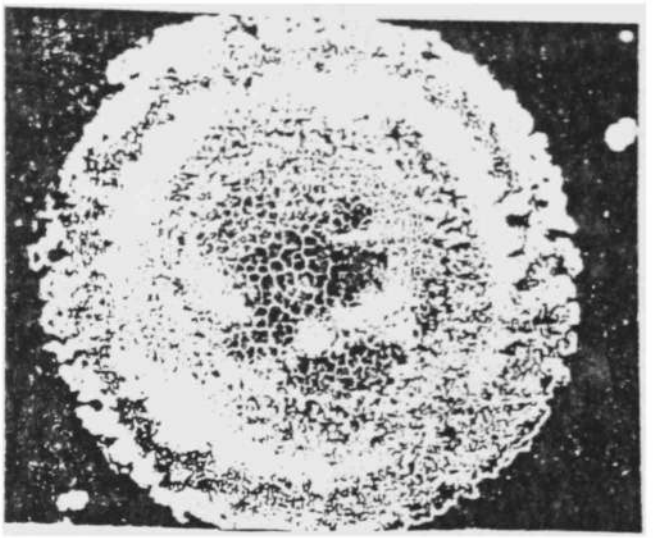

(b) 200μm

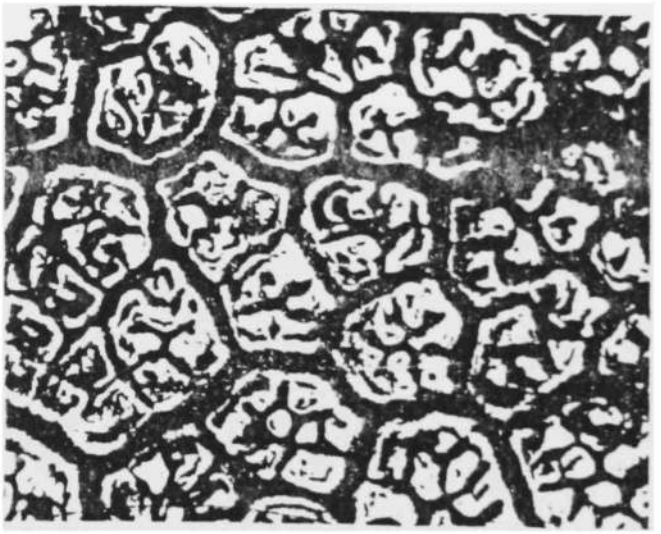

(c) 2mm

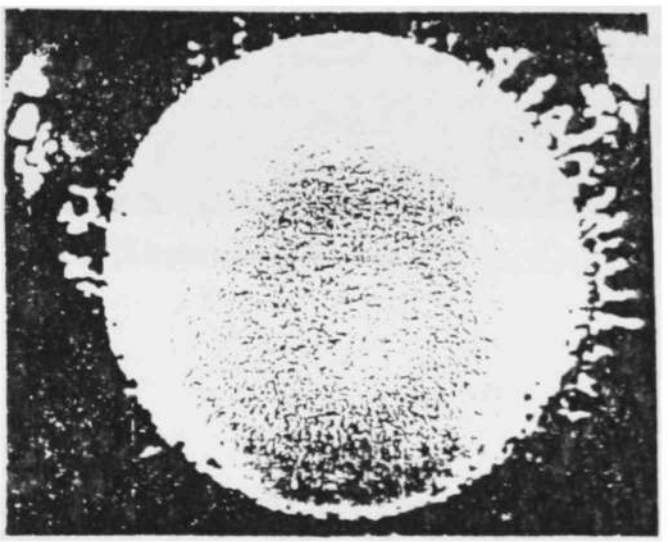

Fig. C.2 Surfaces of Stainless Steel (304) Cathode. ((a) in Air, Low Magnification; (b) in Air, High Magnification; (c) in N_2, Low Magnification)

(a) 50 μm

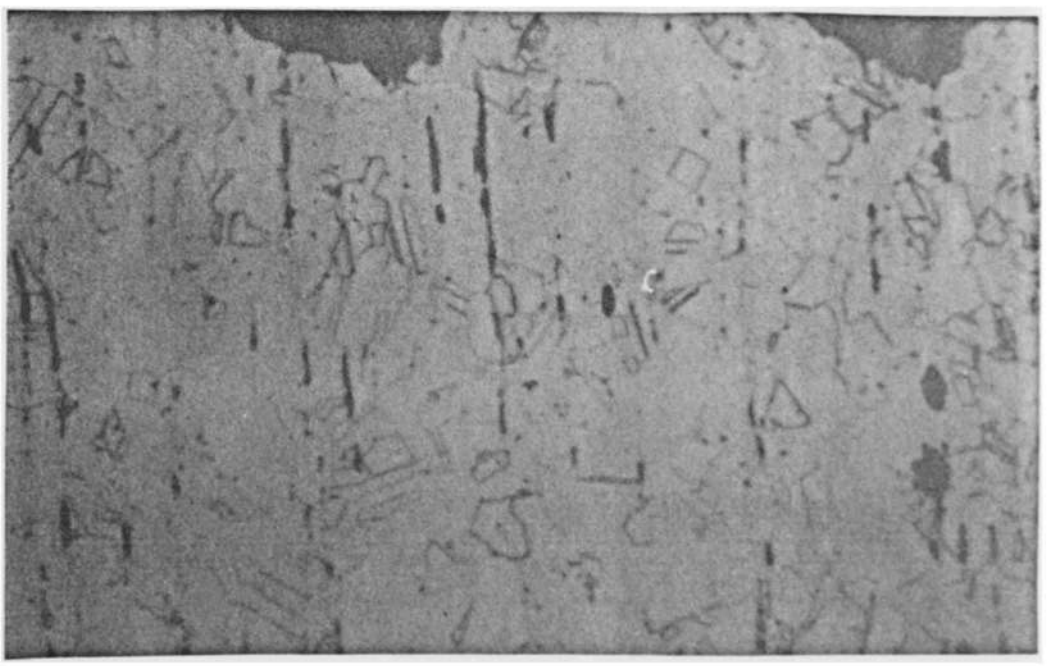

(b) 50μm

Figure C.3 Cross Sections of Stainless Steel (304) Cathode. ((a) in Air, (b) in Nitrogen).

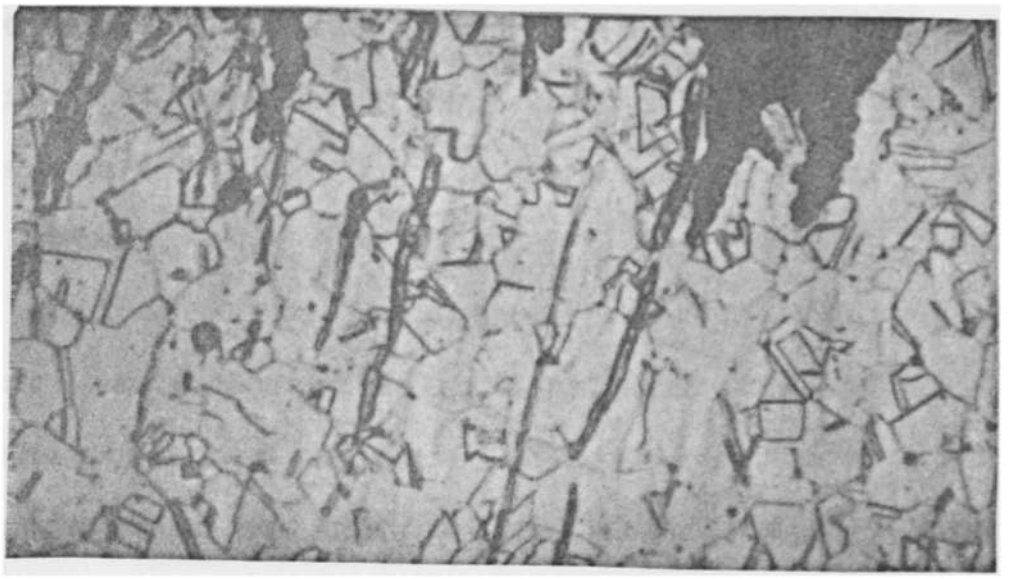

(a) 50μm

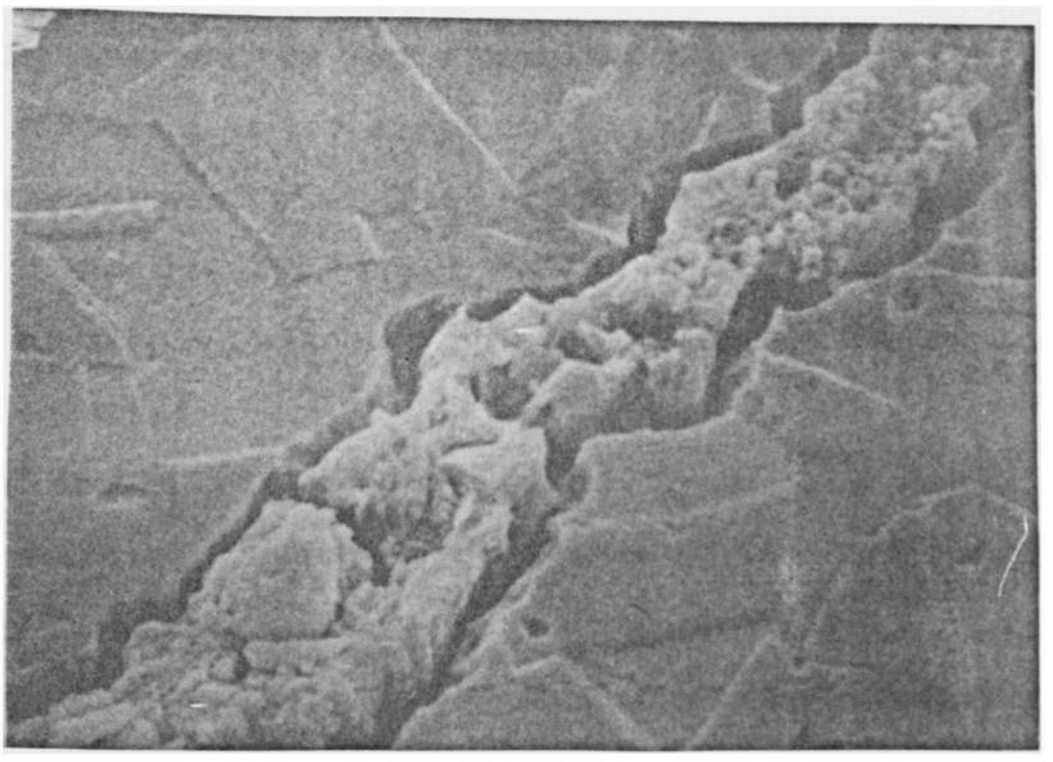

(b) 50μm

Figure C.4 Cross Sections of Stainless Steel (304) Cathode in Air. ((a) on the Outer Edge; (b) SEM Photograph at Region Examined by Auger Analysis)

many more manganese sites exist than those occurring just at the cracks, it was concluded that the resulting surface formation was a combination of both temperature cycling and chemical attack.

To validate the importance of the stringers, an experiment was performed using a cathode (304) which was cut so that the stringers ran parallel to the surface of the steel and an anode which had the original orientation to serve as a control. The resulting surfaces shown in Fig. C.5 indicated that no surface cracking occurred in the cathode (as expected), whereas the anode remained the same.

In addition, at the suggestion of the steel manufacturer, a second steel was tried (316) which might have lower sulphur content. The results, shown in Fig. C.6, also indicate an absence of cracks, although no significant reduction in bulk erosion occurred.

One should not conclude from these experiments that surface cracking requires the presence of manganese stringers or even chemical attack--any mechanism which leads to a weakening of the material surface during temperature cycling can prove sufficient to produce the observed structure. Indeed, crack formation has been observed by the authors and others in electrodes made of copper in a tungsten matrix [3-5] and tantalum [6], although the processes leading to the surface cracking are unclear.

Examination of electrodes run for 2,000, 10,000 and 50,000 shots indicated that the depth of the cracks increases

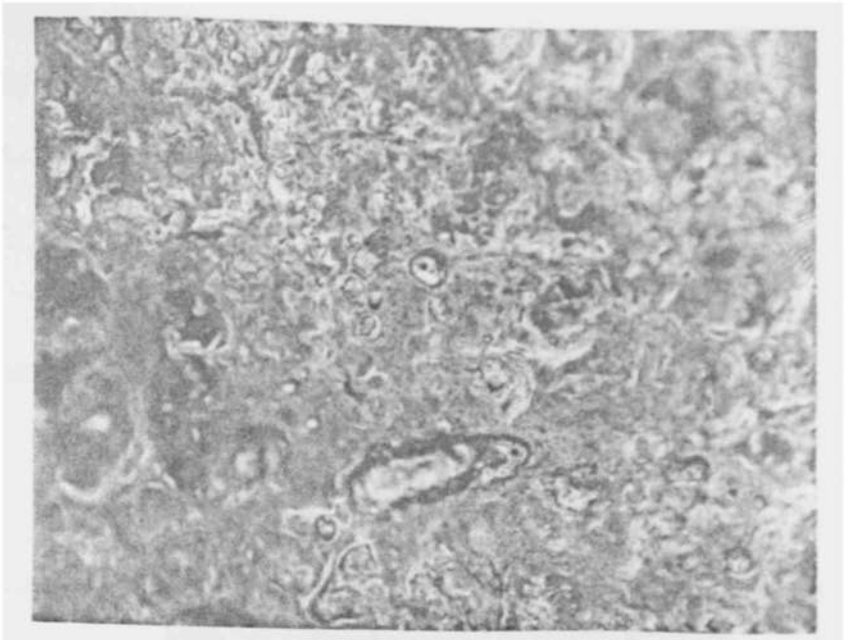

(a) 20 μm

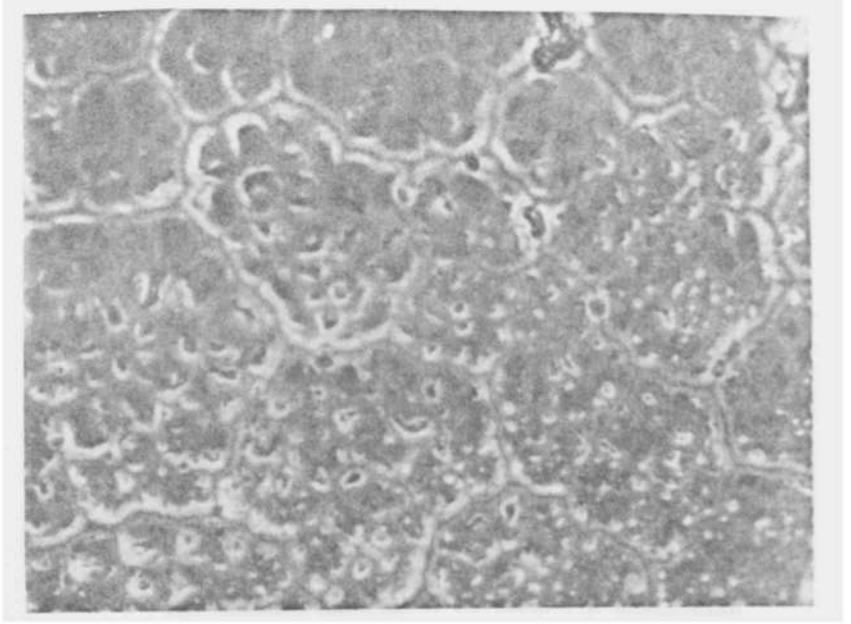

(b) 200 μm

Figure C.5 Surface of Stainless Steel (304) in Air. ((a) cathode--cut so that stringers ran parallel to the surface; (b) anode--the same as previous runs)

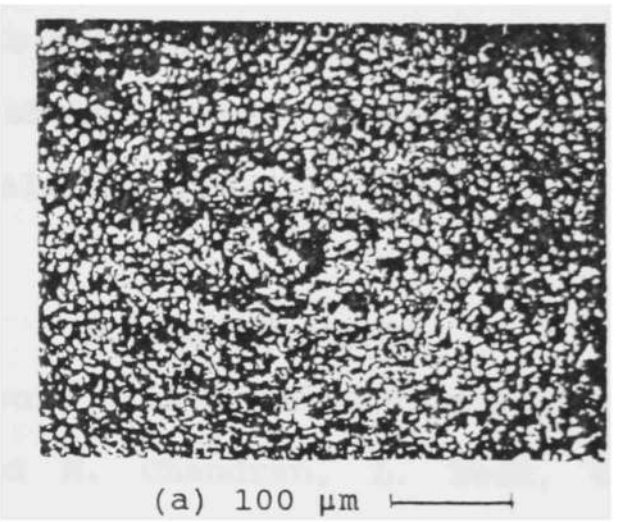

Figure C.6 Comparison of Cathode Surfaces of Two Different Stainless Steels. ((a) 316; (b) 304)

with shot number and, although the damage at 50,000 shots (80 μm cracks) was not enough to produce catastrophic failure of the electrode, it is quite plausible that for normal switching use (10^6 to 10^8 shots) crack formation could present a significant materials problem.

Acknowledgements

The authors would like to thank M. McNeil for her work on the manuscript and M. Chandran, L. Heck, G. Jorden, L. Stephenson, H. Tanumihardja, and B. Tucker for their work on the data acquisition system and experimental facility.

References

[1] G.L. Jackson, L. Hatfield, M. Kristiansen, M. Hagler, A.L. Donaldson, G. Leiker, R. Curry, R. Ness, L. Gordon and D. Johnson, "Surface Studies of Dielectric Materials Used in Spark Gaps," *J. Appl. Phys.*, vol. 55 (1), pp. 262-268, 1984. (EE-1135)

[2] A.L. Donaldson, "Electrode Erosion in a High Energy Spark Gap," Master's Thesis, Texas Tech University, August 1982.

[3] A.L. Donaldson, M.O. Hagler, M. Kristiansen, L.L. Hatfield and G.L. Jackson, "Electrode Erosion Phenomena in a High Energy Pulsed Discharge," *IEEE Trans. on Plasma Science*, vol. PS-12 (1), pp. 28-38, March 1984. (EE-0782)

[4] Y. Suzuki, Y. Kawakita, M. Kume and M. Kawai, "A 150 kV, 100 kA Spark Gap Switch for Marx Generators," *Proceedings of the 3rd IEEE Int. Pulsed Power Conf.*, Albuquerque, NM, pp. 444-447, June 1981. (EE-0884)

[5] M.T. Magnusson, "Erosion and Formation of Cracks in W/Cu Impregnated Materials of Different Tungsten Grain Size," *Elektrotechnische Zeitschrift*, Ausgabe A, vol. 98, pp. 239-240, 1977. (EE-9999)

[6] E.I. Zolotarev, V. Mukhin, L.E. Polyanskii and V.N. Trapeznikov, "Breakdown-voltage Stability of Gas-filled Switches for Voltage Pulse Generator", *Sov. Phys. Tech. Phys.*, vol. 21 (3), pp. 340-344, 1978. (EE-0383)

APPENDIX D

MECHANISM OF ELECTRODE SURFACE DAMAGE AND MATERIAL REMOVAL IN HIGH CURRENT DISCHARGES*

A. Watson, A.L. Donaldson, K. Ikuta, and M. Kristiansen

*This paper was presented at the 4th Electromagnetic Launch Symposium in April 1986, in Austin, Tx. It was subsequently published in the IEEE Trans. on Magnetics, vol. T-MAG-22, pp. 1799-1803, 1986. (EE-0331) The authors were all with the Department of Electrical Engineering/Computer Science at Texas Tech University, Lubbock, Texas 79409. The research was supported by DNA/SDIO.

Abstract

A model of surface damage and material removal is given based upon magnetohydrodynamic phenomena occurring at high current arc electrodes in the microsecond time regime. Experimental observations of the sudden increased erosion rate and surface damage above 250 kA indicate that molten electrode material begins to be driven into jets which break up into droplet streams. Macroprotrusions or "buttes" form by subsequent freezing of the jets which in turn arise from the collective interaction of individual arc filaments. This mechanism has been developed from a model of arc damage due to single filament discharges in the nanosecond time regime. The Stefan problem is considered with Ohmic heating of a liquid metal pool from which material is driven in a hydromagnetic

flow. Alternate models of the liquid jet formation are investigated.

Introduction

At high current levels there is ample evidence to support the conclusion that erosion of material from a pair of electrodes is due to impingement of supersonic jets of metal vapor from one electrode upon the other [1]. It is shown in a companion paper that metallic erosion over a current range from 100-300 kA will take place in proportion to some power of the arc current or of the charge conducted [2]. Within a narrower portion of this range, however, it has been found that one or another of the electrodes will erode excessively while the remaining one appears to lose very little material, (Fig.D.1). Precisely which of the electrodes will erode the most appears to depend upon the geometry but if this is symmetrical it is the anode which loses the most metal. The cathode, although probably losing metal as quickly by vapor jet erosion, is thought to be acquiring material by transfer from the anode. There is hence thought to be two separate and distinct mechanisms operative in metal removal. It will be the purpose here to assemble the evidence in favor of this second process. The discharge current in all experiments described here is supplied by a capacitor bank and is of damped oscillatory form with a frequency of about 100 kHz. When reference is made therefore to the anode or cathode it is intended to imply the state of affairs during the first-half

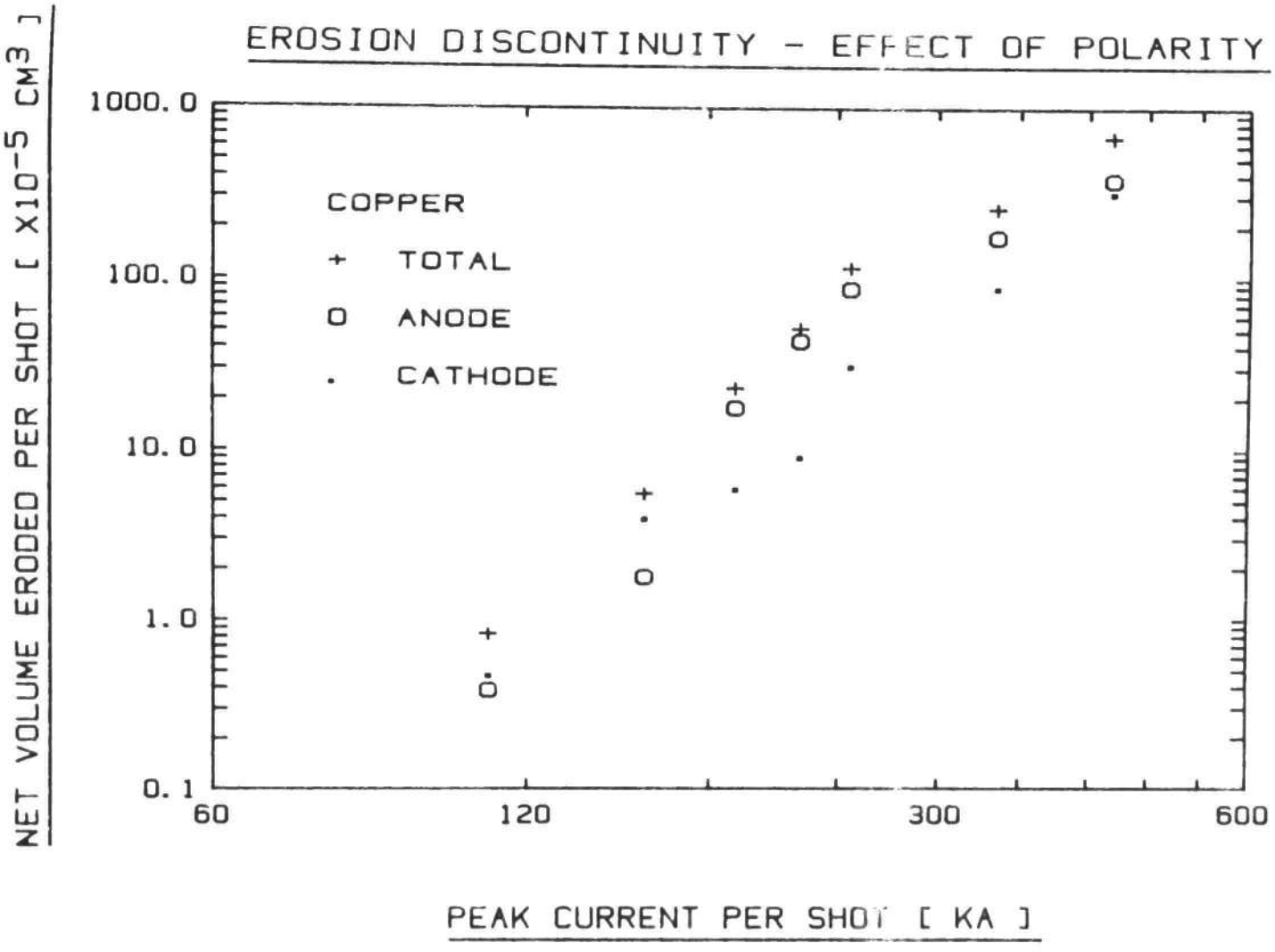

Fig. D.1 Effect of Initial Electrode Polarity Upon Spark Gap Erosion Showing Abrupt Increase in Anode Volume Loss Per Discharge.

cycle of the current pulse, before polarity reversal has occurred.

Investigation of Surface Microtopography and Metallic Debris

Microscopic investigation of both cathode and anode surfaces was carried out after the initial discharge and also at the end of a series of as many as 1500 arcing events. In the former case a characteristic pattern of damage was evident which has led to some conclusions regarding this mode of metal removal. It was found that the surface, in addition to showing widespread evidence of molten liquid flow, occasionally indicated liquid metal displaced in the form of circular rings (Fig. D.2) which bear a strong resemblance to those observed in submicrosecond heavy current spark damage [4]. In addition to this there were frequent incidences of columns of frozen metal rising from the surface, appearing as "buttes" standing out from a flat "landscape" (Fig. D.3) and these were connected by somewhat lower ridges of metal. The buttes appeared in the case of a 230 kA discharge with copper electrodes to be about 100 μm high (Fig. D.4). A remarkable characteristic shared by almost all of these features was that the tip of each protrusion was slightly depressed in the form of a dimple. At this current level the anode erosion rate is shown in Fig. D.1 to be in the heavier loss regime. In contrast, the pictures in Fig. D.3 were obtained for 100 kA and show no such dimples. Although this dimpling of the butte tops may not have been noteworthy alone,it assumes a greater

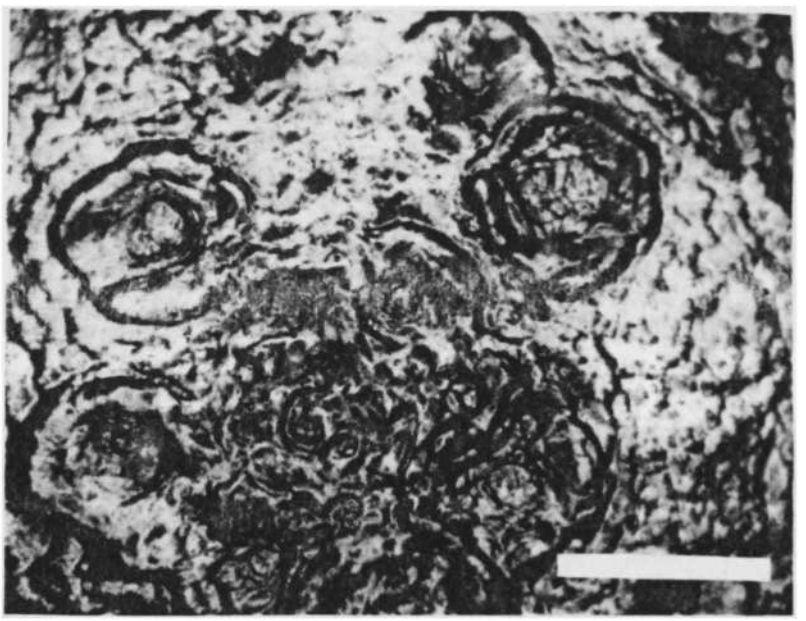

Fig. D.2 Optical Micrograph (50X magnification) of Surface Damage to Cu/Cr Alloy Cathode from a Single 120 kA Discharge.

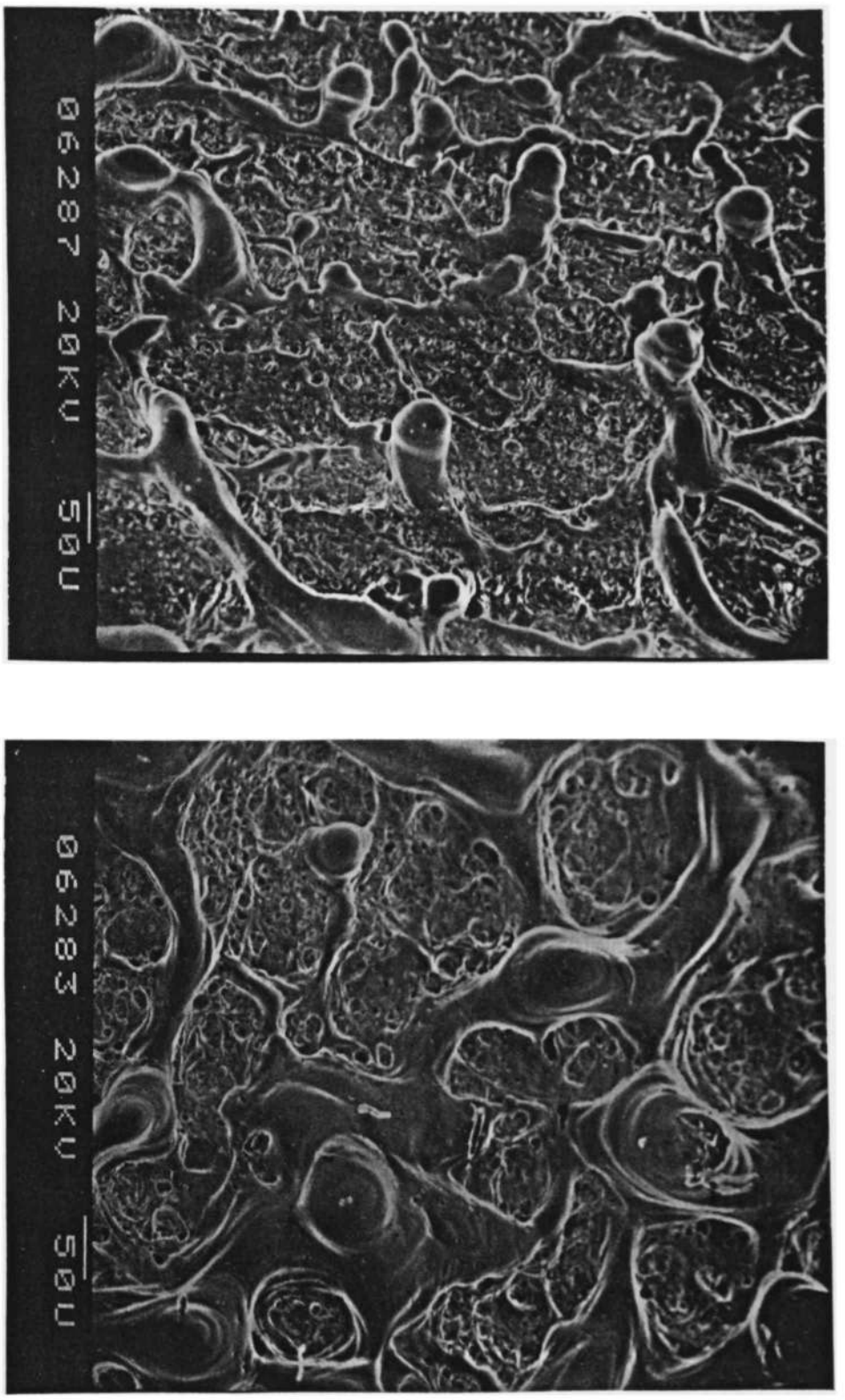

Fig. D.3 Scanning Electron Micrograph of the Surface of a Copper Electrode after 24 discharges at 100 kA. (for a) an oblique angle where the protrusions indicate the presence of purturbing oscillations in diameter leading to tip separations, and b) looking vertically down on the same surface.)

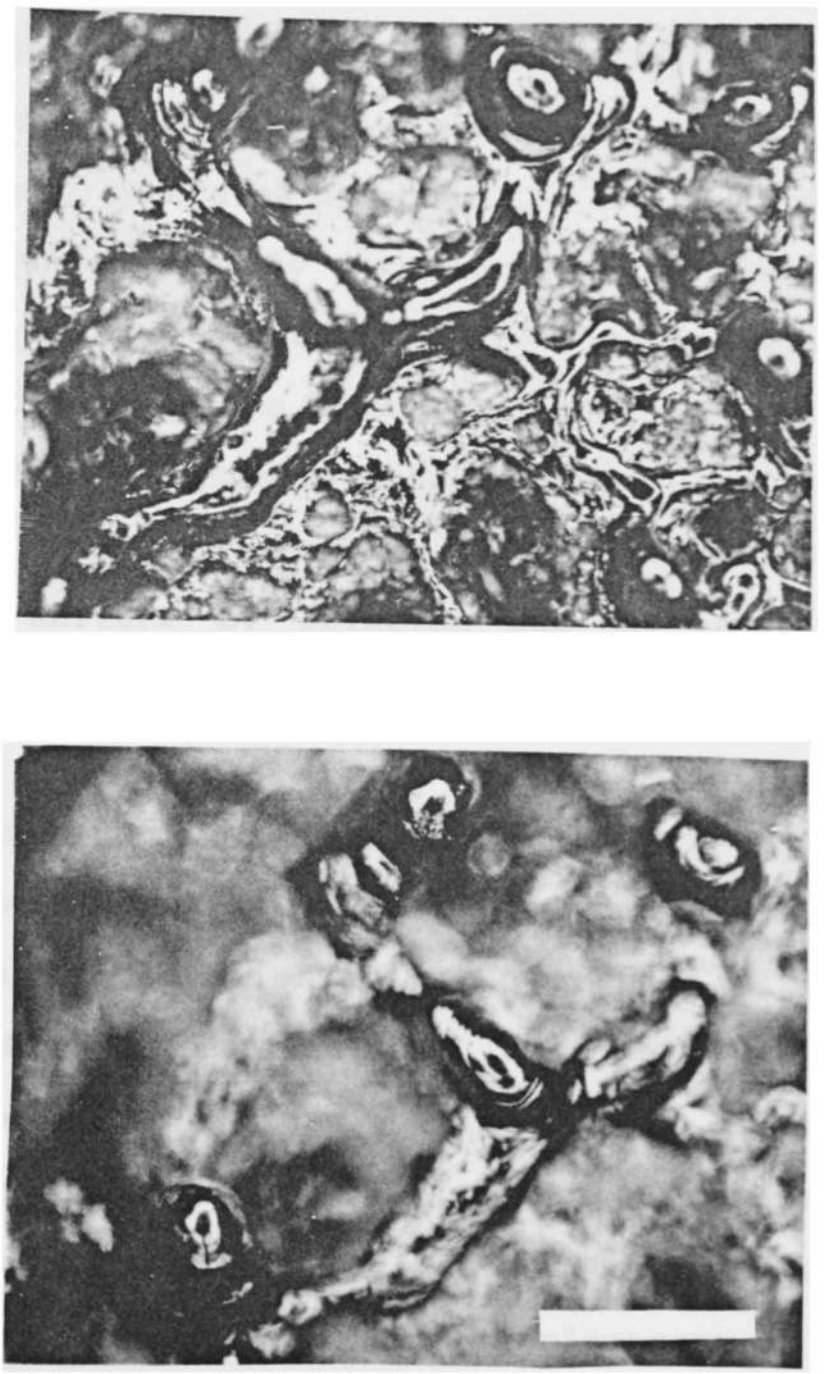

Fig. D.4 Optical Micrograph (100X magnification) Focused on the Dimpled Tips of a Group of Buttes Rising From a Copper Cathode Surface After 300 Discharges at 230 kA.

importance when considered together with the evidence gathered from a microscopic investigation of debris collected from the arc chamber. A typical sample of such debris, photographed and appearing in Fig. D.5, indicates two distinct forms, one of which is quite irregular in shape while the other is comprised of small spherules of about 10- 100 μm in diameter, almost all of which display a characteristic dimple. The diameter of the spherules closely matched the diameter of the tip of the electrode buttes from which they are believed to have originated. Irregularly shaped and, in general, much larger items of debris are thought to have been removed from the electrode surface by ablation due to the impinging supersonic vapor jet.

The Mechanism of Metal Displacement

The dimpled spherules and butte tips constitute evidence that, while in the molten state, the rounded tips of the buttes were undergoing oscillations in shape leading to the ultimate separation of a globule (Fig. D.3). It seems that the shedding of globules fails to shorten the height of the buttes at 230 kA because they all appear to be of about the same size. There is thus a continuing replacement of material lost as globules and in the molten state therefore, there appears to be a flow up the butte which assumes the form of a spout of liquid metal. The instability of such spouts or jets of liquid has been well documented by several authors for over a century [3]. In classical studies liquid emerging from a

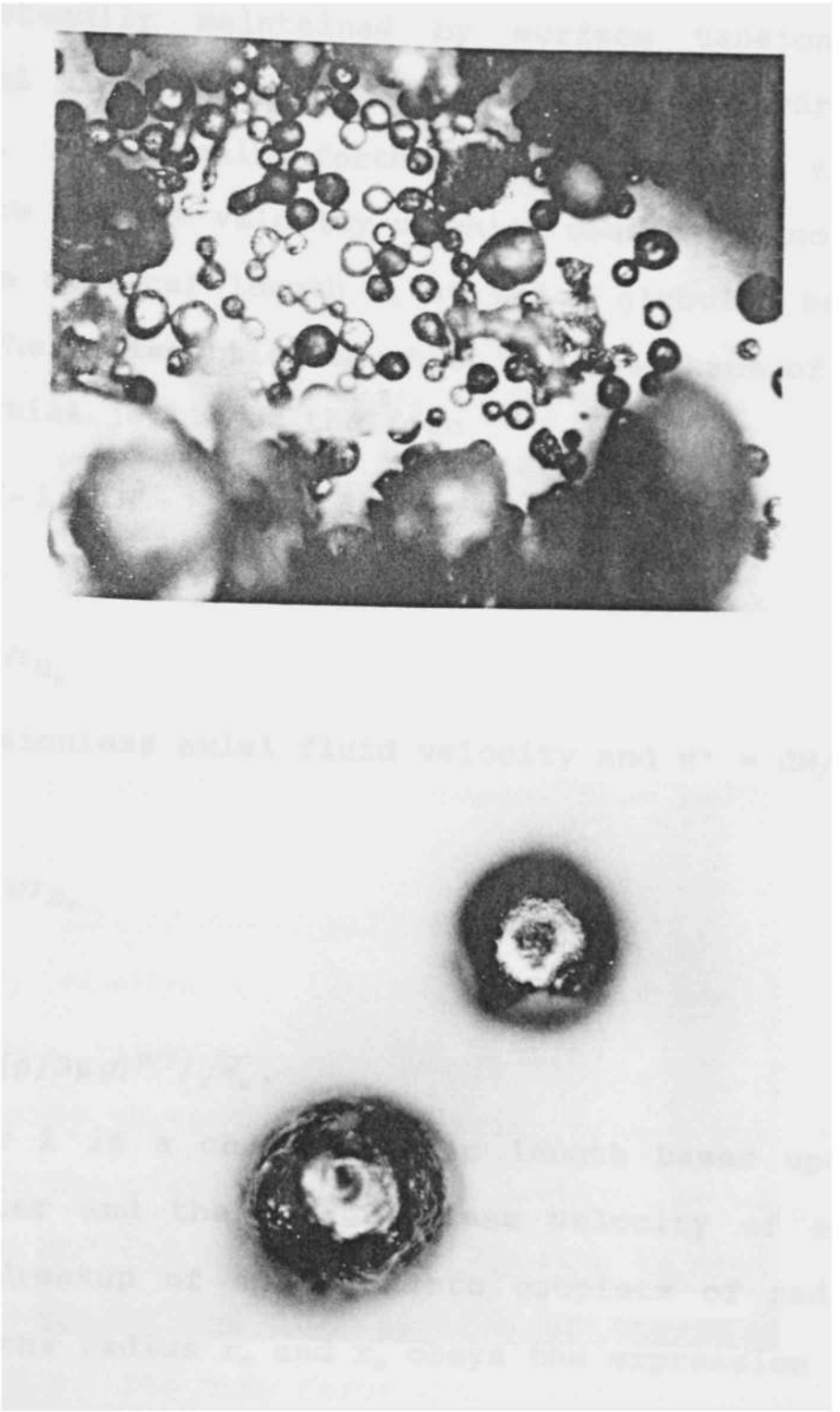

Fig. D.5 Optical Micrograph of a Pair of Dimpled Spherules (100X magnification) Obtained from Spark Chamber Debris.

nozzle with a specific diameter $2r_o$ will form into a jet culminating at the tip in a hemisphere of radius r_c which would be steadily maintained by surface tension under gravitational force were the system to be in hydrostatic equilibrium. When issuing forth as a jet, however, there is an axial flow rate at velocity u_z which causes the column to stretch to a critical length z_c at which globules begin to separate. The differential equation for the shape of such a viscous inertial jet is of the form

$$W'' = (W + W'/W - \lambda/W)\,W' - 1, \tag{D.1}$$

where

$$W = (\rho/3\mu g)^{1/3} u_z \tag{D.2}$$

is the dimensionless axial fluid velocity and $W' = dW/d\xi$, where

$$\xi = g(\rho/3\mu g)^{2/3} z, \tag{D.3}$$

and

$$\lambda = (\gamma/2r_o\rho)\,(\rho/3\mu g)^{2/3}/\sqrt{W_o}. \tag{D.4}$$

The parameter λ is a characteristic length based upon the nozzle diameter and the dimensionless velocity of exhaust therefrom. Breakup of the jet into droplets of radius r_o depends upon the radius r_c and r_o obeys the expression

$$\frac{r_o}{r_c} = \frac{2}{1 - \dfrac{\mu r_c}{\gamma}\left[\dfrac{\partial u_z}{\partial z}\left(1 - \dfrac{\rho r_c^2}{18\mu}\,\dfrac{\partial u_z}{\partial z}\right)\right]_{z=z_c}} \tag{D.5}$$

where μ and γ are the viscosity and surface tension, respectively. For relatively low values of $\partial u_z/\partial z$ the ratio of droplet to jet tip radius approaches the inviscid value of two which is determined from hydrostatic equilibrium. The critical length, z_c, has been demonstrated by dimensional analysis to be related to the jet diameter, d, according to

$$z_c/d = k\ (R_e)^x\ (W_e)^y, \qquad (D.6)$$

where $R_e = vd/\nu$ is the Reynolds' number based upon the characteristic jet velocity, v, and diameter, d, and ν is the dynamic viscosity. The remaining term W_e is the Weber number defined as $W_e = v^2\rho d/\gamma$ in which γ represents the surface tension. The constants and exponents x and y are arbitrarily chosen. An exact theory of jet breakup has yet to be developed due to the theoretical complexities involved.

The Hydromagnetic Spout Model

Classical studies of liquid jet formation have been conducted for viscous, incompressible, and sometimes electrostatically charged fluid emerging from a well defined nozzle [3]. In the present situation, however, no such nozzle is discernable and the spout in fact appears to emerge from a non-circular base at the intersection of the metal ridges shown in Fig. D.3. The body force upon liquid metal subjected to several hundred kiloampere discharges is, moreover, most likely to be hydromagnetic in nature rather than inertial and a model inclusive of this consideration has been sought. As

a starting point the theory of electrode damage from fast transient arcs of 10-100 ns duration has been extended from a previous analysis and compared with experimental data [4]. In this submicrosecond model such a very short duration arc of several hundred kiloamperes strikes an electrode most frequently in a single, well defined, filamentary column and the ensuing current flow causes surface melting and flow in response to a hydromagnetic skin effect. The current rise is so rapid as to be considered instantaneous and flux thereafter is transported into the solid electrode, passing through the molten surface pool of depth h. Hydromagnetic thrust is totally directed normal to the free surface with no radial component and flow in that direction is consequently force-free. The downward thrust and Ohmic power dissipation are each most intense near the arc root and so a decline in both pressure and melting rate occur from the center outwards. Fluid is thus driven radially outward where the floor of the molten pool gradually becomes more shallow. The situation is similar to that of the tidal bore observed at the estuary of some rivers and a similar standing wave accordingly forms in this case at a radius, r_c, from the arc root. This radius has been shown experimentally and theoretically to be directly proportional to the square root of the current, I, flowing in the arc. What is less evident from the short duration experimental observations is that, as melting proceeds while liquid is driven out radially, the floor and the free surface of the pool sink together at the rate h (Fig. D.6). Given

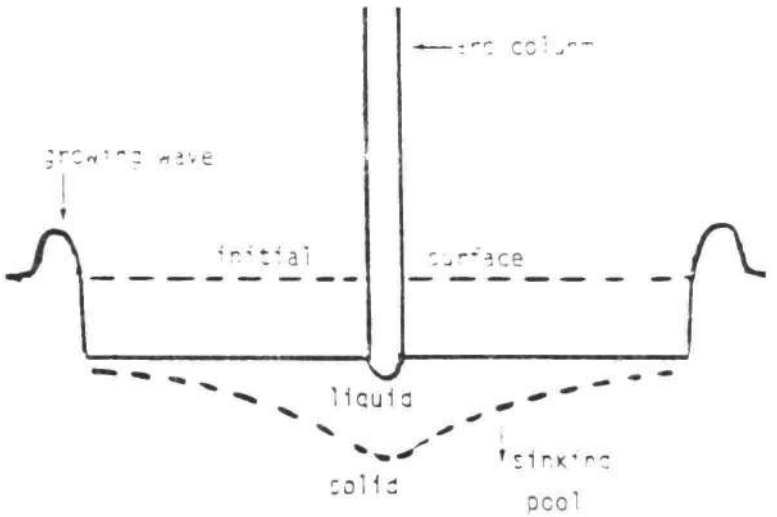

Fig. D.6 Schematic of Cross Section of Arc Column and Electrode Surface. Skin current melts the surface, driving molten metal into a standing wave. As this proceeds the molten pool sinks into the solid.

sufficient time the surface would in fact sink to form a shallow cylindrical depression set into the electrode, as shown in Fig. D.6. The major difference between results obtained in the two time regimes is that arcs tend to divide at the cathode into multiple filaments when they flow for some microseconds duration. Each of the filaments however can separately cause melting and hydromagnetic flow of the surface according to the model described. The radius of each filament will depend upon the square root of the current carried by it and the number density of such filaments as well as the current carried by them will determine whether or not the waves at the lips around their edges will merge. This criterion is fundamental to the mechanism whereby molten liquid can be driven into a spout from which droplets can separate, as has been indicated. The single filament model is based upon the premise that for a flat topped applied current pulse the system is quasisteady, all quantities varying slowly in time at an exponential rate according to $e^{t/\tau}$ where τ is the characteristic time for the system and $t<<\tau$. Upon extension of this model to describe the 100 kHz ringing current system described here it is necessary to observe that individual filaments are created and annihilated continuously and can at least be approximated by a random succession of rapidly rising square pulses. One half cycle of the current waveform lasts for 5 μs and so each pulse will be much shorter than this. The quasisteady flow criterion has been validated in this case by evaluating τ. According to the basic theory $\tau^{-1} = h^{\bullet}/h$ and

the magnetic diffusivity $(\sigma\mu_0)^{-1} = \eta = hh^{\bullet}$. As magnetic flux diffuses into the solid the skin melts and the interface between phases sinks at the rate $h^{\bullet}$ while liquid flows steadily outward at the radial velocity u_r. Conductive heat transport takes place and the Stefan problem for the mobile boundary has been considered. This interface constitutes the melting isotherm at temperature T_{mp} while all other isotherms move together with an associated flux density. From consideration of the similarity between the two transport equations for flux density and temperature it has been found that τ is given by the expression

$$\tau = \eta/2cT = hh^{\bullet}/2ct, \qquad (D.7)$$

where c represents the specific heat of the molten metal and $T = T_m$ is the melting temperature. An estimate of τ has been made for copper, taking into account the elevated resistivity in the molten state and it appears to be of the order of milliseconds. Thus the oscillatory discharge qualifies equally with the 10-100 ns system as being quasisteady. The characteristic time τ is also equal to the ratio of the magnetic field H to its rate of change $H^{\bullet}$ so $\tau = H/H^{\bullet}$ and a second such parameter, $\tau_T = T/T^{\bullet}$, applies to temperature relaxation. It turns out that $\tau = 2\tau_T$ and expression (D.7) can hence be written as $\partial/\partial t\ (cT - h^{\bullet 2}/2) = 0$ and thus

$$h^{\bullet} = \sqrt{2}\, cT_{mp}. \qquad (D.8)$$

An estimate of the value of $h^{\bullet}$ for copper indicates that it is

about 10^3 ms^{-1}. The sinking acceleration $h^{\bullet\bullet}$ is moreover given from the preceding two expressions by

$$H^{\bullet\bullet} = h^{\bullet}/\tau = \sqrt{2}\,(cT_m)^{3/2}/\eta = \sqrt{2}\,h^{\bullet 3}/\eta\,. \qquad (D.9)$$

The pool thus sinks at an accelerated rate which is estimated to be about 10^5 ms^{-2} or 10,000 times the acceleration of gravity. In the accelerated reference frame of the sinking pool there will be an upward thrust of 10,000 g which will be balanced by the JxB body force at the arc root but since JxB falls off in strength radially from this site there will be a resultant upward acceleration of about this order at the standing wave. In about 100 ns (approximate duration of short pulse observations) the pool can only sink about 100 μm and the wave crest rises about the same distance, which is consistent with observations. Since buttes rise above the electrode surface by 100 μm it also appears that only 100 ns is required for this and such a time duration lies well within the 5 μs half wave period of a current oscillation in the present series of experiments.

Discussion

The precise mechanism of metal removal from electrodes during arcing has been under study for many years due to its significance to the electrodischarge machining process. Although the current levels involved in this process are many orders of magnitude lower than those encountered in switching

arcs of current interest it is nevertheless evident that in each case metal is mainly removed as a liquid [5]. The formation and ejection of molten droplets was identified by van Dijck [5] as the most likely cause of erosion in his studies although the precise mechanism will not be the same as that proposed here for the heavy current regime. Ejection of liquid metal was considered by van Dijck due to forces of electrostatic, electromagnetic, hydraulic, and aerodynamic nature as well as from boiling of superheated metal [5]. He concluded that metal can be ejected by electromagnetic forces during the first microsecond of a 400 A current pulse during which the heat source on the surface remains small enough in size before it expands and cools by conductive heat transfer. High speed photographic investigations were quoted in his study which indicated the ejection of tiny balls of metal at 60 ms^{-1} at the beginning of such pulses.

Belkin and Kiselev [7] have also observed that a large percentage of the eroded electrode material is removed in molten form (up to 90% by weight), however, no mention is made concerning the shape of the debris or the mechanism for removal.

Electrode material displacement due to heavy current arcs of much shorter duration than this has been observed and attributed to hydromagnetic forces introduced during widespread surface melting by the skin current [4]. The detailed analysis of this mechanism is being completed and will soon be published. Extension of this mechanism from the

case of a single filament arc to multiple filaments appears feasible from the observations reported here. Such a theoretical extension is predicated upon the propensity of heavy current arcs to divide into multiple cathode spots with individual associated current filaments, each carrying some thousands of Amperes. It is the packing together of such spots (or spot groups) which is responsible for spout formation and droplet shedding. Anode spot formation is moreover a concurrent source for the formation of spouts and the packing of anode spots would then be the definitive factor in determining erosion. For symmetrical electrode geometry the greater metal loss from the node would seem to imply that anode spots are more tightly grouped together.

Although various mechanisms have been investigated theoretically for their potential ability to raise a spout of liquid metal from the electrode surface there is one more which has been observed experimentally as well. In the work of Gobovich and Portitskii an ion beam of up to 500 V energy was projected on to a liquid metal surface which was thereby excited by the growth of nonlinear capillary waves due to the electric field arising from interaction with the plasma [6]. This is known as a Tonks-Frenkel instability and the resulting protrusions of liquid metal resemble the buttes observed on arc damaged electrodes. The Tonks-Frenkel instability however does not operate with the plasma in the arc mode because the plasma interaction region wherein the perturbing electric field is developed becomes highly contracted and does not

uniformly cover a wide area of the surface.

It is possible that a nonlinearly growing hydromagnetic surface wave could contribute to spout formation. The analysis has not, however, been attempted and would necessarily be further complicated in order to account for various sites to which arc filaments are attached. It might be argued that the proposed mechanism is indeed an example of such a nonlinear growing wave.

Acknowledgements

The authors extend their thanks to K. Zinsmeyer, and D. Garcia for their assistance with data acquisition and to I. S. Son for his work in microphotography as well as to S. D. Prien for expertise in scanning electron micrography. Extra thanks are due to Jeannette Davis for her work in preparation of the manuscript.

References

[1] M.A. Sultanov, "Hydrodynamic Processes in a High Power Pulsed Discharge," *Sov. Phys. Tech. Phys.*, vol. 21, pp. 815-821, 1976. (EE-0007)

[2] A.L. Donaldson, E. Kristiansen, M. Kristiansen, A. Watson, K. Zinsmeyer, "Electrode Erosion in High Current, High Energy Spark Gaps," *Proceedings of the 3rd Electromagnetic Launch Conf.*, Austin, TX, 1986. (EE-0136)

[3] J. N. Anno, *The Mechanics of Liquid Jets*, Lexington Books, D.C. Heath & Co. Lexington, MA, 1977.

[4] A. Watson, "Fast Rising Transient Heavy Current Spark Damage to Electrodes," *Proceedings of the 2nd IEEE Int. Pulsed Power Conf.*, Lubbock, TX, pp. 471-474. (EE-0737)

[5] F. van Dijck, "Physico-Mathematical Analysis of the Electro Discharge Machining Process", Doctoral Thesis Catholic University of Leuven, 1973. (EE-1137)

[6] M.D. Gabovich and V. Ya, Poritskii, "Mechanism of Excitation of Nonlinear Capillary Waves of the Surface of a Liquid Metal in Contact with a Dense Plasma," *Sov. Phys. JETP*, vol. 58(1), pp. 86-90, July 1983. (EE-0745)

[7] G.S. Belkin and V. Ya Kiselev "Influence of Electrode Material on Erosion at High Currents," *Sov. Phys. Tech. Phys.*, vol. 12, pp. 702-703, 1967. (EE-0864)

APPENDIX E

MODELING OF MOVING ARC ELECTRODE EROSION

The question has arisen--is it possible to determine moving arc electrode performance and scaling laws by extending both theory and experimental results from stationary arc studies? The answer is yes, provided the erosion in the moving arc is dominated by joule heating in the arc and not the electrode. (This is likely to be the case for many of the operating regimes of interest). For example, the breech end of an electromagnetic launcher, which experiences the greatest erosion, is subject to large heat fluxes, q, produced during arc formation. In addition, the dwell time of the heat flux, t_d, is largest in the breech, which is important because the parameter, $q(t_d)^{1/2}$, determines the onset of bulk melting [1].

A first cut at incorporating the effects of arc motion on electrode erosion has been performed by the author and others [2-4]. However, the curve (Fig. E.1) presented in [2] was intuitive and had not been derived. In the following discussion a derivation is given which suggests that the curve of Fig. E.1 should be modified as shown in Fig. E.2 for the case of constant arc velocity. A more generalized expression which takes into account the time and peak current variation of arc velocity and arc attachment area could easily be implemented on a computer.

It has been previously shown experimentally and theoretically (see Chapter 4) that the stationary arc curve

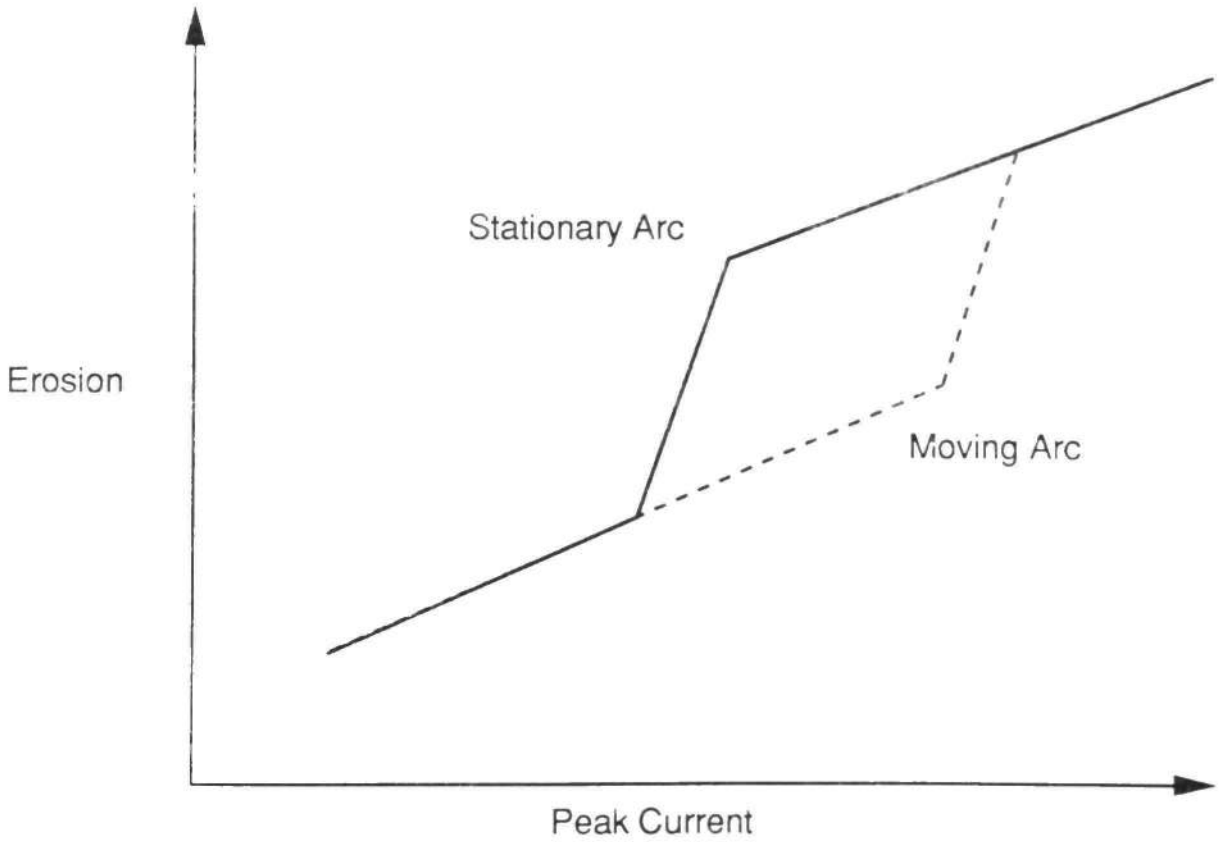

Fig. E.1 A Previous View of the Effect of Arc Motion on Stationary Arc Electrode Erosion Curves. (From [2], [3] - for a physical interpretation see Ref. [3].)

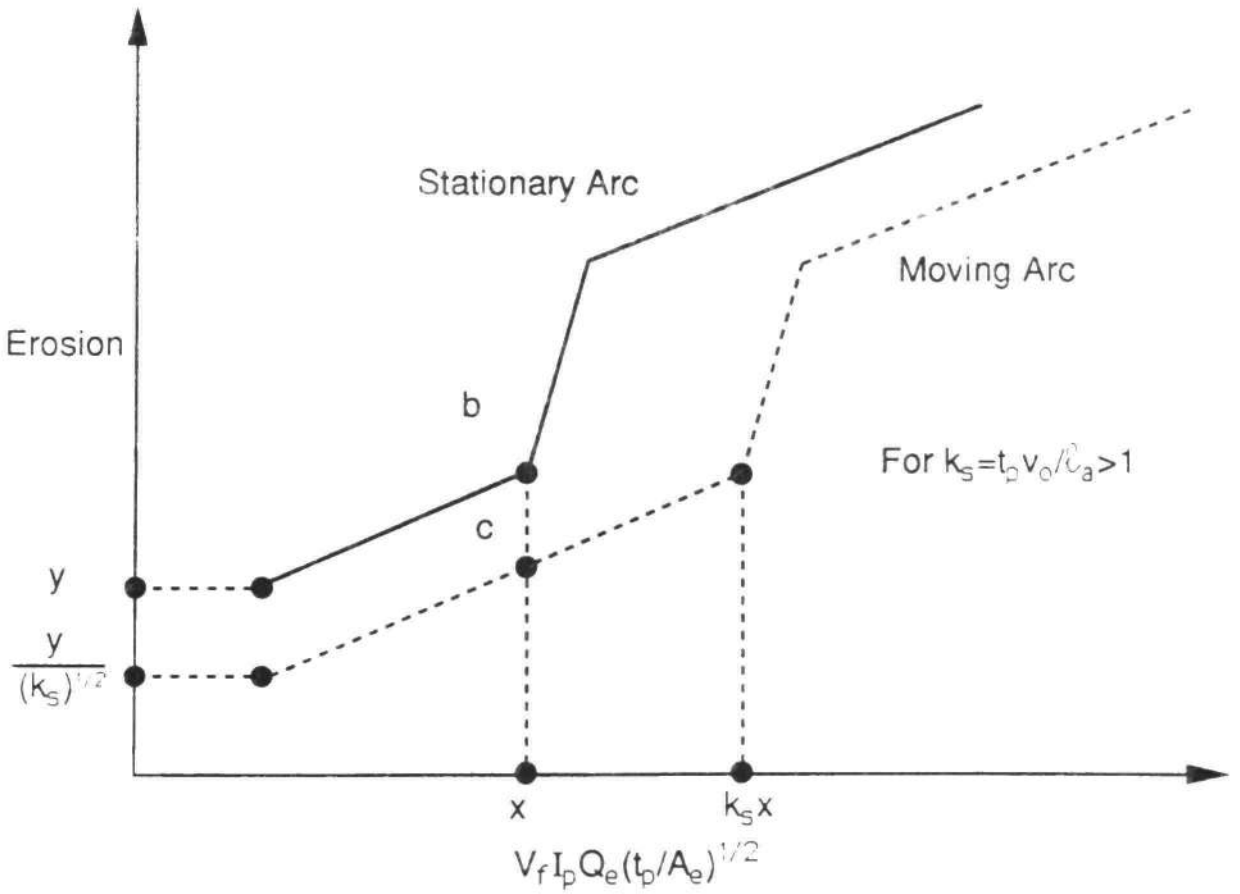

Fig. E.2 The Effect of Arc Motion on Stationary Arc Electrode Erosion Curves for the Case of Constant Velocity, v_o. (where t_p is the pulse width, ℓ_a is the length of the arc in the direction of motion, I_p is the peak current, Q_e is the effective charge transferred ($\int_0^{t_p} |I_a(t)|/dt$), V_f is the fall voltage at each electrode and A_e is the effective area of the arc attachment with the electrode surface)

shown in Fig. E.1 has a slope proportional to $V_f I_p (t_p)^{1/2}/A_e$. For a unipolar current pulse this expression becomes $V_f I_p^2 t_p^{3/2}/A_e$. In addition the point of transition is given in Reference [1] as

$$q^*(t)^{1/2} = V_f I_p (t_p)^{1/2}/A_e T_{mp} (k\rho c)^{1/2} = \pi/4. \qquad \text{(E.1)}$$

To determine how these parameters change for the moving arc of constant velocity v_o consider point b on Fig. E.2. If I_p, t_p and A_e are held constant while the velocity of the arc is increased, the effective dwell time of the arc at any point on the rail electrode is given by

$$t_d^* = (\ell_a/v_o)^{1/2}, \qquad \text{(E.2)}$$

where ℓ_a is the length of the arc in the direction of propagation (typically 1-10 cm). If the rail is divided into segments, each ℓ_a in length, then the total number of segments exposed to the arc during the pulse t_p is

$$n_s = t_p/t_d^*. \qquad \text{(E.3)}$$

If one neglects temperature diffusion effects in the direction of propagation then the erosion, E_c, at point c, is given by the product of the number of segments and the erosion per segment. Thus,

$$E_c \sim (t_p/t_d^*)\,(I_p^2 t_d^{*3/2}/A_e), \qquad \text{(E.4a)}$$

or

$$E_c \sim I_p^2 t_p (t_d^*)^{1/2} / A_e . \qquad \text{(E.4b)}$$

The ratio of the erosion at points b and c is given by

$$E_b / E_c = (t_p / t_d^*)^{1/2} = (t_p v_o / \ell_a)^{1/2} . \qquad \text{(E.5)}$$

The quantity, $t_p v_o / \ell_a$, is designated by the constant, k_s. Thus, the erosion curve in region 1 is lowered for increasing arc velocity. The other important feature of the erosion curve is the location of the transition region on the x axis. For the moving arc, the onset condition is the same quantity,

$$q^* (t_p)^{1/2} = \pi / 4 , \qquad \text{(E.6)}$$

except that t_p is now the dwell time, t_d^*, at any point on the rail rather than the entire pulse width t_p. Thus, since $(t_p)^{1/2}$ is reduced to $(t_d^*)^{1/2}$, by the factor, $(t_d^*/t_p)^{1/2}$, or, $1/(k_s)^{1/2}$, then q^* must be increased by $(k_s)^{1/2}$ to satisfy Equation (E.5). The only variable on the axis which is allowed to change in order to increase q^* is I_p, (V_f, and the material properties are fixed). Thus, I_p becomes $(k_s)^{1/2} I_p$ to get the same $q^* (t)^{1/2}$ and the quantity, $I_p^2 t_p^{3/2} / A_e$, is increased to $k_s I_p^2 t_p^{1/2} / A_e$. The net result is a new expression for the onset of bulk erosion for the moving arc, namely,

$$(V_f I_p (\ell_a / v_o)^{1/2}) / A_e T_{mp} (k \rho c)^{1/2} = \pi / 4 . \qquad \text{(E.7)}$$

One interesting result is that for an actual moving arc, where the velocity increases as a function of the current, the slope of the erosion curve will <u>decrease</u> from the present $I_p^2 t_p^{3/2}$ dependency. The nature of that dependency (i.e., the scaling

laws for moving arcs) could readily be solved on a computer using the considerations presented here.

References

[1] A.L. Donaldson and M. Kristiansen, "Electrode Erosion Resulting from High Current Transient Arcing," *The First Meeting of the Non-Nuclear Space Power Consortium*, Auburn, AL, December 8-9, 1986. (EE-1132)

[2] F.M. Lehr, B.D. Smith, A.L. Donaldson and M. Kristiansen, "The Influence of Arc Motion on Electrode Erosion in High Current, High Energy Switches," *Proceedings of the Sixth IEEE Pulsed Power Conf.*, Arlington, VA, pp. 529-533, June 29-July 1, 1986. (EE-1133)

[3] F.M. Lehr, "Electrode Erosion from High Current, High Energy Moving Arcs," M.S. Thesis, Texas Tech University, pp. 1-68, August 1988.

[4] G.S. Belkin, "Dependence of Electrode Erosion on Heat Flux and Duration of Current Flow," *Sov. Phys. Tech. Phys.*, vol. 15(7), pp. 1167-1170, 1971. (EE-0435)

APPENDIX F

AN ASSESSMENT OF THE ROLE OF ELECTRODE JOULE HEATING (EJH)

This Appendix contains a brief review of previous work which considered the effect of EJH. Many references are cited in Table F.1 but the references discussed are those for which a condition for the importance of EJH was given or could be derived. Also included is the author's own derivations for the onset of skin effect enhanced EJH (SEEEJH) and for the material scaling of the SEEEJH erosion based on the work of Comstock and Williams [3] and Watson [18].

A Brief Review of Previous Work

The importance of electrode joule heating (EJH) versus the importance of arc joule heating (AJH) has been a hotly contested subject since the time when both mechanisms were considered. Many attempts have been made to evaluate the role of EJH both as a source of thermal energy for erosion and as a mechanism active in the cathode spot. Some of these attempts are classified in the listings given in Table F.1. In most cases, the different conclusions regarding the importance of EJH are not a result of the different analytical methods used to calculate the effect of EJH but rather the result of different values which are assumed for the current density, J, and the resistivity, η, of the metal at high temperatures. Since J and η, are not precisely known the

Table F.1 Classification of Various People Who Have Considered the Role of EJH

Important	Not Important	Conditional
Lebedev 1950 [1]	Zingerman 1955 [2]	Comstock and Williams 1959 [3]
Kidder 1959 [4]	Sukhodrev 1962 [6]	Rich 1961 [5]
Ilin & Lebedev 1963 [7]	Zolotykh 1964 [8]	Goloveiko 1968 [10]
Daalder 1978 [15]	Belkin 1966 [9]	Dethlefsen 1968 [11]
Hantzche 1981 [16]	Van Dijck 1973 [12]	Zekster 1977 [14]
Watson 1986 [18]	Kalyatskii 1976 [13]	
	Juttner 1981 [17]	

criteria for defining their role are best left in terms of J and η.

That a pulse condition exists which guarantees the dominance of EJH (really SEEEJH) over AJH has been verified experimentally by Watson [19]. Figure F.1 shows the electrode surface damage resulting from a high current (250 kA), fast rising (< 10 ns) pulse, 50 ns in length. For this time scale the arc column has not expanded appreciably, as indicated by the small crater damage in the center. What is clear is the much larger damage region which extends beyond the area of arc attachment. This damage could only have been done by the SEEEJH as the author has shown. Whether the AJH or SEEEJH dominates in the arc crater is inconsequential since this represents such a small fraction of the overall damage region.

Comstock and Williams [3] obtained fairly complex integral expressions for the time-varying radial and axial current densities resulting from the initiation of a cylindrical current source on a planar electrode surface. For the small values of the normalized time parameter, τ, given by

$$\tau = t/\mu\sigma_e r_s^2, \qquad \text{(F.1)}$$

the asymptotic solutions for the radial current density, J_r, for $r>r_s$ and $r<r_s$, were given as

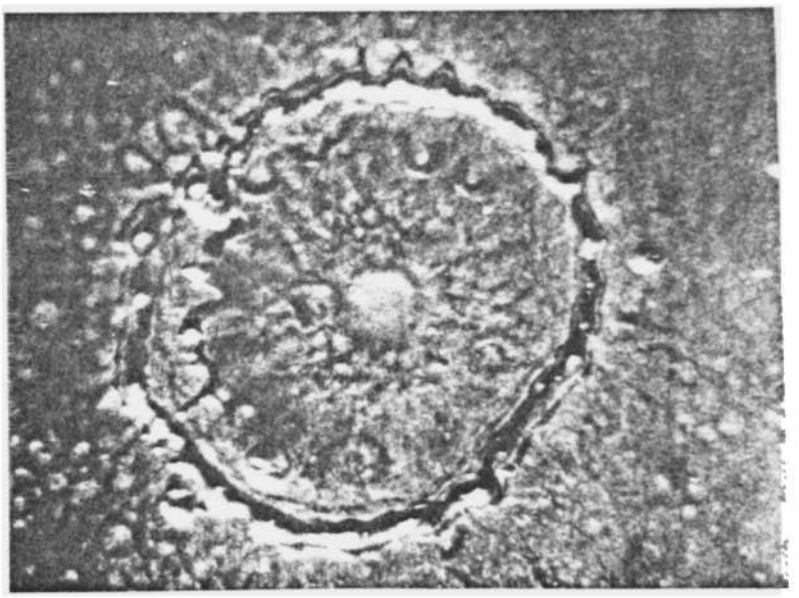

Fig. F.1 Electrode Surface Damage Resulting from a Fast Rising High Current Pulse Which Shows the Dominance of SEEEJH [18]. (Conditions: breakdown voltage - 5.5 MV, output impedance - 57 Ω, estimated current - 100 kA, discharge duration - 25 ns and magnification - 30 X.)

$$J_r \cong \frac{J_o e^{-(z^2 \mu \sigma_e / 4t)}}{2(\pi\tau)^{1/2}} \frac{r}{r_s}, \qquad (F.2)$$

for $r/r_s<1$,

and

$$J_r \cong \frac{J_o e^{-(z^2 \mu \sigma_e / 4t)}}{2(\pi\tau)^{1/2}} \frac{r_s}{r}, \qquad (F.3)$$

for $r/r_s>1$. The asymptotic solution for the axial current density, J_z, for $r>r_s$ and $r<r_s$, were also given as

$$J_z \cong J_o Erfc\left(z\left(\frac{\mu\sigma_e}{4t}\right)^{1/2}\right), \qquad (F.4)$$

for $r/r_s<1$,

and

$$J_z \cong 0, \qquad (F.5)$$

for $r/r_s>1$, where Erfc is the complementary error function. The integral expressions for the general case are difficult to evaluate (the authors themselves chose not to), however, Eqn's. (F.1)-(F.5) will be used by this author to derive the effects of material properties on the skin effect enhanced EJH (SEEEJH).

Rich [5] finds the steady state current density in the electrode due to a constant surface source by first solving approximately the 3-D Laplace equation for the potential. A numerical solution is then obtained for the joule heating as a function of position. The ratio of the energy input to a

cathode spot from the volume power source (EJH), P_v, and the surface power source (AJH), P_s, is given by

$$\frac{P_v}{P_s} = 0.32 r_s J_s (k_o V_f \sigma_e), \qquad (F.6)$$

where k_o is a material-dependent constant in the range of 0.02-0.09.

The work of Goloveiko [10] was reviewed in detail in Chapter 2. Basically, he obtained the steady state expressions for the current densities which determined when EJH was important when melting and vaporization was occurring at the electrode surface. The power density is due to EJH approximated by a 1-D exponentially decaying function of z.

Dethlefsen [11] determines a critical current density for which EJH is important by comparing the terms $\rho c \frac{\partial T}{\partial t}$ and $\frac{J_e^2}{\sigma_e}$ in the heat conduction equation (see Eqn. (2.3)). His criterion

$$\frac{J^2}{\sigma_e} = \frac{\rho c T}{t}. \qquad (F.7)$$

In Chapter 4 the author modified this criterion to obtain some of the following expressions in terms of material properties only. An expression which differs from Dethlefsen by only a constant is cited by Kalyatskii [13].

Zekster [14] derives an analytical solution to Poisson's equation for the temperature, i.e. the steady state problem, given by

$$\frac{k\partial^2 T}{\partial z^2} = \frac{-J_e^2}{\sigma_e} \tag{F.8}$$

by assuming a particular functional form for J. The resulting criteria for the onset current density which leads to melting is determined by setting $T = T_{mp}$ in the expression given for the temperature, namely,

$$T = \left(\frac{qr_s}{k}\right)\left[1 + 0.32J_e^2 r_s/\sigma_e q\right], \tag{F.9}$$

where q is the heat flux. He mentions that this criteria differs only by a constant from the one given by Ecker [19]. An expression is also obtained for the temperature at the surface resulting from any current distribution J(r,z), i.e.,

$$T(0,0) = \frac{qr_s}{k} + \int_0^\infty\int_0^\infty \frac{J(r,z)^2}{\sigma_e}\,\frac{rdrdz}{(r^2+z^2)^{1/2}}. \tag{F.10}$$

In addition, he derives the following condition for which EJH can be neglected, namely,

$$\frac{J^2 r_s}{\sigma_e q} < 1. \tag{F.11}$$

For

$$q = V_f J_e, \tag{F.12}$$

Eq. (F.11) becomes

$$\frac{J_e r_s}{\sigma_e V_f} < 1, \qquad \text{(F.13)}$$

which is essentially the same as Rich's criterion (Eqn. (F.6)).

Kidder [4] derived an onset condition for melting due to SEEEJH in rail electrodes. His criterion is given as the linear current density, J_ℓ, which will produce melting, defined as the current per rail width, namely,

$$J_\ell = \left(\left(\frac{\rho c T_{mp}}{2\mu} \right) \left(\frac{1}{\ell n \left(1 + \pi/2 \left(\frac{\rho c}{\sigma_e \mu k} \right)^{1/2} \right)} \right) \right)^{1/2} . \qquad \text{(F.14)}$$

Derivation of the Onset of SEEEJH

Let us assume that early in the current pulse a current density, J_{eo}, exists at the electrode surface as shown in Fig. F.2. An enhanced current density, J_{eo}^*, will then exist perpendicular to surface at $r=r_s$ as shown in Fig. F.2. J_{eo} is enhanced as a result of the finite rate of propagation of the electromagnetic field into the conductor, i.e., the skin effect. J_{eo}^* is given by

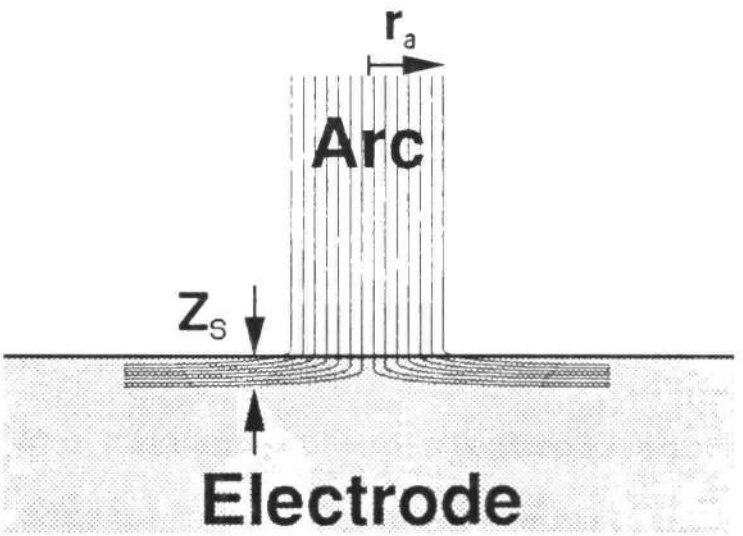

Fig. F.2 Current Density in the Electrode When the Skin Effect is Present.

$$J'_{eo} = \frac{I^{*}_{eo}}{A'_{e}}, \qquad \text{(F.15)}$$

where I'_{eo} is the current flowing through the area, A'_{e}, perpendicular to the surface and equal to

$$A'_{e} = 2\pi r_{s} z_{\delta}, \qquad \text{(F.16)}$$

where z_{δ} is the depth of the field penetration at any time, t, or the "skin depth." The skin depth is defined as that distance where the field has been reduced by a factor of 1/e and for the case of a plane wave on an infinite surface is given by

$$z_{\delta} = (t/\pi\mu\sigma_{e})^{1/2}, \qquad \text{(F.17)}$$

where μ and σ_e are the material's permeability and conductivity, respectively. Thus,

$$I'_{eo} = (1-1/e)\, I_{eo}, \qquad \text{(F.18)}$$

where I_{eo} is the current at the electrode surface and e is the logarithmic constant approximately equal to 2.72. Combining Eqn.'s (F.15) - (F.18) yields

$$J'_{eo} = \frac{J_{eo} A_{e}}{2\pi r_{s} z_{\delta}} \, (1-1/e), \qquad \text{(F.19)}$$

or

$$J'_{eo} = \frac{J_{eo} r_{s}}{2 z_{\delta}} \, (1-1/e), \qquad \text{(F.20)}$$

where A_e, the area of the arc attachment is given by

$$A_e = \pi r_s^2. \tag{F.21}$$

To determine the "onset" for SEEEJH let us find the condition when the skin-effect electrode joule heating term is equal to the heat flux term. For small penetration depths the comparison is

$$\frac{q}{z_\delta} = \frac{J_{eo}'^2}{\sigma_e}, \tag{F.22}$$

where q is the surface heat flux given by

$$q = J_{eo}V_f \tag{F.23}$$

and V_f is the electrode "fall" voltage.

Combining Eqn's. (F.20)-(F.23) yields

$$(1-1/e)\frac{Jr_s^2}{4z_\delta\sigma_e} = V_f, \tag{F.24}$$

or

$$\frac{J^2 r_s^4 \mu}{16\sigma_e} = \frac{V_f^2 t}{(1-1/e)^2}, \tag{F.25}$$

which yields,

$$J^2 = \frac{16\pi^2 V_f^2 \sigma_e t}{\mu A_e^2 (1-1/e)^2} \approx \frac{20\pi^2 V_f^2 \sigma_e t}{\mu A_e^2}, \tag{F.26}$$

or

$$J^2 = k_{j2} t, \tag{F.27}$$

where the onset constant, k_{j2}, is defined by

$$k_{j2} = \frac{20\pi^2 V_f^2 \sigma_e}{\mu A_e^2}. \tag{F.28}$$

Derivation of Material Scaling from Comstock and Williams

From their exact integral expressions, valid anywhere in the electrode, Comstock and Williams [28] derived the following approximate expression for the current density in the electrode valid for small τ and for radial distances somewhat greater than the discharge radius r_s.

$$J_e(r,z,t) = \frac{r_s^2 J_e e^{-z^2\mu\sigma_e/4t}}{r\left(\frac{\pi t}{\mu\sigma_e}\right)^{1/2}}, \qquad (F.29)$$

for $r>r_s$, where J_e is the electrode current density. Now, from Eq. (2.3), with the conduction term set equal to zero, i.e. like Zekster in Eq. (F.8),

$$\frac{J_e^2}{\sigma_e} = \frac{\rho c T}{t}, \qquad (F.30)$$

which, combined with Eq. (F.29), yields

$$\frac{\mu J_e^2 r_s^4 e^{-z^2\mu\sigma_e/kt}}{\pi r^2} = \rho c T. \qquad (F.31)$$

By setting $T = T_m$, the effective melting temperature, Eq. (F.31) can be solved for the depth of melting z_m as a function of r. Namely,

$$z_m^2 = \frac{2t}{\mu\sigma_e} \ell n\left(\frac{\mu J_e^2 r_s^4}{\pi\rho c T_m r^2}\right). \qquad (F.32)$$

The maximum z_m depth of melting, z_{mx}, in the range $r \geq r_s$, occurs at $r=r_s$, and is given by

$$z_{mx} = \left(\frac{2t}{\mu \sigma_e} \ln \left(\frac{\mu I_e J_e}{\pi^2 \rho c T_m} \right) \right)^{1/2} . \qquad \text{(F.33)}$$

Now, let

$$a = \left(\frac{t}{\mu \sigma_e} \right)^{1/2} , \qquad \text{(F.34a)}$$

$$k_1 = \frac{\mu I_e J_e}{\pi^2 \rho c T_m} , \qquad \text{(F.34b)}$$

and r_u, the upper limit of the radius, r, is given by

$$r_u = (k_1)^{1/2} e^{-(z/a)^2} . \qquad \text{(F.34c)}$$

Then, the melted volume, v_m, is given by

$$v_m = 2\pi \int_0^{z_{mx}} \int_{r_s}^{r_u(z)} r dr dz . \qquad \text{(F.35)}$$

Thus,

$$v_m = 2\pi \int_0^{z_{mx}} \left(\frac{k_1}{2} e^{-\left(\frac{2z^2}{a^2}\right)} - r_s^2 \right) dz , \qquad \text{(F.36)}$$

$$v_m = 2\pi \left[\frac{k_1}{2} \int_0^{z_{mx}} e^{-\left(\frac{2z^2}{a^2}\right)} dz - r_s^2 z_{mx} \right] , \qquad \text{(F.37)}$$

or

$$v_m = \sqrt{2}\, \pi^{3/2} a k_1 Erf(x) - 2\pi r_s^2 z_{mx} , \qquad \text{(F.38)}$$

where

$$x = \sqrt{2}\, z_{mx}/a = (2\ell n(k_1))^{1/2}. \qquad \text{(F.39)}$$

Evaluation of this expression indicates that the Erf(x) is only a weak function of the material properties and thus,

$$v_m \propto a k_1, \qquad \text{(F.40)}$$

or

$$v_m \propto \frac{I_e J_e t}{\pi^2}\left(\frac{\mu}{\sigma_e}\right)^{1/2}\left(\frac{1}{\rho c T_m}\right). \qquad \text{(F.41)}$$

Thus, in terms of material properties, the higher the parameter $\left(\frac{\sigma_e}{\mu}\right)^{1/2} \rho c T_m$, the lower the erosion.

Derivation of Material Scaling from Watson

Watson [18] has derived the following expressions for the JxB driven molten metal removal from the electrode for a unipolar current pulse of magnitude, I_p, and pulse duration, t_p:

$$\frac{I}{2\pi r^2} = \left(\frac{\mu}{\rho}\right)\sigma_e^2 \rho c T_m, \qquad \text{(F.42)}$$

and

$$\dot{v}_m(r) = Ir\left(\frac{\mu}{\rho}\right)^{1/2}. \qquad \text{(F.43)}$$

The total melted volume removed is then

$$V_m = \int_0^{t_p} \frac{1}{r_{mx}} \int_0^{r_{mx}} \dot{v}_m(r)\, dr dt, \tag{F.44}$$

where r_{mx} is the maximum radius corresponding to I_p and using Eq. (F.42), is given by

$$r_{mx} = \left(\frac{I}{2\pi}\right)^{1/2} \left(\frac{\rho}{\mu}\right)^{3/4} \frac{1}{\sigma_e (\rho c T_m)^{1/2}}. \tag{F.45}$$

Thus, evaluating Eq. (F.44) yields

$$V_m = \frac{I_p^{3/2} t_p}{4\pi} \left(\frac{1}{\mu\rho}\right)^{1/4} \left(\frac{1}{\sigma_e (c T_m)^{1/2}}\right). \tag{F.46}$$

Thus, in terms of material properties, the larger the parameter $\sigma_e (c T_m)^{1/2} (\mu\rho)^{1/4}$, the smaller the erosion.

References

[1] S.V. Lebedev, "Title Unknown," *Izv. AN Arm. USSR*, vol. 3, pp. 33-?, 1950. (EE-0339-2)

[2] A.S. Zingerman, "The Role of Joule-Lenz Heat in the Electrical Erosion of Metals," Translation of *Sov. Phys. Tech. Phys.*, vol. 25(11), pp. 1931-1943, 1955. FSTC-HT-703-86. (EE-0418)

[3] W.D. Comstock and E.M. Williams, "Current Distribution in the Cylindrical Source Plane-Electrode Configuration," *Trans. of AIEE Comm. and Elec.*, vol. 43(6), pp. 252-256, 1959. (EE-0338)

[4] R.E. Kidder, "Nonlinear Diffusion of Strong Magnetic Fields into a Conducting Half-Space," *Lawrence Livermore National Laboratory Document # UCRL-5467*, Livermore, CA, 1959. (EE-0792-1)

[5] J.A. Rich, "Resistance Heating in the Arc Cathode Spot Zone," *J. of Appl. Phys.*, vol. 32(6), pp. 1023-1031, 1961. (EE-0337)

[6] N.K. Sukhodrev, "On Spectral Excitation in a Spark Discharge," *Transactions (Trudy) of the P.N. Lebedev Physics Institute*, Volume 15- Research on Spectroscopy and Luminescence Part 3, Chapter 4, pp. 29-44, Consultants Bureau, New York, 1962. (EE-0097)

[7] V.E. Il'in and S.V. Lebedev, "Destruction of Electrodes by Electric Discharges of High Current Density," *Sov. Phys. Tech. Phys.*, vol. 7(8), pp. 717-721, 1963. (EE-0339)

[8] B.N. Zolotykh, "The Nature of Energy Transfer to Electrodes in a Pulse Discharge with Small Gaps," in the book: *Electrical Contacts*, M. Energy:, pp. 5-20, 1964. NASA #TTF-339, (EE-0005)

[9] G.S. Belkin, "Dependence of Electrode Erosion on Heat Flux and Duration of Current Flow," *Sov. Phys. Tech. Phys.*, vol. 15(7), pp. 1167-1170, 1971. (EE-0435)

[10] A.G. Goloveiko, "Thermal Processes at the Anode During an Intense Pulse Discharge," *Sov. J. of Eng. Phys.*, vol. 15(6), pp. 1168-1174, 1968. (EE-0344)

[11] R. Dethlefsen, "Investigation of Electrode Erosion in High Current Arcs," *Aerospace Research Laboratories Report # 68-0112*, Wright Patterson AFB, Dayton, OH, June 1968.

[12] F. van Dijck, "Physico-mathematical Analysis of the Electric Discharge Machining Process," PhD - Afdeling Werkplaatstechniek, Katholieke Universitiet Leuven, Belgium, 1972. (EE-1137)

[13] I.I. Kalyatskii, V.I. Kurets, and E.N. Tarakanovskii, "The Relationship of Heat Fluxes Entering the Electrode Surfaces During Breakdown of Solids by Pulse Discharges," *Elek. Obrab. Maters.*, vol. ?(4), pp. 45-48, 1976. (EE-1012)

[14] M.P. Zekster, "Effect of Joule Heat Liberation in a Metal Cathode on the Temperature of the Cathode Arc Spot," *High Temperature (USSR)*, vol. 15(1), pp. 190-193, 1977. (EE-0355)

[15] J.E. Daalder, "A Cathode Spot Model and Its Energy Balance for Metal Vapor Arcs," *J. Phys. D:Appl. Phys.*, vol. 11, pp. 1667-1676, 1978. (EE-0163)

[16] E. Hantzche, "Theory of Cathode Spot Phenomena," *Physica*, vol. 104C, pp. 3-16, 1981. (EE-0175)

[17] B. Juttner, "Formation Time and Heating Mechanism of Arc Cathode Craters in Vacuum," *J. Phys. D:Appl. Phys.*, vol. 14, pp. 1265-1275, 1981. (EE-0174)

[18] A. Watson, "Electrode Damage from Strong Transient Arcs Due to Surface Material Displaced by Hydromagnetic Flow, I-Basic Principles," to be submitted to the *J. of Appl. Phys.* (EE-0493)

[19] A. Watson, "Fast Rising Transient Heavy Current Spark Damage to Electrodes," *Proceedings of the 2nd Int. Pulsed Power Conf.*, Lubbock, TX, pp. 471-474, June 1976. (EE-0737)

[20] G. Ecker, *Ergebnisse der Exakten Naturwissenschaften*, vol. 33, pp. 1-114, 1961. (EE-0833)

APPENDIX G

DERIVATION OF THE SCALING LAWS FOR ABLATION AND VAPORIZATION

In order to derive the scaling laws for both the ablation and the vaporization cases mentioned in Chapter 4, Fig. G.1 will be used. The solution $y = f(x)$, which represents the ablation and vaporization curves shown in Fig. 4.1, is bounded in the region $x_1 \leq x \leq x_2$, by two solutions $y = f_u(x)$ and $y = f_\ell(x)$, as indicated, where

$$f_u(x) = m_u x^{1/n} + b_u, \tag{G.1a}$$

and

$$f_\ell(x) = m_\ell x + b_\ell, \tag{G.1b}$$

with

$$m_u = y_{ss}/(x_2^{1/n} - x_1^{1/n}), \tag{G.2a}$$

$$m_\ell = y_{ss}/(x_2 - x_1), \tag{G.2b}$$

$$b_u = -m_u x_1^{1/n}, \tag{G.2c}$$

and

$$b_\ell = -m_\ell x_1. \tag{G.2d}$$

In the above equation y_{ss} is the steady state value of y beginning at x_2 and corresponding to a large time and x_1 is the thermal onset value. Now $f_u(x)$ and $f_\ell(x)$ can be written as the same function, $g_n(x)$, with a different n value, namely,

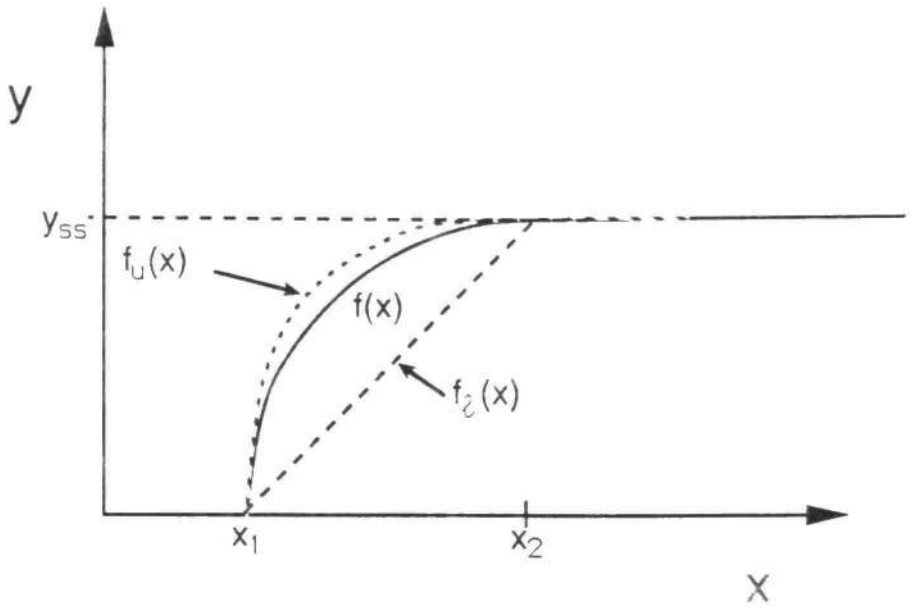

a) y = f(x) bounded by the functions $f_\ell(x)$ and $f_u(x)$

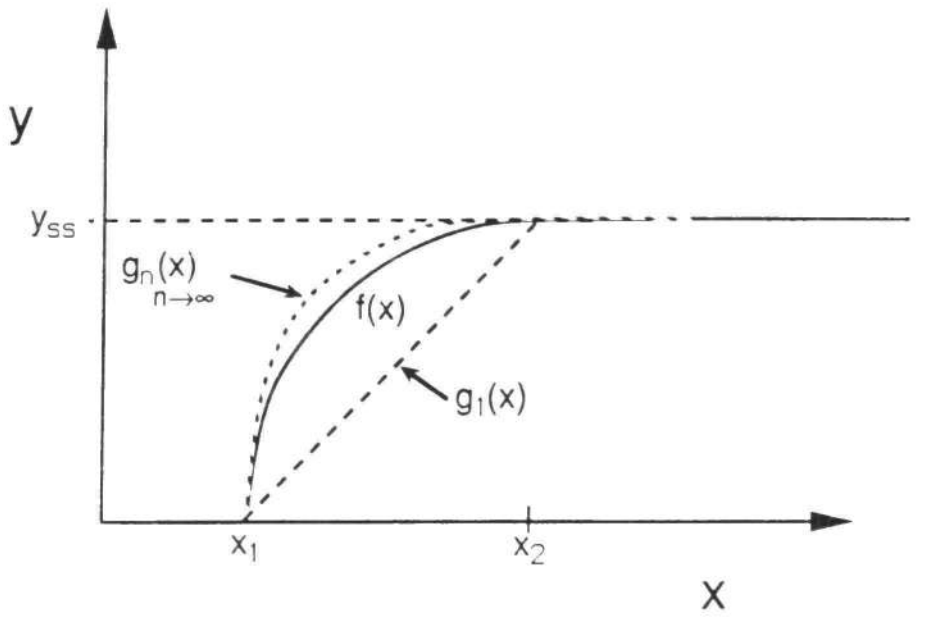

b) y = f(x) bounded by the function $g_n(x)$ as n goes from 1 to ∞

Fig. G.1 The Functions Used to Describe How the Scaling Laws are Bounded for $x>x_1$.

$$f_u(x) = g_n(x) = mx^{1/n} + b \text{ for } n > 1 \qquad (G.3)$$

and

$$f_\ell(x) = g_n(x) = g_1(x) = mx^{1/n} + b \text{ for } n=1. \qquad (G.4)$$

Note: in the limit as n goes to ∞,

$$f_u(x) = g_\infty(x) = m + b, \qquad (G.5a)$$

where

$$m = m_u \text{ and } b = b_u. \qquad (G.5b)$$

Additionally, for $x > x_2$, $y = g_n(x)$ is approximated by the constant y_{ss}.

For the ablation case

$$y = v_a^* = v_a \rho c T_m / (V_f Q_e) = v_a E_m / V_f Q_e, \qquad (G.6)$$

$$x = q^* (t_p)^{1/2} = q_m (t_p)^{1/2} / M_I, \qquad (G.7)$$

and

$$x_1 = k_1 (\pi/4)^{1/2},\ x_2 = k_2 (\pi/4)^{1/2} \text{ and } y_{ss} = 1; \qquad (G.8)$$

where M_I, the material impulsivity, is defined by

$$M_I = M_{Im} = T_m (k \rho c)^{1/2}, \qquad (G.9)$$

with

$$T_m = T_{mp} - T_o + L_f / c_{mp}, \qquad (G.10)$$

and E_m is the energy required to melt a unit volume of electrode material. Thus, combining Eqn's. (G.2-4) and (G.6-10), one obtains

$$v_a = \left(\frac{V_f Q_e}{\rho c T_m}\right)\left(\frac{1}{(\pi/4)^{1/2n}(k_2^{1/n} - k_1^{1/n})}\right), \qquad \text{(G.11a)}$$

$$\left((q^*(t_p)^{1/2})^{1/n} - k_1^{1/n}(\pi/4)^{1/2n}\right)$$

i.e.,

$$v_a = \frac{V_f Q_e}{E_m}\left(\frac{x^{1/n} - x_1^{1/n}}{x_2^{1/n} - x_1^{1/n}}\right), \qquad \text{(G.11b)}$$

for

$x_1 < x < x_2$, *i.e.*, $k_1(\pi/4)^{1/2} < q^*(t_p)^{1/2} < k_2(\pi/4)^{1/2}$.

Also,

$$v_a = \frac{V_f Q_e}{E_m}, \qquad \text{(G.12)}$$

for $x > x_2$, *i.e.* $q^*(t_p)^{1/2} > k_2(\pi/4)^{1/2}$.

For the vaporization case

$$y = v_v^* = v_v\left(\frac{\rho c T_m}{Q_e V_f}\right) = v_v\left(\frac{E_m}{Q_e V_f}\right), \qquad \text{(G.13)}$$

$$x = q^*(t_p)^{1/2} = q_m(t_p)^{1/2}/M_I, \qquad \text{(G.14)}$$

$$x_1 = k_1(\pi/4)^{1/2},\ x_2 = k_2(\pi/4)^{1/2}, \qquad \text{(G.15)}$$

and

$$y_{ss} = (cT_m)/(cT_m + c_{mp}T_v) = E_m/E_v, \qquad \text{(G.16)}$$

where

$$T_v = T_b - T_{mp} + L_v/c_b, \qquad \text{(G.17)}$$

and E_v is the energy required to vaporize a unit volume of electrode material. Thus, combining Eqn's. (G.2-4) and (G.13-16), one obtains,

$$V_v = \left(\frac{V_f Q_e}{\rho (cT_m + c_{mp} T_v)}\right)\left(\frac{1}{(k_2^{1/n} - k_1^{1/n})\,(\pi/4)^{1/2n}}\right) \qquad \text{(G.18a)}$$

$$X\left((q^*(t_p)^{1/2})^{1/n} - k_1^{1/n}(\pi/4)^{1/2n}\right)$$

i.e.,

$$V_v = \left(\frac{V_f Q_e}{E_v}\right)\left(\frac{x^{1/n} - x_1^{1/n}}{x_2^{1/n} - x_1^{1/n}}\right) \qquad \text{(G.18b)}$$

for $x_1 < x < x_2$, i.e., $k_1(\pi/4)^{1/2} < q^*(t_p)^{1/2} < k_2(\pi/4)^{1/2}$.

Also,

$$V_v = \frac{V_f Q_e}{E_v}, \qquad \text{(G.18c)}$$

for $x > x_2$, i.e., $q^*(t_p)^{1/2} > k_2(\pi/4)^{1/2}$.

Now, for $x_1 \le x \le x_2$, the lower limit (n=1) gives

$$V_a = \left(\frac{V_f Q_e}{\rho c T_m}\right)\left(\frac{1}{(k_2 - k_1)\,(\pi/4)^{1/2}}\right)\left(q^*(t_p)^{1/2} - k_1(\pi/4)^{1/2}\right), \qquad \text{(G.19a)}$$

i.e.,

$$V_a = \left(\frac{V_f Q_e}{E_m}\right)\left(\frac{x - x_1}{x_2 - x_1}\right), \qquad \text{(G.19b)}$$

and

$$v_v = \left(\frac{V_f Q_e}{\rho\,(cT_m + c_{mp}T_v)}\right)\left(\frac{1}{(k_2-k_1)\,(\pi/4)^{1/2}}\right) \qquad \text{(G.20a)}$$
$$X\left(q^*\,(t_p)^{1/2} - k_1\,(\pi/4)^{1/2}\right),$$

i.e.,

$$v_v = \left(\frac{V_f Q_e}{E_v}\right)\left(\frac{x-x_1}{x_2-x_1}\right). \qquad \text{(G.20b)}$$

Thus, for $x >> x_1$, v_a and v_v scale as $Q_e q^*(t_p)^{1/2}$.

For q^*, given by

$$q^* = \frac{V_f I_p}{A_e M_I}, \qquad \text{(G.21)}$$

the scaling is proportional to $Q_e I_p (t_p)^{1/2}$. Thus, for $x_1 \le x \le x_2$, and $x >> x_1$, the upper limit (n large) gives v_a and $v_v \sim Q_e I_p^{1/n} (t_p)^{1/2n}$, which becomes Q_e for large n.

To summarize, for $x_1 \le x \le x_2$ the function g(x) is bounded by the scaling Q_e and $Q_e I_p (t_p)^{1/2}$. Note: we could have arrived at this result intuitively by observing that as n goes to ∞, the function $g_\infty(x)$ looks like $g_1(x)$ when x is close to x_1 (i.e., it has a steeper slope but it basically can be approximated by a straight line, albeit, with a larger slope, but the magnitude of the slope does not affect the scaling) and $g_\infty(x)$ looks like $g_n(x)$ for $x > x_2$ when it gets close to x_2. Typical values of k_1 and k_2 are 1 and 5 for the ablation case or 5 and 20 for the vaporization case.

One final note: the constant k_1 is related to the onset constants k_{mo} and k_{vo} used in Chapter 4 by the equations

$$k_1 = \left(\frac{4}{\pi}\, k_{mo}\right)^{1/2} \frac{V_f}{M_{Im}}, \qquad \text{(G.22)}$$

for the melting onset, and

$$k_1 = (4/\pi\ k_{vo})^{1/2} \frac{V_f}{M_{Im}} \qquad \text{(G.23)}$$

for the vaporization onset. Values of k_1 for each case can be calculated using Eqn's. (4.23), (4.24) and (4.26).

APPENDIX H

DERIVATION OF THE EQUATIONS USED TO CALCULATE THE EROSION OF COMPOSITE MATERIALS

It has been known for some time that a minimum exists in the erosion rate as a function of material composition for two component composite materials such as copper-tungsten [1]. Physically this may be explained by considering the amounts of energy required to remove each material in a given phase state. Table H.1 contains the pertinent information needed to describe the process.

For a pure copper electrode, melting will occur at 1356 K and the majority of the metal will be removed in the liquid state, thus requiring 5.53 X 10^9 J/m^3 of material. Likewise for a pure tungsten electrode, melting will occur at 3673 K and the majority of the metal will be removed in the liquid state, thus requiring 1.25 X 10^{10} J/m^3 of material. If, however, the copper exists in a tungsten "sponge" or matrix (which will remain intact at the melting point of copper) then a portion of the copper may be held in its liquid state in the tungsten matrix until the material reaches the vaporization temperature of copper. This process is able to take place since the vaporization temperature of copper is less than the melting temperature of tungsten. The amount of energy required to vaporize copper is significantly higher than the

Table H.1 The Thermophysical Properties of Copper and Tungsten Needed to Explain the Minimum in the Erosion Rate For Composite Materials

Material	T_{mp} (K)	T_v (K)	$E_l \times 10^9$ (J/m^3)	$E_v \times 10^{10}$ (J/m^3)
Cu	1356	2840	5.53	5.37
W	3673	5933	12.5	10.3

amount required to melt copper or tungsten, thus, a minimum in the erosion can occur as a function of copper content. The minimum will be more pronounced if the amount of vaporized copper increases with increasing tungsten content. Physically this is probable since the ability of the tungsten material to retain the liquid copper should increase with increasing tungsten content (e.g., the sponge has smaller pores). These physical considerations are the basis for four different theoretical curves which have been derived below and are plotted in Fig. H.1. The four cases are: 1 - both copper and tungsten ablate, that is they erode as soon as they melt, 2 - all the tungsten ablates but an increasing percentage of copper is removed only as it is vaporized (a linear increase was assumed - that is, no copper is vaporized when the material is 100% copper and all of the copper is vaporized in the limit when all the material is tungsten), 3 - all the copper vaporizes and all the tungsten ablates, 4 - both copper and tungsten vaporize, that is, they only erode when they are vaporized. As can be seen in Fig. H.1, curves 1 and 4 represent the upper and lower limits on the erosion. Curve 2 represents the most likely case from a physical standpoint. It indicates a minimum in the erosion at about 30% copper by weight, which has been shown experimentally [1].

The volume of material which is capable of being removed in either the liquid or vapor state by a unit amount of energy E_u, is simply

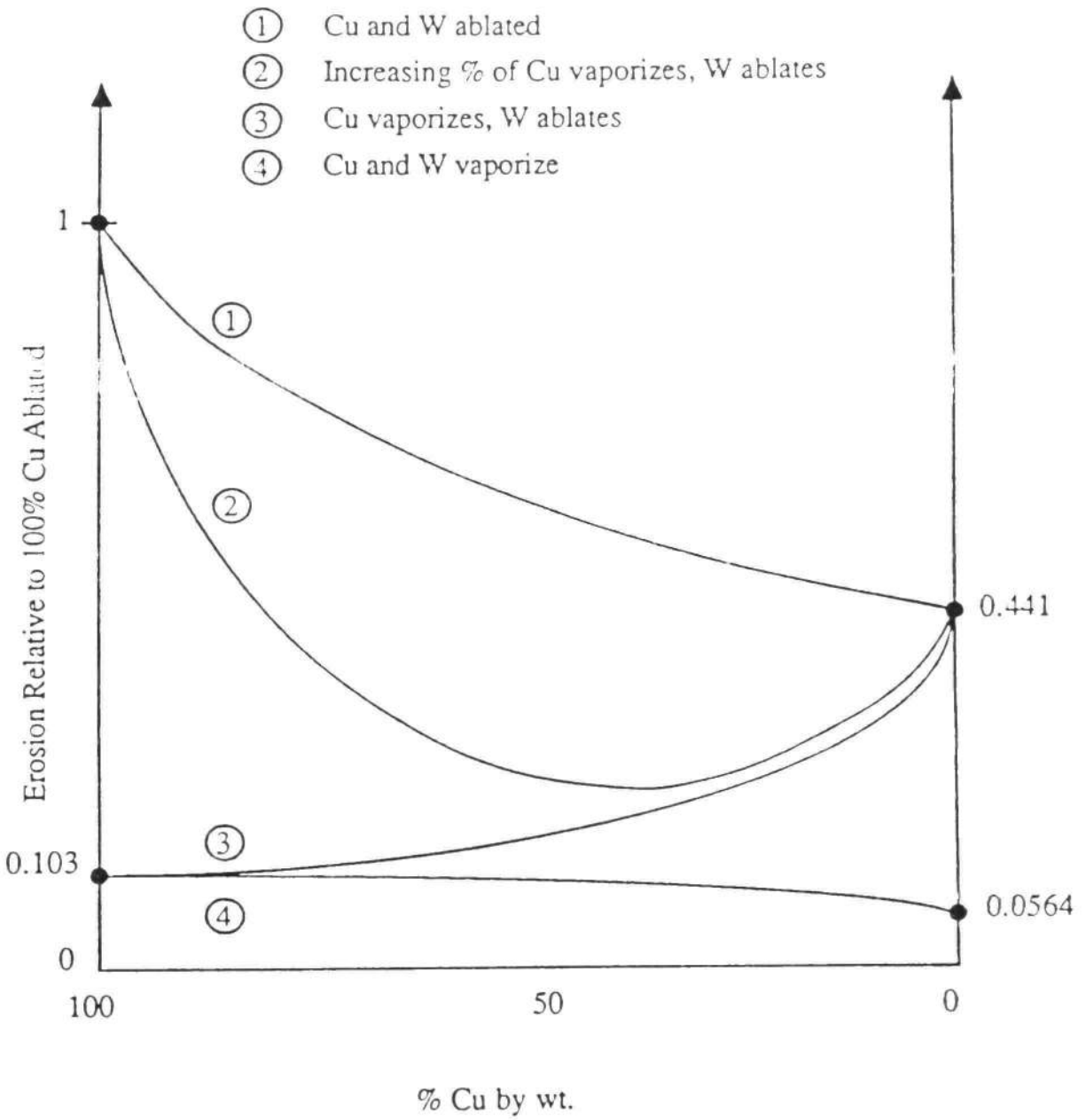

Fig. H.1 Modeling of Composite Material Erosion (CuW).

$$vol_1 = E_u / ((a_{\ell 1} E_{\ell 1} + b_{v1} E_{v1}) \rho_1) \qquad (H.1)$$

where $a_{\ell 1}$ and b_{v1} represent the fraction of material removed in the liquid and vapor state, respectively, $E_{\ell 1}$ and E_{v1} are the amount of energy per mass required to melt or vaporize the material, respectively, and ρ_1 is the density. Similarly, for a two constituent material the volume becomes

$$vol_2 = E_u / (P_{w1} (a_{\ell 1} E_{\ell 1} + b_{v1} E_{v1}) + (1-P_{w1}) (a_{\ell 2} E_{\ell 2} + b_{v2} E_{v2}) \rho_{12}) \qquad (H.2)$$

where P_{w1} is the fraction by weight of the first material, ρ_{12} is the density of the material, given by

$$\rho_{12} = \frac{1}{\frac{P_{w1}}{\rho_1} + \frac{P_{w2}}{\rho_2}} \qquad (H.3)$$

and the subscript 2 is used to indicate the same properties given for material 1 in Eq. (H.1). Thus the ratio of the eroded volume of a two constituent material to the volume of a single constituent material which is eroded only by melting is

$$\Gamma_r = vol_2/vol_1 \text{ (ablation only)} \qquad (H.4a)$$

$$\Gamma_r = \frac{E_{\ell 1}[P_{w1} (1-\rho_1/\rho_2) + \rho_1/\rho_2]}{P_{w1} (a_{\ell 1} E_{\ell 1} + b_{v1} E_{v1}) + (1-P_{w1}) (a_{\ell 2} E_{\ell 2} + b_{v2} E_{v2})} \qquad (H.4b)$$

or

$$\Gamma_r = \frac{P_{w1} (1-\rho_1/\rho_2) + \rho_1/\rho_2}{P_{w1} (a_{\ell 1} + b_{v1} E_{v1}/E_{\ell 1}) + (1-P_{w1}) (a_{\ell 2} E_{\ell 2}/E_{\ell 1} + b_{v2} E_{v2}/E_{\ell 1})} \qquad (H.4c)$$

Equation (H.4C) was plotted in Fig. H.1 for several different conditions, namely

1) $a_{\ell 1} = 1$, $a_{\ell 2} = 1$, $b_{v2} = 0$, $b_{v1} = 0$, (both materials ablate)

2) $a_{\ell 1} = P_{w1}$, $a_{\ell 2} = 1$, $b_{v2} = 0$, $b_{v1} = (1-P_{w1})$, (an increasing percent of the first material vaporizes)

3) $a_{\ell 1} = 0$, $a_{\ell 2} = 1$, $b_{v1} = 1$, $b_{v2} = 0$ (one ablates, one vaporizes)

4) $a_{\ell 1} = 0$, $a_{\ell 2} = 0$, $b_{v1} = 1$, $b_{v2} = 1$ (both vaporize).

Reference

[1] W. Haufe, W. Reichel and H. Schreiner, "Losses of Varying Types of CuW Sintered Impregnation Material in the Air at High Current Levels," *Transaction of Zeitschrift für Metallkunde*, vol. 63(10), pp. 651-654, 1972. (EE-0802)

APPENDIX I

MISCELLANEOUS EXPERIMENTAL RESULTS

This appendix shows plots of the effect of polarity (Fig. I.1), gas type (Figs. I.2-I.5), gas pressure (Figs. I.6-I.15) and inductance (Figs. I.16-I.18) on electrode erosion. The pressure effects are plotted as a function of f_1, Q_s, Q_e, I_p and E_s to show that the plotting variable dramatically changes the conclusions concerning the influence of pressure. Namely, for increasing pressure the erosion as a function of I_p and E_s decreases, whereas for f_1, Q_s and Q_e it increases in the region of transition and decreases slightly for higher values of f_1, Q_s and Q_c. For the gases studied, Air, N_2, Ar and He, it was found that the erosion could be reduced by up to an order of magnitude for He and Ar, at the expense of holdoff voltage. Thus, various mixtures of these gases with SF_6 etc. should be tried in the future. For C#2 and Cu#1 decreasing the inductance by using the SDS III switch [1] led to increased erosion but for CuW#1 no change in the erosion was observed.

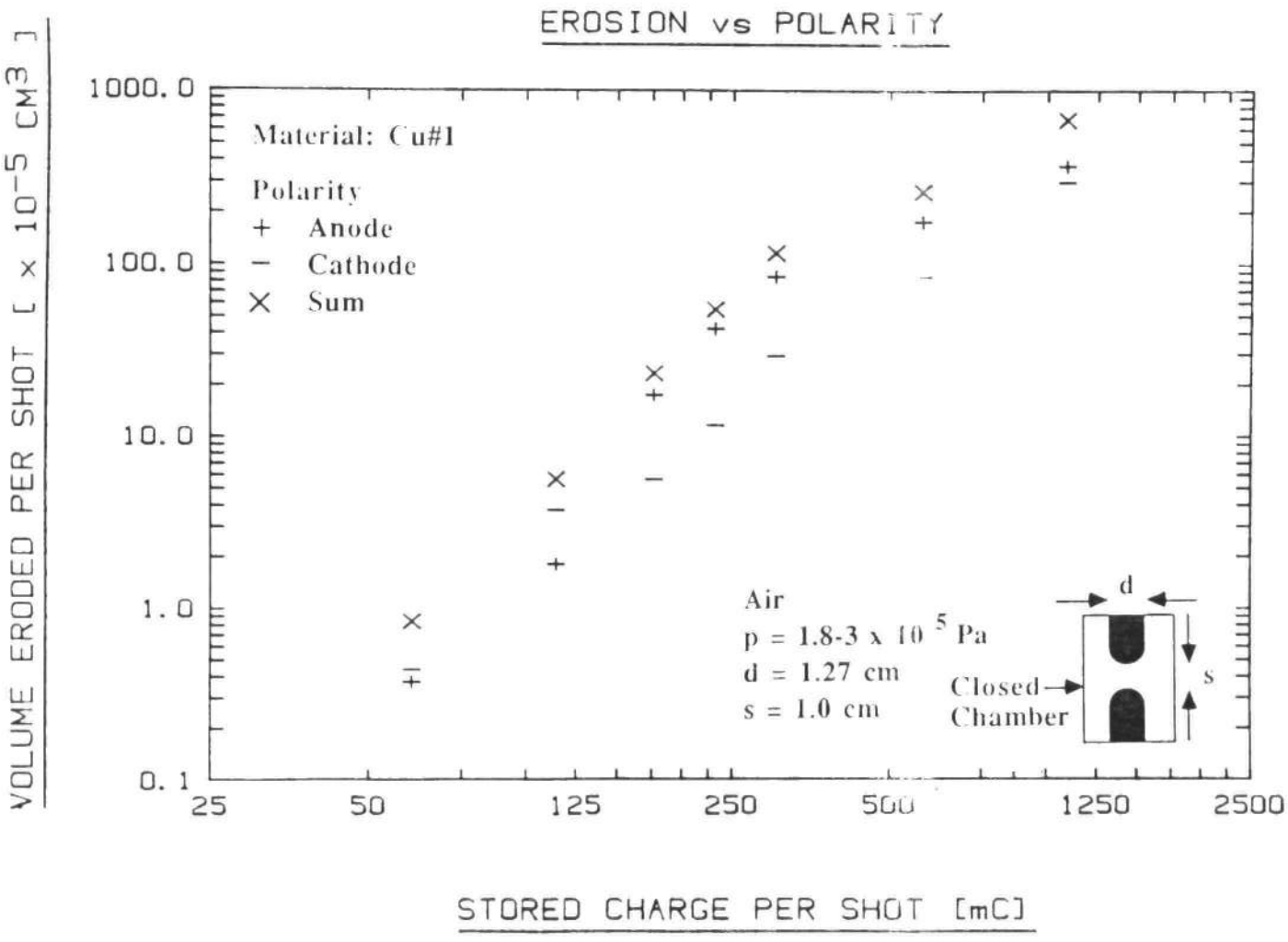

Fig. I.1 Electrode Erosion vs. Polarity.

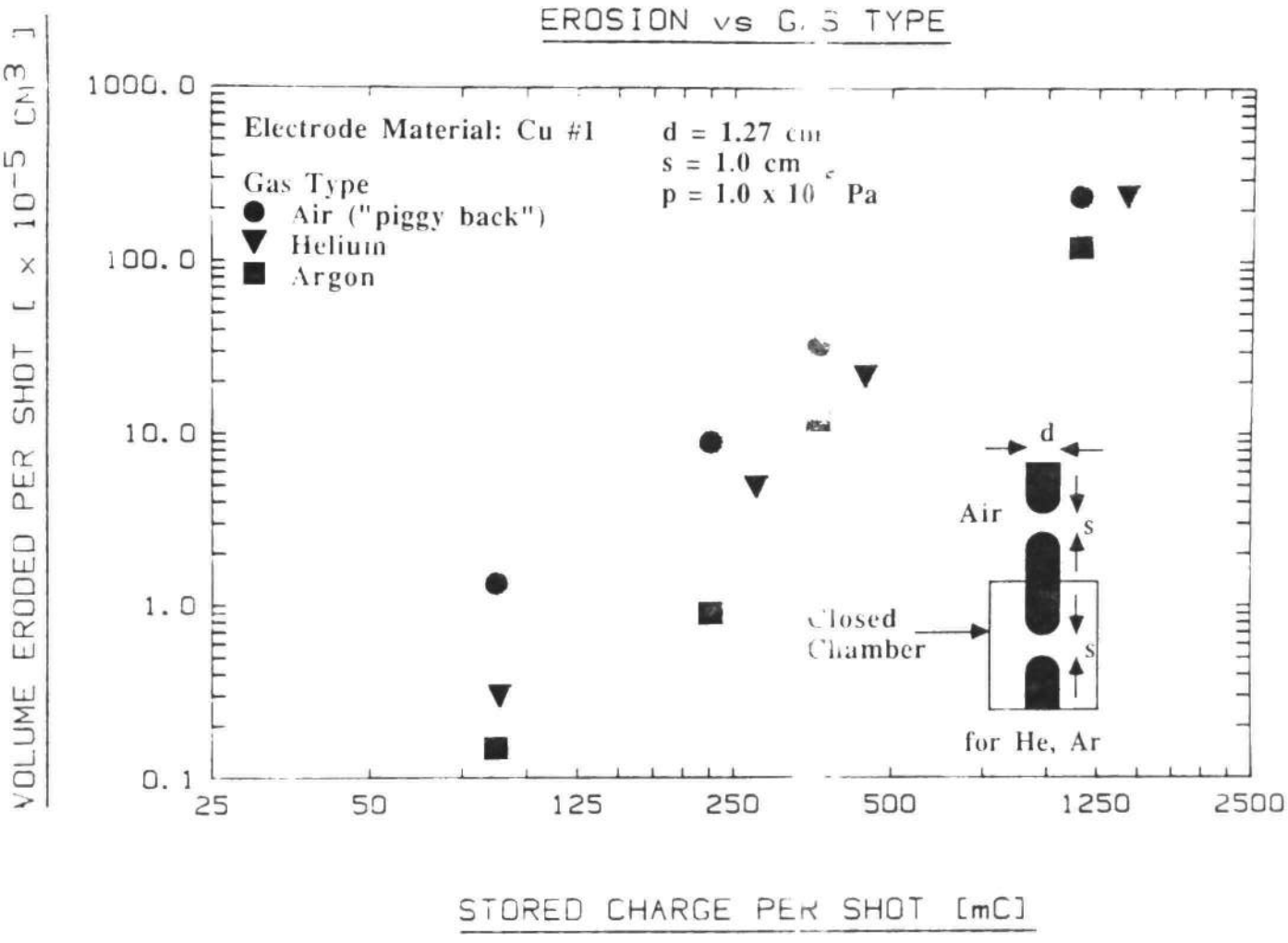

Fig. I.2 Cu#1 Electrode Erosion vs. Gas Type.(Comparing the piggy back erosion with erosion in He and Ar)

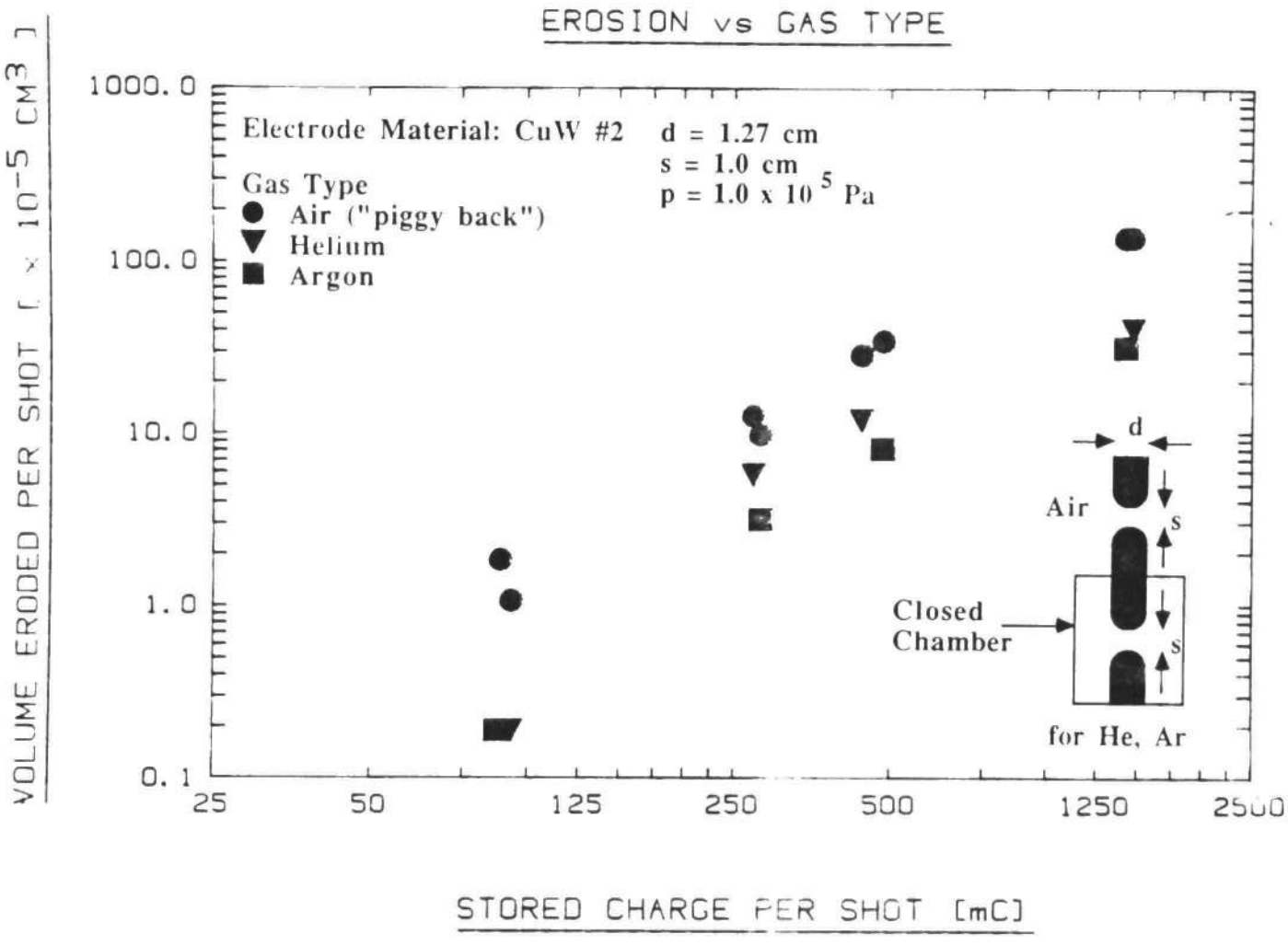

Fig. I.3 CuW#2 Electrode Erosion vs. Gas Type. (Comparing the piggy back erosion with the erosion in He and Ar)

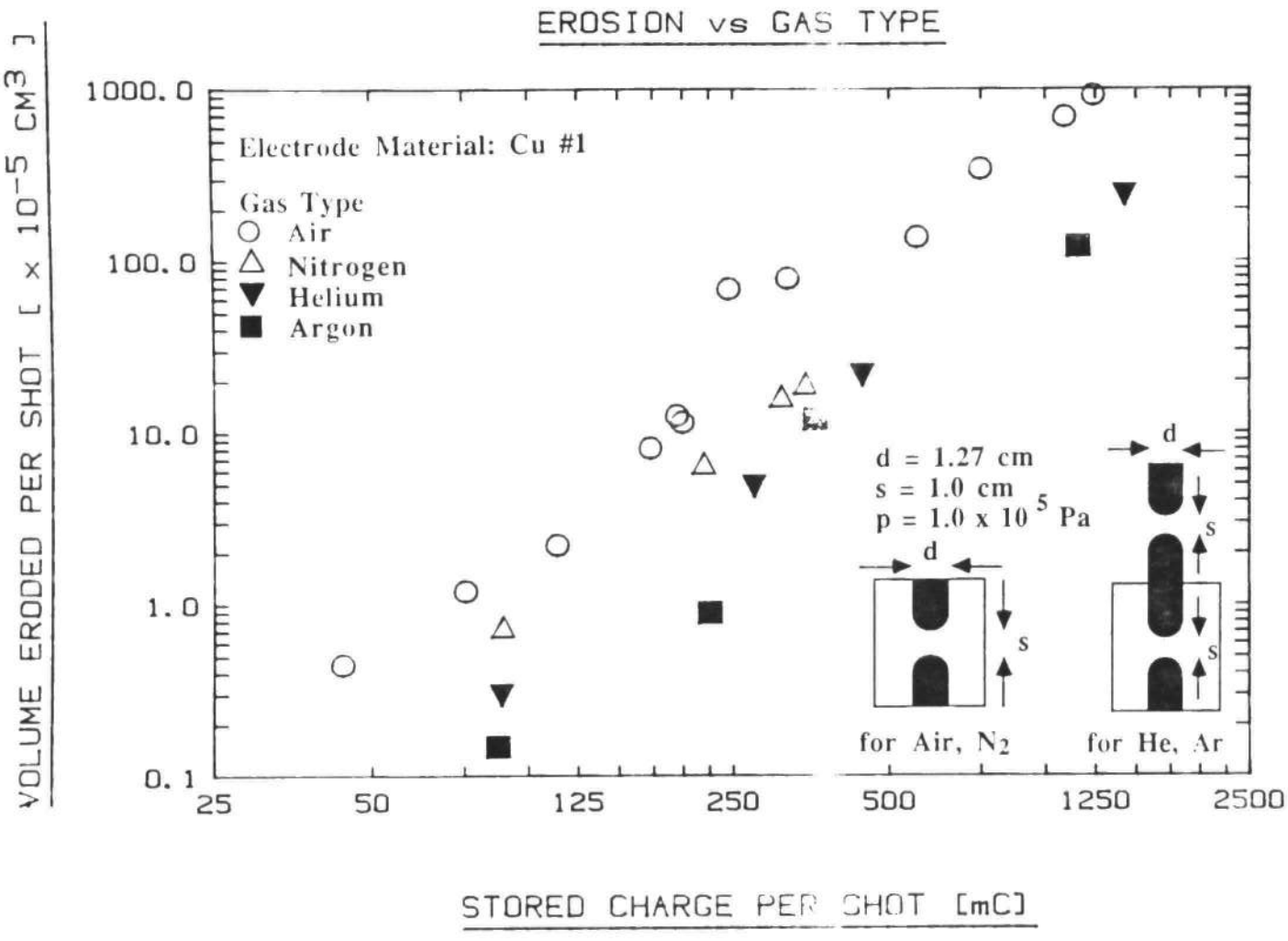

Fig. I.4 Cu#1 Electrode Erosion vs. Gas Type.(Comparing the standard switch erosion in air with the erosion in He, Ar and N_2)

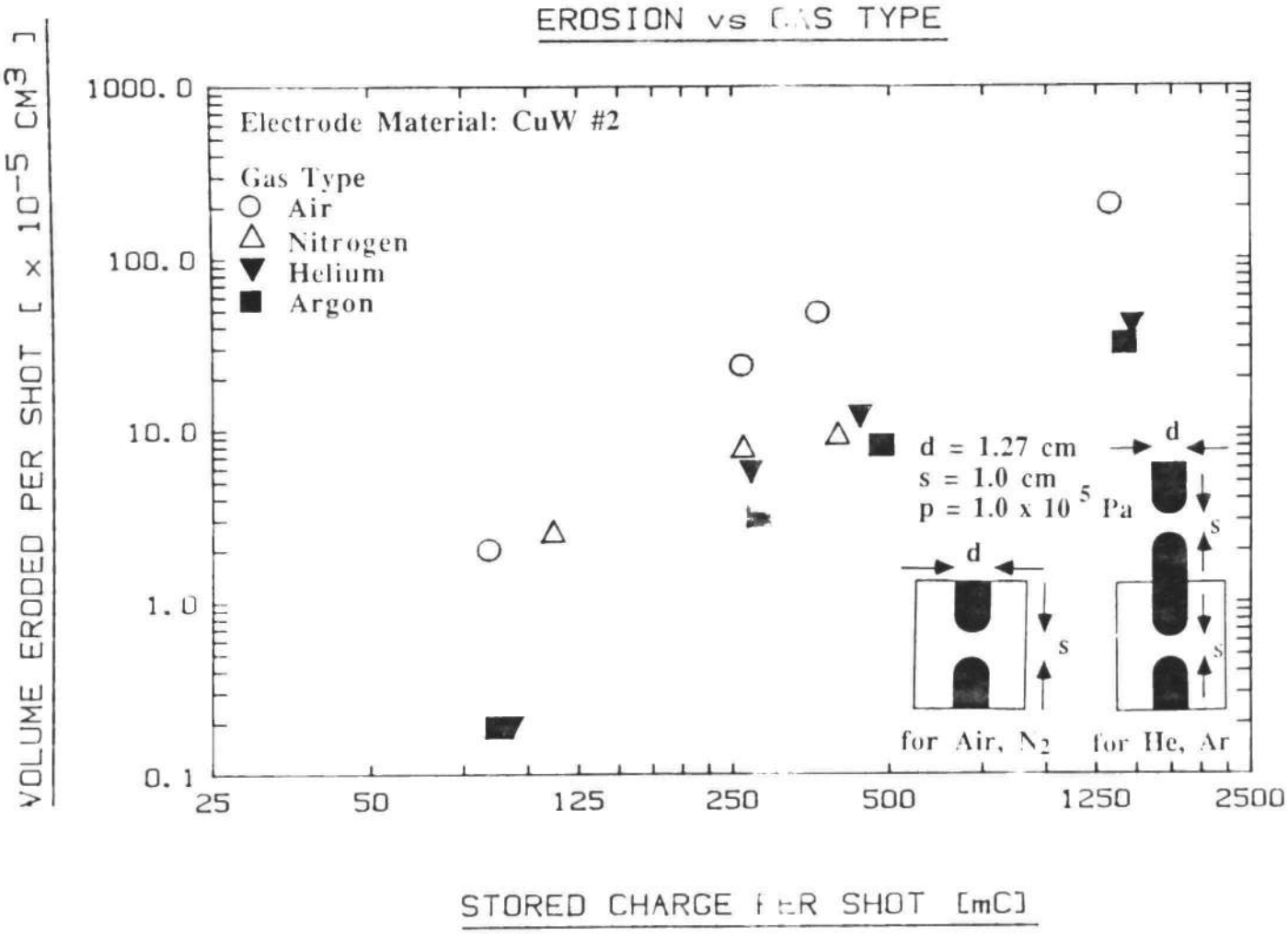

Fig. I.5 CuW#2 Electrode Erosion vs. Gas Type. (Comparing the standard switch erosion in air with the erosion in He, Ar and N_2)

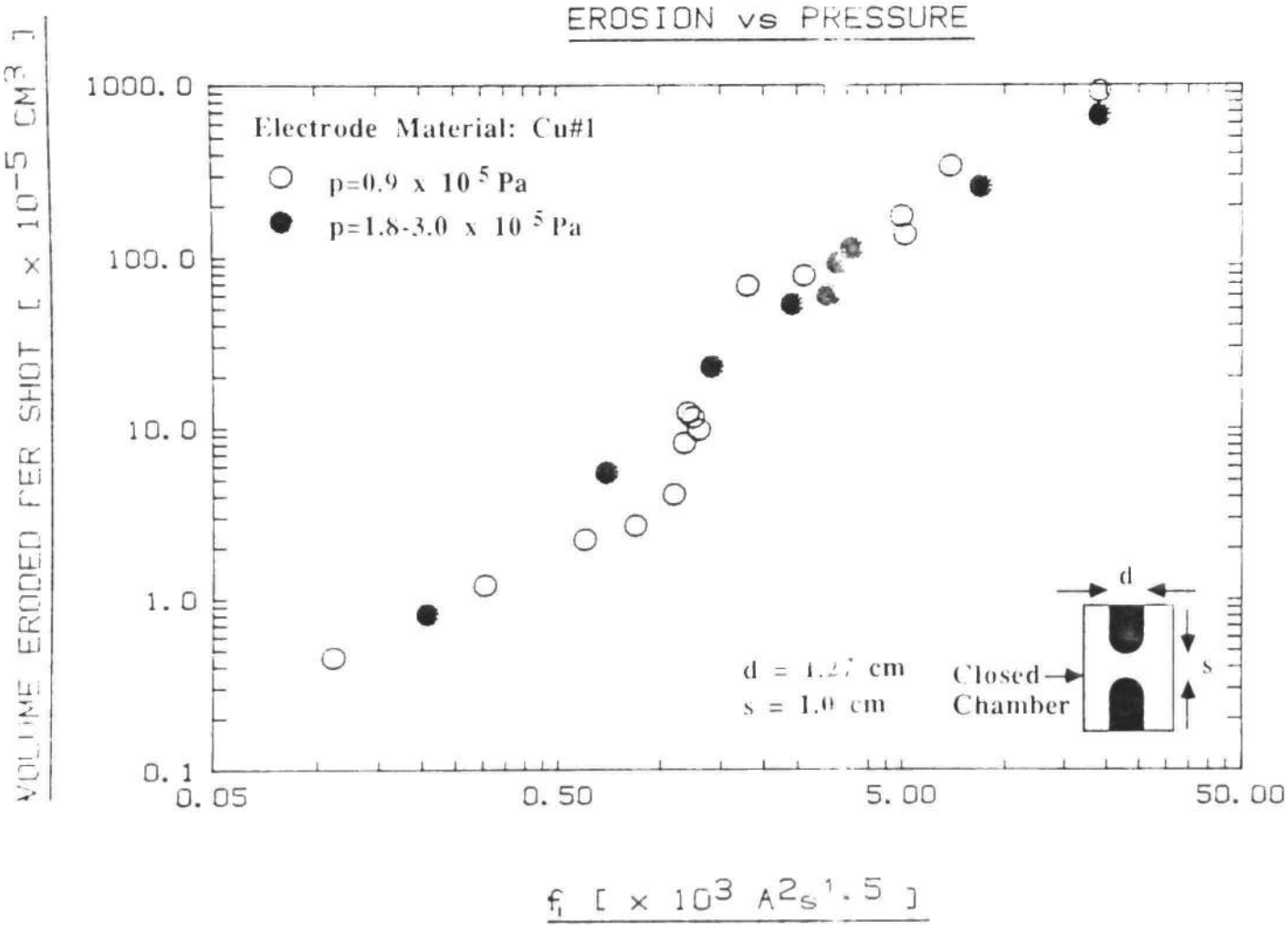

Fig. 1.6 1.27 cm Diameter Cu#1 Electrode Erosion for Two Ditferent Pressures vs. I_1.

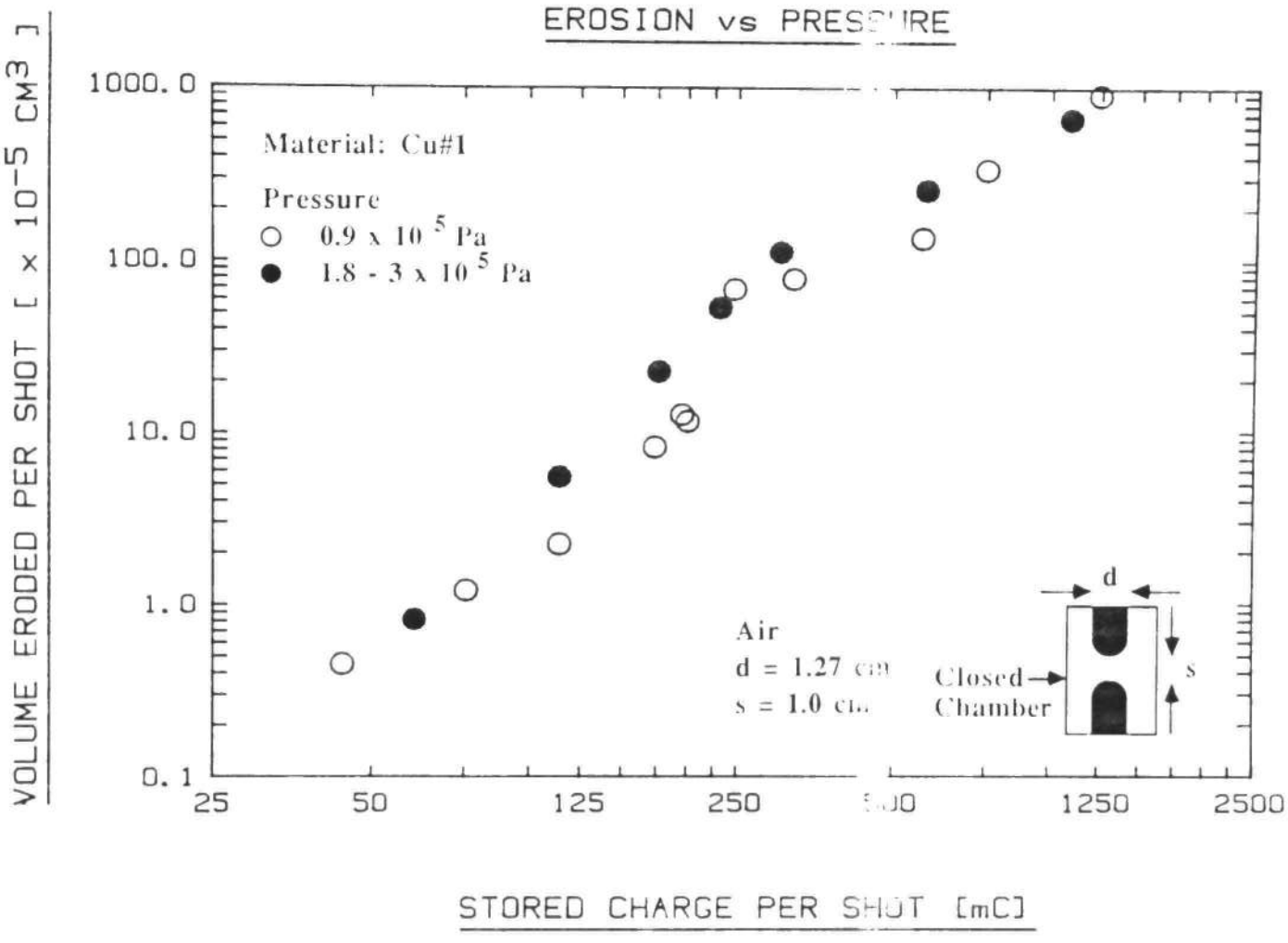

Fig. I.7 1.27 cm Diameter Cu#1 Electrode Erosion for Two Different Pressures vs. Q_S.

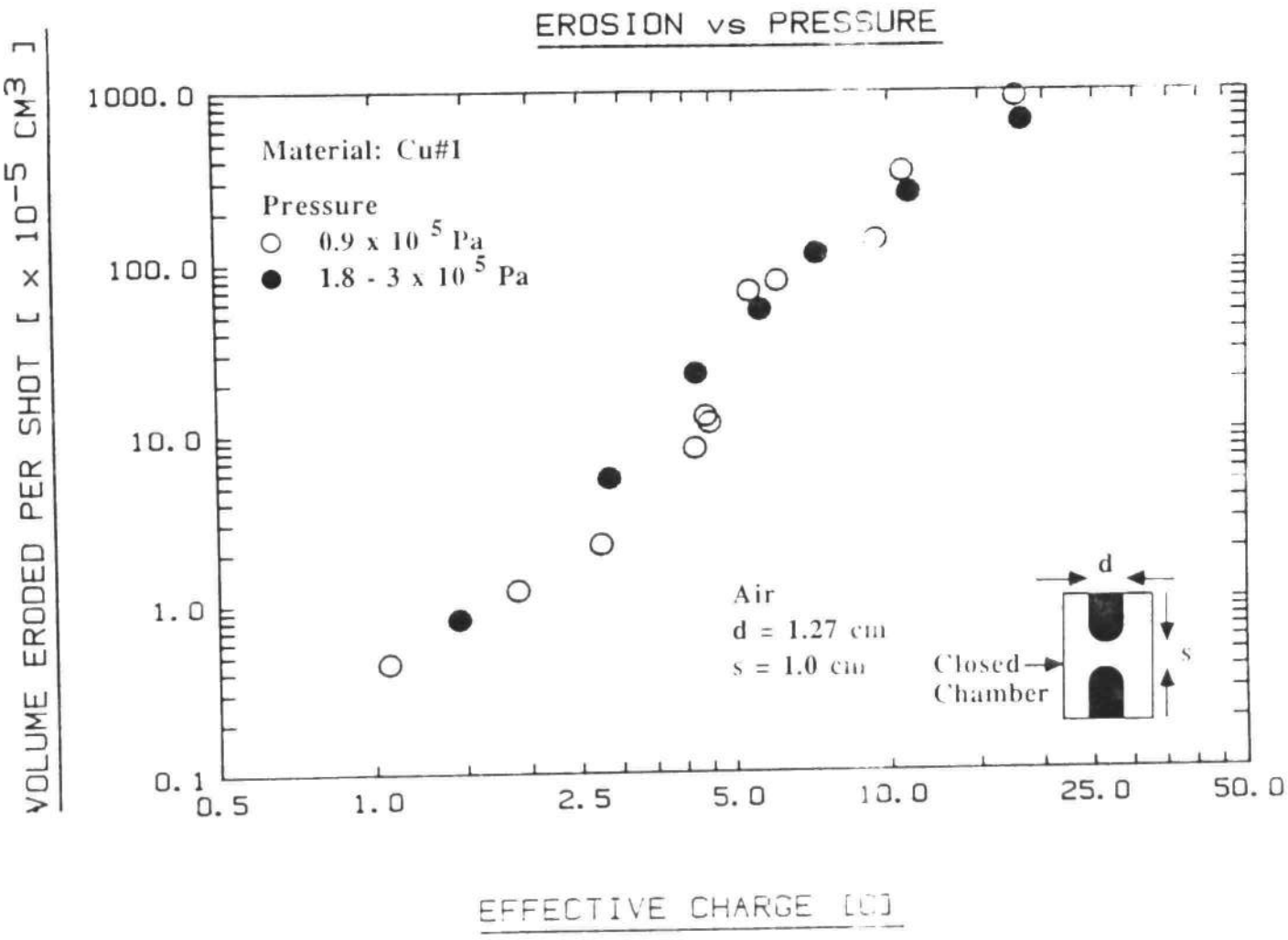

Fig. I.8 1.27 cm Diameter Cu#1 Electrode Erosion for Two Different Pressures vs. Q_e.

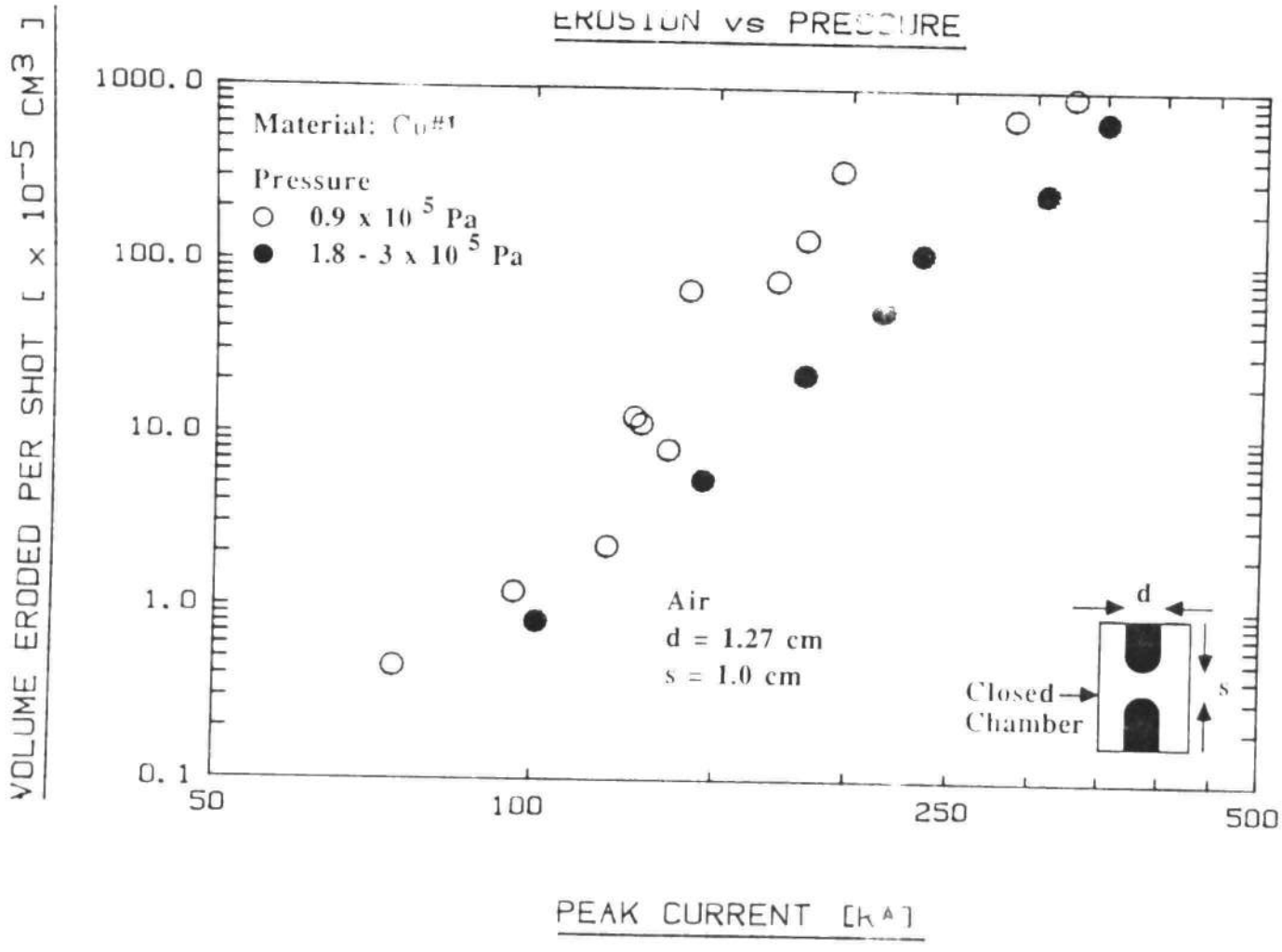

Fig. I.9 1.27 cm Diameter Cu#1 Electrode Erosion for Two Different Pressures vs. I_p.

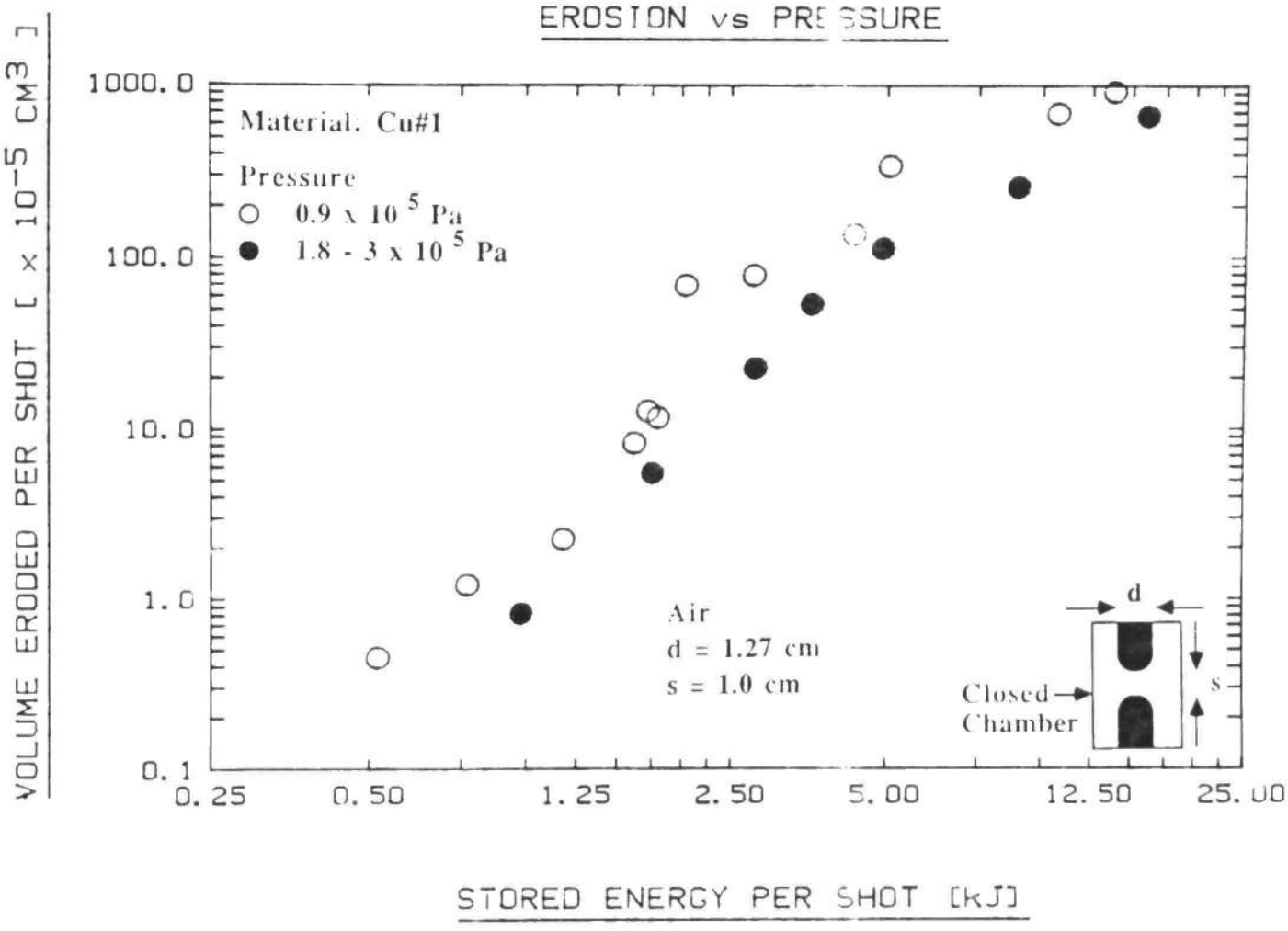

Fig. I.10 1.27 cm Diameter Cu#1 Electrode Erosion for Two Different Pressures vs. E_{ss}.

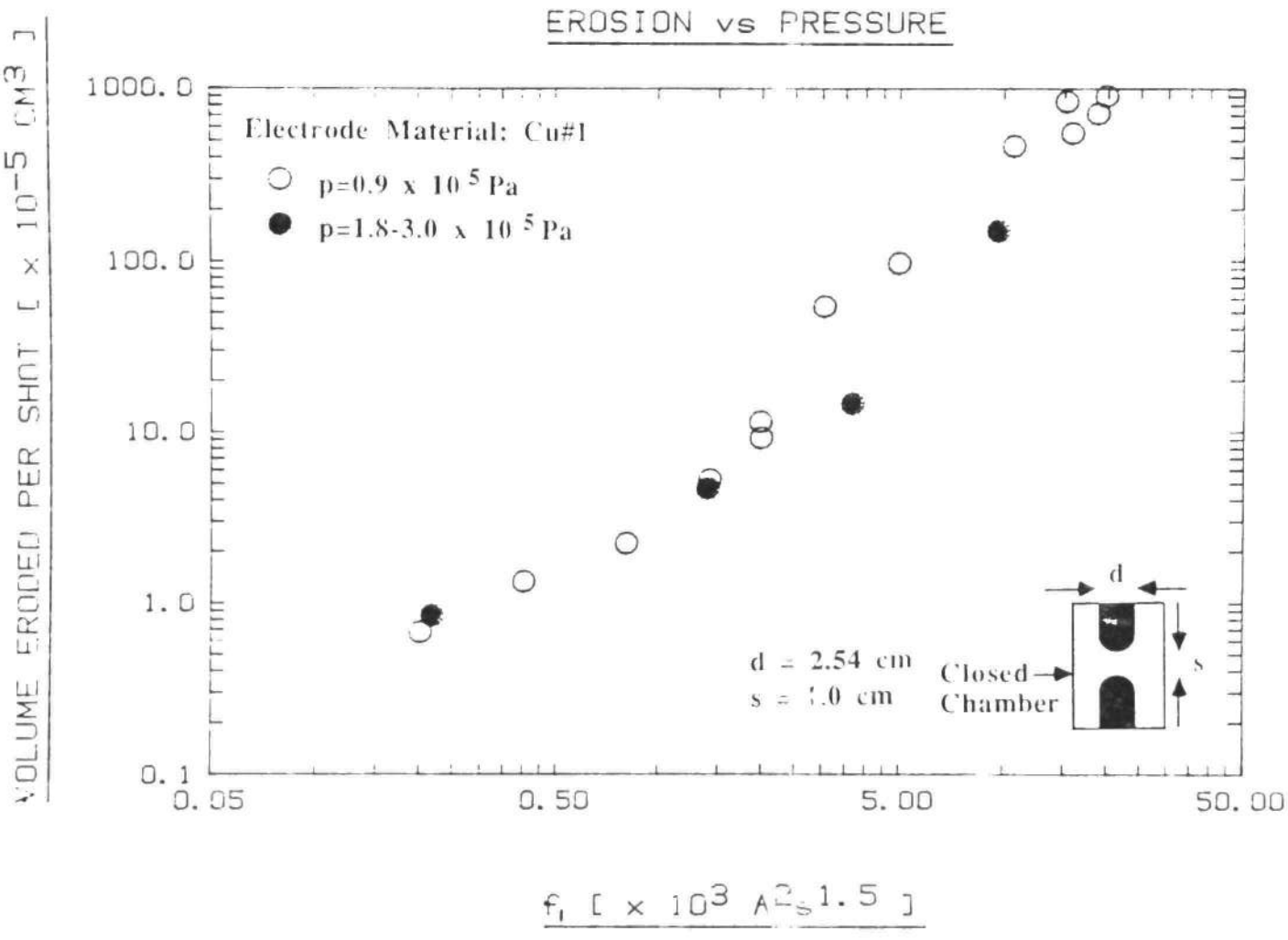

Fig. I.11 2.54 cm Diameter Cu#1 Electrode Erosion for Two Different Pressures vs. f_1.

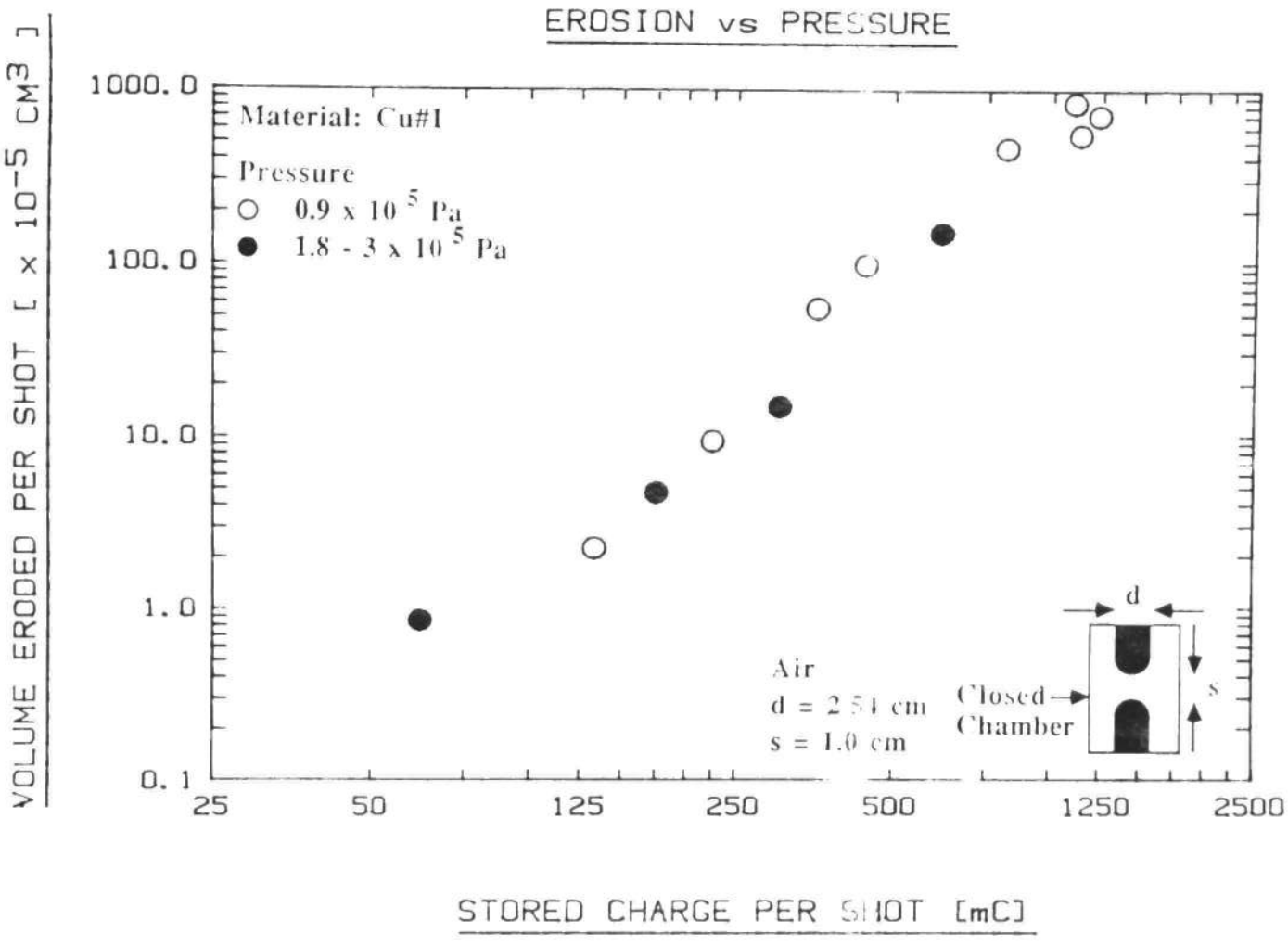

Fig. I.12 2.54 cm Diameter Cu#1 Electrode Erosion for Two Different Pressures vs. Q_s.

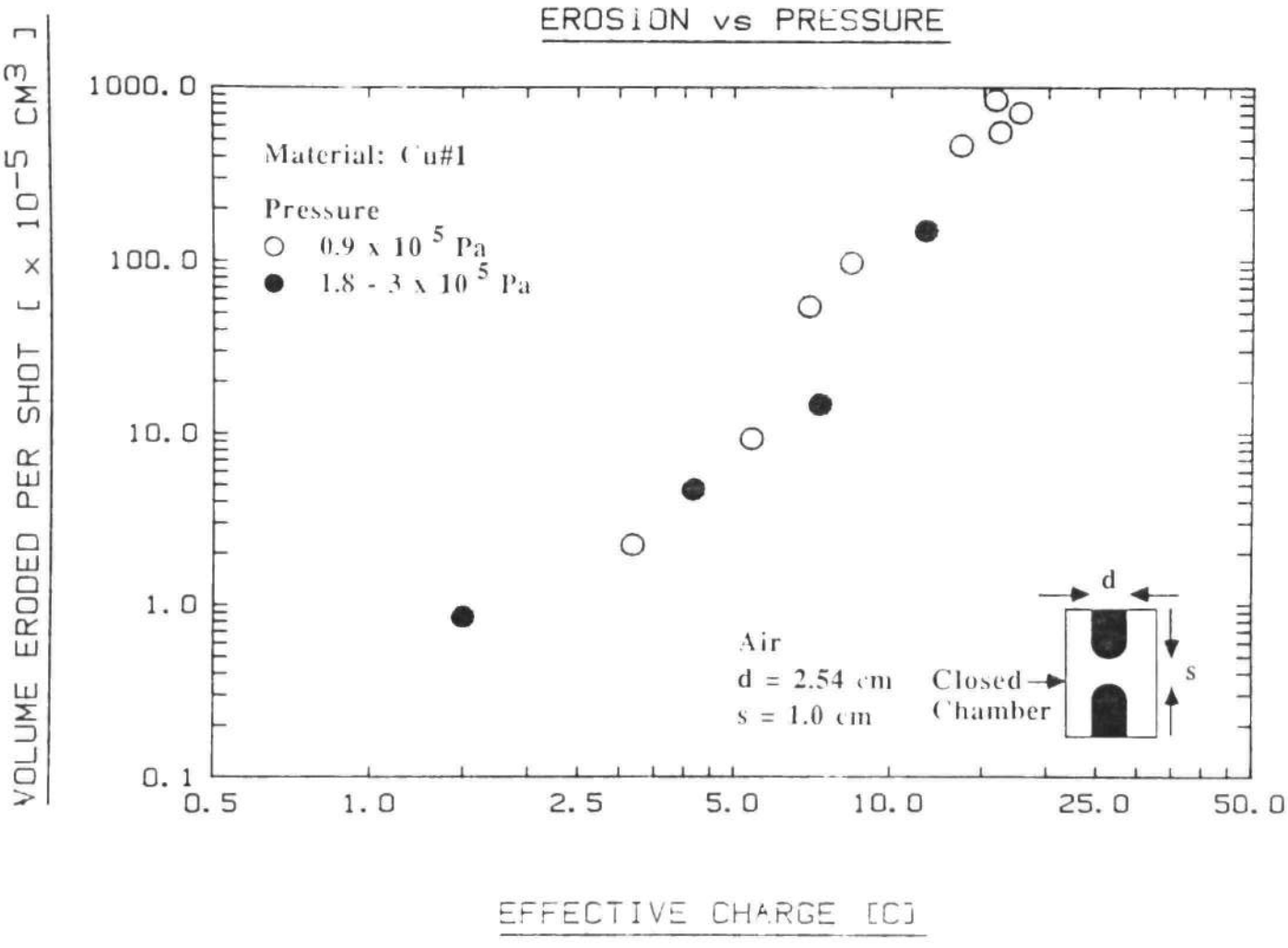

Fig. 1.13 2.54 cm Diameter Cu#1 Electrode Erosion for Two Different Pressures vs. Q_e.

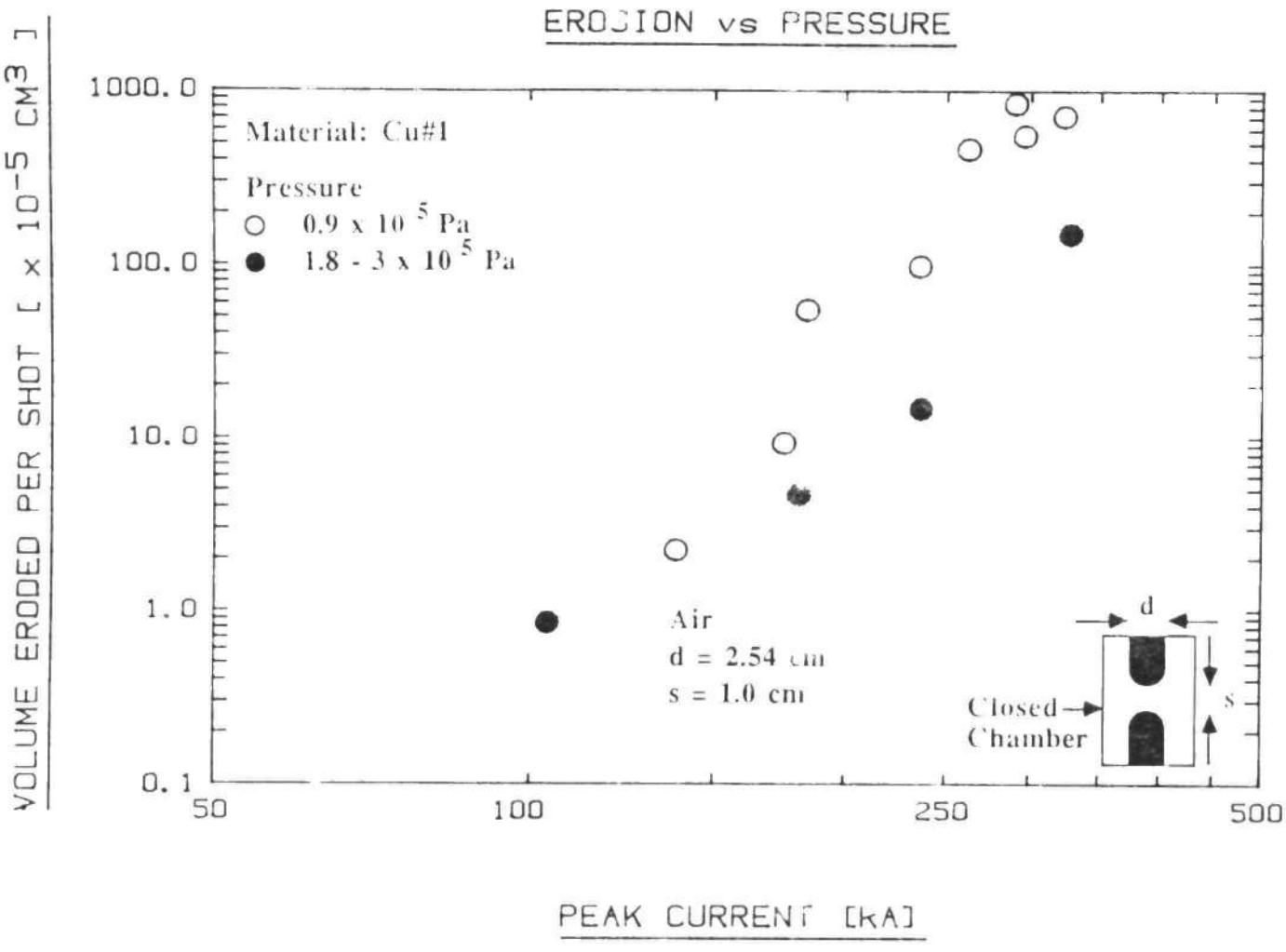

Fig. I.14 2.54 cm Diameter Cu#1 Electrode Erosion for Two Different Pressures vs. I_p.

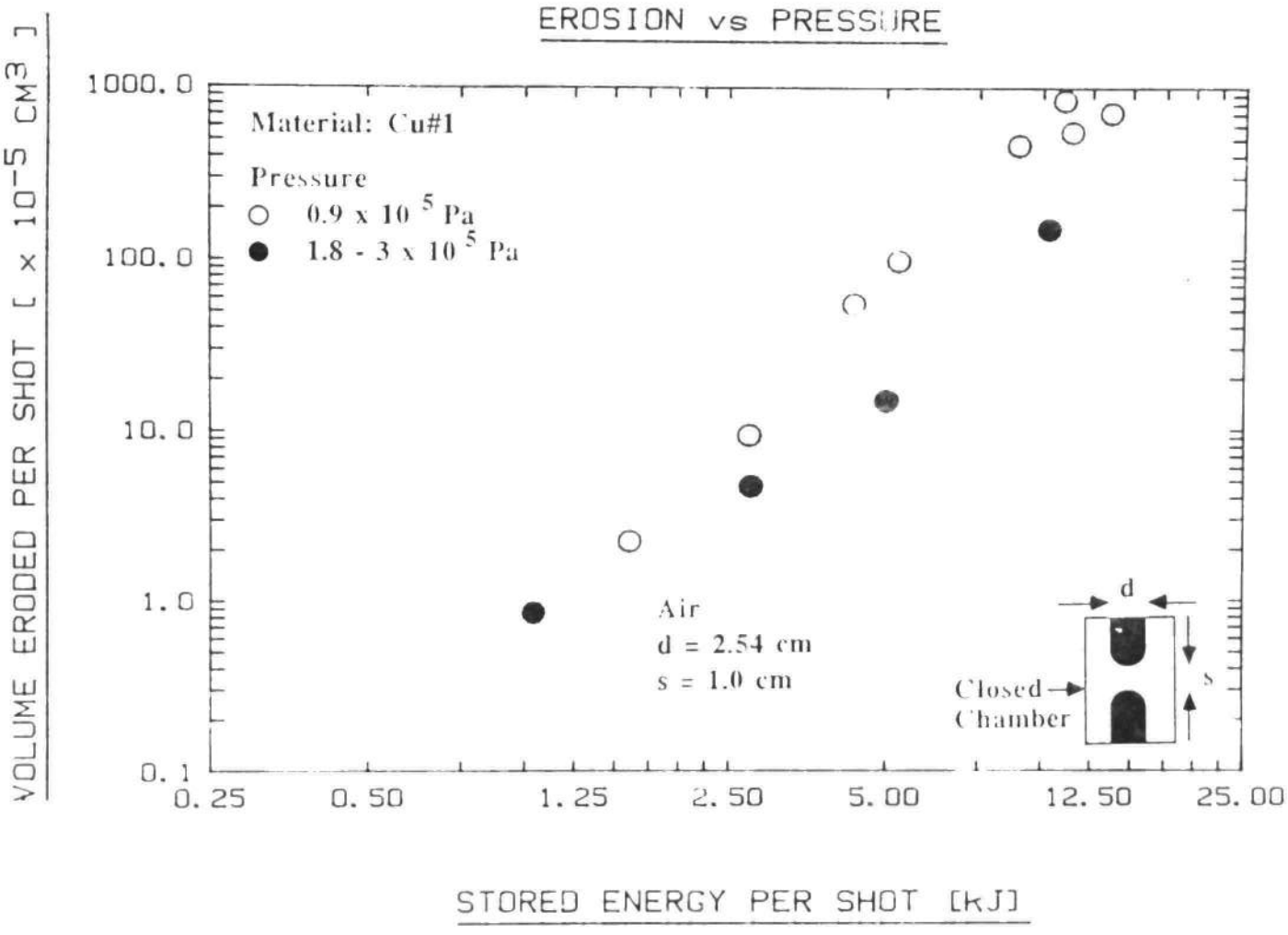

Fig. 1.15 2.54 cm Diameter Cu#1 Electrode Erosion for Two Different Pressures vs. E_s.

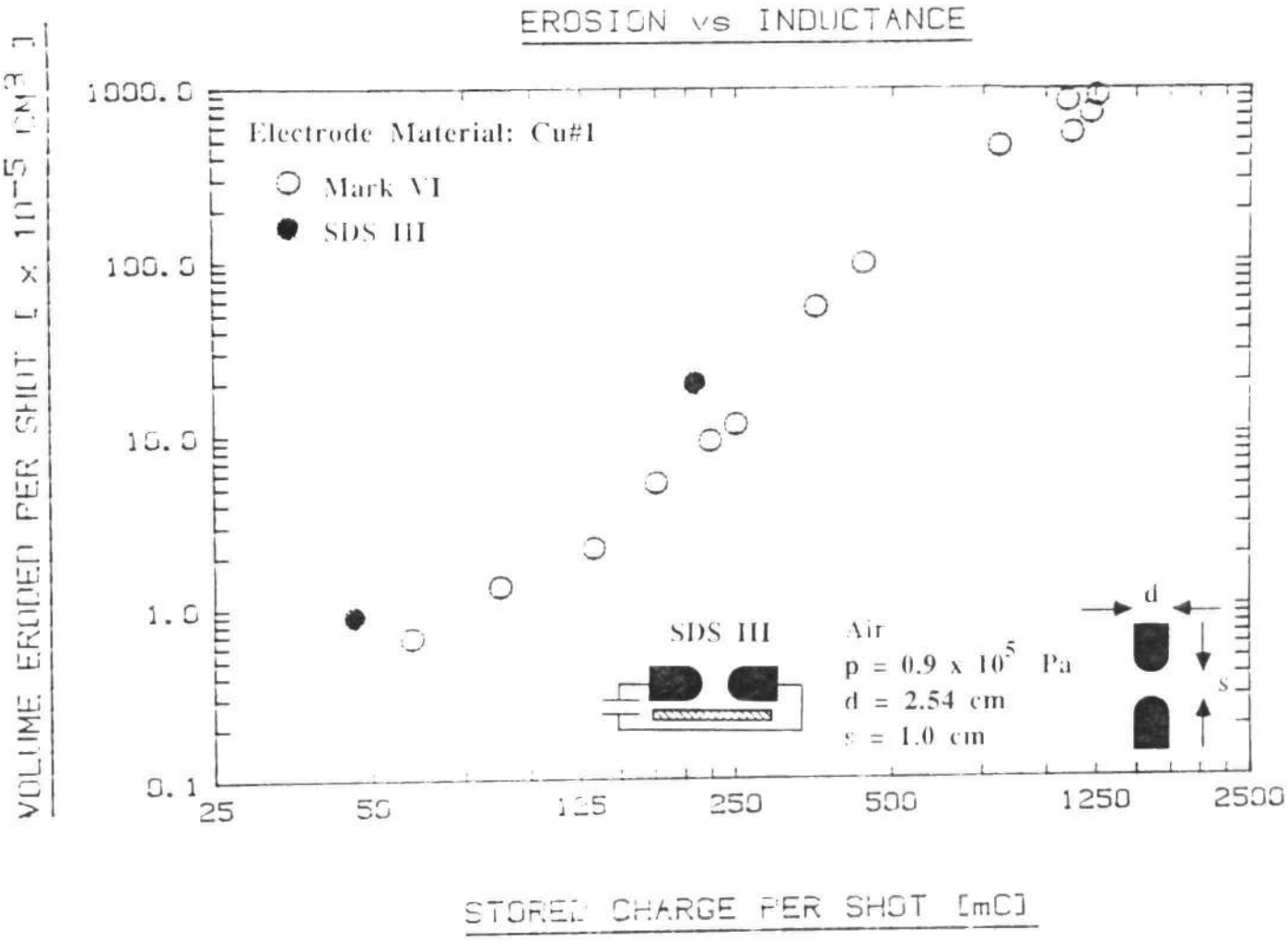

Fig. I.16 Cu#1 Electrode Erosion vs. Inductance (SDS III ~ 100nH, Mark VI ~ 230nH).

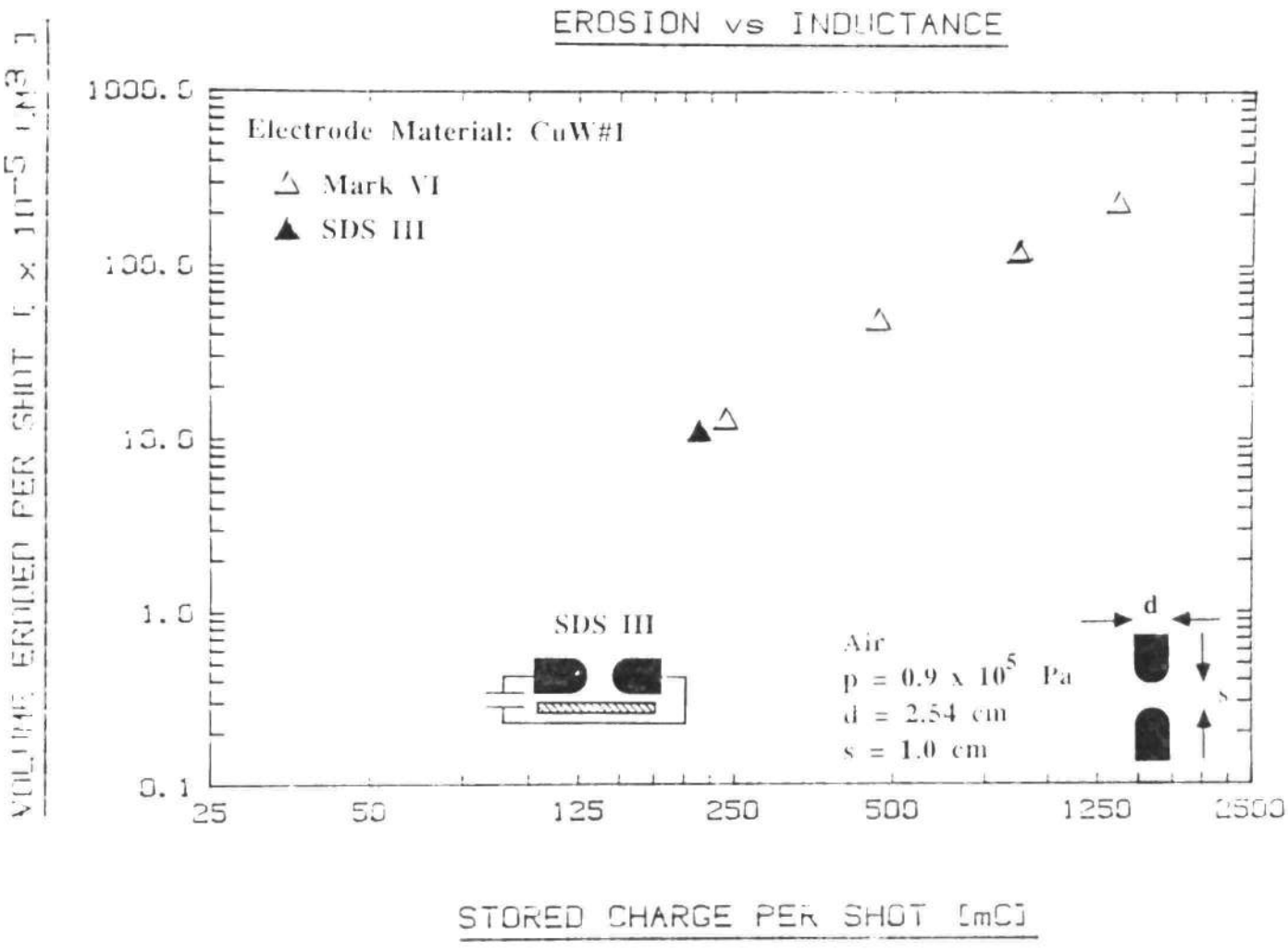

Fig. I.17 CuW#1 Electrode Erosion vs. Inductance (SDS III ~ 100nH, Mark VI ~ 230nH).

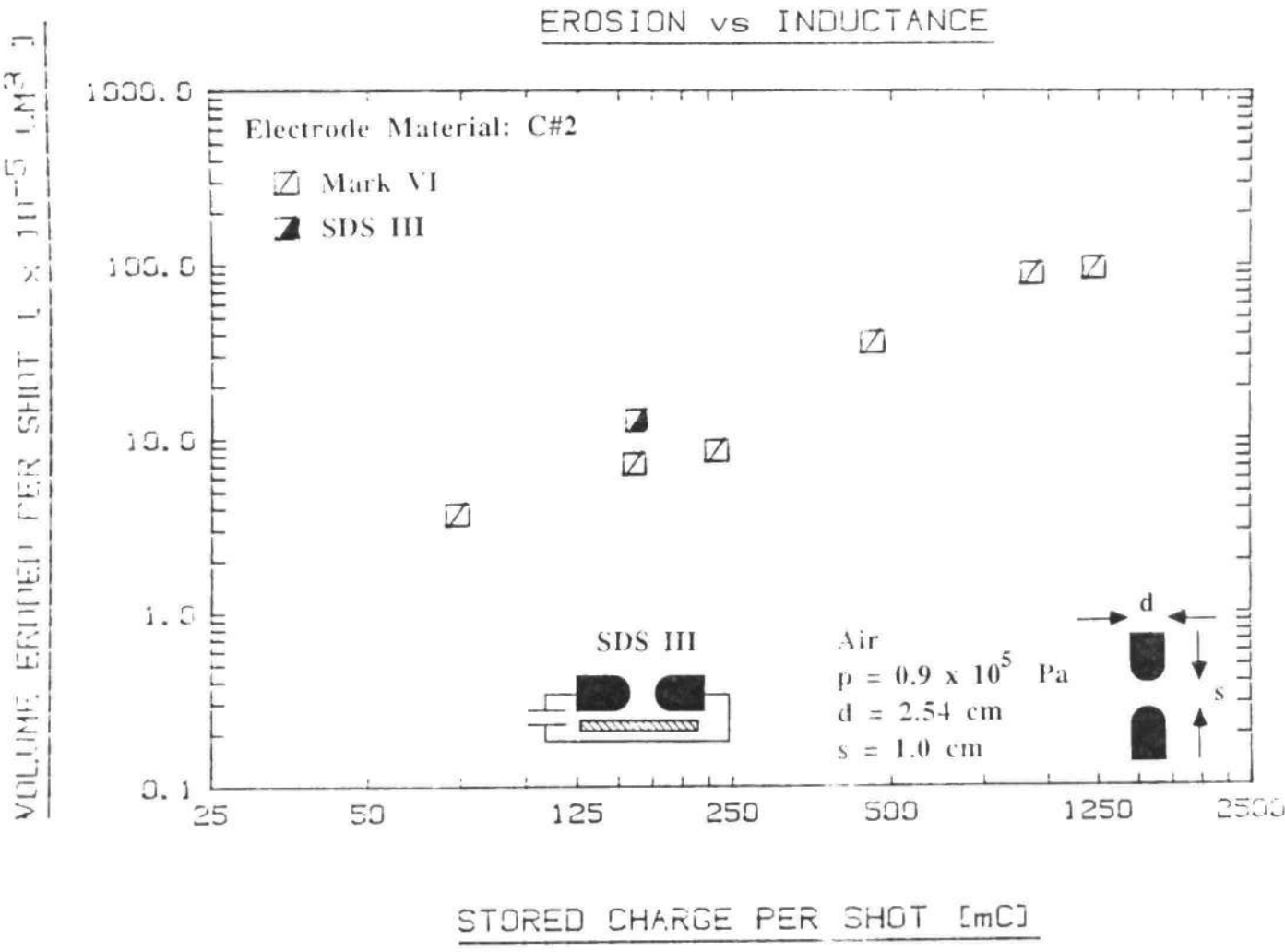

Fig. 1.18 C#2 Electrode Erosion vs. Inductance (SDS III ~ 100nH, Mark VI ~ 230nH).

Reference

[1] G. Engel, "Insulator Degradation by High Current Discharges," Ph.D. Dissertation, Texas Tech University, December 1990.